Structural Geology in Reservoir Characterization

edited by M. P. Coward, T. S. Daltaban and H. Johnson

Structural Geology in
Reservoir Characterization

Geological Society Special Publications

Series Editor A. J. FLEET

Structural Geology in Reservoir Characterization

EDITED BY

M. P. COWARD, T. S. DALTABAN & H. JOHNSON

Royal School of Mines
Imperial College
London
UK

1998

THE GEOLOGICAL SOCIETY

The Society was founded in 1807 as The Geological Society of London and is the oldest geological society in the world. It received its Royal Charter in 1825 for the purpose of 'investigating the mineral structure of the Earth'. The Society is Britain's national society for geology with a membership of around 8000. It has countrywide coverage and approximately 1000 members reside overseas. The Society is responsible for all aspects of the geological sciences including professional matters. The Society has its own publishing house, which produces the Society's international journals, books and maps, and which acts as the European distributor for publications of the American Association of Petroleum Geologists, SEPM and the Geological Society of America.

Fellowship is open to those holding a recognized honours degree in geology or cognate subject and who have at least two years' relevant postgraduate experience, or who have not less than six years' relevant experience in geology or a cognate subject. A Fellow who has not less than five years' relevant postgraduate experience in the practice of geology may apply for validation and, subject to approval, may be able to use the designatory letters C Geol (Chartered Geologist).

Further information about the Society is available from the Membership Manager, The Geological Society, Burlington House, Piccadilly, London W1V 0JU, UK. The Society is a Registered Charity, No. 210161.

The publishers make no representation, express or implied, with regard to the accuracy of the information contained in this book and cannot accept any legal responsibility for any errors or omissions that may be made.

Contents

Preface

This volume is for geologists, geophysicists and reservoir simulation/petroleum engineers studying faulted and fractured reservoirs, particularly those interested in studying petroleum traps, predicting fluid flow or modelling structurally heterogeneous reservoirs.

The two main aims of the volume are to capture the wide range of rapidly expanding research in this area, which reflects the increasing importance of comprehensive 'structural characterization' in static reservoir descriptions, and to help promote synergy between the geosciences and petroleum engineering disciplines. The first aim is addressed by the sixteen papers of the volume, the majority of which cover a range of structural geological features, particularly faulted and fractured reservoirs, fault gouge properties, fault seal potential and fluid flow/simulation modelling in faulted and fractured reservoirs. The papers draw heavily on experience obtained in the North Sea.

The first two papers set the theme of the subject area. The remainder of the book is divided into two parts: faults and fractures (ten papers), and case studies (four papers).

In the introduction, **Cosgrove** reviews the role of structural geology in reservoir characterization and contrasts traditional aspects of structural geology, which focused on the three-dimensional geometry and spatial distribution of structures, with recent trends, which consider the dynamics of structure formation and the interplay of stress and fluid migration.

This is complimented by **Archer**, who provides a broad, petroleum engineering view of reservoir characterization, covering both static description and dynamic modelling aspects, and reviews some of current industry challenges in field development and reservoir management.

The majority of the volume is devoted to various aspects of faults and fractures. **Freeman et al.** present a methodology for predicting fault seal potential, the Gouge Ratio method, which integrates seismically based geometrical data with well-based lithological and compositional information. Application of this method in the Oseberg South field is demonstrated. Experimental aspects of fault plane characteristics are considered by **Crawford**, who quantifies the magnitude of permeability reduction in a series of experiments on artificially-induced shear bands.

Gabrielsen et al. emphasize the importance of evaluating the complete fracture system in subsurface structural reservoir characterization, including the full deformation history, lithology (grain size, composition, bed thickness, etc.), rheological properties and the relationship of the well under investigation to nearby larger structures. The impact of fault geometries on compartmentalization, effective permeability and fluid flow in high porosity sandstones has been assessed by **Manzocchi et al.** in a series of numerical flow simulations. **Gibson** also considers faulted sandstone reservoirs and emphasizes the importance of understanding the nature (e.g. lithology, composition, clay content, etc.) and fluid flow properties (e.g. permeability and capillary displacement pressures) of the sandstone-derived fault zones, of which two main types are highlighted: deformation bands, derived from quartz-rich sandstones, and clay matrix gouge zones, derived from mineralogically immature sandstones. **Walsh et al.** present a range of fault and fault array models, to investigate the impact of variations in fault density, spatial distribution, orientation distribution and fault zone permeability (relative to the bulk permeability of the host rock) on the overall single phase horizontal bulk permeability of a typical North Sea Brent Group reservoir. Results demonstrate that fault densities are much more significant than spatial

and orientational variations, but prediction of fault zone hydraulic properties is a crucial uncertainty in all these, and similar, modelling studies. One approach to improving the description of fault-related heterogeneities in reservoirs is to use seismic anisotropy, as pointed-out by **Owen** *et al.*, who demonstrate its value in predicting fault aggregate alignments and cluster distribution. **Foley** *et al.* consider numerical fluid flow modelling techniques in faulted reservoirs, noting limitations in many modelling programs, and conclude that the Boundary-Fitted Co-ordinate Technique allows for more realistic fault geometries to be modelled. Reiterating previous conclusions, they emphasize the importance of information on fault zone characteristics to enable confident predictions of permeability distribution in faulted reservoirs. The curvature analysis of gridded surfaces, particularly those generated from 3D seismic data, offers a means of predicting fracture distribution according to **Stewart & Podolski.** They argue that the sum of the absolute values of principal curvature reflects the spatial variance in strain, and hence to fracture density, and that these data could form an inexpensively-derived surface attribute of horizons mapped on 3D seismic data. **Couples** *et al.* emphasize the importance of strain partitioning during flexural (bedding plane) slip folding. They note that most petroleum reservoirs are created by fracture networks related to flexural deformation and that fracture characteristics reflect structural position within the fold.

The final part of the volume is devoted to four case studies, where some of the previously discussed concepts are applied to a range of different structural settings. **Younes** *et al.* evaluate fracture development and its preservation in complexly faulted basement blocks in the Gulf of Suez, Egypt. Outcrop and sub-surface examples are discussed, the latter using high-resolution FMS and FMI image logs for fracture detection, and variations in fracture development noted as follows: (1) enhanced fracture density resulted from sheeting, faulting and dyke emplacement, and (2) reduced fracture density occurs as depth of erosion of basement blocks increases. **Lonergan** *et al.* note the presence of pervasive polygonal extensional fault networks in Tertiary mud-dominated slope and basin floor depositional systems in the North Sea. Based on the detailed analysis of 3D seismic data they conclude that these types of faults formed during sedimentation and early burial and may be important conduits for fluid migration, both compaction/dewatering and secondary petroleum migration.

Both 3D seismic data and a continuous, 120 m long oriented core have been used by **Aarland & Skjerven** to characterize a major normal fault in the Brage field (Northern North Sea), which highlights the heterogeneous nature of the fault zone and variations in fracture density. This may have implications for other rift-related fault blocks in the North Sea and elsewhere.

Finally, **Fossen & Hesthammer** present an integrated structural geological analysis of one of the Northern North Sea's most complexly deformed rotated fault blocks, which contains the giant Gullfaks oil field. Most of the shear deformation is thought to have occurred by strain-dependent grain reorganization in the poorly consolidated Jurassic sediments, which resulted in reduced porosity. Forward modelling studies and detailed evaluation of the field's various structurally defined subareas are fully described.

This volume arose from the meeting of the Petroleum Group of the Geological Society on 'Structural Geology in Reservoir Characterization' which was held in March 1995 at Imperial College, London. We thank all the contributors to the meeting for stimulating this volume, and the authors and referees who brought it to fruition.

Michael Coward, Sezgin Daltaban and Howard Johnson
July 1997

The role of structural geology in reservoir characterization

J. W. COSGROVE

*Department of Geology, Imperial College of Science, Technology and Medicine,
London SW7 2BP, UK*

Abstract: In this brief review of the role of structural geology in reservoir characterization a comparison is made between the original role of structural geology, which focused on the three-dimensional geometry and spatial organization of structures and which involved a statistical treatment of the spatial arrangement of structures such as faults and folds and on static analyses, and the more recent trend in structural geology which is concerned with the dynamics of structure formation and the associated interplay of stress and fluid migration.

Traditionally the role of structural geology in the location and definition of hydrocarbon reservoirs has been to define the geometry and spatial organization of structures such as folds and fractures. Field observations, theoretical analyses and analogue modelling of these various structures has led to a sound understanding of their likely three-dimensional geometry and their spatial relationships. For example field observations and analogue modelling of buckle folds has shown that these structures have a periclinal geometry, i.e. have the form of an elongate dome, basin or saddle, and that this geometry is characteristic of buckle folds on all scales. Figure 1 shows three examples which illustrate this point. The folds range in scale between folds with a wavelength of less than a centimetre to folds with wavelengths in excess of 10 km.

It is clear from Fig. 1a that in plan view the folds are arranged statistically in an en echelon manner. Analogue modelling (e.g. Dubey & Cobbold 1977; Blay *et al.* 1977) has shown how this pattern of distribution emerges as the folds are initiated and amplify into finite structures. Initially isolated folds form and as deformation continues these amplify and extend along their hinges. As they do so they may approach other folds. The way in which they interact is found to depend on the separation between the hinges of the two folds (Fig. 2). If the hinges of two interfering folds are off-set but the amount of off-set is only a small fraction of the wavelength, the folds link to form a larger fold with a deflection in the hinge line (Fig. 2a). Experimental observations also show that if the hinges of two folds are separated by more than about half their maximum wavelength but are still close enough to interact, they lock up, each preventing further propagation of the other, so that they become arranged in an en echelon fashion (Fig. 2b).

In the above discussion the linking and blocking of individual folds is considered. However, as an individual fold amplifies, it may cause the initiation of other folds on either side and so begin the formation of a wave-train. The work of Dubey & Cobbold (1977) has shown that as adjacent wave-trains propagate, they too may interact with each other by the process of 'linking' or 'blocking' depending on the relative wavelengths and positions of the two trains. Some of the different ways in which they can interact are shown in Fig. 3. It can be seen that linking of folds from two fold-trains can also give rise to structures which, in plan view, have deflections in their hinges (Fig. 3c(ii)). Alternatively folds may bifurcate (Figs 3c(iii) & d(ii)).

As well as having a limited extent along their hinges, folds often die out relatively rapidly in profile section. A typical profile section through a fold in a multilayer is shown in Fig. 4a. The random initiation of folds within a multilayer would give rise to the type of fold distribution shown in Fig. 4e. It can be seen therefore that the folds are arranged in an en echelon manner both in plan view and in plan. For an extended discussion of this the reader is referred to Price & Cosgrove (1990).

Exactly the same spatial arrangement can be found for faults. For example normal faults are often arranged in an en echelon manner in both profile and plan view and considerable work is at present being carried out in an attempt to understand the stress distribution and fracture patterns likely to develop in the relay zones between these overlapping fractures.

It can be seen from the above discussion that the shortening along any line normal to the fold hinges or the extension along any line normal to the strike of the faults will be constant regardless of where the line is drawn, but the exact location of the individual folds or faults along any particular line cannot be determined.

Although an understanding of the three-dimensional geometry and spatial organization

(a)
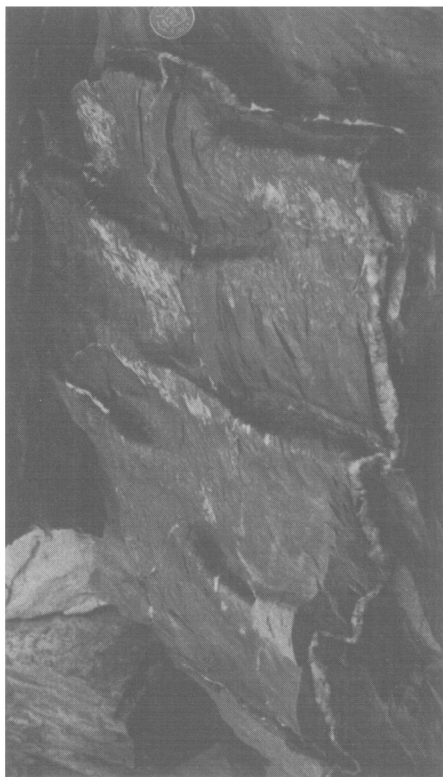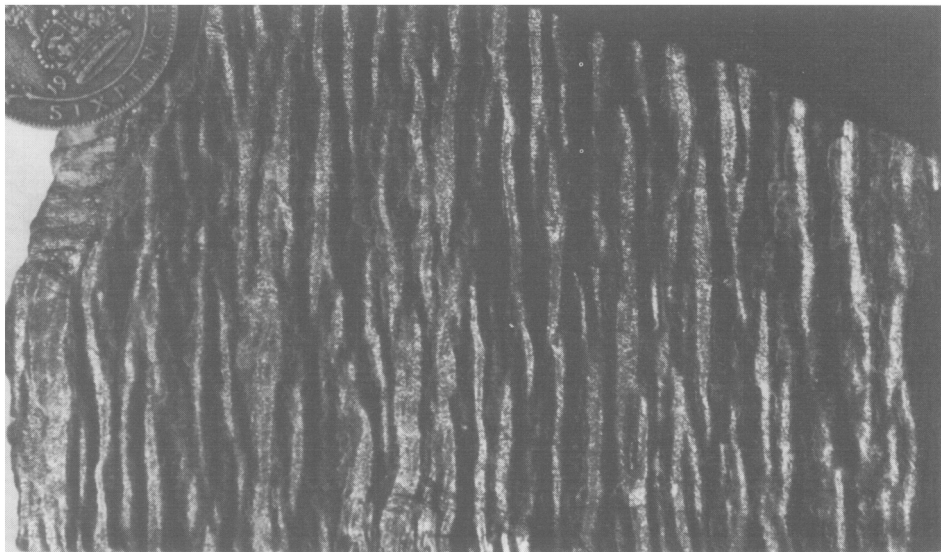
(b)
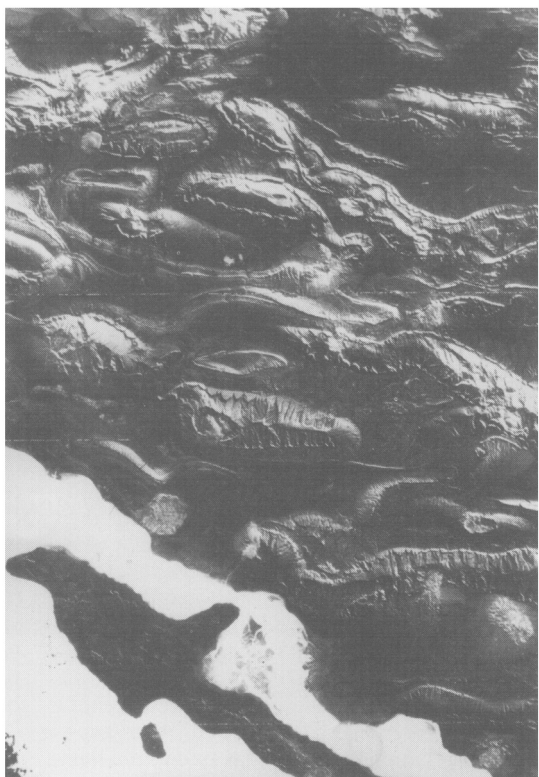
(c)

Fig. 1. Three examples of folds displaying periclinal geometry and an en echelon spatial organization. (**a**) A crenulated mica schist from the Lukmanier Pass, Switzerland. Coin 1 cm. (**b**) En echelon periclines in a folded metasediment near Luarca, North Spain. Coin 2 cm. (**c**) Large periclinal folds in the Zargros mountains. The pericline in the centre of the image is 20 km long.
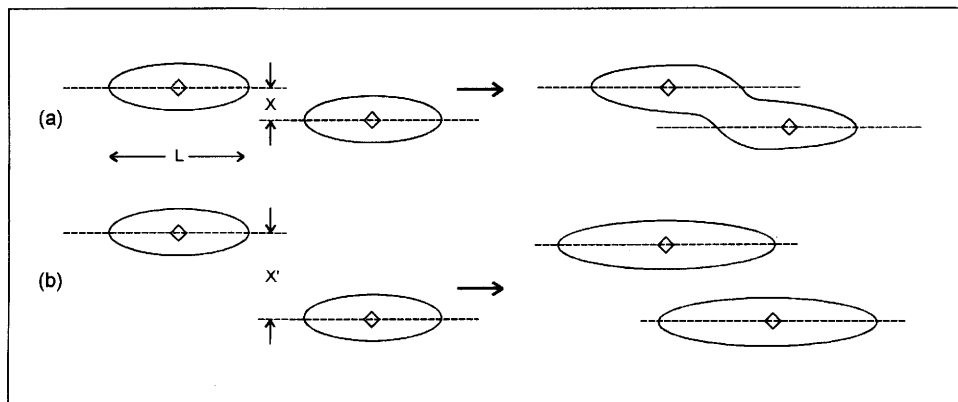
Fig. 2. (a) The amplification and coalescence of two periclines (shown in plan) separated by a distance X which is somewhat less than half the wavelength of the structure. **(b)** Two periclines separated by X' which is greater than half the wavelength. The structures overlap and lock up, each preventing further propagation of the other.

of folds and faults has proved extremely useful in the location of potential reservoirs, it does not provide any insight into the possible fluid migration paths that may have operated during the initiation and amplification of these structures. More recent studies (e.g. Sibson 1990; Sibson *et al.* 1975, 1988; Cosgrove 1993) have been concerned with dynamics of deformation and the interplay of deformation, stress and fluid flow.

In the following section, brittle failure and hydraulic fracturing are briefly considered together with the stress fields that generate them in order to illustrate this approach and show its possible relevance to the migration and concentration of hydrocarbons.

The discussion is then extended to include the links between brittle structures and fluid flow and ductile structures and fluid flow.

Brittle failure and hydraulic fracturing

In this section the geological expression of hydraulic fracturing is considered with particular reference to fracturing of a sedimentary succession during burial and diagenesis. The theory of brittle failure and hydraulic fracturing is discussed in most structural texts (e.g. Price 1966; Phillips 1972; Price & Cosgrove 1990), to which the reader is referred, and only a brief summary of these concepts relevant to the ideas discussed in this paper are presented here.

Figure 5a is a summary diagram showing the failure envelope for brittle failure. This is determined in part by the Navier–Coulomb criteria for shear failure and in part by the Griffith criteria of extensional failure. Figure 5b and c show extensional fractures and shear fractures respectively, and the principal stresses with which they are associated. These stress states are represented as Mohr circles on Fig. 5a where it is clear that in order for shear failure to occur the Mohr circle must be sufficiently large to touch the shear failure envelope. It follows from the geometry of the failure envelope that this can only occur if the diameter of the Mohr circle (i.e. the differential stress $\sigma_1 - \sigma_3$) is greater than four times the tensile strength of the rock (T). It also follows from the geometry of the failure envelope that the angle 2θ between the normal stress axis and the line joining the centre of the Mohr circle to the point A where it touches the failure envelope, is the angle between the two conjugate shear fractures (Fig. 5c). For extensional failure to occur the Mohr circle must touch the failure envelope at point B. This can only occur if the differential stress is less than four times the tensile strength of the rock.

Thus the type of brittle failure indicates whether the differential stress during fracturing was greater or less than $4T$. Occasionally it is clear that both extensional and shear failure occurred together during a single deformation event. An example where this has occurred is illustrated in Fig. 6, which shows a line drawing of incipient boudinage in a relatively thick sandstone layer in the Carboniferous turbidites at Millook, north Cornwall. The individual boudins are separated from each other by quartz veins; some of these are single extensional veins which cut completely across the layer and are an expression of extensional failure; others
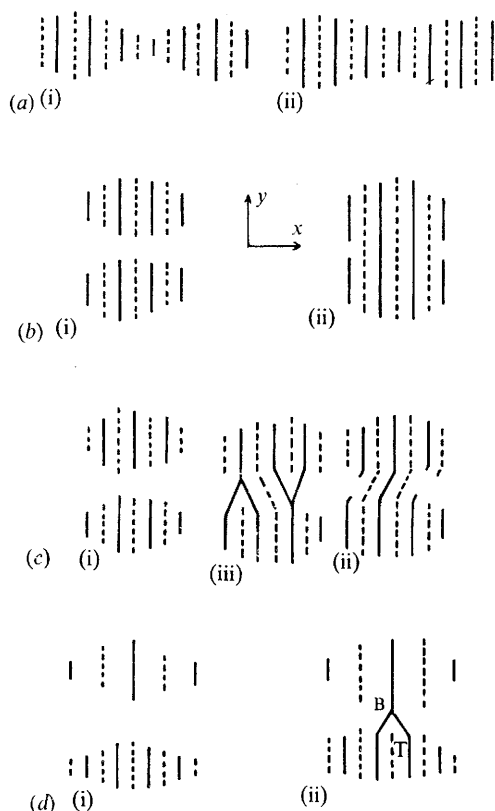
Fig. 3. Simplified plan view illustration of the interference between two fold complexes of different phase and wavelength. The continuous and broken lines represent anticlinal and synclinal axes respectively. (**a**) (i) Wave-trains in phase approaching along *z* resulting in direct linking along *z* (ii). (**b**) (i) Wave-trains in phase approaching along *y* resulting in direct linking along *y* (ii). (**c**) (i) Wave-train out of phase approaching along *y* resulting in oblique linking (ii) and fold bifurcation (iii). (**d**) (i) Wave-trains of different wavelengths approaching along *y* resulting in fold bifurcation, B (ii), and blocking, producing steeply plunging terminations, T (after Dubey & Cobbold 1977).

form part of an en echelon array and are a manifestation of shear failure. It can be concluded therefore that the differential stress during boudin formation was around four times the tensile strength of the sandstone at that time.

It is interesting to note that the boudin necks defined by shear failure and extensional failure zones are both made up of tensile fractures and that the only difference between the two is the spatial organization of these fractures. In general, in a rock undergoing extensional failure, the individual tensile fractures, although aligned, are randomly distributed whereas during shear failure they are organized in such a way as to define either one or a conjugate pair of en echelon extension fractures (see Kidan & Cosgrove 1996).

The orientation of extensional fractures

The stress states represented by the Mohr circles shown in Fig. 7a all have a differential stress less than $4T$ and because they all touch the failure envelope they will all generate extensional failure. The differential stresses vary between just less than $4T$ (circle i, Fig. 7a) and zero (circle iv, Fig. 7a). When $\sigma_1 - \sigma_3$ is zero the stress state is hydrostatic and the Mohr circle collapses to a point.

The relationship between extensional fractures and the principal stresses generating them is shown in Fig. 7b (e.g. Anderson 1951; Price 1966). These fractures form parallel to the maximum principal compression σ_1 and open against the least principal compression σ_3. In the stress state represented by Mohr circle i (Fig. 7a), which has a relatively large differential stress, there is a definite direction of easy opening for the tensile fractures, i.e. parallel to σ_3. Thus the fractures that form will have a marked alignment normal to this direction (Fig. 7b(i)). However, the differential stress for the stress states represented by the Mohr circles ii–iv becomes progressively smaller until, for the hydrostatic stress represented by the Mohr circle iv, the differential stress is zero. In a hydrostatic stress field the normal stress acting across all planes is the same and therefore it is equally easy to open fractures in all directions. Thus the fractures will show no preferred orientation and if they form sufficiently close to each other they will generate a breccia texture (Fig. 7b(iv)). It can be argued therefore that as the differential stress becomes progressively lower the tendency for the extension fractures to be aligned will become less and less (Cosgrove 1995).

Hydraulic fracturing

The state of stress in the Earth's crust tends to be compressional and true tensile stresses are thought to be uncommon. This will be particularly true for the stress states in a sedimentary pile undergoing burial and diagenesis in a tectonically relaxed basin. Nevertheless extensional fractures occur commonly and this
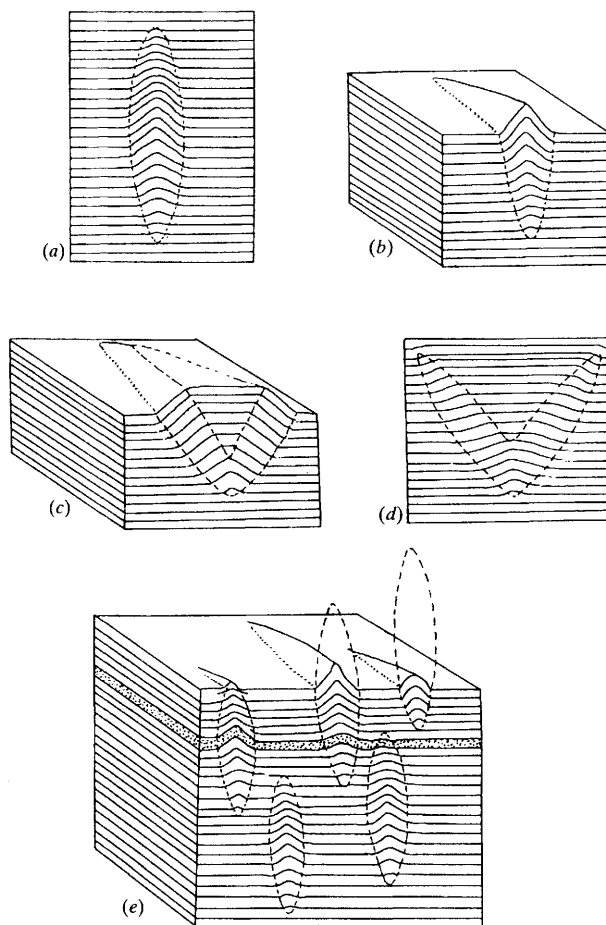
Fig. 4. Typical three-dimensional geometry and spatial organization of multilayer folds.

apparent contradiction has been satisfactorily explained by arguing that failure occurs by hydraulic fracturing (e.g. Phillips 1972). It is argued that the internal fluid pressure in the sediment or rock acts so as to oppose the applied stresses and that the rocks respond to the effective stresses $\sigma_1 - p$, $\sigma_2 - p$, $\sigma_3 - p$, where p is the fluid pressure. Thus a state of lithostatic stress in a rock will be modified by the fluid pressure to an effective stress state $\sigma_1 - p$ and $\sigma_3 - p$ and the Mohr circle will be moved to the left by an amount equal to the fluid pressure. The three stress states represented by the solid Mohr circles shown in Fig. 8 are all stable stress fields in that they do not touch the failure envelope and therefore will not cause failure. However, all three circles can be driven to the left by a fluid pressure until they intersect the failure envelope, when hydraulic fracturing will

occur. It can be seen that stress state i will cause shear failure, stress state ii will cause aligned extensional failure and stress state iii will cause brecciation of the rock by the formation of an almost random array of extension fractures.

It is a common misconception that the result of hydraulic fracturing in sediments and rocks is the formation of randomly oriented extension fractures and the generation of breccia textures (Fig. 7b(iv)). It is clear from the above discussion that the expression of hydraulic fracturing can vary, ranging from randomly oriented extensional fractures through aligned extensional fractures to shear fractures.

Having briefly considered brittle failure, the relationship between stress and fractures and the process of hydraulic fracturing, we can proceed to consider the factors that affect the state
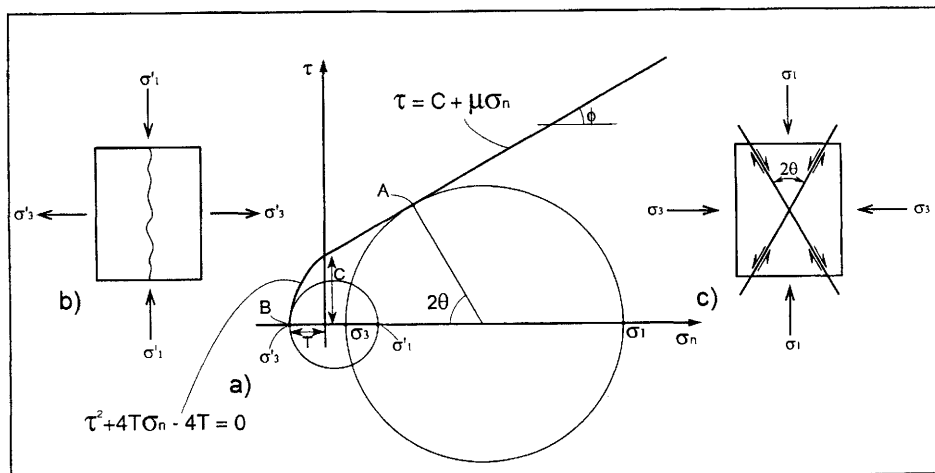
Fig. 5. (a) The Navier–Coulomb/Griffith brittle failure envelope. The two Mohr circles represent stress states that would give rise to extensional failure (the smaller circle) and shear failure. (b) and (c) show the relationship between the principal stresses and extensional failure and shear failure planes respectively.

of stress in a sedimentary succession and the type and orientation of the hydraulic fractures that might develop in them.

Stress variation with depth

In this section the state of stress in sediments being buried in a basin is briefly considered in order to predict the type and orientation of hydraulic fractures that might form. The stress state will depend on the material properties of the sediment or rock and upon the boundary conditions. Consider the relatively simple boundary conditions which affect sediments in a tectonically relaxed basin, i.e. one in which

the main source of stress is due to the overburden. If the boundary conditions are such that horizontal strains are prevented by the constraints of the rock mass surrounding the area of interest, then it can be shown (e.g. Price 1966) that the vertical and horizontal stresses are related as follows:

$$\sigma_H = \sigma_V/(m - 1) \tag{1}$$

where m is Poisson's number, the reciprocal of Poisson's ratio. The vertical stress will be σ_1 and its magnitude given by:

$$\sigma_V = \sigma_1 = z\rho g \tag{2}$$

where z is the depth, ρ the average density of the overlying rocks and g the acceleration due to
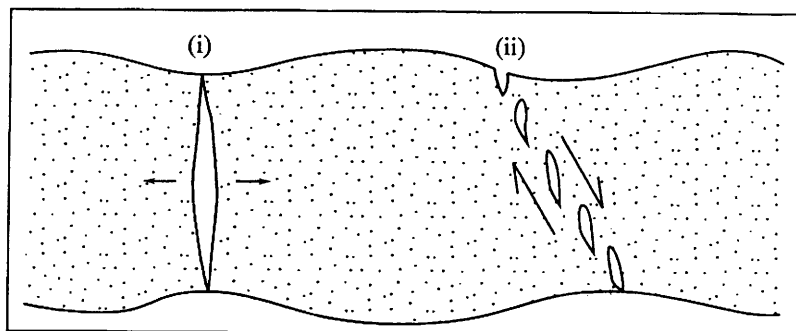
Fig. 6. Line drawing of incipient boudins formed in a sandstone layer in the Carboniferous turbidites at Millook, north Cornwall. Some boudins are separated from each other by a single extensional gash (i) and others by an array of extensional fractures (ii).
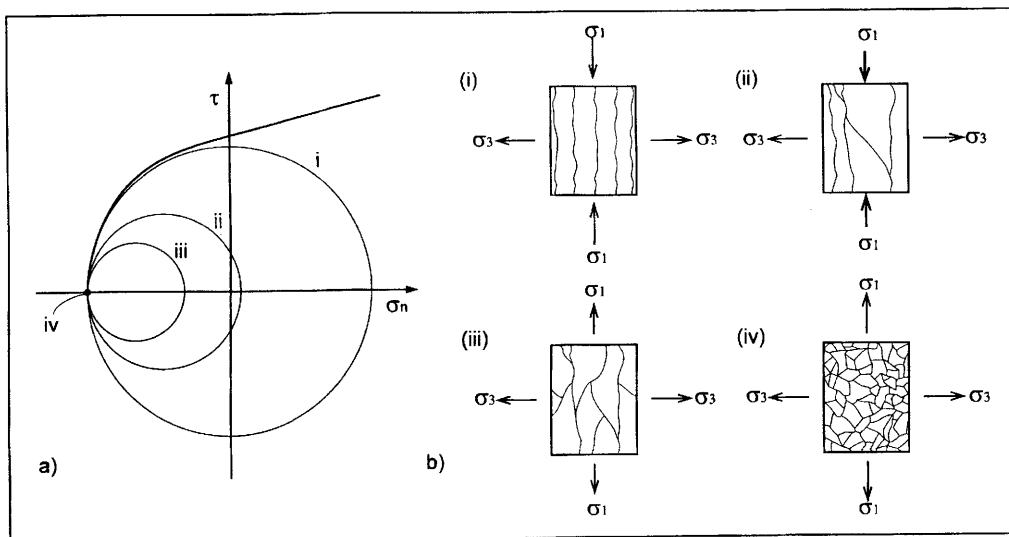
Fig. 7. (a) Four Mohr circles that represent four stress states that will give rise to extensional failure (i.e. $\sigma_1 - \sigma_3 < 4T$). **(b)** (i)–(iv) show the organization of the extensional fractures for each stress state.

gravity. These equations show that if the overburden has a constant density and Poisson's number does not change with depth, then the vertical and horizontal stresses increase linearly with depth (Fig. 9).

It can be seen from Fig, 9 that the differential stress ($\sigma_V - \sigma_H$) will also increase linearly with depth. From the discussion of brittle failure given earlier it follows that the type of hydraulic fractures that will form in the upper section of the sedimentary pile, where the differential stress is less than four times the tensile strength of the rock, will be vertical extensional fractures opening against the least principal stress σ_3 and the fractures that form at depths where the

differential stress is greater than $4T$ will be shear fractures dipping at around 60° and striking normal to σ_3.

Thus when the vertical stress is the maximum principal compression and when the two horizontal principal stresses are not equal, the fracture patterns generated by hydraulic fracturing in the upper and lower zones indicated on Fig. 9 will be as shown in Fig. 10a and b. In the upper zone where extensional failure occurs, the fractures will be vertical and will be aligned normal to σ_3. In the lower zone where shear failure occurs, conjugate fractures will form dipping at 60° and intersecting (and striking) parallel to σ_2. It can be seen from Fig. 10a and b that in
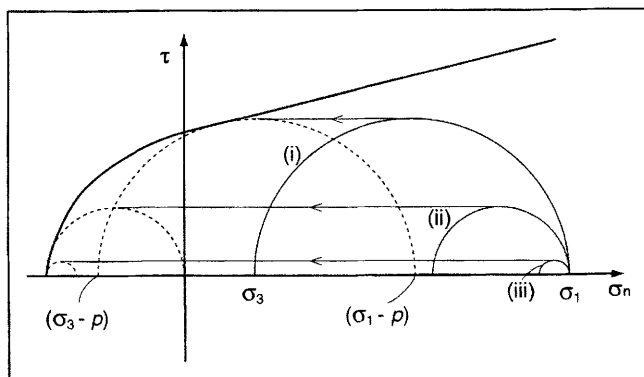
Fig. 8. The influence of an increase of fluid pressure on three stable stress fields i, ii and iii (see text).
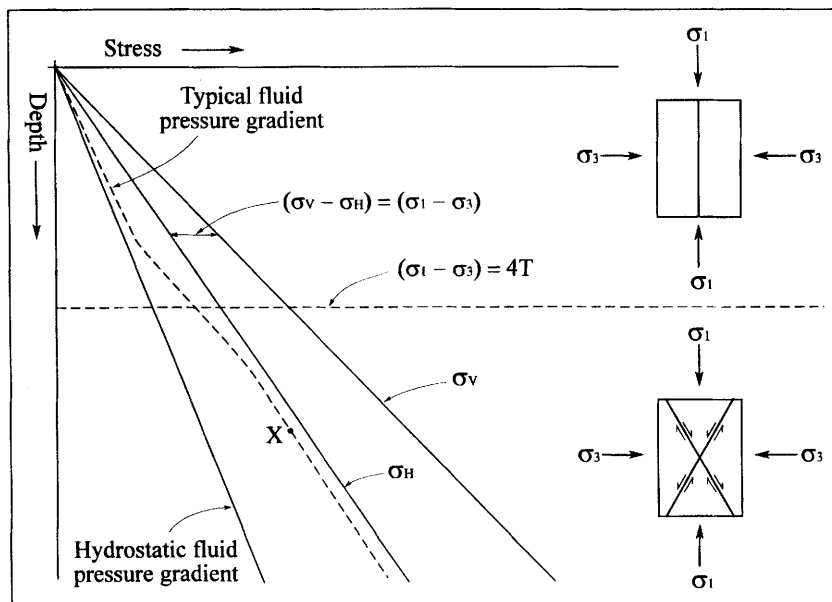
Fig. 9. Plot of variation of vertical and horizontal stress and fluid pressure with depths according to Eqns 1 and 2 which assume that the stresses are generated by the overburden in a tectonically relaxed basin. The expression of the hydraulic fractures is determined by the differential stress which increases with depth. At the depth when it exceeds $4T$ the fractures change from extensional to shear.

the upper zone characterized by extensional failure, the dip of the fractures will be vertical on any vertical face. In the lower shear fracture zone, the apparent dip of the fractures will vary between 60° and 0°. However, on any particular plane the apparent dip will be constant.

The three-dimensional array of fractures that would form in the extensional and shear fracture zones if the two principal horizontal stresses, σ_2 and σ_3, are equal are shown in Fig. 10c and d. In the upper zone, because the horizontal stresses are the same in all directions, there is no horizontal direction of relatively easy opening and therefore no tendency for the alignment of fractures in any particular direction. The result would be the formation of vertical fractures with random strikes. If these fractures are spaced closely enough to interfere, they would generate a polygonal array (Fig. 10c). It is clear from this figure that the dip of the fractures would be vertical on any vertical face.

Similarly, in the zone in which shear fractures form, because the horizontal stress is the same in all directions the strike of the shear fractures would also be random. Thus if they were spaced closely enough they too would interfere to form a polygonal array. The apparent dip of these fractures on any vertical face would vary

between the true dip of around 60° and zero (Fig. 10d).

In the above discussion the state of stress at any depth has been assumed to be determined by Eqns 1 and 2 and it was assumed that the density of the rock or sediment and Poisson's number remained unchanged with depth. These assumptions are clearly unreasonable (e.g. Price (1958) and Eaton (1969) for a discussion of the change of m with depth) and direct measurements of the stress state in several present-day basins show that the stresses change in a non-linear manner with increasing depth (Fertl 1976; Breckels & van Eekelen 1982).

Field evidence for hydraulic fractures

The arguments outlined above indicate that as sediments undergo burial and diagenesis in a basin, conditions of stress and fluid pressure are likely to be encountered that will lead to the formation of hydraulic fractures. Indeed, these fractures would provide a transient increase in permeability that would facilitate the dewatering of relatively impermeable horizons. Unfortunately these fractures are generally not preserved, forming as they do at relatively shallow depths
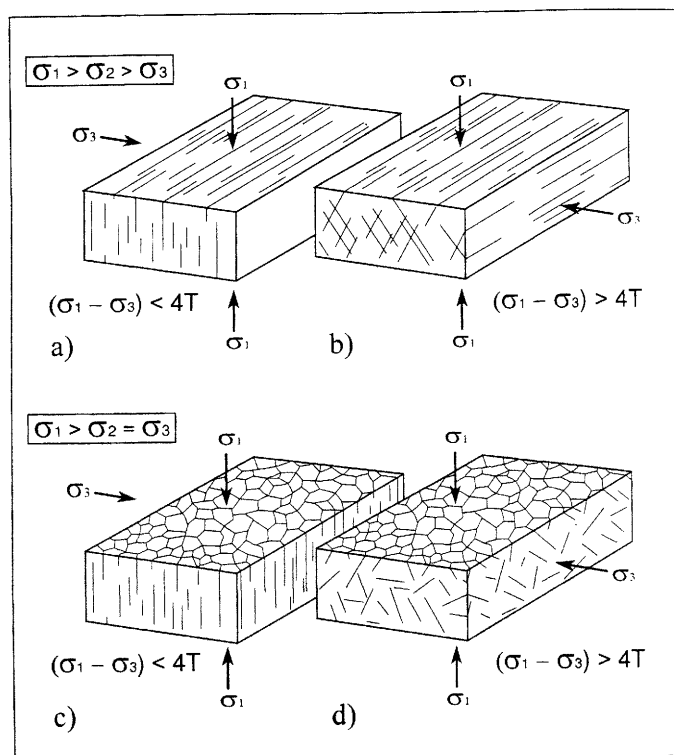
Fig. 10. The three-dimensional organisation of hydraulic fractures: (**a**) when $\sigma_1 - \sigma_3 < 4T$ and the two horizontal principal stresses are unequal; (**b**) when $\sigma_1 - \sigma_3 > 4T$ and the two horizontal principal stresses are unequal; (**c**) when $\sigma_1 - \sigma_3 < 4T$ and $\sigma_2 = \sigma_3$; (**d**) when $\sigma_1 - \sigma_2 > 4T$ and $\sigma_2 = \sigma_3$.

where they are unlikely to be preserved as vein systems and where the rock properties are such that barren fractures would tend to heal once the excess fluid pressure has been dissipated.

The author has examined a number of quarries and other outcrops of low permeability shales thought to have been overpressured during their burial. Remarkably little evidence was found of such fracturing. Occasionally, thin (1–2 mm thick) bedding-parallel veins of fibrous calcite occur, with the fibres oriented normal to the bedding fractures, as for example in the Kimmeridge shales at Kimmeridge Bay in Dorset. 'Chicken wire' texture has been recorded in cores from shales known to have been previously overpressured (Powey 1990, pers. comm.). These are polygonal arrays of fractures along which very thin veins of calcite have been precipitated. Hydraulic fractures are sometimes preserved as sedimentary dykes in the regions around sandstone bodies in shales if the fluid pressures are sufficiently high to fluidize the sands. Sedimentary dykes provide one of the most convincing demonstrations of hydraulic fracturing in sedimentary successions.

Recently, Cartwright (1994) has reported the occurrence of large polygonal fracture arrays in Early Cainozoic mudrock-dominated sequences from the North Sea. The fractures have been mapped using regional two- and three-dimensional seismic data. They occur in the stratigraphically bounded tiers in deep-water sequences bounded by regionally condensed sequences (seals). The faults are organized into cellular networks comprising polygonal prismatic and pyramidal forms and Cartwright suggests that these faults are the result of hydraulic fracturing. The polygonal cells are between 500 and 1000 m in diameter and a synoptic block diagram illustrating the structural framework of the faults is shown in Fig. 11.

Despite the impressive seismic images of hydraulic fracture patterns presented by Cartwright (1994), evidence for the occurrence of hydraulic fractures in low-permeability rocks known to have been overpressured at some stage in their history, is remarkably scanty.
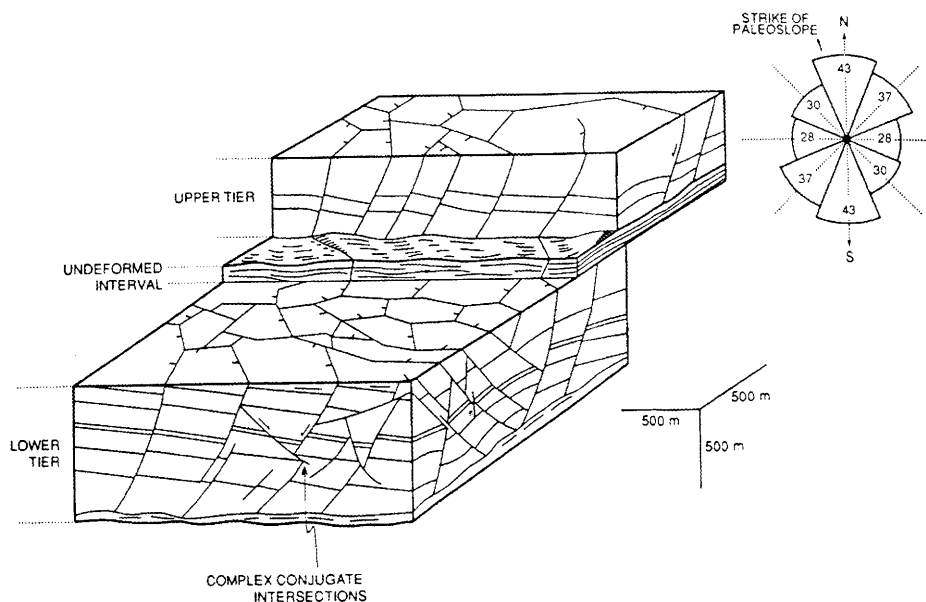
Fig. 11. A structural synopsis of a three-dimensional seismic survey of block 30/19, located in the basin centre, showing a polygonal network of small extensional faults affecting the lower Tertiary (from Cartwright 1994).

Even when fractures are found in such rocks it is difficult to demonstrate convincingly that they are the result of hydraulic fracturing. For example, the barren fractures frequently exhibited by shales at outcrop often form polygonal arrays when viewed on the bedding plane and are normal to bedding. Exposures of such rocks are often characterized by polygonal prisms. This is a fracture pattern that might be expected to form during the burial and overpressuring of the rock (Fig. 10c). Nevertheless it is difficult to determine , whether these fractures represent ancient hydraulic fractures generated during burial and dewatering which have been reopened as a result of the release of residual stresses during exhumation, or whether they represent desiccation fractures resulting from the drying out of the shales on exposure.

This similarity in the geometric organization of desiccation fractures and extensional hydraulic fractures reflects an underlying similarity in the mechanism of formation of both structures. This can be exploited when hydraulic fracturing is studied using analogue models.

The experimental investigation of the initiation and development of hydraulic fractures in overpressured shales and semi-lithified rocks is extremely difficult. However, if it can be argued that the process is directly analogous to the formation of cooling fractures or desiccation fracture, then the formation of these fractures under a variety of boundary conditions can be studied with relative ease.

The association of thrusts and high fluid pressures

In the above discussion the build-up of fluid pressure and the formation of hydraulic fracturing in a tectonically relaxed basin was considered. Such a fluid pressure build-up will also occur in tectonic regimes, particularly those associated with compressional tectonics. In this section the association of thrusts and high fluid pressures are considered.

The recognition of overthrusts, large blocks of rock up to 10 km thick and with lengths and widths often in excess of 100 km, which had been transported tens of kilometres along sub-horizontal fault planes, presented geologists with the challenge of understanding the mechanism by which these blocks were moved. An early study of this problem was carried out by Smoluchowski who represented the overthrust block as a single rectangular prism caused to move over a flat, dry surface by the application of a horizontal push from one end. By selecting the appropriate values for the coefficient of sliding friction and rock strength it can be shown that overthrusts with lengths greater than a few tens of kilometres cannot be moved

by this mechanism unless the applied stress exceeds the strength of the rock.

Alternative mechanisms for the movement of large overthrusts were presented. For example, Oldham (1921) suggested that movement on a thrust plane may not be synchronous and that decoupling and displacement may occur locally and migrate along the thrust plane in a caterpillar-like manner. This mechanism would allow the overthrust block to move forward without having to overcome the total frictional resistance of the block to movement at any one time. In this way, it was argued, large overthrust blocks could be moved at stresses below the strength of the rock. Despite such innovative thinking it was not until 1959 that a widely accepted solution appeared to the mechanical problems associated with the movement of large-scale thrusts.

In their classic paper, Hubbert & Rubey (1959) argued that the existence of high fluid pressures would reduce the effective normal stress across a potential thrust plane and thus reduce the horizontal compressive stress necessary to move the thrust to below the brittle strength of the rock. This idea represented a major step forward in the understanding of the generation and movement of large overthrusts and, following this work, the association of overthrusting and high fluid pressures became almost axiomatic. More recently the overthrust 'paradox' has been reassessed (Price 1989) and this association questioned.

Although Hubbert & Rubey's work on high fluid pressures provided a great insight into the role that fluid pressures may play in thrust initiation, it says nothing about the migration of fluids during thrusting.

Faults, folds and fluid migration

The migration of fluids along major faults during and immediately after reshear has been discussed by Sibson *et al.* (1975), who introduced the idea of seismic pumping. This concept sprang from observations of hydrothermal vein deposits found in the upper, brittle regions of ancient fault zones. The textures of these deposits usually indicate that mineralization took place episodically and it was suggested that episodic injection of hydrothermal fluids could be accounted for by the dilatancy–fluid diffusion model for energy release in shallow earthquakes proposed by Scholtz *et al.* (1973). In later papers, Sibson *et al.* (1988) and Sibson (1990) proposed two other mechanisms, the suction-pump and fault-valve mechanisms which also predict periodic variations in fluid pressure along faults associated with fault reactivation.

In contrast, the migration of fluids in association with the development of folds has received comparatively little attention. It is, however, possible to determine the stress gradients within and around a fold from the equations that govern the buckling behaviour of anisotropic bodies such as a sedimentary sequence. They show that there is a difference between the mean stress inside and outside a fold and that this difference (i.e. the stress gradient) changes as the fold amplifies. For a box fold the gradient is initially such that fluids are drawn into the fold from the surrounding region. However, beyond a certain amplification the gradient is reversed and fluids are driven out of the fold. This process can be inferred from the geometric changes that accompany the amplification of a kink-band in a layered material where the layers remain a constant thickness during the deformation (Fig. 12a–c). Initially there is an increase in volume within the kink-band. This continues until the layering inside the kink-band is normal to the kink-band boundary, i.e. $\omega = \theta$ (Fig. 12b), when it reaches a maximum. Up to this point fluids will be drawn into the fold from the surrounding unfolded region. As the kink-band amplifies beyond this point, the volume of the kink-band is reduced and fluids will be expelled from the fold. When $\omega = 2\theta$ (Fig. 12c), the volume of the kink-band is the same as it was before the fold was initiated. Any further amplification would require the layering inside the kink-band to thin and if there is no mechanism by which this thinning can be achieved, the fold locks up.

The magnitude of the stress gradient between the fold and its surroundings has been quantified by Summers, who shows that the difference in mean stress inside ($\bar{\sigma}_i$) and outside ($\bar{\sigma}_e$) a fold is given by:

$$\bar{\sigma}_i - \bar{\sigma}_e$$
$$= \tau_e^m \left[\frac{(N/Q - 1)\{\cos 2\theta - c\,2(2\omega - \theta)\}}{(N/Q + 1) - (N/Q - 1)\cos 4(\theta - \omega)} \right]$$
$$\text{(3)}$$

where θ and ω are defined as in Fig. 12d, N and Q are measures of the resistance to compression and shear respectively, in the direction of the applied maximum principal compressive stress, and τ_e^m is the maximum shear stress in the layering adjacent to (i.e. outside) the fold. The variation in mean stress gradient as the fold amplifies can be clearly seen by expressing Eqn 3 graphically (Fig. 12e). As the fold begins to amplify, there is an increase in the stress difference which would tend to draw fluids *into the*
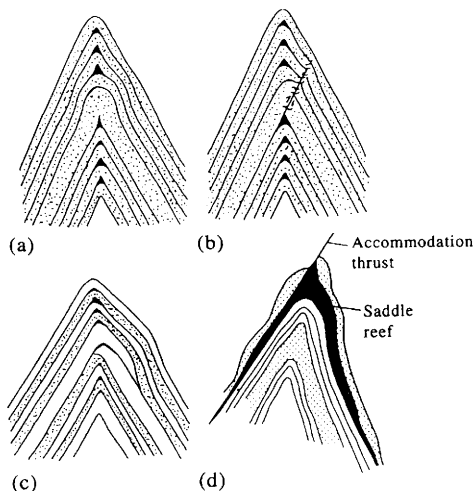
(a)   (b)   (c)

(d)

(e)
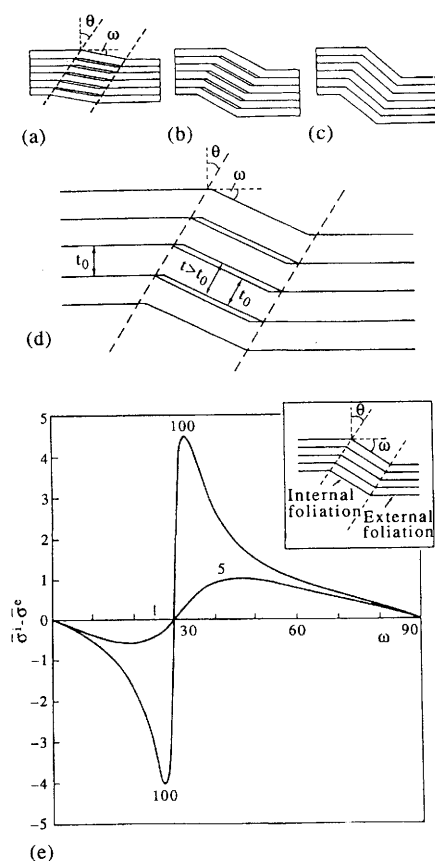
Fig. 12. (**a**)–(**d**) Volume changes that accompany the amplification of a kink-band. During the early stages the volume increases and fluids are drawn into the fold (**a**–**b**). However, as the structure amplifies beyond the stage where $\omega = \theta$ (**b**), the volume decreases and fluids are expelled. (**d**) Detail of (**b**) showing the dilation within the kink-band. (**e**) The graphical expression of Eqn 3 showing the relationship between the difference in mean stress inside and outside the kink-band and the orientation ω of the foliation within the kink-band. Graphs for materials with anisotropies (N/Q) of 5 and 100 are shown ((**e**) after Summers).

fold. The stress difference rises sharply until the layering inside the kink-band is normal to the kink-band boundary ($\omega = \theta$). The gradient then drops dramatically and reverses so that a large gradient is established which will tend to drive fluids *out of* the fold as it continues to amplify.

During the buckling of a complex multilayer, that is a multilayer made up of a variety of different rock types and layer thicknesses, the individual layers will attempt to develop their own characteristic wavelengths. However, the multilayer will impose its own characteristic

wavelength on to these layers and, as they accommodate themselves to the multilayer wavelength, they often develop second-order structures known as accommodation structures (Ramsay 1974; Price & Cosgrove 1990, pp. 319–321). These structures, which form predominantly in the hinge region of folds, may be either ductile or brittle (Fig. 13a–d). In addition to accommodation structures, the high stresses generated in the inner and outer arcs of the hinge region often lead to localized brittle failure. These fractures, combined with the brittle accommodation structures shown in Fig. 13b–d, can dramatically increase the permeability of the hinge regions and become channels of easy fluid migration. Thus, during the expulsion of fluids from a fold during the late stages of its amplification in response to the stress gradients illustrated in Fig. 12e, the fluids are likely to be expelled along these zones of high fracture-induced permeability.

It can be seen from the above discussion that in a deforming sedimentary succession, both folding and faulting can be expected to cause episodic variations in pore pressure and stress. The expulsion of fluids along faults and out of folds as they amplify and lock up may help to generate new structures in the adjacent, relatively undeformed parts of the succession. This insight into the fluid dynamics associated with the formation of

(a)   (b)   — Accommodation
                              thrust

                              — Saddle
                                reef

(c)   (d)

Fig. 13. (**a**)–(**d**) Various accommodation structures that develop during multilayer buckling as layers with anomalous thicknesses adjust to fit into the overall wavelength and amplitude of the multilayer buckles. These may considerably increase the permeability of the hinge region of the fold ((a) and (b) after Ramsay 1974; (c) after Price & Cosgrove 1990; (d) after Herman 1923).

structures such as folds and faults, which are potential hydrocarbon traps, provides a fertile area of research which will doubtless have an important impact on the role that structural geology plays in hydrocarbon exploration.

Conclusions

Knowledge of the three-dimensional geometry and spatial organization of structural traps has for many years been one of the most powerful tools in hydrocarbon exploration. Nevertheless, these models of structure geometry and organization are essentially static and do not consider the interaction of fluids and structures during deformation when the structure is being initiated and amplified. However, recent advances in the understanding of the role of fluid pressure in the initiation of faults and folds and the subsequent influence of these structures on the migration and concentration of fluids, has opened a new chapter in the role of structural geology in reservoir characterization.

References

ANDERSON, E. M. 1951. *The Dynamics of Faulting*, Oliver and Boyd, Edinburgh.

BLAY, P. K., COSGROVE, J. W. & SUMMERS, J. M. 1977. An experimental investigation of the development of structures in multilayers under the influence of gravity. *Journal of the Geological Society, London*, **133**, 329–342.

BRECKELS, I. M. & VAN EEKELEN, H. A. M. 1982. Relationship between horizontal stress and depth in sedimentary basins. *Journal of Petroleum Technology*, Technical Paper SPE **11282**, 2191–2199.

CARTWRIGHT, J. A. Episodic basin-wide hydrofracturing of overpressured Early Cainozoic mudrock sequences in the North Sea Basin. *Marine and Petroleum Geology*, **11**, 587–607.

COSGROVE, J. W. 1993. The interplay between fluids, folds and thrusts during the deformation of a sedimentary succession. *Journal of Structural Geology*, **15**(3–5), 491–500.

——1995. The expression of hydraulic fracturing in rocks and sediments. *In*: AMEEN, M. S. (ed.) *Fractography: fracture topography as a tool in fracture mechanics and stress analysis*. Geological Society, London, Special Publication **92**, 187–196.

DUBEY, A. K. & COBBOLD, P. R. 1977. Non-cylindrical flexural slip folds in nature and experiment. *Tectonophysics*, **38**, 223–239.

EATON, B. A. 1969. Fracture gradient prediction and its application in oilfield operations. *Journal of Petroleum Technology*, Paper **1353-60**; *Trans.*, AIME, 246.

FERTL, W. H. 1976. *Abnormal Formation Pressures*. Elsevier, 382 pp.

HERMAN, H. 1923. Structure of the Bendigo gold field. *Bulletin of the Geological Society, Victoria*, **47**.

HUBBERT, M. K. & RUBEY, W. W. 1959. The role of fluid pressure in the mechanics of overthrusting. *Bulletin of the Geological Society of America*, **70**, 115–166.

KIDAN, T. W. & COSGROVE, J. W. 1996. The deformation of multilayers by layer-normal compression. *Journal of Structural Geology*, **18**, 461–474.

OLDHAM, R. D. 1921. Know your faults. *Quarterly Journal of the Geological Society, London*, **77**, 77–92.

PHILLIPS, W. J. 1972. Hydraulic fracturing and mineralisation. *Journal of the Geological Society, London*, **128**, 337–359.

PRICE, N. J. 1958. A study of rock properties in conditions of triaxial stress. Proceedings of a Conference on the Mechanical Properties of Non-metallic Brittle Materials, Butterworth, London.

——1966. *Fault and Joint Development in Brittle and Semi-brittle Rock*. Pergamon, Oxford.

—— & COSGROVE, J. W. 1990. *Analysis of Geological Structures*. Cambridge University Press.

PRICE, R. A. 1989. The mechanical paradox of large overthrusts. *Bulletin of the Geological Society of America*, **100**, 1898–1908.

RAMSAY, J. G. 1974. Development of chevron folds. *Bulletin of the Geological Society of America*, **85**, 1741–1754.

SCHOLZ, C. H., SYKES, L. R. & AGGARWAL, Y. P. 1973. Earthquake prediction: a physical basis. *Science*, **181**, 803–809.

SIBSON, R. H. 1990. Conditions for fault-valve behaviour. *In*: KNIPE, R. J. & RUTTER, E. H. (eds) *Deformation Mechanism, Rheology and Tectonics*. Geological Society, London, Special Publication **54**, 15–28.

——, MOORE, J. McA. & RANKIN, A. H. 1975. Seismic pumping – a hydrothermal fluid transport mechanism. *Journal of the Geological Society, London*, **131**, 653–659.

——, ROBERT, F. & POULSEN, K. H. 1988. High angle reverse faults, fluid pressure cycling and meso-thermal gold–quartz deposits. *Geology*, **16**, 551–555.

Reservoir characterization and modelling: a framework for field development

JOHN ARCHER[†]

Centre for Petroleum Studies, Imperial College of Science, Technology and Medicine, Prince Consort Road, London SW7 2BP, UK

Abstract: This introductory paper seeks to highlight some of the challenges for reservoir simulation modelling that are presented by proper reservoir characterization and by appropriate cross-scaling of petrophysical parameters. The significance of tensorial representation of effective fluid-phase permeabilities is indicted by a number of examples.

In the UKCS (United Kingdom Continental Shelf) an important contribution to increased recoverable reserves is being made by the application of technology and by the reduction of reservoir description uncertainty. Some developments in reservoir simulation are indicated by examples from innovative well technologies: infill drilling locations indicated from enhanced understanding of flow directions; gas injection and gas condensate behaviour; and fractured reservoir performance.

The paper aims to provide a framework for the design and modelling of improved hydrocarbon recovery processes.

The debate on Structural Geology in Reservoir Characterization and Field Development is timely, as many of the North Sea fields might be regarded as having reached maturity and are posing questions for engineers and geoscientists about suitable locations for infill wells. This debate is taking place against a background of a 'flat' oil price and new ways of doing business. The petroleum industry has largely embraced the concept of 'CRINE', which stands for cost reduction in the new era. Cost-effective solutions in exploration and production are emerging from partnerships between operators, contractors and the research community. There is a greater appreciation of risk and uncertainty and an increased willingness to share the risk and costs in the search for solutions and business opportunities.

The UK Department of Trade and Industry (DTI) publishes its estimates of remaining UKCS reserves at regular intervals. There has been a slow but steady increase over the last ten years or so in the number of years remaining of feasible production life at current production rates. The trend of this reserves:production (R:P) ratio in recent years masks some significant changes. For example, the rate of replacement of produced reserves by new economic discoveries has slowed down. This is not particularly surprising when the oil price for planning purposes is generally assumed to be flat at $16 per barrel.

Even with substantial competition, exploration costs have not reduced dramatically and targets are generally in deeper and more hostile environments. What appears to be happening is that both technology and maturity are having impact.

In the UKCS area the application of four-dimensional seismic (effectively time-lapsed three-dimensional) and its interpretation in a more holistic geoscience environment is paying dividends. The application of information technology to the processes of data acquisition, interpretation and modelling have enabled greater insights into probable fluid movement in producing reservoirs. This, in turn, has justified utilization of innovative extended reach and multilateral wells. It has also prompted and renewed interest in the management of high water cut wells and in the design of more cost-effective water handling facilities.

The DTI survey of likely contributions by technology to the remaining reserves of the UKCS contains the suggestion that three techniques may be of particular significance. They highlight the contribution of innovative well technology and well placement; the role of gas injection and gas condensate management; and the opportunities for late field depressurization of high-pressure water-flooded reservoirs. If application of these technologies is to be effective it seems obvious that reliable information will be needed concerning the quantities and distribution of remaining oil within heterogeneous reservoirs. It will also need reliable interactive modelling tools to investigate design alternatives for oil recovery.

[†] Currently Principal and Vice Chancellor, Heriot-Watt University, Edinburgh, and visiting Professor at Imperial College.

Opportunities

Scaling of reservoir characteristics

Reservoir characterization for reservoir simulation modelling is essentially a multidisciplinary team effort. It does, however, require definition of a particular parameter at the scale in which it will be utilized in the calculation process – usually at the scale of a simulation model grid cell. The rules for generating appropriate values at grid cell scale from, for example, small-scale observations in core, are relatively easy to codify, and are guided by successive simulation scale-up to produce 'effective' or 'pseudo' quantities at the required scale. The main constraint in such an exercise is the need to respect the principles of the physics which governs the displacement process, rather than utilize empirical and limited relationships.

It has long been recognized that scale change 'rules' tend to apply within regions of similar wettability and petrophysical character, often described as 'rock-type' regions. The Leverett pore geometry factor (J-function) has proved a useful correlation concept for scale change within a rock-type and it has been particularly valuable in correlating end-point relative permeability with end-point saturations. At pore scale levels it has been observed that distribution functions describing co-ordination numbers, aspect ratios and pore size distributions also have influence in representing displacement processes.

Effective phase permeability

For multiphase flow of fluids in porous, permeable rocks, the effective phase directional permeability $(\bar{k} \cdot kr)$ is particularly important. As a simplification this is usually regarded as the product of absolute permeability and relative permeability and can be thought of as a tensor. In most current applications in reservoir simulation, all the possible directions of flow are reduced to three directions oriented to coincide with the principal orientations of the grid cell faces.

Relative permeability characteristics have traditionally been related to the saturation of a particular fluid phase. There is now an increasing body of evidence which suggests that saturation alone is an insufficient parameter on which to interpret relative permeability. At pore scale both the Leverett pore geometry factor (the square root of permeability divided by porosity) and wettability effects which control the surface physics play a role in displacement processes.

Reservoir engineers are rightly concerned with the problems of obtaining an estimate of dynamic $(\bar{k} \cdot kr)$ tensors from observations in a particular reservoir and from samples obtained from it, and from analogies with similar rock–fluid systems. The reservoir characteristics of porosity and effective phase permeability tensors are broadly associated with petrophysical and lithological rock types which form the essential correlation framework. At larger scales the effects of structural and diagenetic modifications are important in defining flow paths for the movement of reservoir fluids. Outcrop data can provide a useful guide to directional permeability variations influenced by sedimentary processes. Since the development of the first really portable mini permeameters or probe permeameters designed for field use by teams at the University of Texas, Austin, and at Imperial College in the mid-1980s, a significant quantity of data has been collected. It has of course been single-phase flow information. The rock–fluid interactions, which must be understood in order to translate the measurements to define the effective phase directional permeability tensor, are rarely addressed in a rigorous and systematic fashion. There is a strong case for a national collaborative research programme to understand the controls on effective phase permeability and to develop the capability to scale measurements to grid cell sized representations of petroleum reservoirs in reservoir simulation models.

Fractures and arbitrary geometry

There have been a number of significant developments in the way in which reservoirs are modelled mathematically. The use of permeability tensors has opened the way for representing fluid flow in directions which are not orthogonal with the faces of model grid cells. This has given new capabilities in modelling high contrast permeability regions with non-orthogonal and fault fracture patterns. The use of boundary element mathematics has given insight into representing rock-type regions in arbitrary shapes, closer to natural variations and unconstrained by the need to force a 'layer-cake' geometry. The challenge for the research workers in this area is to combine the prevailing grid cell based technology with the freedom of arbitrary geometries. A similar style of problem is being addressed by research workers engaged in tracer modelling, where mixed finite element schemes are being explored.

Dynamic permeability

During the course of a reservoir's producing lifetime, the absolute permeability at a given location may change. This might result from local stress changes in the porous rock system (due to depressurization, for example) which can alter pore shape or dimensions as well as from dynamic diagenetic changes in the pore system, perhaps induced by injected fluids. The reservoir simulation research community are able to model such behaviour either explicitly or implicitly, but the rules for doing so currently appear to be more empirical than firmly based on physical principles. There is a considerable amount of experimental work still to be done on reservoir rock systems of interest.

Gas condensate reservoir management

If it is assumed that thermodynamic equilibrium exists, then gas condensate systems are predicted to exhibit retrograde behaviour in the pore spaces of reservoirs as they are depressurized under isothermal conditions. It is extremely difficult to obtain representative fluid samples from gas condensate reservoirs and the hydrocarbon mixtures obtained may or may not be reliable for design of recovery processes. Furthermore, the phase partitioning that occurs in a gas condensate located in a porous reservoir rock may or may not be simulated in a PVT cell. The near-wellbore condition of a producing gas condensate reservoir may not represent thermodynamic equilibrium. The consequence of present understanding is that gas condensate reservoir management, in which one of the objectives is to minimize liquid loss within the reservoir, is something closer to art than science. The DTI estimate of gas condensate reserves in the UKCS is such that a major collaborative research programme into the fundamentals of the recovery processes appears to be warranted.

Gas injection into oil reservoirs

Gas injection has tended to be employed in order to maintain oil production rates and is often a temporary solution to restriction on flaring of produced gas or the lack of a market or transportation system for gas. Within a reservoir the gas may stay immiscible with the oil it contacts or in some circumstances it may become miscible or graded. Since gas is generally more mobile than liquids it will have a tendency to bypass some of the liquid under the influence of gravity or a potential gradient. Gas injection may be used in the design of recovery processes which involve creation of over-ride regions or secondary gas caps in regions which are structurally high. This can increase oil recovery from otherwise inaccessible attic regions with respect to particular well placements. There is some evidence that successive pulses of water and gas injection will lead to increased oil recovery in heterogeneous reservoirs where different flow paths are exploited.

The mechanisms for water alternating gas (WAG) displacement schemes are different depending on whether the process is considered immiscible or miscible. The ability to model the process in reservoir simulation is present as far as the programming is concerned, but is questionable in terms of an understanding of the physics or the ability to describe the dynamic effective phase permeability characteristics of the reservoir.

Well technology

Well technology is an important aspect of improved hydrocarbon recovery in many reservoirs. The design of high angle wells and, more recently, of multibranch wells has allowed penetration of distant parts of a reservoir from a fixed platform or pad. It can be important in accessing attic oil and in minimizing coning by spreading out near-wellbore pressure gradients. Much research has been conducted on generating relationships for horizontal well productivity of a single phase in an equivalent grid-based simulation model domain. At Imperial College this has been tackled through conformal mapping in cylindrical geometry to develop the base case for comparisons with a grid-based geometry. The multiphase flow relationships can be established mathematically but they are empirical rather than founded on theory. Our most recent research in this area has concentrated on modelling productivity indices in the presence of complex heterogeneities and with application to unstructured grid domains. The work has extended to modelling the kind of multilateral wells which are being drilled in the UKCS. One of the difficulties in modelling such wells is the attribution of flow to given positions in the reservoir. This is particularly so when branches develop from the same horizontal well. In history matching applications, the identification of flow paths and the pressure distribution indicate that attention is necessary to the design of data acquisition and reservoir characterization.

Conclusions

This introductory paper has attempted to high-
light some of the contributions to increased
recoverable reserves that are being made by the
application of technology and by the reduction
of reservoir description uncertainty. In the
UKCS it is noted that enhanced hydrocarbon
recovery is likely to focus on innovative well
technologies, infill drilling, and combined water
and gas injection and improved water handling.
In mature reservoirs, which may be depressur-
ized, there will be a need to understand and
model dynamic permeability change such as
pressure-dependent permeability and the effects
of local three-phase flow.

Some of the challenges of reservoir character-
ization for application in reservoir simulation
models have been indicated. The most important
aspects appear to be understanding multiphase
flow characteristics across a number of scales
on which data are gathered.

With much of the reservoir characterization
challenge, the ability of mathematics to represent
a particular process has progressed faster than
the ability to understand the physics of that
process or to describe the system in which it
operates. The framework for the design of hydro-
carbon recovery processes is firmly established as
the multidisciplinary field of reservoir simulation
modelling.

Fault seal prediction: the gouge ratio method

B. FREEMAN, G. YIELDING, D. T. NEEDHAM & M. E. BADLEY

Badley Earth Sciences Ltd, North Beck House, North Beck Lane, Hundleby, Spilsby, Lincolnshire PE23 5NB, UK

Abstract: The reduction in pore throat size attributable to the enhanced clay content in the fault rock between two juxtaposed reservoir bodies is able to produce an effective seal to hydrocarbon migration. The gouge ratio, when applied to sand–shale sequences, indicates the proportion of phyllosilicate material that is expected to be incorporated into the fault rock, hence it provides a measure of the seal capacity. Gouge ratios for faulted reservoir sequences are computed from data that are routinely available from fields at the appraisal or production stage. We present a repeatable methodology that maximizes the use of seismically based geometric data and well-based stratigraphic and compositional data. The resulting gouge ratio calculations can be used comparatively at the scale of individual faults, fields or basins. We examine an example fault from the Oseberg Syd Field that is known to seal and we show that a threshold shale gouge ratio of 18% will support a cross-fault pressure difference of *c.* 8 bar.

Structural geology has an important contribution to make to reservoir characterization, particularly the interpretation and analysis of faults. Traditionally, oil industry interpretation has focused on the delineation of horizon surfaces. Faults are often either left uninterpreted or are not interpreted in a manner which produces a consistent three-dimensional model when combined with horizon interpretation. The result of such neglect is that fault planes are frequently regarded as vertical for the purposes of reservoir volume estimation and for hydrocarbon flow simulation. Although faults have always been recognized as key structures in defining the architecture of reservoirs, it is only recently that there has been renewed interest in their behaviour as lateral seals.

Fault seals fall into two broad categories: (1) reservoir against non-reservoir in which case the juxtaposition of permeable rocks against non-permeable rocks provides a sealing mechanism; and (2) reservoir against reservoir in which case the fault itself must provide a barrier to hydrocarbon migration. Knipe (1992) provides a review of the mechanisms leading to fault seal. This paper is concerned only with the second type of seal – reservoir juxtaposed to reservoir. In this case the estimation of the seal potential of a fault has been approached from at least three different angles. Work by Weber *et al.* (1978) indicated that in some faulted sequences, where reservoir rocks are interbedded with shales, the shale units are drawn into the fault zone. The shale layers showed normal-drag geometries and it is implied that there should be a barrier to hydrocarbon migration where a reservoir unit is in contact with shale that has been sheared into the fault plane.

Within the fault zone the shape of the shale units tapers from the shale source bed towards the centre of offset. The shape, hence thickness, of the shale wedge can be computed as a function of fault throw and shale bed thickness. In turn, the fault zone shale thicknesses are used to estimate seal potential. This type of method has been used to explain the distribution of hydrocarbon reservoirs in sand–shale sequences of the Niger Delta (Bouvier *et al.* 1989; Jev *et al.* 1993).

A related method (Lindsay *et al.* 1993) predicts the likelihood of shale source beds producing a continuous smear of clay material across a reservoir–reservoir contact. This method too has been applied successfully to stacked hydrocarbon accumulations in the Columbus Basin (Gibson 1994).

A second approach is to quantify selected attributes on sets of faults which are known either to seal or to leak and then to make predictions about unknown behaviour by comparison. This method has been outlined by Knott (1994). Possible drawbacks to such a method are that an extensive regional database is required and there is some reliance on there being a relatively simple and continuous stratigraphy. It also embodies a notion that faults either seal or leak, whereas it is more realistic to think of faults as having spatially heterogeneous sealing characteristics.

Finally, a third approach is based on consideration of the capillarity of the rocks which are deformed in the fault zone (Knipe 1992). Watts (1987) and Vavra *et al.* (1992) review the mechanisms by which capillarity is able to trap substantial hydrocarbon accumulations. Watts (1987) and Knipe (1992) argue that the equations of capillarity used previously for vertical traps

may also be applied to faults provided that representative measurements can be obtained from analysis of core. Ultimately this type of analysis should be able to make 'standalone' predictions of accumulation without recourse to the 'calibration' required for the first two methods. However, it must encounter scaling problems. Since samples are analysed from core, and reservoir–reservoir juxtaposition areas can be several hundred thousand square metres, there needs to be some means of up-scaling, or averaging, of the capillarity information. There is also a difficulty in obtaining representative core. For a number of reasons, oil companies avoid drilling through known fault zones, for example to avoid early water breakthrough. Therefore faults that are sampled in core are at a scale that may be important in controlling reservoir performance but are unlikely to be responsible for the gross sealing characteristics of the larger faults that trap economic reserves.

Our approach is similar to that of Bouvier *et al.* (1989) in that it considers the entire fault plane. It also attempts to address some of the scaling difficulties associated with the capillarity work. We take the simple view that reservoir characterization is most useful if one is able to apply a repeatable methodology to all faults in a prospect, field, basin and between basins. This means capitalizing on the primary data that are routinely available, i.e. horizon and fault interpretation for geometry, wireline logs for reservoir zone thickness, content of clay or other impermeable material, and, if available, drilling and production information on reservoir zone pressures. From the geometric data one can derive a precise model of the fault's shape and displacement distribution. Combining this with stratigraphy and detailed lithology it is possible to produce fault-wide maps predicting the distribution of clay and other impermeable lithologies (in the fault rock) as a proportion of the total fault-rock volume (gouge ratio maps).

Unlike the work of Weber *et al.* (1978) and Bouvier *et al.* (1989) that implies a single mechanism for incorporating shale into a fault zone, we simply infer that the composition of the fault rock closely reflects that of the undeformed walls. Hence as the overall composition of clay and other impermeable material increases then we would expect the seal potential to increase. For example, this means that faulted sequences from dirty sandstones would have similar seal potentials to sequences of interbedded clean sands and shales, provided the overall clay volume fractions are the same. In the case where the impermeable material is

dominantly shale we refer to the calculation as the shale gouge ratio. The rationale for this stems from the observation that phyllosilicates become concentrated along shear planes in the fault zone and clog the larger pores. They are then effective in reducing the maximum radius of interconnected pores (e.g. Knipe 1992).

Gibson (1998) shows from a study of small-displacement faults of varied mineralogy that there is a clear inverse trend between clay content and porosity. He also shows that of the structures observed in faults, clay gouge zones are the most efficient at reducing pore throat size and permeability.

The purpose of this note is to describe a methodology that we have applied to the study of lateral seals in many producing oil fields. We do this with reference to a specific example from the Oseberg Syd Field (Fig. 1). A full description of the sealing characteristics of faults in the Oseberg Syd Field is given in Fristad *et al.* (1996).

Geological setting

The Oseberg Syd Field is in an area of Mesozoic extension located within Block 30/9 on the Norwegian Continental Shelf between the Horda Platform and the Viking Graben. Most faults within the Oseberg/Oseberg Syd region strike N–S to NNW–SSE in an anastomosing pattern sub-parallel with the Viking Graben. The fault blocks range in size from less than $10 \, km^2$ to $250 \, km^2$. Almost all of the individual fault blocks that have been drilled contain oil and gas. Furthermore, depths to the fluid contacts differ between blocks, indicating that the bounding faults are also sealing faults.

The fault discussed here separates two hydrocarbon columns in Middle Jurassic Brent reservoirs encountered in Wells 30/9-13s and 30/9-14 with a maximum cross-fault pressure difference of 9.5 bar (fault A in Fig. 1). The throw maximum is close to the centre of the fault, diminishing to zero at its southern end. On the same fault there is considerable overlap of Brent reservoirs, the maximum offset being about half of the local Brent Group thickness. The burial depth of the Brent Group at the time of faulting is estimated to have been less than 500 m.

Geometric information

It is important, before performing fault seal analysis, to maximize the use of the basic
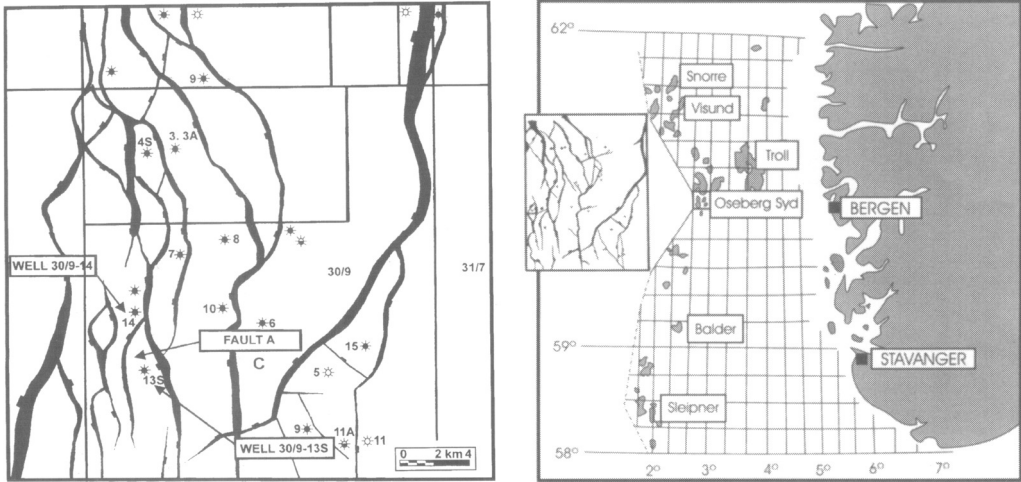
Fig. 1. Location map of the Oseberg Syd Field off the western coast of Norway. Fault A, shown between Wells 30/9-13s and 30/9-14, is the fault referred to in this paper.

geological interpretation. This is usually in the form of horizon surfaces from maps or cross-sections and from fault traces interpreted in cross-section.

Bringing together these two sets of information in a single, topologically consistent model is non-trivial. First the fault surface has to be modelled, in the algorithmic sense, from the raw data, in this case the (x, y, z) values of the traces picked on vertical sections. Ideally, the z-values should be in depth (as in the example discussed here). We use a proprietary grid-based method, referenced to a base plane, that estimates the elevations at grid nodes from the projection of least-squares, best-fit planes through the control points. Data points to be used in both the plane fitting and in the final, weighted estimation of values at the nodes are selected by an octant search strategy. By modifying the numbers of points required in each octant and by changing the weights, we are able to exercise a great deal of control over the resulting surface model. This is important because it means that if the starting data are good our fault model can be forced to honour the control points very closely. On the other hand, if data quality is poor, for example when fault traces are mis-tied, then we need to be able to smooth through the ambiguities and picking errors. Typically, for good quality data, we expect to see root-mean-square (RMS) residuals between the modelled surface and constitutive control points to be of the order of a few metres or less. These errors are smaller than the horizontal resolution of the seismic data.

Despite the maturity of methods employed for interpretation of horizon surfaces, these surfaces are rarely in a form amenable to 'instant' analysis. The main problem is usually an overestimation of the heave which can lead to incorrect throw computations and erroneous juxtapositions (see Needham *et al.* (1996) for a discussion). During our modelling procedure we apply corrections to horizon interpretation in the vicinity of a fault which ensure a single, consistent fault/horizon topology with no gaps or overlaps. We refer to this model as the framework topology (Fig. 2).

This framework topology forms the basis of an analysis. From it we are able to derive quantities such as throw, gouge ratio, thickness variations, reservoir overlap areas, etc. It is used as a template for refining stratigraphy from seismically mappable scale to reservoir zone scale and for computing pressure variations as projected from well information.

It is possible to short-cut some of the steps in the geometric analysis by producing strike projections of horizon terminations directly from horizon maps (e.g. Allan 1989). However, there are always vertical inaccuracies introduced by using hand-drawn fault polygons, but more importantly strike projections do not conserve area. Hence reservoir–reservoir juxtapositions that may be significant in a reservoir engineering sense may be lost on a strike projection. In our view it is better to maximize the geometric data by producing a fully three-dimensional topology rather than degrading it by using a two-dimensional approach.
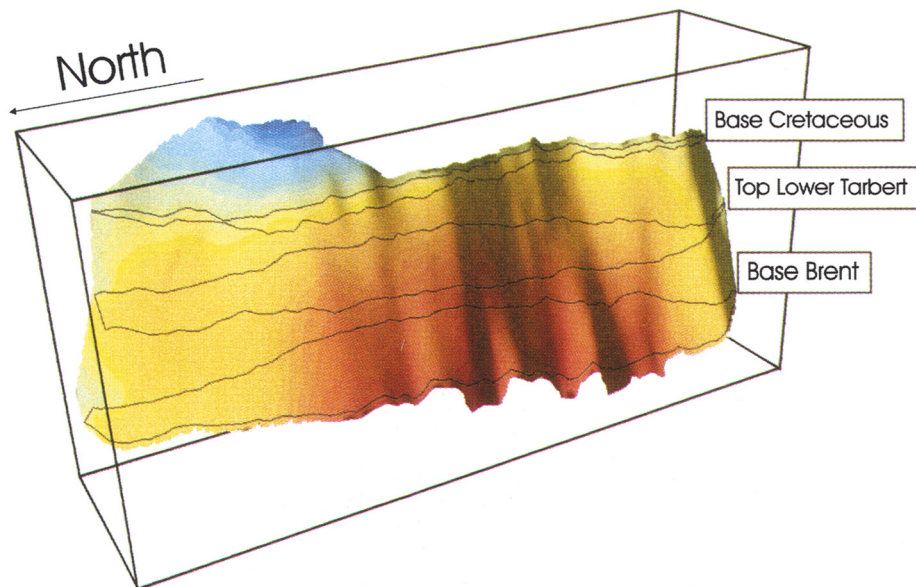
Fig. 2. Three-dimensional model of fault A shaded in throw with illumination perpendicular to the page; vertical exaggeration is a factor of three. Maximum throws (red) are approximately 250 m diminishing to zero (blue) where the fault is mapped above the Base Cretaceous. Marked on the surface are hangingwall and footwall terminations of the seismically mapped horizons: Base Brent, Top Lower Tarbert and Base Cretaceous.

Stratigraphic and compositional information

In most cases it is not feasible to use the large-scale stratigraphic model, defining the framework topology, directly to predict across-fault reservoir characteristics. This is because a mappable seismic interval may contain many individual reservoir zones. Moreover, in geological settings where the seismic image is very much degraded, e.g. in sub-salt plays, it is common for there to be only one picked horizon, say top reservoir. Hence, the framework topology needs to be augmented with stratigraphic detail derived from alternative sources, namely wireline logs. Although it is possible to divide the log curves explicitly into reservoir and non-reservoir units, this in itself can present a major problem of lateral correlation. Usually it is
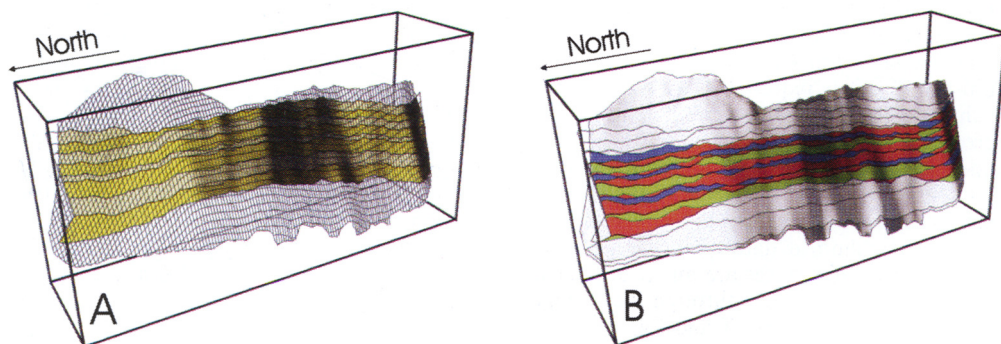
Fig. 3. View, scale and illumination as for Fig. 2. (**A**) Modelled fault as a grid with the intersection of the footwall reservoir zones (two shades of yellow). (**B**) Brent–Brent juxtaposition (red, blue and green). All the zones within the Brent Group are potential reservoirs hence all the shaded region represents an area for potential leakage. The overlap is shaded on a zone-by-zone basis to emphasize the complexity of juxtapositions that can arise from a relatively simple, layer-cake, stratigraphic model.

more practical to interpret the curves in terms of reservoir zones, for which one can be confident that their lateral continuity exceeds the length of the fault in question.

Having sub-divided seismic intervals into zones and measured their relative (or absolute) vertical thicknesses, we compute the locations of the zone intervals within the framework topology. In the Oseberg Syd example the reservoirs of interest occupy the Brent Group, for which we recognize eight zones of alternating good sands and poor sands. Zone compositions were derived from computer-processed petrophysical logs, specifically the shale volume fraction curve. All zones contain some clay. The goods sands have a clay content of $c.15\%$ and the most shaly sands have a clay content of $c.30\%$. Above the Brent Group the average clay content is $c.50\%$, beneath it, the clay content is $c.62\%$. Figure 3A shows the fault surface with intersecting reservoir zones of the footwall. Note that the upper footwall zones are eroded beneath the Base Cretaceous unconformity. Combining the footwall and hangingwall stratigraphies reveals the extent of the Brent–Brent juxtaposition (Fig. 3B). Figure 3B also shows the complexity of juxtaposition geometries that arise from relatively simple stratigraphic relationships. There is potential for cross-leak at all Brent–Brent overlap, although it is the good sand–good sand juxtapositions that represent the locations of greatest risk. The next stage in the process is to quantify this risk by computing the shale gouge ratio.

Gouge ratio computations

Gouge ratios can be computed for any impermeable material that is likely to be incorporated into the fault zone. Most commonly the impermeable material is clay, when we refer to the parameter as the shale gouge ratio. The gouge ratio calculation is performed, once again, as a grid-based operation. The spacing of the grid nodes is chosen such that the thinnest stratigraphic units are adequately represented in raster form. This grid is usually very much finer than that for the surface model. For convenience, the parameters of the gouge ratio grid are always integer multiples of those from the suface models. Hence it is straightforward to interpolate structural information, i.e. throw from the surface model onto the gouge ratio grid.

At every node on the gouge ratio grid we perform the same operation. We estimate the proportion of shale that is present within the

fault zone at that node. Practically, this means quantifying the volume fraction of shale in the window of rock that has slipped past the node, where the height of the window is equal to the throw. In order to be able to deal with geological situations that involve post-faulting erosion we are able to define the window to lie either entirely in one wall or to straddle the node with half in the footwall and half in the hangingwall. Figure 4 is a schematic diagram describing the calculation at a single node using a window of throw in the hangingwall. The gouge ratio method may be applied to stratigraphies that isolate units explicitly as shale and reservoir units (Fig. 4a) or to strati-
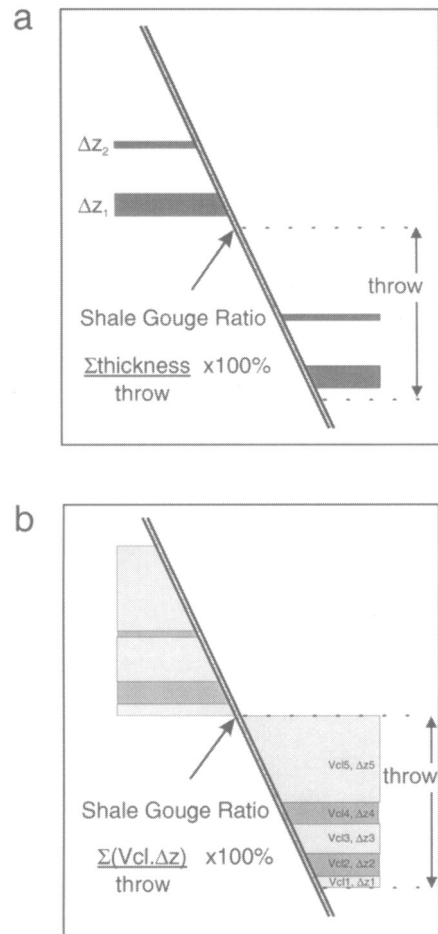
Fig. 4. (a) Computation of shale gouge ratio at a point from a discrete sequence of sands (unlabelled) and shales (Z_1 and Z_2). **(b)** Computation of shale gouge ratio at a point when the clay content is considered as an average value over defined zones. V_{cl} indicates the volume fraction of clay in an interval of thickness Z.
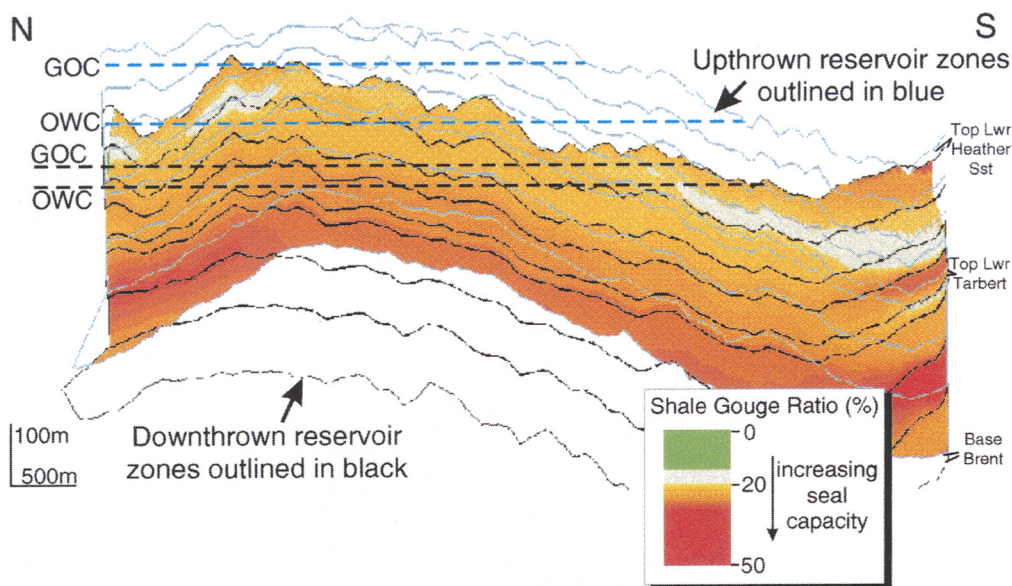
Fig. 5. Isometric view of fault A seen from the west. Vertical exaggeration is a factor of five. Footwall and hangingwall interval boundaries are shown as solid lines and the Brent–Brent overlap is shaded in shale gouge ratio. Fluid contacts (GOC, gas–oil contact; OWC, oil–water contact) are projected from Well 30/9-13s in the footwall and from Well 30/9-14 in the hangingwall.

graphies that are defined more generally as shaly members and reservoir members (Fig. 4b). In the latter case the shale gouge ratio is computed from the sum of the volume fractions of clay in both reservoir and non-reservoir units.

This flexibility in the interpretation of the gouge ratio model means that it is suitable to apply to a broad range of scales. One may also represent the probability of encountering shale beds of given thickness as a volume fraction of clay in a broader zone. Although we do not discuss this aspect any further, it opens the possibility of using gouge ratio calculations in stochastic models.

Figure 4 shows that the gouge ratio computations involve throw and vertical thicknesses. Geometrically this is equivalent to dip separation and bed thickness measured in the direction of fault dip. Furthermore, providing there are no significant lateral thickness changes on the scale of the displacement, the throw and vertical thickness model can be applied to faults of dip-slip, oblique-slip or strike-slip origin.

For our Oseberg Syd example, Fig. 5 shows shale gouge ratio computed over all of the Brent–Brent juxtaposition. Shale gouge ratio varies between 15% and 30%. The lowest

value, 15%, lies in the saddle towards the southern end of the structure. This point is deeper than the structural spill point, hence it is of little interest. The critical region, with a shale gouge ratio of 18%, lies towards the crest of the structure in the oil leg of the footwall and in the gas leg of the hangingwall. Repeat formation tester data from wells on either side of the fault are summarized in Fig. 6. This clearly demonstrates that fault A seals and that the shale gouge ratio of 18% is a threshold value able to support a minimum pressure difference of *c*. 8 bar.

In order to make maximum use of shale gouge ratio calculations it is important to review the threshold values on all of the faults in the field that are known to seal. This provides a calibration. It is then possible to calculate the shale gouge ratio for faults that have not been drilled in one or both walls and to predict whether or not the fault is likely to be able to support a pressure difference, hence trap hydrocarbons. Fristad *et al.* (1996) provide a complete description of all the sealing faults in the Oseberg Syd Field. They find consistently that a shale gouge ratio less than 15% will not seal, between 15% and 18% will support small pressure differences (*c*. 0.5 bar) and that above 18% will support pressure differences in excess of 8 bar.
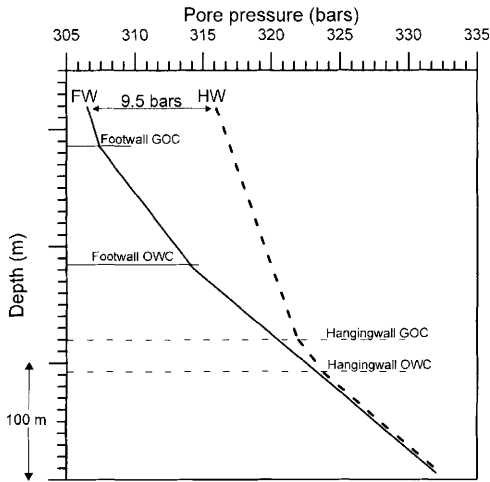
Fig. 6. Summary of the repeat formation tester data showing the maximum pressure difference at the top of the structure between the footwall and hangingwall gas legs.

Remarks

(1) Gouge ratio calculations show that the spatial sealing characteristics of a single fault are likely to be heterogeneous, i.e. it may seal over some of the sand–sand contacts but leak over others.

(2) In the example from the Oseberg Syd Field we show that a shale gouge ratio in excess of 18% will support a pressure difference of c. 8 bar. In our experience from the Oseberg Syd Field and several other fields we find, as a rule of thumb, that shale gouge ratios less than 15% are likely to leak. As the shale gouge ratio increases above 20% the likelihood that the fault will seal also increases.

(3) An important step in the context of appraisal/production is to constrain the threshold value as closely as possible by considering as many sealing faults as possible from the same field. However, using the rule of thumb (above), shale gouge ratio may also be used in exploration provided rudimentary information on zone thicknesses and composition is known. Various possibilities, using different well prognoses, could be used in an exploration setting to assist risk calculation for a prospect.

(4) Nearly all fields in appraisal or production have, as standard, the relevant information required to perform a shale gouge ratio analysis, i.e. seismic interpretation (in time or depth), wireline logs, drilling and production pressure data.

(5) The gouge ratio method embodies a notion of upscaling, is straightforward to apply and produces usable results very rapidly.

References

ALLAN, U. S. 1989. Model for hydrocarbon migration and entrapment within faulted structures. *AAPG Bulletin*, **73**, 803–811.

BOUVIER, J. D., KAARS-SIJPESTEIJN, C. H., KLUESNER, D. F., ONYEJEKWE, C. C. & VAN DER PAL, R. C. 1989. Three-dimensional seismic interpretation and fault sealing investigations, Nun River Field, Nigeria. *AAPG Bulletin*, **73**, 1397–1414.

FRISTAD, T., GROTH, A., YIELDING, G. & FREEMAN, B. 1996. Quantitative fault seal prediction – a case study from the Oseberg Syd area. *In*: Norwegian Petroleum Society (eds) *Hydrocarbon Seals – Importance for Exploration and Production (Conference Abstracts)*. Norwegian Petroleum Society, Oslo.

GIBSON, R. G. 1994. Fault-zone seals in siliciclastic strata of the Columbus Basin, offshore Trinidad. *AAPG Bulletin*, **78**, 1372–1385.

——1998. Physical character and fluid-flow properties of sandstone-derived fault zones. *This volume*.

JEV, B. I., KAARS-SIJPESTEIJN, C. H., PETERS, M. P. A. M., WATTS, N. L. & WILKIE, J. T. 1993. Akaso Field, Nigeria: use of integrated 3D seismic, fault-slicing, clay smearing and RFT pressure data on fault trapping and dynamic leakage. *AAPG Bulletin*, **77**, 1389–1404.

KNIPE, R. J. 1992. Faulting processes and fault seal. *In*: LARSEN, R. M., BREKKE, H., LARSEN, B. T. & TALLERAS, E. (eds) *Structural and Tectonic Modelling and its Application to Petroleum Geology*. Elsevier, Amsterdam, 325–342.

KNOTT, S. D. 1994. Fault seal analysis in the North Sea. *AAPG Bulletin*, **77**, 778–792.

LINDSAY, N. G., MURPHY, F. C., WALSH, J. J. & WATTERSON, J. 1993. *Outcrop Studies of Shale Smear on Fault Surfaces*. International Association of Sedimentologists Special Publication, **15**, 113–123.

NEEDHAM, D. T., YIELDING, G. & FREEMAN, B. 1996. Analysis of fault geometry and displacement patterns. *In*: BUCHANAN, P. G. & NIEUWLAND, D. A. (eds) *Modern Developments in Structural Interpretation, Validation and Modelling*. Geological Society, London, Special Publication, **99**, 189–199.

VAVRA, C. L., KALDI, G. G. & SNEIDER, R. M. 1992. Geological applications of capillary pressure: a review. *AAPG Bulletin*, **76**, 840–850.

WATTS, N. 1987. Theoretical aspects of cap-rock and fault seals for single- and two-phase hydrocarbon columns. *Marine and Petroleum Geology*, **4**, 274–307.

WEBER, K. J., MANDL, G., PILAAR, W. F., LEHNER, F. & PRECIOUS, R. G. 1978. The role of faults in hydrocarbon migration and trapping in Nigerian growth fault structures. *Offshore Technology Conference No. 10*. Paper OTC 3356, 2643–2653.

Experimental fault sealing: shear band permeability dependency on cataclastic fault gouge characteristics

B. R. CRAWFORD

Department of Petroleum Engineering, Heriot-Watt University, Edinburgh, EHI4 4AS, UK

Abstract: An experimental rock mechanics facility was used to assess the finite permeability of shear bands artificially induced in cylindrical core plugs of high porosity sandstone under triaxially compressive stress states of varying magnitude. A method of estimating shear band permeability from axial transient pulse-decay measurements is presented, based on certain assumptions including a linear thickness decrease with resolved normal stress across the fault. Computed permeability reductions range from 2.5 to 3.5 orders of magnitude, with cataclastic sealing exhibiting an order of magnitude increase with increasing normal stress and angular shear strain imposed on the gouge zone. A laser particle sizing technique was applied to the experimentally generated fault gouge samples to appraise any differences in their distributions down to 0.1 μm particle size. By defining the peak (relative fineness) and width of distribution (closeness of grading) of each, the Rosin–Rammler exponential function was able to quantify 'cataclastic intensity' via a 'coefficient of variation' statistical parameter. An empirical relation demonstrated between fault seal and degree of cataclasis is rationalized through consideration of the Kozeny–Carman relation, which analyses permeability in terms of its constituent parameters of tortuosity, porosity and surface area.

Whilst developments in probe permeametry have enabled quantification of sedimentary heterogeneity down to the lamina scale, with such fine detail being incorporated directly into numerical reservoir simulation packages at a scale of the gridblock (Ringrose *et al.* 1993), no parallel advance has been evident in similarly quantifying the flow characteristics of tectonic discontinuities which cross-cut the stratigraphy. To fully incorporate fault architecture into reservoir simulation model gridblocks, reliable predictions of their size population, spatial distribution and hydraulic characteristics are a prerequisite. Heath *et al.* (1994) successfully modelled power law populations of sub-seismic faults with realistic North Sea densities, although the faults were approximated to impermeable (zero transmissibility) baffles. Although Heath *et al.* considered uncertainty concerning the hydraulic characteristics of real faults to be the most important limitation on the modelling procedure, to date work on the petrophysical properties of faults, and in particular their hydraulic nature, has received at best only sparse attention.

Excellent initial studies aimed at quantifying the porosity and permeability of fault surfaces include textural, porosity and gas permeability measurements made on cataclastic slip bands from the Locharbriggs sandstone of SW Scotland by Fowles & Burley (1994) and the mini-permeameter work of Antonellini & Aydin (1994) on deformation bands in the Navajo and Entrada sandstones of SE Utah. To complement these, results are reported here based on an experimental rock mechanics approach, which has focused on transient pulse-decay liquid permeability measurement of cylindrical sandstone specimens faulted in shear under triaxially compressive stress states. A method of estimating these experimentally generated shear band (morphologically similar to natural granulation seams) permeabilities is presented, and the observed stress-sensitive nature of the sealing potential considered in terms of 'cataclastic intensity' derived from fault gouge distributions quantified using novel laser particle sizing technology.

Theory

Fault permeability measurement

Whilst steady-state permeability is determined from measurements of flow rate through a sample under a constant pressure gradient, for shear band permeability estimation, it was found more convenient to use a transient technique, that is, to observe the decay of a small pressure pulse imposed at the upstream end of the core. The transient method was introduced by Brace *et al.* (1968) to measure the permeability of Westerly granite core plugs. The 'pulse-decay' technique utilized here is based on an integration of Darcy's law over the duration of the pressure pulse-decay. From a system initially at

equilibrium with a given pore pressure, a pressure pulse is introduced into the upstream reservoir and allowed to decay through the test specimen from time t_1 to time t_2 against a constant pore pressure, for which it can be shown that permeability, k, results from:

$$k = \frac{\mu C L (\Delta P_{t_1} - \Delta P_{t_2})}{A} \left(\frac{1}{\int_{t_1}^{t_2} \Delta P \, \mathrm{d}t} \right) \quad (1)$$

where μ is fluid viscosity, C system compressibility, L core specimen length, A specimen cross-sectional area, and ΔP the pressure drop across the specimen. The integral in Eqn 1 represents the area under a computer-logged ΔP–time decay curve.

A very simple method for estimating the permeability of an inclined shear fracture (induced under triaxial compression of a cylindrical specimen), from transient axial permeability measurement conducted on the host core plug, is outlined below. The two main assumptions which tend to restrict application of the basic analysis are that: (i) the permeability of the shear band is very much less than the permeability of the stressed rock matrix forming the two specimen halves; (ii) the shear fracture conforms to a shear band geometry with finite and uniform thickness.

Nevertheless, if the above suppositions are generally valid, then the following analysis provides a robust rational approximation for shear band permeability. For high-porosity sandstones, assumption (i) is satisfactory, and carries the implication that virtually all the pressure drop measured across the specimen is occurring across the shear band, so that with $k_{\text{fault}} \ll k_{\text{core}}$, $\Delta P_{\text{fault}} \approx \Delta P_{\text{core}}$ (ΔP_{core} being experimentally measured). Using Eqn 1 this assumption can be expressed as:

$$\frac{k_{\text{fault}} A_{\text{fault}} \int_{t_1}^{t_2} \Delta P \, \mathrm{d}t}{C \mu \varepsilon} = \frac{k_{\text{core}} A_{\text{core}} \int_{t_1}^{t_2} \Delta P \, \mathrm{d}t}{C \mu L} \quad (2)$$

where the core possesses permeability k_{core}, cross-sectional area A_{core}, length L, and the shear band possesses permeability k_{fault}, elliptical area A_{fault}, and thickness ε. The experimental arrangement is shown in Fig. 1, in terms of assumptions (i) and (ii). A constant pressure exists from the upstream end of the core to the shear band, a pressure drop occurs across the fault zone, and a lesser constant pressure exists to the downstream end of the core. On rearrangement and cancellation Eqn 2 reduces to an
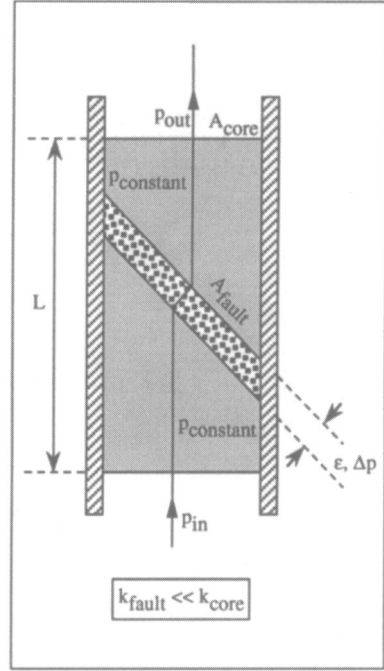

Fig. 1. Schematic illustration of faulted core plug geometry with inclined shear band.

approximate expression for shear band permeability, in terms of a geometric constant incorporating core specimen dimensions and the elliptical fault surface area, shear band thickness and the measured core permeability:

$$k_{\text{fault}} = \left(\frac{A_{\text{core}}}{L A_{\text{fault}}} \right) k_{\text{core}} \varepsilon \quad (3)$$

Cataclastic intensity measurement

Rosin & Rammler (1933) developed a distribution function for broken coal which they later claimed to be 'a universal law of size distribution valid for all powders, irrespective of the nature of the material and the method of grinding'. For a mass of particles (the percentage oversize or residue, R) whose diameter is greater than a stated size, x, Rosin & Rammler deduced from probability considerations that the residual weight distribution is governed by the law:

$$R = 100 - G(x) = 100 \mathrm{e}^{-bx^n} \quad (4)$$

where G is the total weight of particles in the sample and n and b are constants, n being independent of fineness but characteristic of the

material, and b increasing with increasing fineness, thus being comparable to a measure of spread. The distribution (Eqn 4) can be represented in iterated logarithmic form as a straight line relationship between R and x:

$$\log[\log(100/R)] = \log(b) + \log[\log(e)]$$
$$+ n\log(x) \quad (5)$$

Bennett (1936) provided a physical interpretation of the constants in the above Rosin–Rammler law, calling n the 'distribution constant' and $\bar{x} = [1/(n\sqrt{b})]$ the 'absolute size constant'. For theoretically perfect grading so that all the particles are the same size, $n \to \infty$; for a material obeying the simple exponential law $n = 1$ with steady size reduction; whilst for more rapid size reduction, $n < 1$, characteristic of a 'dusty' material. Thus the distribution constant, n, standing for the distribution of size, is a measure of the closeness of grading and fixes the distribution of particle size: the greater its value the more closely sized the material, the smaller its value the more dispersed the sizes. The absolute size constant, $\bar{x}$, measures the actual size of the material, large values meaning coarse material and small values fine material. Rewriting Eqn 4 in terms of the absolute size constant, $\bar{x}$, gives:

$$R = 100\exp\left[-\left(\frac{x}{\bar{x}}\right)^n\right] \quad (6)$$

The peak of the particle size weight distribution curve is theoretically for $n = 1$ at $R = 100/e = 36.8\%$, for if we denote the mode of the distribution curve by $\bar{x}$, then Eqn 6 becomes for $n = 1$, $R = 100e^{-1} = 36.8\%$. Bennett observed that the sieve opening $\bar{x}$ corresponding to R = 36.8% could be conveniently used as a characteristic of the degree of comminution of the material, and since the slope of the straight line on the Rosin–Rammler graph depends upon the range of particle size, the ratio of the angle α ($n = \tan\alpha$) and the mode $\bar{x}$ epitomizes very effectively the distribution curve as regards both mode and range of particle size. Herdan (1960) likened the quantity $(\alpha/\bar{x})$ to a quasi-'coefficient of variation', enabling direct comparison of the degree of dispersion (slope of the line) in samples from different materials which may possess different modes (position of the line). Thus, as noted by Herdan, characterization of particle size distribution by means of $(\alpha/\bar{x})$ has a powerful potential for tracking and describing the process of grinding. In this study, $(\alpha/\bar{x})$ is used to quantify the 'intensity of cataclasis' of experimentally produced fault gouge.

Equipment configuration

Stress-sensitive core plug permeability measurement

Coupled permeability measurement and microseismics monitoring of Clashach specimens, fractured and sheared under triaxial stress states of varying magnitude, was achieved within the experimental 'wet' rock mechanics facility shown schematically in Fig. 2, and described below. The system centres around a 1000 kN stiff, servo-controlled hydraulic press which generates an axial load parallel to the rock specimen long axis, whilst independently, uniform radial confining pressure is applied to the curved surface of the rock specimen via a servo-controlled hydraulic pressure vessel, rated to 68.9 MPa (10 000 psi).

Permeability measurement utilized a peripheral pulse-decay system as opposed to a steady-state procedure for shear band permeability quantification. Traditionally, liquid permeabilities are determined by the steady-state dynamic displacement technique, whereby the rate of flow through a core sample is monitored as a function of the applied constant pressure gradient, so that permeability is readily computable through application of Darcy's law to the rate and pressure data. During such measurements, however, relatively large permeant volumes have to be passed through the sample before rate and pressure stability is achieved, resulting in a real potential for damage to fine pore structure due to the passage of large pore fluid volumes, and especially in fines migration throughout the core plug. Consequently the transient pulse-decay technique is far better suited to the estimation of shear band permeabilities from axial core plug measurements.

With reference to Fig. 2 the system is based around a high pressure/low volume syringe pump able to deliver at a constant flow rate to the specimen's upstream end, at pore pressures up to 68.9 MPa (10 000 psi) and on a differential pressure transducer able to measure a differential pressure across the specimen ends of up to ±0.7 MPa (100 psi) over the system pressure. A chart recorder is used to provide a hardcopy pressure–time decay curve, the integration of which provides a measure of plug permeability. In order to keep the experimental methodology as simple as possible, each test was conducted under drained conditions with the downstream reservoir open to atmosphere, so that effectively zero pore pressure was maintained throughout the core specimen for all tests reported here.
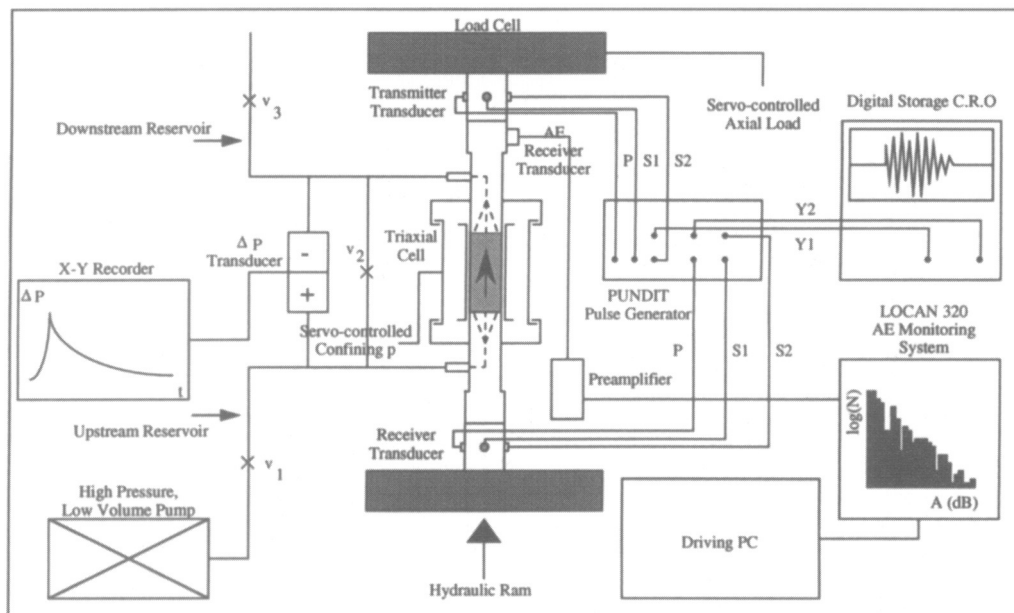
Fig. 2. Schematic illustration of the experimental rock mechanics testing facility, showing peripheral transient permeability and microseismic monitoring systems.

Peripheral active (compressional- and orthogonal shear wave velocity measurement) and passive (acoustic emission monitoring) microseismic systems allow measured changes in permeability, resulting from variation of the experimentally applied triaxial effective stress state, to be related to microstructural deformation occurring in response, within the rock specimen. Equipment specifics and results from the active and passive microseismic systems can be found in Crawford *et al.* (1995) and Liakopoulou-Morris *et al.* (1994) respectively, and will not be discussed further here.

Fault gouge laser particle sizing

To characterize fault gouge size distributions, a high-resolution 'Mastersizer' laser light scattering-based particle size analyser, commercially available from © Malvern Instruments Ltd, was employed. The system utilizes composite laser light diffraction patterns produced by the dispersed particles to compute size distributions. Figure 3 is a schematic representation of the device.

The Mastersizer has three standard user-defined size ranges: 600–1.2, 180–0.5 and 80–0.1 μm. It cannot simultaneously cover the complete dynamic range in one measurement,

so the total span is broken down into the above size ranges, each selected by fitting the appropriate receiver lens, of focal length 300 mm, 100 mm and 45 mm respectively. The Mastersizer employs two forms of optical configuration to achieve its wide range. Whilst conventional Fourier optics are used for the two greater focal length lenses, the 45 mm lens utilizes a reverse Fourier optical configuration to minimize aberrations associated with large angle scattering detection (typically >10°) from small particles. When a particle scatters light, in this case sourced from a low-powered laser, it produces a unique light intensity characteristic with angle of observation. This light is scattered so that the measured energy on a detector has a peak at a favoured scattering angle which is related to the particle diameter. Large particles have peak energies in small angles of scatter and vice versa for small particles. In Mastersizer the range of detection has been extended to in excess of 50° in order to measure sizes down to 0.1 μm.

The conventional Fourier optical configuration is shown schematically in Fig. 3. Laser light (2 mW He-Ne laser of 633 nm wavelength) is used to form a collimated and monochromatic beam known as the 'analyser beam'. Any particles present within the analyser beam will scatter the laser light. The light scattered by the particles and the unscattered remainder are incident onto
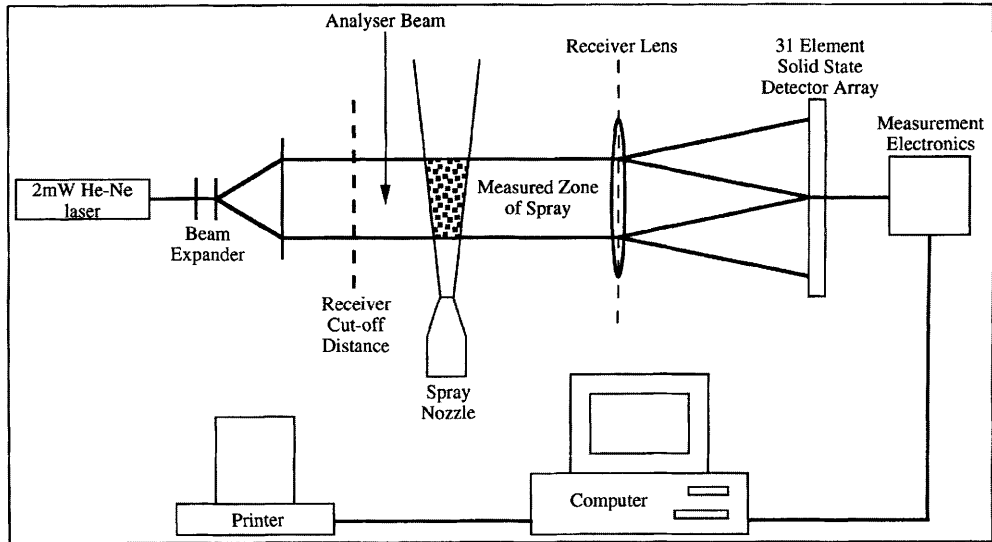
Fig. 3. Schematic illustration of the optical configuration employed for laser particle sizing, comprising a sample recirculating system, an optics module and a microcomputer.

a receiver lens known as the 'range lens', which operates as a Fourier transform lens, forming the far-field diffraction pattern of the scattered light at its focal plane, where a 31-element solid-state detector, in the form of a series of 31 concentric annular sectors, gathers the light over a range of solid angles of scatter.

The time-averaged diffraction pattern shape is a convolution of the contributions of all of the particles of the composite sample. Signals from the measurement windows are deconvolved into a multichannel histogram of the particle size distribution by a complex algorithm. The algorithms used to calculate particle size distribution from composite diffraction patterns are manufacturer-dependent and proprietary; however, from relationships in Weiss & Frock (1976) it is evident that the angle through which the light is diffracted is inversely related to particle size, and the diffracted light intensity is directly related to particle quantity. For a detection range which has been extended up to $>50°$ in order to measure down to $0.1\,\mu m$, the scattering from such small particles at such high angles becomes heavily dependent on the optical properties of the material, necessitating use of the 'Mie' optical theory to model light scattering. Mie theory is an exact solution to Maxwell's equations for the case of a spherical particle, providing a complete description of the light scattering from optically homogeneous spheres, and requires data input on the differential refractive index between dispersant and particle, and particle absorption

Thus it is possible for the computer to predict the scattering signal that would be received from a wide range of materials at a given size. It formulates a table that characterizes how a unit volume of material, of a range of sizes throughout the working range, scatters light. Using this theoretical data, the computer deduces the volume size distribution that gives rise to the observed scattering characteristics by a process of constrained least squares fitting of the theoretical scattering characteristics to the observed data. This best fit result can either be obtained with no assumed form of size distribution (model-independent) allowing the characterization of multimodal distributions with high resolution, or else the analysis can be constrained to three known forms of volume distribution, the normal, log-normal or Rosin–Rammler, in which volume distribution is constrained to have a single peak which can be completely specified by two parameters of a characterizing equation, describing the position of the peak on the size scale and the width of the distribution.

Experimental methodology

The development of macroscopic shear faulting is examined over a timescale of a few tens of minutes, under servo-controlled triaxially com-
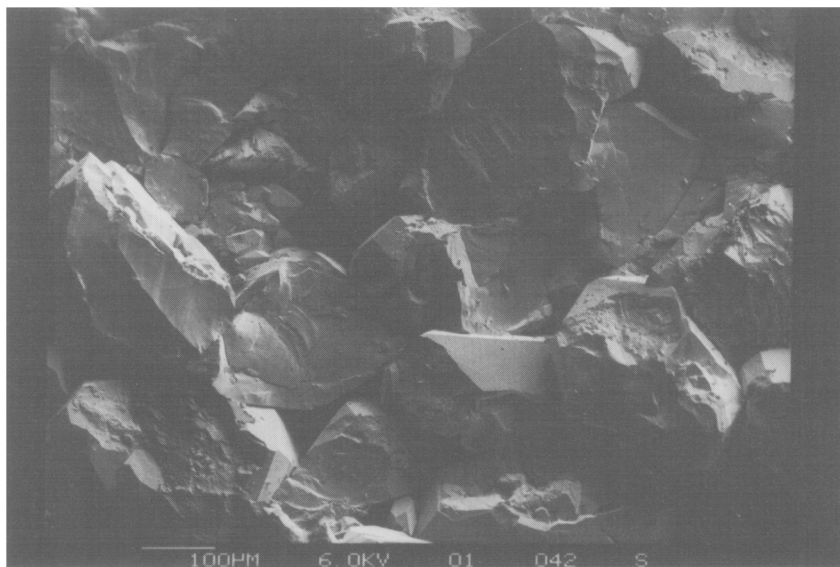
Fig. 4. Scanning electron photomicrograph of a fresh fracture face of undeformed Clashach sandstone, illustrating the nature of its primary porosity.

pressive stress states applied to initially intact specimens of relatively homogeneous Clashach sandstone, saturated in a chemically inert pore fluid (oil). In this paper the influence of triaxial stress magnitude on fluid permeability is examined, with particular regard to the structural effects of sliding-induced fault gouge characteristics on shear band permeability. In a paper (Liakopoulou-Morris *et al.* 1994) describing the same suite of tests, natural acoustic emission (AE) results are interpreted in terms of a mean field theory for damage evolution (Main 1991).

Test specimens were sourced from the Clashach commercial quarry, near Hopeman Village in the Elgin area of NE Scotland. Stratigraphically the test rock-type is drawn from the Hopeman Sandstone, which outcrops in Permo-Triassic aeolian outliers on the shores of the Moray Firth basin (Lovell 1983). The Clashach sandstone is a pale-fawn homogeneous (on the core plug scale), high-porosity (*c.* 18–21%), well-sorted, medium- to coarse-grained subarkosic arenite, composed predominantly of subrounded quartz grains (*c.* 90%) and fresh to altered potassium feldspar (*c.* 10%). Detrital grains appear hardly affected by diagenetic changes, except for the presence of well-developed secondary quartz overgrowths in optical continuity with the host grains. Figure 4 shows a scanning electron photomicrograph of a broken surface of Clashach sandstone, illustrating the nature of its primary porosity. Right-

cylindrical cores were taken at 38.1 mm (1.5 inch) diameter (length-to-diameter ratios of 2:1) from a single recovered block, and were prepared with flat and parallel end-faces. After preparation, the plugs were oven-dried at 100°C for 24 hours, prior to being saturated under vacuum with a refined mineral oil (Shell Tellus Oil 15).

Each specimen was subjected to a three-stage stress path as illustrated schematically in Fig. 5. The aim of the above test procedure was to allow comparison of fluid transport and of acoustic properties measured following Stage I fault nucleation, Stage II dynamic slip weakening, and Stage III reshearing after mechanical strengthening. Following Stage II residual sliding and permeability (C) measurement, the confining pressure was increased by an arbitrary 6.9 MPa (1000 psi) prior to Stage III sliding and permeability (D) determination. This had the effect of mechanically strengthening the fault, and mimics to some extent the quasi-static strength recovery which may result in the Earth from combined physico-chemical processes over larger timescales.

Whilst transient permeability measurements were conducted under constant triaxial stress states by holding the applied axial load, AE was monitored over conditions of changing triaxial stress, associated with a constant rate of axial specimen shortening ($\approx 1.25\,\mu m$ per second). As depicted in Fig. 5, four transient
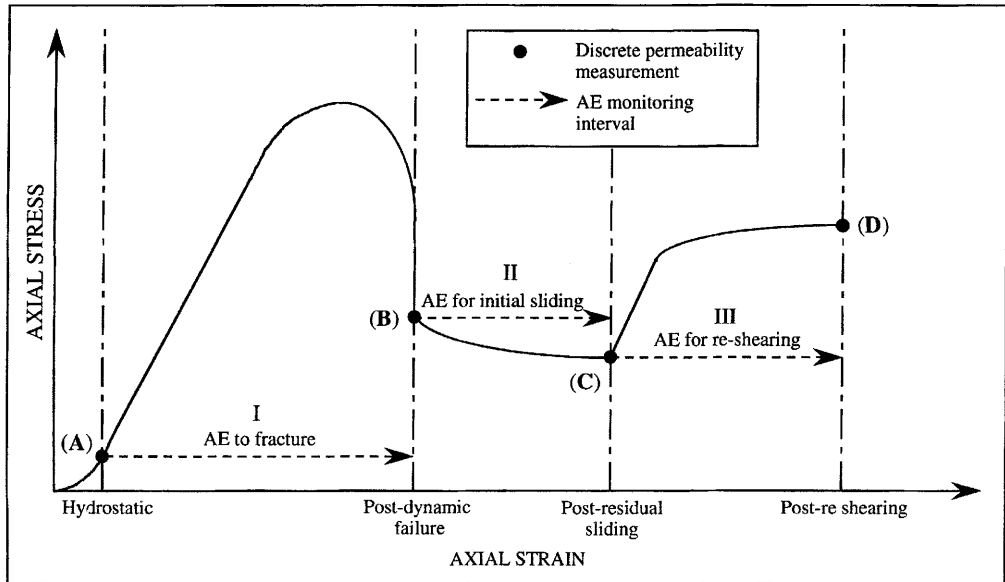
Fig. 5. Schematic illustration of the experimental programme for coupled permeability and microseismics triaxial compression testing.

plug permeabilities were taken for each discrete specimen tested, under constant stress conditions corresponding to: (A) hydrostatic; (B) immediate post-dynamic failure; (C) post-initial slip weakening; (D) post-reshearing on mechanical strengthening.

In total, seven Clashach sandstone specimens were tested, with the magnitude of the initial hydrostatic stress state representing the principal experimental variable (Table 1). From this it is evident that five specimens were tested under initial confining pressures of 6.9, 20.7, 34.5, 48.3 and 62.1 MPa (1000, 3000, 5000, 7000 and 9000 psi respectively) whilst a further two dupli-cate specimens were also tested under 20.7 MPa

and 62.1 MPa pressures, to check data repro-ducibility. With a maximum applied confining pressure following mechanical strengthening of 68.9 MPa (10 000 psi) representing the upper working limit of the pressure vessel, the experi-ments therefore mimicked an *in situ* depth ranging from approximately 0.3 km to 3 km (based on an overburden stress gradient of 1.0 psi/ft and assum-ing a uniform increase in overburden stress with depth).

Following unloading of each test specimen, a 'post-mortem' examination of the induced fault gouge was conducted using laser particle sizing techniques. The powdered comminution products were washed from both the upper and

Table 1. *Summary table of initial confining pressures for permeabilities (A), (B) and (C) and final confining pressures for post-reshearing permeability (D)*

Specimen I.D.	Confinement permeabilities A, B & C phases I & II MPa (psi)	Confinement permeability D phase III MPa (psi)
#15	6.9 (1000)	13.8 (2000)
#16	34.5 (5000)	41.4 (6000)
#18	48.3 (7000)	55.2 (8000)
#19	20.7 (3000)	27.6 (4000)
#20	62.1 (9000)	68.9 (10 000)
#21	20.7 (3000)	27.6 (4000)
#22	62.1 (9000)	68.9 (10 000)

lower shear fracture wall rock faces using acetone. The powder/organic solvent mixture was then placed in a sonic water-bath to separate any remnant oil permeant from the gouge sample. The powder was then dried in an oven at 100°C for 24 hours before being sieved into $>500\,\mu m$ and $<500\,\mu m$ fractions, the latter being used for particle sizing analysis.

Results

Transient permeability

The influence of applied stress state on axial liquid permeability is shown in Fig. 6. In plot (a) permeability (A) values are graphed against the hydrostatic stress magnitudes at which each was measured, whilst immediate post-dynamic faulting permeability (B) values are graphed against normal stress magnitudes resolved across the induced faults. The shear stress, τ, and normal stress, σ_n, may be computed from knowledge of the applied principal stresses σ_1 and σ_3, and of fault inclination with respect to the direction of maximum compression, $\theta = $ fault σ_1, using the well-known biaxial stress equations (e.g. Byerlee 1967).

From Fig. 6a it is evident that the magnitude of hydrostatic stress has no effect on initial permeability (A) which ranges between 685 mD (#22) and 1037 mD (#20), most likely reflecting a variation in initial rock microstructure. Here compaction is probably accommodated via elastic pore closure, so that for the relatively high-porosity Clashach rock-type, although pore size may be decreased, connectivity and hence permeability will remain relatively unchanged.

In contrast, following immediate dynamic fault formation with minimal frictional sliding, permeability (B) measurement shows a moderate linear negative correlation with normal stress resolved across the failure plane. In Fig. 6b post-slip weakening and post-reshearing permeabilities (C) and (D) respectively are also plotted against normal stress, the correlations appearing considerably improved with frictional sliding. Whilst it is tempting to assign these axial plug permeability versus stress correlations solely to the development of a layer of comminuted frictional wear debris along each fault plane, the dependency of (B) on σ_n suggests that an additional stress-sensitive variable might also be instrumental in controlling the measured reductions in axial permeability. Little fault gouge would be expected to have developed at the stage of permeability (B) measurement, frictional sliding on the fault plane being only about 0.01 to

0.1 mm (from knowledge of a measured axial specimen shortening, $\Delta\ell_a$, the slip displacement, δ_s, on a shear plane inclined at an angle, θ, can be ascertained from application of elementary trigonometry as being $\delta_s = \Delta\ell_a / \cos\theta$).

Fault inclination, θ, was also found to be stress-sensitive, and increased systematically from 20° to 40° with increasing σ_3, as a consequence of the parabolic Griffith-type fracture strength envelope, the slope of which decreases with increasing σ_3 (see the discussion in Paterson (1978, pp 24–28) on the relation between fracture inclination and slope of the failure envelope). This stress-dependency is immediately imparted to fault orientation, θ, and hence to fault area, A_{fault}, which is a variable in Eqn 3. Thus defining a 'geometric constant', $G = [A_{core}/(LA_{fault})]$ in Eqn 3 where k_{core} varies inversely with G, it is probable that the inverse relationship between permeability (B) and normal stress is due to the stress-dependency transmitted to the geometric constant, as a result of θ increasing with σ_3. This inverse relation between k_{core} and G will also exist for permeabilities (C) and (D), tending to mask any stress dependency associated with the shear band, k_{fault}. Thus to investigate the control of triaxial stress state on induced fracture permeability, in terms of potentially stress-sensitive fault gouge characteristics, geometric variability must also be accounted for via Eqn 3, necessitating estimation of shear band thickness, ε.

Rosin–Rammler distribution functions

As far as is known, the first published example of the application of laser sizing technology to rock fragmentation is that of Crawford et al. (1994), who studied the relation between frictional strength of a wide variety of lithologies measured under direct shear conditions, and the distribution characteristics of their resultant frictional wear products. Unlike the direct shear specimen study, in which the analysis mode was set to model-independent, so that no assumptions were made about the form of each result with regard to its distribution, for the Clashach suite the Rosin–Rammler two-parameter analysis model was selected, constraining the volume distribution to have a single peak completely identified by the two parameters $\bar{x}$ and n (describing the position of the peak on the size scale and the width of the distribution respectively).

Graphical representation of the Mastersizer Rosin–Rammler particle size distribution analyses are given in Fig. 7a and b for the 300 mm and 45 mm range lenses respectively. Tabulated
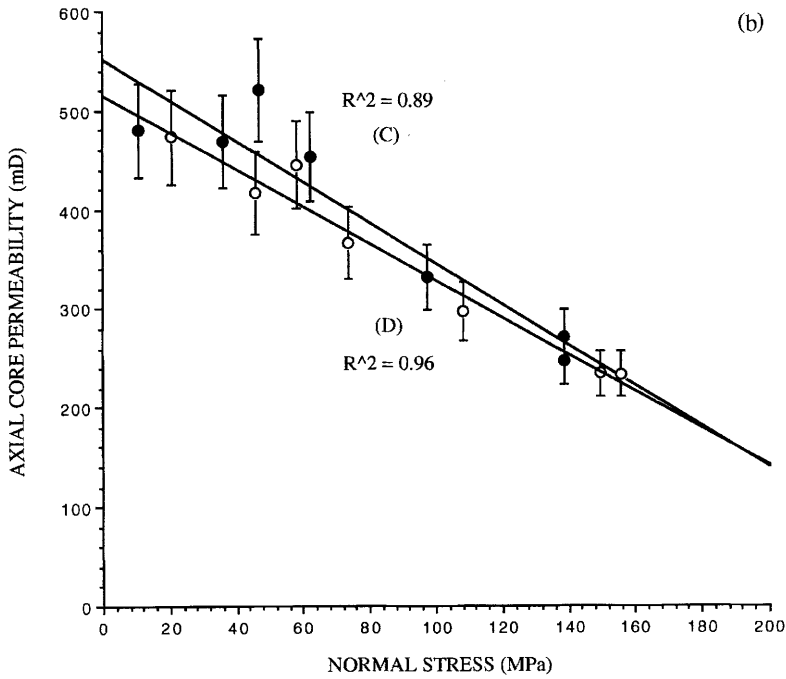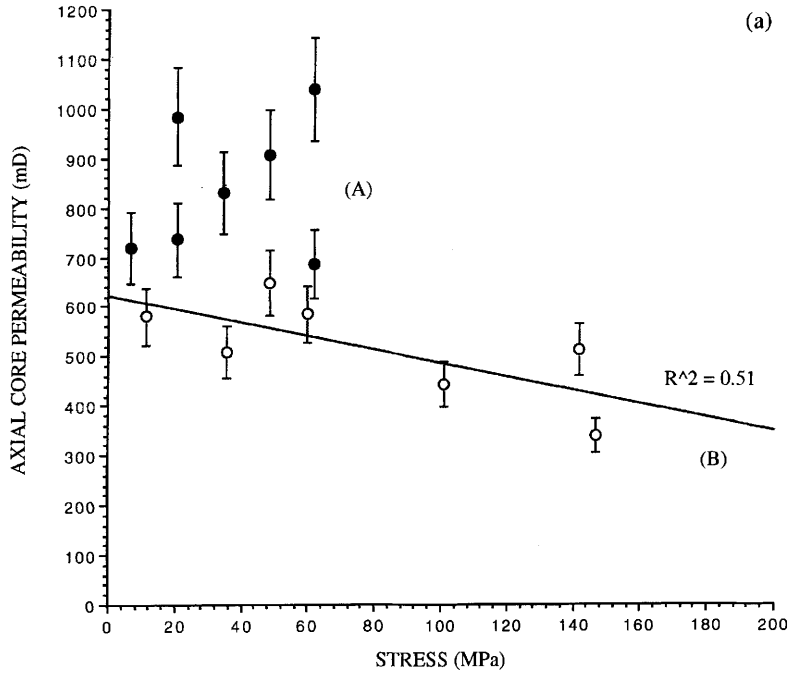
Fig. 6. Influence of applied stress state on core plug axial liquid permeability: (**a**) permeability (A) versus hydrostatic stress plus permeability (B) versus resolved normal stress ● (A) hydrostatic; ○ (B) post-dynamic failure; (**b**) permeabilities (C) and (D) versus resolved normal stress, ● (C) post-residual sliding; ○ (D) post-reshearing.
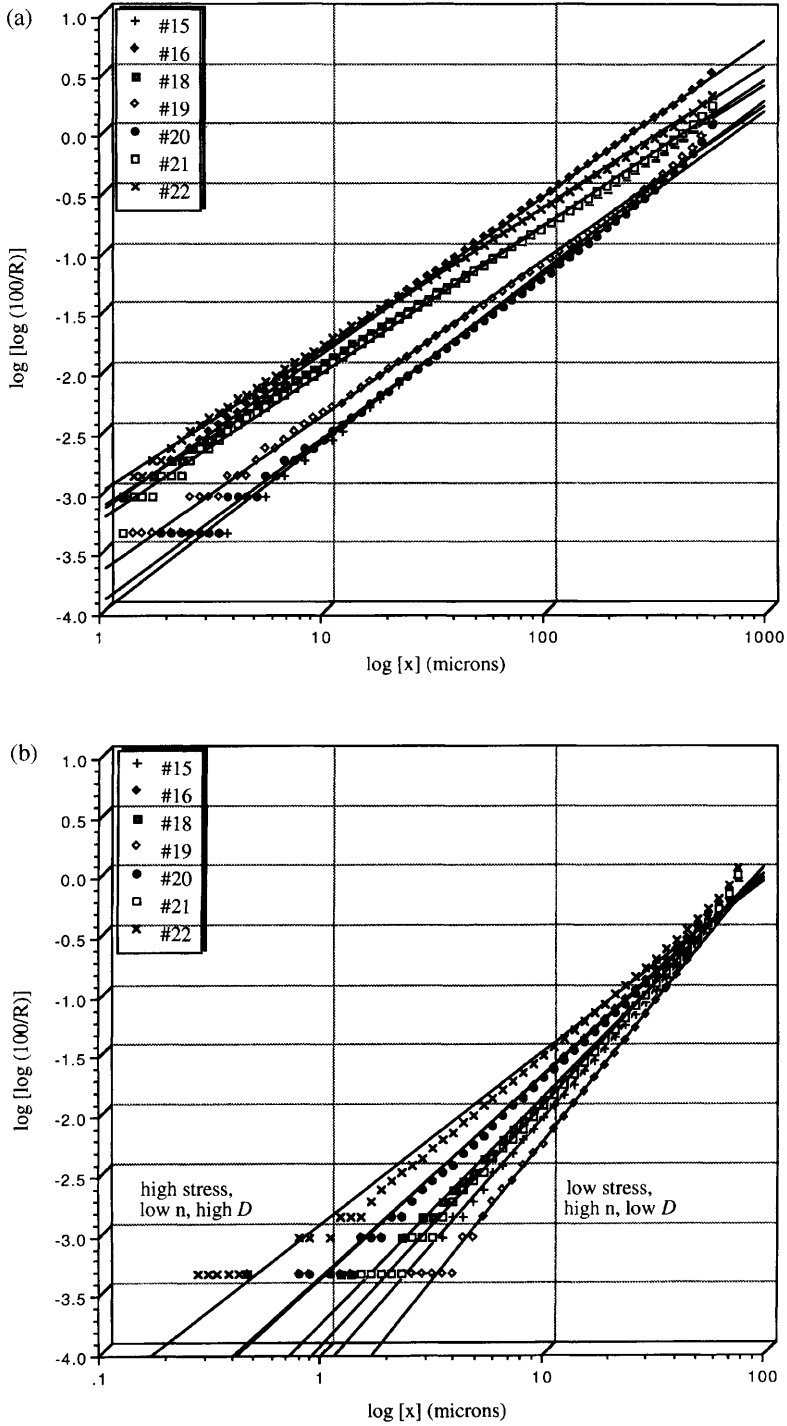
Fig. 7. Straight-line graphical representations of the Rosin–Rammler function for laser sized fault gouge distributions: (**a**) 300 mm range lens giving 500–1.2 μm particle size range; (**b**) 45 mm range lens giving 80–0.1 μm particle size range.

Table 2. *Tabulated Rosin–Rammler constants for laser sized fault gouge distributions*

Specimen I.D.	n	$\alpha(°)$	b	$\bar{x}$ (μm)	$(\alpha/\bar{x})$
$f = 300$ mm range lens $1.2 < x < 600 \,\mu$m					
#15	1.43	55	2.29e-4	347	0.16
#16	1.32	53	1.62e-3	130	0.41
#18	1.18	50	1.74e-3	219	0.23
#19	1.30	52	5.12e-4	341	0.15
#20	1.38	54	2.81e-4	381	0.14
#21	1.23	51	1.36e-3	213	0.24
#22	1.19	50	2.39e-3	163	0.31
$f = 45$ mm range lens $0.1 < x < 80 \,\mu$m					
#15	2.12	65	1.76e-4	59	1.09
#16	1.70	60	1.03e-3	57	1.04
#18	1.89	62	4.25e-4	61	1.03
#19	2.32	67	7.16e-5	62	1.08
#20	1.68	59	1.04e-3	60	0.98
#21	2.01	64	2.87e-4	58	1.10
#22	1.44	55	2.87e-3	58	0.96

constants n, α, b, $\bar{x}$ and $(\alpha/\bar{x})$ are presented in Table 2. From the particle size distribution plots and tabulated Rosin–Rammler constants, it is evident that the 300 mm range lens data show a relatively wide spread in actual particle size, as denoted by the position of each line, with $\bar{x}$ ranging from 130 μm to 380 μm, whilst the between-specimen distribution of particle size remains relatively constant, with $n \approx 1.3 \pm 0.1$. In direct contrast, however, the 45 mm range lens data show relative uniformity in absolute particle size, $\bar{x} \approx 59 \pm 2$, whilst between-sample distribution contrasts, denoted by variance in the slope of each line, show n ranging broadly from 1.4 to 2.3. Thus the relatively large size range data $(1.2 < x < 600 \,\mu$m$)$ imply a wide diversity in the coarseness of the fault gouge from sample to sample, with, however, all samples showing the same closeness of grading, whereas the relatively small size range data $(0.1 < x < 80 \,\mu$m$)$ imply a similar degree of fineness for all samples but a spread in their individual size reduction characteristics.

## Shear band permeability estimation

Thickness determination

As fault gouge induced by frictional slip of the Clashach specimens was removed for laser particle sizing, no quantitative estimation of shear band thickness could be made with any accuracy, so that, instead, two additional, identical specimens (#23R and #24R) were subjected to the same stress paths, at initial confining pressures of 6.9 MPa (1000 psi) and 62.1 MPa

(9000 psi) respectively, representing the minimum and maximum triaxial stress states imposed on the specimens in which permeability was measured. Specimens #23R and #24R (also saturated with Shell Tellus mineral oil under drained conditions with the downstream end open to atmosphere), following removal from the pressure vessel, were then washed in acetone to remove the oil pore fluid, dried and injected with a low-viscosity epoxy resin. Thin sections were prepared from these resin-impregnated specimens, so that the plane of the section was taken perpendicular to the strike of the induced fault plane. From such sections, the observation was made that specimen #23R, sheared at a relatively low normal stress magnitude, produced a relatively thick shear band compared with specimen #24R, sheared under a seven times greater normal stress level. The thickness of the shear band granulated zone approximately perpendicular to the bounding wall rock was measured from thin section under 25× magnification, at regular 0.2 mm intervals along the fault zone. This was achieved by drawing chords on a captured video image of each thin section, utilizing an image processing and analysis program.

Thin section photomicrographs of shear bands from specimens #23R and #24R are shown in Fig. 8a and b respectively. Mean shear band thickness for #23R was measured at 1.00 mm with a population standard deviation of 0.31 mm. This shear band, displaced under conditions of low normal stress, exhibits relatively rough bounding wall-rock surfaces (reflected in the high thickness standard deviation) and shows numerous intact quartz grains 'floating' within the gouge zone of cataclastically comminuted debris, indicating
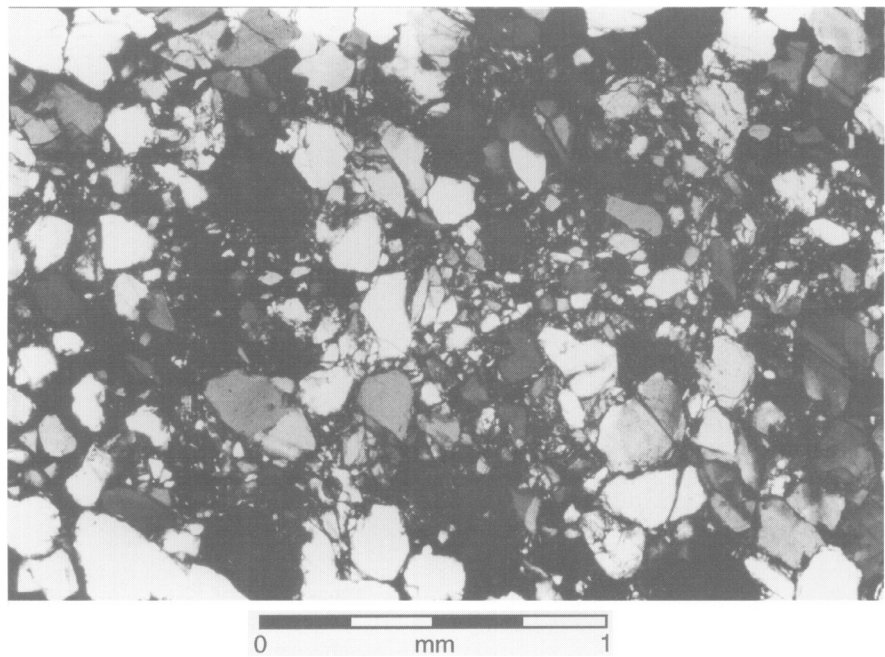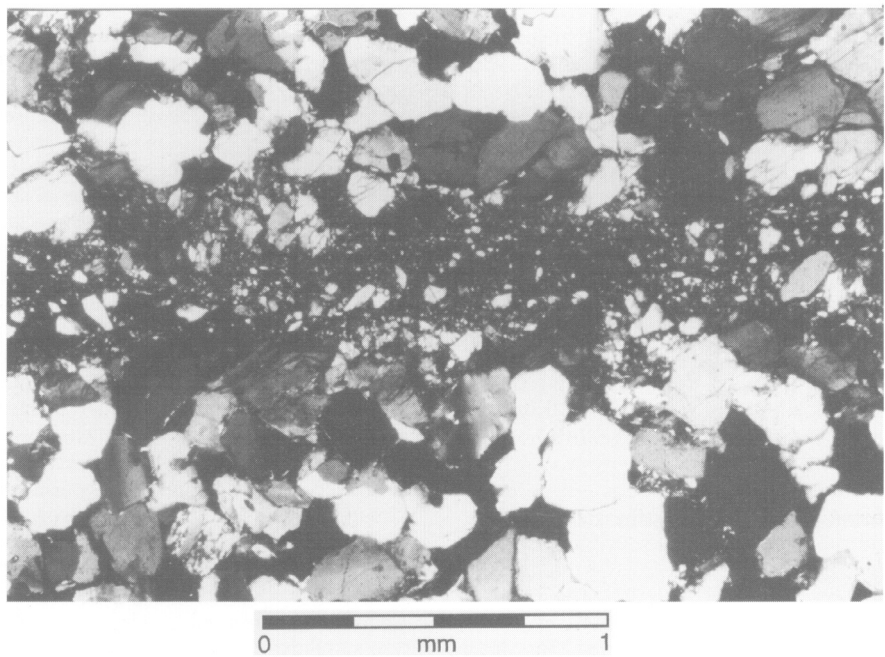
Fig. 8. Thin section photomicrographs of resin-impregnated shear bands: (a) specimen #23R mechanically strengthened under 13.8 MPa (2000 psi); (b) specimen #24R mechanically strengthened under 68.9 MPa (10 000 psi).
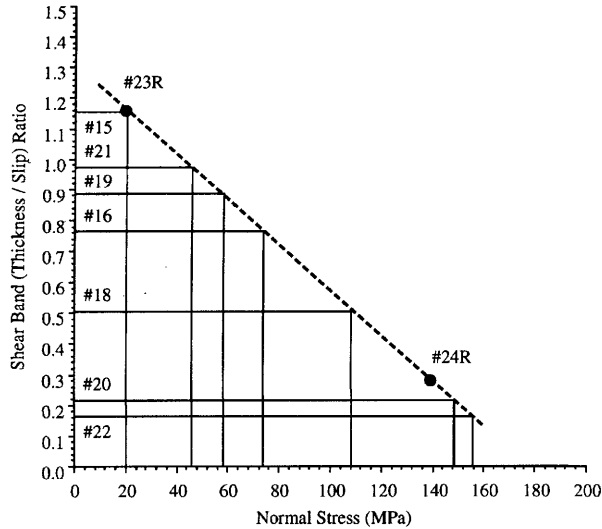
Fig. 9. Shear band thickness/slip (ε/δ_s) ratios versus resolved normal stress.

that both grain-boundary sliding and intra-granular fracturing contributed to the cataclastic deformation mechanism. Mean shear band thickness for #24R was measured at 0.31 mm with a population standard deviation of 0.13 mm; that is, at higher normal stress levels fault thickness has been suppressed to around one-third of that observed at low stress levels. The shear band formed within specimen #24R appears highly localized, with smooth, planar and sub-parallel wall-rock surfaces, bounding a gouge zone composed of highly comminuted grain fragments in which intra-granular cracking has exclusively dominated the cataclastic process. Such observations are supported by those of Tullis & Yund (1992) on the effects of an increasing σ_3 on the nature of faulting in feldspar (Bushveld anorthosite) aggregates. Tullis & Yund noted that at lower pressures the gouge zone was wider, which they attributed to its development from more irregular surfaces which break off more material as they slide, whilst at higher pressures the faults were sharp and smooth from the start, so that they could slide with less gouge development.

In order to estimate the shear band thicknesses of Clashach specimens #15 to #22, from upper (specimen #23R, low normal stress) and lower (specimen #24R, high normal stress) limiting thickness determinations derived from thin section measurements, (ε/δ_s) values for #23R and #24R were plotted against the resolved normal stress magnitudes recorded for reshearing conditions under confining pressures of 13.8 MPa (2000 psi) and 68.9 MPa (10 000 psi)

respectively (Fig. 9). The simplest case of a linear negative correlation between (ε/δ_s) and σ_n was assumed, so that laying off of the known σ_n magnitudes for specimens #15 to #22 yielded corresponding (ε/δ_s) values from which thickness estimates could be derived by multiplying by the measured slip displacement.

Fault sealing potential

Thickness/slip ratios (ε/δ_s) can also be expressed in terms of shear strain, $\gamma = \delta_s/\varepsilon$, and angular shear strain, $\Psi = \tan^{-1}\gamma$. Tabulated values of shear and normal stress magnitudes for reshearing, slip displacements, estimated shear band thicknesses and resultant angular shear strains are presented in Table 3. Estimates of shear band permeability can thus be made by substituting measured core plug permeability values, geometric constants and estimated thicknesses into Eqn 3. Only reshearing core permeabilities (D) are suitable for shear band permeability estimation, as the microstructures associated with thickness determination correspond to end frictional sliding conditions only. An indication of fault sealing potential which encompasses any initial between-sample variations due to microstructural dissimilarities between specimens, can be gained by normalizing each estimate of fault permeability $k_{\text{fault}}(D)$ by the permeability values measured under initial hydrostatic stress conditions $k_{\text{core}}(A)$. Shear band permeability estimates and fault sealing

Table 3. *Stress, strain and permeability values for shear bands induced under triaxial compression*

Specimen I.D.	τ (MPa)	σ_n (MPa)	θ (°)	δ_s (mm)	ε (mm)	Ψ (°)	k_{core}(A) (mD)	k_{core}(D) (mD)	k_{fault}(D) (mD)	$\dfrac{k_{fault}(D)}{k_{core}(A)}$ (%)
#15	18.6	20.6	20	1.02	1.18	41	720	473	2.49	0.35
#16	55.9	73.7	30	1.06	0.81	53	828	365	2.16	0.26
#18	75.8	108.3	35	1.23	0.62	63	903	296	1.27	0.14
#19	53.1	58.3	30	1.01	0.88	49	982	444	2.50	0.26
#20	95.9	149.3	40	1.03	0.21	78	1036	235	0.43	0.04
#21	39.6	46.0	25	0.92	0.89	46	734	415	2.23	0.30
#22	103.4	155.6	40	1.56	0.25	81	684	234	0.51	0.08

potentials (expressed as percentages of hydrostatic permeabilities) are also given in Table 3 for reshearing following mechanical fault strengthening.

From Table 3 it is evident that percentage fault sealing potential ranges from 0.35% at low stress to 0.04% at high stress, representing a 2.5 to 3.5 order of magnitude permeability reduction due to cataclasis alone (as the pore fluids were chemically inert, both hydrolytic weakening and pressure solution are inferred to have been absent). Such magnitudes are in agreement with outcrop mini-permeameter measurements reported by Antonellini & Aydin (1994) on granulation seams in the Navajo and Entrada sandstones of the Arches National Park, Utah, where, on average, a permeability three orders of magnitude less than the host rock was quantified. Antonellini & Aydin contended that the 'intensity of cataclasis' and the clay content controlled the amount of permeability reduction as measured perpendicular to the band; however, the nitrogen mini-permeameter method is conducted under zero-stress conditions so that extrapolation of measured magnitudes to reservoir conditions is necessarily tenuous. In contrast, the Clashach triaxial compression measurements, conducted under stress states associated with shear slippage, show an order of magnitude dependency on applied stress, as illustrated in Fig. 10a where sealing potential, permeability $k_{fault}(D)/k_{core}(A)$%, is plotted against normal stress resolved across the fault, giving a robust linear negative correlation. The effect of the main experimental variable, that of applied triaxial stress state, is also evident in first-order control on both fault inclination and thus on slip displacement (axial closure being the experimentally controlled parameter) as well as on shear band thickness. Taken together, such trends in the magnitude of both δ_s and ε result in a wide between-specimen variability in angular shear strain, Ψ. Thus sealing potential

$k_{fault}(D)/k_{core}(A)$% also shows a strong linear negative correlation with Ψ, as illustrated in Fig. 10b.

Discussion

Degree of cataclastic intensity

In Fig. 11, the 'coefficient of variation' $(\alpha/\bar{x})$ for both the 300 mm and 45 mm range lens data is plotted against (a) normal stress resolved across each shear band, σ_n, and (b) the total angular shear strain, Ψ, imposed on each shear band. Strong linear negative correlations are evident between $(\alpha/\bar{x})$ measured on the 45 mm range lens, and both variables σ_n and Ψ. No such correlations were evident for the 300 mm range lens data. This correlation for $(\alpha/\bar{x})$ determined on particle size ranging from 80 tp 0.1 μm as opposed to the lack of correlation shown by $(\alpha/\bar{x})$ determined on particle size ranging from 600 to 1.2 μm, may be attributed to the fact that the lower size range represents 100% cataclastic products, whereas the larger size range includes both remnant intact grains as well as comminuted grains.

It is evident that for the 45 mm range lens, $(\alpha/\bar{x})$ represents the inverse of 'cataclastic intensity' (modal size $\bar{x}$ approximately constant, α decreasing with increasing rate of size reduction) so that the lower the value of the ratio $(\alpha/\bar{x})$, the greater the degree of comminution. Marone & Scholz (1989) investigated the comminution of simulated fault gouge (Ottawa sand with >99% quartz) under triaxial compression, between rough steel surfaces at 45° to the axis of a cylindrical sample. They found that the fractal dimension, D of the gouge increased from $D = 1.6$ with increasing shear strain to Ψ values of about 52° to 56°, then levelled off to an asymptotic value of $D \sim 2.8$ thereafter (the greater the magnitude of D, the greater the number of small fragments
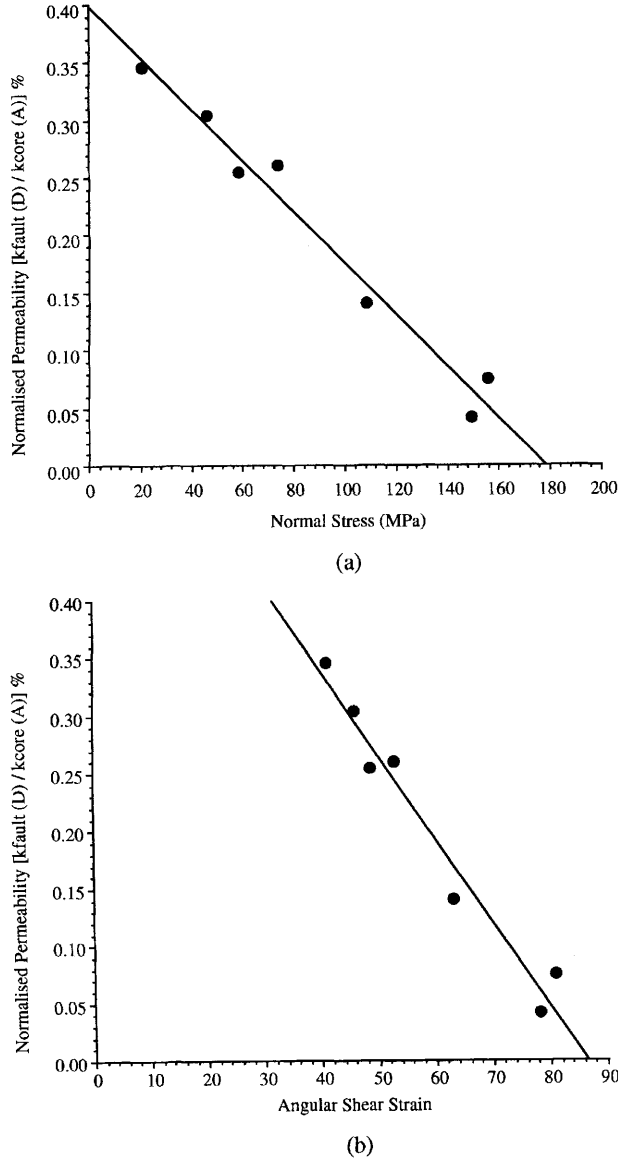
Fig. 10. Sealing potential $k_{fault}(D)/k_{core}(A)\%$ versus: (**a**) resolved normal stress; (**b**) angular shear strain.

relative to large fragments, therefore D varies inversely with n (Turcotte 1992, p. 22)). Marone & Scholz's observation of D increasing with increasing Ψ supports the idea that in fact shear strain represents the primary control on comminution, as all their layer shearing was conducted at a constant effective normal stress of 100 MPa. However, Sammis *et al.* (1986) found that collected samples of natural fault gouge material from the San Andreas fault zone showed a linear decrease in mean particle size with increasing confining pressure (depth) which they attributed to a suppression of micro-fracture extension and subsequent decrease in the spacing of axial microfractures with increasing confinement, leading to smaller particles being produced from denser microfractures at higher pressure. Whilst, with regard to the Clashach tests, the relative influence of a variable normal stress on frictional comminution cannot be
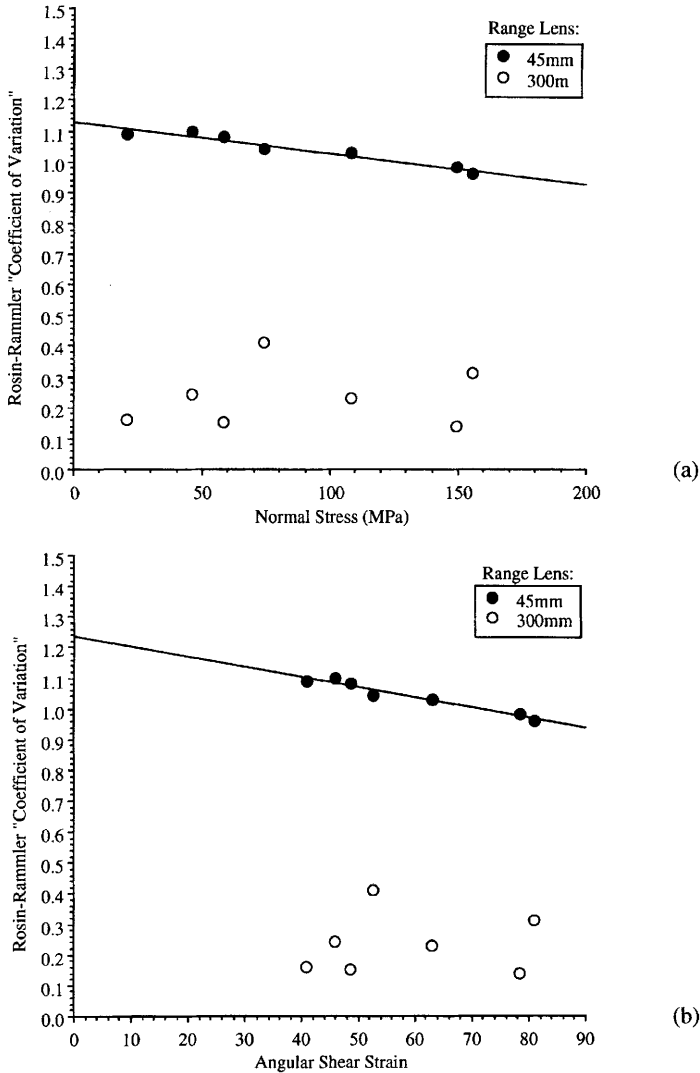
Fig. 11. Cataclastic intensity versus: (**a**) resolved normal stress; (**b**) angular shear strain.

separated from that of shear strain, the above-related studies tend to suggest that both variables will have a complementary, mutually additive, control on cataclastic intensity.

Kozeny–Carman permeability model

Whilst in the previous discussion, the intensity of fault gouge cataclasis has been quantified in terms of a 'coefficient of variation' $(\alpha/\bar{x})$ determined from laser particle sizing, the important question still remains as to what effect this intensity of cataclasis has, if any, on shear band

permeability. In Fig. 12 percentage fault sealing, $k_{\text{fault}}(\text{D})/k_{\text{core}}(\text{A})\%$, is plotted against $(\alpha/\bar{x})$. From this highly correlated direct linear relation it is evident that shear band fluid flow potential increases with increasing $(\alpha/\bar{x})$, that is the lower the degree of cataclastic intensity, the less effective the shear band cataclastic seal.

For the measurement of permeability and indirectly of the specific surface area of powder beds, Kozeny's (1927) equation for the velocity of infiltration of a fluid percolating through porous packings of solid particles has advantages over Darcy's law in that it analyses the permeability constant, k, in terms of its constituent
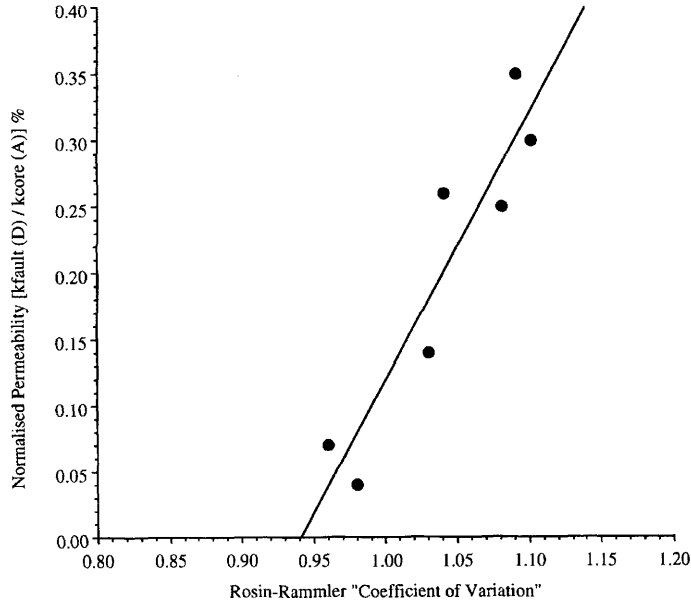
Fig. 12. Sealing potential $k_{fault}(D)/k_{core}(A)\%$ versus cataclastic intensity.

factors. The proportionality constant, k, which according to Darcy's law is a specific property of the material and independent of the viscosity of the fluid and the pressure difference, is proportional to the shape and length of the pores, to a function of the porosity (that is, of the total amount of pores as a fraction of the total volume of the packing) and inversely proportional to the square of the specific surface area of the particles forming the walls of those pores. Assuming spherical particles, the expression for permeability is written as:

$$k = c \frac{l_s}{l_w} \frac{\phi^3}{(1 - \phi)^2} \frac{1}{S_v^2} \qquad [m^2] \qquad (7)$$

where c is an integer dependent only upon the shape of the cross-sectional area of the pores, (l_s/l_w) is the ratio of the apparent straight line length to the real pore length, ϕ is porosity and S_v the specific surface area (surface area per volume of packing). This relation and its various equivalent forms are known as the Kozeny–Carman equation (see, for example, the discussion in Gueguen & Palciauskas (1994, pp. 126–133)). This relation between the permeability of a powder bed and the various parameters given in Eqn 7 can be used to gain insight into the empirically demonstrated dependence of estimated shear band permeability on the degree of fault gouge cataclasis.

Marone & Scholz note that porosity reduction within granular materials can be accommodated through either an increase in packing (a better fit between particles and thus decreased void space) or by a change in particle size distribution (sorting). For less sorted material the range of particle sizes is larger, so that smaller particles can fit between larger ones, thus reducing pore space. From the laser particle sizing studies, the intensity of cataclasis of Clashach sandstone was found quantifiable through the 'coefficient of variation' parameter, $(\alpha/\bar{x})$ varying inversely with the degree of comminution. Whilst the absolute size constant, $\bar{x}$, was found unchanging for all test specimens (porosity being independent of size anyway), the slope α was found to decrease systematically with increasing normal stress and angular shear strain, implying more rapid size reduction leading to 'dustier' powders with more dispersed size ranges. As distributions with greater size ranges possess 'poorer' sorting it is thus intuitive that porosity must be decreasing with increasing cataclastic intensity, changes in sorting occurring via particle size reduction and comminution. Thus the relationship of Fig. 12 may well reflect the permeability versus porosity relationship of Eqn 7 with fluid flow potential increasing with improved sorting. Also, it is possible that increased normal stress across the shear band may have the added effect of increasing compaction within the gouge zone, hence
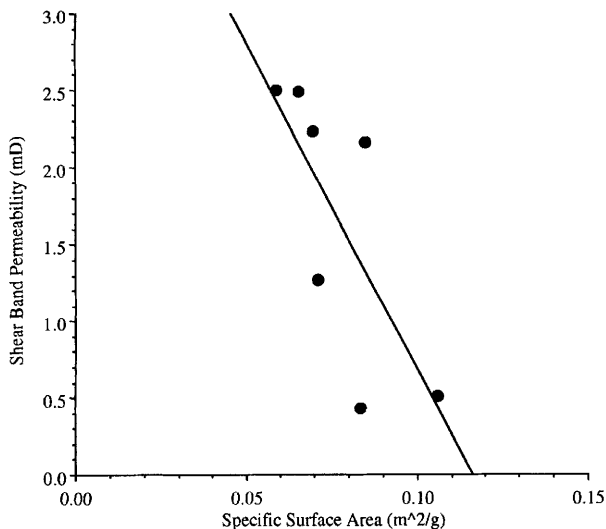
Fig. 13. Estimated shear band permeability $k_{fault}(D)$ versus specific weight surface area.

promoting grain packing over sorting as a mechanism for porosity reduction.

In addition to porosity, other parameters in Eqn 7 may have substantial control on k_{fault}. In Fig. 13, shear band permeability is plotted as a function of the specific weight surface area, S_w (the surface area per unit mass of powder, equivalent to S_v divided by the density of the single mineral phase). S_w is calculated following a method outlined in Herdan (1960, p. 193). In this plot, a negative trend is evident as predicted by Eqn 7. In Fig. 14 a scanning electron photomicrograph of fault gouge from Clashach specimen #22 is presented, to highlight the morphology of the frictional wear products. With individual particles exhibiting high angularity and complex shape, with indeed some fragments tending towards lathe-like forms, it is highly likely that tortuosity, defined as the ratio of real to apparent path length through which the fluid flows (l_w/l_s), will also be increased through comminution, with an attendant inverse effect on fluid flow. Thus the control of 'cataclastic intensity' on gouge permeability can be rationalized through consideration of the Kozeny–Carman relation. Shear band sealing potential increases with the degree of comminution, due to the production of distributions with greater size range and thus poorer sorting, resulting in greater porosity reduction. This effect is accompanied by an attendant increase in specific surface area (surface area varying inversely with particle size) and possibly a rise in tortuosity.

Laboratory to reservoir extrapolation

The sealing capacity of small-scale faulting, commonly well-developed in otherwise unimpaired, high porosity reservoir sandstone horizons, depends firstly on the petrophysical properties of the faults themselves, and secondly on their spatial distribution. In this study, the permeability characteristics of microfaults (shear bands) induced in core plugs of a clean, reservoir sandstone analogue, have been measured in the laboratory under a range of triaxially compressive stress magnitudes. Pulse-decay (refined mineral oil) permeabilities were measured across the shear bands at confining pressures ranging from 13.8 MPa to 68.9 MPa (2000–10 000 psi) corresponding to depths of 0.6–3 km. Such experimental shear bands exhibited permeabilities of 2.5 to 3.5 orders of magnitude less than that of the host rock. This rock mechanical experimental programme thus complements other published single deformation band permeability estimates based on the gas injection mini-permeameter technique, for which the sample microfault is unstressed, and arguably the internal diameter of the probe tip (typically 5 mm) results in a convolved permeability estimate consisting of both wall rock and deformation band responses.

Experimental shear bands exhibited an order of magnitude decrease in permeability with increasing applied stress, implying that microfaults generated under near surface conditions *in situ*, would pose less of a barrier to hydrocarbon migration and entrapment than those
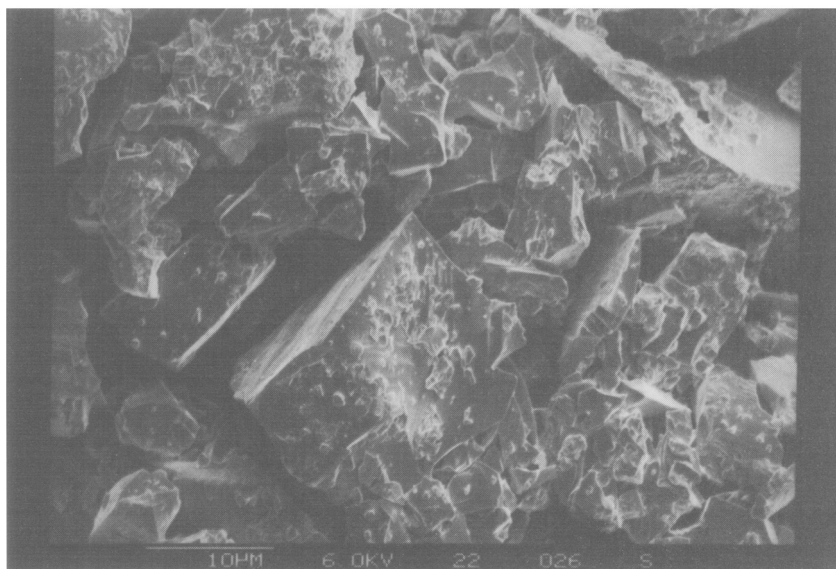
Fig. 14. Scanning electron photomicrograph of fault gouge retrieved from specimen #22.

generated in the same host lithology at greater depth. Induced microfault thickness and wall rock roughness were also observed to decrease with increasing applied stress magnitude, so that for a fairly uniform sliding displacement applied to all test specimens (1 mm) imposed experimental conditions also imparted stress-dependency to angular shear strain across the microfaults (shear strain increasing with applied stress).

The effectiveness of the experimental shear band seals in Clashach sandstone is attributed to the permeability characteristics of their frictional wear products (gouge). Dependency of this sealing potential on stress magnitude and shear strain, in turn reflects variation in internal gouge zone microstructure with these external boundary conditions. Empirically determined linear negative correlations between shear band permeability and the degree of dispersion of the non-indurated, disaggregated shear debris distributions (quantified using laser-sizing techniques) reflect increased shear band sealing with increasing 'cataclastic intensity'. For Clashach sandstone faulted under laboratory stress fields of magnitudes as quoted above, no permeability increase associated with particulate flow-induced dilatancy within the fault zone was recorded. Thin-section analysis shows that 'cataclastic intensity', progressively increasing with applied stress and gouge zone deformation, is micro-structurally manifest in terms of intra-granular fracturing (fine-grained cataclastic matrix)

replacing grain-boundary sliding (intact grains) as the dominant deformation mechanism. Lack of correlation between permeability and the large particle-size distributions (600–1.2 mm range) which incorporate original, undeformed grain-sizes, suggests that permeability is primarily a function of comminuted cataclastic matrix sorting, as opposed to the quantity and distribution of relict grains remaining. Further work will attempt to similarly quantify 'cataclastic intensity' within natural, non-disaggregated (and therefore not conducive to laser-sizing) granulation seam gouge zones, utilising scanning electron microscopy and image analysis to determine particle-size distribution and 2D-porosity, from which application of the Kozeny–Carman relation should enable permeability estimation.

The rock mechanical experiments described here, demonstrate the sealing effects of artificially-induced shear bands in core plugs from the Permo-Triassic Hopeman Sandstone, with, in this case, sealing resulting exclusively from cataclastic deformation alone. However, Edwards et al. (1993), from field studies of natural deformation bands in the same Hopeman sandstone, observed that these tectonic features acted intermittently as both fluid conduits and barriers, with adjacent enhanced cementation testifying to the migration of diagenetic brines along fractures. The underlying processes of such diagenetic fault healing and sealing are presently poorly understood, partly because

they have been thought too slow to observe in the laboratory in a reasonable time frame. However, recent use of state-of-the-art fluid chemistry analysis (high pressure liquid chromatography, Ngwenya et al. 1995) has demonstrated significant real-time permeability changes due to laboratory induced fluid-rock interactions (dissolution of feldspars, precipitation of iron oxide) during fluid flow under stress. Thus the potential exists for empirical quantification of reaction rates associated with diagenetic sealing of cataclastic fault gouge, where the large increase in surface area resulting from comminution provides a chemically reactive substrate for dissolution/precipitation processes.

Conclusions

Transient pulse-decay liquid permeability measurements have been conducted on cylindrical specimens of Clashach sandstone faulted in shear under triaxially compressive stress states equivalent to overburden depths ranging from 0.6 to 3 km. From such measurements, an approximate method of estimating shear band permeabilities is presented, based on the assumptions of fault zone permeability being very much less than host matrix permeability, and a constant linear decrease in shear band thickness with normal stress across it. Fault sealing potential (defined as the ratio of shear band permeability to matrix permeability measured at hydrostatic stress) ranges from 0.35 to 0.04%, representing a 2.5 to 3.5 order of magnitude permeability reduction. The effectiveness of cataclastic seal shows an order of magnitude increase with increasing normal stress and angular shear strain imposed on the gouge zone

A laser particle sizing technique was applied to the collected shear debris samples to assess characteristics of the gouge distributions down to 0.1 μm particle size. The Rosin–Rammler exponential function was used to quantify 'cataclastic intensity' by defining the relative fineness and closeness of grading of the fault gouge distributions via a 'coefficient of variation'. Cataclastic intensity is seen to increase with increasing normal stress and angular shear strain, as indicated by strong linear negative correlations with the coefficient of variation. Fault seal potential is seen to increase with increasing coefficient of variation, indicating that the effectiveness of cataclastic sealing as a fluid baffle decreases as the degree of fault gouge comminution decreases. This empirical relation demonstrated between fault seal and degree of cataclasis was rationalized through consideration

of the Kozeny–Carman relation, which analyses permeability in terms of its constituent parameters of tortuosity, porosity and surface area. Cataclastic intensity was characterized in terms of the relative breadth of the gouge distribution. Less permeable shear bands showed broader ranges of particle size and hence poorer sorting, thus fault sealing may reflect porosity reduction, with smaller fragments fitting between larger ones and thus reducing pore volume. Porosity reduction is shown experimentally to be accompanied by increasing surface area, and an inferred increase in flow path, both of which also impair permeability.

As well as aiding in the understanding of fault sealing by cataclasis, the ability to quantify comminution products through laser particle sizing has great potential in the hydrocarbon industry, including study of the 'crush' characteristics of proppant used to wedge open hydraulic fractures, and the problem of sand production from producing wells, where local shear stresses have exceeded rock strength in the vicinity of the well-bore.

Further work will focus on repeating the experimental method detailed here, but with the addition of finite pore pressures, to investigate the influence of effective stresses and degrees of overpressurization on cataclastic seal integrity and on fault gouge statistics. Reservoir simulation will continue to build stress-sensitivity into numerical modelling studies, so that the process of fault shear with attendant variation in sealing potential can be directly predicted from pressure transients resulting from production.

Nomenclature

b:	$= (1/\bar{x})^n$
c:	Kozeny–Carman constant
k:	absolute permeability constant (see subscripts)
(l_s/l_w):	ratio of apparent to real pore length (=inverse of tortuosity)
n:	Rosin–Rammler distribution constant
$\bar{x}$:	Rosin–Rammler absolute size constant
x:	particle size
A:	area (see subscripts)

C: system compressibility
D: fractal dimension
G: total weight of particles in sample
L: core specimen length
R: residual weight percent
S: specific surface area (see subscripts)
α: $= \arctan(n)$
δ_s: shear displacement
ε: shear band thickness
γ: shear strain $= \delta_s/\varepsilon$
ϕ: porosity
μ: fluid viscosity
θ: shear band inclination, fault σ_1
σ_1: maximum principal stress
σ_3: minimum principal stress
σ_n: normal stress
τ: shear stress
Δl_a: axial specimen shortening
ΔP: pressure drop (see subscripts)
Ψ: angular shear strain $= \arctan(\gamma)$

Subscripts:
v: per unit volume
w: per unit weight
core: cylindrical specimen
fault: shear band

References

ANTONELLINI, A. & AYDIN, A. 1994. Effect of faulting on fluid flow in porous sandstones: petrophysical properties. *AAPG Bulletin*, **78**, 355–377.

BENNETT, J. G. 1936. Broken coal. *Journal of the Institute of Fuel*, **10**, 105–119.

BRACE, W. F., WALSH, J. B. & FRANGOS, W. T. 1968. Permeability of granite under high pressure. *Journal of Geophysical Research*, **73**, 2225–2236.

BYERLEE, J. D. 1967. Frictional characteristics of granite under high confining pressure. *Journal of Geophysical Research*, **72**, 3639–3648.

CRAWFORD, B. R., SMART, B. G. D. & NGWENYA, B. T. 1994. Relationship between frictional strength and fault gouge generation from direct shear testing under constant normal displacement control. *Proceedings of the SPE/ISRM Rock Mechanics in Petroleum Engineering – EUROCK '94*, Delft, 29–31 August. Balkema, Rotterdam, 121–129.

——, ——, MAIN, I.G. & LIAKOPOULOU-MORRIS, F. 1995. Strength characteristics and shear acoustic anisotropy of rock core subjected to true triaxial compression. *International Journal of Rock Mechanics, Mining Sciences & Geomechanics Abstracts*, **32**, 189–200.

EDWARDS, H. W, BECKER, A. D. & HOWELL, J. A. 1993. Compartmentalization of an aeolian sandstone by structural heterogeneities: Permo-Triassic Hopeman Sandstone, Moray Firth, Scotland. *In*: NORTH, C. P. & PROSSER, D. J. (eds) *Characterisation of Fluvial and Aeolian Reservoirs*. Geological Society, London, Special Publication **73**, 339–365.

FOWLES, J. & BURLEY, S. 1994. Textural and permeability characteristics of faulted, high porosity sandstones. *Marine & Petroleum Geology*, **11**, 608–623.

GUEGUEN, Y. & PALCIAUSKAS, V. 1994. *Introduction to the Physics of Rocks*. Princeton University Press, New Jersey.

HEATH, A. E., WALSH, J. J. & WATTERSON, J. 1994. Estimation of the effects of sub-seismic sealing faults on effective permeabilities in sandstone reservoirs. *In*: AASEN, J. O., BERG, E., BULLER, A. T., HJELMELAND, O., HOLT, R. M., KLEPPE, J. and TORSAETER, O. (eds) *North Sea Oil and Gas Reservoirs – III*. Kluwer, Dordrecht, 173–183.

HERDAN, G. 1960. *Small Particle Statistics*. Butterworths, London.

KOZENY, J. 1927. Ueber kapillare Leitung des Wassers in Boden. *Sitz. Ber. Akad. Wiss. Wien, Mathem.-Naturwiss. Abt.*, **136**, 271.

LIAKOPOULOU-MORRIS, F, MAIN, I. G., CRAWFORD, B. R. & SMART, B. G. D. 1994. Microseismic properties of a homogeneous sandstone during fault nucleation and frictional sliding. *Geophysical Journal International*, **119**, 219–230.

LOVELL, J. P. B. 1983. Permian and Triassic. *In*: CRAIG, G. Y. (ed) *Geology of Scotland*. Scottish Academic Press, Edinburgh, 325–342.

MAIN, I. G. 1991. A modified Griffith criterion for the evolution of damage with a fractal distribution of crack lengths: application to seismic event rates and b-values. *Geophysical Journal International*, **107**, 353–362.

MARONE, C. & SCHOLZ, C. H. 1989. Particle-size distribution and microstructures within simulated fault gouge. *Journal of Structural Geology*, **11**, 799–814.

NGWENYA, B. T., SHIMMIELD, G. B. & ELPHICK, S. C. 1995. Reservoir sensitivity to waterflooding: an experimental study. *AAPG Bulletin*, **79**, 285–304.

PATERSON, M. S. 1978. *Experimental Rock Deformation – The Brittle Field*. Springer, New York.

RINGROSE, P. S., SORBIE, K. S., CORBETT, P. W. M. & JENSEN, J. L. 1993. Immiscible flow behaviour in laminated and cross-bedded sandstones. *Journal of Petroleum Science and Engineering*, **9**, 103–124.

ROSIN, P. & RAMMLER, E. 1933. The laws governing the fineness of powdered coal. *Journal of the Institute of Fuel*, **7**, 29–36.

SAMMIS, C. G., OSBORNE, R. H., ANDERSON, J. L., BANERDT, M. & WHITE, P. 1986. Self-similar cataclasis in the formation of fault gouge. *Pure and Applied Geophysics*, **124**, 53–78.

TULLIS, J. & YUND, R. 1992. The brittle–ductile transition in feldspar aggregates: an experimental study. *In*: EVANS, B. & WONG, T.-F. (eds) *Fault Mechanics and Transport Properties of Rocks*. Academic, London, 89–117.

TURCOTTE, D. L. 1992. *Fractals and Chaos In Geology and Geophysics*. Cambridge University Press.

WEISS, E. L. & FROCK, H. N. 1976. Rapid analysis of particle size distribution by laser light scattering. *Powder Technology*, 287–293.

Identification and spatial distribution of fractures in porous, siliciclastic sediments

ROY H. GABRIELSEN[1], RANDI-KRISTIN AARLAND[1,2,3]
& EINAR ALSAKER[1]

[1] Geological Institute, University of Bergen, Allégaten 41, N-5007 Bergen, Norway
[2] Norsk Hydro Research Centre, Sandsliveien 90, N-5020 Bergen, Norway
[3] Present address: ESSO Harge a.s., Grenseveien 6, N-4033 Forus, Norway

Abstract: Spatial and size distribution data of fractures provide essential information in statistical bulk strain estimates and in predictive fracture scaling models for sediments which have undergone brittle deformation. Most fracture populations in naturally deformed sediments include structures which originated at different stages, and in response to different conditions during the deformation history of the rock. Hence, the final fracture population may contain fractures which genetically are related to gravitational (near-surface) instabilities, burial, uplift and unroofing, thermal expansion and contraction, and regional tectonism. Furthermore, grain size, bed thickness and different rheological properties may strongly influence the fracture style and frequency.

Particularly when only well cores are available, identification of fractures of different genetic origin is difficult, and fracture classification and predictive modelling can only be accomplished with data acquired from careful fracture logging. In such logging, information on position of the well relative to major structures, the geometry of nearby faults, and the general geological (sedimentary and tectonic) environment need to be included. Also, fracture frequencies should be compared to, and normalized according to, lithology and bed thickness, and the fracture frequency diagrams should be corrected for eventual well deviation before predictive fracture frequency modelling is performed.

Flow in hydrocarbon reservoirs is commonly influenced by fracture systems, which may either enhance (Narr & Currie 1982; Nelson 1981; Tillman 1983; Tillman & Barnes 1983; Watts 1983) or depress (Stearns & Friedman 1972; Dunn et al. 1973; Pittman 1981; Aydin & Johnson 1983; Wilke et al. 1985; Gabrielsen & Koestler 1987; Antonellini & Aydin 1994) permeability. This emphasizes the need to predict fracture frequencies and spatial distribution of fractures, and to evaluate permeability characteristics of fractures at all scales. The prediction of fracture frequencies is, however, hampered by several methodological and practical restrictions. Firstly, a scale problem exists in fracture studies of hydrocarbon reservoirs, where fracture analysis is frequently based primarily on reflection seismic data, wireline logs and cores. The problem occurs because little information is available on fractures at the scale between faults with throws above the resolution limit in reflection seismic data, which at the very best is in the order of 10 to 20 m, and fractures mapped in cores which typically display offsets of centimetres and occasionally decimetres. Secondly, fracture populations in naturally deformed sediments are generally inhomogeneous in the context that they include fractures that are not necessarily genetically related. The distribution of genetically different fracture sets in a fracture population is likely to be influenced to different degrees by parameters such as history of burial and uplift, bed thickness, fluid pressure, grain size and nearness and position relative to major structures like faults and folds, implying that fractures produced in different settings and at different stages of the geological history of the deforming rock may appear with distinctly different fracture frequencies and spatial distributions.

In a number of recent studies, valuable attempts have been made quantitatively to characterize fracture populations. These works have treated the relation between fault dimensions and fault displacement (Watterson 1986; Barnett et al. 1987; Walsh & Watterson 1987, 1988, 1989; Marrett & Allmendinger 1991; Cowie & Scholz 1992a, b; Gillespie et al. 1992; Jackson & Sanderson 1992), and between fracture frequencies and bulk strain (Childs et al. 1990; Walsh et al. 1991; Scholz & Cowie 1990). Hopefully, such studies will provide tools which will help to make correct predictions of fracture distribution and connectivity in the future, but to obtain this, high quality fracture databases must be available.

It is the scope of the present paper to focus on the quality of fracture data bases used in future studies, and to propose criteria which should be applied in acquiring such data. Hence, we try

to characterize fracture systems of different genesis, and then to evaluate some general parameters that are of importance in fracture development.

The inhomogeneity of natural fracture populations

The idea that individual fractures grow regularly and concentrically from a point of nucleation by stable or simple incremental processes (Walsh & Watterson 1989), and that fracture swarms and faults develop from single fractures into larger composite structures and networks with increasing deformation (Aydin 1978; Aydin & Johnson 1978; Gabrielsen & Koestler 1987) is intuitively feasible. Detailed strain analyses of single structures, however, suggest that these relations may be more complicated for single fractures as well as for complete fracture systems, and that they are influenced to a considerable extent by deformation mechanisms and physical characteristics of the individual fracture (Gillespie *et al.* 1992; Wojtal 1994; Bürgmann *et al.* 1994).

Westaway (1994) suggested that although self-similarity in size distribution of fault populations is not essential for the result of strain estimates, and that several methods for sampling may be successful, such estimates are sensitive to the actual numerical relation between the fracture sub-populations. Also Wojtal (1994), studying contractional faults, demonstrated that mixing of faults of different scales and different genesis or path of development may result in faceted plots, which in turn suggests that the fault population is basically multifractal or pseudofractal. This will be the case if populations of 'bounded' faults ('large' faults that delineate larger structures such as fault blocks or duplexes) and 'unbounded' faults ('small' faults within larger structures) are mixed in the analysis. Hence, in fracture analysis and in the application of scaled fracture frequencies in bulk strain estimates, the identification of the hierarchical status of the fault, as well as the processes of deformation associated with each fracture set, is essential. To obtain meaningful fracture statistics, it is important to acknowledge the effects of such properties as grain size, bed thickness and different rheological characteristics associated with changing lithologies and diagenesis. In the study of cores, structures associated with drilling and core handling also need to be identified and corrected for (Kulander *et al.* 1990).

Description of natural fracture populations

The term 'fracture' is frequently used in a casual manner, and particular nomenclature problems are related to the scale of such features; the distinction between joints and faults is closely linked to the scale at which such features are studied (e.g. Ramsay & Huber 1987, p. 505). In our opinion, this problem sometimes influences the exactness in descriptions of fractures, and this is of particular importance in studies which include classification and statistical handling of fracture sets.

To avoid exclusion of certain fracture types, we propose to include all *planar or subplanar secondary inhomogeneities (in a rock) imposed by outer or inner stresses* in the definition of fractures (Gabrielsen & Aarland 1995). This definition generally follows that of Bates & Jackson (1987) and Nystuen (1989), and includes all types of mode I fractures such as joints and open and mineral-filled fissures (veins), mode II (shear) fractures and mode III (hybrid) fractures (in the terminology of Hancock (1985)). We particularly emphasize that 'deformation bands' (Aydin 1978; Aydin & Johnson 1978), which in early stages of development are identified only as zones of reduced porosity, are included in this definition. The term 'deformation band' is synonymous to granulation seam (Heald 1956), shear fracture (Dunn *et al.* 1973) and band fault (Cruikshank *et al.* 1991).

To obtain a good base for analysis of fracture populations, it is necessary to categorize fractures according to their genesis, in order to prevent mixing of fracture populations in statistical modelling. Fractures related to burial and uplift/unroofing respond to the stresses defined by the reference state and the thermal expansion and contraction (Engelder 1993). Tectonic fractures, on the other hand, may be subdivided into fractures related to 'contemporary tectonic stress', which is defined on a plate-wide scale, and which is presumably related to plate margin interactions (Sbar & Sykes 1973), and 'local tectonic stress', which can be ascribed to local topographic effects or stress fluctuations due to inhomogeneities associated with, for example, fault plane geometries. Residual stresses may contribute to both tectonic- and burial-related fracturing, but is assumed to be of minor practical significance in fracture logging.

The identification of small-scale fractures related to these principal deformation types is not trivial, since characteristics such as morphology and texture may be similar for fractures that have been initiated and developed under different

geological conditions. Therefore, the total geological environment of the fracture population needs to be taken into consideration in fracture analysis. To do this, however, one needs to characterize the fracture populations, which occur in different types of deformation environments, in general terms.

In the following discussion, we distinguish between the different environments of fracturing, namely those associated with burial and unroofing, soft-sedimentary gravitational surface (topographic) instabilities, and contemporary primary and secondary stresses.

Fractures related to burial and unroofing
Fractures associated with loading and volume reduction may be initiated at very shallow levels in the subsurface (a few tens of metres; (Maltman 1988)), and continue to develop throughout the burial history of the sediment (Fig. 1). Also agents other than sediment loading (e.g. ice) can contribute to their initiation.
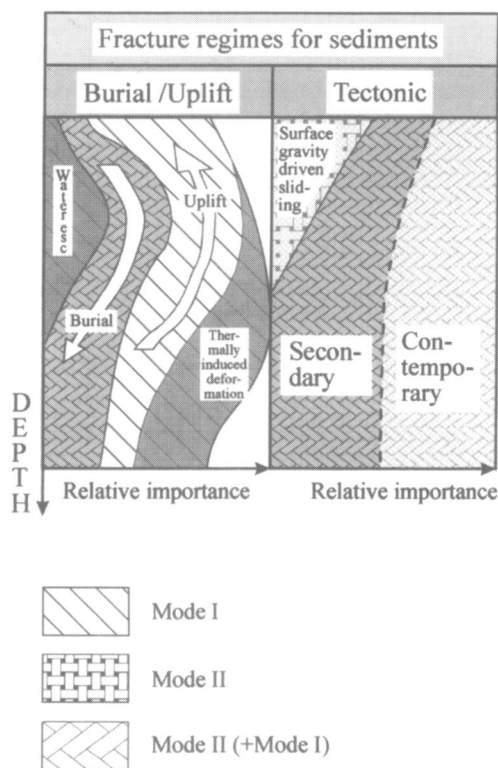

Fig. 1. Schematic relation and relative importance of fractures generated during burial/uplift/unroofing and tectonic deformation. Symbols indicate dominant fracture mode.

According to some authors, fracture populations generated by compaction and decompaction are dominated by tensile (mode I) fractures. Engelder (1985) used the Voight & St.Pierre (1974) relation, which defines the influence of rock mechanical properties and the thermal effect on the state of stress at depth in the uniaxial reference state, to substantiate that sediments that have undergone burial and lithification may reach tensile stresses which are larger than the tensile strength of the rock during unroofing. The practical implication of this is shown in Fig. 2, which suggests that, for example, a sandstone may undergo tensile fracturing at a level where a shale remains undeformed during erosion and uplift. Diagenetic processes and fluid pressure contribute continuously to change the rheological properties of the sediments, and hence may promote fracturing during burial and eventual erosion and upheaval.

However, mode II fractures generated through vertical loading are also frequently reported in unconsolidated and poorly consolidated sediments, and are indeed reproduced in sand box experiments (e.g. Mandl *et al.* 1977). The shear strength of an unconsolidated to poorly consolidated sediment may vary from a few kilopascals to some megapascals (Maltman 1994). Differential stresses of this magnitude are obtained near the surface, and development of shear fractures may continue during burial, eventually promoted by enhanced fluid pressures. In fact, all fracture populations in hydrocarbon wells in the Norwegian continental shelf logged by us are dominated by mode II fractures, and layers with a substantial number of mode I fractures are found only rarely. In outcrop studies (e.g. Montserrat Fan-Delta northeast Spain (Alsaker *et al.* 1996) and Mesaverde Group, Utah (Alsaker unpublished data 1995)), mode I fractures constitute a much larger part of the fracture populations. This is generally in accordance with observations in basins which have been buried, but which are presently exposed at the surface (Engelder 1993, p. 56), and can most easily be explained by stress release during unroofing.

It should of course also be expected that different tectonic histories and contrasting maximum depths of burial of the investigated basins influence fracture frequencies and relation between the fracture modes. Also, the sampling procedures may contribute to the differences (most investigated wells are vertical, implying that cores are cut parallel to the vertical fractures, which accordingly may be strongly under-represented in the fracture logs).

Fracture logging of siliciclastic sediments in cores is most frequently performed in hydrocarbon reservoirs which may constitute siltstone- and
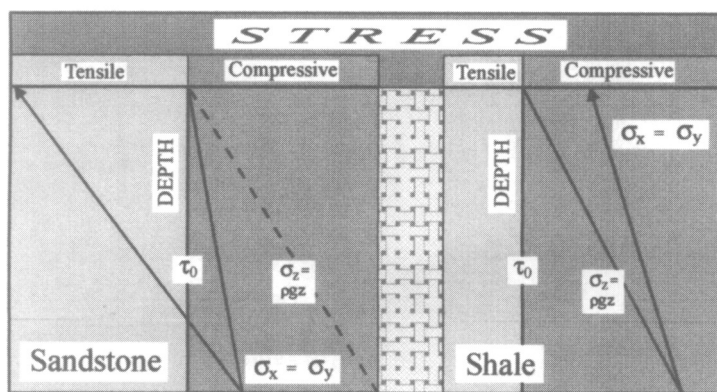
Fig. 2. Stress versus depth for sandstone and shale during burial and uplift. Lithification occurs at maximum depth of burial. Note that the sandstone enters the area of tensile fracturing before the shale during upheaval. From Engelder (1985).

sandstone-dominated intervals up to a few hundred metres thick, presently buried at depths between *c.* 100 and 3000–4000 m. In vertical sediment intervals of, say, 400 m thickness buried at depths of 1000–1400 m, changes in differential stress between the upper and lower part of the sequence will typically be in excess of 10 MPa, and such stress differences may, given that all other parameters (rheological properties, fluid pressure, bed thickness etc.) are constant, be sufficient to explain contrasting fracture frequencies.

Fracture frequency studies in a 350 m thick interval in the Njord Field of mid-Norway (between 2750 and 3100 m below present seabed), and in two intervals of 250 and 150 m in the Oseberg Field in the northern North Sea, where all sequences are dominated by siltstones and sandstones interbedded with mudstones, show no simple relationship between fracture frequency and present depth of burial (Fig. 3). This is in concert with similar results from homogeneous and competent rocks (Haimson & Doe 1983), suggesting that the effect of changes in differential stress in intervals of such magnitudes is almost completely overruled by other parameters (fluid pressure and lithology). Surprisingly, however, no correlation between fracture frequency and overpressured intervals was found in wells studied in the Njord Field in the mid-Norwegian shelf (Pedersen 1992).

In a subsiding, extensional basin where principal horizontal stresses (σ_H and σ_h) are significantly different ($\sigma_H > \sigma_h$) and smaller than the loading stress (i.e. $\sigma_v = \rho g z = \sigma_1$), fractures related to compaction and decompaction would have predictable orientation and geometry. It is also to be expected that fractures related to compaction are more evenly distributed throughout

the deforming sediment (Gabrielsen & Koestler 1987), and that the two conjugate sets of mode II fractures would be planar structures with a dip angle of 60°. Experiments (Mandl *et al.* 1977; Bjørnevoll & Gabrielsen, unpublished) and field observations (Aydin & Johnson 1978; 1983; Gabrielsen & Koestler 1987) suggest that the fractures would be recognized as deformation bands with the characteristics of the early stages of deformation, i.e. grain compaction and porosity reduction (Gabrielsen *et al.* 1993) (Fig. 4). In fine- and medium-grained rocks, this type of fracture has a high potential of preservation (Maltman 1988). Unfortunately, however, such textures are not diagnostic for compactional fractures, because tectonic deformation bands possess similar textures and orientation. Perhaps the best criterion to distinguish compactional fractures is by their spatial distribution.

Water-escape fractures may be seen as a type of compactional fracture which was active during the early stages of burial. In siltstones and sandstones these are typically high-angle, planar structures, usually a few millimetres wide. They are often associated with symmetrical upward- or downward-pointing drag (Fig. 5). Outside the zones affected by drag, there is commonly no relative offset of strata (Burbridge *et al.* 1988). Water-escape fractures may further be subdivided into two classes (Gabrielsen & Aarland 1990): fractures (joints) through which water has escaped (Lowe 1975; Cheel & Rust 1986; Guiraud & Séguret 1987), and fractures (faults) associated with collapse due to volume loss associated with water escape (Burbridge *et al.* 1988; de Lange *et al.* 1988). The deformational style associated with water escape may vary considerably with lithology, from single

fractures in sandstones to fragmentation in shales. Texturally, water-escape fractures in fine- to coarse-grained siliciclastic sediments are characterized by lamination parallel to the fracture walls, laminae being defined by clay particles and other tabular mineral grains (Maltman 1988). Internal wall-parallel laminar elutriation of mineral grains may occur (Lowe 1975; Burbridge *et al.* 1988), and there are indications that packing of grains takes place in this process. The textures may depend upon degree of water saturation in the sediment, grading from hydroplastic through liquefaction to fluidization, the latter representing the highest degree of grain sorting.

In conclusion, fractures related to water escape in sandstones and siltstones are most commonly strata-bound, and are usually associated with other structures related to liquefaction. Hence, they are generally easily identified on the scale of a well core where they happen to be more abundant. Consequently, water-escape fractures contribute significantly to fracture frequency only on the local scale, and are accordingly not believed to represent a great problem in the study of scaling relationships of fracture populations in sandstones and siltstones. In mudstones and shales, however, the problems may be significant (Guiraud & Séguret 1987; Petit & Laville 1987).

Tectonic fractures
Tectonic fractures may affect the entire crust and may be generated near surface as well as in rocks at a deep level of burial (Fig. 1). In many published studies, tectonic fractures are implicitly considered to dominate natural fracture populations. Under moderate stresses, morphologies and texture of the fracture fill of tectonic fractures probably have characteristics that are similar to those of compaction fractures, and distinguishing between the two types may be difficult. However, the textures related to tectonic fractures will frequently reflect strains that exceed those of consolidation fractures. Tectonic fractures have been given thoroughly described in the literature (see Hancock 1985; Groshong 1988; Antonellini *et al.* 1994).

Tectonic fractures may basically be considered to be responses to first-order plate stresses (contemporaneous tectonic stresses), or secondary derivatives or effects of such stresses (Fig. 1). Thus, the second-order tectonic fractures include those associated with gravitational (surface) instabilities and locally deflected stresses in, for example, in the vicinity pre-existing faults, rock borders, along geometrical irregularities in fault planes etc.

Faults related to *soft-sedimentary gravitational surface instabilities* may reach large dimensions,

for example in the form of synsedimentary faults or growth faults, slumps and slides (Hardin & Hardin 1961; Rider 1978; Crans *et al.* 1980; Stow 1986). These structures are related to surface slope, intrinsic instabilities such as inverse gravitational contrasts, or tilted contact surfaces between layers with contrasting shear strength or fluid pressure (Cloos 1968; Bruce 1973; Mandl 1988, pp. 28–29). It is frequently assumed that tectonic tilting or seismicity may contribute to destabilization causing softsedimentary faulting. Local stresses easily exceed the shear strength of sand and other unconsolidated or poorly consolidated sediments in such circumstances, and may result in the development of discrete shear zones. Such shear zones may not be readily distinguishable from shear zones generated during regional-scale tectonic deformation in the field, since morphological and textural characteristics of fractures may not be diagnostically different (Petit & Laville 1987). However, enrichment of clay minerals (Sverdrup & Bjørlykke 1992) and the association with fluidization processes (Owen 1987) may help to identify fractures generated in soft-sedimentary, gravity-induced deformation. In general, however, fractures associated with soft-sedimentary gravitative features may sometimes only be identified as such by their overall geometry and the geological environment in which they occur.

Fracture frequency and spatial distribution are not commonly reported in the literature for soft-sedimentary gravitational faults, but field studies of slides in fluviodeltaic sediments (Sverdrup & Bjørlykke 1992), in marine sediments (Farrell & Eaton 1988) and in accretionary prisms (Behrmann *et al.* 1988) have indicated that fractures related to soft-sediment gravity-driven, near-surface deformation may be abundant, and that they locally may develop frequencies comparable to that of regional (contemporary) or local second-order tectonic deformation (Ord *et al.* 1988; Martinsen & Bakken 1990). It is therefore suggested that fracture systems associated with soft-sedimentary gravitational instabilities may contribute significantly to the bulk fracture strain in fracture populations in sedimentary rocks, and even dominate such populations on the local scale. However, soft-sedimentary gravitational instabilities may be strictly local phenomena, where the strain (e.g. extensional faulting in the upper extensional listric fan of a slump) can be compensated for in the outcropping (compressional) toe-zone.

It is anticipated that fractures generated by near-surface gravity-induced deformation potentially represent a source of error in scaling
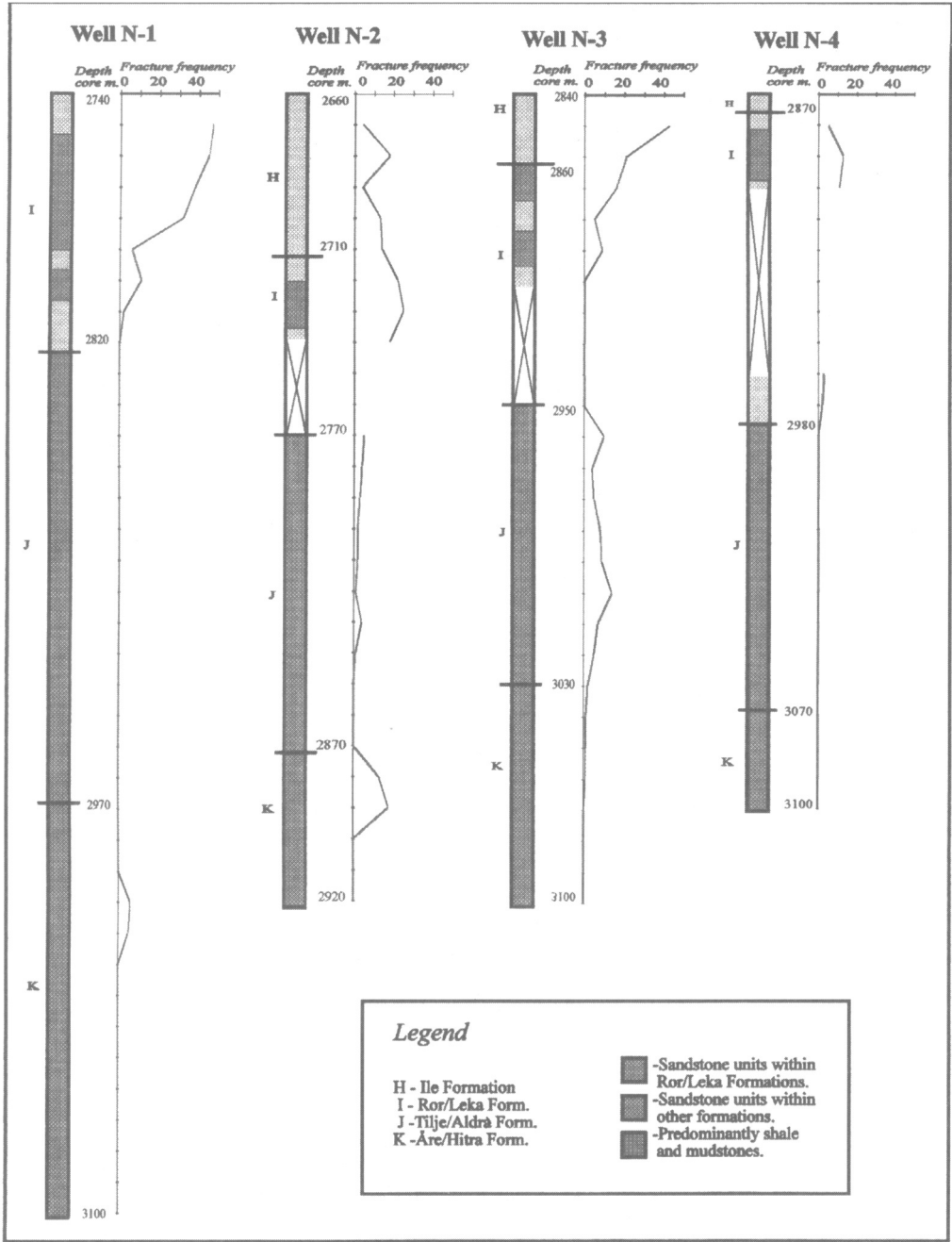
Fig. 3. Depth versus fracture frequency in wells from two Norwegian hydrocarbon fields (Njord (N) and Oseberg (O) fields).
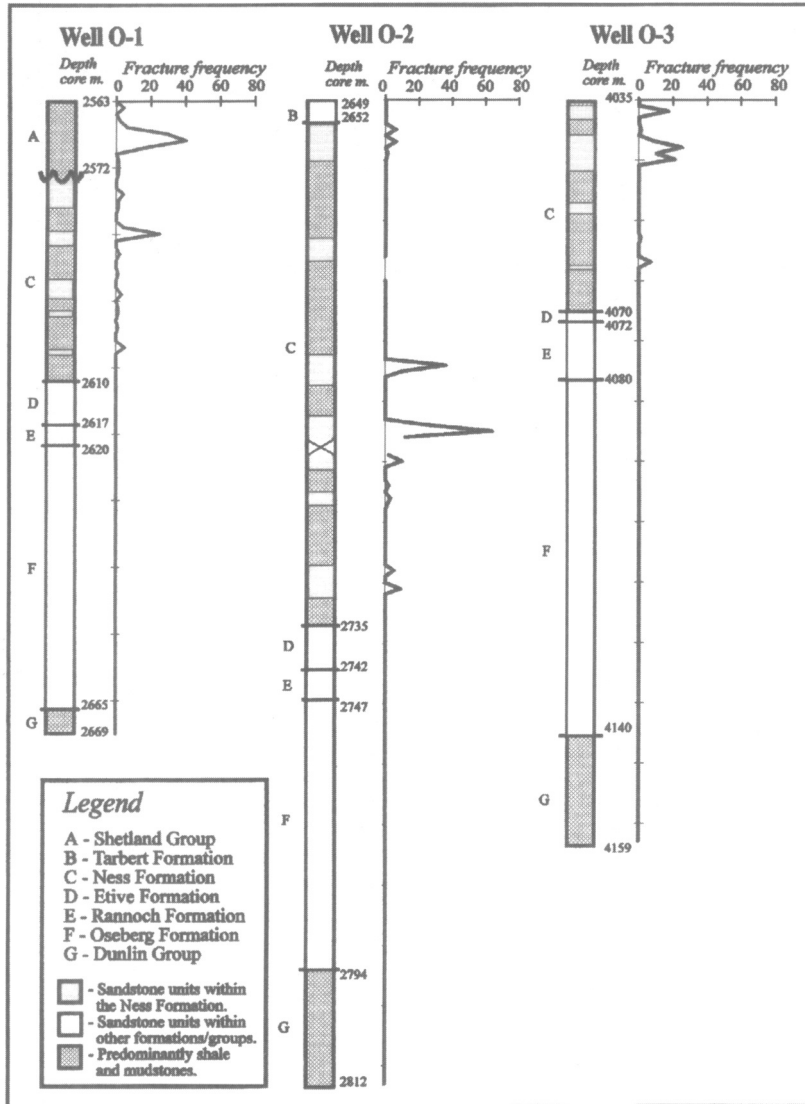
Fig. 3. Continued

relationship studies if one fails to identify such features. Since gravity-induced sliding is not uncommon in the Norwegian shelf at different stratigraphic levels (Gabrielsen & Robinson 1984; Alhilali & Damuth 1987), it may be expected that fractures associated with gravity-induced near-surface sliding locally may contribute significantly to the total fracture frequencies obtained from core logging in this area.

We consider the major faults (those which are above the limit of resolution in reflection seismic data) and those fractures which have first-order

relations to the major faults, to be related to the contemporary (regional) and the secondary (local) stressfield. Where σ_h and σ_H were significantly different during deformation, such structures are characterized by predictable fracture orientations and relations. In most extensional systems investigated by us, fault populations are characterized by relatively uniform fracture frequencies within each fault block, with the fracture frequency increasing both in the hangingwall and the footwall in the proximity of major faults. In our studies, the width of the
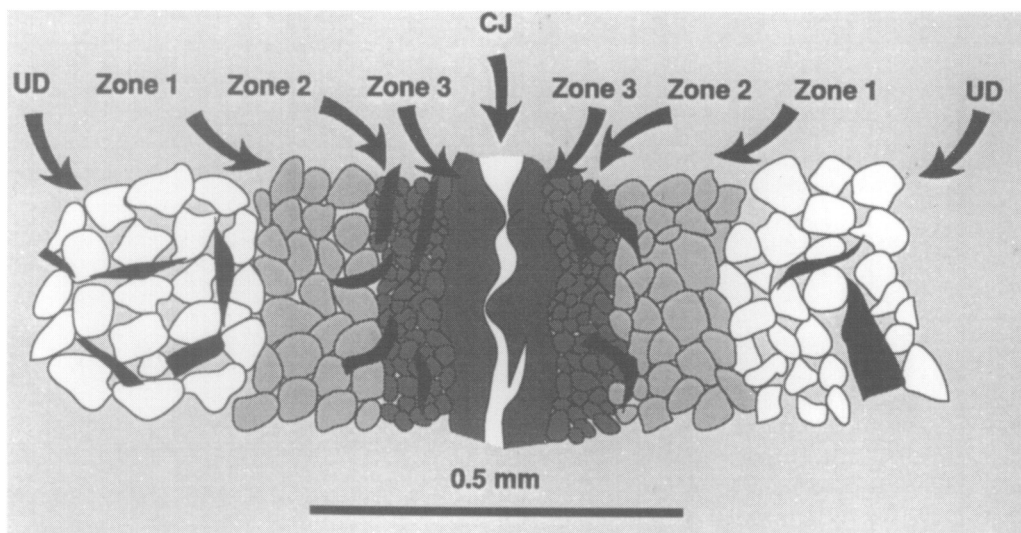
Fig. 4. Schematic zonal symmetric texture in 'complete' deformation band in sandstone. UD: sandstone unaffected by deformation. Zone 1: grain compaction. Zone 2: grain-size reduction and grain reorientation. Zone 3: mineralized central zone. CJ: central joint. Grain compaction in full width of the deformation band usually occurs before grain-size reduction. After Gabrielsen & Aarland (1990).
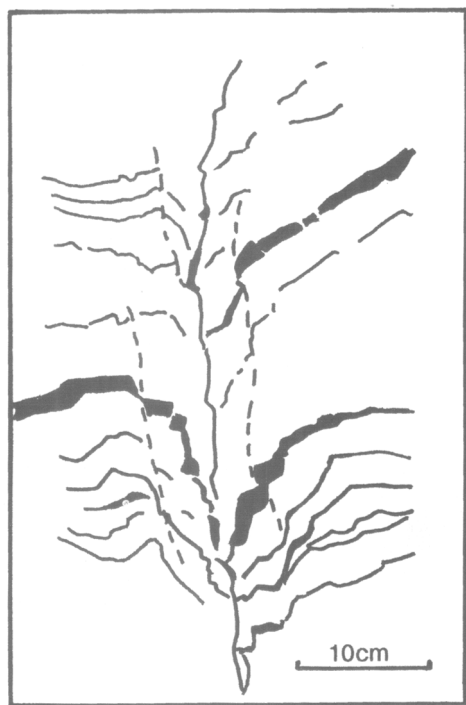
Fig. 5. Fractures associated with water escape. After Burbridge *et al.* (1988).

zones with enhanced fracture frequencies ('the damage zone') in the hangingwalls and footwalls of extensional faults with vertical throws in the order of some tens of metres, is frequently recorded to be less than 20–30 m (Fig. 6). This is in general accordance with several previous studies (Jamison & Stearns 1982; Chester & Logan 1986), although the width of the damage zone is reported to vary (Beach *et al.* 1995). It is also evident that strain, and hence fractures, is commonly concentrated in hangingwalls adjacent to irregularities such as flats or splays, so that abnormally wide damage zones can be expected at such sites (see Fig. 8) (Koestler & Ehrmann 1991; Aarland & Skjerven 1998).

The present data may seem to confirm the general model for growth of fractures (deformation bands) in siliciclastic sediments from single fractures, widening into zones of deformation bands as described by Aydin & Johnson (1978). This may be in general agreement with the model of Walsh & Watterson (1988, 1989) which predicts that shear fractures grow concentrically from a point of nucleation into a surface with elliptic circumference. It is noted, however, that in plaster and sand analogue models faults are frequently seen to nucleate at the surface or at the contact between the deforming 'sediment' and basement (Fossen & Gabrielsen 1995). The development of single deformation bands into deformation zones also suggests that strain
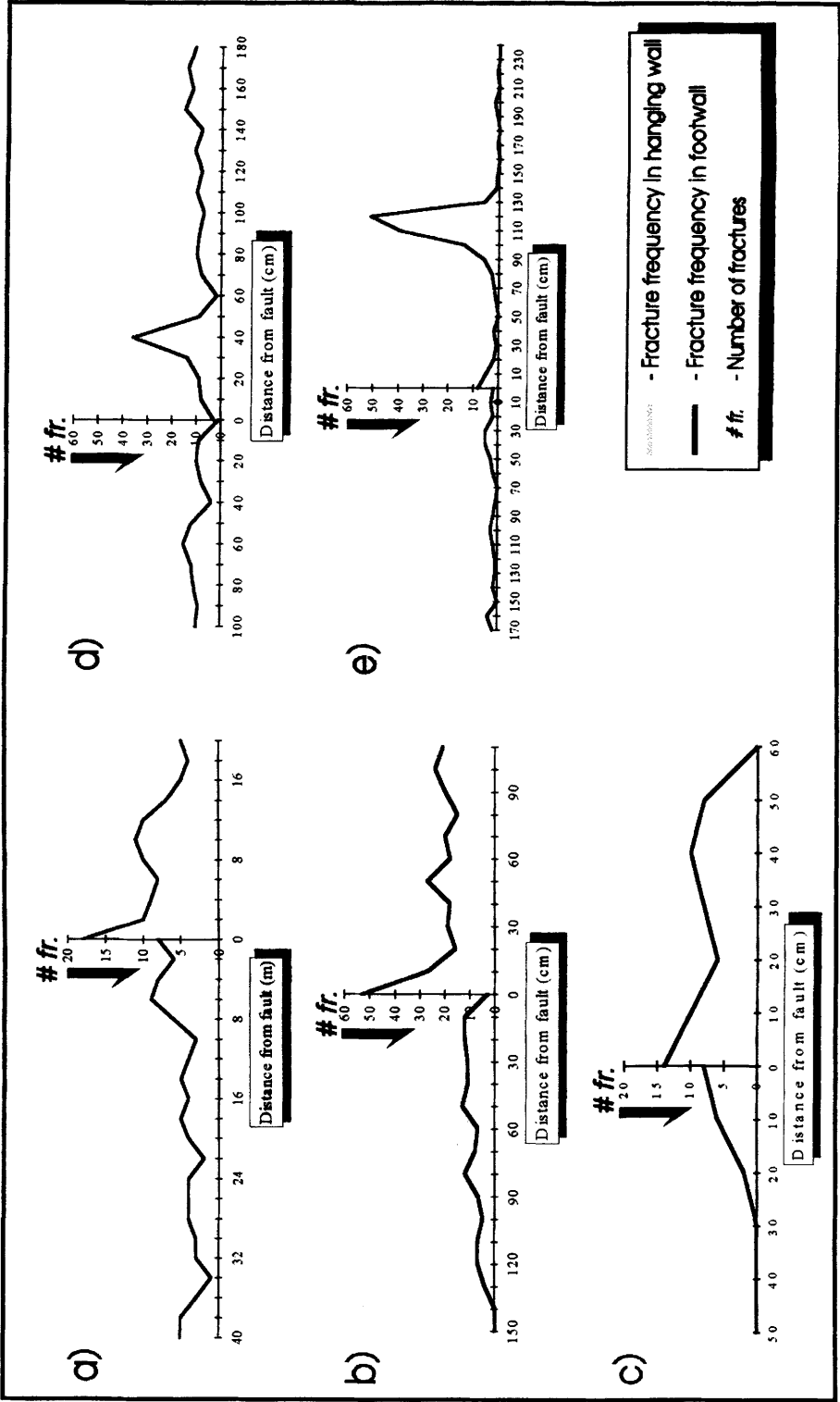
Fig. 6. Fracture distribution in hangingwalls and footwalls of extensional faults. Examples from Price Canyon, SE Utah: Castlegate Formation (Mesaverde Group).

hardening plays an important part in the development of shear fractures in porous siliciclastic sediments. It may also be questioned whether there is an upper limit for such mechanisms to prevail in the development of larger faults.

The influence of bed thickness, grain size and lithology on fracture frequency

It is well-established that bed thickness affects joint spacing (mode I fractures) in sediments (Harris *et al.* 1960; Price 1966; Hobbs 1967), and both linear (Price 1966; Narr & Suppe 1991) and non-linear (Ladeira & Price 1981) relationships have been proposed. Based on plaster experiments, Mandal *et al.* (1994) arrived at a non-linear relationship, and suggested that this relation is also valid for mode II and mode III fractures.

Lithology and grain size rule rock strength, and accordingly strongly influence fracturing. Based on fracture mapping in fine- and medium-grained sandstones of the Oseberg and Njord Fields in the Norwegian shelf, Gabrielsen *et al.* (1993) reported enhanced fracture frequencies in fine- to medium-grained sandstones as compared to siltstones and coarse-grained sandstones. In some cases, the number of fractures was enhanced by a factor of five in the fine-grained sequences. Figure 7 shows an example from two small, oblique faults in sandstones of the late Cretaceous Mesaverde Group in Utah. In this example, fracture frequencies have been recorded over a distance of approximately 60 m in sandy sequences with different thicknesses and grain size. Fracture frequencies in all the units increase in the vicinity of the faults, but the thinner layer with fine-grained sandstones displays an average fracture frequency enhanced by a factor of approximately 2.6 compared to that of medium-grained sandstones of twice the thickness, and a factor of four compared to coarse-grained sandstones five times its thickness.

It is also noted that tectonic and compactional fractures in mudstones and shales both in the field and in well cores, represent a particular problem since intense deformation or volume reduction caused by compaction and water escape in such lithologies frequently generate rubble zones, which completely prevent the evaluation of fracture frequency. This problem is exaggerated by the difficulty in separating tectonic fractures, particularly in cores, from those associated with volume reduction and water escape in the most fine-grained sediments (Petit & Laville 1987; Guiraud & Séguret 1987).

Some practical consequences of dealing with complex fracture data sets

By use of established (Mohr–Coulomb and Griffith) fracture criteria in combination with stress–depth–strength relations and statistical approaches in scaling relationships, structural geologists possess powerful tools for the prediction of fracture distribution in reservoirs. Still, a question may be posed as to whether the fracture sub-populations which are defined at different scales, and which make up the total fracture population, need to be genetically related to obey the mathematical relations described in the literature. If so, this demands that fracture populations applied in predictive studies of scaling relationships need to be genetically homogeneous. This puts strict constraints on sampling procedures. Previous and present data strongly suggest that fracture populations in siliciclastic sediments are, by nature, inhomogeneous in the context that they are commonly composed of several sub-populations of different genetic origin. Unfortunately, morphologies and textures of these structures are such that both on the meso-scale and on the micro-scale, the different genetic populations may be identified only after careful investigation.

Therefore, procedures for acquisition of fracture data need to be carefully designed, with particular emphasis on the identification of fracture sub-populations during field mapping or core analysis. For fractures in rocks exposed at the surface, the potential for studying structures in three dimensions may, to a large extent, secure the recognition of fracture sub-populations, and frequently provides the possibility of finding criteria for determining the genesis of individual fractures as well as for fracture sets.

For fractures studied in drill-cores, less information is usually available on the genesis of fracture sub-populations, and a total analysis of the fracture population and its tectonic and sedimentary environment should be performed before fracture data are mixed with data from elsewhere in statistical analysis. The problems with fracture modelling in, for instance, wells in the Norwegian continental shelf, are further increased because at the present stage of exploration, wells drilled at the crests of rotated fault blocks are over-represented in the available data. This implies that the data are recorded in a position where footwall collapse is frequent, so that the fracture frequency may be anomalously high.

Furthermore, deviation of the well path and the dip angle of the fractures in the drilled unit influence fracture statistics in wells. Such effects can be corrected for relatively easily (Sikorsky
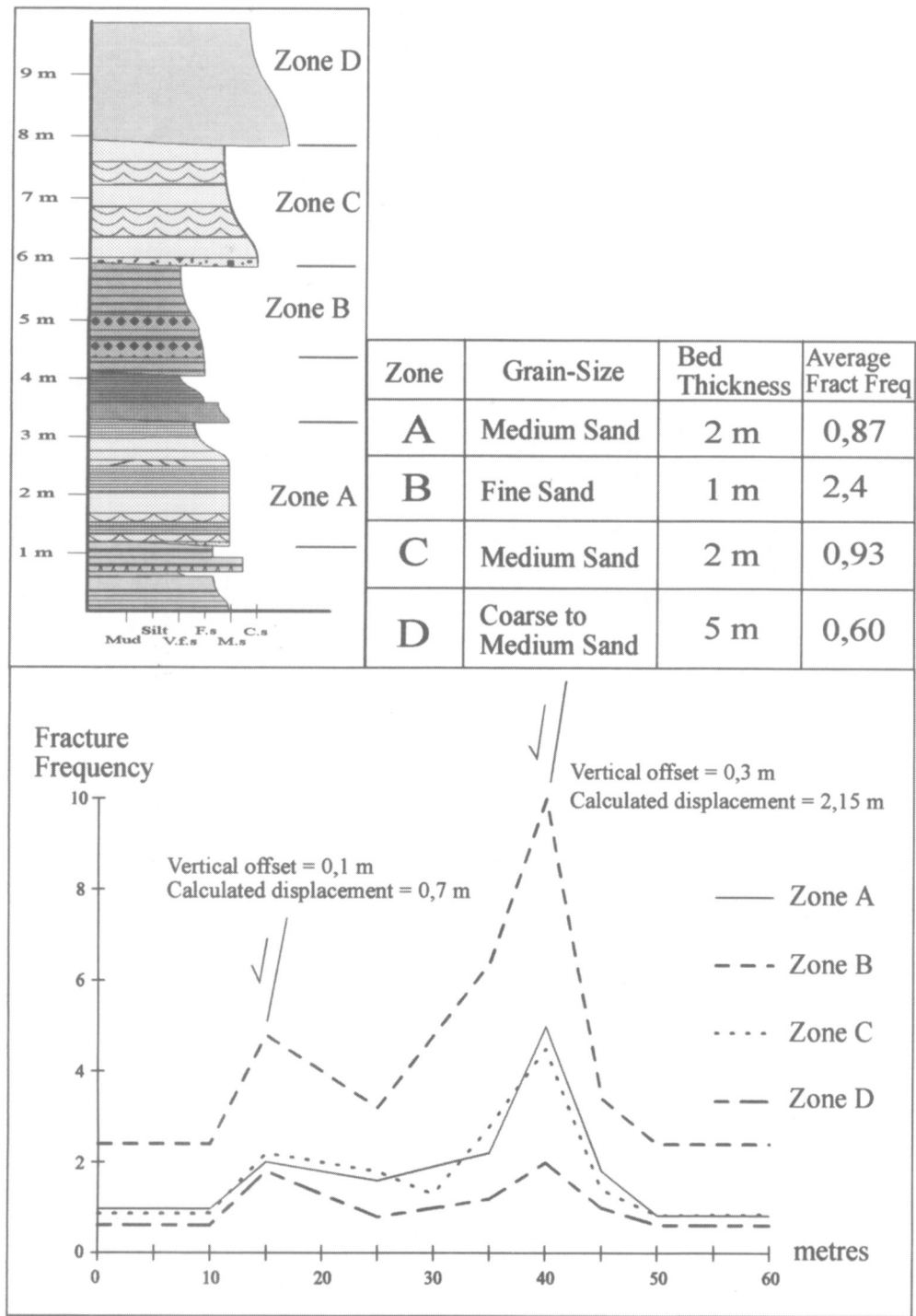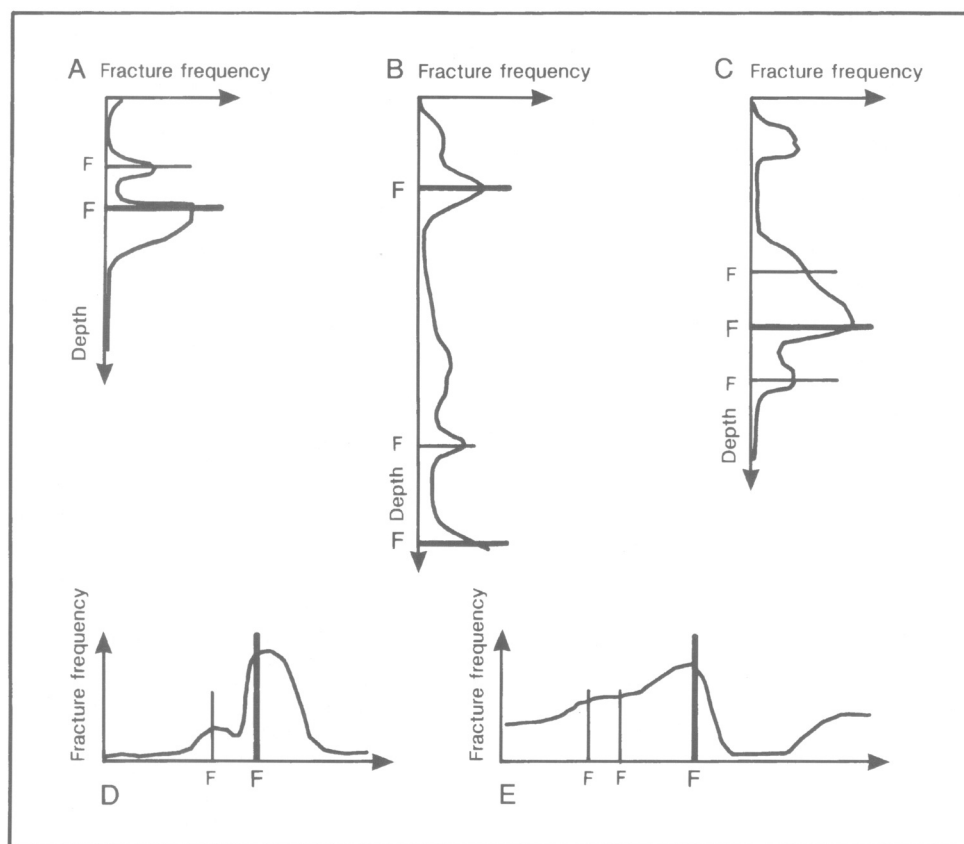
Fig. 7. Fracture frequencies associated with two small, oblique faults from the Late Cretaceous Mesaverde Group, Utah. Fracture frequencies have been recorded over a distance of approximately 60 metres in sandy sequences with different thicknesses and grain size.

(a)
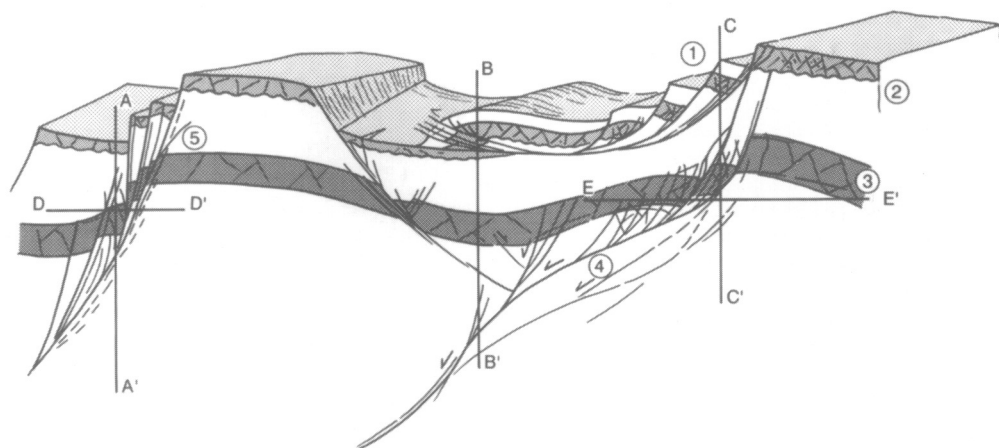
(b)

Fig. 8. Schematic representation of shifting fracture distribution in rotated fault blocks. (**a**). (1) Gravity slide; (2) and (3) sandstone units with different thicknesses; (4) zone of enhanced strain associated with ramp–flat–ramp fault; (5) fault with synthetic accommodation faults. (**b**). Schematic fracture distribution diagrams from vertical wells A and B, and from sections C–C′, D–D′ and E–E′.

1991; Versteeg & Morris 1994), but such corrections do not seem to be frequently reported in published fracture studies where such data are applied.

Figure 8 shows schematically some complexities of fracture distribution which can be expected in an area affected by gravity-driven soft-sedimentary faulting, compaction and tectonic extension. Owing to differences in the fault geometries, fracture logging in two wells crossing the master faults (sections A and B) would give different fracture frequency–depth curves. In section A a minor synthetic fault which is traversed in the hangingwall of the master fault gives two fracture frequency maxima. Section B traverses a gravity slide in its upper part and a high-strain area associated with a flat in the master fault. The flat has also caused the development of accommodation faults in the hangingwall and in the footwall. In both these sections, it is reasonable to assume that the tectonic fractures completely overrule the compactional fractures which are particularly frequent in layer 3.

If these structures were exposed on land, it may be assumed that fracture mapping in arbitrary sections C–C' and D–D' would give results which are significantly different from those obtained from the well logs in sections A and B, because fractures associated with compaction of layer 3 would represent a significant fracture sub-population in section D–D' (Fig. 8).

To obtain the best possible database for statistical fracture studies, we therefore suggest that the following steps should be followed in fracture mapping of cores.

(1) The position of the well relative to major structures, the geometry of near-by faults, and the general geological (sedimentary and tectonic) environment needs to be known. This implies that careful analysis of reflection seismic data should be performed.

(2) Fractures should not be recorded in the fracture logs without classification of fracture mode and assumed genesis.

(3) Fracture frequencies should be compared to lithology and bed thickness.

(4) Fracture frequency diagrams should be corrected for eventual well deviation and fracture orientation relative to well axis.

(5) Core handling should follow standard procedures, and it is an advantage if fracture logging is performed both prior to and after slabbing of the core.

References

AARLAND, R.-K. & SKJERVEN, J. 1998. Fault and fracture characteristics of a major fault zone in the northern North Sea: analysis of 30 seismic and oriented cores in the Brage Field (Block 31/4). This volume

ALHILALI, K. A. & DAMUTH, J. E. 1987. Slide block (?) of Jurassic sandstone and submarine channels in the basal Upper Cretaceous of the Viking Graben, Norwegian North Sea. Marine and Petroleum Geology, 4, 35–48.

ALSAKER, A. et al. 1996. The significance of the fracture pattern of the Palaeocene – early Miocene Montserrat Fan-Delta, Catalan Coastal Range (NE Spain), Tectonophysics, 226, 465–491.

ANTONELLINI, M. & AYDIN, A. 1994. Effect of faulting on fluid flow in porous sandstones. petrophysical properties. AAPG Bulletin, 78, 355–377.

——, —— & POLLARD, D., D. 1994. Microstructure of deformation bands in porous sandstones at Arches National Park, Utah. Journal of Structural Geology, 16, 941–959.

AYDIN, A. 1978. Small faults formed as deformation bands in sandstone. Pure and Applied Geophysics, 116, 913–913.

—— & JOHNSON, A. M. 1978. Development of faults as zones of deformation bands and slip surfaces in sandstone. Pure and Applied Geophysics, 116, 931–942.

—— & ——1983. Analysis of faulting in porous sandstones. Journal of Structural Geology, 5 19–31.

BARNETT, J. A. M., MORTIMER, J., RIPPON, J. H., WALSH, J. J. & WATTERSON, J. 1987. Displacement geometry in the volume containing a single normal fault. AAPG Bulletin, 71, 925–937.

BATES, R. L. & JACKSON, J. A. 1987. Glossary of Geology. American Geological Institute, Virginia.

BEACH, A., BROCKBANK, P., BROWN, L., KNOTT, S., McCULLUM, J. & WELBORN, A. 1995. Structural characterisation of sandstone reservoirs-outcrop analogues for subsurface fault predictions. (abstract). Structural Geology in Reservoir Characterisation and Field Development. Imperial College, London, 1995, 6–7.

BEHRMANN, J. H., BROWN, K., MOORE, J. C., et al. 1988. Evolution of structures and fabrics in the Barbados Accretionary Prism. Insights from Keg 110 of the Ocean Drilling Program. Journal of Structural Geology, 10, 577–592.

BRUCE, C. H. 1973. Pressured shale and related sediment deformation. mechanism for development of regional contemporaneous faults. *AAPG Bulletin*, **57**, 878–886.

BURBRIDGE, G. H., FRENCH, H. M. & RUST, B. R. 1988. Water escape structures resembling ice-wedge casts in Late Quaternary subaqeuous outwash near St.Lazare, Quebec, Canada. *Boreas*, **17**, 33–40.

BÜRGMANN, R., POLLARD, D. D. & MARTEL, S. J. 1994. Slip distribution on faults, effects of stress gradients, inelastic deformation, heterogeneous host-rock stiffness, and fault interaction. *Journal of Structural Geology*, **16**, 1675–1690.

CHEEL, R. J. & RUST, B. R. 1986. A sequence of soft-sediment deformation (dewatering) structures in the late Late Quaternary subaqeuous outwash near Ottawa, Canada. *Sedimentary Geology*, **47**, 77–93.

CHESTER, F. M. & LOGAN, J. M. 1986. Implications for mechanical properties of brittle faults from observations of the Punchbowl fault zone, California. *Pure and Applied Geophysics*, **124**, 79–106.

CHILDS, C., WALSH, J. J. & WATTERSON, J. 1990. A method for elimination of the density of fault displacements below the limits of seismic resolution in reservoir formations. *In:* BULLER, A. (ed.) *North Sea Oil and Gas Reservoirs – II.* Norwegian Petroleum Society (Graham & Trotman), 309–318.

CLOOS, H., 1968. Experimental analysis of Gulf Coast fracture patterns. *AAPG Bulletin*, **52**, 420–441.

COWIE, P. A. & SCHOLZ, C. H. 1992a. Physical explanation for the displacement–length relationship of faults using a post-yield fracture mechanics model. *Journal of Structural Geology*, **14**, 1133–1148.

—— & ——1992b. Displacement–length scaling relationship for faults; data synthesis and discussion. *Journal of Structural Geology*, **14**, 1149–1156.

CRANS, W., MANDL, G. & HARREMBOURRE, J. 1980. On the theory of growth faulting. A geomechanical delta model based on gravity sliding. *Journal of Petroleum Geology*, **2**, 265–307.

CRUIKSHANK, K. M., ZHAO, G. & JOHNSON, A. M. 1991. Duplex structures connecting fault segments in Entrada sandstone. *Journal of Structural Geology*, **13**, 1185–1186.

DE LANGE, G. J., KOK, T. T. J., EBBING, J. & VAN DER KLUGT, P. 1988. Microfault-like structures in unconsolidated Upper Quaternary sediments from the Madeora abyssal plain (eastern North Atlantic). *Marine Geology*, **80**, 155–159.

DUNN, D. E., LEFOUNTAIN, L. J. & JACKSON, R. E. 1973. Porosity dependence and mechanism of brittle fracture in sandstones. *Journal of Geophysical Research*, **78**, 2403–2417.

ENGELDER, T. 1985. Loading paths to joint propagation during a tectonic cycle. an example from the Appalachian Plateau, U.S.A. *Journal of Structural Geology*, **7**, 459–476.

——1993. *Stress Regimes in the Lithosphere.* Princeton University Press.

FARRELL, S. G. & EATON, S. 1988. Foliation developed during slump deformation of Miocene marine sediments, Cyprus. *Journal of Structural Geology*, **10**, 567–576.

FOSSEN, H. & GABRIELSEN, R. H. 1995. Experimental modeling of extensional fault systems by use of plaster. *Journal of Structural Geology*, **18**, 673–687.

GABRIELSEN, R. H. & AARLAND, R.-K. 1990. Characteristics of pre-/syn-consolidation structures and tectonic joints and microfaults in fine- to medium-grained sandstones. *In:* BARTON, N. & STEPANSSON, O. (eds) *Rock Joints.* Balkema, Amsterdam, 4 5–50.

—— & ——1995. How can fracture analysis contribute to the understanding of previous and recent stress systems? *In:* FEJERSKOV, M. & MYHRVANG, A. M. (eds) *Rock Stresses in the North Sea.* NTH/SINTEF, 38–48.

—— & KOESTLER, A. G. 1987. Description and structural implications of fractures in the late Jurassic sandstones of the Troll Field, northern North Sea. *Norsk Geologisk Tidsskrift*, **67**, 371–381.

—— & ROBINSON, C. 1984. Tectonic inhomogeneities of the Kristiansund-Bodø Fault Complex, offshore mid Norway. *In:* SPENCER, A. M. *et al.* (eds) *Petroleum Geology of the North European Margin.* Norwegian Petroleum Society (Graham & Trotman), 397–406.

——, AARLAND, R.-K. & PEDERSEN, T. 1993. Distribution and genesis of natural fracture systems in clastic sediments. *In:* BANKS, S. & BANKS, D. (eds) *Hydrogeology of Hard rocks. Memoirs of the XXIVth Congress International Association of Hydrogeologists,* 52–73.

GILLESPIE, P. A., WALSH, J. J. & WATTERSON, J. 1992. Limitations of dimension and displacement data from single faults and the consequences for data analysis and interpretation. *Journal of Structural Geology*, **14**, 1157–1172.

GROSHONG, R. H. Jr 1988. Low temperature deformation mechanisms and their interpretation. *Geological Society of America, Bulletin*, **100**, 1329–1360.

GUIRAUD, M. & SÉGURET, M. 1987. Soft-sediment micro-faulting related to compaction within the fluvio-deltaic infill of the Soria strike-slip basin, northern Spain. *In:* JONES, K. E. & PRESTON, M. F. (eds) *Deformation of Sediments and Sedimentary Rocks.* Geological Society, London, Special Publication, **29**, 123–136.

HAIMSON, B. C. & DOE, T. W. 1983. State of stress, permeability, and fractures in the Precambrian granite of northern Illinois. *Journal of Geophysical Research*, **88**, 7355–7372.

HANCOCK, P. L. 1985. Brittle microtectonics. Principles and practice. *Journal of Structural Geology*, **7**, 437–457.

HARDIN, F. R. & HARDIN, G. C. Jr 1961. Contemporaneous normal faults of Gulf Coast and their relation to flexures. *AAPG Bulletin*, 45, 238–248.

HARRIS, J. F., TAYLOR, G. L. & WALPER, J. L. 1960. Relation of deformation fractures in sedimentary rocks to regional and local structures. *AAPG Bulletin*, **44**, 1853–1873.

HEALD, M. T. 1956. Cementation of Simpson and St. Peter Sandstone in parts of Oklahoma. *Journal of Geology*, **64**, 16–30.

HOBBS, D. W. 1967. The formation of tension joints in sedimentary rocks. an explanation. *Geological Magazine*, **104**, 550–556.

JACKSON, P. & SANDERSON, D. J. 1992. Scaling of fault displacements from the Badajoz-Cordoba shear zone, SW Spain. *Tectonophysics,* **210**, 179–190.

JAMISON, W. R. & STEARNS, D. W. 1982. Tectonic deformation of Wingate Sandstone, Colorado National Monument. *AAPG Bulletin,* **66**, 2584–2608.

KOESTLER, A. G. & EHRMANN, W. U. 1991. Description of brittle extensional features in chalk on the crest of a salt ridge (NW Germany). *In*: ROBERTS, A. M., YILEDING, G. & FREEMAN, B. (eds) *The Geometry of Normal Faults.* Geological Society, London, Special Publication, **56**, 113–123.

KULANDER, B. R., DEAN, S. L. & WARD, B. J. J. 1990: *Fractured core analysis: Interpretation, logging, and use of natural and induced fractures in core.* AAPG, Methods in Exploration Series No. **8**.

LADEIRA, F. L. & PRICE, N. J. 1981. Relationship between fracture spacing and bed thickness. *Journal of Structural Geology,* **3**, 179–183.

LOWE, D. R. 1975. Water escape structures in coarse-grained sediments. *Sedimentology,* **22**, 157–204.

MALTMAN, A. J. 1988. The importance of shear zones in naturally deformed wet sediments. *Tectonophysics,* **145**, 163–175.

——1994. Deformation structures preserved in rocks. *In*: MALTMAN, A. (ed.) *The Geological Deformation of Sediments.* Chapman & Hall, London, 261–307.

MANDAL, N., DEB, S. K. & KHAN, D. 1994. Evidence for a non-linear relationship between fracture spacing and layer thickness. *Journal of Structural Geology,* **16**, 1275–1281.

MANDL, G. 1988. *Mechanics of Tectonic Faulting. Models and Concepts.* Elsevier, New York.

——, DE JONG, L. N. J. & MALTHA, A. 1977. Shear zones in granular material. an experimental study of their structure and mechanical genesis. *Rock Mechanics,* **9**, 95–144.

MARRETT, R. & ALLMENDINGER, R. W. 1991. Estimates of strain due to brittle faulting. Sampling of fault populations. *Journal of Structural Geology,* **13**, 735–738

MARTINSEN, O. & BAKKEN, B. 1990. Extensional and compressional slumps and slides in the Namurian of County Clare, Ireland. *Journal of the Geological Society of London,* **147**, 153–164.

NARR, W. & CURRIE, J. B. 1982. Origin of fracture porosity – Example from the Altamont Field, Utah. *AAPG Bulletin,* **66**, 1231–1247.

—— & SUPPE, J. 1991. Joint spacing in sedimentary rocks. *Journal of Structural Geology,* **13**, 63–72

NELSON, R. A. 1981. Significance of fracture sets associated with stylolite zones. *AAPG Bulletin,* **65**, 2417–2425.

NYSTUEN, J. P. 1989. Rules and recommendations for naming of geological units in Norway. *Norsk Geologisk Tidsskrift,* **69**, Suppl. 2.

ORD, D. M., CLEMMEY, H. & LEEDER, M. R. 1988. Interaction between faulting and sedimentation during Dinantian extension of the Solway basin, SW Scotland. *Journal of the Geological Society of London,* **145**, 149–259.

OWEN, G. 1987. Deformation processes in unconsolidated sands. *In*: JONES, M. E. & PRESTON, R. M. F. (eds) *Deformation of Sediments and Sedimentary Rocks.* Geological Society, London, Special Publication, **29**, 11–24.

PEDERSEN, T. A. 1992. *Strukturelle strømningsbarrierer og deres betydning for komminikasjon og strømning av hydrokarboner på Njordfeltet.* Cand.scient. thesis, University of Bergen.

PETIT, J.-P. & LAVILLE, E. 1987. Morphology and microstructures of hydroplastic slickensides in sandstone. *In*: JONES, K. E. & PRESTON, M. F. (eds) *Deformation of Sediments and Sedimentary Rocks.* Geological Society, London, Special Publication, **29**, 107–121

PITTMAN, E. D. 1981. Effects of fault-related granulation on porosity and permeability of quartz sandstones. *AAPG Bulletin,* **65**, 2381–2387.

PRICE, N. J. 1966. *Fault and Joint Development in Brittle and Semi-brittle Rock.* Pergamon, Oxford.

RAMSAY, J. G. & HUBER, M. I. 1987. *The Techniques of Modern Structural Geology, Volume 2: Folds and Fractures,* 309–700.

RIDER, M. H. 1978. Growth faults in Carboniferous of western Ireland. *AAPG Bulletin,* **62**, 2191–2213.

SBAR, M. L. & SYKES, L. R. 1973. Contemporary compressive stress and seismicity in eastern North America. An example of intra-plate tectonics. *Geophysical Society of America Bulletin,* **80**, 1231–1264.

SCHOLZ, C.H & COWIE, P. A. 1990. Determining a total geologic strain from faulting. *Nature,* **346**, 837–839.

SIKORSKY, R. I. 1991. A diagram for interpreting orientation data for planar features in core. *Journal of Structural Geology,* **13**, 1085–1089.

STEARNS, D. W. & FRIEDMAN, M. 1972. Reservoirs in fractured rocks. *AAPG Memoir,* **16**, 83–106.

STOW, D. A. V. 1986. Deep clastic seas. *In*: READING, H. G. (ed.) *Sedimentary Environments and Facies.* Blackwell, Oxford, 399–444.

SVERDRUP, E. & BJØRLYKKE, K. 1992. Small faults in sandstones from Spitsbergen and Haltenbanken. A study of diagenetic and deformational structures and their relation to fluid flow. *In*: LARSEN, R. M., BREKKE, H., LARSEN, B. T. & TALLERAAS, E. (eds) *Structural Modelling and its Application to Petroleum Geology.* Norwegian Petroleum Society Special Publication, **1**, 507–517.

TILLMAN, J. E. 1983. Exploration for reservoirs with fractured enhanced permeability. *Oil & Gas Journal,* **81**, 165–180.

—— & BARNES, H. L. 1983. Deciphering fracturing and fluid migration histories in the Northern Appalachian Basin. *AAPG Bulletin,* **67**, 692–705.

VERSTEEG, J. K. & MORRIS, W. A. 1994. Pitfalls and procedures for determining fabric orientations in non-oriented bore core. *Journal of Structural Geology,* **16**, 283–286.

VISSER, J. N. J., COLLISTON, W. P. & TEREBLANCHE, J. C. 1984. The origin of soft-sediment structures in Permo-Carboniferous glacial and proglacial beds, South Africa. *Journal of Sedimentary Petrology,* **54**, 1183–1196.

VOIGHT, B. & ST. PIERRE, B. H. P. 1974. Stress history and rock stress. *In*: *Advances in Rock Mechanics: Proceedings of the 3rd Congress, International Society of Rock Mechanics,* **2**, 580–582.

WALSH, J. J. & WATTERSON, J. 1987. Distribution of cumulative displacement and seismic slip on a single normal fault surface. *Journal of Structural Geology*, **9**, 1039–1046.

—— & ——1988. Analysis of relationship between displacements and dimensions of faults. *Journal of Structural Geology*, **10**, 239–247.

—— & ——1989. Displacement gradients on fault surfaces. *Journal of Structural Geology*, **11**, 307–316.

——, —— & YIELDING, G. 1991. The importance of small-scale faulting in regional extension. *Nature*, **351**, 391–393.

WATTERSON, J. 1986; Fault dimensions, displacements and growth. *Pure and Applied Geophysics*, **124**, 365–373.

WATTS, N. L. 1983. Microfractures in chalks from the Albuskjell Field, Norwegian sector, North Sea. Possible origin and distribution. *AAPG Bulletin*, **67**, 201–234.

WESTAWAY, R. 1994. Quantitative analysis of populations of small faults. *Journal of Structural Geology*, **16**, 1259–1273.

WILKE, S., GUYON, E. & DE MARSILY, G. 1985. Water penetration through fractured rocks. Test of a tridimensional percolation description. *Mathematical Geology*, **17**, 17–27.

WOJTAL, S. F. 1994. Fault scaling and the temporal evolution of fault systems. *Journal of Structural Geology*, **16**, 603–612.

Flow through fault systems in high-porosity sandstones

T. MANZOCCHI[1,2], P. S. RINGROSE[1,3] & J. R. UNDERHILL[4]

[1] Department of Petroleum Engineering, Heriot-Watt University, Edinburgh EH14 4AS, UK
[2] Present address: Fault Analysis Group, Department of Earth Sciences,
University of Liverpool, Liverpool L69 3BX, UK
[3] Present address: Statoil Research Centre, Postuttak, Trondheim 7005, Norway
[4] Department of Geology and Geophysics, The University of Edinburgh,
Edinburgh EH9 3JW, UK

Abstract: Small-scale faults in high-porosity sandstones form highly connected systems over a range of length scales. The effective permeability and oil recovery in such fault systems are strongly controlled by their geometrical architecture. This paper describes partially sealing faults in terms of: (a) characterization of their spatial distribution; (b) their effects on reservoir compartmentalization; and (c) their significance for fluid flow. Four suites of numerical flow simulations in highly compartmentalized fault systems are used to assess the influence of geometrical variability on single- and two-phase flow. The single-phase suites demonstrate that effective permeability is approximately linearly related to the number of fault-enclosed compartments present in a fault system. Use of a fault heterogeneity measure allows effective permeability for a geometrical case to be estimated from fault density and fault and matrix permeability. The two-phase simulations model water-floods, and show the relationships between length scale, fault system geometry and oil recovery. In a self-similar fault system, oil recovery is preferentially inhibited at the smaller length scales. Oil recovery is influenced by compartment volume distribution and is therefore sensitive to fault clustering. The fault density necessary to severely affect either single- or two-phase flow is likely to occur only close to structures which are large relative to the scale under consideration. This improved understanding of the relative influences of fault system geometry, density and petrophysics should lead to significantly improved hydrocarbon recovery from faulted high-porosity sandstones.

Fault system architecture

High-porosity quartz arenitic sandstones often show high fault densities both in outcrop and core. Although individual fault displacements are often less than a centimetre, these faults are characterized by significant reduction in porosity, grain sorting, grain sphericity and pore throat size over a 1–2 mm wide zone. The mechanics of deformation in quartz-rich siliciclastics has been extensively reviewed (e.g. Aydin & Johnson 1983; Underhill & Woodcock 1987; Antonellini *et al.* 1994). Because the strength of a sandstone is proportional to porosity (Dunn *et al.* 1973) and high porosity favours fault strain-hardening, small-scale faulting will tend to be most prevalent in the best quality sandstone reservoirs, and faulting there will be predominantly small-scale.

Figure 1 shows an example of faulting in the Permian Penrith Sandstone in the north of England at George Gill near Espland (Knott 1994). Single-event deformation bands (granulation seams) often form multiple-event zones of bands (Fig. 1a). The faults form in characteristic orientations, and interaction of bands and zones of different orientations produces polyhedral fault-bounded sandstone compartments (Fig. 1b). Although the petrophysical properties of the faults vary with provenance, porosity can be reduced by up to 80%, permeability is frequently around three orders of magnitude less than that of the unfaulted sandstone matrix, and capillary pressures across faults are much higher than in matrix samples (e.g. Pittman 1981; Jamison & Stearns 1982; Underhill & Woodcock 1987; Antonellini & Aydin 1994; Fowles & Burley 1994).

Figure 2 illustrates the nature of faulting in porous sandstones at a range of length scales. The smallest-scale image is a computerized tomograph (CT) scan of a 1 cm thick zone of deformation bands from a sample recovered from core from the North Sea (Fig. 2a). The image has a pixel resolution of 0.2 mm × 0.2 mm and has been processed to display only CT values above an arbitrary threshold. The CT number correlates directly with density, and therefore a high CT number indicates low porosity in monomineralic rock. At this scale the anastomosing nature of the zones of bands is evident, with frequent fault splays and patches of higher porosity sandstone between zones of high density fault gouge.

The second fault map is one order of magnitude larger, and comes from the Penrith Sandstone at

(a)

(b)
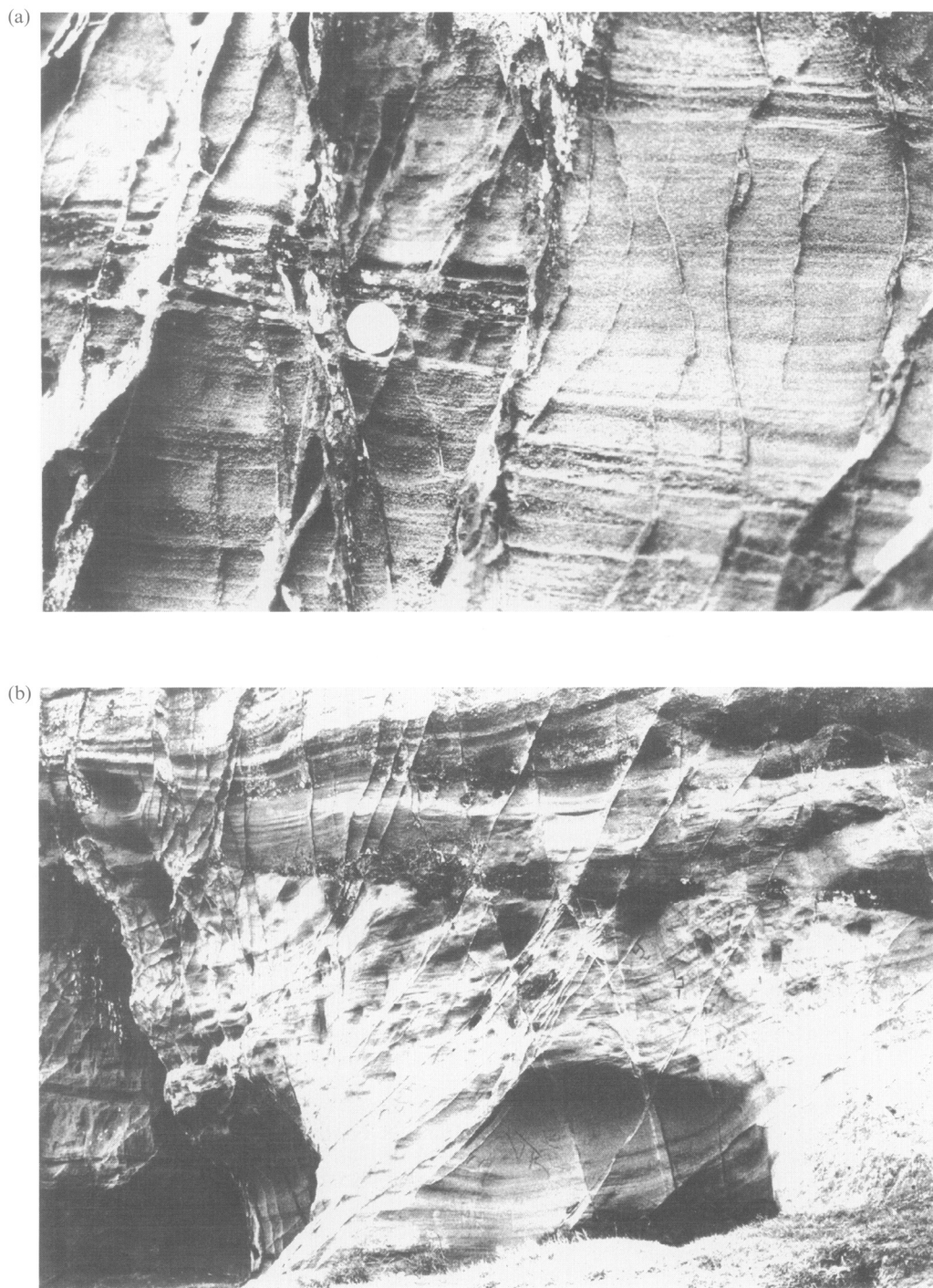
Fig. 1. Small-scale faulting in Penrith Sandstone, George Gill, Vale of Eden. (**a**) Thin anastomosing zones of bands (left) have sub-centimetre displacements. Single wavy deformation bands (right) frequently form splays and terminate as isolated fault tips. Photograph is 35 cm wide. (**b**) Fault traces from two conjugate sets of deformation bands form rhomb-shaped fault-enclosed compartments. Photograph is 8 m wide.
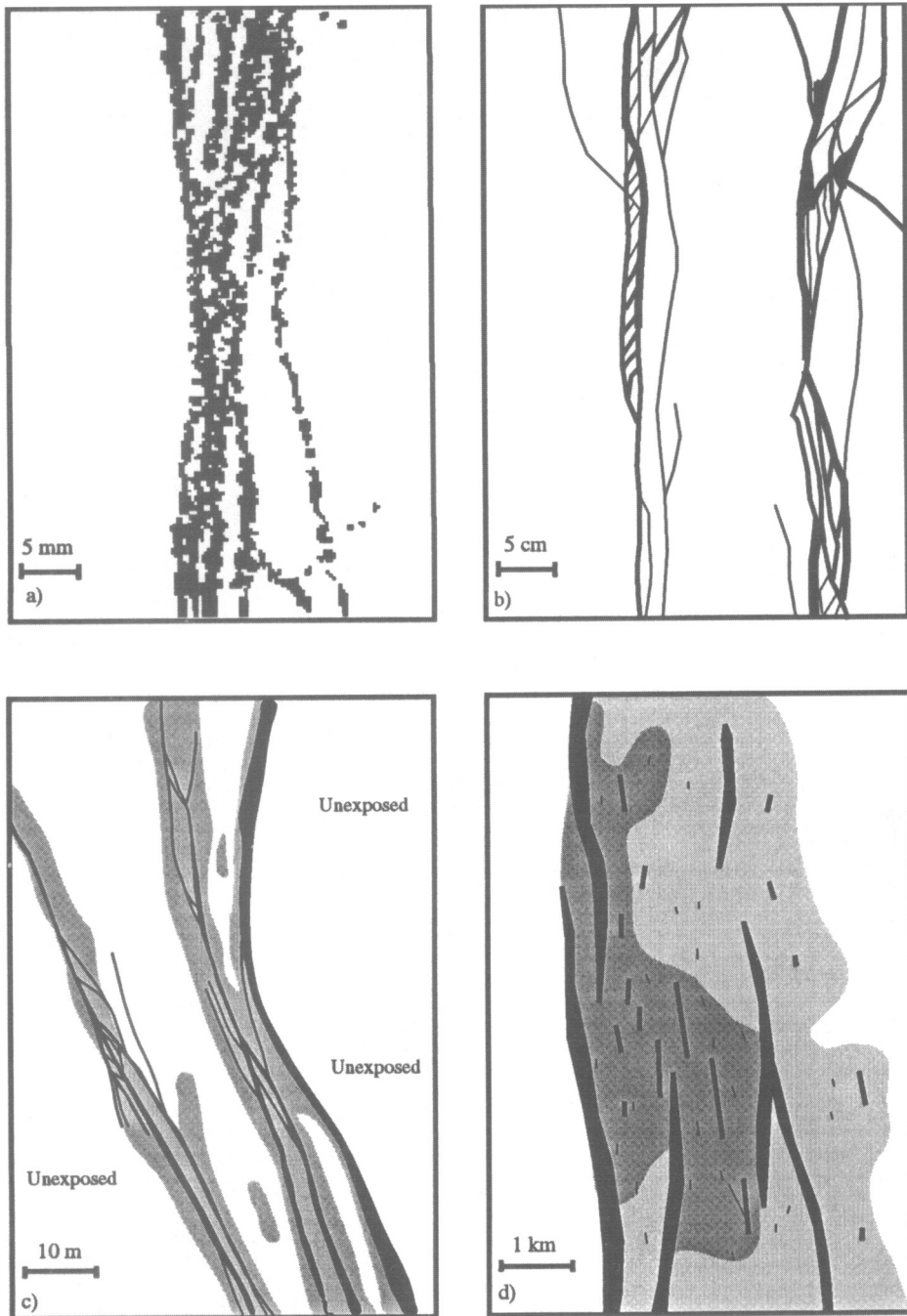
Fig. 2. Faulting at four scales. (**a**) Millimetre-scale CT image of a narrow zone of deformation bands from North Sea core. Pixel resolution is 0.2 mm × 0.2 mm. (**b**) Centimetre-scale fault map from the Permian Penrith Sandstone, Vale of Eden, N England. Resolution is that of the naked eye. (**c**) Tens of metres-scale fault map from a pavement in the Navajo Sandstone, Arches National Park, Utah. Resolution for discrete faults is 10 cm thickness. Contoured fault density for narrower faults is derived from one-dimensional scan lines. The shaded area represents fault density of more than five per metre. (**d**) Hypothetical kilometre-scale reservoir structure map. Seismic fault resolution is approximately 20 m offset.

George Gill (Fig. 2b). Two zones of deformation bands are shown, each with a variable and complex internal morphology. Again, a high frequency of splays and anastomosing strands within the zones is evident. Frequent duplex structures occur within the zones, resulting in variable gouge thicknesses along the zone traces. Duplex structures are common in faulted high-porosity sandstones (Cruikshank *et al.* 1991), and are a common way for zones of deformation bands to terminate. Because of this, the overall connectivity of deformation band systems is often very high. However, both at this and the previous scale, many of the splay faults also have isolated terminations.

Figure 2c is a fault map from the Navajo Sandstone on the Moab anticline in Arches National Park, SE Utah. The 50 m × 80 m area is two orders of magnitude larger than the previous map, and contains faults ranging in width from 1 mm to 1 m. This range is too great to allow construction of a completely scaled map, and only faults thicker than 10 cm are shown. A series of 13 scan lines perpendicular to strike have been averaged to infer the shaded regions which represent areas with over five bands per metre. This average (based on the number of faults) is only one of several possible representations and others are feasible: a fault density average is proportional to gouge thickness, and a strain average is proportional to fault displacements. Thus density and displacement information, as well as data appertaining to connectivity, is not represented by the average selected. The overall fault pattern is similar to the smaller-scale images, with tight fault clusters and frequent duplexes and splays. However, the overall proportion of fault splays to fault terminations is lower than at the previous scale. This is because large faults are frequently transferred onto structures which are below the resolution of the map. The need to average smaller faults has reduced the apparent connectivity of the fault system.

Figure 2d shows a hypothetical reservoir structure map. Only faults with offsets greater than about 20 m are resolvable by three-dimensional seismic, so this is the smallest scale of fault that can be explicitly mapped. The scale of this map is more than five orders of magnitude greater than the CT image (Figure 2a). In order to understand the effect of sub-seismic faulting on flow in this hypothetical sandstone reservoir, the nature of flow and faulting at all relevant scales, from millimetres to kilometres, must therefore be considered. Flow is a function of fault and matrix permeability, the fault system structure, and the fault density and density distribution throughout the reservoir. The object of

this study is to establish which characteristics of the fault system will most affect flow.

Fault data may come from several different sources. Core may yield samples the scale of Fig. 2a. This grain and pore scale is critical as it is the scale at which permeability is determined: cataclasis in quartz arenites or clay smearing in less pure sandstones ultimately determine the petrophysical properties of the fault gouge. The centimetre–decimetre scale shown on Fig. 2b may be resolved by acoustic and electrical wellbore image logs. These may reveal information about fault density and clustering characteristics, but not about permeability which requires core. Information about fault system geometry at scales larger than this, such as that mapped on Fig. 2c, is impossible to gather from wells in anything greater than one-dimensional datasets. Faults between about 1 m and 20 m offset are generally irresolvable by either well or seismic. At these scales the use of analogue or theoretical models of faulting is vital.

Several methods exist to determine areas of likely sub-seismic faulting in reservoirs, including those based on the proximity to large structures (e.g. Gauthier & Lake 1993) or those based on curvature mapping (e.g. Lisle 1994). Field evidence in faulted sandstone systems exists for both these techniques. Jamison & Stearns (1982) have shown small faults clustering around large structures, and a relationship between curvature and fault density has been demonstrated for deformation band systems by Antonellini & Aydin (1995). Here we focus on how small-scale fault density predictions could be used to gain a quantitative assessment of hydrocarbon flow within faulted reservoirs.

An essential step in modelling sub-seismic faulting in reservoirs is to derive a fault density map based on interpretation of the relevant data: seismic, core, regional geological model, tectonic history, rheology, etc. Populating this fault density map with individual faults, each with appropriate petrophysical properties, at all relevant length scales is intractable, so statistical approaches are necessary. Figure 2c illustrates the necessity of fault system averaging, and highlights some of the assumptions and simplifications that must be made in such averaging. Even if populating a deterministic fault map were possible, calculating flow in so complex a model would be computationally exorbitant. A prediction of the flow in a faulted sandstone must therefore rely on some form of fault system averaging, incorporating the effect of flow in the faulted zones as effective properties. A fault system can be characterized by several interrelated geometrical factors. This paper considers some of the

geometrical aspects of fault systems and their significance for flow. Only through an understanding of which fault system attributes are important to flow can reservoir geologists know how to characterize fault systems effectively. Similarly, only through an understanding of natural fault systems can a reservoir engineer know whether the methods or assumptions used in modelling the fault system are valid.

Previous work on predicting flow effects due to sealing or partially sealing faults has focused on the frequency of minor faults at sub-seismic scales (e.g. Gauthier and Lake 1993; Heath *et al.* 1994), with little attention placed on modelling the connectivity characteristics of the system. Conversely, many of the fault characterization and flow performance calculations for hydraulically conductive fracture systems have concentrated on the fault clustering and connectivity characteristics of the system (e.g. Odling 1992*b*). In such systems, most of the flow is concentrated in the fractures and the greater the fracture system connectivity, the greater the flow performance of the reservoir. The opposite is true for partially sealing faults. In these systems the flow is concentrated in the high-permeability matrix, and if the fault system is highly connected, flow is impaired. Fault system geometry is likely to be significant for flow through low-permeability faults, due to compartmentalization of the high-permeability matrix by low-permeability faults.

Fault system modelling

A fracture system can be statistically characterized by only a few geometrical factors (La Pointe & Hudson 1985; Dershowitz & Einstein 1988). The most fundamental factor is fault density and the other factors characterize the distribution of fault density in space. In this study, fault density refers to the total fraction of fault gouge in a volume of rock.

Individual faults (each with particular orientations, sizes, displacements, terminations and positions) occur over a wide range of scales. Fault size and displacement characteristics are governed by the scaling laws of the fault system which define the number of faults at a particular length scale that are present in the system. Fault system connectivity is controlled by the other factors: orientation, termination and position.

Fault scaling

A common technique for determining the frequency of sub-seismic faults assumes scale

invariance. This method (Yielding *et al.* 1992; Gauthier & Lake 1993) relies on self-similarity of fault attribute scaling between seismic and sub-seismic scales. It is based on relationships of the form:

$$N = AL^{-m} \qquad (1)$$

and

$$D = BL^n \qquad (2)$$

where N is the cumulative number of faults of length $\geq L$, D is fault displacement and A, B, m and n are system-specific constants. Equation 1 implies that fault density is scale-invariant (Childs *et al.* 1990; Scholz & Cowie 1990), while Eqn 2 implies scale invariance of fault shape (Gillespie *et al.* 1992). From these relationships it is possible to predict the frequency of faults of any particular length scale, but implicit in the implementation of this method is the belief in a mechanical continuum of faulting at all scales covered by the extrapolation. This is not the case for fault systems in porous sandstones.

Faults in porous sandstones occur in three styles: single deformation bands, zones of deformation bands and slip surfaces (Aydin & Johnson 1978). A continuum of physical processes may exist between the first two styles as both represent strain-hardening processes, but the development of slip surfaces involves a physical transition from shear displacement accommodated across a thickening fault zone to displacement accommodated on a single plane. Slip surfaces strain-soften rather than strain-harden. It is therefore unlikely that fault systems would show a constant power-law distribution over length scales spanning this mechanical transition. In the Penrith Sandstone this transition occurs at fault displacements of about 0.3 m (Knott 1994).

Similarly, the displacement/length relationship (Eqn 2) is process-dependent. Although the relationship is broadly correct for about six orders of magnitude of faulting (Gillespie *et al.* 1992), a mechanical transition between strain-hardening deformation bands and strain-softening slip surfaces negates the possibility of complete scale invariance. High-porosity sandstones are often massively bedded with few good marker laminations and it is notoriously difficult to measure deformation band displacement gradients. Preliminary data reported by Antonellini & Aydin (1995) show that although displacement/length relationships may be scale-invariant for slip surfaces, no such relationship seems to exist for deformation bands. Cowie & Scholz (1992) have shown that an important parameter determining the displacement/length relationship is friction. In deformation bands friction is high, whereas slip surfaces have much lower friction.
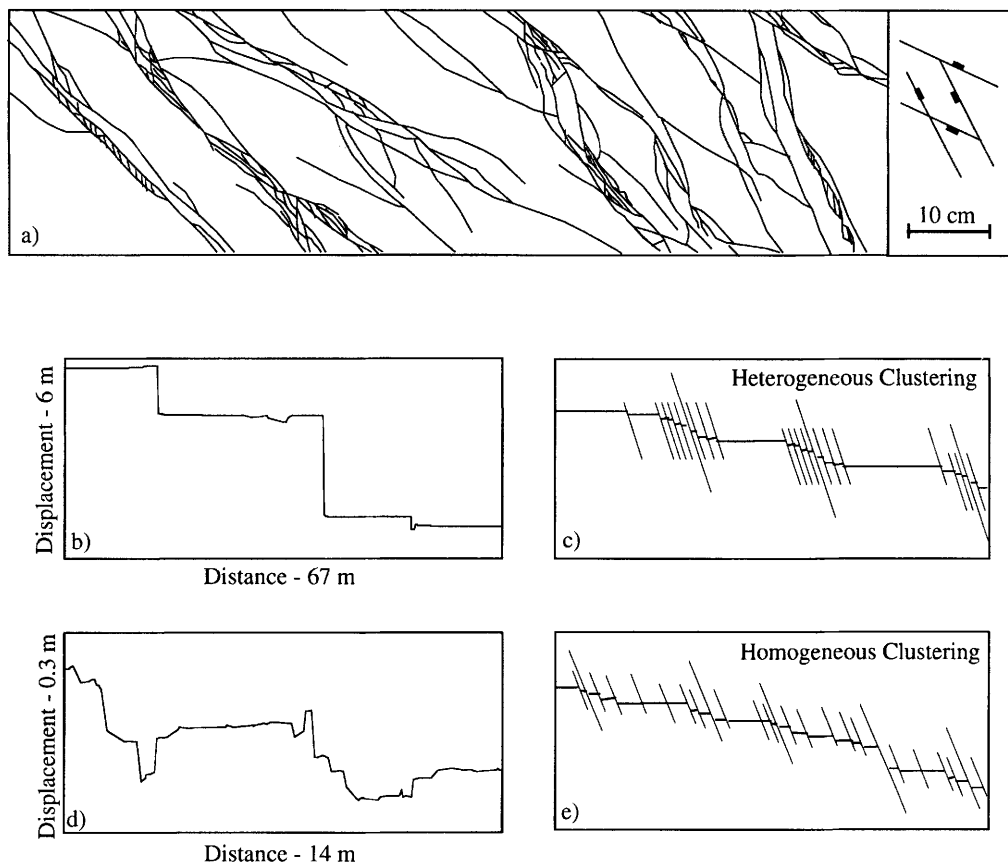
Fig. 3. (**a**) Fault trace map from the Permian Penrith Sandstone, George Gill, Vale of Eden. Fault thickness variation is not represented. (**b**) Fault displacement section for a heterogeneous cluster system, Belah Scar, Vale of Eden. (**c**) Cartoon of heterogeneous clustering – small distinct fault clusters are formed around slip surfaces. (**d**) Fault displacement section from within a cluster, George Gill, Vale of Eden. (**e**) Cartoon of a homogeneous fault system – indistinct overlapping clusters are formed.

Friction is a fundamental control on strain-hardening versus strain-softening faulting processes (Underhill & Woodcock 1987). Therefore it is reasonable to suppose that displacement gradients on deformation bands are markedly different from those on slip surfaces. The strain-hardening/strain-softening transition discussed above is peculiar to high-porosity sandstones; however, analogous mechanical and scaling transitions have been reported from other fracture styles, for example tensile fractures in basalts by Hatton *et al.* (1994).

Fault connectivity

Fault connectivity is governed by fault orientation, termination and placement characteristics. The most essential factor for connectivity is orientation: if all faults are parallel, no faults can connect. Fault systems are usually divided into orientation populations, and the stress state at the time of faulting controls the orientations of the populations present. Four orientation populations are necessary to accommodate triaxial strain (Reches 1977; Krantz 1988) and this is often observed in porous sandstones (Aydin & Reches 1982; Underhill & Woodcock 1987). Figure 3a is a small-scale fault trace map from the Penrith Sandstone, with the four principal orientation populations indicated. Usually a fault system consists of two or more orientation populations, with individual faults dispersed around the principal orientations. For a given length distribution, the fault system becomes more connected as the angle between two populations of parallel faults or the dispersion of fault orientations increases (Robinson 1983).

Fault system termination characteristics directly control fault system connectivity. Termination is characterized by the ratios of I, Y and X nodes present in a fault system. I nodes represent isolated fault tips, Y nodes are formed at fault splays or terminations against other faults, and X nodes represent fault intersections. The proportion of fault terminations in a system is likely to vary as a function of the mechanical evolution of the fault system.

Dershowitz & Einstein (1988) report two joint datasets with 42% and 60% Y nodes (it is unclear in their study whether X nodes are considered equivalent to two Y nodes, or ignored). Gillespie et al. (1993) show a joint map with 91% X nodes. Large-scale (seismic) fault maps often show a preponderance of I nodes (e.g. Gillespie et al. 1993). Fault maps of large sandstone pavements (e.g. Zhao & Johnson 1992) often show high proportions of X nodes, but this could be an effect of fault reactivation in a tensile mode. Our observations suggest that the dominant node type at the small scale in deformation band systems is Y nodes. Figure 2 shows abundant splays; Fig. 3a has $14:73:13$ $I:Y:X$ node proportions.

Antonellini & Aydin (1995) have examined fault terminations in porous sandstones. Both deformation bands and zones of deformation bands form interconnected systems, while slip surfaces often terminate by transference to these smaller structures. Fault system connectivity characteristics are different above and below the mechanical scaling transition: terminations at deformation band and zone length scales are characterized by Y nodes, but slip surface/slip surface Y terminations are rare.

The spatial position of faults relates to fault clustering. In this paper, clustering refers to the relative proximity of faults (e.g. Gillespie et al. 1993), and not the definition used in percolation theory, in which clustering refers to the connectivity of the system (e.g. Odling 1992a). Fault clustering has only an indirect influence on compartmentalization: as clustering in a fault system increases, the sizes of fault-enclosed compartments become more variable.

La Pointe & Hudson (1985) relate clustering to fault system homogeneity. Highly clustered systems are heterogeneous, whereas if the faults are more evenly distributed the system is homogeneous. Clustering of deformation bands around slip surfaces is very common (e.g. Jamison & Stearns 1982; Koestler et al. 1994). Figure 3b is an example of such clustering, showing a displacement profile along a 67 m cliff section roughly parallel to fault dip. Two large faults with metre offsets accommodate most of the 6 m cumulative displacement, and millimetre displacement deformation bands are clustered tightly around these. A cartoon of this heterogeneous fault clustering is shown in Figure 3c.

Figure 3d shows a cross-section through a deformation band/zone of deformation band system. The faulting in this system is much more homogeneous and a simplified cartoon of one orientation population is illustrated in Fig. 3e. The faults in Fig. 3d indicate homogeneous clustering; however, what is sampled is the internal structure of a single cluster. Fault clusters are frequently observed in faulted sandstones. Many of these are not associated with a large fault, although large faults usually display clusters.

The soft-domino fault model (Walsh & Watterson 1991) has shown that linked fault systems need not be ubiquitous. In porous sandstones we observe a population of large slip surfaces which are not linked; the model predicts that the fault blocks respond by internal deformation. In high-porosity sandstones this strain is accommodated by forming deformation bands and zones, rather than by flexural slip and drag around the slip surfaces. These smaller structures form a highly connective system, and are largely responsible for fault compartmentalization.

The number of fault-enclosed compartments in a reservoir can be determined exclusively by orientation and termination characteristics of the fault system. The size distribution of these compartments is controlled by the clustering of the faulting. These influences are illustrated in Fig. 4.

Fault compartmentalization

In this section, we derive a relationship between fault connectivity and reservoir compartmentalization in two dimensions. This provides a measure of compartment density (CD) based on composite geometrical parameters of the fault system and is used in the following section for analysing the flow simulation results. We define compartment density as the number of fault-enclosed compartments present in a system, represented as a fraction of the maximum number of compartments possible for the particular number of fault terminations and intersections. This is a function of the proportion of each fault node type present (Fig. 4c), and the total number of nodes. For given $I:Y:X$ node proportions, the total number of nodes present decreases as the orientation population density ratio, x, decreases (Fig. 4b). This effect is incorporated into the CD measure by normalising
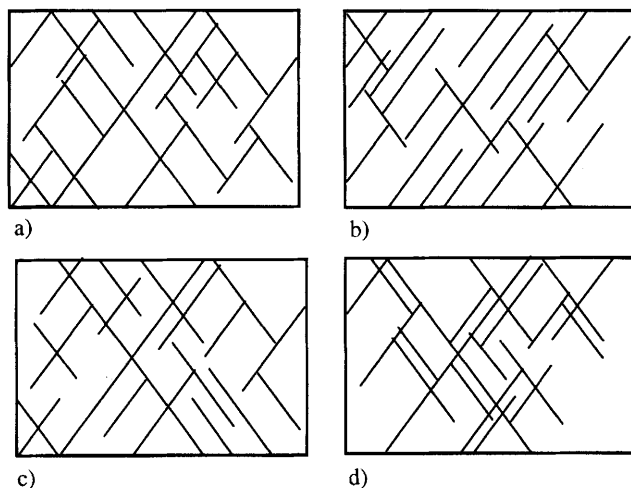
Fig. 4. Geometrical control on fault connectivity. (**a**) Datum fault system. (**b**) Effect of fault orientation: lowering the orientation population density ratio lowers the fault system connectivity. (**c**) Effect of fault termination characteristics: increasing the proportion of isolated terminations lowers the fault system connectivity. (**d**) Effect of fault clustering: increasing the heterogeneity of the system clustering has no influence on fault connectivity, but increases the range of compartment sizes.

the actual number of compartments present for a case of $x \neq 1$ against the number of compartments which would be present for the same $I : Y : X$ proportions at $x = 1$.

Figure 5 shows the fundamental compartmentalization properties of the three fault node types. Each compartment is contained by four Y or X nodes. Each X node separates four compartments (Fig. 5a), but each Y node separates only two compartments (Fig. 5b). Therefore one X node or two Y nodes are

required per compartment. I nodes do not increase compartmentalization, but they can have a dispersive effect. Faults that contain an I node and one or more of any other type of node reduce the number of compartments calculated on the basis of Y and X nodes by one (Fig. 5c). However, faults that contain two I nodes and no other nodes do not affect compartmentalization (Fig. 5d). The compartment density of a fault system may therefore be determined from the proportions of each node type
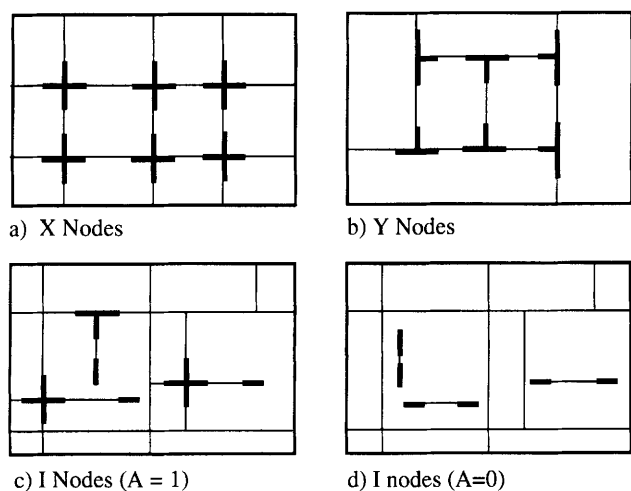
Fig. 5. Contribution of each fault node type to compartmentalization in two dimensions for two orientation populations of parallel faults. One X node (**a**) or two Y nodes (**b**) are required per compartment. I nodes may either reduce compartmentalization (**c**), or have no influence on it (**d**).

a) X nodes, $x = 1$

b) X nodes, $x = 0.33$

c) Y nodes, $x = 1$

d) Y nodes, $x = 0.7$
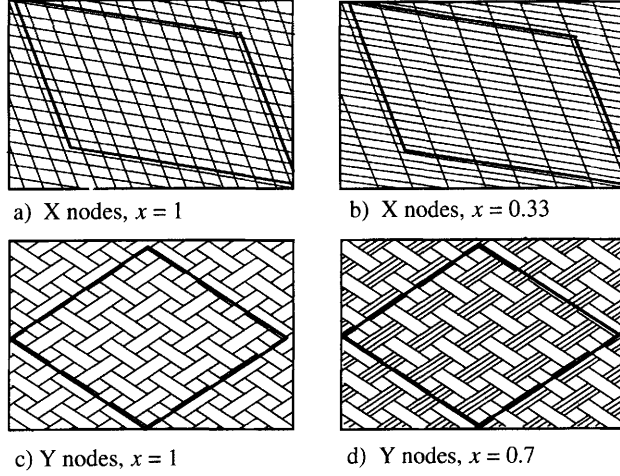
Fig. 6. Influence of the population orientation density ratio (x) on compartmentalization. Compartmentalization due to X nodes is sensitive to x. (**a**) $x = 1$, $n_a = 12$, $n_b = 12$, $n_c = n_a n_b = 144$. (**b**) $x = 0.33$, $n_a = 6$, $n_b = 18$, $n_c = n_a n_b = 108$. Compartmentalization due to Y nodes is not affected by x. (**c**) $x = 1$, $n_a = 36$, $n_b = 36$, $n_c = n_a + n_b = 72$. (**d**) $x = 0.7$, $n_a = 36$, $n_b = 51$, $n_c = n_a + n_b = 87$.

present:

$$CD = p_X + \frac{p_Y}{2} - A p_I \qquad (3)$$

Where CD is compartment density, p_X, p_Y and p_I are the proportions of each node type present, and A is a system-specific constant reflecting the proportion of I nodes that are connected to a Y or X node, and has the range $0 \leq A \leq 1$.

As well as the $I : Y : X$ node proportions, the other variable that affects the number of compartments contained by a specific number of faults is the population orientation density ratio, x (Fig. 4). The maximum number of compartments possible for a fixed number of nodes is attained when all nodes are X nodes (Eqn 3). For a population characterized entirely by X nodes, the total number of compartments (n_C) is given by (Fig. 6):

$$n_C = n_a n_b \qquad (4)$$

where n_a and n_b are the total number of faults from two populations in a given area. If n_T is the total number of faults in an area, and x is the population orientation density ratio, then:

$$n_T = n_a + n_b \qquad (5)$$

and

$$n_a = x n_b \qquad (6)$$

Manipulating Eqns 4, 5 and 6 gives:

$$n_C = \frac{x n_T^2}{(x + 1)^2} \qquad (7)$$

The maximum number of compartments is achieved when $x = 1$:

$$n_{C\max} = \frac{n_T^2}{4} \qquad (8)$$

For any case of $x \neq 1$ and $p_X < 1$, Eqn 3 does not give the maximum number of compartments possible. Maximum compartmentalization occurs when $x = 1$, and the number of X node-bounded compartments is determined by the product of Eqn 8 and the proportion of X nodes present. The actual compartmentalization due to X nodes is given by the product of the X node fraction and Eqn 7. Normalizing Eqn 7 by Eqn 8 provides the x-sensitive $n_C / N_{C\max}$ term for X nodes, which must be incorporated into Eqn 3. The compartmentalization due to Y nodes does not vary as a function of the x (Fig. 6), so the Y node term in Eqn 3 is correct, whatever the value of x.

CD for any case of x is therefore given by:

$$CD = \frac{4 x p_X}{(x + 1)^2} + \frac{p_Y}{2} - A p_I \qquad (9)$$

CD correlates linearly with n_C, is dimensionless and has the range $0 \leq CD \leq 1$. $CD = 0$ implies no compartmentalization (i.e. a case where $p_I = 1$) and $CD = 1$ represents maximum compartmentalization possible at a fixed total number of fault nodes (i.e. a case where $x = 1$ and $p_X = 1$).

Producer wells
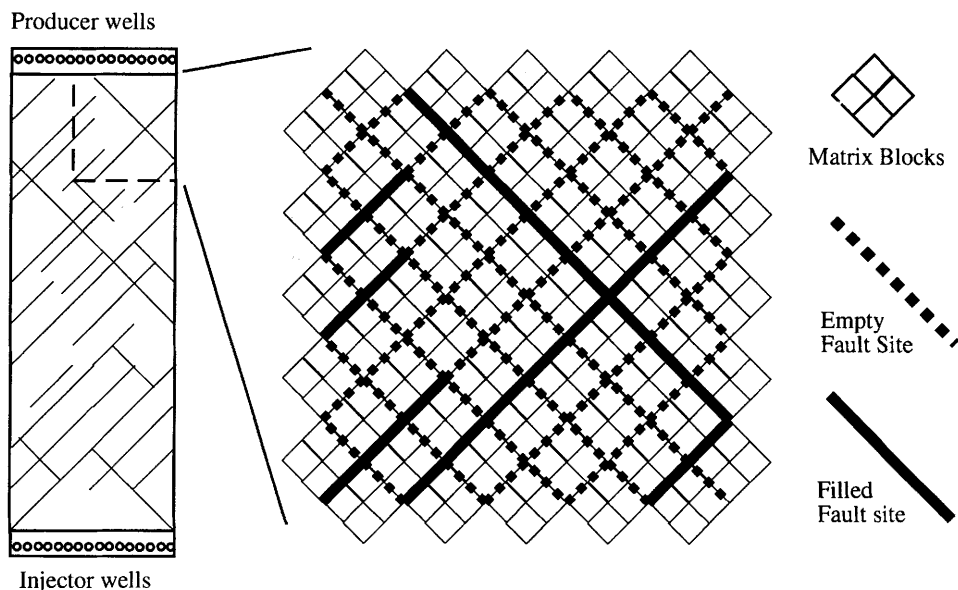
Fig. 7. Simulation grid geometry: 3553 active grid-cells are distributed at 45° to the flow direction. Each block of four matrix sites is bounded by a fault site.

Flow modelling

This section details a series of numerical simulations of single- and two-phase flow through model fault systems with varying fault connectivity characteristics. Flow simulations have been run on the ECLIPSE 100 simulator using discrete grid cells (rather than transmissibility factors) to represent low permeability faults. Fault cells are one block wide, and are separated by at least two matrix blocks (Fig. 7). All models are two-dimensional in the horizontal plane, with no-flow boundary conditions. Two orthogonal fault populations are modelled, and the mean flow direction bisects them. A 90° fault dihedral angle was used, as it allows the desired variability in fault system geometry to be modelled, whilst retaining relatively few grid-blocks in a simple configuration. Flow is modelled by fluid injection and production at controlled rates at each end of the model. The use of no-flow boundary conditions allows us to neglect the cross-flow terms in the full permeability tensor, but see Pickup *et al.* (1994) for a fuller treatment of effective permeability.

Each simulation experiment is designed to investigate the significance of a specific geometrical characteristic of the fault system. Fault density is constant in any particular experiment, and all faults have identical thickness and petrophysical properties. Four series of simulations

are presented: the first investigates effective permeability as a function of compartmentalization; the second considers fault density and permeability variation; the third models oil recovery as a function of fault length scale; and the fourth, oil recovery as a function of fault system connectivity.

Compartmentalization and effective permeability

In the previous section, we showed how the orientation population ratio and termination characteristics of a fault system both contributed to compartmentalization in a faulted reservoir. The significance of these on effective permeability is discussed below.

The effect of population orientation ratio (x) is modelled with a series of 12 fault systems, each with a value of x between 0 and 1 (three are shown in Fig. 8a). A further 20 fault system models were used to calculate effective permeability variation due to fault termination characteristics, of which three are shown in Fig. 8b. The models were run with 1 D matrix and 1 mD fault permeabilities. Each fault block (Fig. 7) is 1 cm thick, and each matrix block 15 cm. The minimum spacing between faults is 30 cm and the vertical thickness of the model is 30 cm. Water was injected and produced at a constant Darcy

a) Orientation Population density ratio, x.
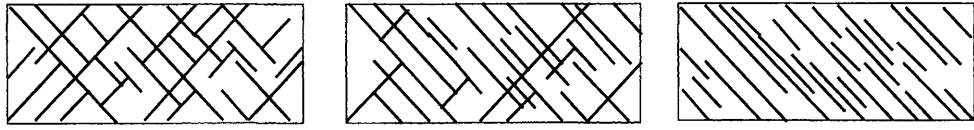
x = 1

x = 1/3

x = 0

b) Termination proportions
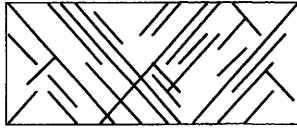
High I node Fraction
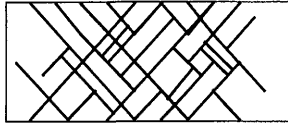
High Y node Fraction
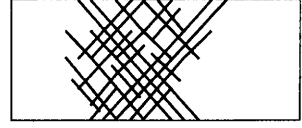
High X node Fraction

Fig. 8. Examples of the fault systems modelled to assess the control of compartmentalization on effective permeability. (**a**) Three of 12 model fault systems with variable orientation population density ratio. (**b**) Three of 20 model fault systems with variable node termination characteristics.

velocity of 0.5 m/day, and well pressures were recorded when flow had stabilized. The effective permeability of the model is calculated from the pressure drop between injector and producer wells using Darcy's law:

$$q = \frac{k_e A \Delta P}{\mu l} \qquad (10)$$

where q is the volumetric flow rate, A is the cross-sectional area, $\Delta P/l$ is the pressure gradient, μ is the water viscosity and k_e is the effective permeability.

The results are shown in Fig. 9. Figure 9a is a plot of model effective permeability against orientation density ratio. Effective permeability decreases non-linearly as the fault system becomes more evenly distributed between the populations present. Figure 9b is a ternary diagram of fault nodes, with effective permeability of the 20 models indicated. Contours show an increase in effective permeability towards I node-dominated fault systems. In Fig. 9c effective permeability from both series of models is plotted against the compartmentalization measure CD (Eqn 9). These results indicate that effective permeability of a fault system decreases approximately linearly with increasing compartment density.

The results were obtained for fault systems at a constant matrix/fault permeability contrast (1000) and constant fault density. Effective permeability (k_e) can be solved analytically for end-member fault systems (Muskat 1937): if flow is perpendicular to a set of faults, effective permeability is the harmonic average permeability (k_h) of the rock-mass, and if parallel the arithmetic average (k_a). In geometrically more

complex fault systems, k_e must lie between these values. The harmonic and arithmetic average permeabilities vary as a function of fault density and fault and matrix permeability, but are independent of fault system structure. The following series of flow simulations quantifies the effect of fault system structure with respect to fault thickness and permeability.

Fault density, permeability and compartmentalization

Figure 10a shows the relationship between arithmetic and harmonic average permeability and fault density for a 1 mD fault system in 1 D matrix. The separation between the two averages is equivalent to the maximum k_e range possible due to the geometrical variability of the fault system. As the matrix/fault permeability contrast (k_m/k_f) increases, the shape of the $k_a - k_h$ curve is similar but retains a higher value to lower fault densities. If we normalize $k_a - k_h$ against k_m/k_f to give $k_f(k_a - k_h)/k_m$, and plot this against fault density for three values of k_m/k_f (Fig. 10b), the distance under each curve at a particular fault density and permeability contrast is a measure of the possible effective permeability range of such a fault system. Fault system geometrical variability can be significant only if the $k_f(k_a - k_h)/k_m$ curve is high.

The term $k_f(k_a - k_h)/k_m$ reflects the heterogeneity of the system, but because it includes the $k_a - k_h$ term, a particular value does not represent a unique case of fault heterogeneity. For instance, a value of $k_f(k_a - k_h)/k_m = 0$ could imply either no faulting in the volume
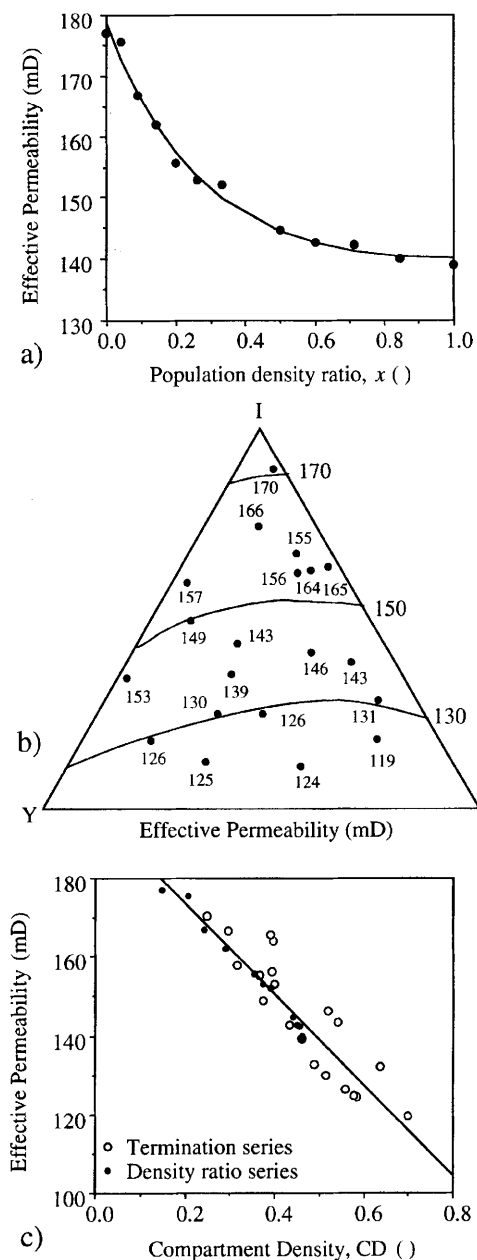
Fig. 9. Compartment density flow simulation results
for 1 mD faults in 1 D matrix. Fault density = 0.015.
(a) Effective permeability vs. orientation population
density ratio. (b) Effective permeability vs. fault node
proportions contoured on an *IYX* node ternary
diagram. (c) Effective permeability vs.
compartmentalization measure *CD* (Eqn 9) combining
both geometrical variables.

under consideration, or that it is composed
entirely of fault gouge. To overcome this equivo-
cality, we use a modified form to represent fault
system heterogeneity (H):

$$H = 1 - \frac{k_h}{k_m} \qquad (11)$$

This function is virtually identical to
$k_f(k_a - k_h)/k_m$ for fault density (d) up to the
turning points (Fig. 10b), but rather than
decreasing to 0 at a fault density of 1, it increases
to 1. H is similar to the Dykstra–Parsons hetero-
geneity measure (Dykstra & Parsons 1950; Lake
& Jensen 1991), and ranges from $H = 0$ (for a
case of $d = 0$ or $k_f = k_m$) to $H = 1$ (for a case
of $d = 1$ or $k_f = 0$).

The nine points on Fig. 10b represent series of
fault systems modelled. All models have uniform
matrix permeabilities of 1 D and fault perme-
abilities of either 0.1 mD, 1 mD or 10 mD.
Three fault densities (0.00047, 0.0047 and
0.015) were obtained by changing the relative
sizes of the fault and matrix grid cells (Fig. 7).
In addition, each density/permeability model is
run with five geometrical templates, with varying
orientation population ratio (x, as above). In this
way the permeability sensitivity due to fault
system structure may be compared with the
permeability sensitivities due to fault thickness
and fault permeability (combined in the H
measure), through a total of 45 effective perme-
ability results.

For each series, the mean of the five k_e values is
shown of Fig. 10c. Unsurprisingly, the highest k_e
is from the fault system with the narrowest and
most permeable faults. Also shown in Fig. 10c
are contours of equal H, which have been calcu-
lated from Eqn 11. The average simulated effec-
tive permeability of the fault systems varies
systematically with this composite average, and
one order of magnitude k_f reduction has the
same effect on a particular geometrical system
as one order of magnitude fault density increase.

Figure 10d shows the range in effective perme-
abilities for the five geometrical cases for each H
case. This range is expressed as a fraction of the
mean k_e of each geometrical series, and plotted
against the series mean, as recorded in Fig. 10c.
The results show that effective permeability is
most sensitive to fault system structure when
k_e is lowest. Thus k_e for the minimum case
is 24 mD ± 36%, and for the maximum is
935 mD ± 0.03%.

These single-phase simulation results indicate
that effective permeability is systematically influ-
enced by fault density and fault and matrix per-
meability (Fig. 10c). As the heterogeneity of the
fault system (H) increases, effective permeability
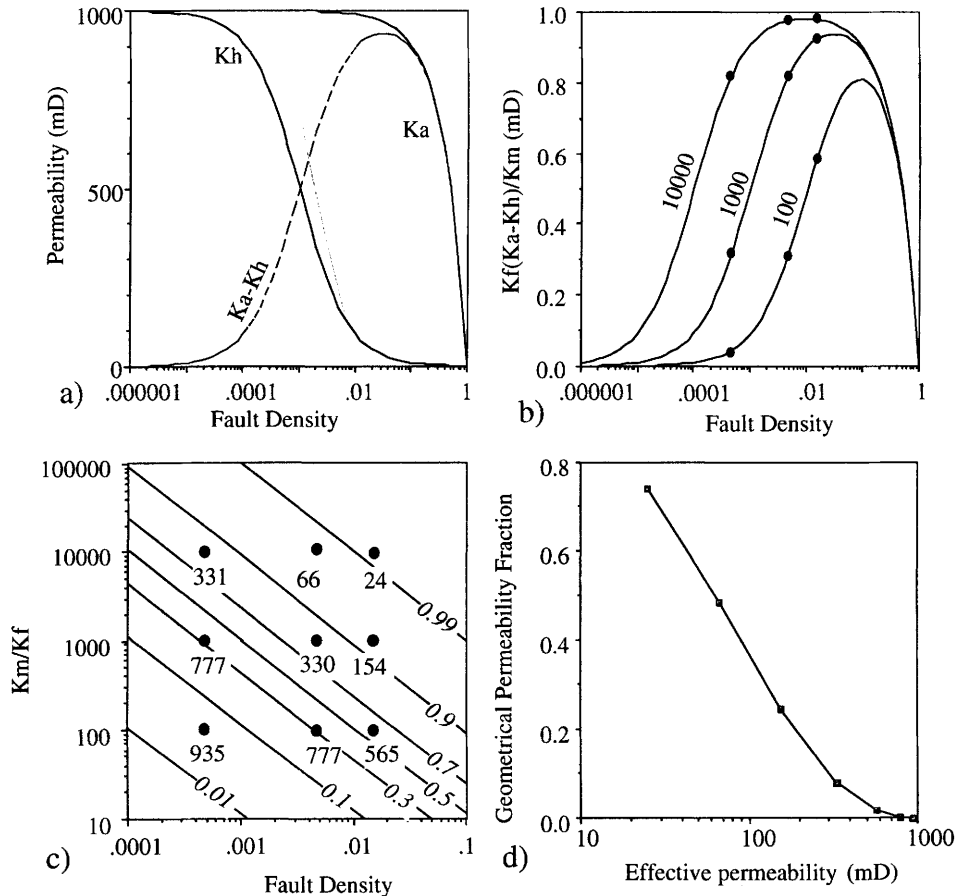
Fig. 10. Fault density, petrophysics and geometry simulation results. (**a**) Permeability vs. fault density for a system of 1 mD faults in 1 D matrix; Ka, arithmetic average permeability; Kh, harmonic average permeability. (**b**) Composite permeability average $K_f(K_a - K_h)/K_m$ vs. fault density for matrix/fault permeability contrasts of 100, 1000 and 10 000. Dots indicate positions of the nine simulation suites. (**c**) Matrix/fault permeability contrast vs. fault density. Spot values are mean effective permeability, and contours are of equal H value. (**d**) Geometrical permeability fraction vs. effective permeability.

becomes increasingly sensitive to the geometrical architecture of the fault system (Fig. 10d).

Oil recovery and length-scale

Unlike effective permeability determination, which is a function exclusively of the medium, two-phase flow processes are controlled also by the properties of the fluids involved. Saturation-dependent relative permeability and capillary pressure functions govern the phase mobilities. In this study, empirical relationships (detailed in Ringrose & Corbett 1994) have been used to generate relative permeability and

capillary pressure curves for 1 D sandstone and 10 mD fault gouge.

The first two-phase simulation examines the influence of scale on oil recovery. A single fault system (Fig. 11a) was modelled at four scales. The four systems have identical H and geometry, and therefore would have identical k_e values. In the smallest model, the faults are 0.1 cm thick and the matrix grid-cells 4.95 cm. These are increased by an order of magnitude in each simulation run, and the largest has 1 m thick faults and 49.5 m matrix cells. The area of the model has been split into four regions (R1 to R4, Fig. 11a), within which the oil recovery has been recorded throughout the run. A cumulative

a)

b)

c)
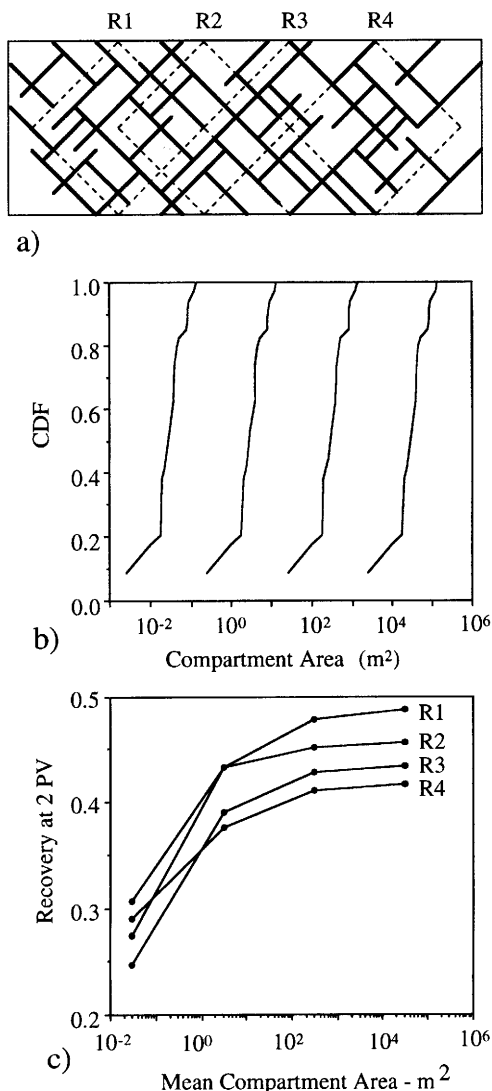
Fig. 11. Oil recovery and length scale flow simulation results for 10 mD faults in 1 D matrix. (**a**) Fault system model and reporting regions. Total flow distance is 3 m, 30 m, 300 m and 3 km. Fault thicknesses are 1 mm, 1 cm, 10 cm and 1 m. Fault density is 0.005 in every case. (**b**) Cumulative density function (CDF) of the compartment area at each length scale. (**c**) Recovery at two pore volumes (2PV) vs. mean compartment area for the four reporting regions.

density function of compartment areas for the four length scales is shown in Fig. 11b. Figure 11c shows a plot of oil recovery at two pore volumes of injected water, plotted against mean compartment area for the four models. These show that in a self-similar fault system, oil

recovery is preferentially inhibited at the smaller length scales.

A set of dimensionless ratios or groups incorporates the fundamental physical processes active in two-phase flow (e.g. Shook *et al.* 1992; Ringrose *et al.* 1993). Gravitational forces can be ignored in this study, as the models are horizontal and two-dimensional, with a constant thickness. The relevant scaling group relates viscous to capillary forces. When the viscous/capillary ratio is high the system tends towards viscous-dominated flow, and recovery is enhanced. Although the Darcy velocity at each scale is modelled at a constant realistic reservoir flow rate (1 ft/day), the volumetric flow rate (q) varies as a function of model size. As the viscous/capillary ratio is directly proportional to q, the ratio increases as a function of length scale, and the flow regime for the larger length scales tends towards viscous-dominated flow with increased recovery (Fig. 11c).

Oil recovery is therefore dependent on the scale of the system, as at smaller length scales the capillary forces in the system become more significant. The fault system structure determines the distribution of high capillary pressure regions, and therefore oil recovery should be most sensitive to the structure of the fault system at capillary-dominated length scales. This sensitivity is investigated by the following simulations.

Oil recovery and fault system connectivity

Figure 12 shows four fault systems with identical fault density and different fault connectivity characteristics. System A is a highly compartmentaliszed system with a high X node fraction. Systems B and C have virtually identical node distributions, but B has continuous faulting across the model, while in C flow paths are possible entirely through the matrix. System D has 100% I nodes and therefore no fault connectivity or compartmentalization. The petrophysics are identical to the previous models, and the systems have been run at the largest and second smallest length scales used previously, which correspond to viscous- and capillary-dominated flow regimes, respectively.

Oil recovery at two pore volumes for the two reporting regions is shown in Fig. 13a and b. Oil recovery for a completely unfaulted homogeneous model should be identical at both length scales, and the discrepancy between the unfaulted recovery at each scale (labelled NF) gives an indication of the error due to numerical dispersion. Ringrose *et al.* (1993) conducted
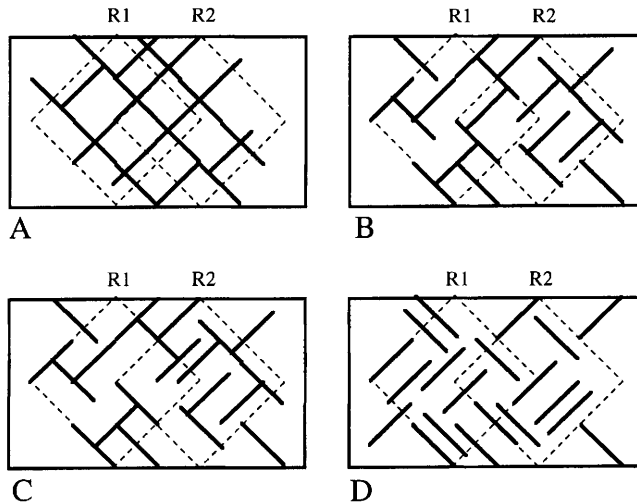
Fig. 12. Fault systems and reporting regions used to determine the influence of fault connectivity on oil recovery. System A: high X node fraction. Systems B and C: high I and Y node fractions. System D: high I node fraction.

sensitivities on numerical dispersion due to grid discretization, and concluded that dispersion is most critical at low viscous/capillary ratios. Because we are modelling different length scales rather than flow rates, the discretization in our capillary-dominated cases is much greater than in the viscous cases, which, coupled with the much shorter time-steps used in the capillary case, results in minimal numerical dispersion. These results confirm those of the previous experiment: at smaller length scales oil recovery is reduced. Numerical dispersion tends to overemphasize the effect. However, scale dependency on recovery is not merely a numerical artefact: an increase in either scale or flow rate increases the viscous forces in the system, and therefore oil recovery.

Figure 13a and b also shows that at capillary length scales the effect of fault connectivity on recovery is more influential that at viscous scales. Figure 13c and d shows recovery throughout the model at two pore volumes for the two length scales, as a fraction of the recovery for the unfaulted matrix. The more connected fault system (A) has lower recovery at both viscous and capillary length scale; however, the reduction compared to the other fault systems is much more marked at the capillary scale.

A subsidiary effect of capillary trapping is shown by fault systems B and C. Region 1 for system B has a complete downstream fault barrier into region 2, but fault system C has continuous matrix flow paths (Fig. 12). Recovery at capillary scales in region 1 is, as expected, lower for system B than for system C; however, in

region 2 the relative recovery switches, and system B has a greater recovery than system C. We believe this is due to the continuous flow path present in system C. Once water has established a flow path through the model, additional injected water will preferentially follow this path, rather than displace the oil trapped in fault compartments. In system B there are no continuous matrix flow paths, and the water-front is more evenly distributed across the model. This allows a greater volume of oil to be displaced, with increased recovery. At large scales, capillary trapping is not significant, and the recovery for system C is greater than for system B (Fig. 13d). Although a completely disconnected fault system (system D) has greater recovery than connected ones, the details of the fault system connectivity, and the presence of flow paths, is significant, and recovery is not simply a function of compartmentalization and connectivity.

Summary and conclusions

This work has focused on evaluating flow behaviour in faulted high-porosity sandstone reservoirs. We have performed flow simulations through highly connected permeability-reducing fault systems. Our fault system models contain no fault scaling relationships and are all modelled with a constant flow direction relative to constant fault orientations. All faults in each model have identical thicknesses and permeabilities. Within these limitations we model fault systems containing only a few discrete faults, and invariably
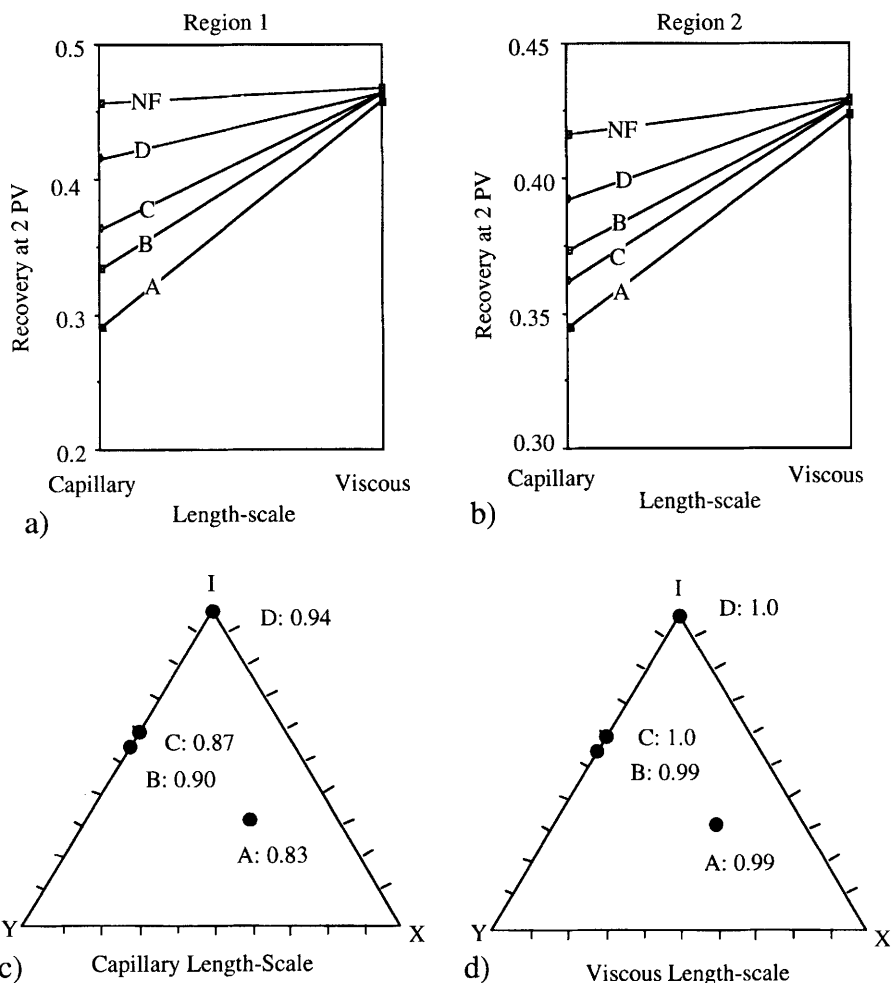
Fig. 13. Oil recovery and fault system connectivity flow simulation results for 10 mD faults in 1 D matrix. Fault density is 0.003. Oil recovery at two pore volumes (2PV) vs. length scale for systems A to D and an unfaulted model (NF) for (**a**) reporting region 1 and (**b**) reporting region 2. Total recovery at 2PV as a fraction of unfaulted recovery at (**c**), the capillary scale and (**d**) the viscous scale.

some faults pass right through the model. The fundamental flow volume we consider is the fault-enclosed compartment rather than the fault itself, and we are concerned primarily with the presence and size of compartments, and only with the thickness and petrophysical properties of the compartment-bounding faults.

Effective permeability calculations have shown that, for any fault density and fault and matrix permeability, a fault heterogeneity measure (H, Eqn 11) may be used to estimate effective permeability (Fig. 10c). Antonellini & Aydin (1994) give an example of an extremely high fault density as 100 deformation bands per metre, with each band 1.5 mm thick. This corresponds to a fault density of 0.15 and is observed only

close to large fault zones. Figure 10c shows that the effective permeability of a compartmentalized system at this density is extremely low for 1 mD faults. The field map on Fig. 2c provides another example. If we take an average fault density in the shaded regions of 10 bands per metre, still assuming 1.5 mm thickness, then fault density is 0.01. Effective permeability might then be around 300 mD for a compartmentalized system of 1 mD faults in 1 D matrix.

Fault clustering appears to be extremely heterogeneous at all scales below the slip surface/zone of bands mechanical scaling transition (Figs 2 and 3), and therefore fault clusters form areas of low effective permeability, which are localized into narrow zones on a larger map. This inference

suggests that the fault density necessary to severely reduce the effective permeability at any scale is likely to exist only very close to structures that are large relative to the scale under consideration.

The composite fault thickness/permeability heterogeneity measure (H) shows that a one order of magnitude change in fault density is equivalent to a one order of magnitude permeability change. The effective permeability estimates calculated above were based on realistic fault and matrix permeabilities. We infer that effective permeability is only significantly reduced at very high fault densities or low fault permeabilities. At high fault densities, increasing compartment density by enhancing fault connectivity can alter the effective permeability by about a factor of two (Figs 9c and 10d).

Antonellini & Aydin (1995) give some estimates of compartment sizes in relation to strata curvature above salt. They describe 30 m wide compartments bounded by 5 mm faults. Our two-phase experiments model a self-similar fault system and predict that compartments of this size, even at the very slow flow rates that occur away from wells during field production, do not have severe capillary trapping effects for 10 mD faults in 1 D matrix (Fig. 10c). Indeed, even in the compartments between the zones on Fig. 3a, recovery is only slightly reduced (about 38% recovery instead of about 45% for 30 m compartments). Oil recovery might be most critical around the percolation threshold of the fault system, in which case significant volumes of hydrocarbon might become trapped in compartments because the water-flood is concentrated into narrow channels exploiting tortuous flow paths through the matrix. Future work aims to carry on addressing the problem with more sensitivity studies with particular attention placed on fault clustering, two-phase flow, boundary conditions and the third dimension.

References

ANTONELLINI, M. & AYDIN, A. 1994. Effect of faulting on fluid flow in porous sandstones: petrophysical properties. *AAPG Bulletin*, **78**, 355–377.
—— & ——1995. Effect of faulting on fluid flow in porous sandstones: geometry and spatial distribution. *AAPG Bulletin*, **79**, 642–671.

——, —— & POLLARD, D. D. 1994. Microstructure of deformation bands in porous sandstones at Arches National Park, Utah. *Journal of Structural Geology*, **16**, 941–959.

AYDIN, A. & JOHNSON, A. M. 1978. Development of faults as zones of deformation bands and as slip surfaces in sandstone. *Pure and Applied Geophysics*, **116**, 931–942.

—— & ——1983. Analysis of faulting in porous sandstones. *Journal of Structural Geology*, **5**, 19–31.

—— & RECHES, Z. 1982. Number and orientation of fault sets in the field and in experiments. *Geology*, **10**, 107–112.

CHILDS, C., WALSH, J. J. & WATTERSON, J. 1990. A method for estimation of the density of fault displacements below the limits of seismic resolution in reservoir formations. *In*: BULLER, A. T. *et al.* (eds) *North Sea oil and Gas Reservoirs II.* Graham and Trotman, London, 309–318.

COWIE, P. A. & SCHOLZ, C. H. 1992. Physical explanation for the displacement–length relationship of faults using a post-yield fracture mechanics model. *Journal of Structural Geology*, **14**, 1133–1148.

CRUIKSHANK, K. M., ZHAO, G. & JOHNSON, A. M. 1991. Duplex structures connecting fault segments in Entrada sandstone. *Journal of Structural Geology*, **13**, 1185–1196.

DERSHOWITZ, W. S. & EINSTEIN, H. H. 1988. Characterizing rock joint geometry with joint system models. *Rock Mechanics and Rock Engineering*, **21**, 21–51.

DUNN, D. E., LaFOUNTAIN, L. J. & JACKSON, R. E. 1973. Porosity dependence and mechanism of brittle fracture in sandstones. *Journal of Geophysical Research*, **78**, 2403–2417.

DYKSTRA, H. & PARSONS, R. L. 1950. The prediction of oil recovery by waterflood. *In: Secondary Recovery of Oil in the United States, Principles and Practice*, 2nd edition. American Petroleum Institute, 160–174.

FOWLES, J. & BURLEY, S. 1994. Textural and permeability characteristics of faulted, high porosity sandstones. *Marine and Petroleum Geology*, **11**, 608–623.

GAUTHIER, B. D. M. & LAKE, S. D. 1993. Probabilistic modeling of faults below the limit of seismic resolution in the Pelican Field, North Sea, offshore United Kingdom. *AAPG Bulletin*, **77**, 761–777.

GILLESPIE, P. A., HOWARD, C. B., WALSH, J. J. & WATTERSON, J. 1993. Measurement and characterisation of spatial distribution of fractures. *Tectonophysics*, **226**, 113–141.

——, WALSH, J. J. & WATTERSON, J. 1992. Limitations of dimension and displacement data from single faults and the consequences for data analysis and interpretation. *Journal of Structural Geology*, **14**, 1157–1172.

HATTON, C. G., MAIN, I. G. & MEREDITH, P. G. 1994. Non-universal scaling of fracture length and opening displacement. *Nature*, **367**, 160–162.

HEATH, A. E., WALSH, J. J. & WATTERSON, J. 1994. Estimation of the effect of sub-seismic sealing faults on effective permeabilities in sandstone reservoirs. *In*: AASEN, J. O. *et al.* (eds) *North Sea Oil and Gas Reservoirs III*. Kluwer, Dordrecht, 173–183.

JAMISON, W. R. & STEARNS, D. W. 1982. Tectonic deformation of Wingate Sandstone, Colorado National Monument. *AAPG Bulletin*, **66**, 2584–2608.

KNOTT, S. D. 1994. Fault zone thickness versus displacement in the Permo-Triassic sandstones of NW England. *Journal of the Geological Society, London*, **151**, 17–25.

KOESTLER, A. G., MILNES, A. G., OLSEN T. S. & BULLER A. T. 1994. A structural simulation tool for faulted sandstone reservoirs: exploratory study using data from Utah and the Gullfaks Field. *In*: AASEN, J. O. *et al.* (eds) *North Sea Oil and Gas Reservoirs III*. Kluwer, Dordrecht, 157–165.

KRANTZ, R. W. 1988. Multiple fault sets and three-dimensional strain: theory and application. *Journal of Structural Geology*, **10**, 225–237.

LA POINTE, P. R. & HUDSON, J. A. 1985. *Characterisation and Interpretation of Rock Mass Joint Patterns*. Geological Society of America, Special Paper **199**.

LAKE, L. W. & JENSEN, J. L. 1991. A review of heterogeneity measures used in reservoir characterisation. *In Situ*, **15**, 409–437.

LISLE, R. J. 1994. Detection of zones of abnormal strains in structures using Gaussian curvature analysis. *AAPG Bulletin*, **78**, 1811–1819.

MUSKAT, M. 1937. *Flow of Homogeneous Fluids*. McGraw-Hill, New York.

ODLING, N. E. 1992*a*. Network properties of a two-dimensional natural fracture pattern. *Pure and Applied Geophysics*, **138**, 95–114.

——1992*b*. Permeability of natural and simulated fracture patterns. *In*: LARSEN, R. M. *et al.* (eds) *Structural and Tectonic Modelling and its Application to Petroleum Geology*. Elsevier, Amsterdam, 365–380.

PICKUP, G. E., RINGROSE, P. S., JENSEN, J. L. & SORBIE, K. S. 1994. Permeability tensors for sedimentary structures. *Mathematical Geology*, **26**, 227–250.

PITTMAN, E. D. 1981. Effect of fault-related granulation on porosity and permeability of quartz sandstones, Simpson Group (Ordovician), Oklahoma. *AAPG Bulletin*, **65**, 2381–2387.

RECHES, Z. 1977. Analysis of faulting in three-dimensional strain field. *Tectonophysics*, **47**, 109–129.

RINGROSE, P. S. & CORBETT, P. W. M. 1994. Controls on two-phase flow in heterogeneous sandstones. *In*: PARNELL, J. (ed.) *Geofluids: Origin, Migration and Evolution of Fluids in Sedimentary Basins*. Geological Society, London, Special Publication, **78**, 141–150.

——, P. S., SORBIE, K. S., CORBETT, P. W. M. & JENSEN, J. L. 1993. Immiscible flow behaviour in laminated and cross-bedded sandstones. *Journal of Petroleum Science and Engineering*, **9**, 103–124.

ROBINSON, P. C. 1983. Connectivity of fracture systems – a percolation theory approach. *Journal of Physics A: Mathematical and General*, **16**, 605–614.

SCHOLZ, C. H. & COWIE, P. A. 1990. Determination of total strain from faulting using slip measurements. *Nature*, **346**, 837–838.

SHOOK, M., LI, D. & LAKE, L. W. 1992. Scaling immiscible flow through permeable media by inspectional analysis. *In Situ*, **16**, 311–349.

UNDERHILL, J. R. & WOODCOCK, N. H. 1987. Faulting mechanisms in high-porosity sandstones; New Red Sandstone, Arran, Scotland. *In*: JONES, M. E. & PRESTON, R. M. F. (eds) *Deformation of Sediments and Sedimentary Rocks*. Geological Society, London, Special Publication, **29**, 91–105.

WALSH, J. J. & WATTERSON, J. 1991. Geometric and kinematic coherence and scale effects in normal fault systems. *In*: ROBERTS, A. M. *et al.* (eds) *The Geometry of Normal Faults*. Geological Society, London, Special Publication, **56**, 193–203.

YIELDING, G., WALSH, J. J. & WATTERSON, J. 1992. The prediction of small-scale faulting in reservoirs. *First Break*, **10**, 449–460.

ZHAO, G. & JOHNSON, A. M. 1992. Sequence of deformation recorded in joints and faults, Arches National Park, Utah. *Journal of Structural Geology*, **14**, 225–236.

Physical character and fluid-flow properties of sandstone-derived fault zones

RICHARD G. GIBSON

*Amoco Exploration and Production Co., 501 Westlake Park Blvd,
Houston, TX 77079, USA*

Abstract: Evaluation of hydrocarbon entrapment and production patterns in faulted
sandstone reservoirs requires understanding of the nature and fluid-flow properties of sand-
stone-derived fault zones. This study documents the interrelationships between sandstone
composition, deformation mechanisms, fault-zone character, and fluid-flow properties
(permeability and capillary properties) using a global sandstone dataset.

Quartz-rich sandstones deform by cataclasis (most commonly), diffusive mass transfer, or
a combination of these processes to form deformation bands. The fluid-flow properties of
these zones depend on deformation mechanism(s). Faulting of mineralogically immature
sandstones results in the formation of clay-matrix gouge zones by a combination of
processes, including cataclasis, intergranular sliding in clay-rich materials, and diffusive
mass transfer. Clay-matrix gouge zones generally have lower permeabilities and higher
capillary displacement pressures than deformation bands.

Most deformation bands have capillary properties sufficient to maintain hydrocarbon
column-height differences of less than 75 m across them, whereas clay-matrix gouge zones
can potentially seal hydrocarbon columns with heights of several hundred metres. Both
low-permeability deformation bands and clay-matrix gouge zones are likely to influence
production patterns, although the magnitude of these effects will depend on the spatial
distribution and abundance of faults and the permeabilities of the fault zones and
undeformed sandstone.

Information about fault zone fluid-flow proper-
ties (e.g. permeability, porosity, capillary proper-
ties) in siliciclastic strata is necessary for accurate
evaluation of fault-seal risk, model simulation of
faulted petroleum reservoirs, and basin-scale
fluid-flow modelling. This paper contains the
results of a petrographic and laboratory study
aimed at determining the fluid-flow properties
of natural fault zones and evaluating the factors
that influence these properties. Because signifi-
cant difficulties are inherent in trying to collect
coherent, representative samples of macroscopic
fault zones for fluid-flow tests, the approach
utilized in this study is to document the character
and properties of small-displacement faults
derived from sandstones of various composi-
tions. Such fault zones are primarily mixtures
of quartz, feldspar and phyllosilicates
(micas + clay minerals) that vary significantly
in character and show many features in
common with macroscopic fault zones in silici-
clastic stratigraphic sequences. Fault zones
similar to some of those examined in this study
have been studied by a number of previous work-
ers (e.g. Aydin 1978; Pittman 1981; Jamison &
Stearns 1982; Nelson 1985; Chester & Logan
1986; Underhill & Woodcock 1987; Trevena
1989; Knipe 1993; Antonellini & Aydin 1994).
However, no previous study has addressed the

spectrum of variability observed among the
samples considered in this paper.

The data presented here demonstrate that
faults formed from porous sandstones range in
character from quartz-rich cataclastic zones to
clay-matrix gouge zones, generally reflecting the
composition of the protolith. Capillary pressure
and permeability data collected on a suite of
samples spanning this spectrum show systematic
variations as a function of both sandstone and
fault-zone composition, as well as the defor-
mational processes active during faulting. Clay-
matrix gouge zones consistently have low
permeabilities and the highest capillary pressures
(smallest effective pore-throat radii). All of the
fault zones studied have permeabilities poten-
tially low enough to influence hydrocarbon
production from a sandstone reservoir. How-
ever, clay-matrix gouge zones also have small
enough pore-throats to form capillary seals for
significant hydrocarbon columns.

Sample description

The specimens used in this study include both
outcrop and core samples collected from a
number of different geographic areas (Table 1).
Arrays of small-displacement faults like those

Table 1. *List of samples, localities, descriptive information, permeability (k), and pore-throat radius (R) data*

Sample number	Stratigraphic Unit and Location (well names and depths in italics)	Fault type*	Fault displ.†	k (mD) (host ss.)	k (mD) (fault zone)	R (μm) (CH₄ inj.)	R (μm) (Hg inj.)
Deformation bands							
Cataclastic							
DAK-1	Dakota Fm, Wet Mountains, W of Canon City, CO, USA	R	meso	—	0.369	1.09	—
DAK-5	Dakota Fm, Wet Mountains, W of Canon City, CO, USA	R	micro	—	0.241	0.18	—
ENT-1	Entrada Fm., Colorado Plateau, near Moab, UT, USA	N	meso	—	—	—	2.1
FOUN-1	Fountain Fm., Front Range, NE of Canon City, CO, USA	N + SS	meso	—	0.123	0.42	—
NAV-1	Navajo Fm, Colorado Plateau, near Moab, UT, USA	N	meso	—	—	—	1.14
NUB-1	Nubia Fm, Gulf of Suez, Egypt (*July 62–86, 1138'*)	N	micro	—	8.002	10.9	—
OCR-1	Oil Creek Ss., Arbuckle Mountains, Mill Creek, OK, USA	SS?	meso	—	0.715	0.66	—
OCR-2	Oil Creek Ss., Arbuckle Mountains, Mill Creek, OK, USA	SS?	meso	—	2.63	—	2.6
RUD-2	Rudeis Fm, Gulf of Suez, Egypt (*July 8, 8812'*)	N	micro	—	1.48	—	—
TRIN-1	Gros Morne Fm, offshore SE Trinidad (*OPR-13, 12400'*)	N	meso	17.8	1.16	2.17	2.7
TRIN-5	Gros Morne Fm, offshore SE Trinidad (*Samaan B-1, 6812'*)	N	micro	—	—	0.72	2.7
TRIN-7	Gros Morne Fm, offshore SE Trinidad (*Poui A-4, 10514'*)	N	micro	210	7.21	—	—
Solution							
FUL-1	Fulmar Fm, North Sea, offshore UK (*30/12b-4, 12968'*)	N	meso	—	—	—	0.15
NUB-3	Nubia Fm, Gulf of Suez, Egypt (*Sidki-7, 10924'*)	N	micro	165	0.084	—	2.7
RUD-3	Nubia Fm, Gulf of Suez, Egypt (*July 8, 9067'*)	N	micro	—	0.081	0.53	—
WIL-1	Wilcox Fm, south TX, USA (*Amoco Peters Estate-1, 13344'*)	N	micro	1.20	0.206	0.80	—
WIL-1	Wilcox Fm, south TX, USA (*Amoco Peters Estate-1, 13352'*)	N	micro	0.314	0.032	0.31	—
Complex							
LYONS-3	Lyons Fm, Front Range, Colorado Spgs., CO, USA	R	micro	—	0.0053	<0.008	—
NUG-1	Nugget Fm, Sevier belt, WY, USA (*Champlin 404-C-1, 14154'*)	R	meso	96.2	0.0155	—	0.23
NUG-2	Nugget Fm, Sevier belt, WY, USA (*Champlin 404-C-1, 14186'*)	R	micro	5.79	0.0106	—	0.23
NUG-3	Nugget Fm, Sevier belt, WY, USA (*Champlin 404-C-1, 14214'*)	R	meso	—	0.0208	0.053	—
Clay-matrix gouge zones							
CA-1	Painted Cyn. fault zone, Mecca Hills, CA, USA	SS	macro	—	—	—	0.04
CA-2	San Andreas fault zone, Mecca Hills, CA, USA	SS	macro	—	0.055	<0.01	0.03
GOR-1	Pliocene ss. near San Andreas fault, S. Of Gorham, CA, USA	SS	micro	—	0.0002	<0.01	0.07
HEM-2	Hemlock Fm, Cook Inlet, AK, USA (*Mid. Ground Shoal-25, 8216'*)	R	micro	1–20	0.002	<0.025	—
HEM-3	Hemlock Fm, Cook Inlet, AK, USA (*Mid. Ground Shoal-25, 8049'*)	N	meso	—	—	—	1.08
MOAB-1	Culter Fm in Moab fault zone, N of Moab, UT, USA	N	macro	—	0.048	<0.01	0.12
MOAB-4	Culter Fm in Moab fault zone, N of Moab, UT, USA	N	macro	—	—	—	0.12
MYAN-1	Tertiary ss., Chindwin basin, Myanmar	N?	micro	5.5–45	0.024	0.034	—
MYAN-2	Tertiary ss., Chindwin basin, Myanmar	N?	micro	5.5–45	0.028	0.053	—
ROM-85	Magaresti Fm, Carpathian belt, central Romania	R	micro	—	—	—	0.04
TRIN-9	Gros Morne(?) Fm, offshore SE Trinidad (*N. Poui 2, 11878'*)	N	micro	4.80	0.034	0.015	0.28

Dashes indicate that parameter was not measured.

* Fault type: N = normal; R = reverse; SS = strike-slip

† Fault displacement magnitude: micro ≤ c. 10 cm; meso = 10 cm to 10 m; macro ≥ c. 10 m

studied here are typical of deformed sandstones in regions of localized high strain, such as in areas of high bedding curvature and within deformation halos adjacent to macroscopic faults (Aydin 1978; Jamison & Stearns 1981; Chester & Logan 1986; Antonellini & Aydin 1994; Knipe *et al.* 1996). Fault types (normal, reverse, strike-slip) and ranges of displacement magnitude are listed in Table 1 for each of the specimens included within the study. In the case of most samples, the fault displacement is small enough that it is clear that the fault-zone material was derived directly from the adjacent sandstone. Two samples (CA-1, CA-2) were collected within major displacement zones within the San Andreas fault system and their protoliths are not known.

The samples were compositionally characterized by (1) point-counting of impregnated, stained thin sections of the protolith sandstone and (2) collecting semi-quantitative X-ray diffraction (XRD) data on the fault-zone material and, where possible, its sandstone protolith. These data are summarized in Table 2 and shown graphically in Fig. 1. XRD analyses have analytical uncertainties on the order of ±10%. Significant XRD mineralogical differences between some of the fault-zone material and the corresponding protoliths are shown in Table 2 and are indicated by arrows in Fig. 1b. Faulted sandstones exhibiting obvious diagenetic modification after faulting were avoided during the sample selection process. Therefore, no distinction is made in either the point-count or XRD data between detrital and authigenic phases, since both contribute to the character of subsequent faults cross-cutting these sandstones.

For descriptive purposes, the suite of fault zones is divided into two broad textural categories, deformation bands and clay-matrix gouge zones (Table 1). The distinction between these two groups is based primarily on fault-zone appearance in outcrop or drill-core and secondarily on characteristics observed in thin section. The criteria by which they are distinguished are outlined below.

Deformation bands

Deformation bands (Aydin 1978) are narrow (< 2 mm thick), planar displacement zones that are a common feature in porous sandstones and have been referred to in the literature by a variety of names (see Pittman 1981; Jamison & Stearns 1981; Nelson 1985; Underhill & Woodcock 1987; Fowles & Burley 1994). In drill-core

or outcrop, they are typically lighter coloured and better indurated than the surrounding sandstone and occur as either complex, intersecting arrays or zones comprising multiple, sub-parallel bands (Fig. 2a). They occur preferentially in mineralogically mature, quartz-rich (>65% of solids) sandstones with less than 30% clay + mica + lithic fragments (Fig. 1a, Table 2). XRD data show that the deformation bands have total phyllosilicate contents below 25% (most below 10%) and do not differ significantly in mineralogy from their sandstone protoliths (Fig. 1b, Table 2). On the basis of the deformation mechanism(s) responsible for their formation, the deformation bands can be sub-divided into three groups.

Cataclastic deformation bands consist of fractured and fragmented detrital grains. They are finer grained, more poorly sorted, and contain smaller pores than the protolith sandstone. Deformation associated with these zones is extremely localized, with sharp boundaries between the zone of grain fragmentation and adjacent undeformed rock (Fig. 2b). Grain fragments within the deformation bands show no apparent preferred orientation and are typically sub-equant, with grain boundaries that do not interpenetrate with neighbouring fragments (Fig. 2c and d). The dominant process responsible for the formation of these deformation bands is interpreted to be cataclasis (see also Aydin 1978; Pittman 1981; Jamison & Stearns 1981; Underhill & Woodcock 1987; Antonellini & Aydin 1994; Fowles & Burley 1994). Of the three types of deformation bands, this is the most common variety within the sample set.

Solution deformation bands consist of tightly packed grains (mostly quartz) with serrated, interpenetrating grain boundaries and irregular concentrations of opaque material and/or phyllosilicates along grain boundaries (Fig. 3a). These zones show little or no indication of fracturing or fragmentation of detrital quartz grains. Instead, grains within them have a weak to strong dimensional alignment parallel to the stylolitic seams and fault-zone margins. The long axes of these aligned grains are comparable in length to the diameter of the detrital grains within the undeformed sandstone (Fig. 3a). The welded grain contacts and grain-shape alignment are interpreted to reflect quartz dissolution along grain boundaries sub-parallel to the fault-zone margin. This diffusive mass transfer may have been superimposed onto pre-existing zones formed by grain-boundary sliding, such as those described by Sverdrup & Prestholm (1990).

Table 2. *Compositional data for samples included in this study*

Sample Number	X-Ray diffraction data				Thin-section point-count data					
	Quartz	Fsp	Phyl	Other	Quartz	Fsp	Lithics	Phyl	Other	Porosity
Deformation bands										
Cataclastic										
DAK-1	98	0	2	0	76.1	0.0	0.0	0.0	0.0	23.9
DAK-5	95	0	5	0	61.9	0.0	0.0	24.0	0.3	13.8
ENT-1	–	–	–	–	76.8	3.2	0.0	3.7	0.4	15.8
FOUN-1	65	13	23	0	50.9	30.3	0.0	10.8	0.6	7.4
NAV-1	–	–	–	–	65.4	8.1	0.0	7.8	0.8	17.8
OCR-1	98	0	2	0	67.1	0.0	0.0	10.3	0.0	22.6
OCR-2	95	0	4	1	–	–	–	–	–	–
RUD-2	90	0	10	0	61.6	1.1	1.2	1.9	19.0	15.2
TRIN-2	95	0	5	0	66.6	3.4	2.3	5.7	0.4	21.6
TRIN-5	–	–	–	–	60.2	2.6	5.0	2.0	1.4	28.8
TRIN-7	–	–	–	–	55.7	4.0	6.8	9.8	0.7	23.1
Solution										
FUL-1	–	–	–	–	60.0	28.0	tr	1.0	2.0	9.0
NUB-3	–	–	–	–	68.5	0.0	0.0	24.3	0.0	7.3
RUD-3	90	0	10	0	65.8	1.7	1.2	4.9	12.5	13.9
WIL-1	85	0	15	0	66.9	0.0	13.5	6.7	2.1	10.8
WIL-2	85	0	15	0	58.4	0.0	16.8	9.3	3.4	12.1
Complex										
LYONS-3	90	3	7	0	59.5	10.2	6.4	10.4	0.0	13.5
NUG-1	80	5	15	0	79.7	8.1	0.4	7.3	0.2	4.3
NUG-2	80	5	15	0	–	–	–	–	–	–
NUG-3	95	3	3	0	82.4	5.5	1.1	2.1	0.0	8.9
Clay-matrix gouge zones										
CA-1	30	5	40	25	–	–	–	–	–	–
CA-2	25	0	55	20	–	–	–	–	–	–
GOR-1	25 (35)	10 (25)	65 (40)	tr	28.7	52.0	0.0	17.7	0.2	1.4
HEM-2	40	15	45	0	34.3	22.3	32.1	6.3	5.0	tr
HEM-3	60 (50)	10	30 (40)	tr	49.5	9.0	35.5	2.0	tr	4.1
MOAB-1	60	5	35	0	32.1	15.9	0.0	48.0	4.1	tr
MOAB-4	25 (35)	0 (15)	75 (40)	0 (10)	29.0	34.1	0.4	30.4	6.1	tr
MYAN-1	40	30	30	0	30.6	16.2	18.2	7.2	14.7	13.1
MYAN-2	50	30	20	0	37.6	25.0	11.8	20.3	3.4	1.8
ROM-85	–	–	–	–	36.4	5.8	19.2	13.6	24.0	1.0
TRIN-9	70	3	28	0	48.0	13.4	26.8	3.1	0.2	8.5

X-ray diffraction data are for fault-zone material and protolith (protolith value in parentheses only where >10% (weight) different from that of fault zone). Point-count data are for undeformed sandstone adjacent to fault zones.
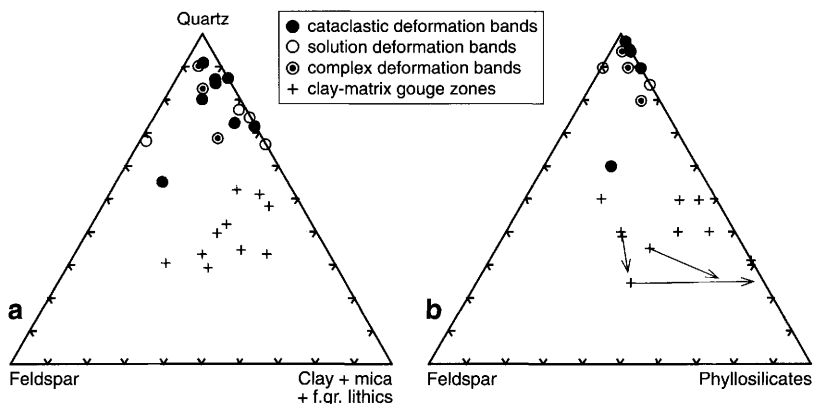
Fig. 1. Porosity-free compositional plots of sandstone and fault-zone samples used in this study. (**a**) Point-counts of thin sections of unfaulted sandstone. (**b**) X-ray diffraction data of sandstone and fault gouge: dashed lines connect sandstone composition (at symbol) with that of fault gouge (arrowhead) for cases where the two are not coincident within analytical uncertainty.

Complex deformation bands are zones of extremely fine grain size with thin, irregular laminae of opaque material parallel or at a low angle to their margins (Fig. 3b). Unlike the cataclastic deformation bands, boundaries of grains within the fine-grained zones tend to be sutured and interlocking (Fig. 3c) and there is locally a grain-shape alignment. Discontinuous mica
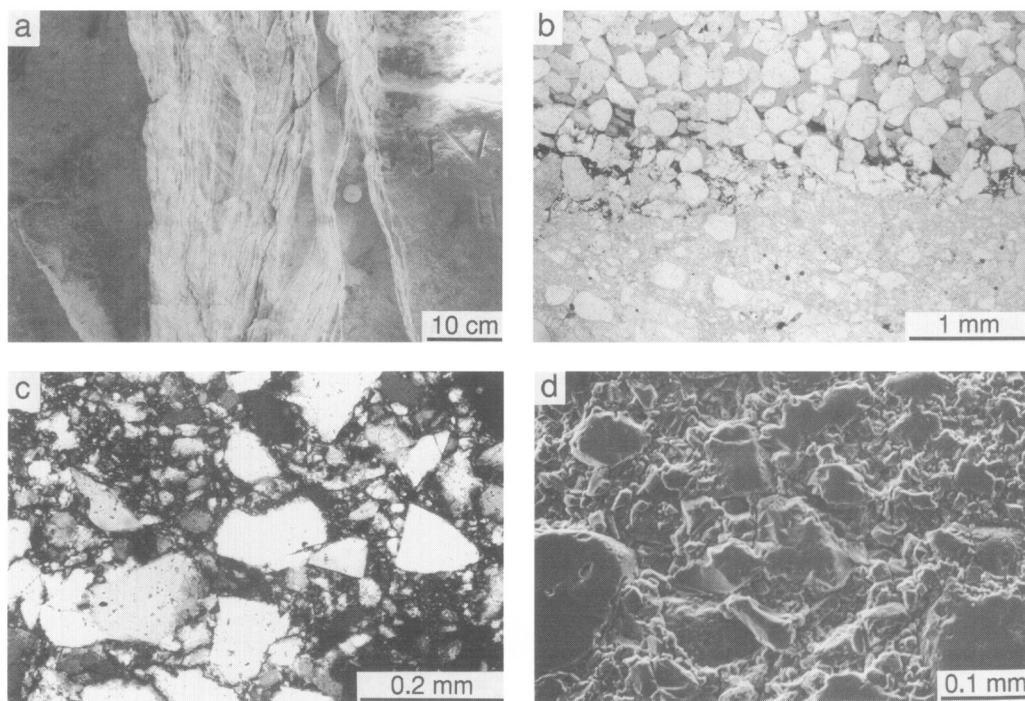
Fig. 2. Cataclastic deformation bands: (**a**) zone of deformation bands in outcrop of Dakota Sandstone, Canon City, Colorado, USA; (**b**) thin section of (a) showing cataclastic deformation band (bottom) and adjacent sandstone (plane light photomicrograph); (**c**) enlargement of (b) showing fractured, angular quartz grains in cataclastic deformation band (crossed polars photomicrograph); (**d**) scanning electron micrograph of (b) showing conchoidal fracture faces on quartz fragments and discrete nature of grain boundaries between fragments.
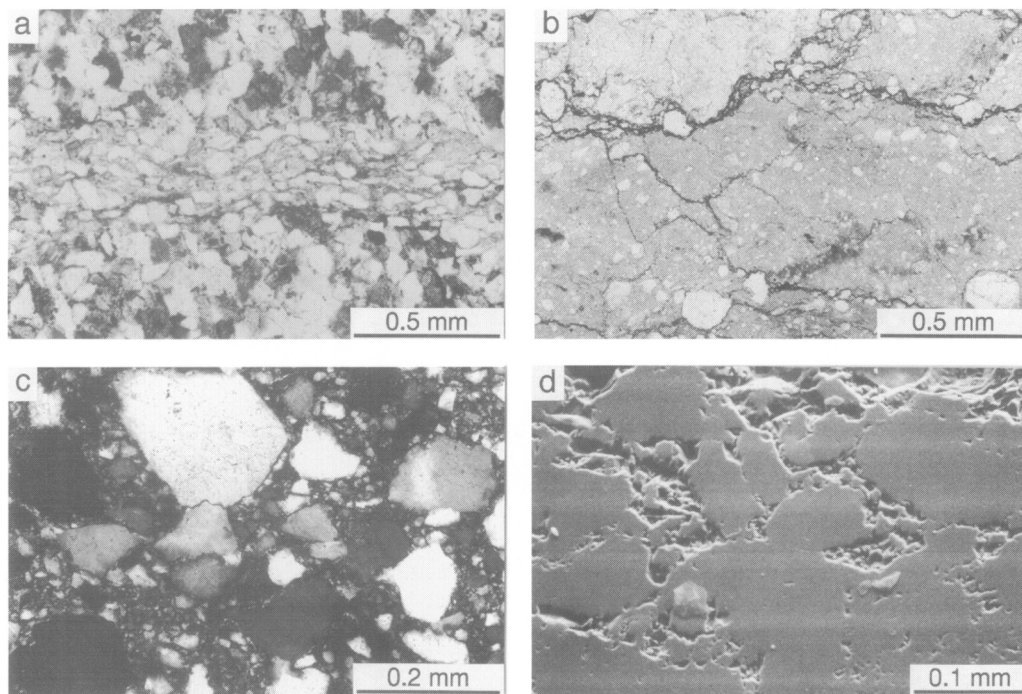
Fig. 3. Solution and complex deformation bands: (**a**) solution deformation band (across centre) showing aligned, unfractured grains bounded by dark, phyllosilicate-rich selvedges, Wilcox Formation (Fm), south Texas, USA (plane light photomicrograph); (**b**) complex deformation band with dark stylolites parallel to deformation band margin (vertical), Nugget Fm, western Wyoming, USA (plane light photomicrograph); (**c**) enlargement of (b) showing sutured quartz grain boundaries within complex deformation band (crossed polars photomicrograph); (**d**) scanning electron micrograph of (b) showing indistinct nature of quartz fragment boundaries resulting from pressure solution and local cementation.

films occur along quartz grain boundaries that are sub-parallel to the fault-zone margin. The textural contrast between these zones and cataclastic deformation bands is especially evident in scanning electron micrographs, where the boundaries between adjacent fragments in the deformed zone appear to be partially to entirely welded (Fig 3d). The microscopic character of these zones is that of cataclastic deformation bands that have been overprinted and modified by pressure solution. Therefore, these zones are interpreted to have formed by a combination of cataclasis and diffusive mass transfer.

Clay-matrix gouge zones

Clay-matrix gouge zones appear in outcrop, drill-core and hand sample as shiny, lineated, dark-coloured surfaces or zones (Fig. 4a) that commonly serve as planes of preferential parting. In many cases, the fault-zone material is poorly indurated and readily disaggregates into platy,

lenticular fragments upon handling. Thin clay-matrix gouge zones in various orientations sometimes form intersecting arrays that separate less-deformed sandstone into polygonal blocks. They are preferentially developed from mineralogically immature sandstones, specifically those with greater than 30% clay + mica + lithics and less than 60% quartz (Fig. 1a, Table 2). Mineralogically, the gouge zones range in composition from 20 to 80% phyllosilicates and, in some cases, show significant differences from their protoliths (Fig. 1b, Table 2).

In thin section, the clay-matrix gouge zones vary in character both within individual samples and between samples from different locations. The principal feature common to all samples is the presence of a fine-grained, clay-bearing matrix within which the phyllosilicate grains are strongly aligned (Fig. 4b). The foliation defined by these phyllosilicates is oriented at low angles or parallel to the fault zone margin (Fig. 4c). In some cases, the phyllosilicate fabric is accompanied by irregular laminae of opaque
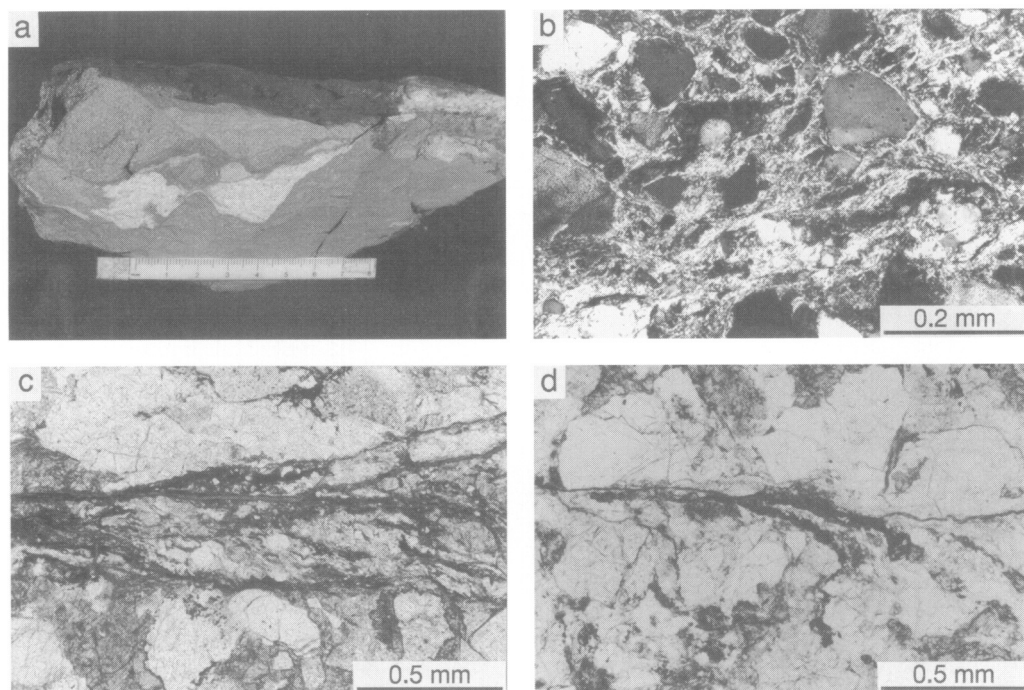
Fig. 4. Clay-matrix gouge zones: (**a**) cut slab of dark-coloured clay-matrix gouge in micaceous Cutler Sandstone from Moab fault zone, central Utah, USA (scale in centimetres); (**b**) thin section of (a) showing aligned, fine-grained phyllosilicates in clay-matrix gouge (crossed polars photomicrograph); (**c**) prominent oblique foliation defined by phyllosilicate aggregates, Hemlock Fm, Cook Inlet, Alaska, USA (plane light photomicrograph); (**d**) deflection of phyllosilicate-rich lithic clast into incipient clay-matrix gouge zone, Hemlock Fm, Cook Inlet, Alaska (plane light photomicrograph).

material. Remnants of the protolith, such as shattered detrital grains and pieces of intact sandstone, occur as porphyroclasts within this foliated matrix. Margins of the gouge zones vary from sharp to diffuse, locally displaying a gradual decrease of foliation intensity into the adjacent rock. Within the sandstone outside of the gouge zones, micaceous detrital grains (e.g. lithic fragments) commonly show evidence of ductile grain distortion and dimensional alignment into parallelism with the foliation (Fig. 4d). In some cases, feldspar grains are partially or completely altered to fine-grained phyllosilicate aggregates in close proximity to the gouge zones.

Sandstone-derived fault rocks similar to the clay-matrix gouge zones discussed above have been previously described by Chester & Logan (1986), Trevena (1989), and Knipe (1993). The complex character of these zones is interpreted to reflect their formation by the simultaneous activity of several deformation mechanisms, including cataclasis, diffusive mass transfer, and intragranular sliding within phyllosilicate-rich domains (detrital fragments or gouge matrix).

Analysis of fluid-flow properties

Fluid-flow tests on the fault-zone samples included analysis of specific permeability and capillary properties. Since permeability is the fundamental factor controlling the rate of fluid flow in response to an applied differential head (see Hubbert 1956), it is the parameter likely to be most important in dictating fluid-flow patterns within a reservoir during production. In contrast, capillary properties dictate the magnitude of the differential hydrocarbon buoyancy pressure (typically manifest as differential hydrocarbon column height) that can be maintained across a lithologic boundary. Capillary properties control the ability or inability of a lithologic boundary to act as a barrier to migrating hydrocarbons (see overview by Schowalter (1979)) on a long-term time frame. Therefore, measurement

of permeability and capillary properties provides information on the potential influence of fault zones on fluid flow over two different time scales.

Permeability

Where possible, 1.9 to 2.5 cm diameter plugs were cut approximately perpendicular to the fault zones, and the plugs were trimmed to maximize the portion consisting of fault-zone material. These plugs were used for Klinkenberg-corrected permeability measurement at 20.7 MPa (3000 psi) hydrostatic confining pressure. Measurement error associated with the permeability tests is estimated to be <15% of the measured value for samples with permeabilities greater than 1 mD and up to 35% for lower permeability samples (G. Potter, Amoco, pers. comm.). Despite these large uncertainties in absolute permeability values, the data are considered sufficient to detect order-of-magnitude differences between samples within the dataset.

Many of the plugs used for permeability analysis consisted of both protolith sandstone and fault-zone material. In these cases, the permeabilities measured in the laboratory represent a harmonic average of the fault-zone and sandstone permeabilities (see Amyx & Bass (1962) for discussion of permeability averaging in heterogeneous media). True fault-zone permeabilities for these samples were calculated from a knowledge of the host sandstone permeability (estimated from previous core analysis results or measured on companion plugs of unfaulted material) and the proportion of the plug (measured parallel to the axial flow direction) consisting of fault-zone material.
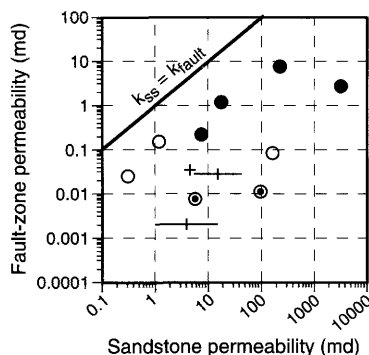
Fig. 5. Comparison of sandstones and fault-zone permeabilities. Symbols as in Fig. 1.

Fault-zone permeabilities span five orders of magnitude (Table 1). For all of the samples in which the permeability of both the sandstone and fault zone were measured, the fault zone has lower permeability (Fig. 5). These results are consistent with the conclusions of other authors (e.g. Aydin 1978; Pittman 1981; Nelson 1985; Trevena 1989; Antonellini & Aydin 1994; Fowles & Burley 1994) who have demonstrated significant permeability reduction associated with faulting of porous sandstones. In the sample set considered here, the permeability reduction relative to the protolith sandstone is one to three orders of magnitude for cataclastic and solution deformation bands, and two to four orders of magnitude for clay-matrix gouge zones and complex deformation bands.

The fault-zone permeabilities generally decrease with decreasing protolith quartz content (Fig. 6a) and increasing fault-zone phyllosilicates (Fig. 6b). Deformation-band permeabilities span
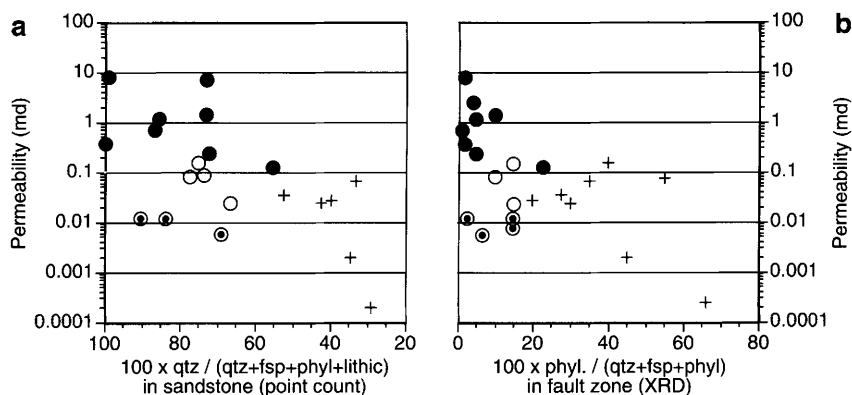
Fig. 6. Fault-zone permeability at 20.7 MPa (3000 psi) hydrostatic confining pressure as a function of (**a**) sandstone protolith composition and (**b**) fault-zone composition. Symbols as in Fig. 1.

a wide range, from 0.008 to 9 mD, showing a strong dependence on the deformation mechanisms active in band formation. Cataclastic deformation bands have the largest permeabilities, whereas the complex deformation bands (cataclasis plus diffusive mass transfer) have the smallest values. Solution deformation bands have permeabilities intermediate between the other two types. Clay-matrix gouge zone permeabilities are below 0.07 mD and, with the exception of a couple of data points, show a crude tendency to decrease with increasing phyllosilicate content (Fig. 6b). The upper part of their permeability range overlaps with that of solution and complex deformation bands.

Measured permeabilities of the cataclastic deformation bands (0.1–9 mD) are similar to those previously determined for cataclastic deformation bands in the Oil Creek Sandstone (Pittman 1981), the Nubia Sandstone (Harper & Moftah 1985), quartzose sandstones in the Colorado Plateau (Antonellini & Aydin 1994), and Permian sandstones of northwest England (Fowles & Burley 1994). Permeabilities of complex deformation bands are similar to other values reported for faults in the Nugget Sandstone (Nelson 1985). The only clay-rich fault-zone permeabilities reported in the literature are those of Morrow et al. (1981) on San Andreas fault gouge. They reported a brine permeability of approximately 0.00001 mD, more than three orders of magnitude lower than the San Andreas gouge permeability measured here (CA-2, Table 1). This difference may be related, in part, to extreme water sensitivity of clays in San Andreas gouge samples.

Capillary properties

Capillary pressure data were collected using two different techniques: (1) methane injection into brine-saturated plugs, and (2) mercury injection into evacuated samples. Because these two test methods utilize different fluid systems, comparison of the resulting pressure measurements cannot be done directly (see Schowalter 1979). In order to allow comparison, the pressure results were converted to effective pore-throat radii (R) using (Washburn 1921):

$$R = 2\gamma \cos\theta / P_d$$

where P_d is the measured pressure at any point during a test, γ is the interfacial tension between the two fluids (480 dyn cm^{-1} for mercury–air; values from Hough et al. (1951) for methane–brine), and θ is the hydrocarbon–brine–solid contact angle (140° for mercury–air; 0° for methane–brine). Capillary pressure results throughout the remainder of this paper are expressed as effective pore-throat radii.

Methane injection was used on plug samples that could be adequately sealed in a Hassler sleeve. In these tests, a brine-saturated (50 000 ppm NaCl, 5000 ppm CaCl) core plug was put under 20.7 MPa (3000 psi) hydrostatic confining pressure and methane was applied to one end. The methane pressure was increased in a stepwise fashion to simulate the build-up of hydrocarbon buoyancy pressure adjacent to a seal. The pressure at the first appearance of methane on the downstream end of the plug is considered the capillary breakthrough pressure of the fault zone. These tests were terminated either at methane breakthrough or when the applied methane pressure was equal to the confining pressure, in which case only a minimum breakthrough pressure could be determined.

Samples that could not be satisfactorily plugged were tested using high-pressure mercury injection. In these tests, the samples were unconfined and mercury could generally enter the sample from all directions. Therefore, these tests measure the pore-throat population of both the fault zone and any undeformed host rock adjacent to it. As a result, interpretation of the fault-zone capillary properties is less straightforward than in the case of methane injection. Figure 7a illustrates the basis for interpretation of composite plugs (sandstone + fault zone). Three samples from the same depth interval within one drill-core of Nugget Sandstone were tested, one consisting of unfaulted sandstone, a second cut entirely from a zone of complex deformation bands, and a third composed of sandstone transected by a complex deformation band. Changes in curve slope indicate significant increases in mercury saturation at 0.4 and 3.4 MPa (60 and 500 psi) for the sandstone and fault-zone samples, respectively. These pressures are interpreted to be the capillary entry pressures of the sandstone and fault zone, and correspond to pore-throat radii of approximately 2 and 0.2 μm. The mercury injection curve for the compound sample shows multiple bends, one at a pressure corresponding to mercury entry into the host sandstone and the other corresponding to entry into the fault zone. Dual inflections of this sort are observed on the mercury injection curves for other compound (sandstone + fault) samples. In these cases (e.g. Fig. 7b), the inflection at the smaller pore-throat radius is interpreted to correspond to the entry of mercury into the finer-grained fault-zone material.

Several samples were tested using both mercury and methane injection in order to understand the
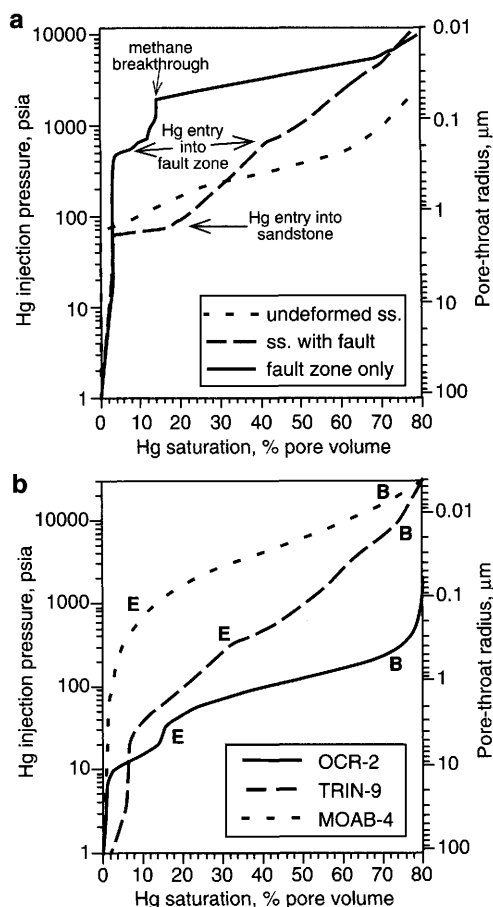
Fig. 7. Examples of capillary pressure data: (**a**) mercury injection data for three samples of Nugget Sandstone discussed in text; (**b**) data for three samples showing comparison between entry pressures (E) determined by mercury injection and breakthrough pressures (B) determined by methane injection.

relationship between the information gained using both techniques. Figure 7a and b illustrate these comparisons. Pore-throat radii corresponding to non-wetting phase entry (mercury injection) into the fault zones are three to 20 times larger than those corresponding to non-wetting phase breakthrough (methane injection). Such disparity between the two techniques is not surprising for several reasons: (1) a greater uncertainty is associated with identifying the fault-zone entry pressures from the mercury-injection data (see above); (2) significant non-wetting phase saturation is typically required to form a connected fluid filament through the sample before breakthrough occurs (Schowalter 1979; Katz & Thompson 1987); (3) the higher confining pressure (20.7 MPa) used in the methane injection tests could have caused pore-throat collapse relative to the samples used for mercury injection; and (4) the samples (especially the clay-matrix gouge zones) are anisotropic and it is likely that the highest capillary pressures would be required for non-wetting phase breakthrough across the fault zones. Despite these data quality limitations, the results are believed to be sufficient for identifying order-of-magnitude differences between similarly analysed samples within the dataset.

Measured fault-zone pore-throat radii corresponding to non-wetting phase entry (small symbols) and breakthrough (large symbols) are plotted as a function of sandstone and fault-zone composition in Fig. 8. Measured values span more than three orders of magnitude, with an overall trend of decreasing pore-throat radii as a function of decreasing sandstone quartz content and increasing fault-zone phyllosilicates. The contrast between capillary entry and breakthrough pressures for materials of equivalent composition clearly shows up on these plots. The general distribution of the data in
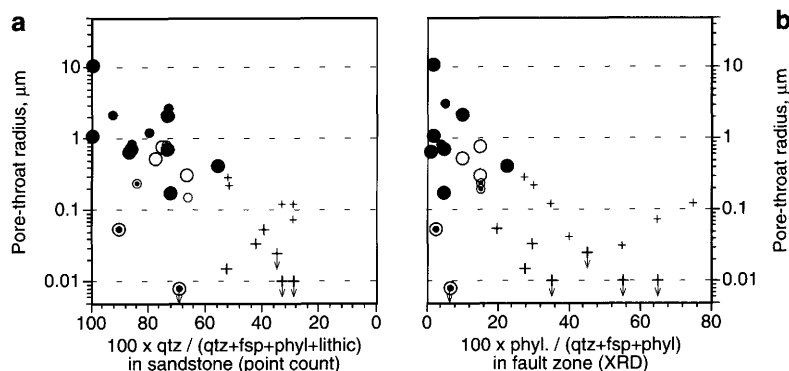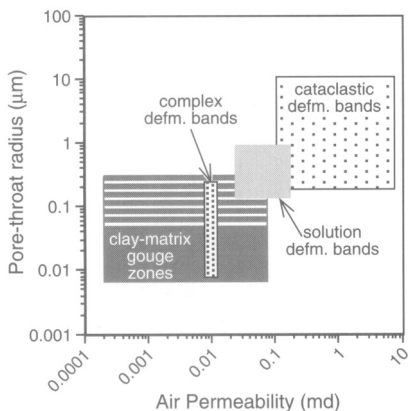

Fig. 8. Effective pore-throat radii of fault zones as a function of (**a**) sandstone composition and (**b**) fault-zone composition. Symbols as in Fig. 1. Arrows connected to some symbols indicate that these are maximum values.

Fig. 8 is similar to that of the permeability data: cataclastic deformation bands have the largest pore-throats, complex deformation bands and clay-matrix gouge zones have the smallest pore-throats, and solution deformation bands have intermediate values.

Discussion

Ranges of permeability (k) and effective pore-throat radius (R) for clay-matrix gouge zones and the various types of deformation bands are summarized in Fig. 9. These results show that the fluid-flow properties of quartz-phyllosilicate fault gouge depend on the gouge composition and deformation mechanisms involved in its formation. Clay-matrix gouge zones, derived from phyllosilicate-bearing sandstones and consisting of more than c. 20% phyllosilicates, have the smallest pore throats and lowest permeabilities ($k < 0.08$ mD, $R \ll 0.3$ μm). The fluid-flow properties of deformation bands derived from quartzose sandstones are more variable ($k = 0.008$–9 mD, $R = 0.02$–10 μm) and show a strong dependence on deformation mechanism(s). Within this compositional range, only those fault zones exhibiting evidence of both cataclastic and diffusive mass transfer processes, have fluid-flow properties comparable to those of the clay-matrix gouge zones. Specimens deformed by either individual deformation mechanism (cataclasis or diffusive mass transfer) have greater permeabilities and larger effective pore-throat radii.

Seals for hydrocarbon entrapment

In order to understand the implications of Fig. 9 for long-term hydrocarbon seals, it is important to consider how much hydrocarbon column could be sealed by fault zones with various pore-throat radii. Capillary pressure equations presented by Schowalter (1979) can be manipulated to the form:

$$H = 2\gamma(\cos\theta)/R(\Delta\rho)$$

which expresses the maximum sealable hydrocarbon column height (H) as a function of seal pore-throat radius (R), hydrocarbon–brine interfacial tension (gγ), hydrocarbon–brine–solid contact angle (θ), and in situ density difference between the hydrocarbons and brine ($\Delta\rho$). This form of the equation assumes that the capillary properties of the reservoir rock can be neglected. Figure 10 is a plot of the equation shown above using input values appropriate for a gas and brine system at the temperature and pressure specified. Superimposed onto this plot are general domains corresponding to the pore-throat radius values determined in this study for cataclastic deformation bands and clay-matrix gouge zones. The clay-matrix gouge zones have pore-throats that are sufficiently small to seal gas columns of 270 m or more, whereas the deformation bands are unlikely to seal columns larger than 140 m. In situ hydrocarbon–brine interfacial tension values are likely to be somewhat lower than those predicted

Fig. 9. Summary plot showing ranges of fault-zone pore-throat radius and air permeability. Ruled portion of clay-matrix gouge zone field indicates pore-throat radii based on mercury injection; solid portion is based on methane injection tests.
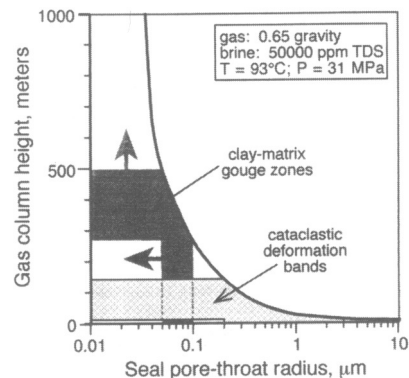
Fig. 10. Maximum sealable gas column height as a function of seal pore-throat radius for the specified physical conditions. Grey and stippled areas indicate ranges of each parameter for clay-matrix gouge zones and cataclastic deformation bands based on experimental data. Only the upper edge of the pore-throat radius range is shown for clay-matrix gouge zones; arrows indicate possible continuation of this field to smaller pore-throats and larger column heights.

based on laboratory interfacial tension data (see
Firoozabadi & Ramey,1988), which were used in
the generation of Fig. 10. Therefore, under nat-
ural sub-surface conditions, sealable column
heights for the fault zones considered are likely
to be closer to the low end of the ranges indi-
cated. For different hydrocarbon–brine systems
and different pressure–temperature conditions,
the absolute column height values will change,
although clay-matrix gouge zones should be
able to seal significantly longer columns than
cataclastic deformation bands under all condi-
tions.

Solution deformation bands and complex
deformation bands are not considered in Fig.
10. Complex deformation bands have very
small pore-throat radii and could seal hydro-
carbon columns comparable to those maintained
by clay-matrix gouge zones. However, their
occurrence cannot be predicted solely from
rock compositional data. Pore-throat radii of
solution deformation bands are intermediate
between those of cataclastic bands and clay-
matrix gouge zones (Fig. 9). Thus, they should
have a correspondingly intermediate seal
capacity.

Previous studies of petroleum fields in
siliciclastic sedimentary sections (Weber *et al.*
1987; Smith 1980; Bouvier *et al.* 1989; Gibson
1994; Fristad *et al.* 1996) have shown that the
best fault seals exist where a phyllosilicate-rich
fault zone is present across the faulted reservoir
termination. In these field examples, the fault
zones are typically formed by a 'shale-smear'

mechanism involving ductile deformation of
shale beds intercalated with the reservoir sands
(Fig. 11a). The clay-matrix gouge zones exam-
ined in this study can be viewed as small-scale,
natural models of these macroscopic fault
zones, with the relatively ductile, phyllosilicate-
bearing components of the sandstones playing
the same role as the shale layers at a larger
scale (Figs 4d and 11b). At the macroscopic
scale, shale-smear zones appear to form along
faults cutting stratigraphic sections containing
in excess of 15–30% shale (see Weber 1987;
Lindsay *et al.* 1993; Gibson 1994; Fristad *et al.*
1996). Similarly, the small-scale clay-matrix
gouge zones examined here formed from sands
containing more than 20–30% phyllosilicate-
bearing components. The correspondence
between the amount of phyllosilicate-rich
material necessary for the generation of fault
gouge with good sealing properties is striking,
and supports the similarity of processes at two
markedly different scales.

One implication of the data presented here is
that fault zones cutting through mineralogically
immature sandstones can form high-quality
seals, even where shale interbeds are not present.
Knipe (1993) reached a similar conclusion and
illustrated the microstructural change associated
with development of a fault rock similar to the
clay-matrix gouge zones discussed in this paper.
Figure 12 is a schematic cross-section that
illustrates one case where the presence of sand-
stone-derived, clay-matix gouge zones could
be important. The cross-section shows two
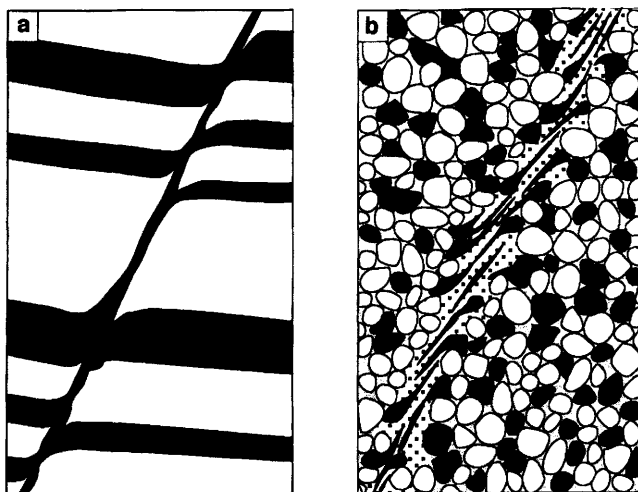
Fig. 11. Comparison of (a) 'shale-smear' mechanism of phyllosilicate-rich fault zone formation from interbedded
sands and shales (black) with (b) formation of clay-matrix gouge from sandstone containing phyllosilicate-bearing
fragments (black). Figure (a) modified from Weber *et al.* (1978).
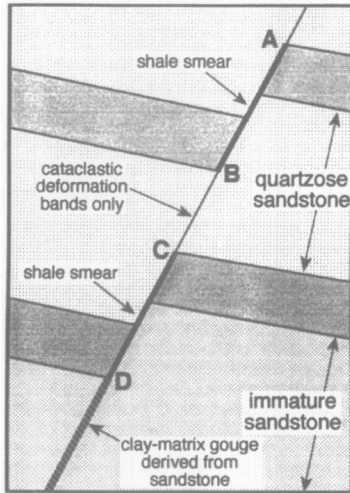
Fig. 12. Schematic cross-section showing phyllosilicate-rich fault zone distribution in siliciclastic sequences containing mineralogically mature sands (top) and immature sands (bottom). Shale beds are

normal-fault traps, the shallower one involving a quartzose sandstone and the deeper one involving a mineralogically immature sandstone. For the shallower trap, the spatial extent of a sealing phyllosilicate-rich fault zone includes only that portion of the fault along which a shale smear is developed (A–B in Fig. 12). Between B and C (Fig. 12), the fault zone is likely to consist solely of deformation bands derived from the quartzose reservoir sandstone. Because of the relatively large pore-throats of most deformation bands, the potential hydrocarbon column that can be sealed in this trap will probably be limited by a spill point near the base of the shale smear (point B). For the deeper reservoir, however, a phyllosilicate-rich fault zone will exist along the entire fault termination of the sandstone, even where no shale has been displaced along the fault (below D, Fig. 12). Thus, no cross-fault spill point exists for this trap, and there is potential to seal a longer hydrocarbon column than in the shallower sandstone. Thus, for a specified fault displacement, fault seals are likely to have greater spatial continuity in siliciclastic sections composed of mineralogically immature sandstones than in sections containing quartzose sandstones.

Seals for hydrocarbon production

From the perspective of hydrocarbon production from a sandstone reservoir, the most important

facet of the fault zones discussed in this paper is that they are of lower permeability than the sands from which they are derived (see also Aydin 1978; Pittman 1981; Nelson 1985, Antonellini & Aydin 1994; Fowles & Burley 1994). The presence of planar zones of low permeability in an otherwise permeable reservoir will influence both the overall (bulk) reservoir permeability and the permeability anisotropy. Permeability parallel to a dominant fault set will be an arithmetic (thickness-weighted) average permeability (Amyx & Bass 1962). Since the fault zones are generally thin, this value will be dominated by sandstone permeability and will probably be only slightly lower than that of the undeformed sandstone. In contrast, flow across the faults will be controlled by a harmonic average permeability (Amyx & Bass 1962) calculated from the permeabilities of the sandstone and fault zones.

Figure 13 illustrates how a harmonic average permeability depends on the proportion of the flow path composed of fault-zone material and the permeabilities of the two components. One of the things evident in this diagram is that as little as 10% low-permeability fault-zone material along a flow path can result in dramatic bulk permeability reduction. The degree of permeability reduction (i.e. number of times reduction) varies depending on the permeability values of the host sandstone and fault zone. Therefore, the presence of fault zones of an arbitrary permeability (e.g. 1 mD) will have a much more damaging effect on the flow characteristics of a high-permeability reservoir than of a low-permeability one (compare solid and dotted curves, Fig. 13). In addition, the lower the permeability of the fault zone cutting a given sandstone, the greater the degree of permeability
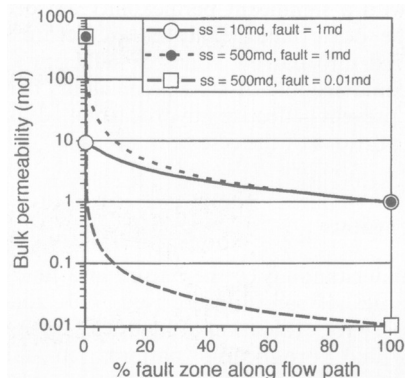
Fig. 13. Effect of low permeability fault zones on bulk permeability of a reservoir along a linear flow path. See text for discussion.

reduction (compare dotted and dashed curves, Fig. 13).

Because of relative permeability effects, the amount of fault-related permeability reduction implied by the test results presented in this paper may underestimate those in a sub-surface hydrocarbon reservoir. At a given elevation in a hydrocarbon column, the contrasting capillary properties of the sandstone and fault zone (e.g. Fig. 6a) will cause the fault zones to either have no hydrocarbon saturation (if the buoyancy pressure in the hydrocarbon column is less than the fault-zone entry pressure) or lower saturation than the undeformed sandstone (if the hydrocarbon buoyancy pressure exceeds the fault-zone entry pressure). In the case of zero fault-zone saturation, which is likely for clay-matrix gouge zones and complex deformation bands, the fault-zone permeability will be effectively zero, producing a no-flow barrier within the reservoir. In cases where the fault zone is partially hydrocarbon saturated, the reduced saturation relative to the undeformed sandstone will result in greater effective permeability contrast between the sandstone and fault zone than indicated by the specific permeabilities presented here. This effect should increase the impact of the faults on the bulk reservoir permeability, although partially hydrocarbon-saturated fault zones may remain somewhat permeable and serve as only partial flow barriers.

In addition to the potential effects outlined above, the overall influence of faults on production behavior will also depend on the spatial fault distribution within the reservoir, including fault interconnectivity and clustering (e.g. Watterson et al. 1995; Manzocchi et al. 1998; Walsh et al. 1998). If the faults are widely distributed throughout the reservoir, the effect may be a general permeability reduction, possibly in conjunction with a significant permeability anisotropy. On the other hand, fault-related deformation localized into narrow zones of sufficient thickness could produce discrete permeability barriers that prevent effective hydrocarbon drainage from portions of the reservoir.

Conclusions

An understanding of the nature and fluid-flow properties of sandstone-derived fault zones is necessary for evaluation of hydrocarbon entrapment and production patterns in faulted sandstone reservoirs. This study of naturally deformed sandstones from various areas shows that deformation of quartzose sandstones results in deformation bands, whereas faulting of

mineralogically immature sandstones produces clay-matrix gouge zones. Clay-matrix gouge zones generally have lower permeabilities and higher capillary displacement pressures than deformation bands. These fluid-flow properties are largely dependent on rock composition, but show a superimposed influence of deformation mechanism, especially in the case of deformation bands.

Most deformation bands have capillary properties sufficient to maintain only small hydrocarbon column-height differences across them, whereas clay-matrix gouge zones can potentially seal hydrocarbon columns with heights of several hundred metres. However, both the low-permeability deformation bands and clay-matrix gouge zones can potentially influence fluid-flow patterns within a producing reservoir, although the magnitude of these effects will depend on the spatial distribution and abundance of faults and the permeabilities of the fault zones and undeformed sandstone.

References

AMYX, J. W. & BASS, D. M. Jr 1962. Properties of Reservoir Rocks, In: Frick, T. C. (ed.) Petroleum Production Handbook, Volume II. McGraw-Hill, Chapter 23, 140.

ANTONELLINI, M. & AYDIN, A. 1994. Effect of faulting on fluid flow in porous sandstones: petrophysical properties: AAPG Bulletin, 78, 355–377.

AYDIN, A. 1978. Small faults formed as deformation bands in sandstone. Pure and Applied Geophysics, 116, 913–930.

BOUVIER, W. F., KAARS-SIJPESTEIJN, C. H., KLUESNER, D. F., ONYEJEKWE, C. C. & VAN DER PAL, R. C. 1989. Three-dimensional seismic interpretation and fault-sealing investigations, Nun River field, Nigeria. AAPG Bulletin, 73, 1397–1414.

CHESTER, F. M. & LOGAN, J. M. 1986. Implications for mechanical properties of brittle faults from observations of the Punchbowl fault zone, California. Pure and Applied Geophysics, 124, 79–106.

FIROOZABADI, A. & RAMEY, H. J. Jr 1988. Surface tension of water–hydrocarbon systems at reservoir conditions. Journal of Canadian Petroleum Technology, 27(3), 41–48.

FOWLES, J. & BURLEY, S. 1994. Textural and permeability characteristics of faulted, high porosity sandstones. *Marine and Petroleum Geology*, **11**, 608–623.

FRISTAD, T; GROTH, A.; YIELDING, G. & FREEMAN, B. 1996. Quantitative fault seal prediction – a case study from Oseberg Syd. *In*: NORWEGIAN PETROLEUM SOCIETY (eds) *Hydrocarbon Seals – Importance for Exploration and Production* (abstracts). Norwegian Petroleum Society, Oslo.

GIBSON, R. G. 1994. Fault-zone seals in siliciclastic strata of the Columbus basin, offshore Trinidad. *AAPG Bulletin*, **78**, 1372–1385.

HARPER, T. R. & MOFTAH, I. 1985. Skin effect and completions options in the Ras Budran reservoir. *Society of Petroleum Engineers, Middle East Oil; Technical Conference and Exhibition*, Bahrain, 211–219.

HOUGH, E. W., RZASA, M. J. & WOOD, B. B. 1951. Interfacial tensions at reservoir pressures and temperatures, apparatus and the water–methane system. *American Institute of Minine Engineers, Petroleum Transactions*, **192**, 57–60.

HUBBERT, M. K. 1956. Darcy's law and the field equations of the flow of underground fluids. *American Institute of Mining Engineers, Petroleum Transactions*, **207**, 222–239.

JAMISON, W. R. & STEARNS, D. W. 1982. Tectonic deformation of Wingate sandstone, Colorado National Monument. *AAPG Bulletin*, **66**, 2584–2608.

KATZ, A. J. & THOMPSON, A. H. 1987. Prediction of rock electrical conductivity from mercury injection measurements, *Journal of Geophysical Research, Series B*, **92**, 599–607.

KNIPE, R. J. 1993. The influence of fault zone processes and diagenesis on fluid flow. *In*: HORBURY, A. D. & ROBINSON, A. G. (eds) *Diagenesis and Basin Development*. AAPG, Studies in Geology, **36**, 135–151.

KNIPE, R. J., FISHER, Q. J., JONES, G., *et al.* 1996. Fault seal prediction: methodologies, applications and successes. *In*: NORWEGIAN PETROLEUM SOCIETY (eds) *Hydrocarbon Seals – Importance for Exploration and Production* (abstracts). Norwegian Petroleum Society, Oslo.

LINDSAY, N. G., MURPHY, F. C., WALSH, J. J. & WATTERSON, J. 1993. Outcrop Studies of Shale Smears on Fault Surfaces. International Association of Sedimentologists, Special Publications, **15**, 113–123.

MANZOCCHI, T., RINGROSE, P. S. & UNDERHILL, J. R. 1998. Flow through fault systems in high-porosity sandstones. *This volume*.

MORROW, C., SHI, L. Q. & BYERLEE, J. 1981. Permeability and strength of San Andreas fault gouge under high pressure. *Geophysical Research Letters*, **8**, 325–328.

NELSON, R. A. 1985. *Geologic Analysis of Naturally Fractured Reservoirs*. Gulf, Houston, TX, 320 pp.

PITTMAN, E. D. 1981. Effect of fault-related granulation on porosity and permeability of quartz sandstones, Simpson Group (Ordovician), Oklahoma. *AAPG Bulletin*, **65**, 2381–2387.

SCHOWALTER, T. T. 1979. Mechanics of secondary hydrocarbon migration and entrapment. *AAPG Bulletin*, **63**, 723–760.

SMITH, D. A. 1980. Sealing and non-sealing faults in Louisiana Gulf Coast salt basin. *AAPG Bulletin*, **64**, 145–172.

SVERDRUP, E. & PRESTHOLM, E. 1990. Synsedimentary deformation structures and their implications for stylolitization during deeper burial. *Sedimentary Geology*, **68**, 201–210.

TREVENA, A. S. 1989. Small faults as barriers to permeability in sandstone gas reservoirs, Pattani Basin, Thailand. *AAPG Bulletin*, **73**, 553.

UNDERHILL, J. R. & WOODCOCK, N. H. 1987 Faulting mechanisms in high-porosity sandstones; New Red sandstone, Arran, Scotland. *In*: JONES, M. E. & PRESTON, R. M. F. (eds) *Deformation of Sediments and Sedimentary Rocks*. Geological Society, London, Special Publications, **29**, 91–105.

WALSH, J. J., WATTERSON, J., HEATH, A., GILLESPIE, P. A. & CHILDS, C. 1998. Assessment of the effects of sub-seismic faults on bulk permeabilities of reservoir sequences. *This volume*.

WASHBURN, E. W. 1921. Note on a method of determining the pore sizes in a porous material. *Proceedings of the National Academy of Science*, **7**, 115–116.

WATTERSON, J., HEATH, A., KNIGHT, S., FLINT, S., WALSH, J., CHILDS, C. & GILLESPIE, P. A. 1995. Estimation of the effects of sub-seismic faults on effective permeabilites of reservoir sequences. *Abstracts of Structural Geology in Reservoir Characterization and Field Development Conference*, Imperial College, London, 34.

WEBER, K. J. 1987. Hydrocarbon distribution patterns in Nigerian growth fault structures controlled by structural style and stratigraphy. *Journal of Petroleum Science and Engineering*, **1**, 91–104.

——, MANDL, G., PILAAR, W. F. & PRECIOUS, R. G. 1978. The role of faults in hydrocarbon migration and trapping in Nigerian growth fault structures. *Offshore Technology Conference Proceedings*, 2643–2653.

Assessment of the effects of sub-seismic faults on bulk permeabilities of reservoir sequences

J. J. WALSH, J. WATTERSON, A. HEATH, P. A. GILLESPIE & C. CHILDS

Fault Analysis Group, Department of Earth Sciences,
University of Liverpool, Liverpool L69 3BX, UK

Abstract: Single-phase horizontal bulk permeabilities for 3 km × 3 km volumes of varying thickness of a typical Brent permeability sequence have been calculated, both before and after faulting by a range of sub-seismic fault arrays, with maximum fault displacements of 20 m–2 m. The models incorporate realistic juxtaposition geometries across fault surfaces. Results are expressed in terms of fractional bulk permeabilities (Kf), i.e. ratio of bulk permeability of faulted model and of pre-faulting model. Fault and fault array variables modelled and tested were fault density, spatial distribution, orientation distribution and fault zone permeability relative to the host rocks, expressed as transmissibility factor (Tf). Realistic fault zone thicknesses were incorporated by use of a scaling factor. Low, moderate and high fault densities have significant and markedly different effects on Kf whereas the effects of spatial and orientation distribution variations are slight except at very low Tf values ($Tf < 0.001$). The relative insignificance of fault spatial distributions is due to closer fault spacing resulting in locally high hydraulic gradients which increase flow through fault surfaces unless these surfaces have very low Tf values. Prediction of fault zone hydraulic properties remains the most important factor contributing to modelling uncertainties.

The degree to which flow in a reservoir is likely to be influenced, either positively or negatively, by the presence of a population of sub-seismic faults is crucial to development decisions for some reservoirs (Sassi *et al.* 1992; Gauthier & Lake 1993; Omre *et al.* 1994). Quantification of the likely effects of sub-seismic faults can be helpful not only where significant effects are likely but also where it can be demonstrated that the effects are likely to be insignificant and that the causes of production problems should be sought elsewhere.

The possibility of assessing the effects of sub-seismic faults arises from recent developments in methods of prediction of sub-seismic fault numbers and sizes by extrapolation from the seismically imaged fault population (Sassi *et al.* 1992; Yielding *et al.* 1992; Gauthier & Lake 1993; Munthe *et al.* 1993). However, in addition to numbers and sizes there are other attributes of fault arrays which are, or could be, significant in modifying flow; these include orientation distribution, spatial distribution and the hydraulic properties of the fault surfaces, or fault zones. Our aim has been to determine which attributes of sub-seismic fault arrays are of most significance to flow and, by implication, which attributes are of little significance. The results can then be used to limit the problem of attribute definition and modelling by concentrating effort on those attributes of most significance.

A principal concern in undertaking this work was the problem of predicting spatial distributions of sub-seismic fault arrays, because there is no satisfactory distribution model on which to base either deterministic or stochastic predictions (Gillespie *et al.* 1993). We report here on the results of testing a variety of spatial distributions for sub-seismic fault arrays of low, moderate and high densities. Fault sizes within the modelled arrays range from 20 m to 2 m maximum displacement on individual faults, which is below the effective limit of seismic resolution for most North Sea reservoirs (Badley *et al.* 1990; Walsh *et al.* 1994).

Flow simulation was carried out using the HOMPER (HOMogenization of PERmeability) routines for simulating single-phase flow, using a finite difference method, provided by the Norwegian Computer Center SAND Group (Holden *et al.* 1990).

Results are expressed in terms of the fractional effective permeability (Kf) of a reservoir volume of 3 km × 3 km × (variable thickness) where Kf = effective permeability of the faulted volume/effective permeability of the volume without faults. Kf was calculated for a range of models with specified fault array attributes and each model was tested with a full range of fault surface hydraulic properties, expressed as transmissibility factor (Tf), which is varied from 1.0 to 0. We use the term 'effective permeability' to refer to the bulk or mass or averaged or homogenized permeability of a heterogeneous volume, even though the flow referred to is single phase.
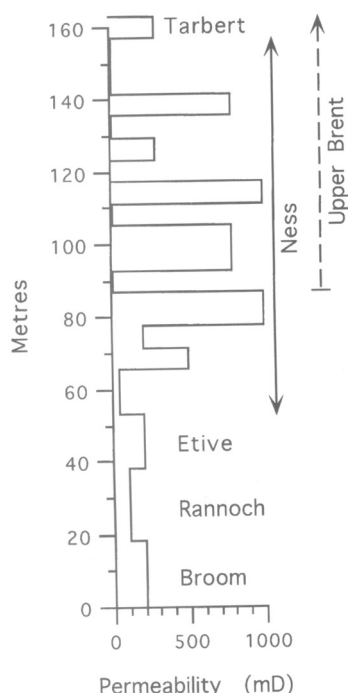
Fig. 1. Brent and Upper Brent permeability sequences used in model construction.

Model construction

The permeability structure used in most models is based on a simplified Brent sequence, 160 m thick, but one model is based on the lower net:gross Upper Brent sequence, 73 m thick (Fig. 1). Use of layer-cake versions of the sequence undoubtedly results in some over-simplification but also means that the effects of different fault arrays are directly comparable. To maintain comparability between models, only sub-seismic faults have been included in the models, although individual seismically imaged faults would usually be explicitly modelled in reservoir simulations.

Realistic tectonic fault-related horizon geometries were added to the model using the method given in Gibson et al. (1989) implemented by an in-house reservoir modelling system, FaMOUS. Fault surfaces are elliptical with aspect ratios of 2:1 and with maximum displacements at the centres reducing approximately linearly (Rippon 1985; Walsh & Watterson 1987; Cowie & Scholz 1992b; Scholz et al. 1993) to zero at tip-lines (Fig. 2). Realistic juxtaposition geometries across fault surfaces are calculated by partitioning of displacements between hangingwall subsidence and footwall uplift in the ratio 2:1, which is a good approximation for tectonic faults (Gibson et al. 1989). For the purpose of this study, precise modelling of displacement partitioning is not required. Modelled faults are vertical but this simplification has an insignificant effect on flow if the fault displacement is taken as equivalent to the throw on a typical steeply dipping tectonic fault. For model construction, fault size is expressed as maximum displacement (D) and maximum dimension of the fault surface ellipse. Most of the results presented are for models in which all faults are parallel.
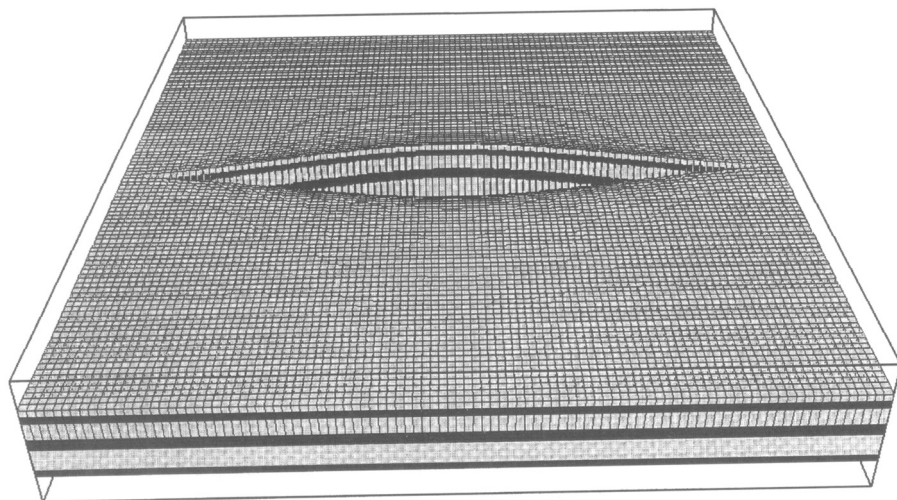
Fig. 2. Cellular volume model showing modelled fault displacements with partitioning of displacement between footwall uplift and hangingwall subsidence giving realistic juxtaposition geometries across the fault surface. Upper and lower parts of the elliptical fault surface are not shown in this view.

A fault system, or array, is defined in a model by the number of faults of given sizes, their distribution and orientation. In addition, fault surfaces, or fault zones, are assigned Tf values and within each model all faults were assigned the same Tf value. $Tf = 1.0$ is equivalent to the fault surface, or fault zone, having the same permeability as the adjacent matrix and $Tf = 0$ is equivalent to an impermeable or sealing fault surface (Omre et al. 1994). Each individual fault is defined by its size, orientation and location (x, y, z) of the centre of the fault surface. The effects of flow-enhancing fractures, where $Tf > 1.0$, are not considered.

Sub-seismic fault population modelling

Fault size definition

Fault size can be measured or expressed in a number of ways and the parameter used depends on the sampling domain (Marrett & Allmendinger 1991; Yielding et al. 1992). If the sampling domain is one-dimensional (1D) (line sampling), size can be expressed only as displacement at the

point on the fault surface intersected by the sample line. With two-dimensional (2D) sampling (maps, sections), fault size can be expressed either as maximum displacement on the fault trace or as the fault trace length. In the three-dimensional (3D) domain, fault size can be expressed either in terms of maximum displacement on the fault surface, maximum dimension of the fault surface or as fault surface area. The various size parameters are not independent variables so one can be derived from another (Marrett & Allmendinger 1991), although the derivation is subject to some uncertainty because there is no consensus defining the detailed relationships between the various parameters (Cowie & Scholz 1992a; Gillespie et al. 1992; Dawers et al. 1993).

It is agreed, however, that for many fault systems each size parameter has a power-law, or fractal, scaling law so that by extrapolation of the straight line plot derived from seismic data, a sub-seismic population can be derived for the plotted parameter (Yielding et al. 1992). The slopes of the straight lines, or power-law exponents, for a given fault population vary systematically according to which parameter is plotted (Fig. 3). Two practical
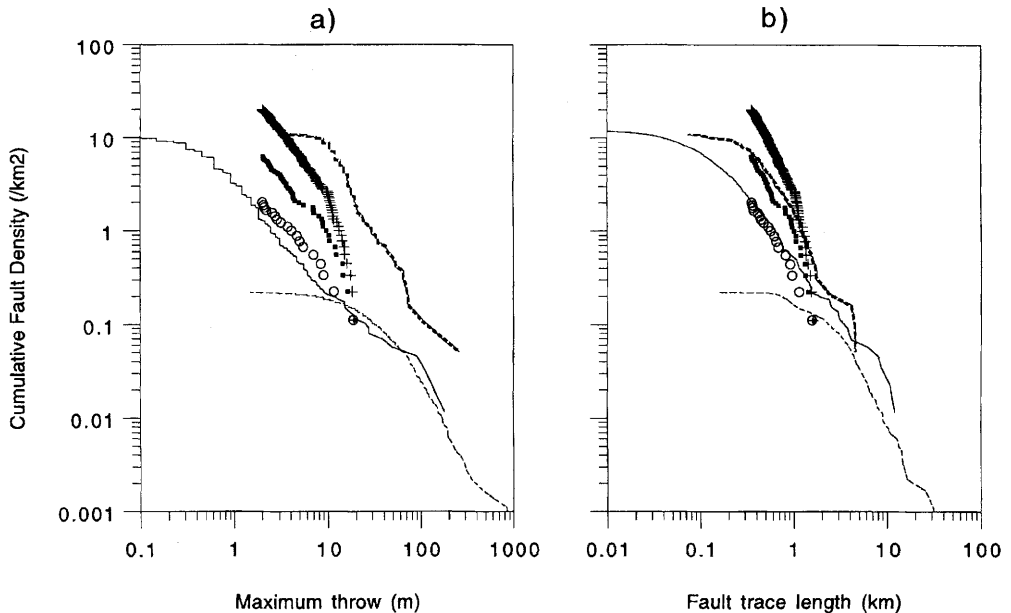
Fig. 3. (a) Maximum fault throw and (b) fault trace length population curves for three fault datasets and for low-, moderate- and high-density fault models. Cumulative fault density is the cumulative number of faults with maximum throws or trace lengths greater than a given size value, per km². Datasets are for a N North Sea oil and gas reservoir (light broken line), S North Sea gas reservoir (heavy broken line) and S Yorkshire coal-field (solid line). Model populations are low (open circles), moderate (filled squares) and high (crosses) density with maximum throws from 20 m–2 m and trace lengths 1650 m–350 m. The model population curves have steep right-hand segments because of random sampling of power-law populations which extend to larger fault sizes.

modelling problems arise from these population domain systematics. The first problem is that the parameters which can be measured, and therefore directly predicted, are either 1D or 2D but the model input required is 3D, i.e. maximum displacement on a fault surface. Derivation of the 3D parameter values from either 1D or 2D data inevitably increases the uncertainty. The second problem arises from the fact that, given a maximum displacement on a fault, the fault surface dimensions must be derived using the, uncertain, relationship between maximum displacement and dimensions (Cowie & Scholz 1992*a*; Gillespie *et al.* 1992; Dawers *et al.* 1993). As flow is likely to be sensitive to total fault surface area, the uncertainties in the derived dimensions must be assessed in terms of their resulting uncertainties in flow. In order to reduce these uncertainties we have used a combination of 3D (maximum displacement) and 2D (maximum fault surface dimension) size attributes to generate the models.

Fault trace length population power-law exponents determined from fault datasets are generally within the range -1.3 to -2.0 (Yielding *et al.* 1992) and trace maximum displacement population exponents within the range -1.0 to -1.4. Our model fault populations are based on a trace length exponent of -1.5 with a trace maximum throw population of -1.0, which is at the lower end of the observed range. Because flow is likely to be more sensitive to fault dimensions than to maximum throw, because across-fault juxtapositions are relatively unimportant for faults of the size range considered (see Results section), more priority is given to correct dimensional input rather than to correct displacement values. The maximum throw and trace length populations used in construction of low-, moderate- and high-density fault array models are shown in Fig. 3 together with populations derived from data from a Northern North Sea reservoir (low density; Clausen *et al.* 1994), a Southern North Sea gas reservoir (high density) and the Yorkshire coal-field (low density; Watterson *et al.* 1996).

Examples of fault trace maps of the modelled fault arrays with low, moderate and high densities are shown in Fig. 4; for a 3 km × 3 km area these densities correspond to 18, 57 and 180 faults, respectively, in the 20 m–2 m maximum displacement size range.

Spatial distribution

The spatial distribution of a predicted sub-seismic fault size population is difficult to model because the systematics of fault spatial distributions have not been determined even for parallel fault arrays (Gillespie *et al.* 1993). We know of no result which would permit deterministic modelling of the locations of sub-seismic faults, in either 1D, 2D or 3D, so stochastic modelling is necessary. Recent work does not support claims that fault patterns are fractal (Gillespie *et al.* 1993; Odling 1992; Walsh & Watterson 1993) but it is obvious from inspection of fault maps that faults are usually irregularly spaced, at least in 2D. Some individual fault system attributes, e.g. size population, may be fractal even though the fault pattern, which is the result of several independent attributes, is not fractal (Gillespie *et al.* 1993). The idea that fault distributions are characterized by some degree of clustering, perhaps modified by repulsion, has a long history arising from qualitative observations of many small faults being spatially associated with larger faults, and fault clustering along 1D sample lines has been demonstrated quantitatively (Gillespie *et al.* 1993). Clustered fault array models have been created according to formal clustering criteria; if required, the distributions can be conditioned on the locations of known, i.e. seismically imaged, faults. Clustered distributions, in 2D, were obtained using the correlated Lévy method in which power-law size populations are distributed by a series of sequential power-law jumps to define locations and which create a fractal clustering; this method is a modification of the Lévy dust structure of Mandelbrot (1982). From a single randomly positioned seed point, faults are positioned sequentially relative to the previous fault using 'jump' and 'anisotropy' ratios. 'Correlated' refers to the correlation of jump length with size of the previous fault. The jump ratio defines the jump length as a proportion of the horizontal dimension of the previous fault, and determines the distance from a randomly chosen point on the trace of the previous fault to the centre point of the new fault trace. The anisotropy ratio is the ratio between the mean jump distance parallel to the fault traces and the mean jump distance normal to the fault traces. To create an isotropic system the direction in which the new fault is positioned relative to the previous fault is chosen randomly, but an anisotropic system can be created by applying an anisotropy ratio when selecting the direction. Anisotropy ratios are axial ratios of nominal ellipses which represent the degree of departure from the isotropic distribution as represented by a circle. Reduction in jump ratio and increase in anisotropy ratio, within individual fault clusters, result in a decreasing mean fault-normal distance between neighbouring faults relative to
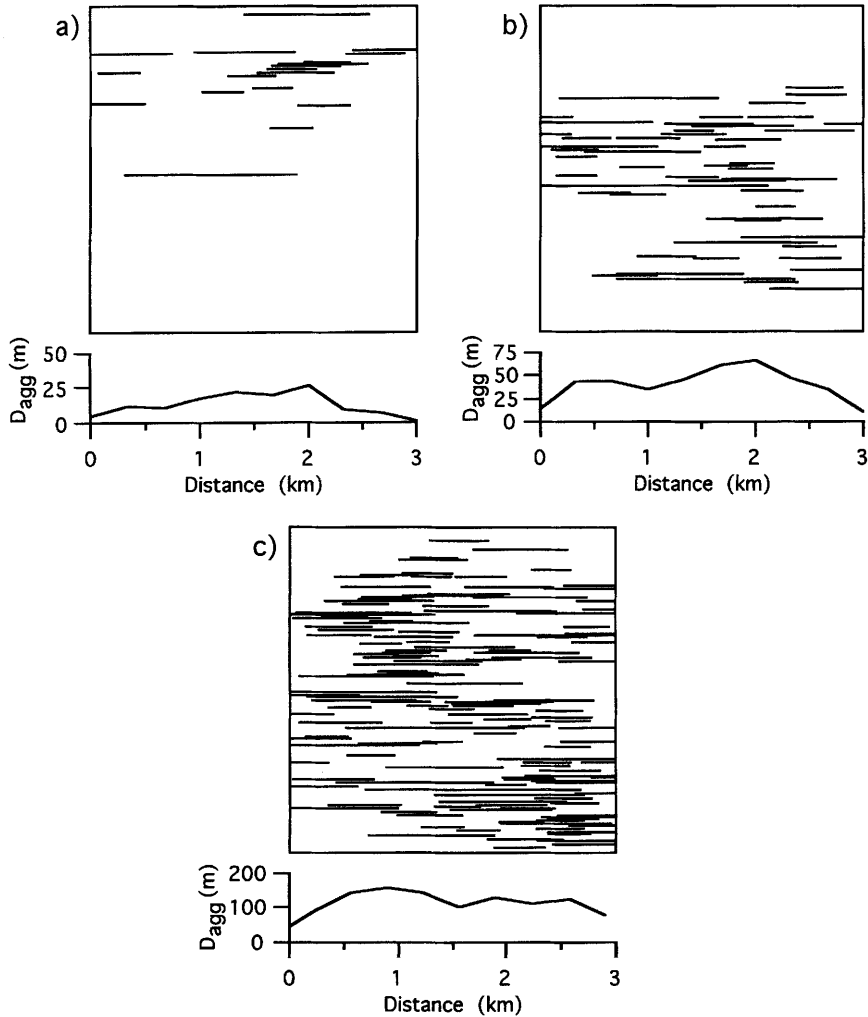
Fig. 4. Typical low-, moderate- and high-density model fault array maps (**a**)–(**c**), all moderately clustered, for 3 km × 3 km models. Below each map is its aggregate displacement profile (D_{agg}). Modelling was performed mainly on array realizations meeting the regular aggregate displacement profile criterion (see text).

mean fault trace length. Jump ratios of 0.3 and 0.5 and anisotropy ratios of 3.33 and 2.0 were applied to create strongly and moderately clustered arrays, respectively, in both of which successive faults usually overlap along strike. Fault centre positions lying outside the model lateral boundaries are rejected, which results in a boundary effect of slightly reduced fault density. Sub-seismic faults can be conditioned on known seismically imaged faults by repeated seeding from traces of seismic faults. Because the clustering procedure used is 2D, fault centres are all located on the horizontal mid-plane of the modelled sequences; this has little effect on flow as all

sizes of faults have vertical surface dimensions greater than model thicknesses. A very slight edge effect on juxtaposition geometries towards the upper and lower model boundaries has negligible effect on the flow results. Examples of clustered and randomly distributed arrays of moderate fault density are shown in Fig. 5. To obtain 3D clustering the procedure can be modified to define also the elevations of fault centres. Random fault distributions were used as bench-marks against which clustering effects could be assessed.

Further conditioning of some of the models was achieved by testing the shapes of aggregate
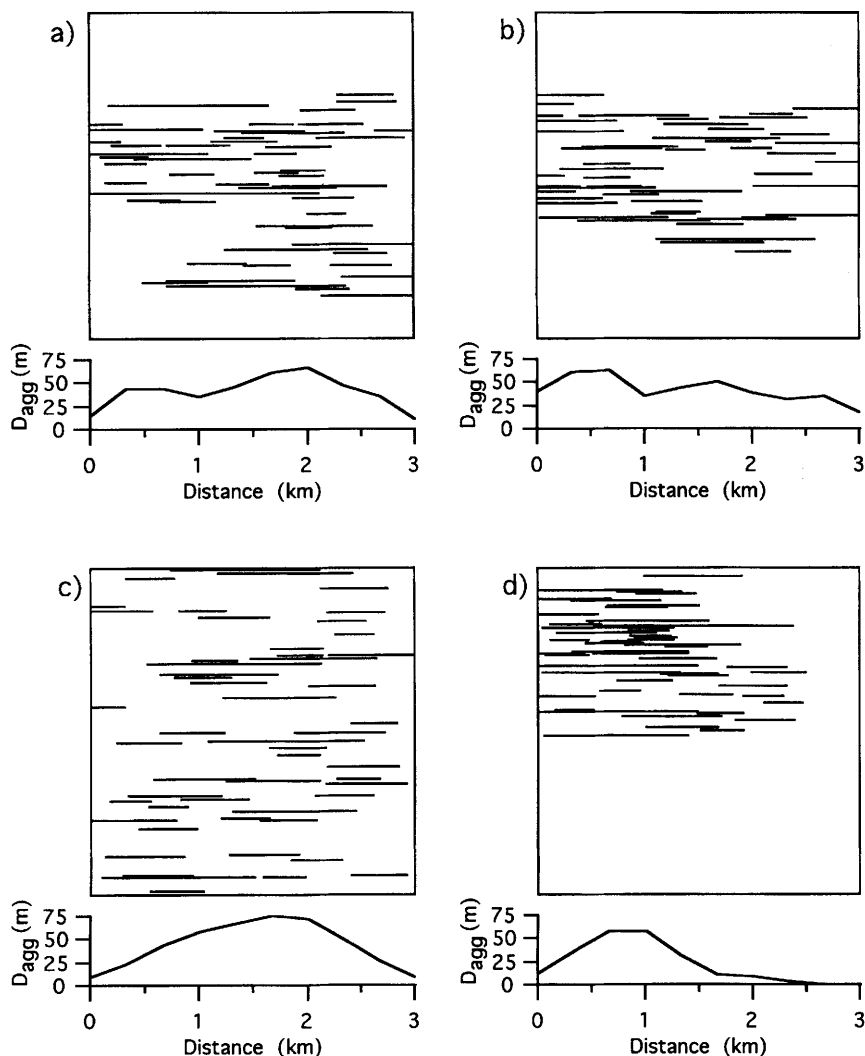
Fig. 5. Examples of (**a**) moderately clustered, (**b**) highly clustered and (**c**) randomly distributed fault array maps of moderate density arrays for 3 km × 3 km models which meet the regular aggregate displacement (D_{agg}) profile criterion. See text for clustering parameters applied to (a) and (b). (**d**) An example of a highly clustered moderate-density array with an irregular aggregate displacement profile (D_{agg}) which does not meet the criterion for regular aggregate displacement profiles (see text).

displacement profiles which for real fault systems are known to have fairly regular forms (Mukherjee 1979; Walsh & Watterson 1993). Model arrays were conditioned by aggregate displacement profiles by selecting from numerous realizations only those for which the minimum aggregate displacement along a profile was >15% of the maximum aggregate displacement on the profile. The model arrays shown in Fig. 4 have acceptable aggregate displacement profiles,

in contrast with the non-conditioned profile shown in Fig. 5d.

Property models and flow models

Geological surface models are converted to property models by cellularization of the model volume using eight-corner point cell definition (Flint *et al.* 1995). As corner points are not

constrained to lie on grid-nodes, a property model honours the geological surface model exactly, except where curves are represented by a series of straight segments corresponding to edges or surfaces of cells. In practice this cellularization is carried out prior to imposing the fault displacement fields.

The only volume property of concern here is the permeability tensor; values were assigned to each of the cells according to the permeability sequence in Fig. 1. The same values were assigned to the x, y and z directions in a cell. Although the property models could be used as flow models without modification, the negative effects of numerical dispersion associated with the irregular cells of a geological model outweigh the benefits of geometrical precision. The property models were therefore sub-sampled onto a regular lattice to produce flow models with orthorhombic cells. For standard 3 km × 3 km area flow models, resolutions were varied from 40 m to 20 m, in x and y, and from 0.5 m to 2 m in z, so typical models comprised $c.3.5$ million cells.

A disadvantage of using orthorhombic cells is that for the sizes of model used, fault zone thickness cannot be correctly represented because a resolution of $c.1$ m would require models with $c.10^9$ cells. Because of the way in which flow simulation software operates, a fault zone thickness is implicitly represented even where a fault is simply represented in the flow model as a surface, with attached Tf value, between adjacent cells. This implicit representation of fault zone thickness arises because the Tf value assigned to an inter-cell fault surface is attached to a notional gridblock spanning the surface; the raw results are therefore highly dependent on model resolution.

As a rule of thumb, fault zone thickness at a point on a fault surface can be taken as one to two orders of magnitude less than the displacement, with zone thicknesses varying by approximately one order of magnitude between 20 m faults and 2 m faults (Robertson 1983; Hull 1988; Knott 1994; Flint et al. 1995). For 2 m–20 m maximum displacement faults, thicknesses are therefore $c.$ two orders of magnitude less than can be represented directly in a model with 30 m lateral resolution. This problem was overcome by applying a scaling technique whereby the modelled thickness of a fault zone is effectively decreased by reducing the fault surface Tf value (Flint et al. 1995).

To express these wide variations of fault zone thickness, two additional abscissa (Tf) scales are given for several figures (e.g. Fig. 7), one showing values appropriate to the lower end of the fault zone thickness range and the other for the upper end of the range. Using these scales the Tf value is equivalent to the ratio of fault zone permeability to host rock permeability, which we refer to as the permeability ratio. Fault rocks commonly have permeabilities some orders of magnitude less than those of the host rock sandstones, and permeability ratios range down at least to 0.0001 (Antonellini & Aydin 1994; Fowles & Burley 1994; Flint et al. 1995). Indirect evidence, from seismically mapped faults and pressure and/or production data, shows that sealing faults are relatively common, but in many of these cases the zero transmissibility is due, at least partly, to juxtaposition effects rather than being due entirely to fault zone hydraulic properties.

Flow modelling

HOMPER routines apply a finite difference method to calculate the effective permeability of a prismatic volume containing an unlimited number of orthorhombic gridblocks, each of which is assigned permeability values in x, y and z directions (Holden et al. 1990). Boundary conditions are defined by a pressure value of 1.0 applied over the upstream and zero over the downstream end of the prism, with no flow through other prism surfaces. Flow simulation results are given only for flow in the x direction of each model, normal to the strike of the modelled faults, and the ratio of the effective permeability values before and after insertion of a sub-seismic fault array gives the Kf value for each model.

The concept of 'homogenization' of a reservoir volume has limitations. Substitution of a heterogeneous volume with a single valued homogeneous volume should, ideally, reproduce exactly the effect of the heterogeneous volume on flow within a larger volume model. Larger scale heterogeneities should therefore be upscaled only within an appropriately large volume or by application of global optimization techniques. In practice, a valid homogenization of an area of 3 km × 3 km should not include fault surfaces longer than approximately 1.5 km or even less if they are close to the upstream or downstream prism faces, so that each end of the upscaled prism is isobaric. As this last requirement is a boundary condition of a HOMPER experiment, we are unable to test the extent to which our models conform with natural boundary conditions.
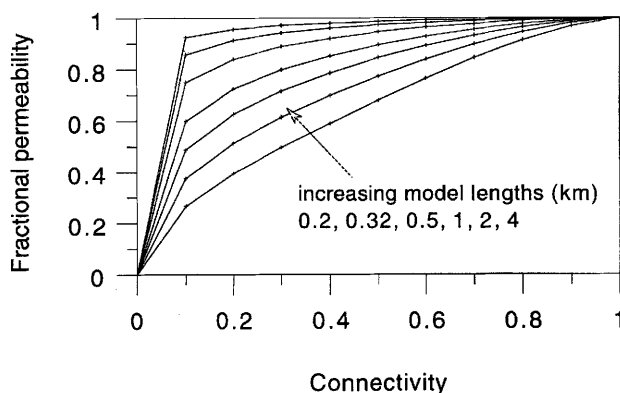
Fig. 6. Fractional permeability versus connectivity, for a model with a single through-going fault offsetting a single flow unit across the width of the model and transverse to the flow direction; the fault entirely offsets the flow unit when the connectivity is zero. The effective permeability increases with an increase in model length in the flow direction. Model dimensions in y and z are 2 km and 220 m respectively, and variable in x. Cell dimensions are 20 m in x and y and 10 m in z.

Results

System dependency

All results are expressed as fractional permeability (Kf), values of which vary from 1.0 to zero with increasing negative fault effects on flow. Kf values >1.0 can occur when faults increase connectivity by connecting originally isolated high permeability volumes, e.g. sand channels, but this does not occur in our layer-cake models. Kf values are highly dependent on system parameters, principally model resolution, so results have to be assessed with this dependency in mind. For simple models with a single fault offsetting a single flow unit across the width of the model, Kf values are dependent both on the model lengths in the flow direction (x) and on model resolution, except for connectivities of 1.0 and 0.0. The shorter the model the lower the value of Kf for a given connectivity (Fig. 6). There is a markedly non-linear relation between fault offset (connectivity) and Kf values (Fig. 6; Omre *et al.* 1994).

For a given model resolution there is a simple relationship between a Tf value assigned to an inter-cell surface and a permeability value assigned to a layer of cells explicitly representing a fault zone. A Tf value of 0.1 is equivalent to assigning a Kf value to the fault zone cells which is one order of magnitude less than that of the matrix cells. A Tf value of 0.1 is also usually equivalent to 90% of the fault surface being assigned zero permeability and 10% assigned a value equal to that of adjacent matrix cells; this equivalence holds when the

two extreme permeability values are distributed regularly or randomly on the fault surface and the surface is large relative to the cell dimensions. Definition of the scaling relationships between fault zone permeabilities and thicknesses on the one hand and gridblock resolution on the other allows results to be expressed as those which would be obtained by explicit representation of true fault zone thicknesses with appropriate permeability values assigned to the fault zone cells. The Tf values are then identical with those of the permeability ratios.

We emphasize that these system dependencies are not peculiar to our systems or methods but apply to all flow modelling based on volume cells or gridblocks. Our method has been to keep system parameters constant and vary only the fault system attributes so that results can be directly compared. Unless stated otherwise the resolution, i.e. cell or gridblock dimensions, is 30 m in x and y and 0.6 m in z, which gives reasonably good definition of juxtaposition geometries across all but the smallest faults, i.e. 2 m maximum displacement. The vertical dimensions of even the smallest faults are greater than the thickness of the reservoir sequences investigated. This method is both realistic and allows use of 2D population systematics (Yielding *et al.* 1992) that are directly comparable with populations derived from seismic interpretations.

Fault density effects — moderate clustering

Figure 7 shows the changes in fractional permeability for Tf values ranging from 1.0 to zero
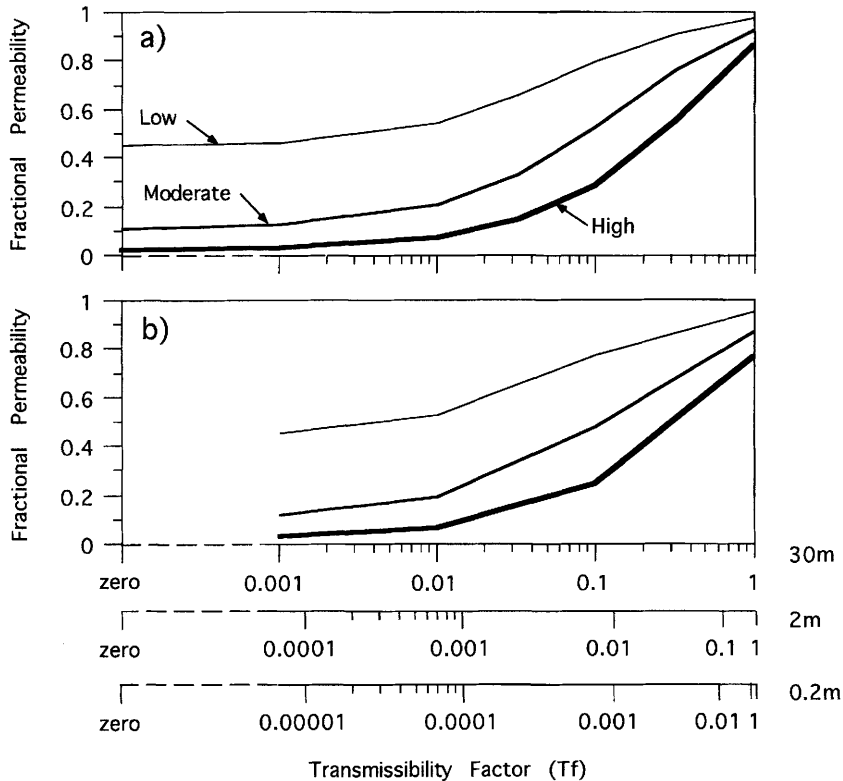
Fig. 7. Fractional permeabilities versus *Tf* for (**a**) Brent and (**b**) Upper Brent sequences with low-, moderate- and high-density fault arrays (arrowed) with moderate clustering. The uppermost abscissa scale is the model scale for 30 m gridblock lateral dimensions, which implicitly ascribes fault zone thickness of 30 m. The two lower scales correspond to the upper and lower range of realistic fault zone thicknesses for the fault size range modelled. Fractional permeability values at *Tf* = 1 are due solely to the effects of juxtaposition geometries across the fault surfaces, which are greater for the lower net:gross Upper Brent sequence.

for low-, moderate- and high-density sub-seismic fault arrays, each spatially distributed with moderate clustering. Figure 7a is for the Brent sequence and Fig. 7b for the Upper Brent sequence.

At a *Tf* value of 1.0 the only effects on flow are due to juxtaposition geometries across fault surfaces, and Fig. 7a shows that, for the fault size range examined, the juxtaposition effects on flow within the Brent sequence are insignificant. The effects are slightly more marked for a lower net:gross sequence, such as the Upper Brent sequence (Fig. 7b), as would be expected. For *Tf* values <1.0 the *Kf* differences due to fault density differences become quite marked and absolute changes in *Kf* are very significant. Fractional permeabilities of the model volume are seriously reduced, i.e. by more than a factor of two, only at *Tf* values <0.01 for realistic fault zone thicknesses of between 2 m and 0.2 m (middle and lower scales).

Fault clustering effects

Three types of spatial distribution were modelled initially, i.e. strongly clustered, moderately clustered and randomly distributed. For each combination of fault density and spatial distribution, five conditioned realizations were tested and examples of the resulting fault arrays are shown in Fig. 5a–c. The results are shown in Fig. 8 and illustrate the relative unimportance of differences between the modelled spatial distributions. Differences between moderately and highly clustered arrays are trivial but their effects are only marginally greater than those of the random array even at *Tf* = 0. Density differences within the expected range are of much greater significance than differences within the expected range of spatial distributions, as shown in Fig. 9a–c.

The value of conditioning models on the basis of aggregate throw profiles is shown by results
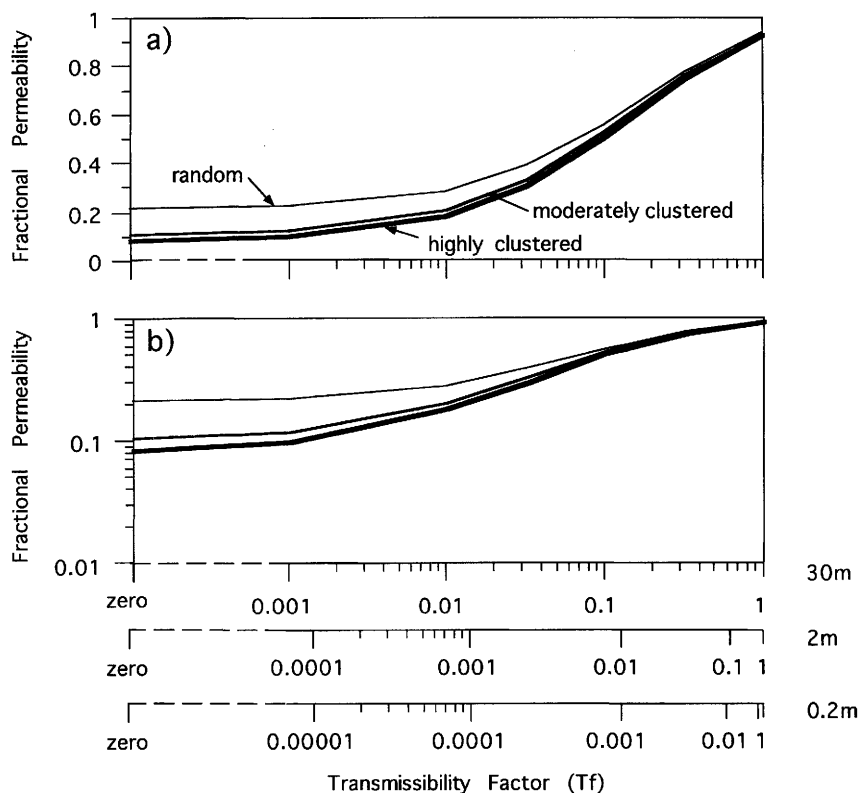
Fig. 8. Fractional permeability versus *Tf* for moderately and highly clustered and randomly distributed fault arrays of moderate density in the Brent sequence, illustrated with (a) linear and (b) log ordinate scales. Even at *Tf* = 0, the flow property differences between the three types of array are small. For significance of multiple abscissa scales, see caption to Fig. 7.

for 20 unconditioned models (Fig. 9d) which produce a wider range of fractional permeabilities than otherwise similar, but conditioned, models (Fig. 9a–c).

In order to test the effects of extreme clustering, a fault array, originally with both moderate density and moderate clustering, was compressed to occupy, in one case, the central 1 km of the model and in another case the central 300 m of the model (Fig. 10). In some parts of the fault array shown in Fig. 10b and in most of that in Fig. 10c the faults are so closely spaced that, given the lateral seismic resolution at depths of 2–3 km, i.e. >*c*. 50 m, the arrays would each be imaged as a single fault zone and no longer be sub-seismic. The resolutions, i.e. gridblock lateral dimensions, required for definition of individual fault surfaces in these very highly clustered models were achieved using high resolution 2D models with $1000 \times 1000 \times 1$ cell arrays giving a lateral resolution of 3 m.

Results of flow simulation of the high resolution 2D models (Fig. 11) show that differences

between extreme and moderate clustering are greatest, at about one order of magnitude, when fault surfaces are sealing, i.e. *Tf* = 0. The *Kf* differences are therefore approximately proportional to the fault spacings in the models, which also vary over one order of magnitude, i.e. the same array is distributed over model distances of 3 km, 1 km and 0.3 km in the three different models. For *Tf* = 1.0 there is, of course, no difference between the degrees of clustering because the fault surfaces have no effect on flow and there is no juxtaposition effect in 2D models. Differences between the models become apparent only where *Tf* < 0.001 and increase gradually towards *Tf* = 0. Increased upstream pressure adjacent to bottlenecks caused by close fault spacing results in an increased proportion of flow through fault surfaces, so far as this is possible. At values of *Tf* > 0.001 the proportion of flow through fault surfaces is so high that fault spacing has an insignificant effect. As diversion of flow through fault surfaces becomes less
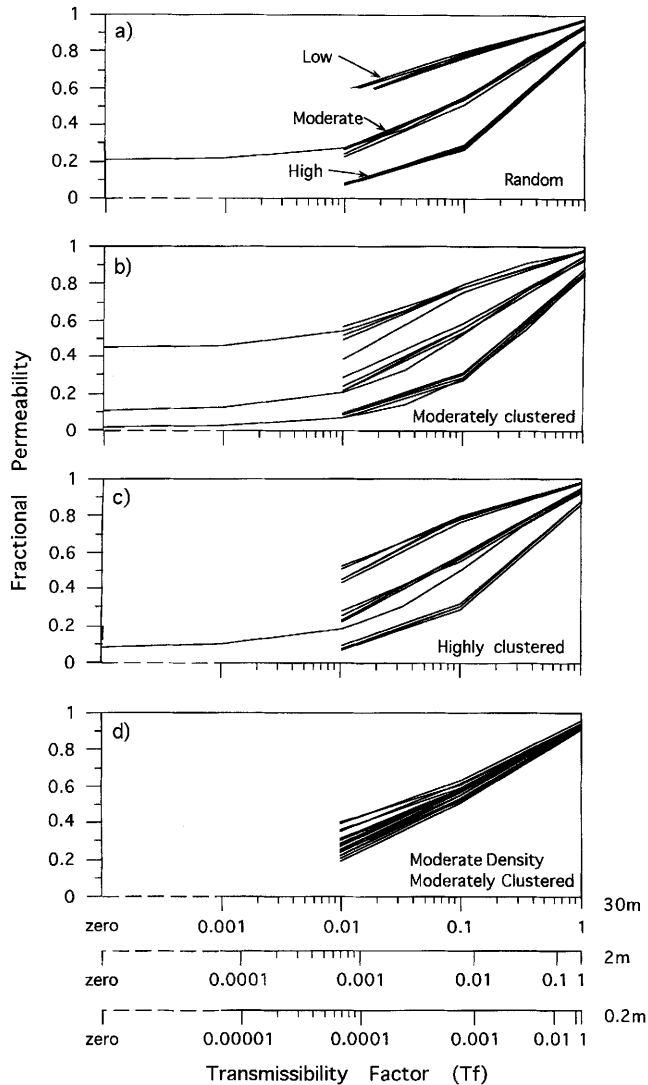
Fig. 9. (a)–(c) Comparison of the effects on Kf of realistic fault density differences with those of realistic spatial distribution differences, for values of Tf from 1.0 to 0, showing the slight effects of spatial distribution differences compared with density differences. Results are shown for five realizations for each combination of density and spatial distribution, conditioned by aggregate displacement profile regularity. (**d**) Fractional permeability curves for 20 non-conditioned realizations (see example in Fig. 5d) of moderate-density, moderately clustered arrays. The range of results for these non-conditioned arrays is significantly greater than for conditioned arrays. For significance of multiple abscissa scales, see caption to Fig. 7.

likely with decreasing Tf, the effects of fault spacing become progressively more pronounced until at $Tf = 0$ there is a near-linear relationship between fault spacing and fractional permeability. Even so, the difference in Kf between moderate and extreme clustering at $Tf = 0$ is no more than the differences between either low- and moderate-density or moderate- and high-density

models. As the extreme degrees of clustering which have been modelled are beyond the expected range for natural fault arrays we conclude that, even where fault surfaces are perfectly sealing ($Tf = 0$), the difficulty of valid modelling of spatial distributions of sub-seismic faults is not of great practical consequence. This conclusion would not apply to modelling
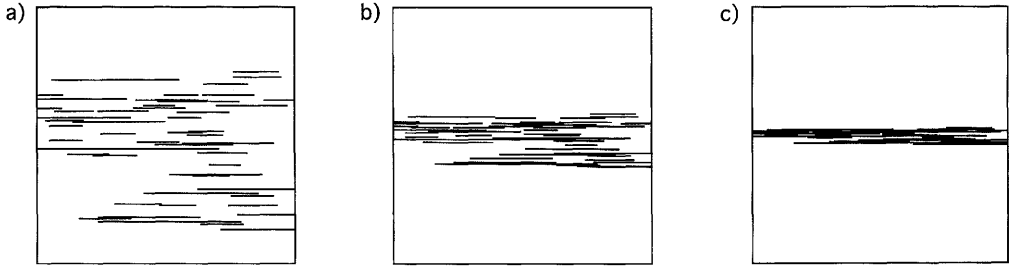
Fig. 10. (a) Moderately clustered, moderate-density array distributed in 3 km × 3 km model. (b) Same array compressed into central one-third of model, i.e. 1 km. (c) Same array compressed into central one-tenth of model, i.e. 300 m.

of well performance in a reservoir with fault surfaces of very low permeability where the well location relative to individual faults could be critical.

The insignificance of even extreme spatial distributions relative to fault density variations is due to the quite different ways in which each of these two variables affect the flow process. Whereas density differences have an approximately linear effect on Kf differences throughout the range of fault surface transmissibilities, spatial distribution differences result in strongly non-linear differences in Kf. Moreover, the range of fault densities occurring in natural
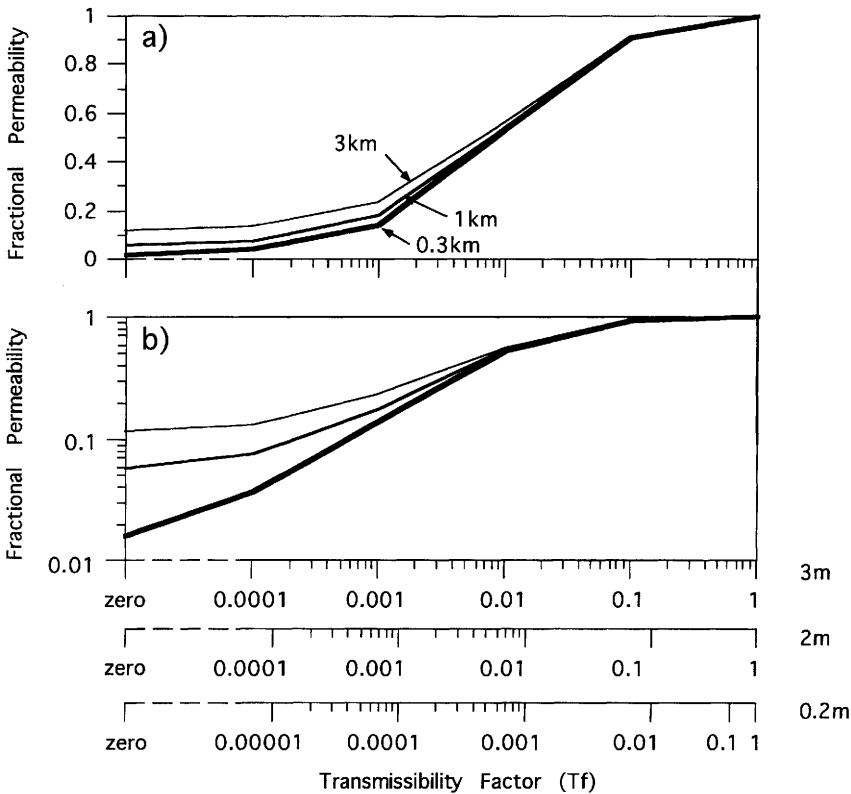
Fig. 11. Flow simulation results for fault array models shown in Fig. 10, illustrated with (a) linear and (b) log ordinate scales. Differences become apparent only when $Tf \leq 0.001$ (3 m scale) and increase towards $Tf = 0$ when the maximum difference between fractional permeabilities is about one order of magnitude; fault spacings also vary by an order of magnitude between least and most clustered arrays. For significance of multiple abscissa scales, see caption to Fig. 7.
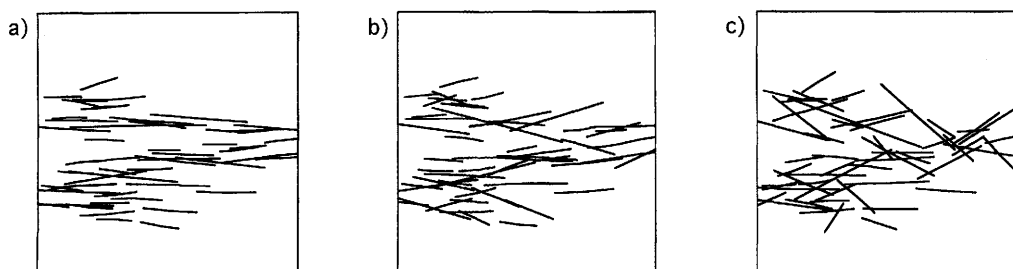
Fig. 12. Fault trace maps for moderate-density, moderately clustered fault arrays with non-parallel faults. Standard deviation from parallelism is 5° in (**a**), 10° in (**b**) and 20° in (**c**). A near-continuous fault baffle is apparent in (b) and faults in (c) are continuous.

fault systems has a much greater influence on Kf than does the normal range of spatial distributions. Only in an extreme case, in which perfectly sealing fault surfaces are contiguous and form continuous or near-continuous transverse baffles, would fault spacing represent a significant problem by compartmentalization of a reservoir. In our parallel fault models this type of fault connectivity does not occur so a series of models with arrays of non-parallel faults were tested.
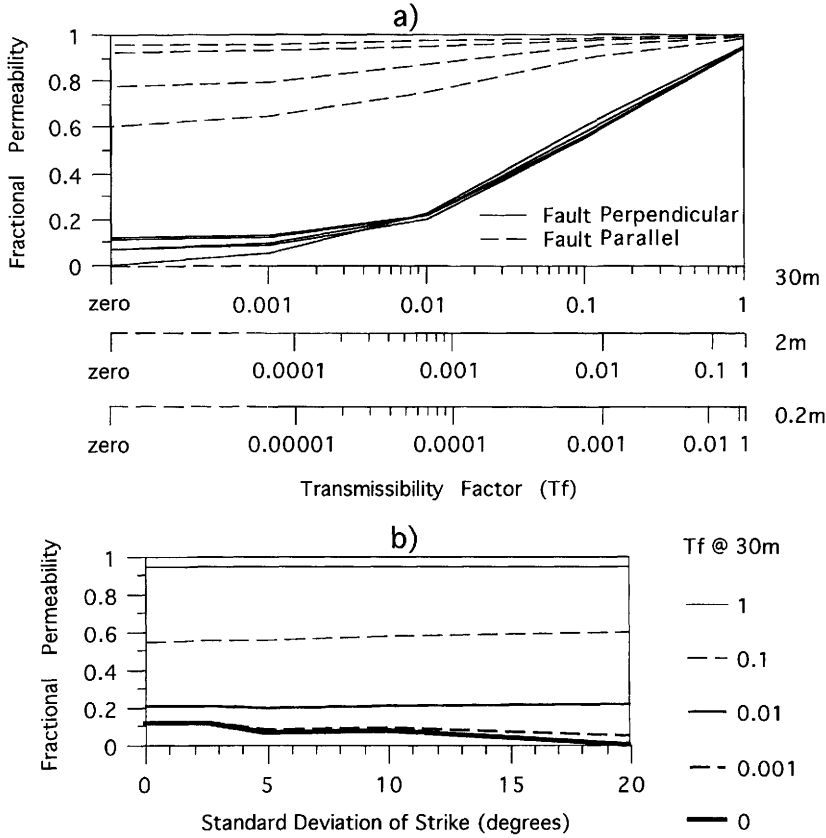
Non-parallel fault arrays

Strike directions were varied for a moderate-density and moderately clustered array by dispersing strike directions about the original direction of parallel faults by standard deviations of 5°, 10° and 20°. The resulting arrays (Fig. 12a–c) have not been conditioned to provide the abutting intersections which would characterize a real fault array with splays, but are adequate for the purpose. Inspection shows that fault surface connectivity provides an almost continuous baffle even in the 10° model and a continuous baffle in the 20° model. Flow results (Fig. 13) are in keeping with the observations on fault continuity. The results indicate that orientation distribution is not significant except when $Tf < 0.001$ and is crucial when $Tf = 0$. Although the significance of fault continuity will be considered in detail elsewhere, the differences in fractional permeabilities between highly connected fault arrays and parallel unconnected arrays are also small at $Tf > 0.001$. The orientation distribution and allied fault pattern characteristics, including the continuity of faults within an array, represent significant variables and further analysis of real fault systems is necessary before well-conditioned models can be generated.

Discussion

To what extent are the results of these simple models of practical interest? An obvious shortcoming is the restriction to single-phase flow. Opinion on the significance of this restriction has been widely canvassed and the opinions expressed vary almost as widely. Our current view is that the conclusions concerning the limited effects of spatial distributions of faults would be much the same for multiphase flow except where the fault surfaces have very different relative permeabilities for the different phases. An obvious step would be to carry out multiphase flow simulations using the same models and this work is planned. However, we know of no published data on relative permeabilities of either fault rocks or fault zones.

A more obvious limitation of the results is that they are expressed in terms of the fractional permeability of a relatively large volume. This scale of model was chosen as representing the smallest volume for which results would be reproducible. Smaller models are each likely to give unique values because of the small lateral dimensions relative to the lateral dimensions of individual faults within the required size range; the concept of a fault population, of the given size range, cannot simply be applied to smaller areas. Nevertheless, the performance of a single well, or paired producer/injector, would clearly vary considerably according to the location within each model and our 'average' results would have little predictive value. However, given that spatial distributions will, for the foreseeable future, be stochastically rather than deterministically modelled, a significant degree of uncertainty in well performance is inevitable. The best that is likely to be achieved in the near future is quantification of this uncertainty by varying well locations within models of the type

Fig. 13. Flow results for non-parallel fault arrays shown in Fig. 12. (a) *Kf* curves are provided for both flow in *x* (i.e. fault perpendicular) and in *y* (i.e. fault parallel). Curves are for parallel faults and for faults with strike directions varying about the direction of parallel faults with standard deviations of 5°, 10° and 20°. Note zero fractional permeability with *Tf* = 0 for fault array in Fig. 12c. For significance of multiple abscissa scales, see caption to Fig. 7. (b) *Kf* versus strike variation for different *Tf* values at 30 m gridblock lateral dimensions.

we have used and this work is planned. However, our results indicate that this type of uncertainty is likely to be significant only where fault surfaces have low *Tf* values.

Conclusions

(1) On the scale examined and for realistic fault zone thicknesses, sub-seismic fault arrays have a significant effect on fractional permeability only when fault surface *Tf* values are less than 0.01, i.e. when fault zone permeabilities are two to three orders of magnitude less than that of the matrix in which they are embedded. Scaling of flow results to take account of realistic fault zone thicknesses is necessary unless the model resolution is the same as the anticipated fault zone thickness.

(2) Juxtaposition geometries across sub-seismic fault surfaces have an insignificant effect on flow.

(3) Flow differences between low, moderate and high fault densities are pronounced. Differences between the effects of different fault densities are approximately linear throughout the full range of fault surface hydraulic properties.

(4) Even with very low values of *Tf*, differences between spatial distributions of parallel fault arrays have little effect on *Kf* values for the range of fault spacings likely to occur in reservoirs. Differences in *Kf* values at *Tf* = 0 are approximately proportional to the fault spacing, but for other *Tf* values the effects are strongly non-linear due to the diversion of flow through fault surfaces.

(5) The lateral dimensions of the models constructed are too large for the results to be

applied to performances of individual wells or pairs of wells but are nevertheless the minimum size to which the concept of systematic fault size populations can be applied. Well performance is expected to vary according to location within each stochastically modelled volume but such variation remains as an unavoidable, but nevertheless quantifiable, uncertainty. This uncertainty will increase as the Tf value of the fault surfaces decreases.

(6) The uncertainty of prediction of fault surface hydraulic properties contributes more than all other factors combined to the uncertainty of flow modelling results.

References

ANTONELLINI, M. & AYDIN, A. 1994. Effect of faulting on fluid flow in porous sandstones: Petrophysical properties. *AAPG Bulletin*, **78**, 355–377.

BADLEY, M. E., FREEMAN, B., ROBERTS, A. M., THATCHER, J. S., WALSH, J. J., WATTERSON, J. & YIELDING, G. 1990. Fault interpretation during seismic interpretation and reservoir evaluation. *In: The Integration of Geology, Geophysics, Petrophysics and Petroleum Engineering in Reservoir Delineation, Description and Management*, Proceedings of the 1st Archie Conference, Houston, Texas. AAPG, 224–241.

CLAUSEN, O.-R., KORSTGÅRD, J. A., PETERSEN, K., *et al.*, 1994. Systematics of faults and fault arrays. *In:* HELBIG, K. (ed.) *Modelling the Earth for Oil Exploration. Final Report of the CEC's Geoscience Program 1990–1993.* Elsevier, 205–316.

COWIE, P. A. & SCHOLZ, C. H. 1992a. Displacement–length scaling relationship for faults: data synthesis and discussion. *Journal of Structural Geology*, **14**, 1149–1156.

—— & ——1992b. Growth of faults by accumulation of seismic slip. *Journal of Geophysical Research*, **97**, 11085–11095.

DAWERS, N. H., ANDERS, M. H. & SCHOLZ, C. H. 1993. Growth of normal faults: Displacement–length scaling. *Geology*, **21**, 1107–1110.

FLINT, S. S., HEATH, A., KNIGHT, S., WALSH, J. J. & WATTERSON, J. 1995. *Sensitivity Analysis of Depositional Architecture vs Faulting on Effective Connectivity in Clastic Hydrocarbon Reservoirs.* Petroleum Science and Technology Institute, Edinburgh, Project Report, February 1995.

FOWLES, J. & BURLEY, S. 1994. Textural and permeability characteristics of faulted, high porosity sandstones. *Marine and Petroleum Geology*, **11**, 608–623.

GAUTHIER, B. D. M. & LAKE, S. D. 1993. Probabilistic modelling of faults below the limit of seismic resolution in the Pelican Field, North Sea, offshore U.K. *AAPG Bulletin*, **77**, 761–777.

GIBSON, J. R., WALSH, J. J. & WATTERSON, J. 1989. Modelling of bed contours and cross-sections adjacent to planar normal faults. *Journal of Structural Geology*, **11**, 317–328.

GILLESPIE, P. A., HOWARD, C. B., WALSH, J. J. & WATTERSON, J. 1993. Measurement and characterization of spatial distributions of fractures. *Tectonophysics*, **226**, 113–141.

——, WALSH, J. J. & WATTERSON, J. 1992. Limitations of dimension and displacement data from single faults and the consequences for data analysis and interpretation. *Journal of Structural Geology*, **14**, 1157–1172.

HOLDEN, L., HØIBERG, J. & LIA, O. 1990. An estimator for the effective permeability. *In:* GUERILLO, D. & GUILLON, O. (eds) *2nd European Conference on the Mathematics for Oil Recovery.* Editions Technip, Paris, 287–290.

HULL, J. 1988. Thickness–displacement relationships for deformation zones. *Journal of Structural Geology*, **10**, 431–435.

KNOTT, S. D. 1994. Fault zone thickness versus displacement in the Permo-Triassic sandstones of NW England. *Journal of the Geological Society of London*, **151**, 17–25.

MANDELBROT, B. B. 1982. *The Fractal Geometry of Nature.* W. H. Freeman, New York.

MARRETT, R. & ALLMENDINGER, R. W. 1991. Estimates of strain due to brittle faulting: sampling of fault populations. *Journal of Structural Geology*, **13**, 735–738.

MUKHERJEE, S. 1979. The structural and tectonic analysis of the Jharia coal basin. *In:* LASKAR, B. & RAO, R. C. (eds) *4th International Gondwana Symposium: Papers*, Hindustan, Delhi, 777–784.

MUNTHE, K. L., OMRE, H., HOLDEN, L., DAMSLETH, E., HEFFER, K., OLSEN, T. S. & WATTERSON, J. 1993. *Subseismic Faults in Reservoir Description and Simulation.* Society of Petroleum Engineers, Paper No. **26500**, 843–850.

ODLING, N. E. 1992. Network properties of a two dimensional natural fracture pattern. *Pure and Applied Geophysics* **138**, 95–114.

OMRE, H., SØLNA, K., DAHL, N. & TØRUDBAKKEN, B. 1994. Impact of fault heterogeneity in fault zones on fluid flow. *In:* AASEN, J. O., BERG, E., BULLER, A. T., HJELMELAND, O., HOLT, R. M., KLEPPE, J.

& TORSÆTER, O. (eds) *North Sea Oil and Gas Reservoirs*, Kluwer, London, 185–200.

RIPPON, J. H. 1985. Contoured patterns of the throw and hade of normal faults in the Coal Measures (Westphalian) of north-east Derbyshire. *Proceedings of the Yorkshire Geological Society*, **45**, 147–161.

ROBERTSON, E. C. 1983. Relationship of fault displacement to gouge and breccia thickness. *Society of Mining Engineers, American Institute of Mining Engineers Transactions*, **35**, 1426–1432.

SASSI, W., LIVERA, S. E. & CALINE, B. P. R. 1992. Reservoir compartmentation by faults in Cormorant Block IV, U.K. northern North Sea. *In*: LARSEN, R. M., BREKKE, H., LARSEN, B. T. & TALLEKAAS, E. (eds) *Structural and Tectonic Modelling and its Application to Petroleum Geology*. Special Publication of the Norwegian Petroleum Society, **1**, 355–364.

SCHOLZ, C. H., DAWERS, N. H., YU, J. Z., ANDERS, M. H. & COWIE, P. A. 1993. Fault growth and fault scaling laws: preliminary results. *Journal of Geophysical Research*, **98**, 21951–21961.

WALSH, J. J. & WATTERSON, J. 1987. Distributions of cumulative displacement and seismic slip on a single normal fault surface. *Journal of Structural Geology*, **9**, 1039–1046.

—— & ——1993. Fractal analysis of fracture patterns using the standard box-counting technique: valid and invalid methodologies. *Journal of Structural Geology*, **15**, 1509–1512.

——, —— & YIELDING, G. 1994. Determination and interpretation of fault size populations: procedures and problems. *In*: AASEN, J. O., BERG, E., BULLER, A. T., HJELMELAND, O., HOLT, R. M., KLEPPE, J. & TORSÆTER, O. (eds) *North Sea Oil and Gas Reservoirs*, Kluwer, London, 141–155.

WATTERSON, J., WALSH, J. J., GILLESPIE, P. A. & EASTON, S. 1996. Scaling systematics of fault sizes on a large-scale range fault map. *Journal of Structural Geology*, **18**, 199–214.

YIELDING, G., WALSH, J. J. & WATTERSON, J. 1992. The prediction of small-scale faulting in reservoirs. *First Break*, **10**, 449–460.

Reservoir characterization: how can anisotropy help?

RODERICK J. OWEN, XIANG-YANG LI, COLIN D. MACBETH &
DAVID C. BOOTH

*Edinburgh Anisotropy Project, British Geological Survey, Murchison House,
West Mains Road, Edinburgh EH9 3LA, UK*

Abstract: We present a brief review on the use of seismic anisotropy for reservoir characterization. Seismic anisotropy utilizes the concept of scattering interference from sub-wavelength heterogeneities and may provide a powerful tool for characterizing these heterogeneities. An ordered system of reservoir heterogeneity may display seismic anisotropy diagnosed by shear-wave splitting, and the polarization of the fast split shear-wave ($qS1$), the time delay between the two split shear-waves ($qS1, qS2$), and the differential reflectivity at normal incidence may be used to quantify the heterogeneities. An example of field data obtained from a multicomponent seismic survey is presented to demonstrate how hydrocarbon production can be correlated with seismic anisotropy, and its potential application to reservoir characterization.

There is now a drive within the hydrocarbons industry to maximize extraction from existing oil-fields, since exploration and development of new oil-fields is becoming much more difficult and expensive. Few existing fields are structurally simple, and most consist of complex formations in which many heterogeneities exist, of which only a small proportion are reservoirs. Thus a more complete understanding of the distribution and the geometry of reservoir heterogeneity is the key to sustained recovery and reserve growth.
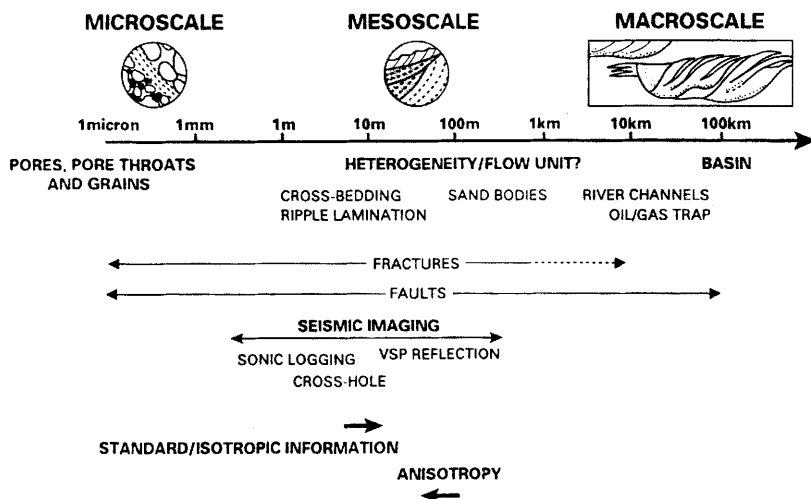
Many methods have been used to study reservoir heterogeneities, of which perhaps combining three-dimensional seismics with well logs is the most popular so far. However, this approach may lack enough detail to represent accurately some significant reservoir heterogeneities, and better definition of small-scale features is indispensible. The use of seismic anisotropy provides an alternative approach to this problem by determining the directional characteristics of the reservoir heterogeneities, such as aggregate alignments and cluster distribution.

The techniques involved utilize the effects of scattering from a distribution of sub-wavelength heterogeneities, which sufficiently alter the transmitted wavefield to carry forward an impression of the group characteristics. These seismic scattering effects can be observed in seismic data acquired by multicomponent surveys which generate and record waves polarized in all three spatial dimensions. The scattering can be simulated by an 'equivalent homogeneous medium' which replaces the heterogeneous medium and acts as a seismic pseudo-function for reservoir complexity (MacBeth 1995). If the heterogeneities possess an aggregate alignment, then the equivalent medium is anisotropic.

By using 'equivalent medium theory' we can process and interpret multicomponent data to understand a diversity of reservoir features such as faulting and fracturing, cross-bedding, channels and facies. Multicomponent seismic data are now commonly used in the study of seismic anisotropy.

Heterogeneities at different scales

Definitions of the term 'reservoir heterogeneity' cover a wide spectrum, and depend very much upon the particular geological features under observation. Nevertheless, it is generally taken to refer to an irregular spatial uniformity of diverse physical constituents, whether structural, lithological, petrophysical or relating to fluid flow, evident at various scales. Scales of reservoir heterogeneities can vary from a large basin ('megascale'), the distribution of stratigraphic and lithologic intervals ('macroscale'), through cross-bedding and ripple laminations ('mesoscale'), to the smallest 'microscale' which includes grains, pores or pore-throats (Fig. 1). Although heterogeneities still tend to be viewed from the basis of the type of data used, it is not sufficient to describe reservoirs in terms of bedding planes, fault distributions or depositional systems alone; successful reservoir characterization depends upon the effective integration of representative data measured at different scales. This can be accomplished through the application of the equivalent medium theory in the study of seismic anisotropy, which is a valuable concept for conserving a detailed level of characterization for reservoir heterogeneity and may also assist in correlating data from one scale to

MICROSCALE   MESOSCALE   MACROSCALE

| 1micron | 1mm | 1m | 10m | 100m | 1km | 10km | 100km |

PORES, PORE THROATS   HETEROGENEITY/FLOW UNIT?   BASIN
AND GRAINS

CROSS-BEDDING   SAND BODIES   RIVER CHANNELS
RIPPLE LAMINATION   OIL/GAS TRAP

◄———————————— FRACTURES ———————·········►

◄———————————— FAULTS ————————————►

SEISMIC IMAGING

SONIC LOGGING   VSP REFLECTION
CROSS-HOLE

STANDARD/ISOTROPIC INFORMATION

ANISOTROPY
◄

Fig. 1. Various heterogeneity scales affecting reservoir processes at different scale lengths. Standard seismics image structures at large scales, whereas the phenomenon of seismic anisotropy helps to image smaller scale features (after MacBeth 1995).

another. MacBeth (1995) also suggests that it may be possible to use equivalent medium theory to identify some reservoir features originally thought to be beyond the resolution of seismic data. Future development of even more versatile anisotropic models gives hope that we may soon be able to make use of seismic anisotropy in reservoir characterization on a routine basis.

Multicomponent seismic survey

The seismic scattering effects of reservoir heterogeneities can only be reliably observed and interpreted from seismic data recorded by multi-component polarized sources and receivers; existing methods include reflection surveys (surface–surface), vertical seismic profiles (VSPs) (surface–borehole) and cross-hole surveys (borehole–borehole). Both seismic body waves are used, the longitudinally polarized P-wave and the transversely-polarized shear-wave. A shear-wave incident on, or generated in, an anisotropic medium generally splits into two orthogonal polarizations, $S1$ and $S2$, which propagate through the medium with different velocities, thus introducing a time delay between them at the receiver. The polarizations and time delay are sensitive to the orientation and degree of anisotropy, and hence shear-waves provide particularly useful information on aligned heterogeneities. Two orthogonal horizontal shear-wave polarizations are usually generated in order to

determine azimuthal variations in the characteristics of the medium. Using different configurations of sources and receivers, up to nine-component data can be recorded which consist of three orthogonally polarized sources and three-component receivers (z, x and y, as shown in Fig. 2). Ideally, a full nine-component survey is required to describe seismic scattering effects in the vector wave-field accurately, but in practice other configurations of sources and receivers can be used, depending on the purpose of the surveys. These include: conventional one-component P-wave seismic surveys for mapping geological structure
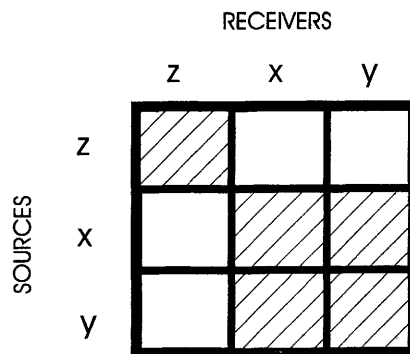
Fig. 2. Full nine-component data acquisition. There are three orthogonal sources represented by the rows, and three orthogonal receivers represented by the columns. The shaded area shows five-component acquisition (after Li 1997).

Table 1. *Seismic effects related to reservoir heterogeneities for seismic parameters recovered from multicomponent data*

Heterogeneity characteristics	Seismic Effects
Structural boundary	Visible reflected wave (A_{qP})
Fluid-filled zones	Amplitude increase of (A_{qP}) and A_{qP}/A_{qS}
Increase in fracture density	Amplitude decrease (dim spots) of reflected shear waves (A_{qS1}, A_{qS2}); time delay increase $(V_{qS2} - V_{qS1})$
Changes in lithology, porosity, etc.	Variations in time delay

The table is not exhaustive, but lists those heterogeneities and effects which are of significance to anisotropy

(Yilmaz 1987); two-component surveys for mapping geological structure and lithology (Dohr 1985); and three-component acquisition in VSPs for correlating seismic horizons (Hardage 1991).

Further study of seismic anisotropy has led to the development of four-component (xx, xy, yx and yy component) and five-component (four component plus zz component) surveys (Alford 1986), as well as total wave-field nine-component surveys (Squires *et al.* 1989). The purpose of these surveys is to investigate the potential of shear-wave anisotropy for characterizing reservoir heterogeneity.

Information content of multicomponent surveys

Table 1 summarizes the seismic effects which are related to different kinds of reservoir heterogeneity. The term 'wave-field attributes' is used to describe the seismic effects of anisotropy, and these wave-field attributes, using appropriate processing techniques, can be extracted from the multicomponent data.

The three most used shear-wave attributes in anisotropic media are the polarization direction of the first split shear-wave (*qS1*) arrival, the time delay between the two split shear-waves (*qS1, qS2*), and the differential reflectivity at normal incidence; these attributes provide different information. The polarization direction of the fast split shear-wave gives fracture strike, and probable direction of fluid flow within a reservoir. The time delay between the two split shear-waves can give information about fracture and crack density, while differential reflectivity can help in identifying more intensely fractured zones in the seismic section and is thus a very useful indicator for fracture concentrations. Other wave-field attributes employed include the v_p/v_s ratio, differential attenuation, differential amplitude, signal-to-noise ratio, scattering and the offset-dependent reflectivity.

Case study

We shall use a field data example to demonstrate how the shear-wave attributes can be used to characterize reservoir heterogeneity. The example comes from a multicomponent reflection survey above the Austin Chalk trend in Texas, USA.

The Austin Chalk is a very fine-grained impermeable carbonate mud containing skeletal debris, and is composed of three units: an upper, fractured massive chalk; a central ductile chalk-marl; and a lower, fractured massive chalk. Sub-surface porosity in the chalk can be less than 5% and therefore oil production is entirely dependent on fractures. Fracture systems in the Austin Chalk are dominantly extensional, a result of downwarping due to subsequent deposition and pre-existent faulting. They are uniformly oriented and parallel to the strike of the structure (Corbett *et al.* 1987). Owing to minor local variations in stress, fractures form clusters and swarms which, once located, can be exploited by horizontal wells drilled to intersect the trend.

The Austin Chalk has attracted considerable interest since oil was first discovered in the 1920s, and over the past few years several authors have discussed the anisotropy of the area. Mueller (1991) identified lateral fracture concentrations from differential amplitudes of shear-waves, Li *et al.* (1993) compared the characteristics of shear-waves in a fractured reservoir, and Li (1997) correlated amplitude dim spots in a seismic section with local fracture swarms indicated by horizontal wells. These studies all show, either directly or indirectly, that oil production can be correlated with anisotropy. For example, it has been found that over the length of the Austin Chalk trend, for areas where commercial oil production is absent, the average time delay of the split shear-waves is less than 10 ms, corresponding to 0.5% anisotropy or less. In areas close to producing fields,
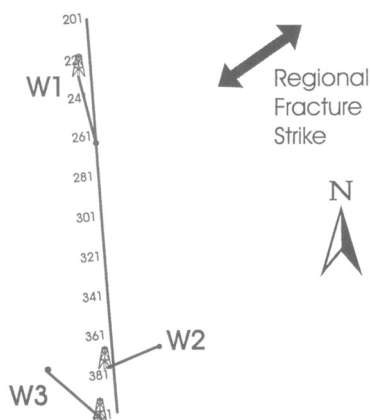
Fig. 3. A survey map showing the orientation of the studied survey line above the Austin Chalk reservoir and the strike of the horizontal wells W1, W2 and W3 (adapted from Li 1997).

the average delay is about 30 ms to 40 ms, corresponding to about 1.5% anisotropy. In major production areas, the delay is 50 ms to 60 ms, corresponding to about 2.5% anisotropy (Li *et al.* 1993).

The example discussed here is from Li (1997), who uses a four-component seismic survey and production data from three nearby horizontal wells to reveal the potential of local variations in shear-wave amplitudes (dim spots) in identifying local fracture zones. The survey line lies N–S, at about 40° from the regional fracture strike (*c.* NE–SW). There are a number of horizontal wells in the area, all drilled along the Austin Chalk; the three selected for study (W1, W2 and W3) are close to the line and have a similar horizontal length. Well W1 is at about 60° from the regional fracture strike, W2 is parallel to the strike and W3 is perpendicular to the strike (Fig. 3). Amongst the three wells (which all penetrate fracture zones), W1 is the most productive, W2 the least productive and W3 is moderately productive. Bearing in mind that the flow rate of a horizontal well is primarily determined by the number of fractures encountered, which in turn is determined by the length and azimuth of the well plus the fracture intensity of the penetrated zone, one can make the following observations from the shear-wave section (Fig. 4).

(i) Well W1, drilled in a relatively more fractured area and into two reflection dim spots of the Austin Chalk horizon (Fig. 4), has substantially higher rates of production than W3, although they both have similar azimuths. In fact, W3 is more favourably oriented; this implies that fracture intensity in the zone penetrated by W1 may be greater than in the zone penetrated by W3.

(ii) Well W3, drilled in a relatively less fractured area and into part of a dim spot, is more
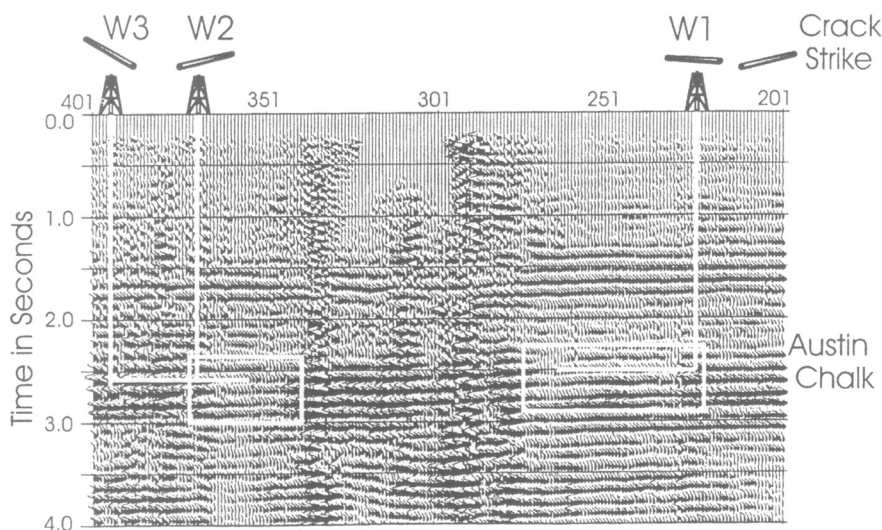
Fig. 4. The stacked shear-wave section. W1, W2 and W3 are horizontal wells; the small bars represent the azimuths of the wells; the bar at the far right indicates the crack (i.e. fracture) strike; the rectangles outline significant dim spots (adapted from Li 1997).

productive than W2, drilled into the same trend of fracture swarms but at the edge of a dim spot (Fig. 4). This shows that wells parallel to fracture strike intercept fewer fractures than wells perpendicular to fracture strike.

After corrections for overburden effects, dim spots in stacked sections along the Austin Chalk can be correlated with the fracture swarms intercepted by horizontal wells, and fracture intensity, which determines production rates, can be qualitatively interpreted from variations in shear-wave attributes.

Conclusions

This paper has discussed the concept of multicomponent surveys and data processing, and has also described various reservoir properties deduced from various attributes of shear-wave splitting. In discussing heterogeneity scales, it has been established that anisotropy can play a major role in reservoir characterization. Finite hydrocarbon reserves combined with increasing demand mean that better reservoir characterization is needed. Hydrocarbon reservoirs containing aligned fractures are anisotropic, and therefore the answer to the question posed in the title is that examination of the resultant split shear-waves can give us vital information about reservoir structure. The example of the use of shear-waves in the Austin Chalk is of particular importance, as it demonstrates not only a proven application, but also the undoubted potential of seismic anisotropy in reservoir characterization.

References

ALFORD, R. M. 1986. Shear data in the presence of azimuthal anisotropy: Dilley, Texas. *56th SEG Meeting, Houston, Expanded Abstracts*, 476–479.

CORBETT, K., FRIEDMAN, M. & SPANG, J. 1987. Fracture development and mechanical stratigraphy of Austin Chalk, Texas. *AAPG Bulletin*, **71**, 17–28.

DOHR, G. P. 1985. *Seismic Shear Waves, Part A: Theory*. Geophysical Press, London.

HARDAGE, B. A. 1991. *Vertical Seismic Profiling, Part A: Principles*. Pergamon, Oxford.

LI, X.-Y. 1997. Fracture reservoir delineation using multicomponent seismic data. *Geophysical Prospecting*, **45**, 39–64.

——, MUELLER, M. C., and CRAMPIN, S. 1993. Case studies of shear-wave splitting in reflection surveys in south Texas. *Canadian Journal of Exploration Geophysics*, **29**, 189–215.

MACBETH, C. 1995. How can anisotropy be used for reservoir characterization? *First Break*, **13**(1), 31–37.

MUELLER, M. C. 1991. Prediction of lateral variability in fracture intensity using multicomponent shear-wave surface seismic as a precursor to horizontal drilling in the Austin Chalk. *Geophysical Journal International*, **107**, 409–415.

SQUIRES, S.G., KIM, C.D. and KIM, D.Y., 1989. Interpretation of total wave-field data over Lost Hills field, Kern County, California. *Geophysics*, **54**, 1420–1429.

YILMAZ, O., 1987. *Seismic Data Processing*. SEG Special Publication.

Numerical simulation of fluid flow in complex faulted regions

L. FOLEY*, T. S. DALTABAN & J. T. WANG

Department of Mineral Resources Engineering, Royal School of Mines, Prince Consort Road, London SW7 2BP, UK

Abstract: Faults exist in most hydrocarbon reservoirs. In general, they interfere with the transport of the fluids within the porous medium, and in other cases they may compartmentalize the reservoir and alter its connectivity. When performing any simulation procedure on a faulted reservoir it is important to take account of the sealing characteristics of the faults, especially (1) the effects of the pressure distribution across a fault and (2) the relationship between the porosity and permeability of the fault zone material and that of the bulk reservoir rock.

Current numerical fluid flow modelling techniques of faults are generally limited to the use of special connections, which involve modifying the transmissibilities between cells of the finite difference simulation grid. In many cases, the simulated flow is allowed to occur only between cells which are physically in contact. This may not be appropriate in the event of flow occurring along the fault plane and thus between a number of blocks which are not adjacent to each other. Modelling of fluid flow in complex faulted regions may be enhanced by implementing a boundary-fitted co-ordinate technique. This allows the geometry of the fault to be represented more accurately by constructing the simulation grid around the fault zone such that the inner boundary of the grid is coincident with the boundary of the fault. The permeability of the reservoir in the vicinity of the fault needs to be described using available information on fault zone characteristics (e.g. cataclastic slip band densities, clay smear potential, cementation etc.) to enable the construction of permeability distributions in the faulted region.

Faults are widespread in many hydrocarbon traps and are responsible for altering reservoir continuity and causing a change in the nature of the material in the immediate vicinity of the fault zone. The two main ways in which a fault might affect fluid flow are by (Smith 1966; Munthe *et al.* 1993):

(1) *geometric effect*, where sedimentary rocks of different petrophysical properties are juxtaposed;
(2) *fault plane effect*, which depends on the nature of the emplaced fault zone material, formed by mechanical or chemical processes in relation to the faulting process.

These effects are shown schematically in Fig. 1.

The permeability characteristics of the reservoir in the vicinity of a fault can differ vastly from those of the parent rock outside the fault zone. Granulation of the rock along the fault reduces pore aperture size, thus increasing the sealing potential of the fault and reducing communication between layers that are laterally juxtaposed across it. On the other hand, increased fracturing during the faulting process may create a high-permeability zone parallel to the fault, providing a path between different layers which are not in physical contact. To simplify the calculations, complexities such as these are often neglected when simulating faulted reservoirs, resulting in a misrepresentation of both the physics and the geological characteristics of the reservoir.

Fault modelling techniques

Background

The flow of fluid in faulted regions is often restricted to those cells physically in contact with each other. This implies that fluid can travel only directly across the fault and not along it. Mrosovsky *et al.* (1980) modelled a reservoir of the Prudhoe Bay field in three dimensions by limiting a fault throw to an integer number of layers. Using this method, the actual number of connections remains constant and only the pointers defining which blocks are connected to a given block need to be changed. In the case of a single fault, the throw can be forced to equal an integer number of gridblocks by increasing the number of mesh cells used to model the reservoir in the direction of the fault. However, in the case of multiple faults, this becomes unfeasible.

* Current address: Department of Geology and Petroleum Geology, University of Aberdeen, Aberdeen AB9 2UE, UK
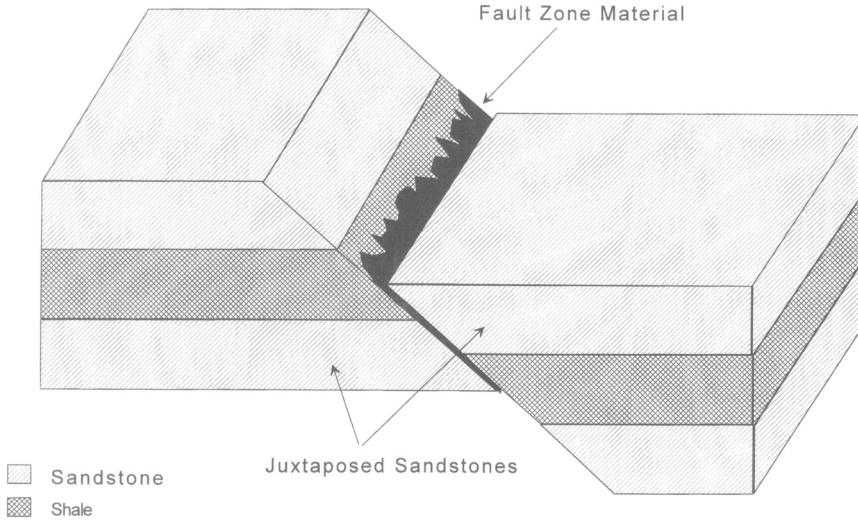
Fig. 1. Schematic diagram showing the juxtaposition of different lithological sequences after faulting and the emplaced fault zone material.

More advanced numerical models permit connections of varying transmissibilities to be made between the gridblocks (Dunlop *et al.* 1982). The transmissibility between two gridblocks of a reservoir simulation model is a function of the effective permeabilities of the gridblocks and their cross-sectional areas. If two gridblocks have been displaced at a fault, the transmissibility is often modified according to the resulting area of contact between the relevant cells of the simulation grid. This procedure, known as non-neighbour connections, introduces greater complexities into the equations and these complexities, though not insurmountable, are rarely addressed.

Other techniques used to model the geometry and throw of a fault are corner-point geometry, which allows the gridblock shape to vary, and local grid refinement. These techniques are discussed in detail by Goldthorpe & Chow (1985) and Forsyth & Sammon (1985).

Non-neighbour connections

As described above, special (non-neighbour) connections are used in numerical reservoir simulators to modify the transmissibilities between gridblocks. This is achieved using a linear interpolation of the transmissibilities of two adjacent blocks with a weighting factor based on the relative size of the overlap between them. In Fig. 2, for example, the normalized interface area between cell i and cell j across the fault could be defined as:
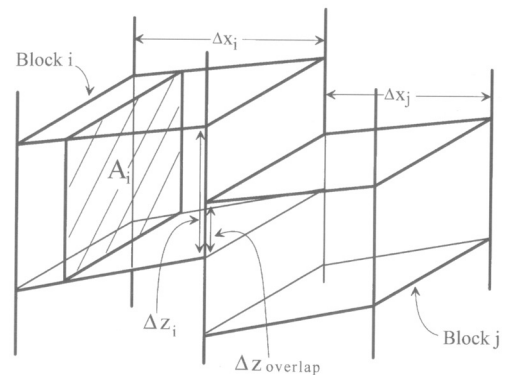
$$A_{ij} = C_{ij} \left[\frac{A_i \times \Delta x_j \times W_i + A_j \times \Delta x_i \times W_j}{\Delta x_i + \Delta x_j} \right] \ (1)$$

where Δx = length of block in the x direction, A = cross-sectional area, C = factor accounting for the dip angle between the cells, and W = weighting factor based on the relative size of the overlap between cells i and j.

That is:

$$W_1 = \Delta z \,(\text{overlap})/\Delta z_1$$

where Δz_1 = thickness of individual block 1 and $\Delta z \,(\text{overlap})$ = thickness of overlap between adjacent cells.

Fig. 2. Apportioning of transmissibilities according to area assumed to be in contact.

In order to allow for flow along, as well as across, the fault plane it is necessary to allow a given gridblock on one side of the fault to communicate with all or any gridblocks on the other side, regardless of whether or not the blocks concerned are in physical contact. In such cases, any modification applied to the transmissibility terms must be specified as an input to the model.

Boundary-fitted co-ordinates

The flow of fluid within a reservoir is generally modelled using partial differential equations. These equations are discretized by overlaying a finite difference grid on the reservoir. This numerical representation is most accurate when the boundaries of the domain being modelled are coincident with some of the co-ordinate lines of the grid because it eliminates the need for interpolation at the boundary. If an irregular shape occurs within the reservoir, it becomes increasingly difficult to match the boundary of the shape and the external boundary of the reservoir simultaneously. Various methods can be used such as curvilinear grids (Lambeth & Dawe 1988) or representing the reservoir using corner-point geometry. This is a technique which distorts the grid so that it assumes the shape of an irregular domain. However, the flow equations are still written for an orthogonal system, thus errors are introduced into the transmissibility terms. Thompson *et al.* (1977) developed a technique, which they termed 'boundary-fitted co-ordinates', for generating a general curvilinear co-ordinate system with co-ordinate lines coincident with all boundaries of a two-dimensional region containing any number of arbitrarily shaped bodies. It was developed specifically for the purpose of solving flow equations in the vicinity of aerofoils of arbitrary shape in aeronautics, but it can be applied to any set of partial differential equations. Folefac *et al.* (1992) applied the technique to modelling single-phase flow in a fractured porous medium. In the current application, the method has been further developed to modelling two-phase flow in the vicinity of faults.

Grid generation The principle of the method is to generate a co-ordinate system such that there is a co-ordinate line coinciding with each boundary (interior and exterior) of the reservoir. The domain and relevant set of partial differential equations are then transformed to a regular grid system where the new equations can be easily approximated using finite difference expressions

and solved numerically. A general method of generating the boundary-fitted co-ordinate system is to let the curvilinear co-ordinates be solutions to two elliptic partial differential equations with Dirichlet boundary conditions (i.e. pressure gradient zero on all boundaries). One co-ordinate is specified to be constant on each boundary. Suppose the reservoir domain lies in a plane $[x, y]$ with boundaries Γ_1 and Γ_2, as shown in Fig. 3, and that a transformation is required to a regular grid $[\xi, \eta]$.

The transformation can be written as:

$$\begin{bmatrix} \xi \\ \eta \end{bmatrix} = \begin{bmatrix} \xi(x, y) \\ \eta(x, y) \end{bmatrix} \qquad (2)$$

so that the inverse transformation is:

$$\begin{bmatrix} x \\ y \end{bmatrix} = \begin{bmatrix} x(\xi, \eta) \\ y(\xi, \eta) \end{bmatrix} \qquad (3)$$

The physical grid is then generated by solving:

$$\xi_{xx} + \xi_{yy} = f(\xi, \eta) \qquad (4)$$

$$\eta_{xx} + \eta_{yy} = g(\xi, \eta) \qquad (5)$$

subject to

$$\begin{bmatrix} \xi \\ \eta \end{bmatrix} = \begin{bmatrix} \xi_1(x, y) \\ \eta_1 \end{bmatrix} \qquad [x, y] \text{ on } \Gamma_1 \qquad (6)$$

$$\begin{bmatrix} \xi \\ \eta \end{bmatrix} = \begin{bmatrix} \xi_2(x, y) \\ \eta_2 \end{bmatrix} \qquad [x, y] \text{ on } \Gamma_2 \qquad (7)$$

where f, g, η_1, η_2 are constants and ξ_1, ξ_2 are specified functions on Γ_1, Γ_2. As all numerical computations will be performed on the Cartesian grid $[\xi, \eta]$, the dependent and independent variables must be interchanged in Eqns 4–7, leading to:

$$\alpha x_{\xi\xi} - 2\beta x_{\xi\eta} + \gamma x_{\eta\eta} = -J^2(fx_\xi + gx_\eta) \qquad (8)$$

$$\alpha y_{\xi\xi} - 2\beta y_{\xi\eta} + \gamma y_{\eta\eta} = -J^2(fy_\xi + gy_\eta) \qquad (9)$$

with boundary conditions:

$$x = x(\xi, \eta_1),\ y = y(\xi, \eta_1) \qquad (\xi\eta) \text{ on } \Gamma_1^* \qquad (10)$$

$$x = x(\xi, \eta_2),\ y = y(\xi, \eta_2) \qquad (\xi\eta) \text{ on } \Gamma_2^* \qquad (11)$$

and where

$$\alpha = x_\eta^2 + y_\eta^2 \qquad (12)$$

$$\beta = x_\eta x_\xi + y_\eta y_\xi \qquad (13)$$

$$\gamma = x_\xi^2 + y_\xi^2 \qquad (14)$$

$$J = x_\xi y_\eta + x_\eta y_\xi \qquad (15)$$

This system of equations can then be discretized over the rectangular mesh by a central difference
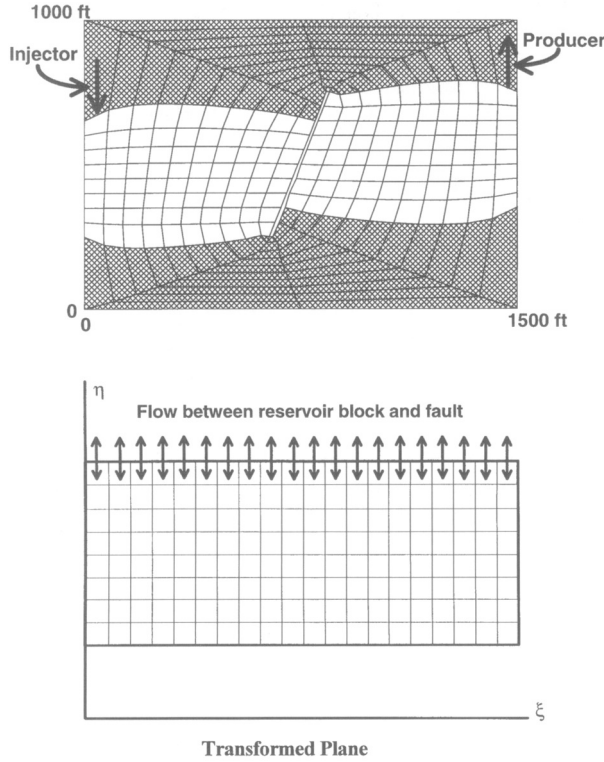
Fig. 3. Field transformation of boundary-fitted co-ordinates applied to a faulted reservoir.

scheme and solved to obtain solutions which are the physical co-ordinates of the x–y plane.

Figure 3 shows how this technique can be applied to a faulted reservoir domain. The unshaded area represents the reservoir region of interest. The shaded regions have been included in the grid generation for mathematical convenience, but the reservoir properties in these areas were made inactive by setting them to zero.

Flow simulation The flow equations needed can be developed from the single-phase flow equation:

$$k_x \frac{\partial^2 P}{\partial x^2} + k_y \frac{\partial^2 P}{\partial y^2} = \phi \mu c \frac{\partial P}{\partial t} \qquad (16)$$

where k_x and k_y are the permeabilities in the x and y directions, and the boundary conditions are specified on the outer boundary of the reservoir and the inner boundary around the fault. Applying a transformation similar to that above leads to the equation:

$$\alpha' P_{\xi\xi} + 2\beta' P_{\xi\eta} + \gamma' P_{\eta\eta} + \tau' P_\xi + \sigma' P_\eta$$
$$= J^2 \phi \mu c P \qquad (17)$$

where c is constant and

$$\alpha' = k_y x_\eta^2 + k_x y_\eta^2 \qquad (18)$$

$$\beta' = k_y x_\xi x_\eta + k_x y_\xi y_\eta \qquad (19)$$

$$\gamma = k_y x_\xi^2 + k_x y_\xi^2 \qquad (20)$$

$$\tau' = (x_\eta D_y - y_\eta D_x)/J \qquad (21)$$

$$\sigma' = (y_\xi D_x - x_\xi D_y)/J \qquad (22)$$

$$D_x = \alpha x_{\xi\xi} - 2\beta x_{\xi\eta} + \gamma x_{\eta\eta} \qquad (23)$$

$$D_y = \alpha y_{\xi\xi} - 2\beta y_{\xi\eta} + \gamma y_{\eta\eta} \qquad (24)$$

J = transformation Jacobian

$$= x_\xi y_\eta + x_\eta y_\xi \qquad (25)$$

Extending this analysis to two phases simply requires the absolute permeability term, k, to be replaced by an effective permeability defined by kk_r. It should be noted that the structure of the coefficient matrix changes as flow must be allowed to occur between the left and right boundaries of the transformed grid.

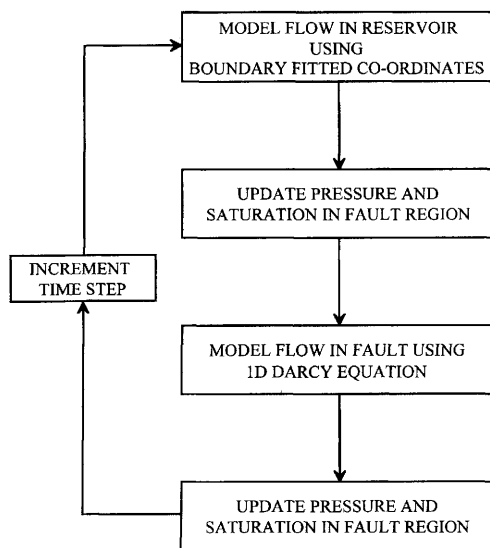*Flow in the fault* The flow of fluid within the fault is modelled using a one-dimensional fluid

Fig. 4. Flow diagram of how fluid flow in the region of a fault is simulated using boundary-fitted co-ordinates.

flow equation based on Darcy's law. The fault properties are specified in the input data file and flow between the reservoir blocks and the fault blocks is represented by an exchange flow rate term. In this application, the fault modelling is done sequentially, i.e. flow within the fault is updated at the end of every time step of the reservoir simulation (Fig. 4). However, it would be possible to incorporate the fault equation fully implicitly so that it can be modelled simultaneously and to replace the Darcy equation with a Navier–Stokes equation if the fault is an open conduit. These developments, together with the extension of the technique into three dimensions, would enable a comparison of boundary-fitted co-ordinates with special connections. Incorporating both procedures into the same reservoir simulator would enable the user to choose the most appropriate fault modelling technique for the problem being considered.

Fault characterization

Applying either the special connection or boundary-fitted co-ordinates techniques in a meaningful way relies on the availability of detailed information on the characteristics of faults within hydrocarbon reservoirs. The current lack of accurate data on the petrophysical properties of fault zones makes modelling of fluid flow in faulted regions extremely difficult.

The most helpful direction forward is probably a paper recently published by Antonellini & Aydin (1994) in which they describe a case study of the fault structure and deformation band distribution in the vicinity of a fault in the Delicate Arch Trail. The permeability of the cataclistic slip bands is estimated to be several orders of magnitude less than that of the host rock, which affects the overall reservoir permeability perpendicular to the fault. Antonellini & Aydin (1994) used this information to calculate the average horizontal permeability in a fault zone using a harmonic mean. In this study, a permeability distribution model in the vicinity of the fault has been constructed as follows.

- The fault zone (i.e. the region around the fault which has been affected by the faulting process) is divided into gridblocks, each of which is 1 m in width.
- For each gridblock, a number of cataclastic slip bands is randomly distributed within the block, such that the density of deformation bands documented for that region is preserved. The cataclastic slip bands all run parallel to the fault and are approximately 2 mm wide.
- In each gridblock, the bands representing the cataclastic slip bands are assigned a permeability which is at least two orders of magnitude smaller than the permeability of the host rock.
- Using a renormalization technique (King 1994), a single permeability value is obtained for each gridblock. This procedure involves coarsening the grid step by step until the required scale is achieved. These permeabilities are then used in the simulation model.

An example of the distribution of deformation bands in the vicinity of a fault (from Antonellini & Aydin 1994) and the resulting permeability distribution is shown in Fig. 5. These permeability values can then be assigned to the gridblocks in the fault zones in either the special connections or boundary-fitted co-ordinates models, to account for changes in the regional characteristics of the reservoir rock as a result of the faulting process.

Case studies

Many test cases in both two and three dimensions have been modelled to test our algorithms, using a variety of fault throws and sealing capacities varying from completely sealing to fully conductive. A selection of examples from
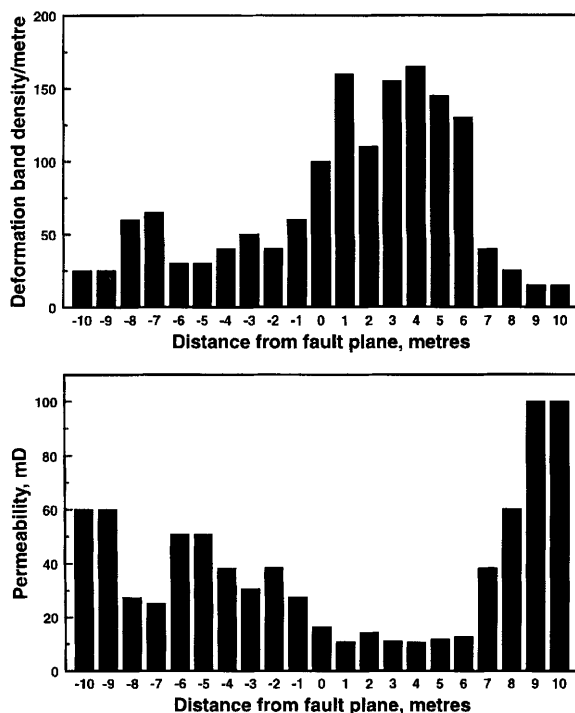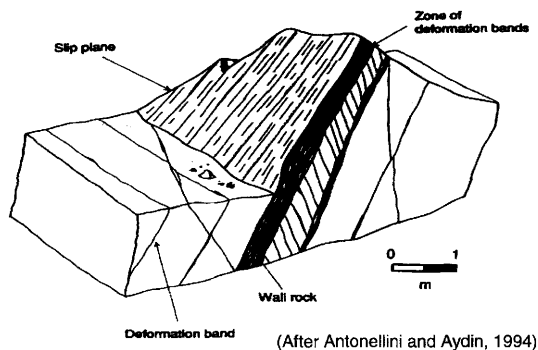
Fig. 5. Deformation band density and effective permeability in a fault zone.

some of the key models are discussed below to show how the faults affect the behaviour of fluid flow within the reservoir and how this, in turn, alters the production profiles of individual wells located in a faulted area. A more comprehensive discussion of the cases can be found in Foley (1994).

Cross-sectional models can be used in cases where areal heterogeneities are not expected to have a significant impact on the flow behaviour within the reservoir or when examining gravity segregation and stratification. They also provide

a window for analysing fluid flow behaviour local to a major heterogeneity. However, when performing field-scale simulation studies, three-dimensional models are essential, especially if multiple layers and/or multiple-completed wells are being considered.

Results using special connections

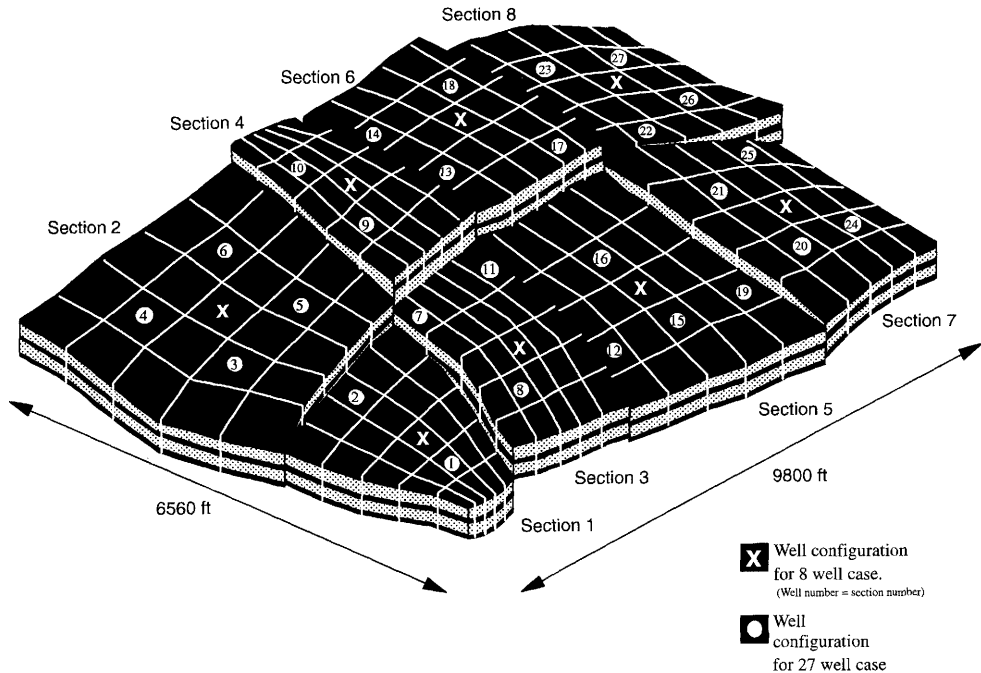The example presented below was produced as part of a study in which a coalbed methane

Fig. 6. Schematic diagram of a faulted reservoir with eight-well and 27-well configurations.

numerical simulator was developed. Methane produced from coal seams is becoming an increasingly important commercial energy resource. Coalbed methane is primarily adsorbed onto the surface of the coal, with free gas only constituting a minor fraction of the total gas content. The methane is held in this adsorbed state by reservoir pressure, and desorption will only occur when the pressure of the coal seam is reduced below the 'critical desorption pressure'. This behaviour leads to fluid flow regimes which differ from those in conventional gas reservoirs.

One test case considered was a three-dimensional realization of a multiseam, multifault model which was run in order to investigate the influence of faults on the overall production of a reservoir. A schematic diagram of the model is shown in Fig. 6. The reservoir consists of three coal seams separated by either sandstone or shale and contains mainly methane gas, most of which is adsorbed onto the surfaces of the coal particles. A gridblock scheme of $10 \times 20 \times 5$ was used. Some cases with just one well per compartment were modelled but, in general, a more realistic well spacing consisting of 27 wells was used. The wells were all completed in each coal seam and each had a bottom hole pressure of 50 psi (345 kPa). The

sealing capacity of the faults varied from 0% (i.e. conducting) to 100% (i.e. completely sealing). Details of the rock and fluid properties are given in Table 1.

In the simplest case eight wells are used (i.e. one well/compartment), with layers of shale separating the three coal seams. Figure 7 shows the individual well performances as a function of time when the faults are completely sealing or completely non-sealing, respectively. When all the faults are sealing (Fig. 7a) the wells in the smaller compartments (i.e. sections 1, 3, 4) drain the free gas more quickly than those in the larger compartments. This in turn causes gas desorption from the pore walls to begin sooner, resulting in an earlier increase in gas production rate. For example, the gas production rate from the well in section 1 begins to increase before the end of the first year of production whereas the well in section 5 takes almost twice as long to reach this stage. When all of the compartments of the reservoir are in communication (i.e. faults are all non-sealing) the performance from each well is more uniform (Fig. 7b). That is to say, at any given time of the simulation, all of the wells display the same trends.

For the 27-well configuration, the individual well performance of each well was examined in

Table 1. *Rock and fluid data for three-dimensional faulted reservoir*

	Field units		SI units
Grid system		$10 \times 20 \times 5$	
Total length in x direction	6560 ft		2000 m
Total length in y direction	9800 ft		2987 m
Thickness of each coal seam	9 ft		2.75 m
Thickness of each seam of sandstone/shale	50 ft		15.25 m
Datum depth	1730 ft		527 m
Matrix permeability			
Coal	0.05 md		5×10^{-17} m^2
Sandstone	10.0 md		1×10^{-14} m^2
Shale	0.0001 md		1×10^{-19} m^2
Cleat permeability: coal	5.0 md		5×10^{-15} m^2
Fracture permeability: sandstone	100.0 md		1×10^{-13} m^2
Matrix porosity			
Coal		0.06	
Sandstone		0.15	
Shale		0.0001	
Cleat porosity: coal		0.01	
Fracture porosity: snadstone		0.015	
Initial reservoir pressure	500.0 psi		3.45 MPa
Initial water saturation		0.85	
Langmuir pressure	883.67 psi		6.1 MPa
Langmuir volume		77.07 vol. gas/vol. res.	
Well radius	0.5 ft		0.15 m
Bottom hole pressure	50.0 psi		345 kPa

detail. It was clear that wells which were located at a distance from any fault boundary are not greatly influenced by the characteristics of the fault. In contrast, wells adjacent to a fault show noticeable differences in their production profiles. The individual gas production rates of well 4 and well 7 are plotted as a function of time in Fig. 8. It can be seen that well 4 reaches a peak production rate of over 44 Mscf/day (1.25 Mscm/day) when the faults are non-sealing compared with 45.5 Mscf/day (1.29 Mscm/day) when the faults are sealing. On the other hand, the peak gas production rate for well 7 when the faults are non-sealing is almost double what it would be if the faults adjacent to it were barriers to flow (63 Mscf/day versus 32 Mscf/day).

This study emphasizes the importance of characterizing faults and investigating their effects on the flow of fluids within a reservoir. If a fault is sealing, it will restrict the production from a well located in close proximity to it as it will act as a boundary to the drainage area of the well. On the other hand, if a fault is behaving as a conduit, it will influence both the distribution of fluid within the reservoir and the flow path taken by the fluid when production begins. Very often, the data available are not sufficient to accurately predict the sealing capacity of the fault. In such cases, using a simulator which can account for the existence of faults with variable transmissibility is beneficial to test the possible scenarios. It is also important that the model should be able to handle both flow along the plane of a fault as well as flow directly across it.

Results using boundary-fitted co-ordinates

A qualitative analysis was conducted in order to test the benefits of using a boundary-fitted co-ordinate system to match the reservoir boundaries in the presence of a single fault more accurately. Data are shown in Table 2. The case shown here consisted of an injector and a producer being placed on either side of a fault. Two immiscible fluids were used. The model was run until the injected fluid (water) had traversed the fault zone. Three examples demonstrated are when the permeability in the fault is equal to, less than and greater than the permeability in the reservoir. The effect of the fault characteristics on the flow of fluid in the vicinity was analysed by comparing the water saturation profiles of each of these cases (Fig. 9). When the fault zone and the reservoir have equal permeabilities (Fig. 9a), no changes of flow behaviour are observed with the water
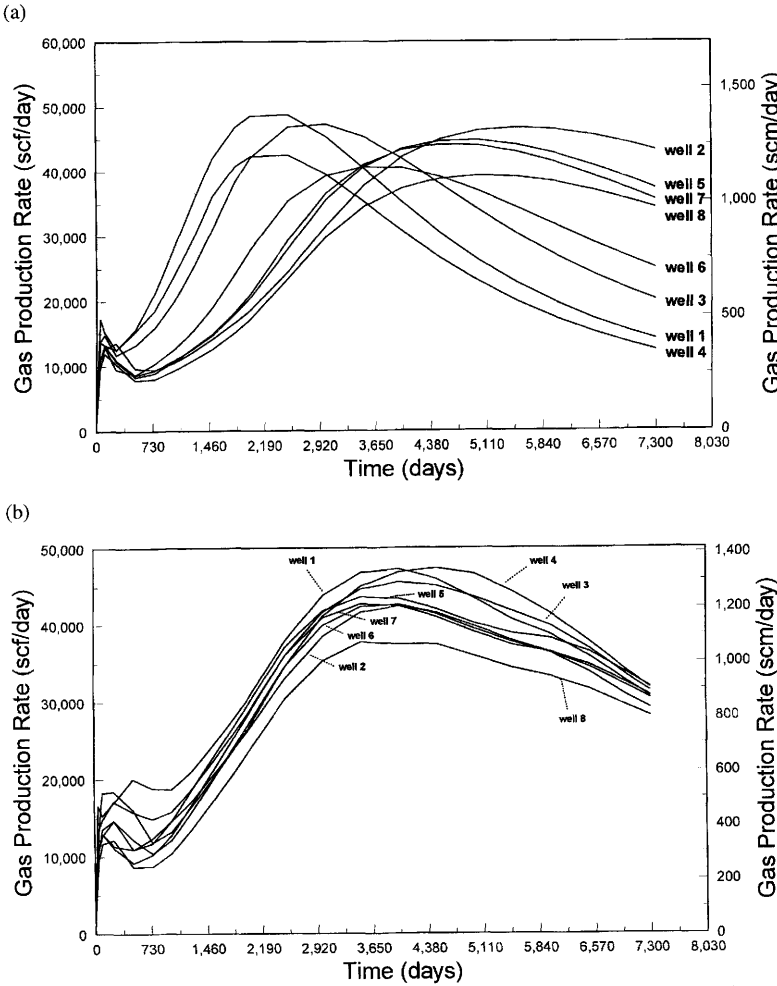
Fig. 7. Gas production rates from each of the eight wells when (**a**) faults are all sealing and (**b**) faults are all non-sealing.
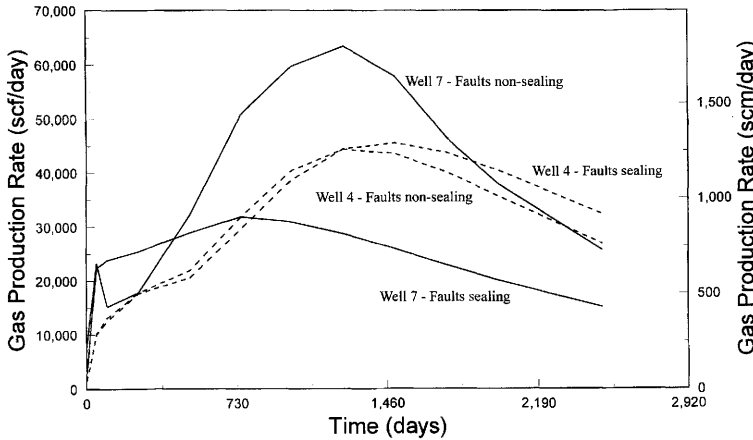

Fig. 8. Gas production rates from well 4 and well 7 in 27-well configuration.

Table 2. *Data used in boundary-fitted co-ordinate cases*

	Field units		SI units
Reservoir dimensions	$1500 \times 400 \times 100$ ft		$457 \times 122 \times 30.5$ m
Fault dimensions	$10 \times 500 \times 100$ ft		$3 \times 152.4 \times 30.5$ m
Initial pressure	1000 psi		6.9 MPa
Initial water saturation		0.2	
Injection rate	1000 bbls/day		$159 \, \text{m}^3/\text{day}$
Production rate	1000 bbls/day		$159 \, \text{m}^3/\text{day}$
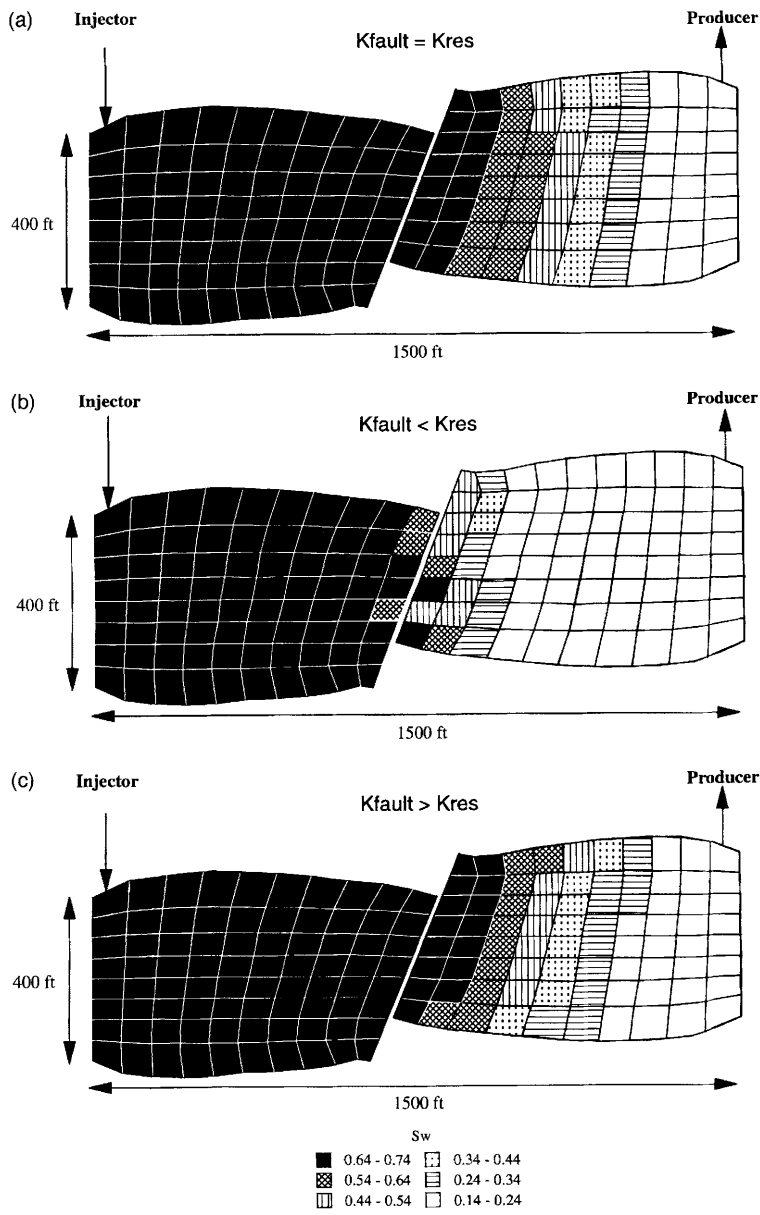
Fig. 9. Application of boundary-fitted co-ordinates to a fault zone with various fault zone characteristics.

flowing directly across the fault and into the upper regions of the reservoir on the right-hand side of the fault. If the permeability in the fault is lower than the permeability of the reservoir (Fig. 9b), the fluid, which enters the fault at the bottom, struggles to move along the fault and re-enters the reservoir in the lower regions on the other side of the fault. Finally, if the permeability of the fault is high, the fluid will travel easily along the fault and will reappear in the upper regions of the reservoir on the other side (Fig. 9c).

Conclusions

It has been shown that fault characteristics within a reservoir have a significant effect on fluid flow, which must be accounted for in any flow simulation. If a fault is sealing, it will act as a boundary to the drainage area of a production well located near to it and affect the sweep of a water flood. On the other hand, if a fault is behaving as a conduit it affects the distribution of fluid within the reservoir and the fluid flow paths during production.

To handle flow in faulted regions within numerical simulators, both along and across the fault plane, two techniques have been developed and implemented in this work.

(a) *Special connections.* Non-neighbour connections allow flow to occur from a block on one side of the fault to a block on the other side which is in a different layer. In this application, the technique has been implemented such that fluid can transfer between two blocks, even if they are not in physical contact, which allows fluid flow to occur both along the plane of the fault as well as directly across it. A number of models, both two- and three-dimensional, were run and the sealing capability of the faults was allowed to vary. These cases demonstrated clearly how the fluid flow behaviour within a reservoir would differ depending on the nature of a fault and its sealing characteristics, thus emphasizing the need for detailed descriptions of faults in reservoir models.

(b) *Boundary-fitted co-ordinates.* This method has been developed separately to investigate the possibility of representing the flow of fluid in the vicinity of a fault with increased precision. As the boundary of the simulation grid is fitted to the boundary of the fault zone, the geometry of the fault can be matched more accurately. Thus, if adequate data are available on the characteristics of the material within a fault zone and its distribution, a detailed study can be made of how the fault will influence fluid flow and hydrocarbon production. A qualitative analysis can then be conducted in which a grid system is fitted around a sloping fault and flow within the fault modelled using Darcy's law. In our work three cases have been modelled, i.e. with the permeability of the fault less than, equal to or greater than the permeability of the reservoir. These preliminary results show how such a technique could be useful in understanding fluid flow through more complex fault zones. As more information on the fault zone is obtained, especially the permeability characteristics of the faulted regions, the applicability of the boundary-fitted co-ordinate systems will increase.

References

ANTONELLINI, M. & AYDIN, A. 1994. Effect of faulting on fluid flow in porous sandstones: petrophysical properties. *AAPG Bulletin*, **78**, 35–377.

DUNLOP, K. N. B., DE BOER, E. T. & WALDREN, D. 1982. Modelling the Piper Field using layer cross flow at faults. *6th SPE Symposium on Reservoir Simulation*, New Orleans, SPE **10527**, 539–551.

FOLEFAC, A. N., WANG, J., DALTABAN, T. S. & ARCHER, J. S. 1992. Explicit representation of flow in a fractured porous medium with boundary fitted co-ordinates. *3rd European Conference on the Mathematics of Oil Recovery*, Delft.

FOLEY, L. M. 1994. *Numerical Modelling of Methane Flow in Coal Seams*. PhD dissertation, Imperial College of Science, Technology and Medicine, University of London, UK.

FORSYTH, P. A. & SAMMON, P. H. 1985. Local mesh refinement and modelling faults and pinchouts. *SPE Reservoir Simulation Symposium*, Dallas, Texas, USA, SPE **13524**, 267–278.

GOLDTHORPE, W. H. & CHOW, Y. S. 1985. Unconventional modelling of faulted reservoirs: a case study. *SPE Reservoir Simulation Symposium*, Dallas, Texas, USA, SPE **13526**, 279–294.

KING, P. R. 1994. Rescaling of flow parameters using renormalisation. *North Sea Oil and Gas Reservoirs*, **III**, 265–271.

LAMBETH, N. & DAWE, R. A. 1988. Boundary and crossflow behaviour during displacement in nodal systems. *SPE Reservoir Engineering*, **3**, 1137–1142.

MROSOVSKY, I., WONG, J. Y. & LAMPE, H. W. 1980. Construction of a large scale simulator on a vector computer. *Journal of Petroleum Technology*, **32**, 2253–2264.

MUNTHE, K. L., OMRE, H., HOLDEN, L., DAMSLETH, E., HEFFER, K., OLSEN, T. S. & WATTERSON, J. 1993. Subseismic faults in reservoir description and simulation. *68th SPE Annual Technical Conference and Exhibition*, Houston, USA, **SPE 26500**, 843–850.

SMITH, D. A. 1966. Theoretical considerations of sealing and non-sealing faults. *AAPG Bulletin*, **50**, 363–374.

THOMPSON, J. F., THAMES, F. C. & MASTIN, C. W. 1977. *Boundary Fitted Curvilinear Co-ordinate Systems for Solution of Partial Differential Equations on Fields Containing any Number of Arbitrary Two-Dimensional Bodies*. Final Report, NASA **CR-2729**.

Curvature analysis of gridded geological surfaces

S. A. STEWART & R. PODOLSKI

Amerada Hess Ltd, 33 Grosvenor Place, London SW1X 7HY, UK

Abstract: Surface curvature is related to strain and hence fracture density in most lithologies relevant to hydrocarbon exploration, and can be calculated at negligible expense as a surface attribute of horizons mapped on three-dimensional (3D) seismic data. Surfaces mapped using 3D seismic exist as data grids. Direct application of strict mathematical approaches to curvature measurement of gridded data is hindered by several problems inherent to discretized data. The grid node spacing in a horizontal plane is initially equal to the 3D seismic bin spacing and is some arbitrary value greater than the infinitely small mathematical limit, so the measured curvature is also arbitrary. Poor resolution of reflectors gives noise which can be removed by smoothing, but this subjective step impacts subsequent curvature extraction.

Fracture distributions also reflect the effect of large- and small-scale fold structures so there is merit in measuring curvature at a range of scales in addition to that defined by the grid node spacing. As curvature varies with direction of measurement, observations in the grid x and y directions alone are unlikely to coincide with the key maximum and minimum curvature values. Resampling a data grid using a large sliding window permits curvature measurement at a range of different wavelengths, and several orientations can be searched in addition to those parallel to the grid axes. Problems which are present regardless of the sample interval include inherent curvature of geological structures, signal aliasing and regional surface tilt relative to the horizontal grid reference plane.

Total, or Gaussian, curvature which is the product of the maximum and minimum curvatures may not be the best format for presenting curvature data, as strata characterized by zero total curvature may be significantly strained within cylindrical fold structures. Instead, the sum of the absolute values of the principal curvatures gives a representation of spatial variance in strain due to maximum and double curvature.

Small-scale faults and fractures may profoundly affect reservoir characteristics. Modern seismic data of reasonable quality can resolve fault structures with throws as small as approximately 20 m, but large numbers of faults and fractures may exist below this limit of seismic resolution. Considerable effort has been directed towards quantifying the population of these 'unmappable' structures on the basis of power-law characteristics of the fault population as a whole, from seismic to sub-seismic and borehole scale (Pickering *et al.* 1996, and references therein). However, these approaches do not yield the spatial distribution of sub-seismic structures.

It is well known that folding of strata may be accompanied by the development of fractures and faults on a variety of scales. Bending strain associated with cylindrical fold growth is related to the curvature of the fold (Eqn 1, from Price & Cosgrove 1990, p. 252).

$$\varepsilon = kt/2 \qquad (1)$$

where ε is the fibre strain on the outer arc of the fold, k is the maximum fold curvature (not necessarily that observed on an arbitrarily oriented section) and t is the thickness of the folded layer, assuming tangential longitudinal strain within that layer. It is clear from this expression

that maps of surface curvature may give a good approximation of the spatial variation in strain, given limited spatial variance in strain mode. A relationship between areas of high surface curvature and fracture density has been noted by several workers, for example Murray (1968), who observed a strong correlation between oil well drill stem test (DST) flow rates and reservoir curvature in the Antelope Sanish Pool fold structure, North Dakota, and Antonellini & Aydin (1995), who found that fault spacing was related to curvature of sandstones deformed above salt structures in the Colorado Plateau.

In the North Sea basin, three-dimensional (3D) seismic acquisition commonly precedes exploration drilling; as 3D seismic coverage has proliferated in mature basins, so opportunities to employ surface attribute analyses (Rijks & Jauffred 1991) at earlier phases in exploration, appraisal and development programmes have arisen. Applications of strain maps in North Sea basin plays include the Central Graben chalk play, and southern North Sea carbonate plays where fractures contribute to reservoir permeability (Watts 1983; Dangerfield & Brown 1987; Foster & Rattay 1993; Cooke-Yarborough 1994), and analysis of dip-closed Jurassic structures in the Central Graben, where topseal

integrity may be compromised by fracturing (Watts 1987). As with most geophysical tools, curvature maps are best used as complements to other techniques, rather than in isolation.

Curvature extraction in the form of 'edge' maps has become a standard supplement to 3D seismic interpretation. However, deficiencies in the algorithms for curvature calculation within commercially available interpretation and mapping software have been highlighted by Lisle (1994) and Lisle & Robinson (1995), who have thoroughly described the geometrical aspects of surface curvature in the context of geological structures. They have shown that there are at least three useful measures of curvature at any point on a surface: the maximum and minimum curvatures (or principal curvatures, k_1 and k_2), and their product, total curvature (or Gaussian curvature, K). They also pointed out that the minimum curvature in addition to the maximum curvature of a surface must be taken into account when attempting quantitative fracture analysis.

The purpose of this paper is to identify and discuss problems encountered in the extraction of curvature from surfaces mapped using 3D seismic data, and propose solutions which might improve algorithms for curvature mapping. A key factor from which many problems arise in curvature extraction is that mapped surfaces usually exist as a data grid which is an inherently discretized version of the original surface, whereas most published descriptions of curvature are based on continuous, relatively simple surfaces. This paper focuses exclusively on the problems of analysing gridded surfaces. Curvature terminology and key features of existing algorithms are introduced first, followed by examination of the problems faced in extracting curvature from grids of sub-surface horizon data. These problems are presented under several broad headings (geological, geophysical, sampling), concluding with a discussion of the best way to present the results.

Definitions

A summary of the nomenclature relevant to this discussion of surface curvature is presented in Fig. 1. Every point on a surface is the centre of
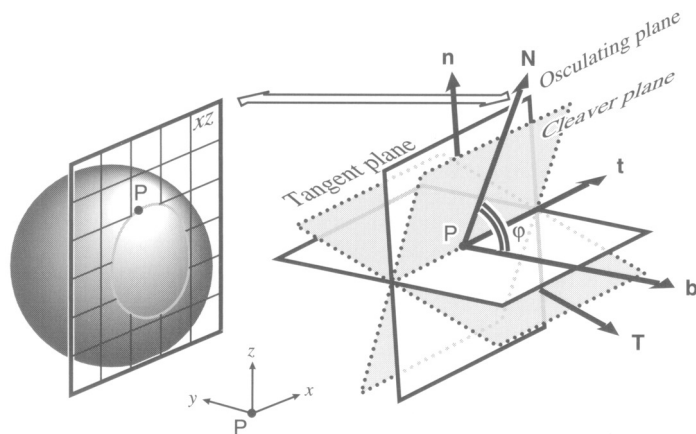
Fig. 1. Illustration of the three frames of reference which are relevant to the measurement of curvature from gridded surfaces. The reference frames are centred upon an example point P which lies on the surface of a sphere. The surface curve frame consists of three orthogonal planes and associated vectors attached to the surface at point P (shaded planes). The vectors within the surface frame are the surface normal (**N**), the tangent to the curve formed by the surface in the line of section at point P (**t**), and an orthogonal vector **T**. Vectors **t** and **T** lie within the surface tangent plane and vectors **N** and **t** lie within the cleaver plane. The space curve frame is attached to the curve formed by the surface in the line of section (unshaded planes). The curve tangent vector (**t**) is shared with the surface curve frame, the normal to the curve is vector (**n**) and the vector orthogonal to **n** and **t** is the binormal vector (**b**). Vectors **n** and **t** lie within the osculating plane, the plane of cross section. Vectors **N**, **n**, **t** and **b** lie in a plane common to both frames. **N**^**b** is φ, a measure of the angular discrepancy between the space and surface curve frames. **T** is not necessarily parallel to the surface dip vector. A third reference frame comprises the coordinate system for storage of the surface as a data grid. The coordinate system usually refers to orthogonal axes x, y and z, where the xy plane is horizontal. The binormal vector **b** will always lie within the xy plane, but the normal vector **n** is not necessarily parallel to the z axis. A more detailed explanation of the reference frames is given in Lisle & Robinson (1995) from which this summary has been drawn.

a surface reference frame which contains the surface tangent plane and surface normal vector. The appearance and properties of the surface (such as curvature) at that point depend upon the orientation of a plane of cross-section. A second reference frame is attached to the curve which is formed by the intersection of the surface and plane of cross-section. This is termed the space curve frame; the plane of cross-section is coincident with a plane termed the osculating plane. The curvature of the curve which appears in the plane of cross-section can be defined as the rate at which the tangent turns with respect to arc length. Surfaces existing as data grids are stored using a third reference frame, the orthogonal system of co-ordinate axes used to specify grid node location. This grid reference frame partially governs the orientation of the second, as planes of cross-section are bound to run parallel to the z axis of the grid reference frame. Since curvature is independent of grid reference frame orientation, it is not related in a simple way to properties of the surface measured with respect to the grid reference frame axes, for example the second derivative of the surface (these relationships are discussed later). It is assumed throughout the discussions presented here that the grid spacing is equal in the x and y directions. The principal curvatures k_1 and k_2 at any point on a surface lie within orthogonal cleaver planes, possess zero surface torsion and are the maximum and minimum values of normal curvature.

Existing algorithms

Commercially available mapping software

Curvature will vary spatially across most geological surfaces, and at any one point, may vary according to the direction in which it is measured; but the directions in which it is possible to make measurements in any gridded surface are limited by the nature of the grid lattice. Many commercially available interpretation and mapping software packages offer second-derivative extraction, although it is not often made clear that the second derivative at a given point is only equal to curvature if the dip at that point is zero (see Discussion section). For this short discussion, the dip is presumed to be zero. One can usually choose to extract the second derivatives in the grid x and y directions at any point (k_x and k_y) or calculate the maximum value of the second derivative. Maximum values of first and second derivatives are typically obtained using an approximation of the following form

(Dalley et al. 1989):

$$k_1 \approx \sqrt{(k_x^2 + k_y^2)} \qquad (2)$$

However, it can be shown that this approximation becomes quite inaccurate for locations with non-zero minimum curvature. For example, the normal curvatures, including principal curvatures, at any point on the surface of a sphere, dome or basin will all be equal in magnitude, yet the above expression would overestimate k_1 by 41%. As these k_1 estimates will always be positive, this approach does not permit a sign convention for curvature measurement (Fig. 1). Few packages are currently able to deliver minimum curvature and hence total curvature maps.

Angular defect method (Calladine 1986; Lisle 1994)

This is a method of directly calculating total curvature (K). In the version described by Lisle (1994), each grid node is considered in turn, and forms the centre of a construction involving its nearest four neighbours. Four triangles are constructed using the offset nodes with the central node forming a common vertex. Total curvature is the quotient of the difference (δ) between the sum of the angles associated with the four vertices and 2π, and A, which is one-third of the sum of the areas of these triangles

$$K = \delta/A \qquad (3)$$

This is a computationally efficient approach which in the form described above has some drawbacks, as will be discussed below, in addition to the inability to deliver principal curvatures.

Mohr circle method (Nutbourne 1986; Lisle & Robinson 1995)

This method exploits the zero surface torsion property of principal curvatures. At each grid node, a best-fit circle is fitted to three co-planar points, which comprise the nearest grid nodes in the grid x orientation about the central node. This process is repeated twice, once in the grid y direction and again in a diagonal direction, using a pair of the second-nearest grid nodes. As a surface becomes more tilted, a discrepancy arises between the curvature of the surface in a vertical plane and the normal curvature of the surface (k_n) at that point (Fig. 1). The measured curvatures k_x, k_y and k_d are converted to normal

curvatures k_{nx}, k_{ny} and k_{nd} (method described later) and are used to define a Mohr circle on a plot of surface torsion against normal curvature, from which the principal curvatures k_1 and k_2 are calculated (the points at which the circle intersects the k_n axis).

A key feature of all three approaches is that they are designed to use the adjacent grid nodes and are therefore limited to measuring curvature over an interval predetermined by the grid node spacing. This issue is discussed further below.

Geological problems influencing curvature extraction

Inherent curvature of sedimentary structures

Not all sedimentary strata accumulate in regular sequences of constant layer thickness. Many sedimentary structures possess surface curvature which reflects the process which created the structure. Examples include clinoforms at the margins of carbonate platforms, and sand waves, dunes and channels (Fig. 2). These structures may range in size from tens of metres to kilometres and their curvature may not be specific to a given lithology; younger layers may also be affected via drape over the underlying structures. Unconformities can also be
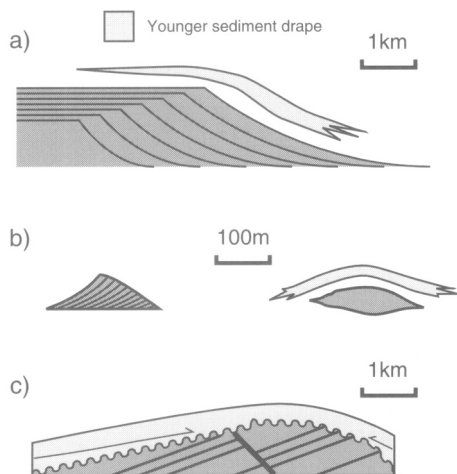
Fig. 2. Examples of geological structures which display curvature unrelated to tectonism and which compromise direct inversion of curvature maps to strain maps. (a) Clinoforms, e.g. carbonate platform margins, deltas. (b) Aeolian/submarine sand features, e.g. dunes, waves and channels. Palaeotopography (unconformity). The curvature of such features may be inherited by younger strata.

placed in this class of problems (Fig. 2): a palaeotopographic surface may display a wide range of curvatures which have no bearing upon finite strain within the strata below.

Little can be done to avoid 'contamination' of curvature extractions by non-tectonic curvatures related to sedimentary structures; however, the presence of such structures should be apparent from the initial mapping. With the benefit of this local knowledge, such effects should be easily recognizable on curvature maps.

Partitioning between brittle and ductile strain

A particular problem with the application of curvature maps to fracture prediction is the degree to which strain is partitioned between brittle and ductile processes. Although it may well be the case that some strain is accommodated by ductile processes, this will not totally compromise the value of curvature maps, whose power lies in provision of a relative measure of the spatial distribution of strain. The problem of ductile deformation in the context of this discussion is probably most acute with structures which form prior to significant lithification, such as folds forced by differential compaction of underlying strata.

Many parameters would have to be taken into account if one were considering calibration of a given curvature map, even given the benefit of control points in the form of cored wells or borehole image logs. Issues such as rheology of the layer in question at the time of deformation (e.g. Gross 1995), strain rate, degree of overpressure in the layer and presence of pre-existing weaknesses combine to ensure that a general calibration for the prediction of brittle structures may be very difficult.

The problem of tectonic structure wavelength: which is relevant to fracturing?

A very common feature of most geological surfaces is that at any one point, the result of curvature measurement depends upon the scale of observation, with apparently superimposed 'fold wavelengths' ranging from tens of metres to kilometres (Fig. 3). In most places it is unlikely to be clear which particular fold wavelengths are significant in terms of fracture generation. This problem forces departure from a strict mathematical approach to curvature measurement. Curvature, by definition, has a unique value for a given orientation at any
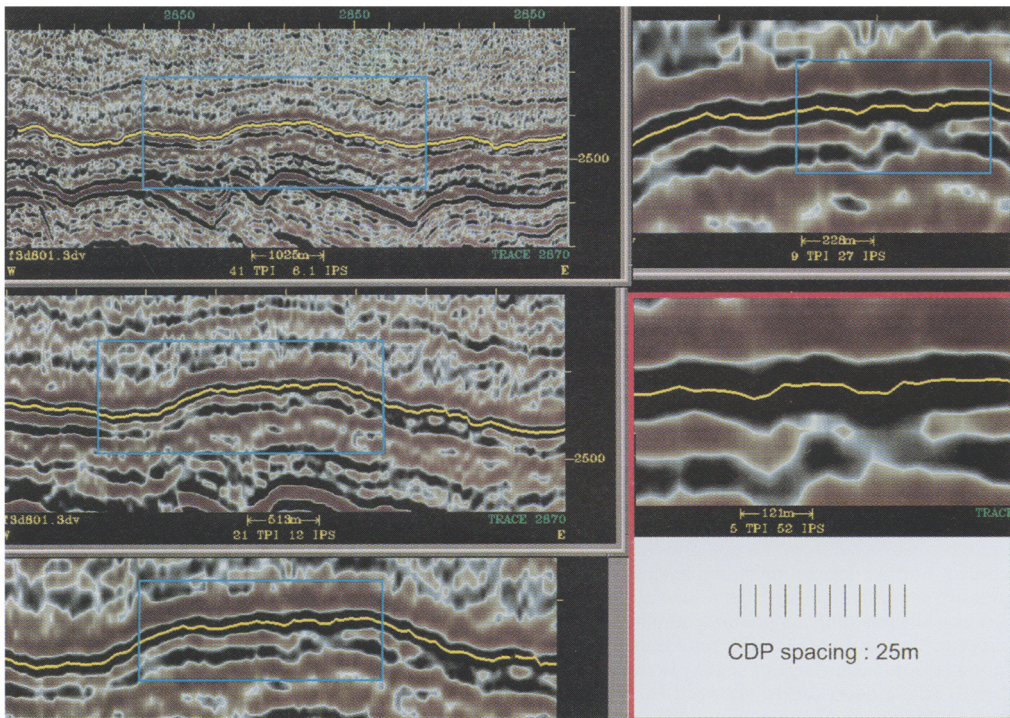
Fig. 3. Illustration of the scale of observation effect, which is relevant to specifying appropriate sampling intervals for curvature calculation. Example from a central North Sea 3D seismic dataset. Autopicked horizon (yellow) is top Chalk. At the scale of a whole survey (top left), large fold structures are apparent. On zooming in, 'fold' structures can be observed at every scale, down to rugosites and spikes in the autopicked horizon between adjacent bins (or CDPs). The bin spacing is depicted below the highest magnification portion (bottom right). At which point does tectonic bending relevant to fracture generation give way to irrelevant noise arising from inadequate imaging?

point on a surface, yet the curvature measured at the smallest possible sampling interval is not necessarily that which would have been obtained at that point had the original, continuous surface been measured. The possibility of structures of relatively large wavelengths having an influence on fracture distribution is another aspect of the problem.

This question should be considered in the context of the algorithms reviewed above, noting that most algorithms only employ adjacent grid nodes. When a number of superimposed wavelengths occur in one place, the fold wavelength which is measured at that point will be predetermined by the grid node spacing, yet fracture density at that point may reflect the superimposition of several tectonic wavelengths, or there may be a single dominant but spatially variable tectonic wavelength.

As the relevant fold wavelength(s) may not be known, algorithms in the forms reviewed above are likely to be inadequate. There is, however, considerable scope for manipulating a surface

grid prior to curvature extraction, with the intention, for example, of enabling measurement of a particular wavelength. Some of the options for grid manipulation and an alternative method for calculating curvature to those already described are considered below.

Decimation Decimation of an initial surface grid will enable measurement of longer structural wavelengths than could have been detected in the initial surface. The choice of new grid spacing interval at which to resample the initial surface is subjective (the relationship between sampling interval and measurable wavelength is described later) (Fig. 4a). This approach is prone to error in that poor choice of resampling interval may lead to omission of key short-wavelength structures. In this context it is noted that surfaces are routinely decimated in the course of mapping projects in the interests of saving computer memory and time, for example during transfer of interpreted surfaces into mapping packages for depth conversion.
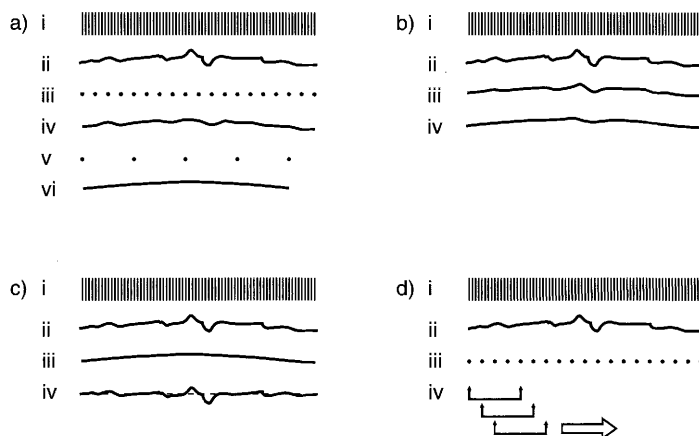
Fig. 4. Alternative options for grid manipulation before or during curvature extraction. Parts i and ii represent a bin grid and autopicked surface respectively, in each example. (**a**) Decimation: a typical bin spacing of 25 m (i) will usually be resampled during export to a mapping package to a new grid spacing of, for example, 100 m (iii). A surface reconstructed from this new grid (iv) shows that short-wavelength features in the intial surface (ii) were not recorded. Further decimation (v and reconstructed surface vi) leads to further loss of information. (**b**) Smoothing: successive smoothing passes over a surface progressively reduce the amplitude of relatively short-wavelength features while retaining the original sampling density. Note that the highest-amplitude spikes may not completely disappear. Factorizing the initial surface into a low-order polynomial surface (iii) and a residual (iv). (**d**) Sliding window: the initial surface, or slightly decimated equivalent, can be locally resampled at some given spatial interval. This window can be allowed to slide across the surface (iv), giving measurements at each grid node.

Smoothing Smoothing filters are available in most interpretation and mapping packages. Use of a smoothing filter to 'remove' short-wavelength features enables one to make more of the information contained in the initial dataset than decimation, as spatial variation in curvature is measured at the initial sampling interval (Fig. 4b). In practice, this approach yields good qualitative results (Fig. 5), but there are several drawbacks. The specification of smoothing parameters is subjective, and the user may not be aware of how the smoothing filter actually works, obscuring the significance of the results in terms of the structural wavelength which one is seeking to measure. A considerable range in results can be obtained by varying the severity of the smoothing pass and sampling interval for curvature measurement. The most flexible approach to smoothing in this context is probably use of a Fourier algorithm to remove specified short-wavelength features. Most gridding algorithms incorporate an element of smoothing whose effect is difficult to quantify; one of the few gridding options free from such hidden smoothing would be a 'snapping' algorithm using single nearest grid nodes.

*Polynomial fitting* The problem of factorizing several superimposed tectonic fold structures with different wavelengths is essentially the same as that of regional-residual separation encountered in gravity and magnetic data interpretation. Approaches which have been developed for these types of data may also be applicable to curvature analysis of geological surfaces. A potentially useful method involves fitting a polynomial function to longer-wavelength features (Oldham & Sutherland 1955); a surface described by such a fitted polynomial could be extracted (via subtraction from the initial dataset) and curvature calculated, and successively higher-order surfaces could be extracted from the residual dataset. This approach is similar to a Fourier analysis of the initial surface; however, a problem with this type of analysis is that the components yielded may not have geological significance over the entire area, i.e. geological structures of short and intermediate wavelengths may be spatially isolated rather than pervasive.

Moving window A way of resampling a surface which is similar to decimation, but without the disadvantage of omitting data, is not to use the adjacent grid nodes in the curvature calculation itself, but to use grid nodes offset by some number, n. This number can be specified by the interpreter to give a curvature 'filter' based on pseudo-grid spacing ns, where s is the initial grid spacing. The calculation of curvature is
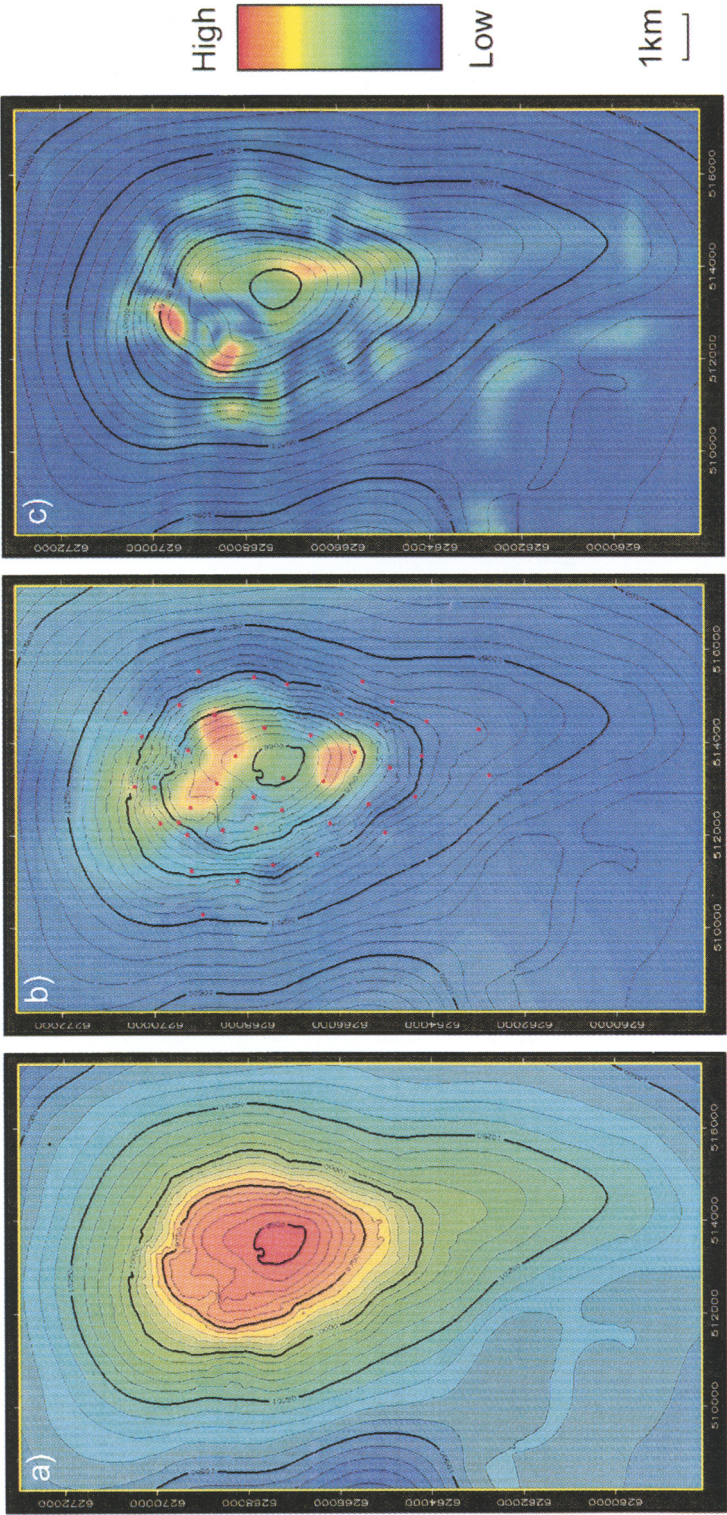
Fig. 5. Ekofisk field topography, fracture intensity and total curvature. (**a**) top Ekofisk Formation depth surface (Fritsen & Corrigan 1990). Grid node spacing 100 m. (**b**) Tor Formation fracture intensity calculated from well-core and test data. Fracture intensity shaded behind top Ekofisk surface contours. Red dots are the wells: data gridded using a convergent algorithm (43 data; Dangerfield & Brown 1987). Total curvature (K_t) map calculated at sample interval of 100 m from following 10 smoothing passes over the top Ekofisk depth surface with a maximum grid node z value change of 5%. Total curvature shaded behind the smoothed topographic surface. Note the steeply plunging curvature accommodation folds (Lisle *et al.* 1990) radially arranged around the flanks of the structure.
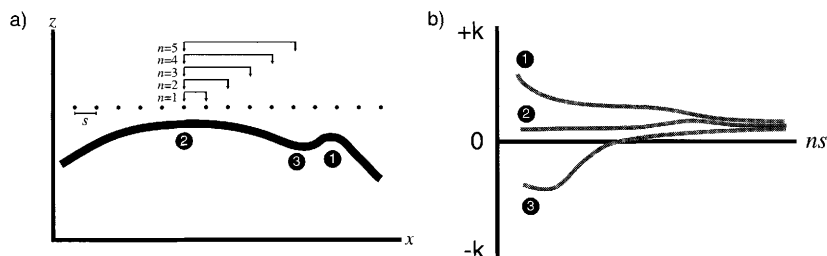
Fig. 6. Variation in curvature with scale of observation. (**a**) Measurement of curvature at each grid node using adjacent nodes, then second nearest in a given direction ($n = 2$), then third nearest ($n = 3$) and so on, could be a way of identifying superimposition of fold structures of different wavelengths. The fluctuation of curvature with offset from each grid node will vary spatially (**b**).

repeated at every grid node. This approach is perhaps the most attractive of those reviewed here, since it is simple, flexible and operates directly on the initial surface.

Multiple curvature extraction   A subjective element is common to all of the above procedures for factorizing various tectonic structure wavelengths; this is unavoidable due to the nature of the problem itself. This problem can be addressed by extracting curvature over a range of intervals at each grid node; all of the approaches described above can form the basis of algorithms which iteratively decimate/ smooth/polynomial fit or simply sub-sample the initial surface and calculate curvature. With the exception of a decimation approach, a range of curvature measurements can be obtained at each grid node; one is then faced with the problem of how to present these measurements. Graphical illustration of curvature against offset (Fig 6) shows that the form of such curves could indicate the nature of tectonic structure superposition; however, a method of collapsing this information into a single parameter which can be presented in map form is not clear. In practice, curvature extractions within three or four 'windows' of varying size should give a good chance of covering those structures likely to have influenced fracture distributions. In choosing which windows to use, one is governed at the smallest end by the grid spacing of the initial surface. For typical modern 3D seismic data, this initial grid spacing will be in the order of 25 m, and it is suggested that a value of approximately 100 m is chosen as the lower limit. The largest window width ultimately depends on the size of the dataset but particular attention should be paid to curvature extractions within window widths close in size to the wavelength of key major fold structures. In the absence of prior knowledge of useful window

sizes, trial and error suggests that a set of curvature maps at 100 m, 400 m and 2000 m window widths ($n = 2$, 8 and 40 for $s = 25$) provides a good visualization of the distribution of tectonic structures.

Large-scale (seismically resolvable) faults

Faults which are large enough to be resolved seismically appear as linear anomalies on curvature maps. While this provides a quick method of fault-trend mapping, such anomalies compromise any of the approaches described above when the grid node offset $n > 1$, because they are included in the curvature calculation up to the nth grid node away from the fault scarp, into the fault block. In the North Sea, this problem is encountered when mapping pre-Upper Cretaceous horizons, but large faults are relatively uncommon in younger strata. A method of resolving fault block surface curvature adjacent to major faults is to shrink the sampling window as a fault is approached until $n = 1$. This can be achieved if grid nodes which fall within resolvable fault planes are assigned some identifying value (e.g. the default indeterminate value used by the interpretation software) which can be recognized by the curvature extraction algorithm. Alternatively, one can apply various filters to the curvature data itself, such as a despiking filter to remove edge anomalies related to the top and base of fault scarps. Or one could map curvature within fault blocks individually.

Other artefacts influencing curvature extraction

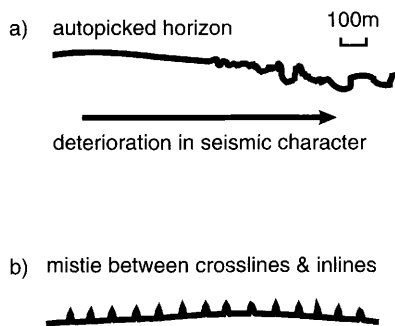There are several sources of noise in surfaces mapped using workstation-based software. This

a) autopicked horizon   100m

deterioration in seismic character

b) mistie between crosslines & inlines

Fig. 7. Sources of artificial noise in interpreted surfaces. (**a**) Autopicker becomes erratic as quality of the seismic reflector decreases. (**b**) Misties between inline and crossline directions in a manually picked surface. It can be difficult to ensure that a surface is completely free from such anomalies, and a conservative smoothing pass prior to curvature calculation should be considered, even if the surface has been resampled/decimated.

noise is purely an artefact of the interpretation method, and some examples are illustrated in Fig. 7. The degree of noise imparted by the autopicker can sometimes be controlled by a smoothing filter built into the autopicker itself, but overly aggressive smoothing at such an early stage in mapping should be avoided, since useful short-wavelength information may be lost.

Sampling problems influencing curvature calculation

Whenever a surface is sub-sampled, it is important to be aware of the relationship between the new sample spacing and the wavelength information which can actually be captured by that density of sampling. A considerable amount of information regarding sampling and associated problems is available in seismic data processing literature (e.g. Telford *et al.* 1976, pp. 376–378); some relevant parts are briefly reviewed here.

Sampling theorem

A fundamental sampling theorem states that a regular sampling interval can record wavelengths no shorter than twice the sample spacing (in the line of section). This theorem determines the maximum sampling interval which can be used to record any given structural wavelength (Fig. 8a).

Aliasing

Aliasing is an unavoidable problem in any situation which involves sub-sampling of a continuous signal or surface, and is summarized on Fig. 8. An interval which is twice the sampling interval (*ns*) can be termed the Nyquist wavelength (λ_n, Fig. 8b). Any regular structural wavelength which is $\delta\lambda$ shorter than the Nyquist will appear in the new sample grid as (will alias as) a non-existent wavelength greater in magnitude than the Nyquist (Fig. 8c). In the frequency domain, the relationship between real and aliased signals is simple, $f_n + \delta f$ being indistinguishable from $f_n - \delta f$, where f_n is the Nyquist frequency. The corresponding relationship in the wavelength domain is shown in expression 4.

$$\lambda_n - \delta\lambda \text{ aliases as } \lambda_n(\lambda_n - \delta\lambda)/(\lambda_n - 2\delta\lambda) \quad (4)$$
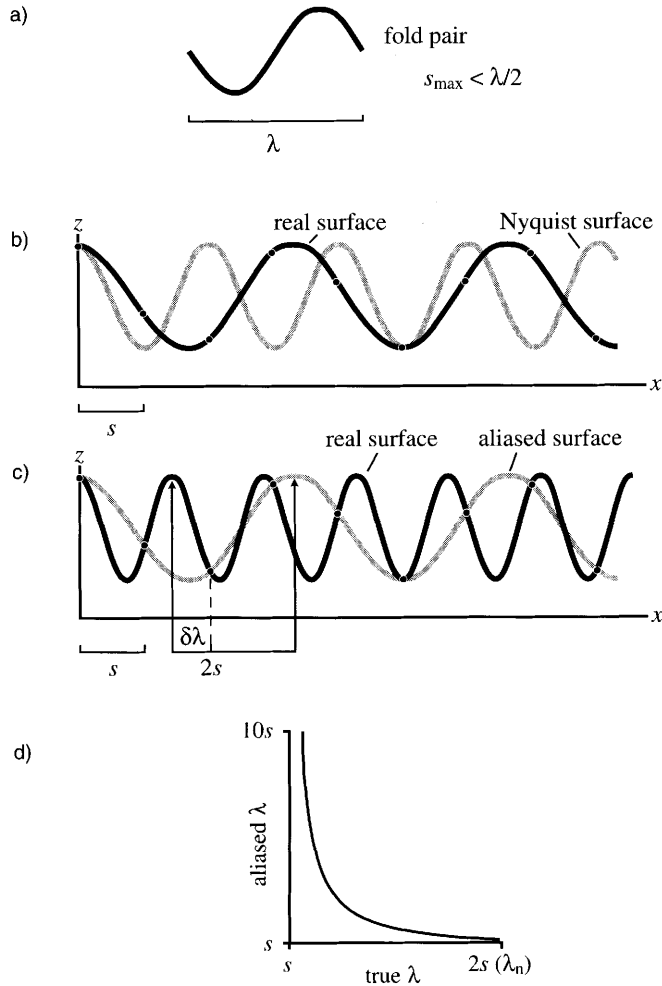
A graph of this relationship (Fig. 8d) shows that if *ns* becomes larger relative to the wavelength of a fold, then the aliased fold wavelength increases markedly.

Anti-aliasing filters are routinely applied during seismic processing, but aliasing is inherent in nearly every subsequent sampling operation in a map-making process. This problem would ideally be addressed by removing any structural features with wavelengths shorter than the sampling interval *ns* prior to curvature extraction. This is most effectively achieved by carrying out a Fourier analysis of the initial surface and removing the harmonics of shorter wavelength than the sub-sampling interval *ns*.

Dip-related problems

The axes to which surface grids relate are usually arranged such that a reference co-ordinate plane (*xy* plane) is horizontal and the grid nodes each have some altitude (*z*) relative to this plane. Tectonic dip *a* within any surface will lead to an under-sampling of the surface relative to the sampling interval *ns* by a factor of $\sec\alpha$, but nothing can be done about this.

Curvature is defined in terms of the rate at which the tangent plane turns with respect to distance along the surface itself. Curvature is therefore independent of orientation of the *xyz* grid reference frame and is not directly related to properties of the surface which are calculated with respect to the axes of this system such as dip (e.g. dz/dx) or rate of change of dip (e.g. d^2z/dx^2). Curvature can, however, be calculated from the first and second derivatives according to the following expression (for a derivation see

a)

fold pair

$s_{max} < \lambda/2$

λ

b)

z

real surface   Nyquist surface

x

s

c)

z

real surface   aliased surface

x

$\delta\lambda$

s   2s

d)

10s

aliased λ

s

s   true λ 2s (λ_n)

Fig. 8. Sampling and aliasing. (**a**) If a given fold pair defines a fold wavelength λ, the maximum sampling interval s which can be used such that the fold could be reconstructed must be less than $\lambda/2$. (**b**) Fold train of arbitrary wavelength and a sampling interval s sufficiently dense to record the surface. The surface consisting of folds of the Nyquist wavelength for that particular sampling interval is also shown (grey), illustrating the shortest fold wavelength which could be captured by the sample grid. The same sample grid as (b) applied to a real fold train with a characteristic wavelength (black) shorter than the Nyquist wavelength λ_n by some length $\delta\lambda$. The sample grid records a non-existent (aliased) fold train with a characteristic wavelength which is greater than λ_n. (**d**) Graph of the relationship between aliased wavelength and real wavelength (see text). Parts (b) and (c) after Telford *et al.* (1976).

Gasson (1983, pp. 82–84)):

$$k_x = \frac{d^2z/dx^2}{[1 + (dz/dx)^2]^{3/2}} \quad (5)$$

Tectonic dip has a further effect upon algorithms which attempt to measure curvature in vertical planes passing through the grid nodes. Any surface cut by a vertical plane will give a curve in

cross-section with a horizontal binormal vector **b** (Fig. 1), however, if the local tectonic dip is non-zero and is not parallel to the vertical osculating plane, the surface cleaver plane will not be parallel to the vertical osculating plane and the vertical section cannot contain a normal, or principal curvature (Fig. 1). The angle between surface normal vector **N** and the binormal vector **b** is φ. The observed curvature (k) is

related to the normal curvature k_n (Lisle & Robinson 1995):

$$k_n = k \sin \varphi \qquad (6)$$

Local orientation of the surface and hence φ is estimated by least-squares fitting of a node and its eight neighbours to a plane. Indirect approaches to curvature measurement from grid nodes, such as the angular defect method, do not suffer from this problem.

Grid lattice and principal curvature orientation mismatch

The principal curvatures k_1 and k_2 are specific members of the set of normal curvatures which it is possible to measure at any point on a surface. Euler's theorem for normal curvature states that k_n is related to the principal curvatures:

$$k_n = k_1 \cos^2 \theta + k_2 \sin^2 \theta \qquad (7)$$

where θ is the angle in the tangent plane between the orientation in which k_n is measured and the orientation of k_1 (Fig. 9). A fundamental problem with curvature extraction from discretized (i.e. gridded) surfaces lies in the fact that the orientations of grid node axes x and y are unlikely to be parallel to k_1 and k_2 at any given grid node, and θ is unknown. In other words, the relationship between measureable normal curvatures k_x and k_y and the principal curvatures k_1 and k_2 is unknown, as is the relationship between measured total curvature K_m and actual total curvature K (Fig. 10). This problem is similar in nature to aliasing in that the initial surface is insufficiently sampled to record the actual curvature, but unlike aliasing (with respect to a given wavelength), the problem is independent of sample interval ns. This problem becomes more significant as the absolute value of total

curvature increases. At points with negative total curvature, for example, angle θ might be such that k_x or k_y is parallel to one of the asymptotic directions, and the point would have an apparent total curvature of zero (Fig. 10). This problem mitigates against using only the adjacent four nodes to any given grid node for curvature calculation.

Monitoring of K_m at a point of negative K during rotation of a synthetic dataset shows the relationship between K and K_m. The same behaviour is shown by a point with positive K (Fig. 11a), graphs of $K_m - K$ when $\theta = 24°$ for various periclinal shapes are shown in Fig. 11b. A relationship between K_m and K can be deduced from these artificial examples:

$$K_m = K[1 \pm c(\cos 4\theta - 1)] \qquad (8)$$

where c is a constant and '$\pm$' is the opposite sign to that of K. An equivalent relationship describing K_m follows from Eqn 7:

$$K_m = K(\sin^4 \theta + \cos^4 \theta) + (k_1^2 + k_2^2) \sin^2 \theta \cos^2 \theta \qquad (9)$$

An important implication of Eqns 8 and 9 is that K is always less than (or equal to the minimum value of) K_m (Fig. 11a), indicating that total curvature maps calculated from grids are liable to be biased towards positive K. The search for principal curvatures is analogous to the search for principal strain axes from deformed markers; in the latter case it is well known that at least three data points are required (Lisle & Ragan 1988). Similarly, curvature measured in two directions is clearly insufficient for determining total curvature. The relationship between K_m and K can be used if employing the angular defect method of calculation: after computing K_m using the nearest four grid nodes, repeat the calculation using the next nearest four (those diagonally offset), and choose the lowest K_m as the best estimate of K (Fig. 12a). Ideally, an algorithm should measure curvature in as many directions as possible; algorithms using offsets greater than $n = 1$ have the opportunity to measure curvature in several directions additional to the grid x and y orientations, searching for principal curvatures, and/or the minimum total curvature (Fig. 12b).
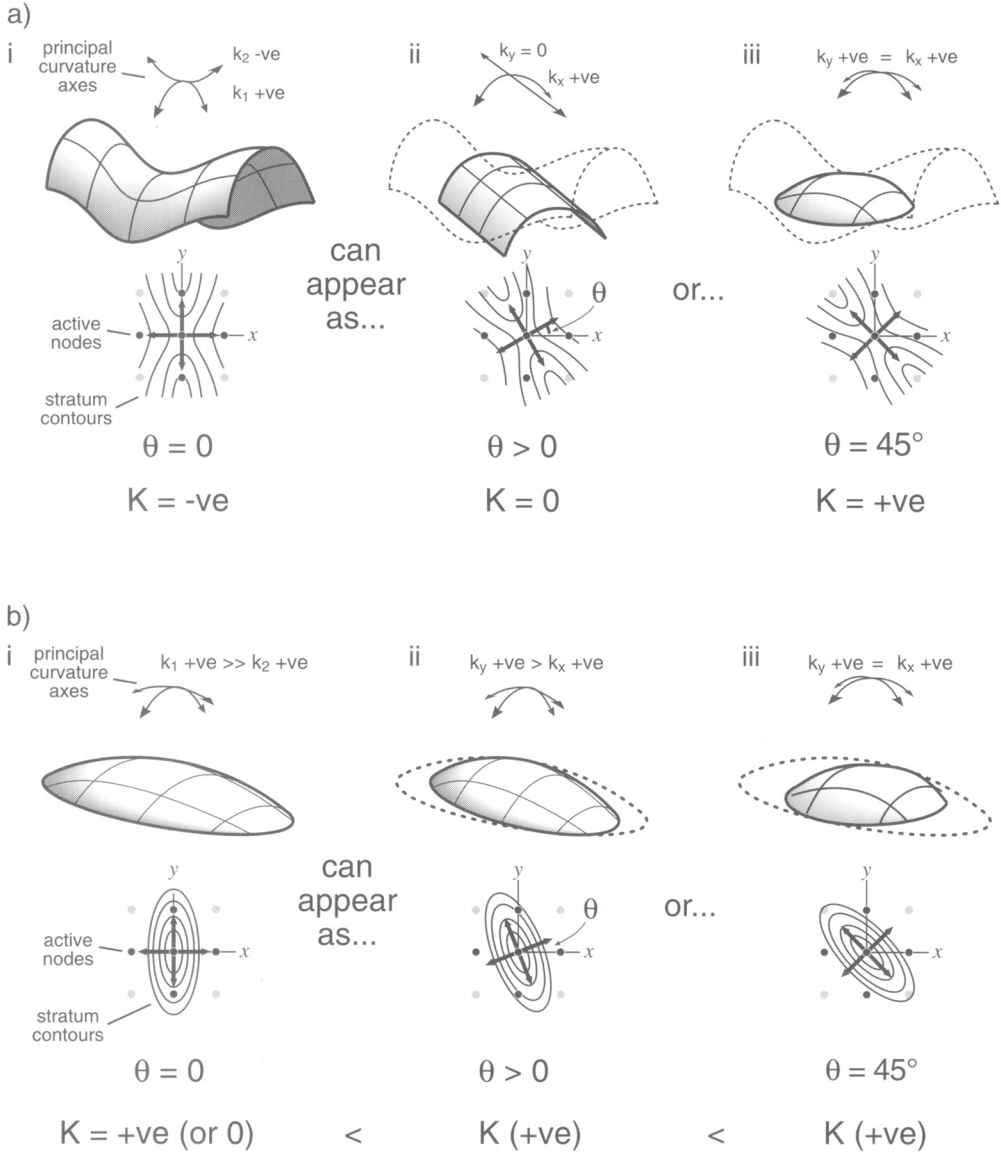
Discussion

Regardless of the preferred method for calculating curvature, considerable variation in the results of these calculations may arise from the manner in which a surface is sampled. Further
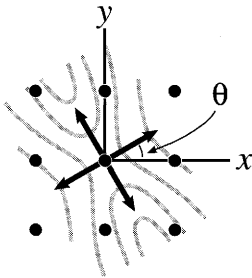
Fig. 9. Angular mismatch between orientation of principal curvatures (black arrows) and grid node axes. Stratum contours in grey.

Fig. 10. Effect of θ on measurement of total curvature K. (**a**) Location with negative K. When $\theta = 0$ (i), k_x and k_y are parallel to the principal curvatures and the shape is faithfully recorded. At certain values of θ (ii), one of the grid axes may be locally parallel to orientations characterized by $k_n = 0$ (asymptotic directions), and the location appears to have zero K. At other values of θ (iii), the grid node lying directly on the saddle may have a higher altitude than its nearest four neighbours, leading to measurement of positive apparent total curvature. (**b**) Location on the crest of a periclinal closure (positive K). As θ increases, k_2 increases in magnitude while k_1 decreases and K increases. This effect would be more pronounced had the initial location been on the crest of a cylindrical fold structure ($k_2 = 0$).

variation occurs if the surface is processed in some way prior to sampling, e.g. decimation or smoothing. Some rules of thumb which emerge from the above discussions include: understand the smoothing elements built into regridding algorithms; restrict initial smoothing to a conservative despiking pass; retain as dense a grid as possible throughout depth conversion; calculate curvature at a range of offset grid nodes in addition to adjacent nodes; search as
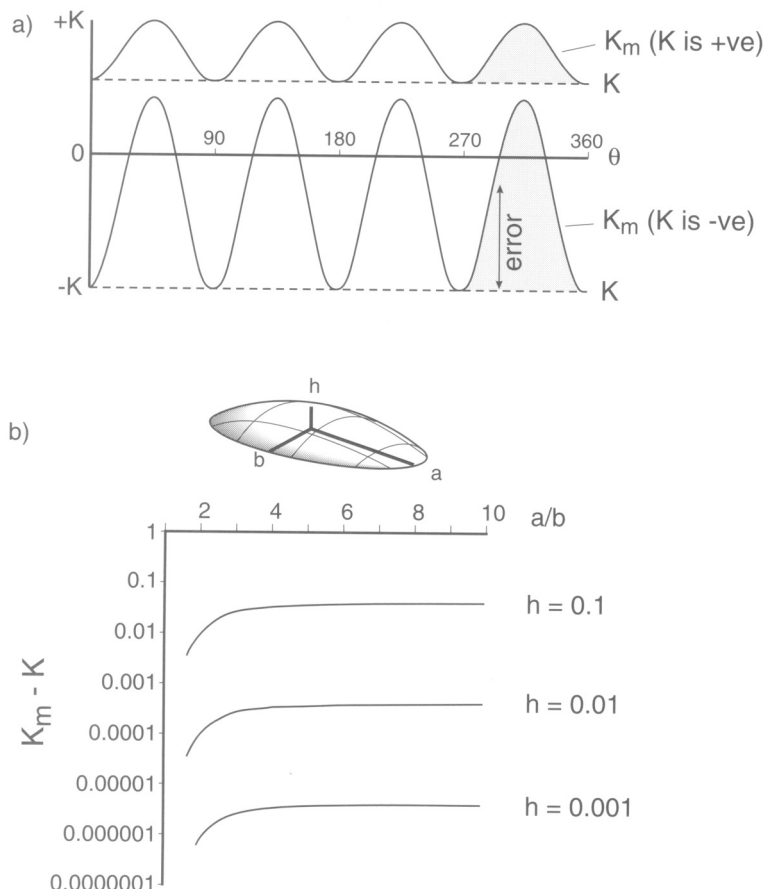
Fig. 11. Results of numerical experiments to examine variation of K with θ. (**a**) Fluctuation of measured K at points of positive (upper curve) and negative (lower curve) total curvature during rotation of the surfaces containing the points about the surface normal vector **N**. Actual values of K at each point are indicated by the broken lines. The variation in measured K (K_m) is similar in each case. (**b**) Calculated difference between measured total curvature (K_m) and actual total curvature (K) when $\theta = 45°$ for points on crests of periclines. By specifying that the ellipse which forms the base of the pericline has semi-axes parallel to grid x and y directions and that the ellipse passes through the points $(\pm 1, \pm 1)$, the length of one semiaxis can be calculated from the other [e.g. $b = a^2 / (2a^2 - 1)$]. The curvatures were calculated using some given fold amplitude (h). The difference in K increases as the eccentricity of the structure in plan view (a/b) increases.

many orientations as grid node offset allows. Whilst steps can be taken to optimize curvature extraction, several factors work against accurate measurements, for example, an arbitrary minimum sampling interval is imposed by the initial data grid; the transition between noise and tectonic curvature may be poorly defined; as the sampling interval increases and more directions can be examined, the effects of aliasing may have to be considered.

Assuming an algorithm yields 'reliable' measurements of principal and total curvatures, each calculated from an appropriate offset range, one would ideally like a representative

curvature map to use alongside other attributes, such as results of seismic inversion for porosity but should maximum, total or some other version of curvature map be used? Lisle (1994) argues for the use of total curvature, but it should be borne in mind that structures with very low or zero total curvatures could still have significant strain and tectonic fracturing (Fig. 13). Although total curvature is very meaningful in a geometrical sense, there are discrepancies between this property and strain which are important if the purpose of the map is to convey the spatial variance in strain or some related factor. On the other hand, k_1 maps do
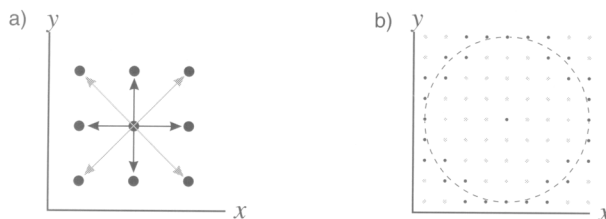
Fig. 12. Options for using additional grid nodes in curvature calculation. (**a**) Use of the second nearest four neighbours would help in the situations illustrated in Fig. 10, although they are 41% farther away. (**b**) A moving window approach has the opportunity to sample grid nodes in many more directions as offset (*n*) increases. At $n = 4$, 16 directions can be searched for principal curvatures, with the maximum departure of actual grid node separation from search radius *ns* (broken line) reduced to 12%.

not discriminate between cylindrical structures and more highly strained non-cylindrical structures. There are many ways of combining the principal curvatures other than multiplying them together, but a simple and meaningful approach would be to add their absolute magnitudes. A reason to use this index is that is takes account of both maximum and minimum curvature without falling to zero as minimum curvature falls to zero. A map of $|k_1| + |k_2|$ may therefore give a more realistic portrayal of finite strain distribution than either K or k_1.

Curvature extraction is similar in principle to the extraction of other surface properties such as dip and azimuth; the sampling issues discussed here are also relevant to the calculation of these attributes. In contrast to these lower-order attributes, curvature maps have the potential to illustrate the spatial variation in fracture density, a key reservoir characteristic. The discussions presented in this paper are intended to illustrate some of the problems which must be considered when designing a curvature algorithm to operate on large grids of sub-surface data such as those which arise from 3D seismic datasets. Calibration

of curvature for a property such as fracture density seems a particularly formidable task, but the ability to depict relative spatial variance in strain for very little cost or computer time makes curvature extraction a valuable part of any prospect evaluation where tectonic fractures are considered to be important.

References

ANTONELLINI, M. & AYDIN, A. 1995. Effect of faulting on fluid flow in porous sandstones: geometry and spatial distribution. *AAPG Bulletin*, **79**, 642–671.

CALLADINE, C. R. 1986. Gaussian curvature and shell structures. *In*: GREGORY, J. A. (ed.) *The mathematics of surfaces.* Clarendon, Oxford, 179–196.

COOKE-YARBOROUGH, P. 1994. Analysis of fractures yields improved gas production from Zechstein carbonates, Hewett Field, UKCS. *First Break*, **12**, 243–252.

DALLEY, R. M., GEVERS, E. C. A., STAMPFLI, G. M., DAVIES, D. J., GASTALDI, C. N., RUIJTENBERG, P. A. & VERMEER, G. J. O. 1989. Dip and azimuth displays for 3D seismic interpretation. *First Break*, **7**, 86–95.

DANGERFIELD, J. A. & BROWN, D. A. 1987. The Ekofisk field. *In* : KLEPPE, J., BERG, E., BULLER, A. T., HJELMLAND, O. & TORSAETER, O. (eds) *North Sea Oil and Gas Reservoirs.* The Norwegian Institute of Technology, Graham and Trotman, London, 3–22.

FOSTER, P. T. & RATTAY, P. R. 1993. The evolution of a fractured chalk reservoir: Machar oilfield, UK North Sea. *In* : PARKER, J. R. (ed.) *Petroleum Geology of Northwest Europe: Proceedings of the 4th Conference.* The Geological Society, London, 1445–1452.
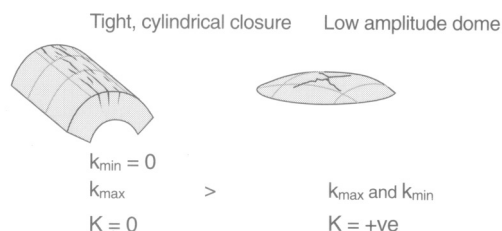
Fig. 13. The problem of which curvature parameter to select when presenting curvature extraction. (**a**) Approximately cylindrical structures, such as monoclines above inverted faults, may well have significant associated fracturing, yet low or zero total curvature; would the crests of such structures necessarily be any less fractured than a location of non-zero K (**b**)?

FRITSEN, A. & CORRIGAN, T. 1990. Establishment of a geological fracture model for dual porosity simulations on the Ekofisk field. *In*: BULLER, A. T., BERG, E., HJELMLAND, O., KLEPPE, J., TORSAETER, O. & AASEN, J. O. (eds) *North Sea Oil and Gas Reservoirs – II*. The Norwegian Institute of Technology, Graham and Trotman, London, 173–184.

GASSON, P. C. 1983. *Geometry of Spatial Forms*. Ellis Horwood, Chichester.

GROSS, M. R. 1995. Fracture partitioning: Failure mode as a function of lithology in the Monterey Formation of coastal California. *Geological Society of America Bulletin*, **107**, 779–792.

LISLE, R. J. 1994. Detection of zones of abnormal strains in structures using Gaussian curvature analysis. *AAPG Bulletin*, **78**, 1811–1819.

——, R. J. & RAGAN, D. M. 1988. Strain from three stretches – a simple Mohr Circle solution. *Journal of Structural Geology*, **8**, 905–906.

——, R. J. & ROBINSON, J. M. 1995. The Mohr circle for curvature and its application to fold description. *Journal of Structural Geology*, **17**, 739–750.

——, STYLES, P. & FREETH, S. J. 1990. Fold interference structures: the influence of layer competence contrast. *Tectonophysics*, **172**, 197–200.

MURRAY, G. H. 1968. Quantitative fracture study – Sanish Pool, McKenzie County, North Dakota. *AAPG Bulletin*, **52**, 57–65.

NUTBOURNE, A. W. 1986. A circle diagram for local differential geometry. *In*: GREGORY, J. A. (ed.) *The Mathematics of Surfaces*. Clarendon, Oxford, 59–71.

OLDHAM, C. H. G. & SUTHERLAND, D. B. 1955. Orthogonal polynomials: their use in estimating the regional effect. *Geophysics*, **20**, 295–306.

PICKERING, G., BULL, J. M. & SANDERSON, D. J. 1996. Scaling of fault displacements and implications for the estimation of sub-seismic strain. *In*: BUCHANAN, P. G. & NIEUWLAND, D. A. (eds) *Modern Developments in Structural Interpretation, Validation and Modelling*. Geological Society, London, Special Publication, **99**, 11–26.

PRICE, N. J. & COSGROVE, J. W. 1990. *Analysis of Geological Structures*. Cambridge University Press, Cambridge.

RIJKS, E. J. H. & JAUFFRED, J. C. E. M. 1991. Attribute extraction: An important application in any detailed 3D interpretation study. *The Leading Edge*, **10**, 11–19.

TELFORD, W. M., GELDART, L. P., SHERIFF, R. E. & KEYS, D. A. 1976. *Applied Geophysics*. Cambridge University Press, Cambridge.

WATTS, N. L. 1983. Microfractures in chalks of Albuskjell Field, Norwegian sector, North Sea: Possible origin and distribution. *AAPG Bulletin*, **67**, 201–234.

——1987. Theoretical aspects of cap-rock and fault seals for single- and two-phase hydrocarbon columns. *Marine and Petroleum Geology*, **4**, 274–307.

Strain partitioning during flexural-slip folding

GARY D. COUPLES, HELEN LEWIS & P. W. GEOFF TANNER

*Department of Geology and Applied Geology, University of Glasgow,
Glasgow G12 8QQ, UK*

Abstract: In upper-crustal structures, folding by flexural slip leads to the partitioning and
ordering of strains, which are commonly expressed by means of faults, fractures and
joints. Flexural slip occurs along only some of the numerous layer-to-layer contacts within
a sedimentary rock sequence, and these active bedding-plane slip surfaces partition the
succession into mechanical units, each of which, although composed of many rock layers,
deforms as though it were a single beam. Thus, in upper-crustal flexural-slip folds, the
strain domains associated with bending are sharply delimited by the active slip horizons
and also are related to structural position within the beam. Progressive folding leads to the
development of additional active slip surfaces and, therefore, to an increased number of
mechanical units which each develop bending strains. As a result of this sequence of
events, there is a hierarchical overprinting of strains, which leads to considerable complexity
in fracture fabrics; nevertheless, order in the fracture patterns is retained. Most petroleum
reservoirs appear to be affected by fracture networks created during flexure, and their fluid
flow characteristics are probably related to a fracture-dominated, flexural deformation
state which is disposed relative to the layering, is inhomogeneous, and is not distributed
stochastically throughout the whole rock volume.

Fractures are an important element of petro-
leum reservoirs. Predicting the distribution of
fractures (orientations, densities, extents),
and creating flow simulations based on the
effects of fracturing, are topics of current inter-
est. Our contribution to this subject is to empha-
size the role of bedding-plane slip in the
partitioning of strain during flexural-slip folding
on scales appropriate to commercial oil-fields.
We argue that some of the major fracture sets
commonly encountered in folds of this size are
directly related to flexural slip. The fractures
are the expression of strains that develop
within the mechanical units that arise as slip
occurs.

Our approach in this paper is to review some
basic concepts concerning flexure, and to exam-
ine these ideas in the context of those structures
typical of the upper crust where slip on bedding
planes, and fracturing, are the dominant expres-
sions of deformation. We establish an 'expected
state' of deformation in a very simple flexure
and then consider the mechanical alterations of
that state which occur as slip takes place on
only some of the available bedding planes.
Examples of flexural deformations show a hier-
archical development of bedding-plane slip,
with complex overprinting of strains. We argue
that a flexural-slip model of fold-associated
fracturing can be used to make predictions as
to the size, location and extent of fractures,
leading to a better understanding of their petro-
physical effects.

Flexures

Some previous work on flexural deformation

There is a considerable body of work which
examines the strain distribution expected within
rock layers affected by folding. The simplest
case is where a single, isolated layer (Fig. 1A) is
deflected into a smooth shape (Billings 1972,
p. 119; Hills 1972, p. 227; Ramsay & Huber
1987, p. 458). A 'neutral surface' (or fibre) is
thought to divide the layer into elongated and
shortened parts, which are thinned and thick-
ened, respectively, and which can be inferred
to have developed contrasting states of stress
(Fig. 1B). This model leads to a major problem
when it is used to create fold pairs (continuous
anticline–syncline couplets): abrupt stress state
reversals, and abrupt changes in position of the
neutral fibre, are predicted in the common limb
of the fold pair (Fig. 1C). This arrangement is
clearly impossible.

The problems associated with this along-limb
change of state are eliminated in the transverse-
longitudinal strain (TLS) model (Fig. 1D)
described by Ramsay (1967, p. 398; see also
Bayly 1992, pp. 30–36). This model assumes
that principal strains are either perpendicular
or parallel to layering, and that the total layer
thickness does not change during folding.
Within the layer, a finite neutral surface is
assumed to exist, and its curvature can be used
to calculate a strain distribution which honours
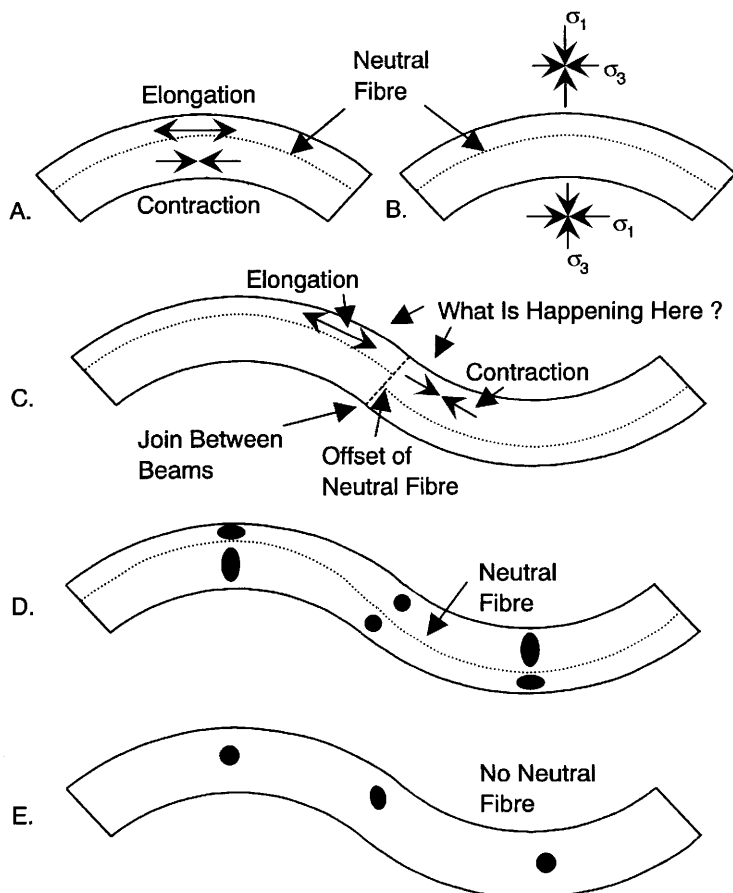
Fig. 1. (**A**) Antiformal deflection of isolated layer (with free ends) showing neutral fibre and regions of elongation and shortening strains. (**B**) Stress states inferred from strains depicted in (**A**), with regions of thinning and thickening. (**C**) Difficulties arising from double flexure (antiform + synform). (**D**) Transverse-longitudinal strain model (after Ramsay 1967) showing strain ellipses. (**E**) Flexural-flow model (after Ramsay 1967).

the above conditions. In this situation, the neutral surface is not parallel to the layer boundaries, but instead it reflects a partitioning of the layer into thickened and thinned parts that have a compensatory relationship such that the total thickness of the layer remains constant. This model has been used to guide and explain a number of studies of folds, including field investigations (e.g. Hara *et al.* 1968; Groshong 1975; Ramsay & Huber 1987), laboratory modelling (e.g. Hudleston 1973), and theoretical analyses (e.g. Fletcher 1979; Hudleston & Lan 1993; Lan & Hudleston 1995).

The flexing of multilayered sequences may, however, involve a major component of motion parallel to the layering, and there is a basis for questioning the relevance of the TLS model in this situation. Flexural-flow (Fig. 1E) and

flexural-slip models have been developed to account for the localization of displacement associated with mechanically weak layers, or weak interfaces within a layered package (Ramberg 1961; Donath & Parker 1964; Ramsay 1967; Ramsay & Huber 1987; Tanner 1989). Hudleston *et al.* (1996) have challenged the validity of the flexural-flow mechanism on the basis of numerical work which suggests that the anisotropies required to produce the geometries and strains predicted by the flexural-flow model are unlikely in natural materials. They argue instead that equivalent fold profiles and strain patterns can be achieved by the deformation of stacks of thin, alternating layers that have a large viscosity contrast. In their suggestion, the stiff layers develop TLS and the weak layers deform by simple shear.

Stress state in bending deformations

Upper-crustal folds which have (or might have) entrapped commercial quantities of petroleum are the primary subjects of this paper. The development of such folds is often dominated by fracturing, faulting and other discontinuities, and an understanding of the distribution of that deformation is important for reservoir management. As the geometries of fracture patterns can be related to the states of stress which caused them (Friedman & Sowers 1970; Stearns *et al.* 1981; Hancock 1985; and references therein), we need to establish the state of stress which is likely to exist in a flexure.

We take as our example a symmetric, double flexure (antiform/synform pair), but we emphasize that the primary elements of the stress state are also shown by asymmetric folds. The stress field we expect in a single-layer flexure (Fig. 2) is derived from studies that use: photoelastic methods (Currie *et al.* 1962; Friedman & Sowers 1970: plane stress); mathematical modelling (Hafner 1951; Couples 1977; Gangi *et al.* 1977: plane strain, results projected onto non-rectangular shape); and experimental models of rock layers folded under confining pressure (Handin *et al.* 1972; Friedman *et al.* 1976*a*, *b*, 1980: approximately plane strain).

This stress distribution (Fig. 2) differs considerably from that which is suggested by either the simple neutral surface approach (Fig. 1B), or which might be inferred from the TLS model (Fig. 1D). In this double flexure, principal-stress trajectories are normal or parallel to layering in only limited areas, and throughout the remainder of the folds they are inclined to the layer boundaries. Nearly everywhere in these flexures, the stress trajectories are curved, and sometimes sharply so. The strains associated with this stress field must be equally complex if they are co-axial with the stresses (as we might expect for low strain magnitudes). They differ markedly from the strains predicted by assuming the presence of a neutral fibre, especially in the limbs. However, the fold-*limb* strain pattern suggested by this stress field compares favourably with that predicted by flexural flow, and with the multilayer model described by Hudleston *et al.* (1996). Later in this paper we will return to these comparisons.
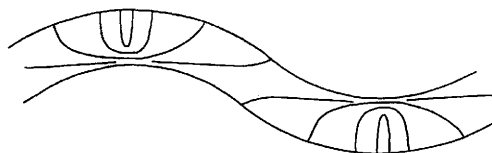
The pattern of deformation illustrated in Fig. 2 is the stress state we expect to develop in a simple, single-layer flexure. We focus on stress because of our interest in the primary deformation mechanism in upper-crustal flexures, i.e. fracturing, whose formation is best understood in these terms.

Expression of fracture strains in natural flexures

Strains in natural folds can, of course, be expressed in a variety of ways. Here, we are concerned with deformation mechanisms that result in joints, fractures, and small faults, with fairly low bulk strains: perhaps a few per cent. Notionally, these responses are typical of deformation occurring in the upper 5–10 km of the crust, and if we seek to make advances in understanding the folding process, our models need to explain the main observations.

Based on the predicted stress state distribution (Fig. 2), flexures developed in upper-crustal locations may be expected to have fracture/fault patterns which indicate regions of both layer-parallel elongations in the outer arc and contractions in the inner arc, as in TLS (Fig. 3). We note that such fracture/joint patterns have been recognized in folded rock sequences by many workers (Price 1967; Stearns 1967; Ramsay & Huber 1987; Hancock 1985; Price & Cosgrove 1990; Ameen 1992; and other references cited by these authors), and we interpret

Fig. 2. Stress trajectories from pure bending of double flexure. Solid lines show orientations of σ_1 (maximum compressive principal stress). Minimum principal stress trajectories (not shown) form orthogonal set to σ_1 orientations. See text for references.
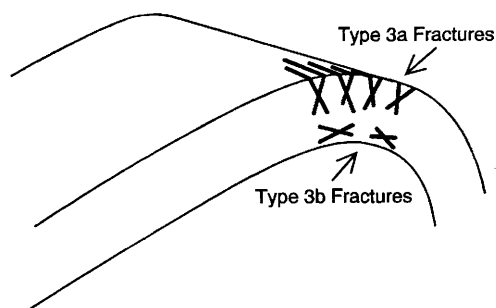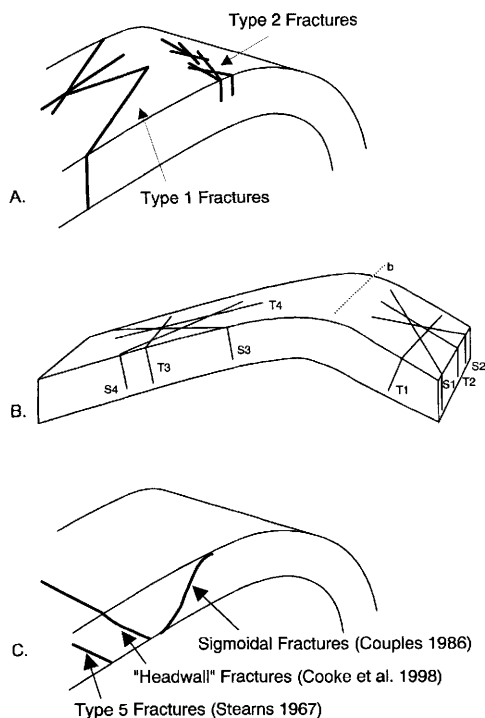

Fig. 3. Fractures and small faults that accommodate bending strains within a single thick layer (terminology after Stearns 1967).

Fig. 4. (**A**) and (**B**) Fracture assemblages indicating within-layer motions. (**A**) Scheme from Stearns (1967); (**B**) scheme from Price (1967). (**C**) Fractures characteristic of fold limbs.

these fracture patterns to be intimately associated with bending.

However, there are additional fracture/joint orientations that are commonly observed in folds which cannot easily be related to the bending stress state. For example, consider the bedding-normal fracture sets of Stearns (1967) and Price (1967) as depicted in Fig. 4. If we accept that the fractures shown in Figs 3 and 4 are conjugate sets, or assemblages, and that implied stress orientations are defined entirely by the geometry of each fracture assemblage, then four different states of stress are suggested in the anticline. Using Stearn's terminology: Type 3a and 3b assemblages have σ_2 lying in the bedding and oriented along the fold axis, but have reversed maximum and minimum stresses; and Type 1 and Type 2 assemblages have σ_2 normal to bedding, but again, these sets indicate a reversal of maximum and minimum stresses. The spatial variation of stress states created by bending (Fig. 2) appears to explain the creation of fracture Types 3a and 3b (Fig. 3), but Type 1 and 2 assemblages have

no apparent mechanical explanation that arises directly from the stresses caused by bending. Below, we suggest an origin for these assemblages associated with the flexural slip process.

There are still other complexities related to the fracture patterns commonly seen in folds. Additional observations (primarily from sandstones; for examples, see Jamison & Stearns (1982), Aydin & Reches (1982) and Antonellini *et al.* (1994)) indicate that fracture orientations in folds can be more complex than those illustrated in Figs 3 and 4. The fracture patterns we have depicted here are those that are expected in plane strain deformation, whereas the patterns typical of many folded sandstones are indicative of triaxial strain (Reches 1978). Although the subject of rheology is not the primary focus of this paper, we note that the 'sandstone' fracture patterns often reflect compactant volume strains (D'Onfro *et al.* 1994; Couples & Lewis 1997, 1998). The stress orientations inferred from these more complicated fracture patterns seen in folded sandstones (Jamison & Stearns 1982; Lewis & Couples 1993) are, nevertheless, similar to those derived from fractures that formed in plane-strain modes.

Still another group of fracture types needs to be considered. Many folds may have more-or-less planar limbs connecting localized hinges. Within these planar limbs, 'bending' fractures (Types 3a and 3b) are infrequent. Type 1 and 2 fractures are present, but there are other fractures which may be related to flexure. These fractures (Fig. 4C) are most easily attributed to the direct effects of bedding-plane slip, as conjugates (Stearns 1967), as incipient ramps or duplexes (Couples 1986; Tanner 1989, 1992*a*), or as the 'headwalls' of slip patches (Cooke & Pollard, 1994, 1996; Cooke *et al.* 1998). The lack of distinct curvature of the layers in these limb locations makes it difficult to associate these fractures with bending, but we believe that they can be related to flexural slip (see below).

However, even though explanations can be offered for the creation of individual fracture sets, there is still the conundrum posed by the concurrent presence of multiple fracture types in a fold. Interpretation problems also arise in situations where fracture patterns are quite complex, and their classification into sets is not straightforward. Still greater difficulties occur when fracture sets are in apparent conflict, such as where Types 3a and 3b are both present. In this paper we develop a model which provides an explanation for many of these complexities as an *expected* mechanical consequence of bedding-plane slip.

Strain evolution and partitioning

Role of Bedding-Plane Slip

Many workers have recognized the importance of bedding-parallel slip in folding (Cloos & Martin 1932; Kuenen & de Sitter 1938; Donath & Parker 1964; Ghosh 1968; Ramsay 1967; Chapple & Spang 1974; Dubey & Cobbold 1977; Johnson 1977; Behzadi & Dubey 1980; Tanner 1989, and other references therein; Higgs *et al.* 1991; Ameen 1992). However, we believe that it is useful to reconsider some of the mechanical concepts which have come to be widely accepted. For example, a common (though not universal) notion is that flexurally induced slip occurs on all bedding surfaces, or at least on each competent/incompetent boundary, within a sequence of layered rocks. This process model is inherent in the 'deck of cards' demonstration of flexural folding that many have encountered in their undergraduate education. However, the deck of cards view is inappropriate on two counts: it is based on free ends (see above), and slip in real folds is not equally distributed onto all available surfaces. Instead, bedding-parallel slip is generally restricted to some bed-to-bed contacts, and other (apparently similar) interfaces appear to remain welded together (Chapple & Spang 1974; Johnson & Page 1976; Behzadi & Dubey 1980; Tanner 1989; Fitches *et al.* 1990; Tanner 1990, 1992*a*). Further examples of this localization of flexural slip are reviewed below.

Some of the questions that arise include: Why are only some surfaces activated, and indeed, what is the mechanical reason for slip along any surface? Do the functioning slip surfaces become active all at once, or is there some sequence to their activation? What are the consequences, for the development of bending strains, of such kinematic partitioning?

We argue here that bedding-plane slip develops in a sequential, hierarchical fashion, and that, although the distribution of the resulting strains (expressed as fractures) is complex, it is ordered. Let us begin by imagining that in a developing fold, *some* bedding planes are experiencing slip. These active bedding-plane slip surfaces serve to separate the stratigraphic succession such that each of two regions (lying above and below the slip surface, and further bounded by adjacent slip surfaces) develops its own bending-caused deformation state (Fig. 5A). If several slip surfaces are active, then each of them bounds bending deformation that is occurring both above and below the surface. The packages of layered rock so delimited
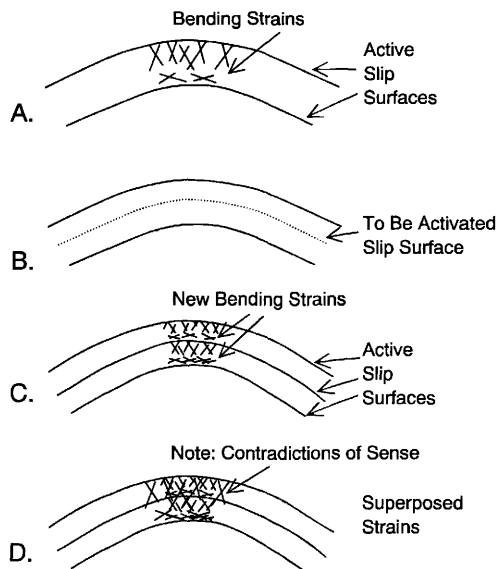
Fig. 5. Mechanical units and superposition of strains. (A) Mechanical units defined by active layer-parallel slip surfaces. (B) Antiformal portion of active mechanical unit showing position of next-to-be-activated slip surface. (C) Bending strains (fractures) developed as a result of segmentation of previous mechanical unit. (D) Illustration of overprinting of previous fabric with new fracture sets created by higher-order mechanical units. Note regions where fabrics are contradictory.

(i.e. above and below the active slip) are here called 'mechanical units' to emphasize that their definition is intimately linked to the mechanics of the process (that is, bending-associated deformation of a package of rock layers delimited by bedding-parallel slip). The package of layers bounded by the slip surfaces in Fig. 5A is such a mechanical unit.

What happens to a current mechanical unit when a new bedding-plane slip surface becomes operative within it? If we focus on the antiformal part of the flexure, an active mechanical unit will have its set of elongational and contractional fracture fabrics (these will transect the individual, but so-far mechanically indistinct layers of rock that constitute the unit; Fig. 5A). When that mechanical unit is subsequently divided by the activation of a new slip surface somewhere within the package of layers (Fig. 5B), the newly defined mechanical units will each develop sets of elongational and contractional strains, probably expressed by fractures (Fig. 5C). The progressive activation of bedding-plane slip surfaces in a flexure will lead to a complex series of deformation states such that the combination

of the earlier fracture fabrics, and those that are newly created, produces patterns of strain (Fig. 5D) that would appear contradictory if they were assumed to be the result of a single stress state. In our view, the interpretation of strain in multilayer flexures cannot be attributed to a single deformation state, but instead, the total state of strain represents a cumulative process in which different stress states, possibly of different sign, are superimposed.

Examples of hierarchical flexural fabrics

This sequential development of active slip horizons seems to be common in cases we have studied. Measurements from chevron-folded turbidite sequences show that the spacing of bedding-plane slip surfaces decreases as the dip of the bedding increases, and as the folds become tighter (Tanner 1989). These data are supported by the work of Hutchinson (1995; developed from previous discussions by Busk (1929), de Sitter (1958) and Ramsay (1974), on folded rocks), who finds that unconsolidated sediments that are being extended can be affected by flexural slip, and that both the net slip and the spacing of slip are related to the dip. In Hutchinson's compilation, flexural slip affects surfaces with dips as low as one degree.

Another example that illustrates the sequential development of flexural slip is from Rattlesnake Mountain anticline, located in northwestern Wyoming. This fold is an asymmetric structure expressed by Palaeozoic carbonate rocks (Fig. 6A); it has a core of faulted crystalline basement, and the structural relief is some 2+ km (Stearns 1971, 1978; Couples 1986). The folding occurred in an uppermost crustal setting (less than 3 km maximum overburden), and the carbonate rocks of this anticline are essentially free of internal strain other than small faults, bedding-plane slip, fractures and joints (twinning strains amount to only a few per cent, where present, and the strain associated with pressure solution is virtually nil). Although the cause of this structural feature remains quite controversial (compare contrasting cross-sections by Stearns (1971) and Brown (1988; see also Stearns 1978; Couples & Lageson 1985; Rodgers 1987; Narr & Suppe 1994), our interest here is only in how the cover rocks achieved their folded shape, and in the way that the folding strains developed. The debate over the origin of the uplift is irrelevant to this paper.

At Rattlesnake Mountain, the Palaeozoic carbonate rocks (Ordovician to Lower Carboniferous: approximately 1 km thick) maintained

their thickness during the folding (Stearns 1971, 1978) except in very localized circumstances (Couples 1986, 1998). As a consequence, and because of the excellent exposure, this structure provides an ideal setting to study flexural-slip folding. The fractures in the folded carbonate rocks conform to the assemblages depicted in Figs 3 and 4A, and there are abundant examples of overprinting as depicted in Fig. 5.

The largest example of this superposition of fracture/fault patterns occurs in the crestal region of the fold (Fig. 6). Here, an earlier episode of layer-elongation strain (small horst/ graben sets) is overprinted (and offset) by a major bedding-plane slip surface and its continuation as a contractional fault where it slightly transects bedding. We interpret these relationships to mean that a thick mechanical unit existed first (with strains expressed as horst/ graben), and that this earlier mechanical unit was segmented into thinner mechanical units by the development of a new bedding-parallel slip horizon. Thus, the anticlinal location depicted in Fig. 6B was in the upper, extensional portion of an initial, thick mechanical unit, and later it became the contractional (lower) part of a thinner mechanical unit.

The interpretation that thick mechanical units are divided into two or more thinner ones (by the activation of previously dormant bedding surfaces) is borne out at Rattlesnake Mountain through a range of scales (Couples 1986, 1998). Indications of slip (such as those described above, plus direct evidence in the form of local detachments and striated bedding surfaces) have been studied throughout the exposure of the fold (which is approximately 25 km long and cut by numerous deep canyons). Overprinting relationships, and the size of the implied mechanical units, permit these observations to be grouped into a hierarchy of slip-surface activations, in which the first-formed slip surfaces bound thick first-order units, and later-activated slip surfaces bound thinner, higher-order units (Couples 1986). In other parts of the Rocky Mountain foreland, similar superposition relationships are noted (D. Weinberg, pers. comm. 1996).

We believe that the evidence from Rattlesnake Mountain records the progressive activation of slip surfaces as bending proceeds. Bending strains and stresses build up in the portions of the fold where flexure (curvature) is higher, but these do not increase indefinitely because of the 'relief' brought about by the creation of higher-order mechanical units caused by activation of additional bedding-plane slip surfaces. That is, the process of creating higher-order mechanical units limits the magnitude of the strains developed
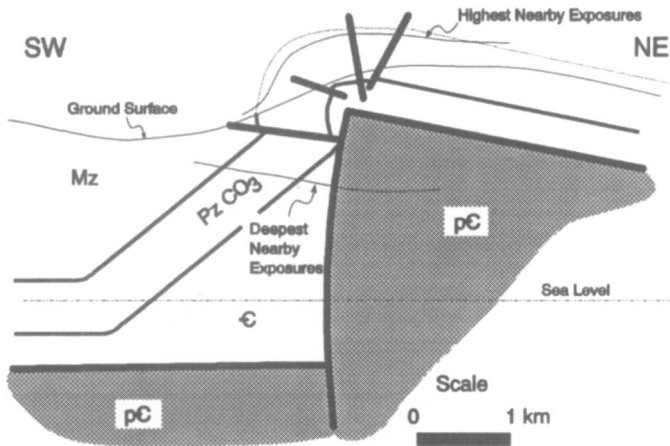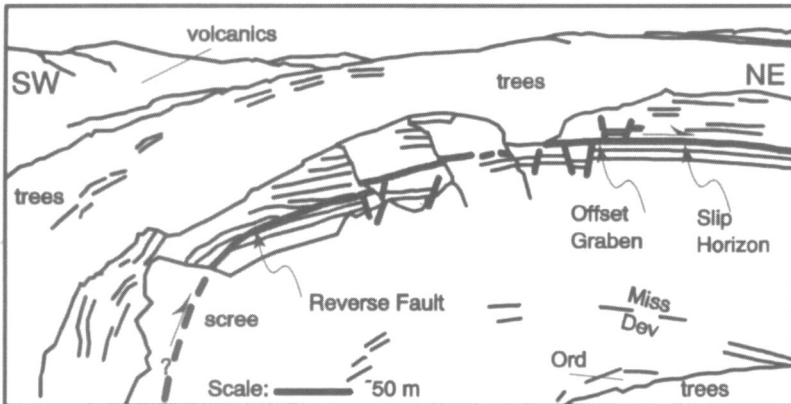
Fig. 6. Rattlesnake Mountain anticline, northwest Wyoming. (**A**) Cross-section (after Couples 1986). Mz = Mesozoic rocks, Pz CO₃ = Palaeozoic carbonates, C = Cambrian shales, pC = Precambrian. (**B**) Line drawing of north wall of Mooncrest Canyon (Sections 27 and 28, T 54 N, R 104 W, projected). Middle portion of Mississippian (Lower Carboniferous) Madison Limestone is at top of canyon, and top of Ordovician Bighorn Dolomite exposed in canyon bottom. Note extensional horsts and grabens (first-order fabrics) offset by second-order slip surface and associated contractional fabrics.

at any point in the fold, and so determines the distribution of, in this instance, the fracture fabrics, and their intensities.

Based on the interpreted sequence of slip activation (Couples 1986, 1998), we conclude that the flexural-slip folding at Rattlesnake Mountain occurred progressively. Early in the flexing, the stratigraphic succession was divided into a small number of thick packages of rock layers (mechanical units), bounded by then-active slip surfaces. Later, and especially where the curvature became more pronounced, more and more slip surfaces developed, thereby creating a larger number of mechanical units. Within each mechanical unit (still composed of a large number of rock layers) strains are expressed by fracturing and faulting.

Verification in models

Although the sequential and hierarchical development of mechanical units in the flexural-slip fold at Rattlesnake Mountain is a well-founded interpretation, we recognize that alternate explanations could be offered. Furthermore, the

cautious geologist might point out that the layer-parallel motions discussed above cannot be proven in many folds, since there generally are no clear markers available for the measurement of offsets, and so slip surfaces cannot be positively identified. These difficulties are overcome (or at least greatly mitigated) by the use of modelling.

Physical models Physical models of the sort described by Weinberg (1979), Couples *et al.* (1994) and Couples & Lewis (1998) have thin (*c.* 1 cm thick) packages of rock layers which are deformed (under realistic confining pressure: 50 MPa) into asymmetric folds by the uplift and rotation of a pre-machined steel-block loading assembly. The resulting fold geometries replicate the anticlinal shape of the Rattlesnake Mountain example described above, and superimposed grids and post-experiment sections permit detailed analysis of the mechanics of the folding process (Couples *et al.* 1994). In this type of model, which comes from a series of studies on folding using rock materials (Handin *et al.* 1972; Friedman *et al.* 1976*a*, *b*, 1980; Couples *et al.* 1994; Patton *et al.* 1997), the (interpreted) stress field which develops in the thick rock layer is that of a 'thick beam bend' (Fig. 2; Friedman *et al.* 1976*b*; Couples 1977; Gangi *et al.* 1977; Couples *et al.* 1994).

The design of these models permits a simple test of the concept that mechanical units are created during flexural-slip folding. The single thick layer of limestone in the models of Couples *et al.* (1994) (Fig. 7A) is replaced in other experiments (Couples 1986; Couples & Lewis 1998) by a package of four thin limestone layers yielding the same overall thickness. During uplift and folding, slip occurs first on only the middle interface of the four-layer package (Fig. 7B), but as the structural relief becomes greater (Fig. 7C), slip occurs on all three of the package's layer-to-layer interfaces. These models provide striking support for strain partitioning as a consequence of layer-parallel slip, demonstrating that mechanical units are created during folding, and that an increased number of mechanical units develops as the folding proceeds.

Numerical simulations
Physical models of the sort described above are limited in terms of the flexibility of their design; for example, rock layers cannot be machined to less than about 1.5 mm in thickness, thus limiting the number of layers in a package, and the friction coefficient of the interfaces can only be that of rock/rock contacts (*c.* 0.6) or of lubricated contacts (*c.* 0.1). On the other hand, numerical models permit investigation of a range of
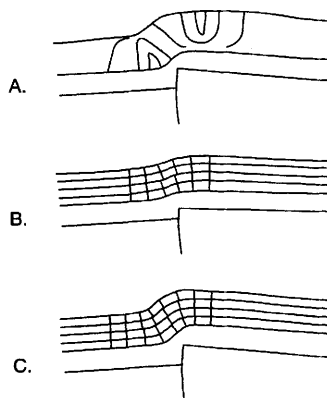
Fig. 7. Hierarchical development of inter-layer slip in limestone layers of folded rock models. (A) Thick (*c.* 1 cm) single-layer limestone beam showing stress state like that of Fig. 2 (after Couples *et al.* 1994). Movement of forcing assembly shown underneath limestone packages. (B) and (C) Offset of marker grid lines in four-layer packages of limestone (each layer *c.* 2 mm thick); models otherwise identical to the single-layer models. In (B), structural relief is small, and only middle interface is activated. In (C), at higher structural relief (comparable to that illustrated in single-layer model (A)), all layer boundaries have experienced slip, and there are four mechanical units (after Couples & Lewis 1998).

variation (in parameters and number of layers), and, in principle, a nearly infinite number of intermediate geometries can be evaluated to define the full path of any process.

We describe here a single numerical example (Fig. 8) in which finite-element methods are used to model the sequential and hierarchical development of layer-parallel slip in a four-layer package (with frictional interfaces) flexed into an antiformal shape (Couples *et al.* 1996). Early in the deflection sequence, no slip occurs (Fig. 8A), but slightly later, the middle interface is activated, thereby creating two new mechanical units (Fig. 8B). Later, all three interfaces are active (Fig. 8C), and four mechanical units exist. Stress state discontinuities occur along the slip horizons, as do strain discontinuities, thereby confirming the creation of separate mechanical units. Layer-parallel slip is progressively developed as flexure increases.

Discussion

Complex strain states

In a developing fold, consider the (temporary) case where only a single first-order mechanical
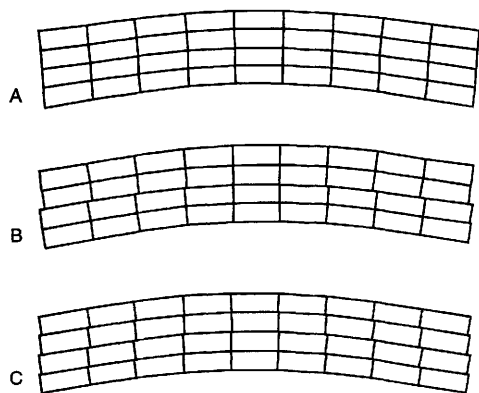
Fig. 8. Numerical model of flexure (bending) of multilayer subjected to half-wavelength sinusoidal deflection at its base. In starting configuration the four layers are planar, and each is 2000 m long and 50 m thick. They are assigned equal elastic constants, and the inter-layer frictional contacts are identical ($\mu = 0.6$) on all interfaces. In these plots, maximum displacement is always shown at same size. Lines represent selected finite-element boundaries. (**A**) At 10 m deflection, no significant slip has yet occurred, and only one mechanical unit exists. (**B**) At 50 m deflection, central interface has slipped, defining two mechanical units (each composed of two layers). (**C**) At 200 m deflection, all interfaces have slipped, and four mechanical units are present. Calculations done in 1979, using ANSYS ©. Top and side boundary conditions are constant pressure, basal b.c. is displacement. Materials are elastic.

unit has been created (that is, there is only one set of bending strains), and focus attention on one such unit bounded above and below by slip horizons. Bending strains in this mechanical unit are localized, both to their appropriate relative positions, and by the spatially variable degree of curvature of the flexure. These strains are heterogeneous across a range of scales, in terms of the intensities (expressed as either spacing or size, or both), and, at the larger scale in terms of the orientations, of the resulting fractures. If an inversion procedure (to define the causative stress state) is applied to this fracture population, it will yield different results as its sampling window is moved and/or resized.

Now consider the (subsequent) case where multiple orders of mechanical units have developed during folding. Each mechanical unit has the heterogeneous strain field described above; in addition, the strains of the higher-order (later-developed) mechanical units are superimposed onto those created earlier. The complexity of the analysis is compounded as a consequence of this overprinting such that effective inversion

of the fracture data is likely to be impossible if only orientations and intensities are considered.

However, the model of flexural-slip folding that we describe here provides a means to understand the partitioning of strain, and a framework for analysing the distribution of discontinuities in folded rock sequences. Overprinting of strain features denotes the likely presence of hierarchies of mechanical units and instigates a search for the bounding surfaces. Reversals of strain state (changes of sign: layer-parallel extension to contraction, or vice versa) along bedding-normal profiles indicate that a significant mechanical boundary has been crossed: either a slip surface, or a 'neutral zone' within a mechanical unit. An integrated analysis can reveal the mechanical sequence of events, and the conceptual model then provides a template for interpreting the heterogeneous strain information.

In the development of flexural-slip folds, inter-layer slip is typically localized to a sub-set of the available bedding horizons. The slip surfaces that are activated by the folding process are initiated in a hierarchical fashion, defining time-dependent sets of active mechanical units. Within each active mechanical unit, strains develop in response to bending, and overprinting of strains occurs as new mechanical units come into existence.

Inchworm motion

However, this model so far accounts for only a portion of the fractures actually observed. Here we consider whether the bedding-plane slip process (in contrast to bending) may be associated with the formation of other fracture sets, such as Stearns' (1967) Type 1 fracture assemblage (Fig. 4), or the equivalent geometry of the S_3, S_4 and T_4 fractures of Price (1967). These fracture assemblages are ubiquitous features of folds around the world, producing the 'flatiron' and 'hogback' geomorphic expressions of dipping rock units (which we argue involve flexural slip), and their presence can hardly fail to have significant petrophysical effects (e.g. Stearns & Friedman 1972). Stearns' Type 2 fractures, although they are generally smaller and consequently have less of a geomorphic impact, nevertheless are significant in terms of their impact on the fluid flow characteristics of reservoirs (Nelson 1991). Even though these two fracture assemblages are important elements produced by the folding, and even though they probably affect the resultant flow characteristics, the mechanical explanation of their development is not clear: the implied responsible stress states

cannot be easily related to any model of fold genesis (including the flexure state described above).

If these fracture assemblages (Types 1 and 2) are each interpreted to represent conjugate sets (following Stearns (1967)), then in-bedding motions are suggested for both assemblages. The shear fractures of the Type 1 assemblage are particularly interesting: in our experience, they are vertically limited by bedding-parallel slip surfaces, and, in cases where it is possible to make observations, they are laterally limited by swarms of Type 2 fractures. Thus, these two assemblages seem to be intimately related to active slip horizons, and to each other. Low-order (thick) mechanical units in some folds may be defined by bedding-plane slip surfaces which may be hundreds of metres apart, and the Type 1 fractures related to these seem to form the boundaries of the major flatirons.

We here suggest the beginning of a more complete mechanical explanation of these 'non-bending' fracture sets: Type 1 shear fractures represent the lateral margins of areally limited (perhaps kilometre scale for the major ones), dynamic(?), bedding-parallel slip events (Fig. 9). In other words, the movement of rock units in fold limbs may occur in an inchworm fashion,

Fig. 9. Inchworm effect of bedding-plane slip. (**A**) Anticline showing two mechanical units, and 'patch' of active bedding-parallel slip is shaded. (**B**) As (**A**) but with shaded volume removed. Note striations on bedding, and on wall of Type 1 fracture, indicating approximately up-dip motion of dynamic block.

with only part of the moving 'sheet' (i.e. mechanical unit) experiencing motion at any time. Energy arguments for such localization in the case of thrusting have been emphasized by Price (1988). Cooke & Pollard (1994, 1996) and Cooke *et al.* (1998) also highlight the importance of localization of bedding-plane slip, and the fractures created as slip varies along a bedding plane (Fig. 4C; see also Means 1989).

Similar spatial/temporal variation of active bedding-plane slip is implied by our model for the formation of Type 1 (and Type 2) fractures. The full analysis of this hypothesis will require the creation of three-dimensional (3D) numerical simulations (see also Cooke & Pollard 1994, 1996; Cooke *et al.* 1998). We consider that it is possible that these ubiquitous, but heretofore unexplained, fracture assemblages are the result of dynamic slip events, and the (temporary?) complexity of stress states that could conceivably result.

Process implications

The progressive activation of bedding-parallel slip surfaces in flexural slip folds is mechanically intriguing. Why does the slip localize onto only *some* surfaces? And why does a hierarchy of slip develop? The following comments set out a conceptual framework for a subsequent phase of analysis and simulation designed to address these questions.

The activation of a new slip surface within a previous mechanical unit must mean that the development of that slip horizon is energetically favoured over other events, such as continued development of the former pattern of bending strains. Slip on inter-layer surfaces is taken to be a frictional process; therefore, the initiation of slip means that the shear stress/normal stress ratio exceeds the criteria that bound 'stable' states of stress. The orientation of the stress trajectories in a flexed unit (Fig. 2) is compatible with this requirement, but the shear/normal stress ratio varies considerably along any given virtual surface within an existing mechanical unit (Cooke *et al.* 1998). It is *possible* that slip is initiated at some location, and conditions favourable for its propagation develop as the stress state is altered in response to the slip, but this possibility seems unlikely to us, since the greatest number of slip surfaces (and hence, mechanical units) is developed in the high-curvature areas of some of the folds we have studied, and the stress trajectories in these sites are expected to be more nearly normal to layering. This observation highlights another difference between our model and those developed by previous workers: the crestal
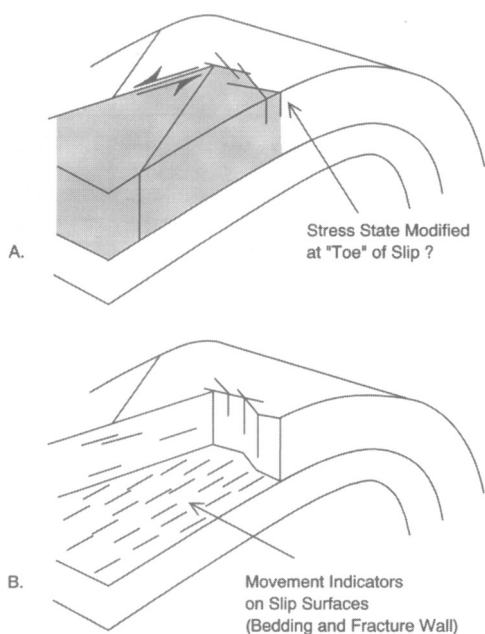
(or trough) regions of folds are often assumed to be pin lines, but the concentration of slip surfaces in these sites suggests that further analysis of this assumption may be necessary.

Another possibility to consider is that fluid-pressure transients facilitate the localization of 'frictional' sliding. Ge & Garven (1994) illustrate this process at a large scale in their numerical analysis of thrust motion (see also Price & Cosgrove (1990) for a discussion of these ideas with respect to folding). It could be that such non-linear (feedback) effects contribute to the explanation of the hierarchical patterns of flexural slip, but the action of multiple slip horizons in close spatial proximity implies that the fluid pressures (and effective stresses) probably vary only slightly from point to point in a fold, especially as there may well be a connecting network of developing fractures. Feedback may be relevant in the sense that slip, abetted by locally anomalous fluid pressure, may alter the porosity/permeability (poro-perm) state of the rock sequence, and that alteration might subsequently localize the mechanical effects of the fluids. This view suggests that, if fluids are involved, they cannot be the only explanation, but must act in concert with other mechanical processes.

Comparison of models

In the model we have described here, a layered sequence is, during flexure, divided into mechanical units by active bedding-plane slip. Each of the mechanical units develops a bending stress state (plus, possibly, others which are more complicated), with 'bending' fractures (Types 3a and 3b) reflecting the small strains. In the fold limbs, bedding-plane slip directly generates other fracture sets (Fig. 4C), and 'patchy' bedding-plane slip events throughout the flexure lead to Types 1 and 2 fracture assemblages. Progressive folding, with the creation of additional mechanical units, leads to considerable overprinting of fracture fabrics.

It is fair to ask how this model compares with previous ideas. If Types 1 and 2 fractures are not directly associated with bending (as we suggest), then we need not address them in our comparison (since they are distinctly associated with 3D strain, and it is not possible to consider them in relation to two-dimensional models). But we must assess how the 'bending' fractures (Types 3a and 3b) and the 'limb' fractures (Fig. 4C) relate to the TLS model, the flexural-flow model and to combination models.

Types 3a and 3b fractures indicate strains which are rather like the strains in the crest and trough regions of the TLS model. However, a significant difference is that the TLS model predicts that the neutral surface lies *above* the mid-point of the layer (in the antiform), but both the bending stress state (Fig. 2) and observed patterns of fractures indicate that the local neutral point is offset low in the beam. So, although there may be a superficial resemblance between 'bending' fractures and the TLS model, there are important differences in the hinge areas of a flexure. Further differences are found in the limbs: our model predicts strain ellipses with inclined axes at the locations where the TLS model predicts no strain. On these grounds, we suggest that the TLS model is inappropriate for upper-crustal flexures, even at the small scale.

The flexural-flow model predicts no significant strain in the hinge areas (if bulk shortening is removed, and many upper-crustal flexures will have minimal or no such bulk shortening) in contrast to the clear evidence of bending deformation we have described. However, the limbs of the flexural-flow model indicate strains that are similar to those described here. Thus, there is an element from the flexural-flow model which is compatible with the geometries we have described.

A flexural model in which a composite multilayer (Biot 1965) experiences relative slip between the competent layers is described by Hudleston et al. (1996). These authors state that competent layers develop TLS and incompetent layers exhibit simple shear (which, in the limit, becomes discrete bedding-plane slip). They state that this composite model tends toward the flexural-slip model as the thickness of the incompetent layers decreases. The predicted strain state within a 'classic' flexural-slip model (Ramsay & Huber 1987, Fig 21.1) has not been developed from the same kinematic approach as is the case for the TLS and flexural-flow models, but if we accept the argument put forward by Hudleston et al. (1996), we can infer that the pattern of strain in the 'classic' flexural-slip model is as they suggest: layers alternating between TLS and simple shear, or layers with TLS bounded by bedding-plane slip *where the strains are similar to the flexural-flow model* (see also Tanner (1989, p. 652) for comments on modifications due to simple shear of the stiff layers). The pattern of strain in the flexural-flow model is not the same as the pattern of strain that we have described here. However, the kinematics of our flexures seem to be what is embodied in the flexural-slip notion, and so we must conclude that the strain patterns we have described are those which appropriately describe the flexural-slip model.

Implications for reservoir management

The preceding discussion has emphasized the mechanical development of fold-associated strains (discontinuities in the form of fractures), and their partitioning, as the folding proceeds. We now turn our attention to the implications of a hierarchy of mechanical units for typical petroleum reservoirs.

Stochastic distribution of fractures in folds?

The view that faults form in scaled arrays such that a power-law distribution provides a method to predict the intensities of 'all' fractures through a region, based on data from sub-sets of the population, is primarily the work of the Fault Analysis Group at Liverpool University (Walsh & Watterson 1989; Walsh *et al.* 1991; Gillespie *et al.* 1993). This idea has gained considerable popularity, and is now in widespread use (Yielding *et al.* 1996). However, scale limitations prevent definitive tests of this hypothesis, and some studies emphasize the significance of real gaps in the distribution (Watterson *et al.* 1995). We suggest that flexural-slip folding of layered rock sequences may be part of the explanation for these discrepancies (Fig. 10).

According to the model developed in this paper, flexural-slip fractures are contained *within* their causative mechanical units. Bedding-normal fractures (such as the Type 1 assemblage) may be very long, but they will not be very tall, since they are bounded by the slip surfaces active at the time of their formation (these surfaces define the mechanical unit whose deformation state controls the fracture locations). For example, Tanner (1992*b*) describes quartz-filled extensional veins linked to fibred veins formed on bedding-plane slip surfaces in chevron-folded turbidite sequences; these extensional
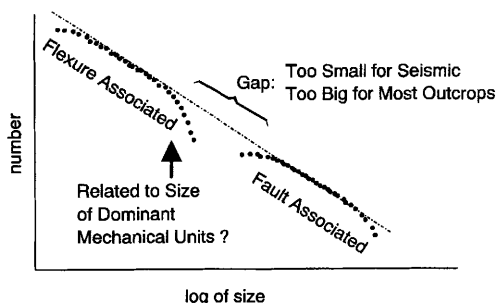
Fig. 10. Hypothetical size–frequency distribution of faults/fractures showing a 'gap' (after Watterson *et al.* 1995). Is the gap 'real'? Is it related to flexural control? See text for explanation.

veins are the result of strains within the mechanical units developed during folding, and do not cross the mechanical-unit boundaries (slip surfaces). Because of this control, the aspect ratios of fold-associated fractures are more pronounced than is usually assumed to be the case where fractures are viewed as being associated with faulting or regional strain (Walsh & Watterson 1989). Fold-associated fractures are likely to have approximately rectangular shapes, rather than elliptical ones, and their length/height ratios may be extreme. However, their distribution can be stochastic within their controlling mechanical unit. If fold-associated fractures are an important element in a reservoir simulation, then the geometrical relationship between fractures and slip horizons needs to be considered, as does the issue of the size and shape of typical fractures.

The flexural-slip process results in the partitioning of strains into layer-delimited domains (Fig. 11). Within each mechanical unit, fracture strains vary with structural position: differences will occur between the top and bottom of the mechanical unit; strains will depend on the
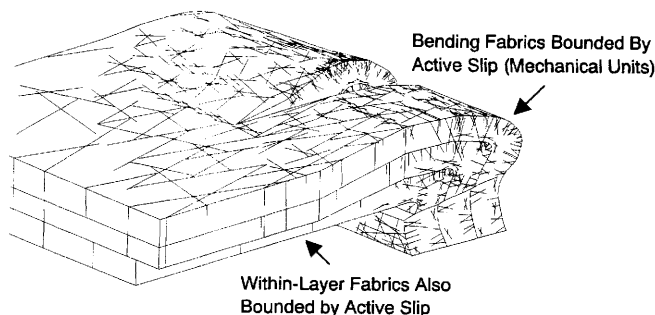
Fig. 11. Distribution of fractures in typical asymmetric anticline illustrating strain partitioning associated with mechanical units and layer-delimiting of fractures (after Lewis & Couples 1993).

amount of curvature; different fracture assemblages characterize 'planar' limbs (Type 1 and others) versus hinges (Types 3a and b); and lithologic differences between layers may result in distinct modes of fracture (e.g. compactant versus constant-volume versus dilatant). The spatial variation of such strain domains is predictable, but, within domains, fractures may well occur in stochastic distributions. If the lithostratigraphic succession at any site consists of dominant units whose properties and thicknesses exert an overriding control on the development of flexural slip (that is, they control the distribution of the low-order mechanical units), then there may well be size 'gaps' in the power-law distributions of the resulting fractures. Where such a gap occurs near the top of the mesoscale portion of the data, and below the seismic resolution, then the resulting distribution might be very like that illustrated in Fig. 10.

Petrophysical effects of fold-associated fractures

The orientations of fold-associated fractures are related to the structural position, and distribution, of mechanical units; these latter are themselves functions of, at least, the structural position in a flexure, and the lithological succession. Whereas the causes of some of the fracture sets remain unclear (see above), the likely fracture patterns are known from empirical studies. In principle, then, the fracture *patterns* of folded rocks can be predicted. Moreover, the extent of fracture surfaces, and particularly the relationship between fractures and bedding-parallel slip horizons, can be specified. Added to this knowledge, the intensities of the fractures can be estimated from information on the shape of the fold, e.g. curvature (see Lisle & Robinson 1995; Stewart & Podolski 1998), and from knowledge of the rheology of the rocks involved (Stearns & Friedman 1972; Nelson & Handin 1977; Aydin & Johnson 1983; Antonellini *et al.* 1994; Knipe 1992; Edwards *et al.* 1993; D'Onfro *et al.* 1994; Crawford 1998; Gabrielsen *et al.* 1998; Gibson 1998; Knipe *et al.* 1997). Combining these aspects provides a means to derive a probable distribution for the fractures in a fold, and their petrophysical characteristics.

How is this depiction to be used in predicting reservoir response? The understanding summarized in the preceding paragraphs permits the creation of a digital fracture network patterned after the geometry of the fold, and perhaps conditioned by *in situ* observations of estimates

arising from other approaches (for example, curvature). The petrophysical properties of individual fracture sets can be derived from experiments, or estimates of these parameters can be made on the basis of theories accounting for volumetric strain and permeability change related to plastic yielding (D'Onfro *et al.* 1994; Couples & Lewis 1997). Scale-up procedures (Begg *et al.* 1989; Lake *et al.* 1990) for such a model are feasible (Manzocchi *et al.* 1998). Network theory (Odling 1992; Cowie *et al.* 1993) is another approach that may hold promise for such complex distributions.

However, most of the research on scaling that has been undertaken thus far has been at best two-dimensional, whereas the fracture arrays in flexural-slip folds are certainly fully three-dimensional. Even for the work now being described on 3D scale-up and simulations (e.g. Watterson *et al.* 1995; Walsh *et al.* 1998), the fracture patterns are primarily of a single set. We draw the conclusion that there is a significant gap between present modelling work, and the view on fold-associated fractures presented here.

Bedding-parallel slip as a sealing mechanism?

We have emphasized the impact of fractures on the bulk petrophysical characteristics of folded rock sequences. Another issue that needs to be addressed is the potential for localized petrophysical alterations (Pitman 1981; Knipe 1992; Antonellini & Aydin 1994; Knipe *et al.* 1997) associated with bedding-parallel slip horizons. Deformation on or along these slip zones can occur in such a fashion that porosity and permeability are substantially reduced (Lewis & Couples 1993). This poro-perm reduction is especially likely if there are small amounts of clays in the rocks (Gibson 1998), which may be a situation common at bedding-parallel slip horizons: the presence of clay, which presumably is important in creating a stratigraphic 'break', could be 'the' factor that makes these particular interfaces 'special' for the localization of slip. If the poro-perm of the rock is reduced in slip zones, it may also be true that entry pressures are raised. In such cases, flexural slip will not only be responsible for determining the distribution of strain within a sequence, but the slip zones themselves will function as flow barriers or baffles in a reservoir. Slip surfaces could, then, conceivably function as a trapping mechanism, although their recognition in such a role might be difficult to distinguish against the normal view of stratigraphically caused trapping.

Conclusions

Flexural-slip folding divides a stratigraphic succession into an evolving hierarchy of mechanical units. These each develop an internal array of bending strains. A complex distribution of strains is created in each unit, both as a result of it being bounded by bedding-parallel slip surfaces, and because of overprinting of earlier strains as new mechanical units are formed. These concepts arise from field observations, but they are supported by the results of physical and numerical modelling.

The work reported here leads to three structural conclusions, and three conclusions directly related to reservoir management.

(1) During upper-crustal folding of layered sequences, slip is activated on only some bedding interfaces, and the slip is accompanied by new deformation patterns (fracture assemblages) which are contained within mechanical units defined by the bedding-plane slip horizons. A new research effort needs to address the concept of competition of mechanical processes: the continuation of one bending event versus the creation of new mechanical units.

(2) The strains developed during bending differ considerably from those predicted by existing folding models. TLS and flexural-flow models are not appropriate for the analysis of upper-crustal structures of the type reported here. The patterns of fold-associated strain described in this paper should become the standard flexural-slip fold model, supplanting previous notions which have been only loosely derived.

(3) The ubiquitous Type 1 fracture assemblage (and its related Type 2 assemblage (Stearns (1967)) may be related to dynamic and localized bedding-plane slip, and possibly to the action of mobile fluids. New multi-physics simulations are needed to address the mode of formation of these assemblages.

(4) Fold-associated fractures are not distributed uniformly through rock volumes, but instead they are distinctly layer-bound, with rules defining intersections, aspect ratios and patterns. There may, however, still be a power-law relationship for fracturing *within* the mechanical units created by slip.

(5) Fracture arrays associated with flexural-slip folding are quite complex, and the complexity may exceed our present ability to perform useful simulations.

(6) Bedding-plane slip surfaces may function as flow barriers. They certainly function to limit the extent of fractures.

The paradigm of folding presented in this paper, and the ramifications that arise from it, open an abundance of new research opportunities.

References

AMEEN, M. S. 1992. Strain pattern in the Purbeck-Isle of Wight monocline: a case study of folding due to dip-slip fault in the basement. *In*: BARTHOLOMEW, M. J., HYNDMAN, D. W., MOGK, D. W. & MASON, R. (eds) *Basement Tectonics 8: Characterization and Comparison of Ancient and Mesozoic Continental Margins.* Kluwer, Dordrecht, 559–578.

ANTONELLINI, M. A. & AYDIN, A. 1994. Effect of faulting on fluid flow in porous sandstones: petrophysical properties. *AAPG Bulletin*, **78**, 335–377.

——, —— & POLLARD, D. D. 1994. Microstructure of deformation bands in porous sandstones at Arches National Park, Utah. *Journal of Structural Geology*, **16**, 941–959.

AYDIN, A. & JOHNSON, A. M. 1983. Analysis of faulting in porous sandstones. *Journal of Structural Geology*, **5**, 19–31.

—— & RECHES, Z. 1982. Number and orientation of fault sets in the field and in experiments. *Geology*, **10**, 107–112.

BAYLY, B. 1992. *Mechanics in Structural Geology.* Springer, New York.

BEGG, S. H., CARTER, R. R. & DRANFIELD, P. 1989. Assigning effective values to simulator grid block parameters for heterogeneous reservoirs. *SPE Reservoir Engineering*, **4**, 455–463.

BEHZADI, H. & DUBEY, A. K. 1980. Variation of interlayer slip in space and time during flexural folding. *Journal of Structural Geology*, **2**, 453–456.

BILLINGS, M. P. 1972. *Structural Geology*, 3rd edition. Prentice-Hall, Englewood Cliffs.

BIOT, M. A. 1965. *Mechanics of Incremental Deformations.* Wiley, New York.

BROWN, W. G. 1988. Deformational style of Laramide uplifts in the Wyoming foreland. *In*: SCHMIDT, C. J. & PERRY, W. J. Jr. (eds) *Interaction of the Rocky Mountains Foreland and the Cordilleran Thrust Belt.* Geological Society of America, Memoir, **171**, 1–25.

BUSK, H. G. 1929. *Earth Flexures: their Geometries and their Representation and Analysis in Geological Section with Special Reference to the Problem of Oil Finding.* Cambridge University Press.

CHAPPLE, W. M. & SPANG, J. H. 1974. Significance of layer-parallel slip during folding of layered sedimentary rocks. *Geological Society of America Bulletin*, **85**, 1523–1534.

CLOOS, H. & MARTIN, H. 1932. Der gang einer Falte. *Fortschr. Geologische Paleontologische Berlin*, **11**, 74.

COOKE, M. & POLLARD, D. D. 1994. Development of bedding plane faults and fracture localization in a flexed multilayer: a numerical model. *In*: NELSON & LAUBACH (eds) *Proceedings of the First North American Rock Mechanics Symposium*. Balkema, Rotterdam, 131–138.

—— & ——1996. Bedding plane slip in the initial stages of fault-related folding. *Journal of Structural Geology*,

——, MOLLEMA, P., POLLARD, D. D. & AYDIN, A. 1998. Joint localization in folds over basement faults: results from numerical modelling and evidence from Kaibab Monocline, Utah, USA. *In*: COSGROVE, J. (ed.) *Forced (Drape) Folds and Associated Fractures*. Geological Society of London, Special Publication, in press.

COUPLES, G. D. 1977. Stress and shear fracture (fault) trajectories resulting from a suite of complicated boundary conditions with applications to the Wind River Mountains. *Pure and Applied Geophysics*, **115**, 113–133.

——1986. *Kinematic and dynamic considerations in the forced folding process as studied in the laboratory (experimental models) and in the field (Rattlesnake Mountain, Wyoming)*. Ph.D dissertation, Texas A&M University, 193 pp.

——1998. Rattlesnake Mountain anticline: a neo-classic forced fold in NW Wyoming. *In*: COSGROVE, J. (ed.) *Forced (Drape) Folds and Associated Fractures*. Geological Society of London, Special Publication, in press.

—— & LAGESON, D. R. 1985. Penrose Conference report: Laramide tectonics of the Rocky Mountain foreland. *Geology*, **13**, 311.

—— & LEWIS, H. 1998. Effects of interlayer slip in model forced folds. *In*: COSGROVE, J. H. (ed.) *Forced (Drape) Folds and Associated Fractures*. Geological Society of London, Special Publication, in press.

—— & ——1997. Critical state approach for poroplastic materials under effective stress conditions. *Terra Nova*, **9**, 644.

——, —— & TANNER, P. W. G. 1996. Hierarchical development of interlayer slip in flexed multilayers. *In*: BICANIC, N. (ed.) *Fourth Annual Meeting, Association for Computational Mechanics in Engineering – UK*, Glasgow, January, 53–56.

——, STEARNS, D. W. & HANDIN, J. W. 1994. Kinematics of experimental forced folds and their relevance to cross-section balancing. *Tectonophysics*, **233**, 193–213.

COWIE, P. A., VANNESTE, C. & SORNETTE, D. 1993. Statistical physics model for the spacio-temporal evolution of faults. *Journal of Geophysical Research*, **98**, 21809–21821.

CRAWFORD, B. R. 1998. Experimental fault sealing: shear band permeability dependency on cataclastic fault gouge characteristics. *This volume*.

CURRIE, J. B., PATNODE, H. W. & TRUMP, R. P. 1962. Development of folds in sedimentary strata. *Geological Society of America Bulletin*, **73**, 655–674.

DE SITTER, L. U. 1958. Boudins and parasitic folds in relation to cleavage and folding. *Geologie Mijnbouw*, **20**, 277–288.

D'ONFRO, P., FAHY, M. F. & RIZER, W. 1994. Geomechanical model for fault sealing in sandstone reservoirs. *AAPG Annual Convention Official Program*, **3**, 130–131.

DONATH, F. A. & PARKER, R. B. 1964. Folds and folding. *Geological Society of America Bulletin*, **75**, 45–62.

DUBEY, A. K. & COBBOLD, P. R. 1977. Noncylindrical flexural slip folds in nature and experiment. *Tectonophysics*, **38**, 223–239.

EDWARDS, H. E., BECKER, A. D. & HOWELL, J. A. 1993. Compartmentalisation of an aeolian sandstone by structural heterogeneities: Permo-Triassic Hopeman Sandstone, Moray Firth, Scotland. *In*: NORTH, C. P. & PROSSER, J. (eds) *Characterisation of Fluvial and Aeolian Reservoirs*. Geological Society, London, Special Publication, **73**, 339–365.

FITCHES, W. R., CAVE, R., CRAIG, J. & MALTMAN, A. J. 1990. The flexural-slip mechanism: Discussion. *Journal of Structural Geology*, **12**, 1081–1087.

FLETCHER, R. C. 1979. The shape of single-layer folds at small but finite amplitude. *Tectonophysics*, **60**, 77–87.

FRIEDMAN, M. & SOWERS, G. M. 1970. Petrofabrics: a critical review. *Canadian Journal of Earth Sciences*, **7**, 477–497.

——, HANDIN, J., LOGAN, J. M., MIN, K. D. & STEARNS, D. W. 1976a. Experimental folding of rocks under confining pressure: Part III. Faulted drape folds in multilithologic layered specimens. *Geological Society of America Bulletin*, **87**, 1049–1066.

——, HUGMAN, R. H.H. & HANDIN, J. 1980. Experimental folding of rocks under confining pressure, Part VIII – Forced folding of unconsolidated sand and of lubricated layers of limestone and sandstone. *Geological Society of America Bulletin*, **91**, 307–312.

——, TEUFEL, L. W. & MORSE, J. D. 1976b. Strain and stress analyses from calcite twin lamellae in experimental buckles and faulted drape-folds. *Philosophical Transactions of the Royal Society of London*, **A283**, 87–107.

GABRIELSEN, R. H., AARLAND, R-K. & ALSAKER, E. 1998. Identification and spatial distribution of fractures in porous, siliciclastic sediments. *This volume*.

GANGI, A. F., MIN, K. D. & LOGAN, J. M. 1977. Experimental folding of rocks under confining pressure: Part IV. Theoretical analysis of faulted drape folds. *Tectonophysics*, **42**, 227–260.

GE, S. & GARVEN, G. 1994. A theoretical model for thrust-induced deep groundwater expulsion with application to the Canadian Rocky Mountains. *Journal of Geophysical Research*, **99**, 13851–13868.

GHOSH, S. K. 1968. Experiments on buckling of multilayers which permit interlayer gliding. *Tectonophysics*, **6**, 207–249.

GIBSON, R. G. 1998. Physical character and fluid-flow properties of sandstone-derived fault zones. *This volume.*

GILLESPIE, P. A., HOWARD, C. B., WALSH, J. J. & WATTERSON, J. 1993. Measurement and characteristics of spatial distributions of fractures. *Tectonophysics,* 226, 113–141.

GROSHONG, R. H. 1975. Strain, fractures and pressure solution in natural single-layer folds. *Geological Society of America Bulletin,* **86**, 1363–1376.

HAFNER, W. 1951. Stress distribution and faulting. *Geological Society of America Bulletin,* **62**, 373–398.

HANCOCK, P. L. 1985. Brittle microtectonics: principles and practice. *Journal of Structural Geology,* 7, 437–457.

HANDIN, J., FRIEDMAN, M., LOGAN, J. M., PATTISON, L. J. & SWOLFS, H. S. 1972. *Experimental folding of rocks under confining pressure: Buckling of single-layer rock beams.* American Geophysical Union, Monograph **16**, 1–28.

HARA, I., UCHIBAYASHI, S., YOKOTA, Y., UMEMURE, H. & ODA, M. 1968. Geometry and internals structures of flexural folds (I): Folding of a single competent layer enclosed in thick incompetent layer. *Hiroshima University Journal of Science, series C,* **6**, 51–113.

HIGGS, W. G., WILLIAMS, G. D. & POWELL, C. M. 1991. Evidence for flexural shear folding associated with extensional faults. *Geological Society of America Bulletin,* **103**, 710–717.

HILLS, E. S. 1972. *Elements of Structural Geology,* Second edition. Chapman and Hall, London.

HUDLESTON, P. J. 1973. An analysis of single-layer folds developed experimentally in viscous media. *Tectonophysics,* **16**, 189–214.

—— & LAN, L. 1993. Information from fold shapes. *Journal of Structural Geology,* **15**, 253–264.

——, TREAGUS, S. H. & LAN, L. 1996. Flexural flow folding: does it occur in nature? *Geology,* **24**, 203–206.

HUTCHINSON, J. N. 1995. The significance of tectonically produced pre-existing shears. *11th European Conference on Soil Mechanics and Foundation Engineering.* Danish Geotechnical Society, *DGF Bulletin,* **4**, 59–68.

JAMISON, W. R. & STEARNS, D. W. 1982. Tectonic deformation of Wingate Sandstone, Colorado National Monument. *AAPG Bulletin,* **66**, 2584–2608.

JOHNSON, A. M. 1977. *Styles of Folding: Mechanics and Mechanisms of Natural Elastic Materials.* Elsevier.

JOHNSON, A. M. & PAGE, B. M. 1976. A theory of concentric, kink and sinusoidal folding and of monoclinal flexuring of compressible elastic multilayers. VII. Development of folds within Huasna suncline, San Luis Obispo County, California. *Tectonophysics,* **33**, 97–143.

KNIPE, R. J. 1992. Faulting processes and fault seals. *In:* LARSEN, R. M. (ed.) *Structural and Tectonic Modelling and its Application to Petroleum Geology.* NPT Special Publication **1**, 325–343.

——, FISHER, Q. J., JONES, G., *et al.* 1997. Fault seal analysis: successful methodologies, application, and future directions. *In: Hydrocarbon Seals – Importance for Exploration and Production.* Norwegian Petroleum Society, Special Publication, in press.

KUENEN, Ph. H. & DE SITTER, L. U. 1938. Experimental investigation into the mechanism of folding. *Leidsche Geol. Meded.,* **10**, 217–239.

LAKE, L. W., KASAP, E. & SHOOK, M. 1990. Pseudofunctions – the key to practical use for reservoir description. *In:* BULLER, A. T., BERG, E., HJELMLAND, O., KLEPPE, J., TORSÆTER, O. & AASEN, J. O. (eds.) *North Sea Oil and Gas Reservoirs II.* Norwegian Institute of Technology, Graham, and Trottman, London, 297–308.

LAN, L. & HUDLESTON, P. J. 1995. Strain distribution in single-layer buckle folds in non-linear materials, *Journal of Structural Geology,* **17**, 727–738.

LEWIS, H. & COUPLES, G. D. 1993. Production evidence for geological heterogeneities in the Anschutz Ranch East field, western USA. *In:* NORTH, C. P. & PROSSER, J. (eds) *Characterisation of Fluvial and Aeolian Reservoirs.* Geological Society, London, Special Publication **73**, 321–338.

LISLE, R. J. & ROBINSON, J. M. 1995. The Mohr circle for curvature and its application to fold description. *Journal of Structural Geology,* **17**, 739–750.

MANZOCCHI, T., RINGROSE, P. S. & UNDERHILL, J. R. 1998. Flow through fault systems in high porosity sandstones. *This volume.*

MEANS, W. D. 1989. Stretching faults. *Geology,* **17**, 893–896.

NARR, W. & SUPPE, J. 1994. Kinematics of basement-involved compressive structures. *American Journal of Science,* **294**, 802–860.

NELSON, R. A. 1991. Multi-scale natural fracture development and its effect on reservoir modeling (abstract). *AAPG Bulletin,* **75**, 645.

—— & HANDIN, J. W. 1977. Experimental study of fracture permeability in porous rocks. *AAPG Bulletin,* **61**, 227–236.

ODLING, N. E. 1992. Network properties of a two dimensional natural fracture pattern. *Pure and Applied Geophysics,* **138**, 95–114.

PATTON, T. L., LOGAN, J. M. & FRIEDMAN, M. 1997. Experimentally generated normal faults in single- and multilayer linestone beams at confining pressure. *Tectonophysics* in press.

PITMAN, E. D. 1981. Effect of fault-related granulation on porosity and permeability of quartz sandstones, Simpson Group (Ordovician), Oklahoma. *AAPG Bulletin,* **65**, 2381–2387.

PRICE, N. J. 1967. *Fault and Joint Development in Brittle and Semi-brittle Rock.* Pergamon, New York.

PRICE, N. J. & COSGROVE, J. W. 1990. *Analysis of Geological Structures.* Cambridge University Press.

PRICE, R. A. 1988. The mechanical paradox of large overthrusts. *Geological Society of America Bulletin,* **100**, 1898–1908.

RAMBERG, H. 1961. Relationship between concentric longitudinal strain and concentric shearing strain during folding of homogeneous sheets of rocks. *American Journal of Science,* **259**, 382–390.

RAMSAY, J. G. 1967. *Folding and Fracturing of Rocks.* McGraw-Hill.

——1974. Development of chevron folds. *Geological Society of America Bulletin,* **85**, 1741–1754.

—— & HUBER, M. I. 1987. *The Techniques of Modern Structural Geology. Volume 2. Folds and Fractures.* Academic, New York.

RECHES, Z. 1978. Analysis of faulting in three-dimensional strain field. *Tectonophysics,* **47**, 109–129.

RODGERS, J. 1987. Chains of basement uplifts within cratons marginal to orogenic belts. *American Journal of Science,* **287**, 661–692.

STEARNS, D. W. 1967. Certain aspects of fracture in naturally deformed rocks. *In*: RIECKER, R. E. (ed.) *Rock Mechanics Seminar.* US Air Force Cambridge Research Laboratories, Contribution **AD 669375**, 97–118.

——1971. Mechanisms of drape folding in the Wyoming province. *Wyoming Geological Association, 23rd Annual Field Conference Guidebook,* 125–144.

——1978. Faulting and forced folding in the Rocky Mountains foreland. *In*: MATTHEWS, V. (ed.), *Laramide Folding Associated with Basement Block Faulting in the Western United States.* Geological Society of America, Memoir **151**, 1–37.

—— & FRIEDMAN, M. 1972. *Reservoirs in Fractured Rock. AAPG,* Memoir, **16**, 82–106.

——, COUPLES, G. D., JAMISON, W. R. & MORSE, J. D. 1981. Understanding of faulting in the shallow crust: the contributions of selected experimental and theoretical studies. *In*: CARTER, N. L., FRIEDMAN, M., LOGAN, J. M. & STEARNS, D. W. (eds) *Mechanical Behavior of Crustal Rocks (the Handin Volume).* American Geophysical Union, Monograph **24**, 215–229.

STEWART, S. A. & PODOLSKI, R. 1998. Curvature analysis of gridded geological surfaces. *This volume.*

TANNER, P. W. G. 1989. The flexural-slip mechanism. *Journal of Structural Geology,* **11**, 635–655.

——1990. The flexural-slip mechanism: Reply. *Journal of Structural Geology,* **12**, 1081–1087.

——1992*a*. Morphology and geometry of duplexes formed during flexural-slip folding. *Journal of Structural Geology,* **14**, 1173–1192.

——1992*b*. Vein morphology, host rock deformation and the origin of fabrics of echelon mineral veins: Discussion. *Journal of Structural Geology,* **14**, 273–275.

WALSH, J. & WATTERSON, J. 1989. Displacements gradients on fault surfaces. *Journal of Structural Geology,* **11**, 307–316.

——, —— & YIELDING, G. 1991. The importance of small-scale faulting in regional extension. *Nature,* **351**, 391–393.

——, ——, HEATH, A., GILLESPIE, P. A. G. & CHILDS, C. 1998. Assessment of the effects of sub-seismic faults on bulk permeabilities of reservoir sequences. *This volume.*

WATTERSON, J., HEATH, A., KNIGHT, S., FLINT, S., WALSH, J., CHILDS, C. & GILLESPIE, P. A. 1995. Estimation of the effects of sub-seismic faults on effective permeabilities of reservoir sequences. *In*: *Structural Geology in Reservoir Characterisation and Field Development.* Imperial College, London, March, 43.

WEINBERG, D. M. 1979. Experimental folding of rocks under confining pressure, Part VII – Partially scaled models of drape folds. *Tectonophysics,* **54**, 1–24.

YIELDING, G., NEEDHAM, T. & JONES, H. 1996. Sampling of fault populations using sub-surface data: a review. *Journal of Structural Geology,* **18**, 135–146.

Fracture distribution in faulted basement blocks: Gulf of Suez, Egypt

AMGAD I. YOUNES[1,*], TERRY ENGELDER[1] & WILLIAM BOSWORTH[2]

[1] *Department of Geosciences, The Pennsylvania State University, University Park, PA 16802, USA*
[2] *Marathon Petroleum Egypt Ltd, PO Box 52, Maadi, Cairo, Egypt*

Abstract: Fractures in basement rocks of Gebel El Zeit and Esh El Mallaha fault blocks, Egypt, occur in three nearly orthogonal sets: a SE-dipping, cross-rift set that parallels ENE faults and dykes; a SW-dipping set sub-parallel to bedding in overlying clastic rocks; and a NE-dipping, rift-parallel set that parallels the rift-border faults. Restoration to pre-rift orientations puts these sets into vertical, horizontal and vertical attitudes respectively. All fracture sets are present throughout the fault blocks, except for the horizontal set which is absent on the NE side of Gebel El Zeit and in the Nubia Sandstone. Fracture density increases near the top of basement where sheet fracturing is common, near faults, and in and around dykes. The distribution of similar fracture sets is recorded from sub-surface Formation Micro Scanner and Formation Micro Imager logs in the basement of the Ashrafi Oil-field, southern Gulf of Suez. The similarity of the fracture pattern between Gebel El Zeit and the Ashrafi Field suggests that surface fault blocks can be adequate analogues to the sub-surface blocks.

The intersection of sheet and fault-parallel fractures localizes the maximum fracture density at the edges and near the top of the fault blocks. Block faulting and subsequent depth of erosion govern the distribution of fractures within the blocks. Block rotation during rifting relocated the maximum fracture density at an upper corner or structural crest, whereas block faulting without rotation maintained the maximum fracture density at block edges. In both styles, erosion of an exhumed block removed rocks of high fracture density by eroding the crest in the first case, and by stripping off the sheet fractures in the second. The first style is an analogue for half-graben reservoirs, e.g. the southern Gulf of Suez, while the second style is an analogue for full-graben reservoirs, e.g. the Mekong Basin, southern Vietnam.

Fractured basement reservoirs are promising yet challenging targets for oil exploration and production. Recent discoveries such as the Zeit Bay and Ashrafi Fields in the Gulf of Suez, Egypt, are basement reservoirs that yield as much as 25 000 barrels of oil per day (BOPD). Other promising plays of this type are found in offshore southern Vietnam where the oil column reaches over 3000 feet high in two fields, the White Tiger and Big Bear (Chan *et al.* 1994; Arechev *et al.* 1992). One of the first steps associated with drilling and evaluating fractured basement reservoirs is to define the fracture network since it controls both porosity and permeability. Fractured granite, for example, has a bulk permeability that generally exceeds its intrinsic permeability by several orders of magnitude (Heath 1985; Freeze and Chenry 1987). Hence, data on the location and density of fractures become essential for evaluation of porosity and hydraulic parameters of a basement reservoir.

Although several borehole logging tools (e.g. Formation Micro Scanner (developed by Schlumberger), Fracture Identification Log, and BoreHole TeleViewer (developed by Schlumberger and Mobil) can detect fracture attitude and spacing, other fracture characterization parameters, such as fracture size, are difficult to judge from these tools. In order to construct a set of rules that constrain the extent and geometric relationship among different fracture sets, the reservoir engineer may resort to direct observations in outcrop. Extrapolation of surface fracture data to the sub-surface requires knowledge of how the fracture density and development are affected by differences in fault-block size, attitude, rotation, and depth of erosion.

This study focuses on some of the factors that influence the fracture density in a faulted basement block in Egypt, the Gebel El Zeit block. This rotated fault block along the western side of the Gulf of Suez was selected for its proximity to the offshore Ashrafi Field which is an oil reservoir in fractured basement (Fig. 1). First, we introduce the study area and present fracture data. Then, we present two models for fracture

---

* Present address: Royal Holloway College, University of London, Department of Geology, Egham, Surrey, TW20 0EX, UK
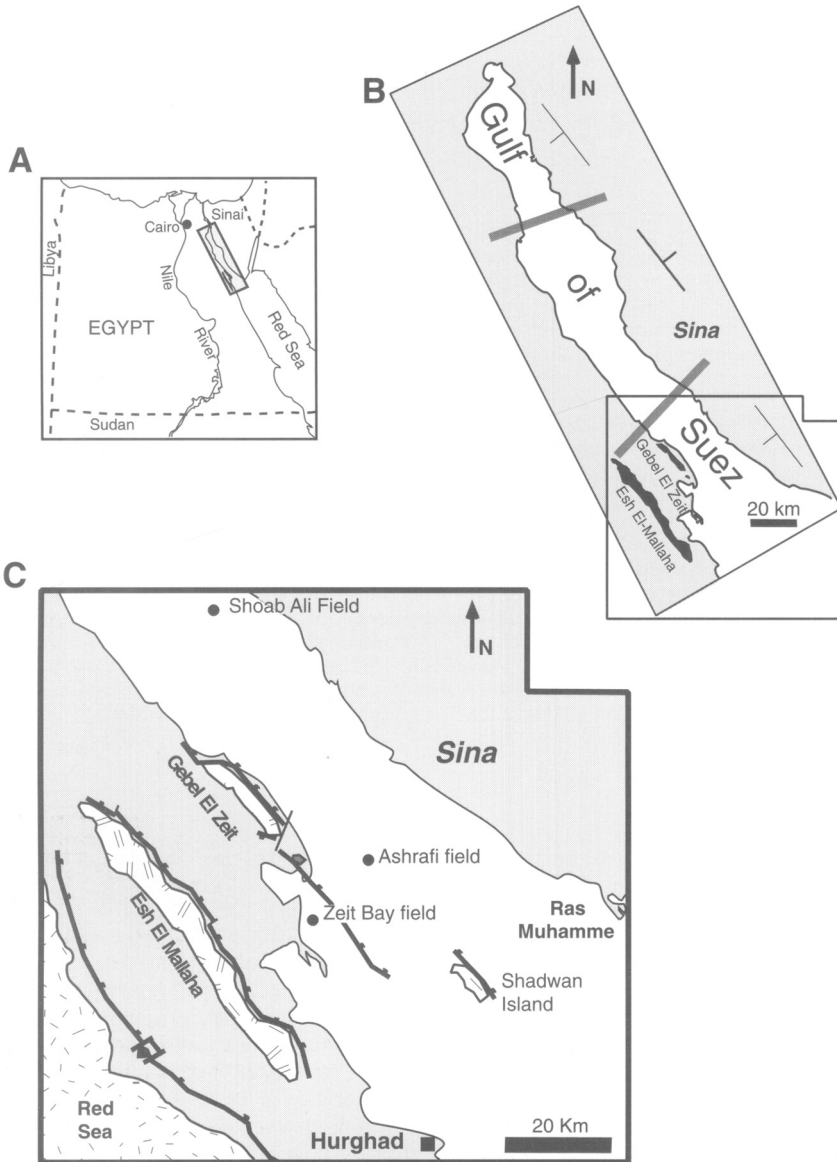
Fig. 1. (A) Location map of the study area. (B) The Gulf of Suez is divided into three half grabens (dip symbols) separated by large transverse fault zones (stripes). (C) The Gebel El Zeit and Esh El Mallaha fault blocks have rotated along faults that dip to the northeast (hachuring is on the downthrown side) exposing basement rocks in the core of the fault blocks (double-line hachuring). At the Gebel El Zeit block, overlying sedimentary cover dips 42° to the southwest at its contact with the basement (see Fig. 5 for detailed map). The Esh El Mallaha block dips only 7–8° to the southwest. The Shoab Ali, Ashrafi and Zeit Bay Fields produce from fractured basement reservoirs.

distribution in faulted basement blocks. We correlate the first model with a sub-surface example, the Ashrafi Field, Egypt, and then suggest a possible sub-surface analogue for the second. Finally, we discuss the significance of the fracture distribution

on basement-rock permeability and reservoir potential.

Throughout the paper we use the term 'fault' to indicate a discontinuity along which significant motion (>0.5 m) took place and/or fault

surface structures are observed (Petit 1987). We use the term 'fracture' to indicate a discontinuity where displacement was not observed and thus the discontinuity can be a joint or faulted joint. A 'joint' is a fracture that opened perpendicular to a discontinuity plane and remained open (Engelder 1982). We refer to fracture rather than joint since the long history of the basement, including multiple rifting and peneplanation, makes it inevitable that some joints have slipped and become faults. Thus, it is difficult to discriminate between a reactivated joint and a discontinuity that started as a fault. Fracture orientations were measured using the right-hand rule.

Geological setting

The Gulf of Suez is a continental rift that extends for 325 km, with a maximum width of 90 km at the northern terminus of the Red Sea. Extension commenced at the southern end of the rift during the lower Miocene. There is a progressive decrease in total extension both towards the north and away from the rift axis. Shoulders of the rift extend into the African continent and are manifest as a series of rift-parallel faults along which several blocks rotated up to 45°, exposing basement-cored fault blocks such as the Gebel El Zeit and Esh El Mallaha fault blocks (Fig. 1).

Basement rocks of the Gebel El Zeit block consist of multiple intrusions of granitic to granodioritic rocks known as the Younger Granite (pink) and the Older Granite (grey), both of which were emplaced during the Precambrian cratonization of the Arabo-Nubian shield (Patton et al. 1994; Stern & Hedge 1985). The Older Granite (610–670 Ma) is a calc-alkaline, orogenic, mesozonal type that may be related to subduction (Stern et al. 1984). Conversely, the Younger Granite represents an anorogenic epizonal type that is related to a magmatic pulse associated with Cambrian rifting (Greenberg 1981). Isotope age dates from the basement exposed along the western side of the Gulf of Suez range between 620 and 570 Ma (Patton et al. 1994; Stern & Menton 1987; Stern & Hedge 1985; Stern et al. 1984; Greenberg 1981). Except for a few Cretaceous granite plutons surrounding Esh El Mallaha (Stern 1995, pers. comm.), no age dates are available for the Esh El Mallaha granite intrusion. However, because this granite intrudes late Proterozoic volcanic rocks, its age is late Proterozoic or younger. Following cratonization, the basement complex was affected by NNW extension as manifested by the formation

of a series of ENE-oriented longitudinal basins in northeastern Egypt, and the simultaneous emplacement of dykes. Dykes occur in swarms oriented ENE with minor populations oriented N–S and WNW (Schurmann 1966), and show a bimodal composition that varies from rhyolite and andesite, to basalt with several textures. In Gebel El Zeit, the ENE dykes are mainly andesitic while those at Esh El Mallaha are mainly rhyolitic and are much less frequent in occurrence.

The age and depositional history of the units directly overlying the basement rocks at Gebel El Zeit are controversial (Fig. 2). For example, the age of the Nubia Sandstone varies from Cambrian or Permian (Perry 1983; Bhattacharyya & Dunn 1986; Allam 1988; Klitzsch & Squyres 1990), to early Cretaceous (Prat et al. 1986; Colletta et al. 1986). Nevertheless, after an early phase of WNW extension with ENE basement rifting, the area was exposed to erosion for long periods followed by the deposition of up to 350 m of Nubia Sandstone. The Nubia Sandstone is overlain by a sequence of marls, shales and fine sands that mark the onset of the mid-Cretaceous transgression. Miocene sediments unconformably overlie the Cretaceous section and are divided into two distinct groups: a lower Miocene clastic series that

Age		Thk	Lithology	Rock unit
CENEOZOIC	Ph-Qr			Sand, gravel, reef
CENEOZOIC	Miocene	240-360 m		Belayim Fm. Hammam Faraun Mmbr.
CENEOZOIC	Miocene	240-360 m		Kareem/Rudeis
CENEOZOIC	Miocene	240-360 m		Nukhul
MEZOZOIC	Cretaceous	0 - 200 m		Matulla/Wata & younger
PALEOZOIC	Cambrian / Permian (?)	260-350 m		Nubia Sst.
				BASEMENT

Fig. 2. Stratigraphic column of Gebel EL Zeit measured at the northern end of Wadi Kabrit.

marks the initiation of rifting (Nukhul, Rudeis and Kareem), and a middle to upper Miocene thick cover of evaporites, representing the post-rifting closure and abandonment.

The Miocene Gulf of Suez rift basin is bounded by two fault sets: a rift-parallel set (310–330°) and a cross-rift set (055–065°). The first set forms oblique- and dip-slip normal faults that are related to block rotation during the rifting of the Gulf of Suez. A left-lateral sense of slip is often recorded in the outcrop, and large ENE faults have a right-stepping arrangement (Bosworth 1995). These two fault sets divide the rift basin into a series of rotated blocks with variable sizes. Two large fault zones transect the Gulf of Suez dividing the rift basin into three dip domains (Moustafa 1976) (Fig. 1). The southern zone passes to the north of Gebel El Zeit, separating it from the structurally distinct area further north where kilometre-scale folds and greater deformation exist. Dyke swarms in the southern Gulf of Suez strike almost parallel to the previous zone. Except for syn-sedimentary folds and minor folds associated with strike-slip motion on ENE faults, no evidence for pervasive folding was observed, and has not been reported in the literature of the Gebel El Zeit area.

Although rotation of both the Gebel El Zeit and Esh El Mallaha blocks is a manifestation of the Gulf of Suez rifting, the timing and rates of exhumation of these blocks are significantly different. Apatite fission tracks show that basement rocks of the Gebel El Zeit block were at least 2–3 km deep during the early Carboniferous whereas rocks of Esh El Mallaha were at the same depth as late as the early Jurassic (Omar *et al.* 1989). The age difference implies that the onset of exhumation at Gebel El Zeit predates that at Esh El Mallaha. Therefore, if rocks of both fault blocks are of the same age, then the amount of uplift and erosion will be considerably different. Most of the present-day relief on the western margin of the Gulf of Suez is due to early Miocene rifting, at approximately 20 Ma (Omar *et al.* 1989).

Data from oil and gas exploration in the Gulf of Suez constrain the rift's structural and stratigraphic styles. A few papers (e.g. El-Shazly *et al.* 1979; Huang & Angelier 1985; Zahran & Ismail 1986) discuss the characteristics and general statistics of fractures around the Gebel El Zeit area. Recently, the discovery of hydrocarbon within fractured basement and the advance of high-resolution resistivity tools that can detect fractures in a borehole has stimulated interest in analysis of fractured basement rock.

Fractured basement of the Gebel El Zeit and Esh El Mallaha fault blocks

The basement rocks of the Gebel El Zeit block were fractured intensely during the ENE (Cambrian) and the NW (Miocene) rifting events (Husseini 1988), and systematic fracture sets were developed approximately parallel to dykes and faults associated with rifting. During rotation accompanying the Miocene rifting event, the Gebel El Zeit and Esh El Mallaha fault blocks tilted to the west by 42° and 8°, respectively. The fault slip and rotation of the Gebel El Zeit block contributed ≥9 km to the 35 km total extension of the Southern Gulf of Suez, whereas the rotation of Esh El Mallaha lead to ≤2 km of extension (Bosworth 1995). The different amounts of extension are reflected in the intensity of fracturing and faulting within the Gebel El Zeit and Esh El Mallaha fault blocks.

In the Gebel El Zeit and Esh El Mallaha blocks, fractures occur in different sets and may have different origins. Identifying the origin of a fracture set largely relies on its pervasiveness, persistence, and orientation relative to larger structures. In this paper, we are concerned only with systematic fracture sets, that is, groups of fractures that are persistent in attitude and character over large areas.

Joint sets typically form as vertical or horizontal discontinuities. Rotation of a fault block will cause a reorientation of joints so that dip changes from a minimum of 0° if joints are perpendicular to the rotation axis, to a maximum equal to the block rotation if joints are parallel to the rotation axis. Joints, or fractures, that are oriented obliquely to the rotation axis will change attitude (strike and dip) by an amount directly proportional to the amount of rotation and the angle between the rotation axis and the fracture strike. The block rotation of the Gebel El Zeit (42°) and Esh El Mallaha (8°) fault blocks illustrates this effect. In the Gebel El Zeit block, three nearly orthogonal fracture sets exist, two of which are affected by block rotation: the first, sheet fractures, show a maximum tilt equivalent to the dip of the overlying Nubia Sandstone beds (42°–45° SW); and the second, a rift-parallel set, dips 69° NE and shows less tilt because it strikes 15°–30° west of the rotation axis (Fig. 3). Only the set that is perpendicular to the rotation axis (and the rift), the cross-rift set, remains sub-vertical, dipping approximately 80° SE (this cross-rift set constitutes the face of outcrop in Fig. 3). In the Esh El Mallaha block, where rotation is only 7–10°, the sheet fracture set retains a sub-horizontal attitude
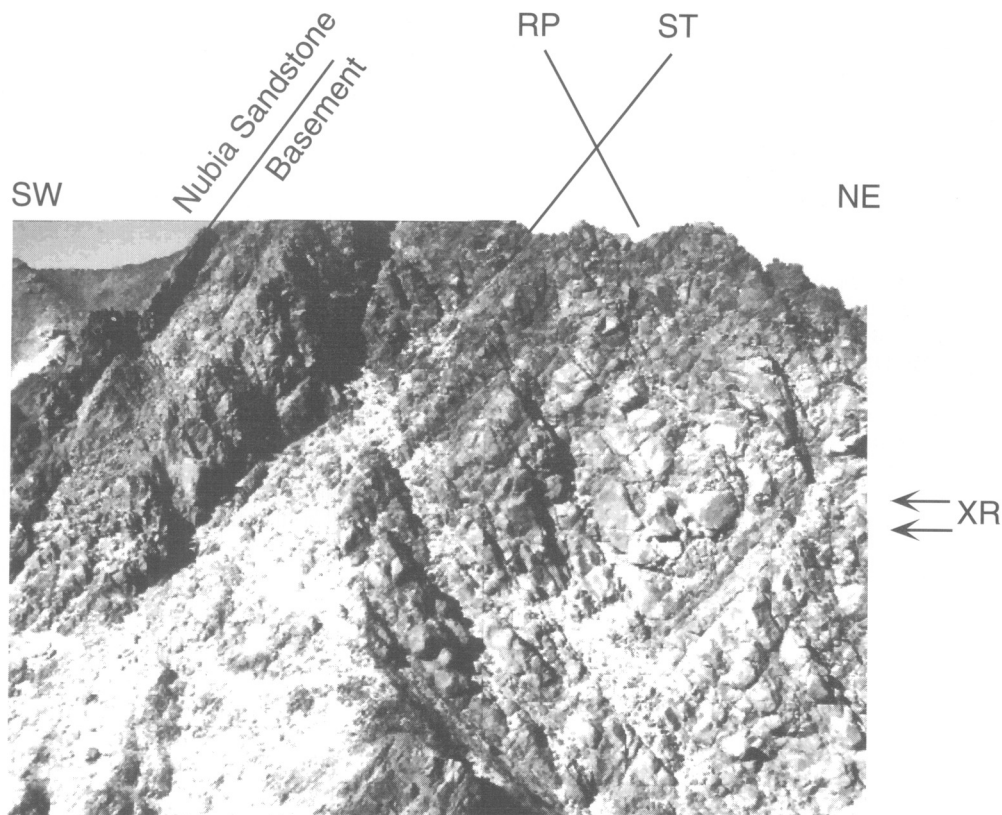
SW Gebel El Zeit

Fig. 3. Photograph showing the three mutually perpendicular fracture sets near the entrance of Wadi Kabrit, Gulf of Suez, looking NW. The sedimentary cover is exposed on the upper left corner of the photograph and dips 42° to the SW. Notice the gradual decrease in fracture density of the bedding- parallel set towards the NE. XR = cross-rift set dipping SE, ST = SW-dipping fracture set, RP = rift-parallel NE-dipping fracture set. The field of view is approximately 35 × 20 m.

and rift-parallel and cross-rift retain vertical to sub-vertical attitudes in agreement with the small rotation amount (Fig. 4).

In addition to the change of attitude by rotation, fractures in the Gebel El Zeit block differ from those at Esh El Mallaha in other aspects. For example, in the Gebel El Zeit block, the cross-rift fractures are the best developed (uniform and persistent), extending up to 15 m in length, and are distinguished by a chlorite coating on fracture walls. The rift-parallel set is less developed and is frequently found as zones lined with vug-filling quartz.

In contrast to the Gebel El Zeit block, cross-rift fractures in the Esh El Mallaha block are less developed whereas rift-parallel fractures are

the best developed showing plumose structures, no fill, and reaching several tens of metres in length (Fig. 4). The sheet fractures can reach over 50 m in length, cut other fractures, and are well-developed just below the base of the Nubia Sandstone (Fig. 3). In the Gebel El Zeit block, the sheet fractures occasionally have a few pockets of vug-filling quartz, slickensides and other fracture-surface structures. On a meso-scopic scale, sheet fractures appear as planar, narrowly spaced fracture zones approximately 10–30 cm thick. The abutting relationships indicate that the rift-parallel set is younger than the sheet and cross-rift sets. The abutting relationship between the cross-rift and sheet fractures is not clear. The youngest set oriented
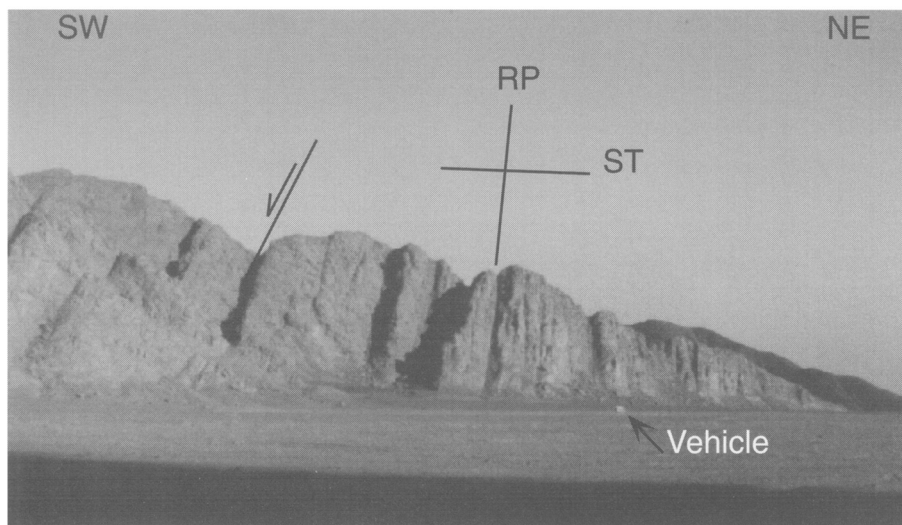
Fig. 4. Photograph of fractures in Esh El Mallaha granite. The large fracture sets are approximately 100 m high, a few metres wide, and trend NW, parallel to the Gulf of Suez. RP = rift-parallel fractures, ST = sheet fractures. Half-arrow indicates the downthrown side of a rift-parallel normal fault. Car is approximately 40 m from outcrop.

NNE has a vector mean strike at 025° and is best developed within the Esh El Mallaha block, but frequently occurs in the Gebel El Zeit block as well. The age relationships of fractures, absolute ages of basement and significance for the structural evolution of the southern Gulf of Suez will be discussed elsewhere.

Field data

Orientation, and other parameters (e.g. spacing, height, length and termination), from over 3000 fractures were systematically measured along scanlines on the eastern and western sides of the Gebel El Zeit fault block (Fig. 5). Lack of pavements on which joints are exposed and inaccessibility of outcrop faces limited our data collection to scanline surveys. Fracture orientation data from the NE side, the SW side, the Nubia Sandstone of the Gebel El Zeit, and the Esh El Mallaha fault blocks are plotted on lower-hemisphere equal-area stereonets as poles to fractures (Fig. 6). On the SW side of the Gebel El Zeit block, the basement carries three sub-orthogonal fracture sets (see also Fig. 3): cross-rift fractures form a northeasterly set with a vector mean strike and dip at 055°/79°, rift-parallel fractures form a northwesterly set with a vector mean at 315°/70°, and sheet fractures constitute a southeasterly set with a vector mean 140°/45° (the right-hand rule is followed throughout the paper) (Fig. 6). On the NE side

of the fault block, and in the Nubia Sandstone, only the cross-rift and the rift-parallel sets exist. Except for a fourth fracture set at 025°/82°, fractures in the basement of the Esh El Mallaha block are similar to those found in basement on the SW side of the Gebel El Zeit. Table 1 summarizes the present-day and restored vector means of all fracture sets in the NE and SW sides of the Gebel El Zeit and Esh El Mallaha blocks.

All fracture sets in the basement were restored to their pre-Nubia datum by rotating the Gebel El Zeit block 42° (average dip of the Nubia Sandstone bedding) in a clockwise sense (looking NW) along an axis at 320° (Fig. 6). Fractures in the Nubia Sandstone were restored by rotating the block 35° along the same axis of rotation. The difference in the amount of rotation required to restore the basement (42°) and the Nubia Sandstone (35°) may indicate that the basement was tilted 7–10° prior to the deposition of the Nubia Sandstone, or that there was 7–10° of rotation between the formation of the basement and Nubia Sandstone joints. The restoration brings the 315°/70° and 055°/79° sets into a vertical attitude and the 140°/45° planes into a horizontal attitude. After restoration, only samples from the SW side of the Gebel El Zeit block and Esh El Mallaha block show a fracture set that restores to a horizontal attitude. The NW and ENE sets are found throughout the basement of the Gebel El Zeit and Esh El Mallaha blocks and the Nubia Sandstone but no fractures
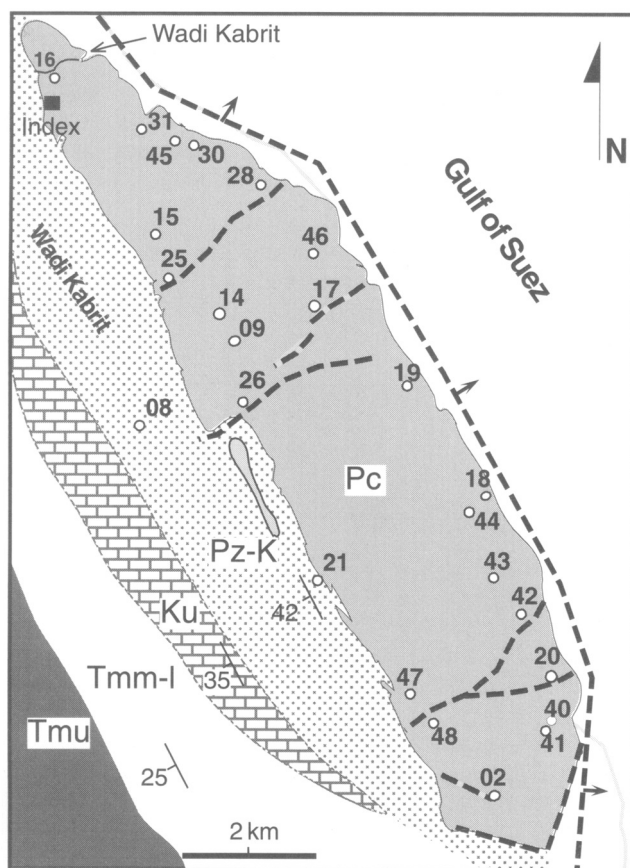
Fig. 5. A detailed map of the Gebel El Zeit main block. White circles represent the locations of measured scanlines. The solid black square is the station at which the 'background fracture spacing' is measured. Pc = Precambrian basement (granite), Pz-K = Nubia Sandstone, Ku = Cretaceous Matullah shales, sands and marls, Tmm-l = Lower Miocene, and Tmu = upper Miocene. Dashed lines are faults, and the arrows on the border fault show the dip direction. Many smaller faults were mapped within the block but are not shown for clarity. Wadi Kabrit is a strike-parallel valley formed by the erosion of the Nubia Sandstone along its contact with the basement.

were observed to continue from the basement into the Nubia Sandstone. The absence of a bedding-parallel fracture set (i.e. sheet) in the Nubia Sandstone indicates that it predates the Nubia whereas its absence on the NE side of the fault block reflects the limited depth at which the sheet fracture set formed.

Assessment of fracture distribution in a rock mass (e.g. a fault block) requires measurement of fracture orientation and spacing in outcrop or from well logs by two widely used methods: the scanline method (Terzaghi 1965; Priest & Hudson 1976; La Pointe 1980) and the area method (Davis 1984; Wu & Pollard 1995). The scanline method accounts for the angle between the scanline and measured fractures, and yields data such as median fracture spacing and fracture frequency. These data can be statistically

analysed and extrapolated to other wells or fault blocks. The area method gives the fracture density within the rock mass and takes into account the length of the fracture in addition to its orientation. The fracture density is defined as 'the total surface area of fractures divided by the volume of the rock in three dimensions, or the total length of fracture traces divided by the surface area of rock exposures in two dimensions' (Rouleau & Gale 1985).

The term 'fracture frequency' is sometimes used indiscriminately to refer to fracture frequency of more than one set. In this paper, the term 'fracture frequency' is restricted to the ratio of the number of fractures in one set to the length of the scanline perpendicular to that set. The ratio of the number of fractures from all sets to the length of the scanline, regardless
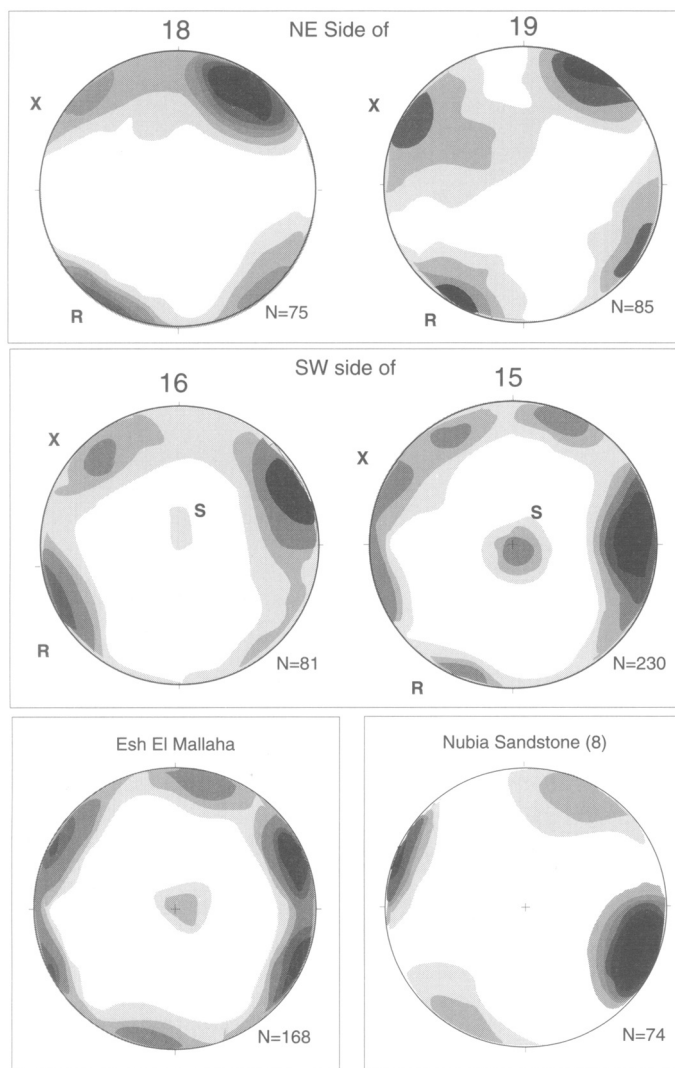
Fig. 6. Kamb contours of poles to restored fractures. Restoration is based on the average dip of the Nubia Sandstone (42°/230°). XR = cross-rift, RP = rift-parallel, and SF = sheet fractures. Only the SW side of Gebel El Zeit and Esh El Mallaha block show a fracture set that restores to horizontal. N = number of fractures. The number on the top of each diagram is the station number. Contour interval = 2 sigma.

of the orientation of the scanline, is referred to as the 'total fracture frequency'. Thus, this ratio may vary with the orientation of the scanline. Total fracture frequency is particularly useful when documenting fractures sampled by well logs. Fracture frequency may be a suitable description for uniformly developed fracture spacings; however, when the fracture spacing changes either gradually or abruptly, fracture frequency is not a suitable description for fracture development. If the fractures are well-developed, the total fracture frequency can be used as a qualitative measure of fracture density, especially when referring to a volume of rock (Wu & Pollard 1995).

In the Gebel El Zeit block, the cross-rift set is well-developed and has a uniform spacing (≤ 0.5 m) on both the SW and NE sides of the fault block (Fig. 7). On the other hand, the local spacing of the rift-parallel set shows an increase with distance from the fault: the spacing is a minimum (≤0.5 m) near the border fault, larger at the SW side of the block (0.3–1.15 m), and a maximum within the Esh El Mallaha

Table 1. *Present-day/restored vector means of fracture orientations in the Gebel EL Zeit and Esh El Mallaha fault blocks, Gulf of Suez*

Set/Area	NE GZ	SW GZ	EEM
RP or RP′	320/67 [301/88]	330/70 [335/88]	(055/88)
XR	56/78 [66/83]	45/77 [34/81]	(055/88)
SF	–	155/45 [158/2]	143/7
RP or RP′	320/67 [301/88]	330/70 [335/88]	325/85
NNE	(037/83)	(025/82)	026/88

Parentheses indicate that the fracture set is poorly developed in that area, and brackets enclose restored vector mean orientations. At least 200 fractures were used to determine the vector mean. NE GZ and SW GZ = northeast and southwest sides of the Gebel El Zeit block, respectively, and EEM = Esh El Mallaha fault block. XR = cross-rift fractures, SF = sheet fractures, RP = rift-parallel fractures, NNE = north-northeast fractures.

block (0.65–1.25 m). The NNE set within the Gebel El Zeit block has a local spacing that ranges from 0.9 m to 0.24 m whereas in the Esh El Mallaha block it averages 0.3 m. Sheet fractures have a local spacing that varies between 0.25 m at the top of the Esh El Mallaha block to 0.6–1.2 m in the SW side of the Gebel El Zeit block, but they are absent in the NE side. Sheet fractures and the distribution of their fracture frequency will be discussed in the next section.

In this paper, we distinguish between a local fracture spacing and a background spacing. The first is the median spacing for fractures of a single set at any site of interest. The second is the spacing measured at an arbitrary reference site (i.e. the index station in Fig. 5), some distance away from either faults or dykes. In a sense, this background spacing is a measure of fracture development in basement unaffected by local structures. By taking the ratio of the local spacing of a particular fracture set to its background spacing, we obtain a normalized fracture spacing that gives an indication of local fracture development.

In order to compare spacing data at different stations, we normalized the local fracture spacing using data from the index station (Table 2). Only vertical fracture sets are normalized because they occur throughout the granite blocks (horizontal fractures have background spacing equal to infinity, i.e. deep basement was not fractured in this orientation). Thus, a normalized spacing of 1 indicates that the local outcrop has a set of fractures spaced equivalent to the background fracture spacing. Therefore, if the normalized spacing is <1, the local fracture set is better developed, and if normalized spacing is >1, the local fracture set is less developed. In other words, if normalized spacing is <1, the local fracture frequency is high, whereas if normalized spacing >1, the local fracture frequency is low.

Figure 8 shows that fracture development of the rift-parallel set in the NE side of the Gebel El Zeit block is twofold higher than in the SW side, and threefold higher than in the Esh El Mallaha block. Thus, the regional fracture frequency determined from scanline measured at the Gebel El Zeit and the Esh El Mallaha blocks changes regionally, according to location relative to the border fault.

Normalized fracture spacings in the Gebel El Zeit and Esh El Mallaha blocks not only show the degree of fracture development, but can also reflect the correlation between a fracture set and its relative age. This correlation stems from the observation that the first, or oldest, fracture set will tend to be more developed (i.e. longer, more closely and uniformly spaced, and higher in frequency) than the later, or younger, fracture sets. The decrease in fracture development is related to the heterogeneities in the stress field induced by the presence of older fractures. For example, the NNE, the youngest fracture set, is well-developed (background spacing = 0.6) in the Esh El Mallaha block but is less developed in the Gebel El Zeit block (background spacing = 1.29–1.54) whereas the cross-rift (ENE) set is best developed in the Gebel El Zeit block and least developed in the Esh El Mallaha block (Fig. 8). In summary, the older sets, cross-rift and rift-parallel, are well-developed in the Gebel El Zeit block, whereas the youngest set, NNE, is well-developed in the less-fractured, Esh El Mallaha block.

Factors affecting fracture spacing

Extension fractures develop in response to the tectonic stresses by propagating in the orientation of maximum horizontal stresses (Engelder & Geiser 1980). The extent (regional or local)
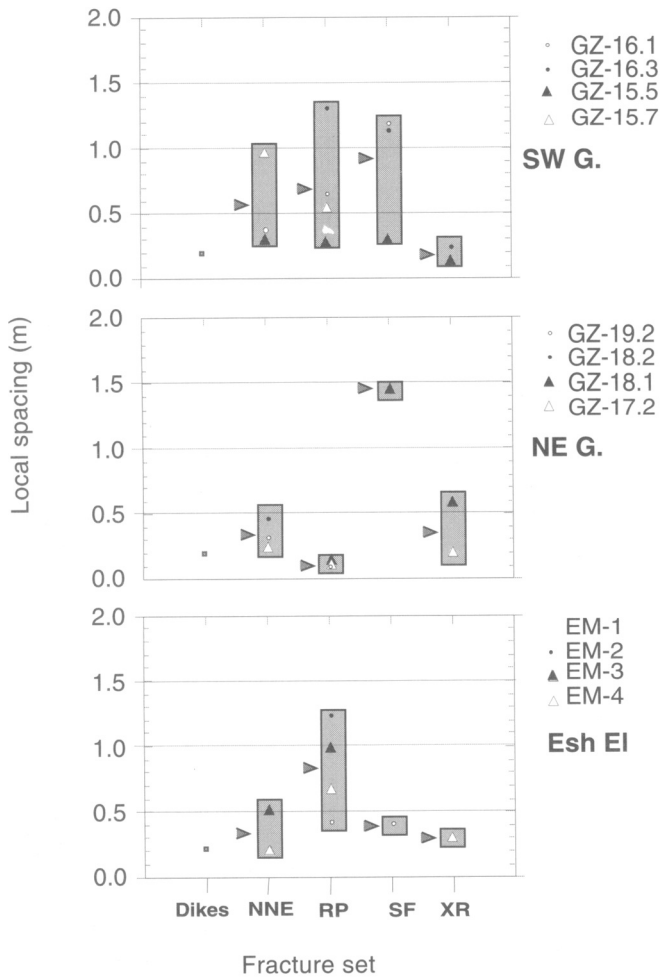
Fig. 7. Median spacing of fracture sets measured at different stations (legend on right) in the Gebel El Zeit (GZ) and Esh El Mallaha (EEM) blocks. The rift-parallel set has the smallest spacing near the border fault (NE side), and the largest spacing is recorded at the Esh El Mallaha block. Fracture spacing of dykes is plotted for comparison. RP = rift-parallel, XR = cross-rift, SF = sheet fractures, and NNE = north-northeast fractures. The small arrows to the left of the grey boxes marks the average of fracture spacings measured along different scanlines.

of the stress field, homogeneity of rock and its elastic properties all contribute to determining the intensity of fracturing in rock. For a particular rock type, the fracture spacing, as defined in the previous section, is rather uniform unless other local structures (e.g. faults) contribute to the deformation. This uniform spacing is thought to be controlled by stress shadows ranging from reduced crack-normal tensile stress in the vicinity of joints (Gross *et al.* 1995). A uniform fracture

Table 2. *Background spacing data used to normalize fracture spacing data at different stations*

Set	XR	SF	RP	NNE
Background spacing	0.34	–	0.66	0.44

Each number represents the median of the particular set spacing at the index station (see Fig. 5). Notation as in Table 1.
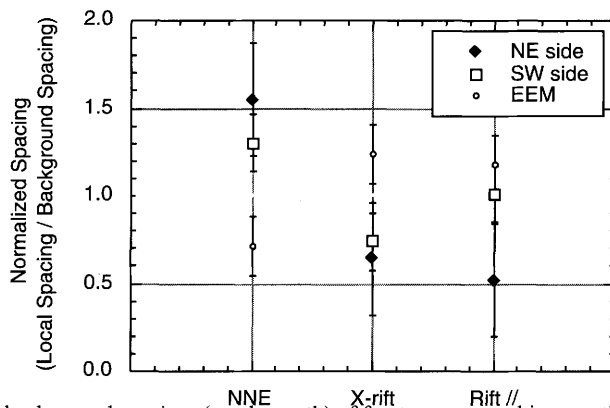
Fig. 8. Normalized background spacings (north–south) of fractures restored into vertical. The background spacing is defined in the text. A normalized spacing of 1 indicates that the fracture set has a 'normal' fracture spacing, while a normalized spacing greater than or less than 1 indicates that the fracture set is either poorly, or well developed respectively. The bars are one standard error from the mean. EEM = Esh El Mallaha block.

spacing implies that the fracture spacing is approximately constant along the scanline. Within the Gebel El Zeit and the Esh El Mallaha blocks, such uniformity in fracture spacing is not common. Fracture spacing of systematic sets varies from one set to the other, within a single set, and from one station to the other. Below, we discuss three processes that reduce the fracture spacing and, consequently, increase total fracture frequency (and density).

Sheet fracturing

Axial splitting is a process by which joints propagate parallel to the topographic surface as long, broad sheet fractures that reach up to 200 m in length (Nemat-Nasser & Horri 1982; Holzhausen 1989). Sheet fractures are well-developed in granitic rocks and sandstones (e.g. the Colorado Plateau), but are less common in mafic or other sedimentary rocks. Sheet fractures form as extension cracks having apertures of 1–2 mm and are likely to remain open because of surface asperities. Accordingly, sheet fractures permit fluid flow and will greatly enhance the interconnectivity of a fractured basement rock. We follow Holzhausen (1989) in making the distinction between sheet fractures and exfoliation fractures: the former are driven by non-thermal horizontal stresses, whereas the latter are driven by thermal stresses induced by annual or daily ambient temperature cycles.

In the Gebel El Zeit block, the sheet fracture set (140°/45°) is found on the SW side of the fault block but is almost absent on the NE side (Fig. 6). After restoring the Gebel El Zeit block

to its pre-Nubia datum, the SW side becomes the top of the basement whereas the NE side rotates to a deeper portion of the basement (Fig. 9). Because the 'bedding-parallel' fractures on the SW side (top of basement) of the Gebel El Zeit block are restored to the horizontal and because they are rarely present on the NE side of the block, we interpret these as sheet fractures. The local fracture spacing of the sheet set gradually increases with depth from this contact with the Nubia Sandstone so that its fracture density decreases with depth (Fig. 10). Although these fractures are apparent as much as 40 m below the top of basement, outcrop limitations restricted our scanlines to 14 m. Data from sub-surface fracture logs of the Ashrafi Field show that sheet fractures exist down to 150 m from the top of basement. In addition, very rare occurrences of sheet fractures are observed in the NE side of the Gebel El Zeit block which projects to 1.7 km below the top of basement. The behaviour of the sheet fractures within the Gebel El Zeit block resembles that of the Chelmsford Granite, New England, where Holzhausen (1989) and Jahns (1943) similarly observed a decreasing sheet-fracture frequency with depth.

Regionally, sheets between fractures at the top of basement in the Gulf of Suez become progressively thicker, from 0.2 m at Esh El Mallaha to 0.6–1.2 m SW of Gebel El Zeit. This pattern arises since Gebel El Zeit basement was uplifted approximately 150 Ma prior to Esh El Mallaha, therefore erosion exposed deeper and thicker sheets. Except for very rare occurrences, no sheet fractures were found to have a present-day horizontal attitude, or to be parallel to the
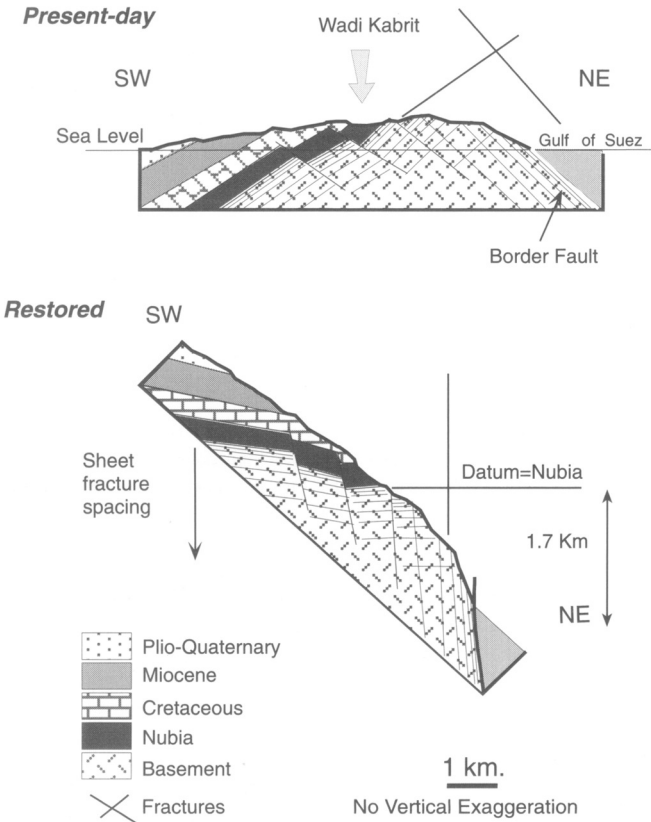
Fig. 9. A cross-section of Gebel El Zeit showing the restoration of basement rock on the SW side as the top of basement, while the NE side becomes a deeper basement.
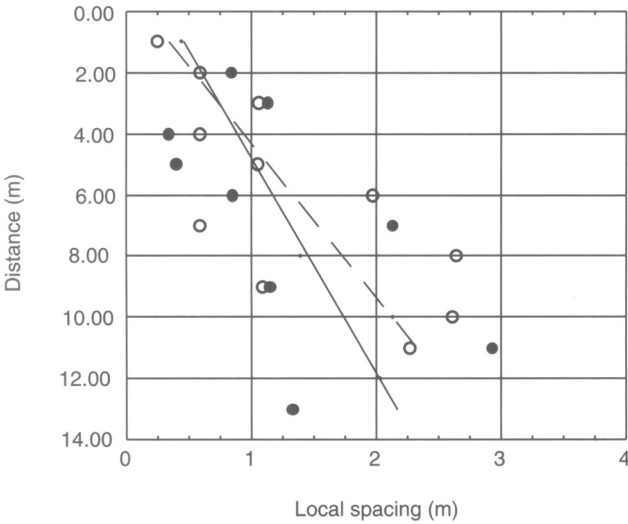
Fig. 10. Distribution of sheet fractures with depth as indicated by the data from two scanlines (solid and open dots). Solid and dashed lines are best fits of the two scanlines. Outcrop limitations restricted length of scanlines, but sheet fractures can be traced in some outcrops down to 40.0 m.

present-day topographic surface. Lack of post-Nubia sheet fractures is due to the intense fracturing of the basement which dissipates the stresses necessary to form large horizontal fractures.

Faulting

In the basement of the Gebel El Zeit and Esh El Mallaha blocks, faults strike parallel to the dominant ENE and NW fracture sets and mainly occur as dip-slip normal faults. These faults are commonly accompanied by features such as pinnate joints, tail cracks, mullions and tension gashes that are often lined or filled with vug-filling quartz. Although fracture spacing is rather uniform at a distance from faults, deviations from this uniformity occur near faults,

particularly in footwalls (Fig. 11). The fracture spacing of a fault-parallel fracture set is usually less than 0.75 m but becomes much smaller in proximity to faults (Fig. 7). In other words, the fracture frequency, for example, of the rift-parallel set, gradually increases towards the border fault (Fig. 8). A similar behaviour is observed on a single-fault scale. Here, the fault-parallel fracture spacing decreases near individual cross-rift and rift-parallel faults (Fig. 12). In Fig. 12, the spacing data of a fault-parallel set are plotted against the distance from the fault. The data show that: (1) the frequency of a fault-parallel set increases near the fault; and (2) the rift-parallel fracture set has a higher fracture frequency than the cross-rift set at distances greater than 5 m from the fault.

In addition to the increase in the fracture frequency near faults, movement along faults
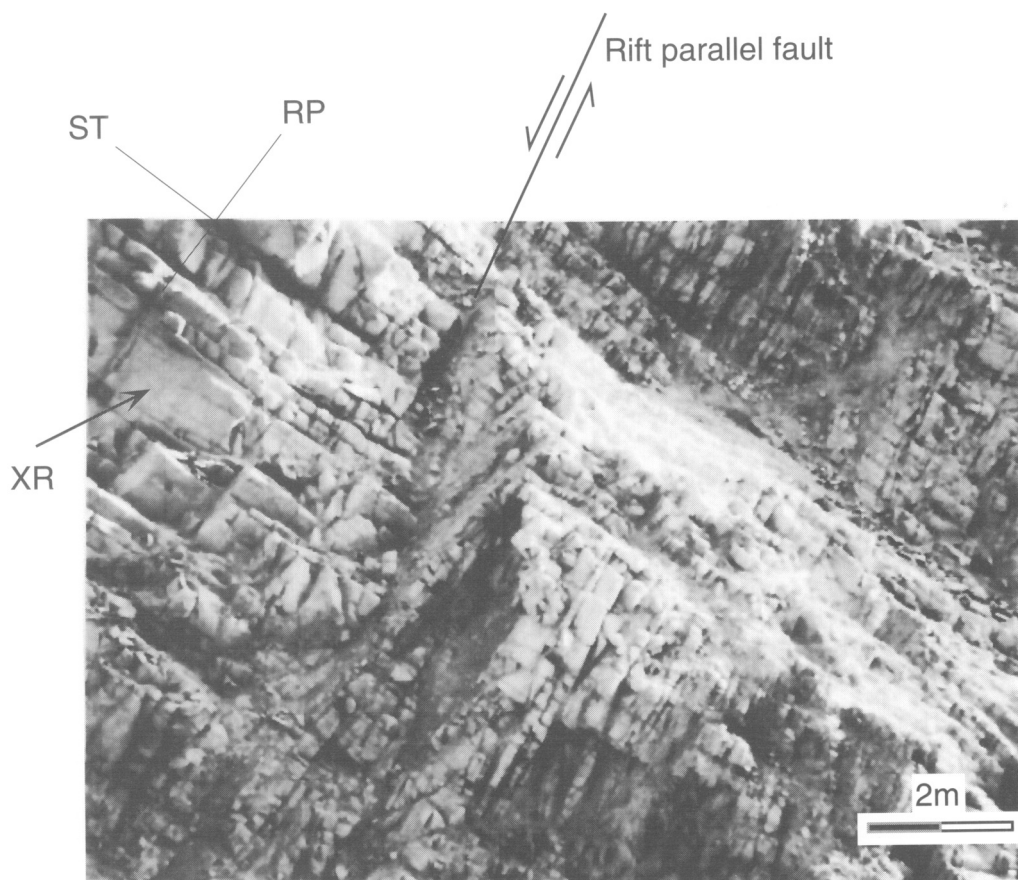
Fig. 11. Photograph of a rift-parallel fault in granite of the Gebel El Zeit block, looking SE. Wadi Kabrit is to the right of the photo. The fracture density near the fault is very high (compare to Fig. 3), especially in the footwall. Note the higher fracture density in the hangingwall within 1 m from fault surface. Fracture set symbols are as in Fig. 3.
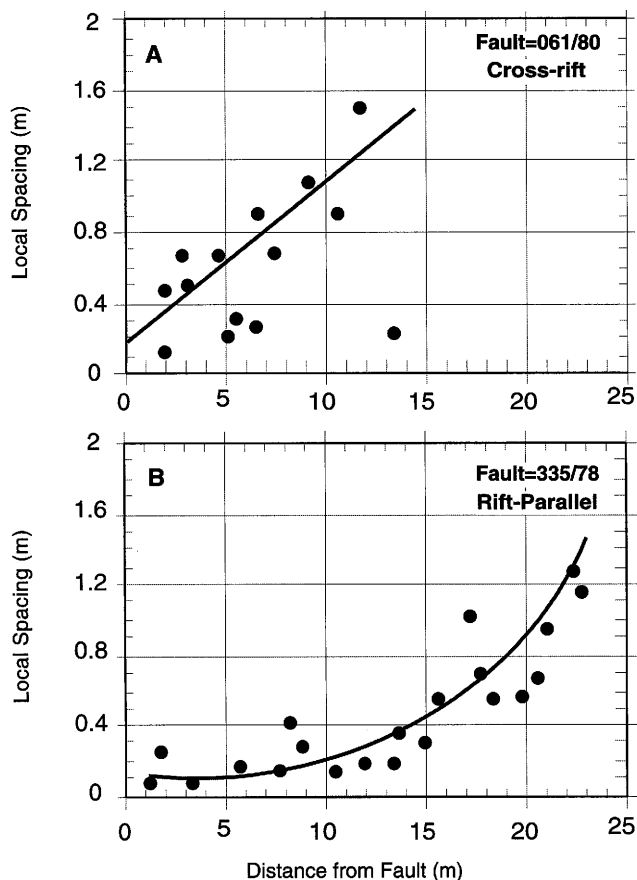
Fig. 12. Distribution of fracture spacing of fault-parallel fractures. Fracture spacing tends to increase with distance away from the fault. Cross-rift fractures tend to have a linear distribution (**A**) whereas rift-parallel fractures tend to have an exponential distribution (**B**).

causes block rotation and this may influence propagation of later fractures. The addition of fractures and block rotation leads to a larger scatter in fracture orientations so that fractures near faults plot as a girdle whereas those measured away from faults plot as well-clustered maxima (Fig. 13).

Dyke emplacement

Andesitic and rhyolitic dykes in the Gebel El Zeit block extend for distances of more than 500 m parallel to the ENE cross-rift faults and fractures. Sills strike parallel to the Gulf of Suez and dip to the SW parallel to the Nubia-basement contact. The small thickness (*c.* 1 m), weathering and infrequent occurrence limited field work on sills, hence the data presented here are for dykes only.

The fracture spacing within dykes averages approximately 0.18 m and thus leads to the highest fracture frequency anywhere in the Gebel El Zeit and Esh El Mallaha blocks. In a dyke, the majority of fractures strike parallel to the orientation of the dyke itself, implying that there is a genetic relationship between dykes and fractures (Fig. 14). In addition to their high internal fracture frequency, some dykes are bordered by a zone of dyke-parallel fractures that gradually become less frequent away from the dyke walls (Fig. 14). The adjacent zone is approximately equivalent to the dyke in thickness. Such fractured zones may be interpreted as a process zone ahead of the dyke tip (Delaney *et al.* 1986) or as a manifestation of thermal stresses developed in the host rock after dyke intrusion. Alternatively, this may be a zone of weakness that was exploited during the intrusion of the dyke.
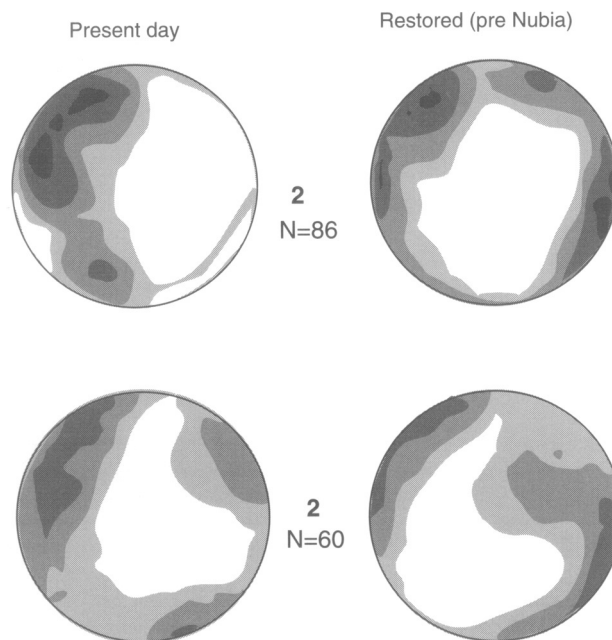
Fig. 13. Variation of fracture orientations in proximity of faults. Fractures plot on equal-area plots as a girdle instead of as well-defined maxima. Data from the NE and SW sides of Gebel El Zeit.

The Ashrafi Oil-field

The Ashrafi Oil-field (Fig. 1) is located within a series of southwesterly dipping fault blocks that were rotated along rift-parallel, NE-dipping faults. Composition of the cover and basement rocks, and structure of the Ashrafi Field resemble that of the Gebel El Zeit block. The basement is mainly granitic (alkali granites) and is intruded by andesitic and rhyolitic dykes. Well logs show that the basement is covered by pre-rift strata in some wells and by the post-rift Miocene clastics or evaporites in other wells. For example, the basement of wells A3 and C-1X is covered by the Nubia Sandstone whereas that of well B3 is covered by lower–middle Miocene clastics and evaporites (Fig. 15). The contact between the basement and the overlying sediments is defined by discontinuity in the gamma-ray and density logs. Dykes within the granite can also be resolved using the same logs.

Formation Micro Scanner (FMS) and Formation Micro Imager (FMI) data in the Ashrafi basement are available from several wells. The average total fracture frequency is calculated from corrected fracture orientations and plotted as a fracture density curve plot (FVDC) (Fig. 15). Similar to a scanline, the FVDC is calculated as the number of fractures recorded by the FMS

tool per unit depth (an increase in frequency = a right shift in FVDC). Sub-surface fracture data from the Ashrafi Field show three dominant sets: a rift-parallel, cross- rift and sheet fracture sets similar to those in the Gebel El Zeit block. Fracture sets in the basement rocks of the Zeit Bay Field (Fig. 1) also resemble those in outcrop (Zahran & Ismail 1986). However, fracture attitudes may differ owing to the difference in the fault-block orientation or amount of block rotation.

The distribution of fracture density in the sub-surface varies according to the factors defined before (sheet fracturing, faulting, and dyke emplacement). In both the Ashrafi and Zeit Bay Fields (Fig. 1), the fracture density in the sub-surface shows an abrupt increase if the borehole intersects a dyke (Fig. 16). In addition, boreholes intersecting a rift-parallel fault, e.g. wells B2X, and A3, show two dominant fracture sets similar to the NE side of the Gebel El Zeit block. Furthermore, the fracture density in the basement of the Ashrafi Field shows a correlation between the presence or absence of pre-rift sediments and total fracture frequency indicated by the FVDC. Wells where the basement is overlain by the Nubia Sandstone, e.g. A3, show a higher total fracture frequency than those where the basement is overlain by the Miocene section, e.g. well B2X (Fig. 15).
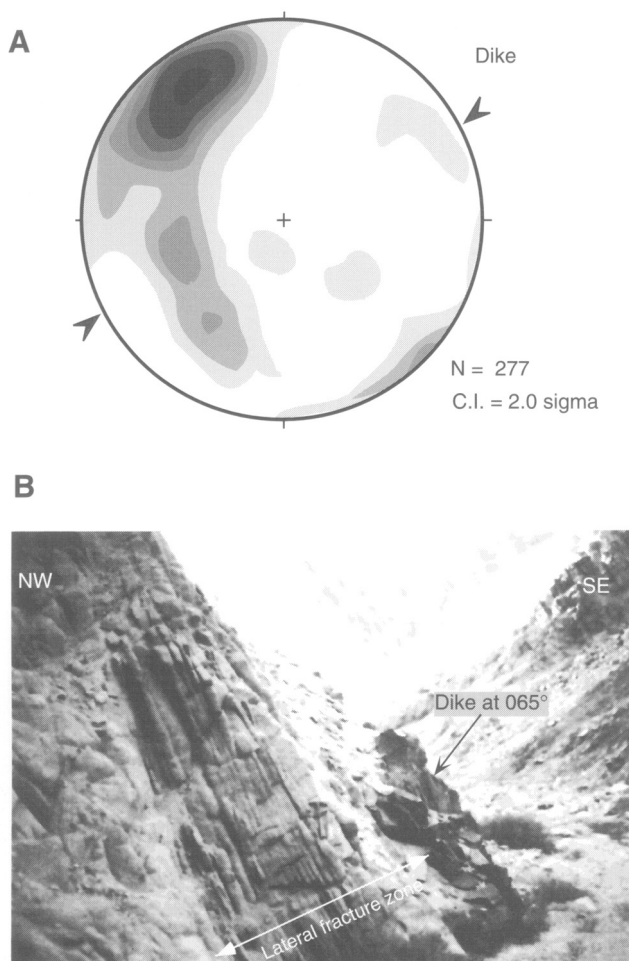
Fig. 14. (**A**) Kamb contour, and (**B**) field photograph of a fractured andesitic dyke exposed at the Gebel EL Zeit block. Most of the fractures within the dyke strike parallel to the dyke. In addition, dyke walls are fractured by a lateral fracture zone that, again, strikes parallel to the dyke. Note the areal extent of the dykes shown in the background of the photo.

In order to test this correlation between pre-rift sediments and fracture frequency, scatter diagrams of poles to fractures from the Nubia-covered A3 well and the Miocene-covered B2X well are compared in Fig. 17. In the top row, equal intervals of basement are compared but the A3 basement is deeper than the B2X. In the lower row, data from the bottom 25 m in both wells are compared. Fracture orientations in A3 are similar to the rift-parallel, cross-rift and sheet orientations of the Gebel El Zeit and Esh El Mallaha blocks. Although both wells show a decrease in fracture frequency with depth, the deeper interval of A3 has a higher fracture density than the shallower interval of B2X. In

addition, sheet fractures are abundant in the A3 well but are almost absent in the B2X basement. This situation is similar to comparing the SW side of the Gebel El Zeit block (A3) with its NE side (B2X). The same relationships were observed for all the wells where the sheet fracture and total fracture frequency are higher in the first than in the second. In other words, basement rocks covered by pre-rift sediments (e.g. Nubia Sandstone) have a higher fracture density than those covered by syn- or post-rift sediments (e.g. Rudeis Formation). Therefore, the presence of pre-rift cover appears to preserve the fractured rock beneath it (especially sheet fractures) from erosion, while post-Nubia
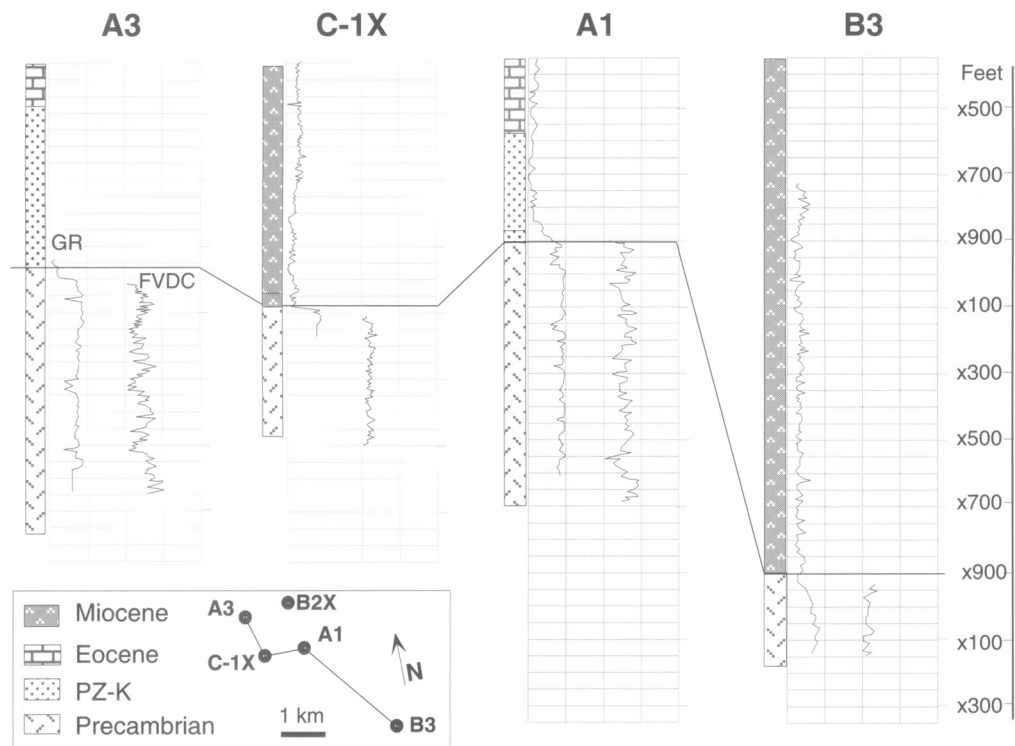
Fig. 15. Four well logs from the Ashrafi Field. The strike of the cross-section is NW, parallel to the Gulf of Suez. In terms of stratigraphy and structure, the A3 well is similar to the A1, A2, A5 and C-1X; and the B3 well is similar to the B2X and B1X. Grid is 50 ft intervals, GR is the gamma-ray log, and FVDC is the fracture frequency curve from FMS data. The FVDC shows an increase in the total fracture frequency if the curve shifts to the right, and vice versa. Log data modified from Deri (1993).

exhumation of the basement subjects it to erosion and loss of significant fracture density with the removal of rocks containing sheet fractures.
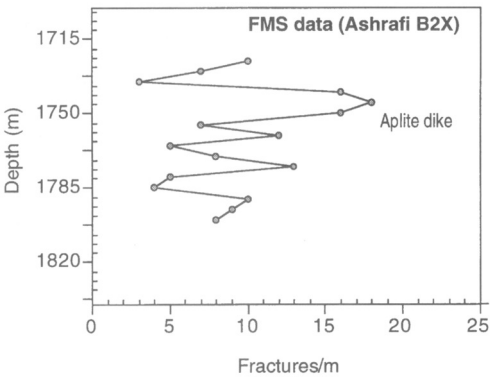
Fig. 16. Sub-surface example of increase in fracture density along zones intruded by dykes: Ashrafi B2X well.

The similarities of fracture orientation and distribution in sub-surface (Ashrafi and Zeit Bay) and surface (Gebel El Zeit and Esh El Mallaha) fault blocks justify the use of surface fault blocks as analogues for the sub-surface rocks. However, differences in fracture frequency as illustrated above (B2X versus A3) and the lack of strong 'stratigraphic markers' in the basement may lead to incorrect interpretations. For example, B2X was drilled near the crest of a rotated fault block, a customary target for drilling, yet the fracture density in the basement was low at this well.

In order to completely understand the fracture density distribution in basement, these fractures must be considered in a tectonic context. The style of uplift, proximity to block-bounding faults, the depth of erosion, and the interaction of more than one fracture set are important factors. Based on the tectonic style of the rift basin, the following section presents two models where fracture distribution differs according to the nature of the block uplift and erosion.

B2X

A3
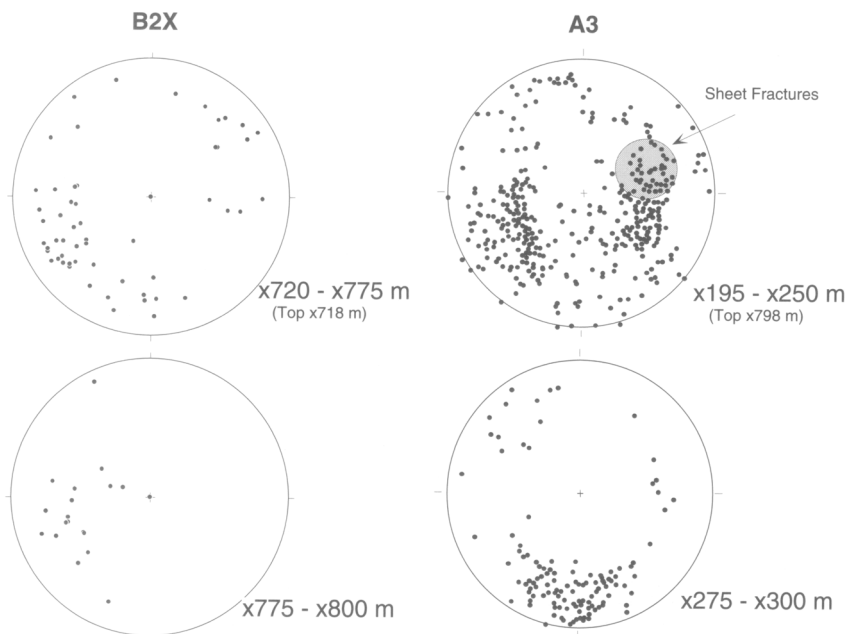
Fig. 17. Lower-hemisphere stereonet projections of poles to fractures in the Ashrafi B2X and A3 wells; sheet fractures plot in the eastern side of the stereo plot (shaded). The fracture density in both wells decreases with increasing depth, particularly sheet fractures in A3. The higher fracture density is present in the Nubia-covered A3 well while the lower fracture density is present in the Miocene-covered B2X well. The last 25 m of the A3 well were drilled through the youngest granite intrusion which was fractured under a different, more easterly compression than the older granites on top of it.

Discussion

Fracture distribution in faulted basement blocks

The local fracture density of a fault block is largely controlled by sheet fracturing, faulting, dyke emplacement and erosion. The term 'fracture density' is used here qualitatively to indicate those portions of a fault block which are more fractured than others. Except for erosion, the style of deformation (rifting) will control the location of maximum fracture density. We propose two models that illustrate this effect: a rotated-block model fitting the behaviour of the fault blocks exposed along the shoulders of the Gulf of Suez, and an uplifted-block model fitting the behaviour of the fault blocks off the southern coast of Vietnam (Khy 1986). Block rotation is typical for half grabens, whereas block uplift is typical for full grabens (Morley 1995).

Theoretically, fractures related to faulting dip at an acute angle to the fault surface, such as those presented in the block-uplift model (e.g. Hancock 1985). However, in the block-rotation model, rift-parallel fractures are modelled parallel to faults of that orientation as documented from field work. The discrepancy between the two models arises because faults in the Gebel El Zeit block were initiated utilizing previously existing rift-parallel fracture fabric, and consequently fractures and faults parallel each other (Younes 1996).

In the block-rotation model, we assumed the absence of post-rifting sheet fractures. This assumption is based on field data from the Gebel El Zeit block where occurrences of present-day sheet fractures are very rare. The lack of present-day sheet fractures may be attributed to the high fracture density of the fault block, which inhibits the formation of large, uniform fractures. Alternatively, sheet fractures are best developed when uplifted block has undergone peneplanation. Thus, the rugged topography of the fractured basement of the Gebel El Zeit block would relieve the horizontal stresses necessary to propagate sheet fractures. The abundance of pre-Nubia sheet fractures thus suggests some degree of peneplanation which has been documented from the non-conformable relationships between the lower Nubia Sandstone and the

underlying igneous rocks, and from textural and mineralogical data of the lower Palaeozoic rocks (Klitzsch & Squyres 1990).

Block-rotation model

Rotation of fault blocks along listric or planar faults is a common style of deformation in half grabens (e.g. the Gulf of Suez) and leads to the exhumation of the uplifted edge of the block. Large amounts of rotation, proximity of the rotation axis to a fault, and large block sizes cause larger amounts of uplift, and consequently greater depths of erosion into the basement. The effect of rotation and erosion on the fracture density of a fault block is illustrated by a cross-section of the Gebel El Zeit block (Fig. 18). The fracture frequency of the sheet fractures increases towards the top of the block whereas
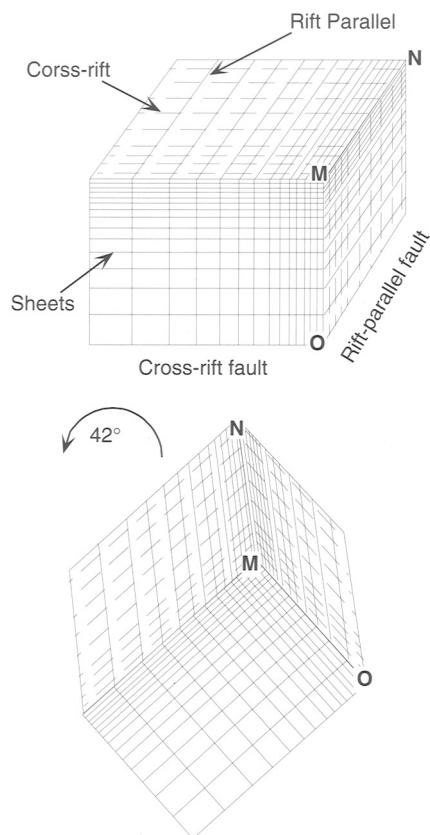
Fig. 18. Rotation of a fault block relocates the most fractured portion of a fault block as the crest of the block, MN. Subsequent erosion will strip off this part, leaving the block with lower fracture density. Point M is the most fractured portion of the block.

that of the fault-parallel fractures increases towards the block-bounding faults.

The intersection of three mutually perpendicular fracture sets localizes the fracture density along the edges of the block, and particularly towards a point where the three fracture sets intersect. Rotation and uplift of the fault block causes the uplifted edge to become the crest, where erosion will strip off rocks containing a high fracture density. A large amount of erosion will leave rocks of widely spaced fractures at the top of the basement (Fig. 19). Meanwhile, the graben receives sediments and will be filled, thereby protecting the underlying basement rock, with its relatively higher fracture density, from erosion. Because the frequency of sheet fractures gradually decreases with depth, higher fracture densities are found only where the basement cover was not deeply eroded. For example, the basement of the A3 well is overlain by the Nubia Sandstone, and thus shows higher fracture density largely because abundant sheet and rift-parallel fractures have not been exposed to erosion (Fig. 15). The Shoab Ali Field is located in the central Gulf of Suez, and is another example of a Nubia-covered basement producing field (Nagaty 1982). In contrast, the Ashrafi B2X block is a Miocene-covered, deeply eroded block and is not a basement producer.

Block-uplift model

Block uplift refers to a rifting style where the basement is faulted in a horst-and-graben style with little or no rotation. This style is typical in the central troughs of large rift basins and continental shelf margins (e.g. the Cuu Long (Mekong) and the Con Son rift basins, Vietnam; Chan et al. 1994). In contrast to block rotation, the block-uplift style differs in having smaller amounts of rotation and larger vertical displacements.

The model illustrated in Fig. 20 represents a horst uplifted along two sub-perpendicular faults with initial fracture density similar to that of Fig. 16, where fault-parallel fracture frequency gradually increases from the centre of the block towards the block edges. If the basement is exhumed, erosion will gradually remove the sheet fractures at the top while the graben will receive sediments from the eroded rocks. The removal of sheet fractures lowers the fracture density of the horst, while the sediment-filling of the graben protects the high fracture density in the underlying basement.

In this tectonic style, the maximum fracture density is localized at block-bounding fault
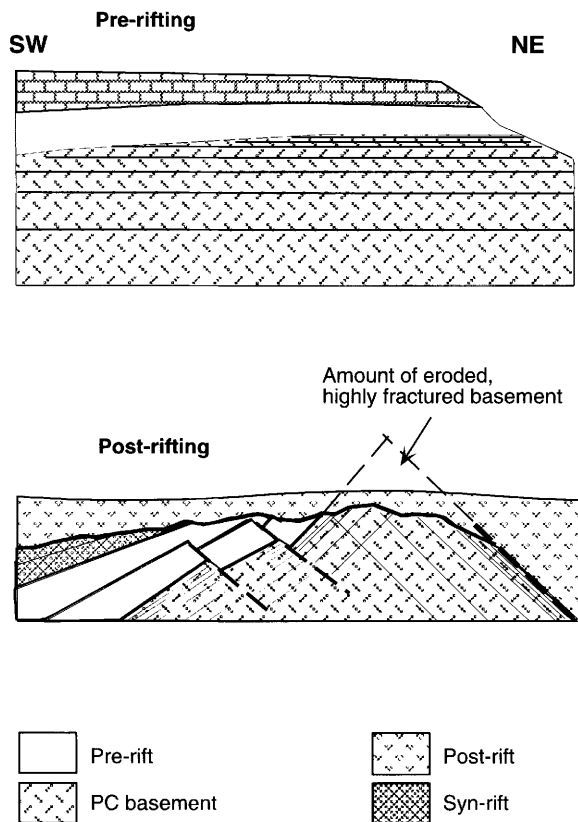
Fig. 19. Block-rotation model. The eroded basement crest is covered by post-rifting sediments (Middle and Upper Miocene) at the southern end of Gebel El Zeit. Dashed lines are faults and the NE fault is the border fault.

intersections (Fig. 20). The large vertical displacements on these faults (3–6 km; Chan *et al.* 1994; Arechev *et al.* 1992) reflect larger amounts of extension, and consequently larger fault-related fracture zones. In addition, the thick sedimentary column in the graben will allow lateral migration of oil from the source rock, or other reservoir rock, into the fractured basement. Thus, if the horst is eroded, fractures will be localized only at fault intersections, and there will be reduced chances for lateral oil migration, and hence oil accumulation in the horst block.

Alternatively, if the amount of uplift of a horst is insufficient to erode the entire sedimentary cover on top, the horst will have its highest fracture density at fault intersections and near the top of the block. In this case, penetrating the crest of a fractured basement reservoir block is recommended. Deep wells (4.5 km) penetrating over 1 km of fractured basement of the Cuu Long basin, Vietnam, could have intersected such large fault-intersection zones.

Where do fractured basement reservoirs occur?

In Fig. 21, we examine three possible fractured basement reservoir targets for each tectonic style as discussed above (Figs 19 and 20). Targeting the crest of the structure is routine in oil exploration; however, in fractured basement, crests are the most eroded. For example, well X was drilled on the crest of the structure in both tectonic styles where the basement is less fractured, and hence lower permeability values, such as those of B2X, are expected in both wells. Well Y, on the other hand, is drilled near fault intersections where fault-parallel fractures are well-developed and provide high permeability. Because well Y in the rotated block lacks sheet fracture intersections, it will show lower fracture density (and permeability) than an uplifted block. In addition, the decrease in the fracture density away from the fault will govern the 'thickness' of the reservoir in the

Erosion   Sheet fracture

Deposition   Fault -parallel

▨ Basement   ▨ Syn- and Pre- rift   ☐ Post-rift
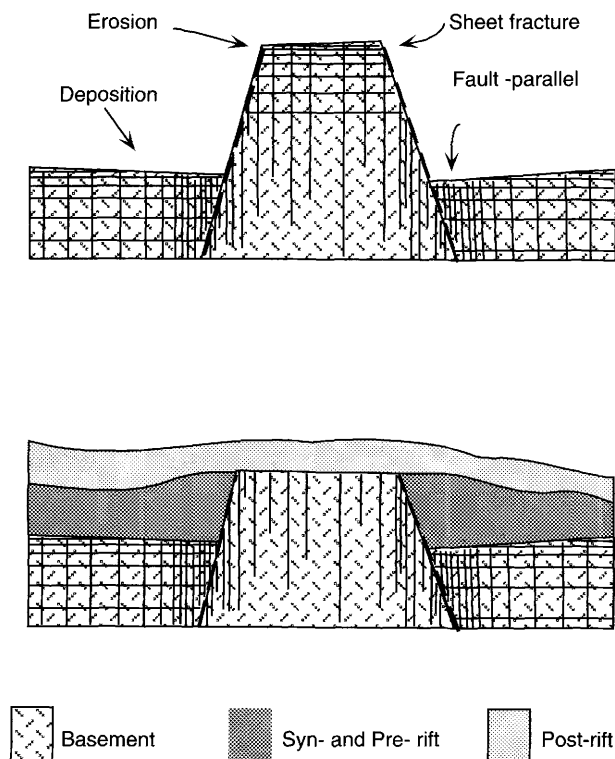
Fig. 20. Block-uplift model. Dashed lines are faults bounding the horst structure. Erosion of the horst will reduce the overall fracture density . Deposition of eroded material in the graben protects the basement's fracture density. The maximum fracture density occurs at fault intersections.

rotated block example, whereas the parallelism of the well bore to fractures in the uplifted block may be a disadvantage. Overall, well Y in block uplift is a better target than that in block rotation. Well Z is drilled in a highly fractured basement that is covered by pre- or syn-rift sediments where it is likely to encounter high fracture density in both wells. However, the well of the block-rotation model is a more promising target than that of the block-uplift model, simply because oil can migrate upwards through faults in the rotated block, but it is less likely that it will move laterally into the down-thrown block of the block-uplift model.

Other controls may influence the productivity of fractured basement rotated fault blocks. For example, some wells around the Ashrafi Field have fractured basement that is covered by the Nubia Sandstone. However, these wells were not basement producers simply because the fractured portions were below the oil–water contact, whereas the crests, the less fractured portion, were above it. Another situation arises if the fault and bedding attitudes inhibit the

upward migration of oil into the fractured basement (e.g. if the fault and the beds dip in opposite directions). Despite these exceptions, fracture density within a basement fault block generally increases away from its eroded crest, and reaches a maximum below the uneroded portions.

Effect of fractures on permeability

Basement rocks, unless fractured, have very low permeability and porosity. Vertical fractures are generally abundant in basement rocks and provide conduits with high directional permeability and porosity. However, lateral communication may be reduced because of low fracture interconnectivity. Sheet fractures, with their large dimensions, can greatly enhance interconnectivity, especially at the top of basement. For example, basement in well A3, where high flow rates were recorded during production tests (28 BOPD/PSI on average), is highly fractured with an abundance of sheet fractures

Block Rotation Style

Block Uplift Style

Pre-rift		Post-rift		Fractures
Basement		Syn-rift		Faults
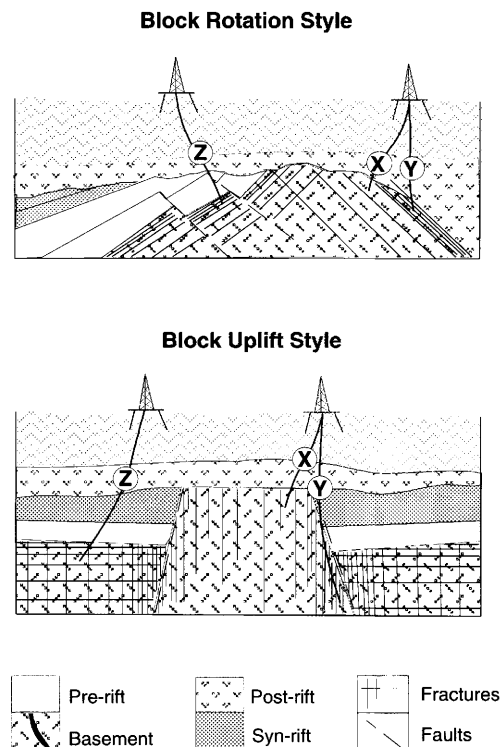
Fig. 21. Possible potential targets for fractured reservoirs. See text for discussion.

(Fig. 17). On the contrary, basement lacking sheet fracturing (e.g. B2X) is less permeable and porous as indicated by the low rates of production tests (4 BOPD/PSI). The extent, depth and distribution of sheet fractures is critical to the production of fractured basement reservoirs, particularly in fault blocks where the crest is eroded.

The presence of sheet and fault-related fractures is possibly the most significant factor in determining the quality of a fractured basement reservoir. Their presence localizes the fracture density at the edges of a fault block, and consequently creates potential high-permeability targets. In addition, the scatter of fracture orientations near faults increases the number of possible fracture intersections and hence the opportunity to develop a wellconnected fracture network that would increase the overall permeability.

Dyke geometry in the Gebel El Zeit block indicates that they were intruded through previously existing fractures. The high fracture density and the occurrence of lateral fracture zones marginal to dykes make them potential zones of high permeability. The strong parallelism of fractures within and around the dykes and the lower fracture density in the surrounding granite, could increase the permeability anisotropy. In Zeit Bay Field, such increases in permeability at dyke intersections are matched by an increase in production (Ismail & Abd-Elmoula 1992; Younes 1996).

Conclusions

Outcrop studies of the Gebel El Zeit and Esh El Mallaha blocks show that the fracture density of basement rocks increases by three geological processes: sheet fracturing, faulting and dyke emplacement. Sheet fracturing increases a block's fracture density near the top and provides the block with horizontal permeability. The continuous formation of sheet fractures depends on the intensity of fracturing of the block and may control the potential of reservoirs in uplifted blocks. Faulting is associated with veining and zones of higher fracture density that also increase rock permeability. In addition, fracture orientations show a wider scatter that may contribute to the increase of permeability near faults. Dykes have the highest fracture density, but the majority of these fractures strike parallel to the dyke orientation and thus may provide a path of permeability anisotropy. The existence of a dyke-parallel lateral fracture zone in the host rock will enhance this anisotropy.

Sub-surface studies in the Ashrafi Field show that rotation of a fault block relocates the highly fractured edge of the block as the crest of the block, whereas uplift of basement as a horst localizes the fracture density along the boundaries of the horst. In either mode of uplift, erosion will strip the rock of its highly fractured portions. Thus distribution of fracture density in a fault block depends on the depth of erosion, or the length of hiatus between the basement and the overlying cover. Fractured reservoirs are best-developed where the fractured basement was protected by the pre-rift cover and was not eroded.

Finally, the Gebel El Zeit and Esh El Mallaha fault blocks can be analogues to sub-surface Ashrafi blocks and outcrop characterization of fractures is necessary to properly evaluate fractured reservoirs.

Neil Hurley at Colorado School of Mines in pursuing the funds for this project and revising an earlier version of the manuscript. The authors wish to thank Adham Gouda, of Marathon Petroleum Egypt Ltd, for helping with the field work, and David Pollard and John Lorenz for helpful comments and review.

References

ALLAM, A. 1988. A lithostratigraphical and structural study on Gebel El-Zeit area, Gulf of Suez, Egypt. *Journal of African Earth Sciences*, **7**, 933–944.

ARECHEV, E., DONG, T., SAN, N. & SHNIP, O. 1992. Reservoirs in fractured basement on the continental shelf of southern Vietnam. *Journal of Petroleum Geology*, **15**, 451–464.

BHATTACHARYYA, D. P. & DUNN, L. G. 1986. Sedimentologic evidence for repeated pre-Cenozoic vertical movements along the northeast margin of the Nubian Craton. *Journal of African Earth Sciences*, **5**, 147–153.

BOSWORTH, W. 1995. A high strain model for the southern Gulf of Suez (Egypt). *In*: LAMBIASE, J. J. (ed.) *Hydrocarbon Habitat in Rift Basins*. Geological Society, London Special Publication **80**, 75–102.

CHAN, T., HA, V., CARSTENS, H. & BERSTAD, S. 1994. Viet Nam, attractive plays in a new geological province. *Oil and Gas Journal*, **92**(11), 78–83.

COLLETTA, B., MORETTI, I., CHENET, P. Y., MULLER, C. & GERARD, P. 1986. The structure of the Gebel El Zeit area: A field example of tilted block crest in the Suez rift. *Eighth Egyptian General Petroleum Corporation Conference*, Cairo, November 1986.

DAVIS, G. 1984. *Structural Geology of Rocks and Regions*. Wiley, New York.

DELANEY, P. T., POLLARD, D. D., ZIONY, J. I. & McKEE, E. H. 1986. Field relations between dikes and joints: Emplacement processes and paleostress analysis. *Journal of Geophysical Research*, **91**, 4920–4938.

DERI, S. 1993. *Structural Analysis of the Ashrafi Field, Gulf of Suez*. AGIP, internal report.

EL-SHAZLY, E., EL-KASSAS, I. & MOUSTAFA, M. 1979. Comparative fracture analysis and its relation to radioactivity in the pink granite of Um Had pluton, Central Eastern Desert, Egypt. *Egyptian Journal of Geology*, **23**, 95–110.

ENGELDER, T. 1982. Is there a genetic relationship between selected regional joints and contemporary stress within the lithosphere of North America?, *Tectonics*, **1**, 161–177.

—— & GEISER, P. 1980. Use of joints as paleostress indicators. *Journal of Geophysical Research*, **85**, 6319–6341.

FREEZE, R. & CHERRY, J. 1987. *Hydrogeology*. McGraw Hill, New York.

GREENBERG, J. K. 1981. Characteristics and origin of Egyptian Younger Granites: Summary. *Geological Society of America Bulletin*, **92**, 749–840.

GROSS, M., FISCHER, M., ENGELDER, T. & GREENFIELD, R. 1995. Factors controlling joint spacing in

interbedded sedimentary rocks: integrating numerical models with field observations from the Monterey Formation, USA. *In*: AMEEN, M. (ed.) *Fractography: Fracture Topography as a Tool in Fracture Mechanics and Stress Analysis*. Geological Society, London, Special Publication **92**, 215–233.

HANCOCK, P. L. 1985. Brittle microtectonics: Principles and practice. *Journal of Structural Geology*, **7**, 437–457.

HEATH, M. 1985. Geological control of fracture permeability in Carnmenellis granite, Cornwall: implications for radionuclide migration. *Mineralogical Magazine*, **49**, 233–244.

HOLZHAUSEN, G. 1989. Origin of sheet structures: 1. Morphology and boundary conditions. *Engineering Geology*, **27**, 225–278.

HUANG, Q. & ANGELIE, J. 1985. Fracture spacing and its relation to bed thickness. *Geological Magazine*, **126**, 355–362.

HUSSEINI, M. I. 1988. The Arabian infracambrian extensional system. *Tectonophysics*, **148**, 93–103.

ISMAIL, F. & ABD-ELMOULA, I. 1992. The impact of dyke and brecciated zones on production from fractured basement reservoir of Zeit Bay field, Gulf of Suez, Egypt. *Egyptian General Petroleum Corporation Twelfth Exploration and Production Conference*, Cairo, November 1992.

JAHNS, R. 1943. Sheet structure in granites: Its origin and use as a measure of glacial erosion in New England. *Journal of Geology*, **LI**, 71–98.

KHY, L. 1986. The Structure of the Mekong trough. *International Geological Review*, **28**, 87–95.

KLITZSCH, E. & SQUYRES, C. H. 1990. Paleozoic and Mesozoic geologic history of Northeastern Africa based upon new interpretation of Nubia strata. *AAPG Bulletin*, **74**, 1203–1211.

LA POINTE, P. 1980. Analysis of the spatial variation in rock mass properties through geostatistics. *Proceedings of the 21st US Rock Mechanics Symposium*, 570–580.

MORLEY, C. K. 1995. Developments in the structural geology of rifts over the last decade and their impact on hydrocarbon exploration. In: LAMBIASE, J. J. (ed.) *Hydrocarbon Habitat in Rift Basins*. Geological Society, London, Special Publication **80**, 5–17.

——, NELSON, R. A., PATTON, T. L. & MUNN, S. G. 1990. Transfer zones in the east African rift system and their relevance to hydrocarbon exploration in rifts. *AAPG Bulletin*, **74**, 1234–1253.

MOUSTAFA, A. M. 1976. Block faulting of the Gulf of Suez. *Fifth Egyptian General Petroleum Corporation Exploration Seminar*, Cairo, 1–19.

NAGATY, M. 1982. The seven reservoirs of the Shoab Ali field. *Sixth Egyptian General Petroleum Corporation Exploration Seminar*, Cairo.

NELSON, R. 1985. *Geologic Analysis of Naturally Fractured Reservoirs*. Gulf.

NEMAT-NASSER, S. & HORII, H. 1982. Compression-induced nonplanar crack extension with application to splitting, exfoliation, and rockburst. *Journal of Geophysical Research*, **87**, 6805–6821.

OMAR, G. I., STECKLER, M. S., BUCK, W. R. & KOHN, B. P. 1989. Fission-track analysis of basement apatites at the western margin of the Gulf of Suez rift, Egypt: evidence for synchronoeity of uplift and subsidence. *Earth and Planetary Science Letters*, **94**, 316–328.

PATTON, T. L., MOUSTAFA, A. R., NELSON, R. A. & ABDINE, S. A. 1994. Tectonic evolution of the Suez rift. In: LANDON, S. M. *Interior Rift Basins*. AAPG Memoir, **59**, 9–55.

PERRY, S. K. 1983. *The Geology of the Gebel El Zeit Region, Gulf of Suez, Egypt*. University of South Carolina, Earth Science Resources Institute.

PETIT, J. P. 1987. Criteria for the sense of movement on fault surfaces in brittle rocks. *Journal of Structural Geology*, **9**, 597–608.

PRAT, P., MONTENEANT, C., OTT D' ESTEVOU, P. & BOLZE, J. 1986. La marge occidentale du Golfe de Suez d'apres l'etude des Gebels Zeit et Mellaha. *Documents et Travaux Institut Geologique Albert de Lapparent*, **10**, 45–74.

PRICE, N. J. & COSGROVE, J. W. 1994. *Analysis of Geological Structures*. Cambridge University Press.

PRIEST, S. D. & HUDSON, J. A. 1976. Discontinuity spacings in rock. *International Journal of Rock Mechanics and Mining Science and Geomechanics Abstracts*, **13**, 135–148.

ROULEAU, A. & GALE, J. E. 1985. Statistical characterization of the fracture system in the Stripa granite, Sweden. *International Journal of Rock Mechanics and Mining Science and Geomechanics Abstracts*, **22**, 353–367.

SCHURMANN, H. M. E. 1966. *The Pre-Cambrian along the Gulf of Suez and the northern part of the Red Sea*. E. J. Brill, Leiden.

STERN, R. J. & HEDGE, C. E. 1985. Geochronological and isotopic constrains on late Precambrian crustal evolution in the Eastern Desert of Egypt. *American Journal of Science*, **258**, 97–127.

—— & MENTON, W. I. 1987. Age of Fieran basement rocks, Sinai: implications for late Precambrian crustal evolution in the northern Arabian-Nubian shield. *Journal of the Geological Society, London*, **144**, 569–575.

STERN, R. J., GOTTFRIED, D. & HEDGE, C. E. 1984. Late Precambrian rifting and crustal evolution in the Northeastern Desert of Egypt. *Geology*, **12**, 168–172.

TERZAGHI, R. D. 1965. Sources of error in joint surveys. *Geotechnique*, **15**, 287–304.

WU, H. & POLLARD, D. D. 1995. An experimental study of the relationship between joint spacing and layer thickness. *Journal of Structural Geology*, **17**, 887–905.

YOUNES, A. I. 1996. *Fracture distribution in faulted basement blocks, Gulf of Suez, Egypt: Reservoir characterization and tectonic implications*. PhD thesis, Pennsylvania State University.

ZAHRAN, I. & ISMAIL, F. 1986. Similarity in composition and tectonic style between basement exposed in Gebel El Zeit and Zeit Bay subsurface. *Proceedings of the Eighth Egyptian General Petroleum Corporation Special Exploration Conference*, Cairo, November 1986, 183–205.

Polygonal faulting in the Tertiary of the central North Sea: implications for reservoir geology

LIDIA LONERGAN[1], JOE CARTWRIGHT[1], ROD LAVER[2] & JOE STAFFURTH[2]

[1] Department of Geology, Imperial College of Science, Technology and Medicine, London SW7 2BP, UK

[2] Fina Exploration, Fina House, Ashley Avenue, Epsom Surrey KT18 5AD, UK

Abstract: Interpretation of regional two-dimensional seismic surveys and three-dimensional seismic surveys in the central North Sea has demonstrated the existence of a pervasive polygonal network of normal faults affecting Tertiary shale-dominated slope and basin-floor depositional systems. The area affected by the faulting encompasses most areas of hydrocarbon production from Tertiary sandstone reservoirs. The polygonal fault networks were active during sedimentation and early burial. Throws measured on individual faults range from 8 to 100 m, with average fault plane dips of 45°. Lengths of individual fault segments range from 80 to 1400 m, and average fault spacings range from 100 to 500 m. The high density and the polygonal geometry of the faults make seismic interpretation of the Lower Tertiary interval problematic, and can lead to misinterpretation of faults as apparent seismic-stratigraphic features.

The recognition of this fault system has consequences for the development of fields in Tertiary reservoirs. The remaining hydrocarbon potential in the Lower Tertiary could be considered predominantly to be stratigraphic plays, but the presence of faults active during sedimentation and early burial implies that this play concept is too simplistic, particularly for Eocene reservoirs. The role of both syn-depositional and early-burial normal faulting on original reservoir distribution and post-depositional modification should be considered further. The presence of this fault system may also be important for secondary migration into Lower Tertiary reservoirs from Kimmeridge Clay Formation source rocks. The existence of an interconnected fault and fracture network in the low-permeability mudrocks may have provided an efficient vertical migration pathway for charging isolated lower Tertiary sandstone reservoirs. Finally, the maximum fault throws of between 50 and 100 m are large enough to represent potential barriers for lateral communication in sandstone reservoirs where individual sand bodies are commonly 25–100 m thick.

With the recent widespread application of sequence-stratigraphic concepts to the petroleum geology of the North Sea, the Lower Tertiary sandstone reservoirs (e.g. Forties-Montrose, Nelson (Paleocene) and Forth, Gryphon and Alba (Eocene)) in deep-water successions are interpreted as basin-floor or slope deposits developing in a lowstand systems tract (Stewart 1987; Milton et al. 1990). Within this model, basin-floor fans are predicted to be sand-rich and hence are considered to be attractive hydrocarbon prospects (Posamentier & Vail 1988). The dominant role of the sequence-stratigraphic approach has meant that subtle structural features affecting the Paleocene–Eocene reservoir intervals have been either neglected or relegated to minor significance, in comparison to stratigraphic controls on reservoir geometry and occurrence. In this paper, we describe the development of a pervasive, polygonal network of small-scale extensional faults affecting slope and basin-floor depositional systems in the central North Sea (Cartwright 1994a, b). We

illustrate the detailed geometry of this polygonal fault system using as an example one of the six three-dimensional (3D) seismic datasets studied to date in the central North Sea, and discuss the implications for development and exploration strategies for Eocene reservoirs.

Stratigraphic setting of the tertiary sandstone play

The polygonal fault systems described here affect Paleocene to Miocene clastic sedimentary sequences in the central North Sea Basin (Fig. 1). The lithostratigraphy of the deformed units is dominated by mudstones and silty mudstones that accumulated in prodelta, slope, and basin-plain depositional environments in a partly enclosed marine basin (Parker 1975; Lovell 1990). Commencing in the Paleocene, a large volume of sand-rich sediment was eroded off the uplifted Scottish Highlands–Shetland Platform and transported into depocentres
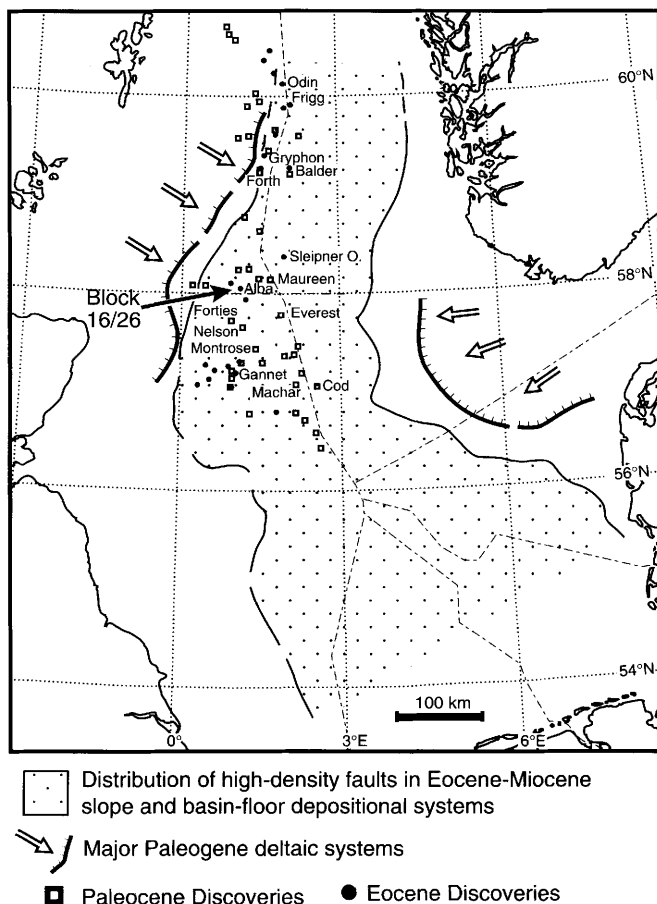
Fig. 1. Distribution of faulted Tertiary slope and basin-floor facies in the central–northern North Sea and location of main Tertiary discoveries in sandstone reservoirs.

located over the buried Mesozoic Central and Viking Grabens (Morton 1979). Large fluvial deltas built out into the Moray Firth and East Shetland Platform. At times during the Paleocene (Maureen, Andrew and Forties Formations) and during the Eocene (Balder and Frigg Formations), submarine sand-prone complexes were deposited in the deeper water environments of the Viking and Central Grabens. Channel sandstone complexes form the Paleocene (post-chalk) and Eocene reservoirs. During breaks in clastic input large areas of the shelf and coast were drowned and mudstone-dominated packages separate the major sandstone units. Channel development was much more extensive during the Paleocene than the Eocene. It is considered that during the Eocene, sands were fed to the basin during times of relative sea-level fall via canyons (e.g. the Frigg Fan (Den

Hartog Jager *et al.* 1993) and the Alba sands (Harding *et al.* 1990; Newton & Flanagan 1993)), or due to slump failure of the shelf edge (Forth Field sands (Alexander *et al.* 1993)). The Paleocene sand-rich complexes tend to be more laterally extensive and have a sheet-like geometry in comparison to some of the Eocene facies, which exhibit restricted mound-like geometries with massive sandstone units (e.g. Gryphon, Forth and Balder Fields).

Three different trapping mechanisms have been described for Tertiary sandstone fields (Parsley 1990; Bain 1993).

(1)   Structural dip closures have developed by differential compaction over Jurassic tilted fault blocks. Typical examples are the Paleocene Forties, Montrose and Nelson Fields.

(2) Salt-induced structural traps occur, such as the Cod, Maureen and Machar Fields.

(3) Stratigraphic traps occur where sand-rich depositional bodies are sealed and enclosed by hemipelagic shales (e.g. Alba and Frigg Fields). Later drape and differential compaction forms the trap with a mound-like morphology. Another successful stratigraphic trapping mechanism is the pinch-out of mounded sands against pre-existing topography in the basin. In Gannet East, the Eocene Tay Formation sands pinch out towards the shelf and the salt-induced highs of Gannet North and Central to the SW. The Everest field also shows a similar relationship where the sand lobes pinch out eastwards onto a topographic high in the basin (O'Connor & Walker 1993).

A stratigraphic trapping style is frequently considered more typical of the Eocene fields. Recently however, the improved high-resolution 3D seismic data acquired over fields such as Balder, have shown that trapping is achieved by a combination of structural and stratigraphic mechanisms with small faults defining the trap geometry on the sides of the sedimentary mounds (Jenssen et al. 1993).

Recent exploration targets in the Tertiary of the central and northern North Sea have focused on remaining subtle stratigraphic traps. If such plays are to be successful, the effect that pervasive polygonal fault systems might have on influencing the geometry of reservoir bodies must be considered. Much drilling activity aimed at Tertiary objectives is concentrating on the appraisal and development of existing discoveries. Again, success will rely on an understanding of the depositional processes and the role of faults during and after sedimentation.

Fault geometries

The structural expression of the Lower Tertiary fault system on two-dimensional (2D) seismic data has been described previously by Rundberg (1989), Higgs & McClay (1993), Clausen & Korstgård (1993), and Cartwright (1994a,b). Examples of the 2D seismic expression of these faults can be found in Fig. 2 of Cartwright (1994b) and Fig. 2 of Higgs & McClay (1993). The small extensional faults are generally poorly resolved on 2D seismic data. This is because the fault spacing is dense relative to the spatial resolution of the data, and because the polygonal geometry means that any 2D section will always consist of many oblique fault intersections which cannot

be migrated properly. Hence 3D seismic data are required to image the faults properly. The faults are best imaged in the high-reflectivity parts of the Lower Tertiary section in mudstone-dominated lithologies. Regionally, in the central North Sea, they are most pervasively developed in slope and basin-floor depositional facies in the Eocene to Middle Miocene interval, but are recognized to a lesser extent in the more sand-prone Paleocene succession.

3D seismic case study: Block 16/26

As an example of the deformational style, two orthogonal seismic lines and two horizon maps from a 3D seismic survey in Block 16/26 (UK sector, central North Sea) are illustrated in Fig. 2. Two levels with clearly faulted horizons are visible on the seismic sections (Fig. 2A and B) at approximately 1.5 and 2.0 s two-way-travel time (TWTT) respectively. In between there is a zone of low-amplitude reflectivity where it is difficult to be confident of interpreting faults. Individual faults are thus restricted in vertical extent to only part of the entire deformed interval with only the occasional faults appearing to cross the entire interval. The deformation is layer bound and concentrated between the Middle Miocene marker and the prominent Balder horizon (base Eocene). The lower levels of the fault system affect reservoir sandstone bodies distributed within the middle Eocene interval. The faults on this dataset are best resolved in the mudrock-dominated lithologies of the uppermost Oligo-Miocene interval. Horizon data from this interval are used to illustrate the main geometrical attributes of the polygonal fault network.

We have found that structural interpretation of this highly complex fault system is best approached via a horizon-based interpretation rather than by interpreting faults on sequential vertical sections. Fault interpretation is relatively straightforward if the section intersects a fault approximately orthogonally and the faults are well imaged (e.g. centre portion of Fig. 2A). However, as a result of the polygonal organization of the fault system, most sections will have low-angle oblique or strike cuts through faults, and these cut-outs are responsible for the poor continuity of stratigraphic markers. This means that it is difficult to reproduce a unique fault interpretation on vertical sections, but it is possible to obtain accurate fault maps by interpreting clear marker horizons, on a line-by-line basis. The dense sampling of fault cuts then eliminates aliasing problems, and mis-ties are
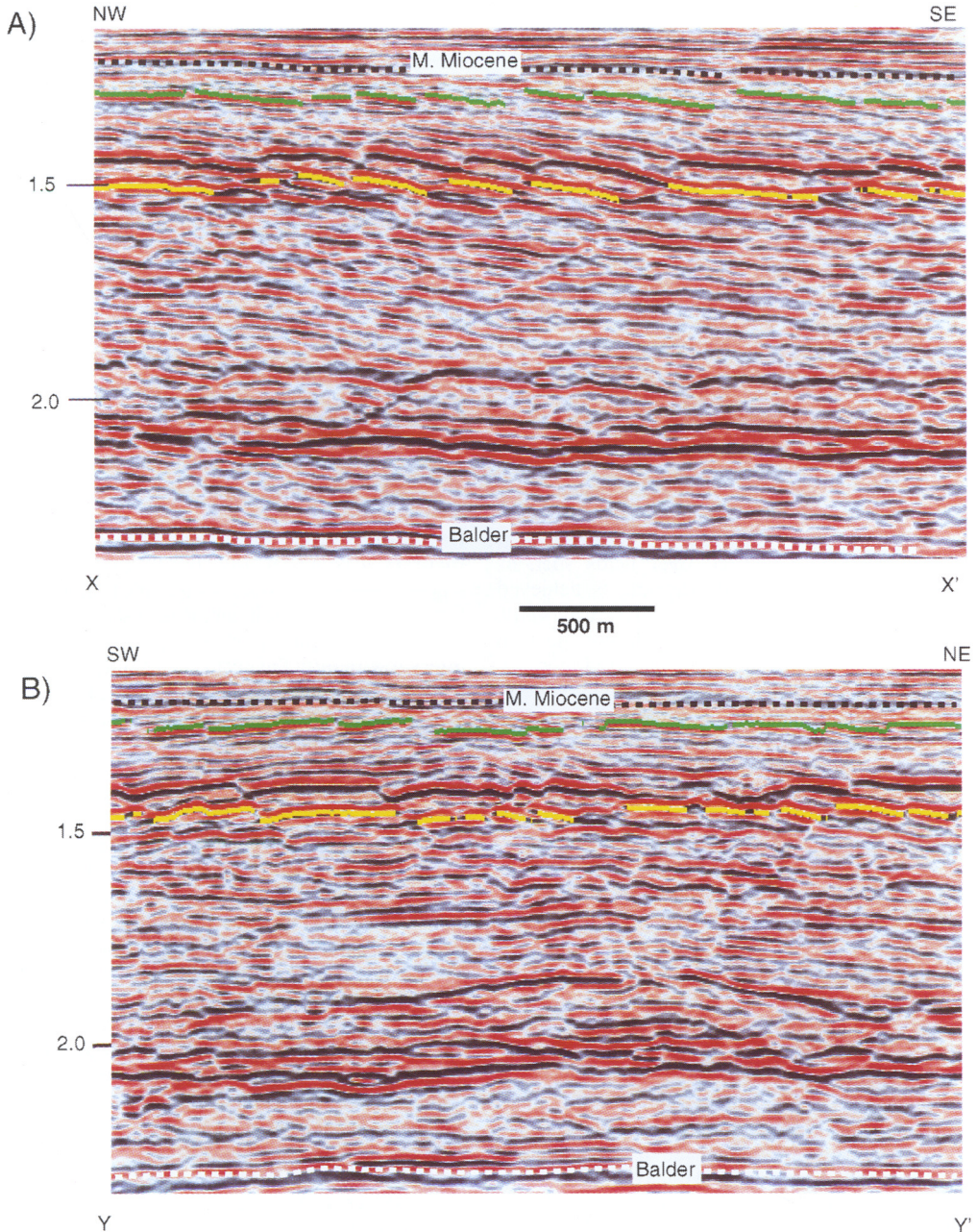
Fig. 2. (**A**) and (**B**) NW–SE (XX′) and SW–NE (YY′) seismic sections from a 3D survey of Block 16/26, in the UK Sector of the North Sea. Two interpreted horizons of Lower Miocene age (green) and Oligocene age (yellow) are illustrated on each section. The vertical scale is two-way travel time. The seismic sections (A and B) show the faulted interval bounded at the top (Middle Miocene and younger) and bottom (Balder Formation) by undeformed sequences. Faults are recognized from normal-sense offsets of stratal reflections. Seismic section XX′ (A) is perpendicular to the strike of a group of faults in the centre of the Oligocene map and hence most of the fault planes appear to dip uniformly to the NW. On the orthogonal seismic section YY′ (B) faults can be identified dipping in opposite directions, but a comparison of the fault maps and seismic sections shows that the sections intersect other faults obliquely resulting in very low angle fault offsets of horizons.
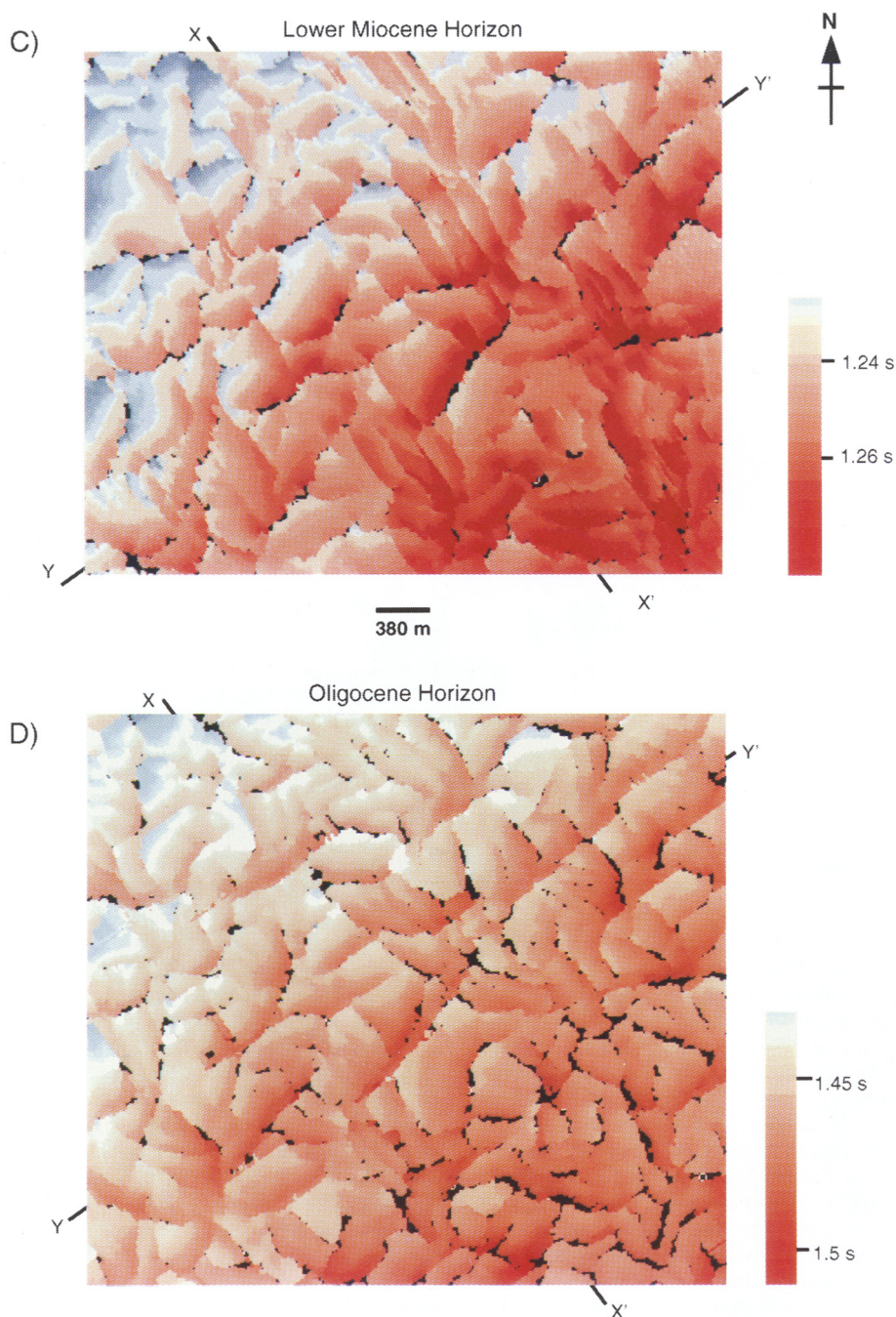
(**C**) and (**D**) Structural maps in two-way travel time of the interpreted Oligocene and Lower Miocene horizons. The horizon maps were constructed by line-by-line interpretation at 12.5 m spacing of sections oriented NW–SE and SW–NE. Each horizon is deformed by small extensional faults that are organized in a polygonal pattern.
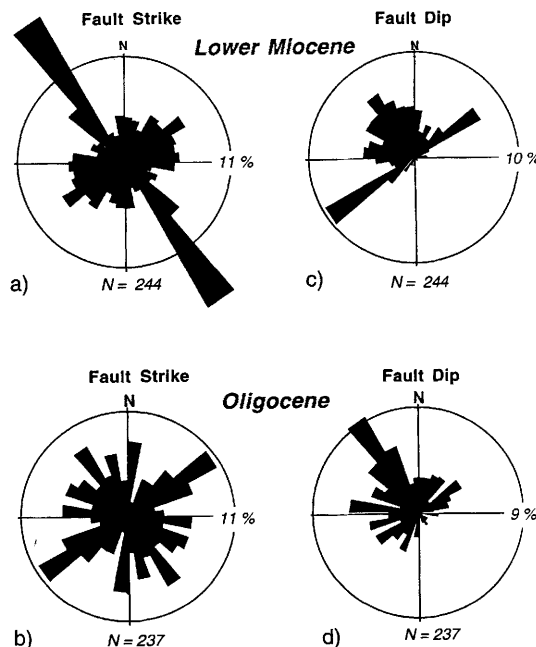
Fig. 3. Equal-area rose diagrams of fault strikes (**a**) and (**b**) and dip direction (**c**) and (**d**) for faults offsetting the Lower Miocene and Oligocene horizons. Despite the horizons being separated by only 250 m they exhibit different preferred orientations of fault strike. The Oligocene fault map has an almost equal number of faults oriented in all directions, whereas the Lower Miocene horizon has a background radial distribution of fault strikes with a superimposed strong preferred orientation of NW-striking faults. For both horizons, faults that strike between N and E, dip (and downthrow) towards the NW quadrant.

readily observable. The 3D fault structure can then be inferred by mapping several closely spaced horizons.

Figure 2C and D are fault maps constructed by interpreting a Lower Miocene and an Oligocene horizon on closely spaced lines (12.5 m intervals) throughout the 3D survey. The horizons are gently dipping at less than 1° to the SE as seen by the broad change in TWTT from grey in the NW to reds in the SE. The faults are identifiable as linear or arcuate gaps or jumps in the time contour colours. The gaps represent the fault heave and the irregularities in the fault traces reflect the resolution accuracy in interpreting fault plane positions from horizon offsets. The polygonal organization of the fault system is the most obvious characteristic of these maps, with many examples of triple and even quadruple fault intersections. The Oligocene fault map has an almost equal number of faults oriented in all directions (see rose diagram, Fig. 3b). In comparison, the Lower Miocene horizon has a background radial distribution of fault strikes, with a superimposed strong preferred orientation of NW-striking faults (Fig. 3a).

Although the two horizons are only separated by about 250 m they exhibit different fault patterns and not all of the faults connect between the two horizons. A close examination of the dataset shows that the NW-striking faults deforming the Lower Miocene tend to be short faults (in a depth direction), have small throws (<15 m), and do not extend down to the Oligocene horizon. Faults that can be traced through the two horizons tend to have accumulated the largest displacements. Closely spaced horizons with different biases in fault orientation are not unique to the Block 16/26 data and have been described from other 3D datasets (Cartwright & Lonergan 1996). An interesting feature of the deformation pattern is that faults striking between N and E preferentially dip to the NW quadrant (Fig. 3c and d), i.e. up-dip of the regional shallow tilt of the succession. Why this should be so is as yet not fully understood, but may represent a response to the palaeoslope during fault formation. Fault patterns affecting horizontal basin-floor successions do not show such a marked preferred fault dip direction. Higgs & McClay (1993) first observed the

preferred dip direction to the NW in the Outer Moray Firth, which they attributed to gravitational collapse of the slope due to a tilting event in the Middle Miocene. However, their model fails to account for the polygonality of the fault system or for the occurrence of extensional faults in the horizontal region of the basin axis.

The throws on the faults shown on the two horizon maps (Figs 2C and D) range from 8 m to a maximum of 50 m, assuming a velocity of 2000 m s^{-1} for this interval (Fig. 4A). In general the throw measured on the upper portions of the faults (Lower Miocene level) is less than at the Oligocene level. Fault throws of up to 100 m have been measured on other 3D datasets from the central North Sea. In section the faults within this interval have dips ranging from 30° to 70°, with an average of 45° (Fig. 4B). Faults with arcuate map traces are often gently listric in section, and short linear fault segments tend to be planar. In plan view, lengths of individual fault segments range from 80 m to 1400 m, with the majority of the faults having segment lengths of 100–400 m on the Oligocene horizon and 200–600 m on the Lower Miocene horizon (Fig. 4C).

Timing of fault movement

The Middle Miocene 'unconformity' is a regional marker in the central–northern North Sea and other workers have assumed that the faulting affecting the Tertiary interval took place at this time (Harding *et al.* 1990; Higgs & McClay 1993; Clausen & Korstgård 1993). The fact that different levels within the deformed interval have different densities, spacings and patterns of faults (Figs 3 and 4) implies that the entire interval cannot have been faulted at the same time. Even stratigraphic horizons separated by only 250 m have different fault populations suggesting that faults must be active during early burial within the time interval separating the horizons.

Evidence for syn-sedimentary movement on the faults has been found at at least two stratigrapic levels within the 16/26 survey area. In the youngest portion of deformed succession divergent, wedge-shaped groups of reflectors observed in the hangingwall of the faults in the Oligo-Miocene interval imply that syn-sedimentary movement took place on the faults in the early Miocene. The seismic panel in Fig. 5a is a random line chosen perpendicular to the strike of a group of planar faults dipping to the NW which affect the Oligo-Miocene interval. On the centre fault block, beneath the Middle Miocene

unconformity, wedge-shaped reflectors can be clearly seen.

Older syn-sedimentary fault movement is apparent from reflection configurations at deeper levels within the Eocene (Fig. 5B). The horizon map detail in Fig. 5B illustrates two faults which intersect in the SE corner of the map. The westerly fault dips and downthrows to the NE, whereas the easterly fault downthrows to the SW forming a small asymmetric depression between the two faults. On the seismic line, orthogonal to the westerly fault, a distinct thickening of strata is visible in the hangingwall of the fault above the interpreted horizon (grey marker). Other examples similar to this imply that some of the faults propagated to the sea-floor generating local topography during Eocene times.

It is apparent from this description of reflection geometries associated with different sets of faults in the 16/26 survey area that the deformation occurred at different times during sediment deposition. Similar conclusions have been reached for other survey areas in the central North Sea, where up to four 'tiers' of faults have been interpreted based on fault population analysis from horizon maps (Cartwright 1996). Evidence for several episodes of fault movement places constraints on the type of process involved in the genesis of the polygonal faults. The evidence for syn-sedimentary fault activity as early as the middle Eocene also raises the possibility that faulting influenced the depositional processes at a time when reservoir-prone units were being deposited.

Fault genesis

Cartwright & Lonergan (1996) have measured the amounts of extension on Lower Tertiary faults on differently oriented sections through two 3D seismic survey areas. They found that the extensional strain in two separated areas was radially isotropic as measured on sub-horizontal marker horizons within the layer-bound deformed interval. Two explanations for this bulk strain are possible: either the extension is a true extension, and compactional flattening was accompanied by radial outward movement of the original stratigraphic horizons (Fig. 6A), or the extension is an apparent strain, and compaction was accompanied by radially uniform volumetric contraction of the beds (Fig. 6B). Since the deformation is clearly layer-bound and there is no evidence for displacement transfer to basement structures, Cartwright & Lonergan (1996) argue that the only explanation

A. FAULT THROW

Lwr Miocene Horizon

Oligocene Horizon

B. FAULT DIP IN OLIGO-MIOCENE LAYER

C. FAULT SEGMENT LENGTHS

Lwr Miocene Horizon
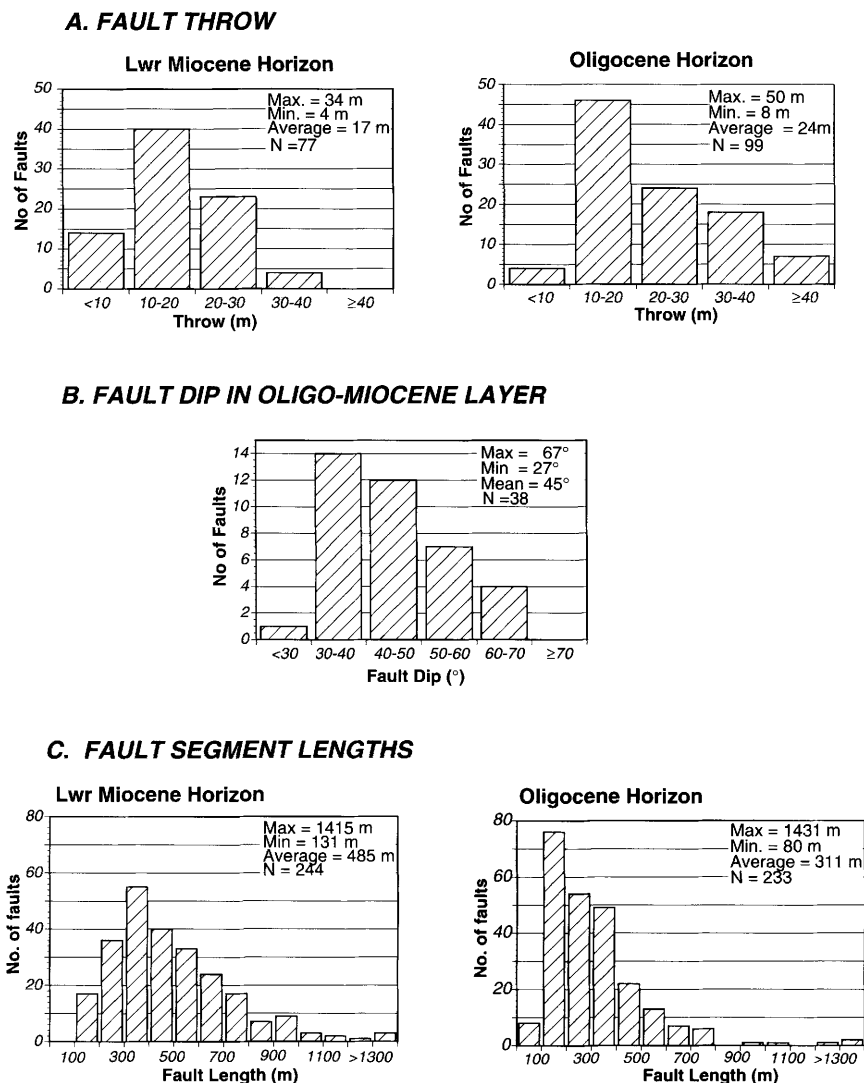
Oligocene Horizon

Fig. 4. Statistics for faults in the Oligo-Miocene deformed interval. (**A**) Range of throws measured on faults offsetting the mapped Oligocene and Lower Miocene horizons. Throws are maxima for each fault measured on seismic sections perpendicular to the fault strike and depth, converted assuming a seismic velocity of 2000 ms^{-1}. Dips of faults (**B**) were measured on true-scale seismic sections perpendicular to fault strike. (**C**) Histograms illustrating the range in fault segment lengths for faults intersecting the two mapped horizons.

for this apparent extension is by layer-parallel volumetric contraction. Were it to be a 'true' extension, the 10–20% measured values of apparent extension would require a totally unrealistic extrusion of 20–30 km of Lower Tertiary rocks outward at the basin margins in order to conserve volume across the 200×400 km dimensions of the deformed region of the basin (Fig. 1). Further evidence suggesting that the polygonal faults have not formed in response to

a regional tectonic event is the observation that the fault orientation statistics and map geometries change between closely spaced horizons within one deformed interval (Figs 2 and 3; Cartwright,1996), a feature that is atypical of tectonic fault patterns.

The mechanism of faulting by volumetric contraction can be considered partly analogous to the development of shrinkage cracks during the desiccation of muddy sediments. When mud

(a) Miocene growth
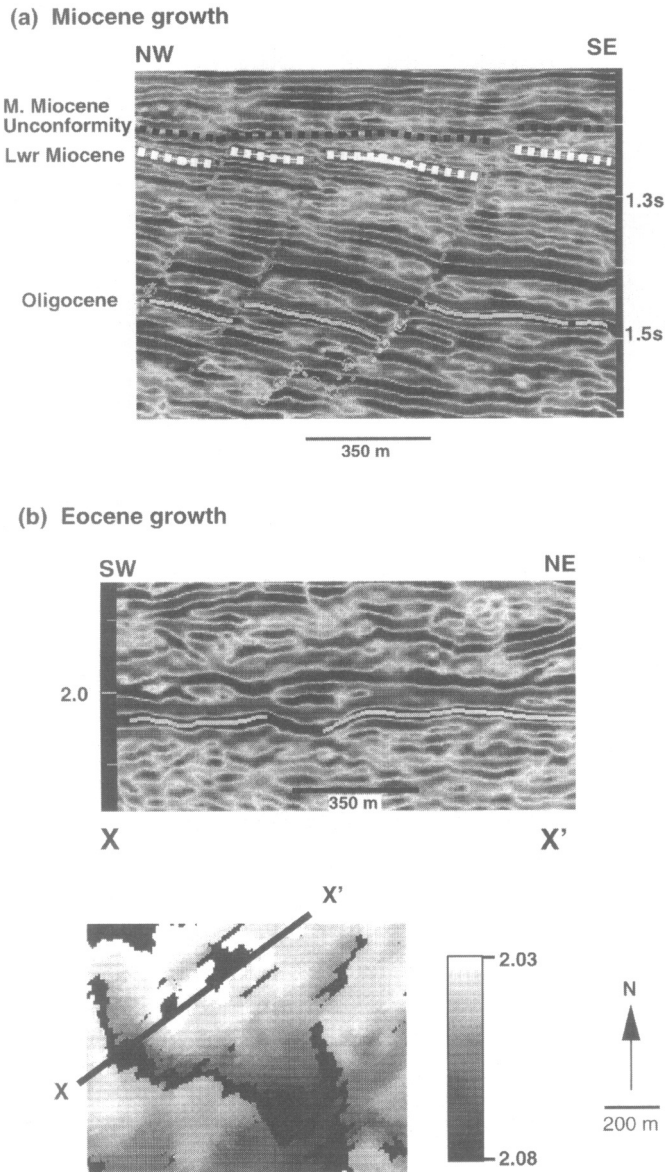
(b) Eocene growth

Fig. 5. Seismic sections showing syn-sedimentary fault growth in lower Miocene and Eocene times. (**A**) The seismic panel is a random line chosen perpendicular to the strike of a group of planar faults dipping to the NW in the Oligo-Miocene tier. The dashed grey lines with circles are interpreted faults. Note the low-angle strike cut of a fault parallel to the section below 1.5 s. (Not all possible faults have been interpreted on the section.) (**B**) Seismic line and map (contoured in TWTT) of an Eocene horizon (pale grey marker below 2 s on seismic line). The map shows the fault traces (black gap) and location of the seismic line. The seismic line illustrates the thickening of hangingwall strata into the fault. The grey loop above the pale marker splits into an extra back-loop close to the fault.

cracks develop there is a net loss of pore fluid resulting in the development of tension cracks creating voids, but no net extension of the shrinking mud layer. Both processes result in polygonal extensional structures, but in the case of the fault system in the Lower Tertiary, the polygonal structures are inclined normal faults, not vertical tensile fissures.

Cartwright & Lonergan (1996) propose that faults forming by volumetric contraction occur

A) *Compaction & Extension*   **B)** *Compaction (with contraction)*

$$\text{EXTENSION} = \frac{L_1 - L_0}{L_0} \text{ , Where } \Sigma L_i = L_0$$

$$\Delta W + Z_1 < Z_0$$

$$\begin{aligned}\text{APPARENT}\\\text{EXTENSION}\end{aligned} = \frac{L_0 - \Sigma L_i}{L_0} \text{ , Where } \Sigma L_i < L_0$$

$$\Delta W + Z_1 = Z_0$$
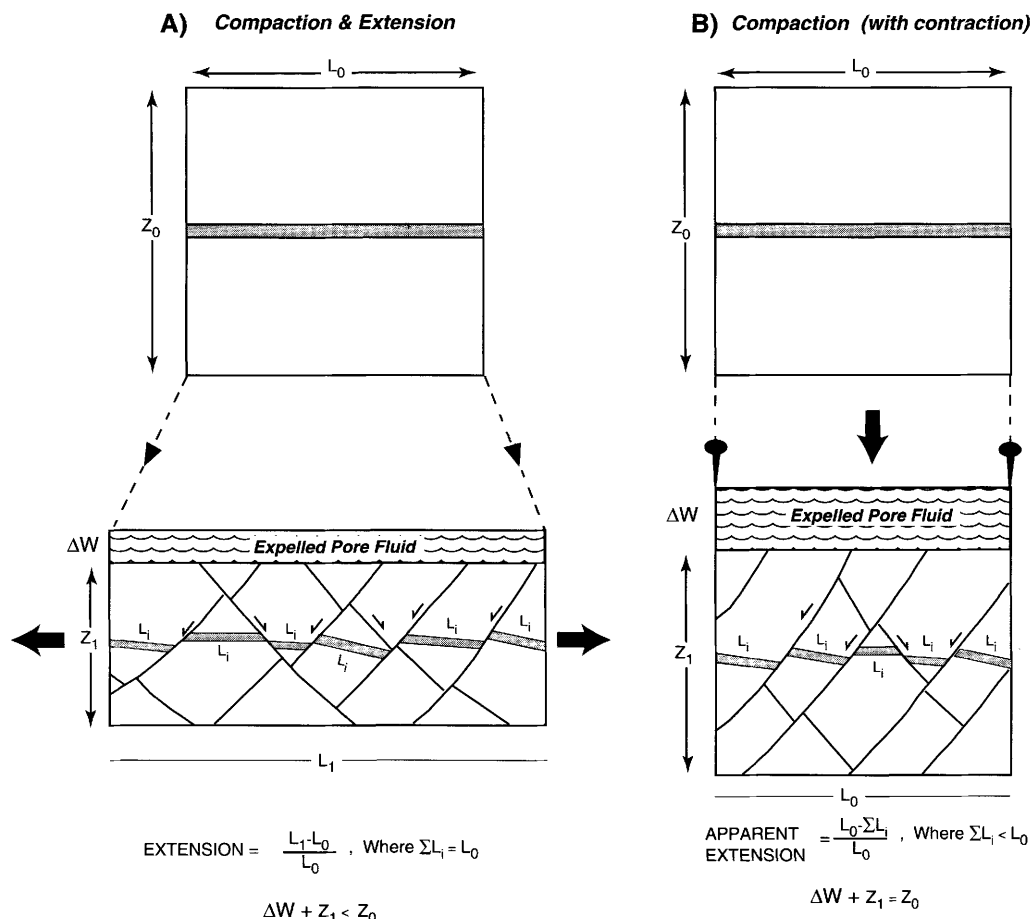
Fig. 6. Alternative mechanisms for the observed 3D deformation in the Tertiary sequence. For simplicity, the strain paths are illustrated in 2D, because the polygonal distribution of faults implies that any orientation of cross-section exhibits the same structural relationships. In both cases there is a reduction in volume due to compaction during burial. In (**A**) the compaction is accompanied by a net extension, whereas in (**B**) there is no net extension (the rectangle sides are pinned) and hence the bed lengths must contract (from Cartwright & Lonergan 1996).

in response to fluid expulsion from the mudrocks during early compaction, which is consistent with the seismic evidence for fault movement during shallow burial (Fig. 5), and that within the first two kilometres of burial mudrocks reduce their volume by up to 50% due to loss of pore fluid. The build-up of fluid overpressures may have triggered failure in the cohesive muddy sediments (e.g. Henriet *et al.* 1991; Verschuren 1992; Cartwright 1994*a, b*) allowing some dewatering due to enhanced permeability along and in the vicinity of faults and fractures. Alternatively, the driving force for failure may well be partly provided by physical interactions between clay minerals induced by pore fluid expulsion, rather than solely by a critical fluid overpressure

(Cartwright & Lonergan 1996). The faults would continue to grow as the rock mass contracted volumetrically. With increasing burial, and less and less pore fluid to expel, the fault system probably ceased to be an important dewatering mechanism and became inactive beneath a threshold depth. In the meantime new sediments within the top few hundred metres beneath the sea floor began to deform in a similar way, forming a new and different set of polygonal faults.

This model explains many aspects of the fault system, including the basin-scale distribution in the low-permeability slope and basin floor lithofacies, the layer-bound distribution of the deformed intervals and the polygonal organisation

of the faults. In slope settings the slope dip or wedge geometry of the sedimentary package may have had some influence on fault propagation direction, with faults dipping up-slope developing preferentially.

Implications for reservoir geology

Field development strategies

The widespread distribution of the polygonal fault network encompassing most of the areas of commercial production from Tertiary reservoirs in the North Sea (Fig. 1) means that many Lower Tertiary reservoir intervals could be intersected by normal faults with throws of up to 50–100 m. The main Lower Tertiary reservoir units have thicknesses varying between 25 m and 400 m (Fig. 7). In general the Paleocene reservoirs are thickest, but many Eocene reservoirs have thicknesses of less than 100 m over substantial parts of the productive volume, and the likelihood of the productive reservoir interval being faulted against mudrocks is high.

Given that mud-rich rocks dominate the lithostratigraphy of the Lower Tertiary, the sealing potential of faults by clay-smear along the fault plane is high. Therefore even if the throws on the faults are not large enough to offset reservoir sands, they may still be responsible for compartmentalizing the reservoirs.

Sandstone injection features are commonly associated with Eocene reservoirs (Alexander *et al.* 1993; Newman *et al.* 1993; Dixon *et al.* 1995) and from both core and seismic studies are observed to be injected along fault planes. If such injected sandstones occur they could be expected to offset the effects of clay-smear along the fault plane and to improve reservoir connectivity.

When planning horizontal wells, the possibility of drilling from reservoir into shale and then back into reservoir due to <50 m offsets on faults that are seismically difficult to resolve should not be discounted (Fig. 8). Detailed horizon mapping is the best way of identifying faults. Finer resolution of subtle smaller faults, with offsets less than the cycle of seismic reflection, that only cause an inflection in the horizon can be made by making attribute (azimuth, dip, edge and amplitude) maps from interpreted horizon maps. To confirm the existence of faults that are poorly resolved in cross-section, maps of closely spaced horizons above and below the reservoir interval should be made. Faults can then be traced from one map to another and their position through the reservoir interval tracked. Although it is time-consuming, careful fault mapping will help identify small-scale faults difficult to observe on seismic sections through the reservoir body. This added information is obviously crucial when planning reservoir development and well locations.
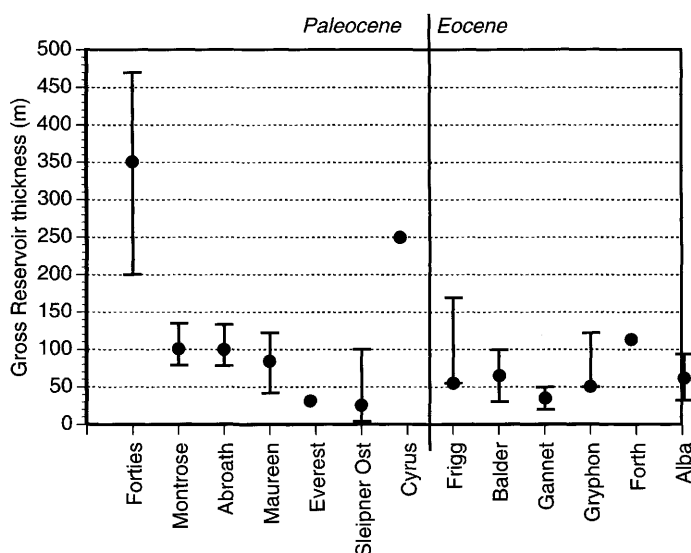
Fig. 7. Gross reservoir thicknesses for Lower Tertiary sandstone fields. Ranges in reservoir thicknesses have been plotted where available. Data compiled from numerous published sources.

Stratigraphic "mound" or faulted unit ?
Implication for field development
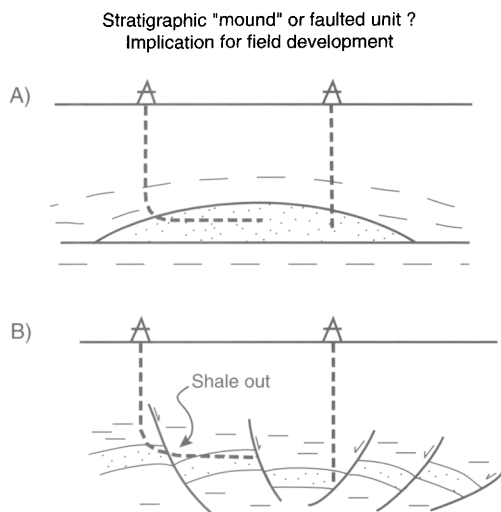
Fig. 8. Implications of polygonal faulting for reservoir geology. The misinterpretation of a complex faulted structure (**B**) for an apparently simple stratigraphic mound (**A**) may lead to surprises during field development, where horizontal wells may shale out due to small offsets on normal faults.

Seismic interpretation

Cartwright (1994*b*) has summarized the potential interpretational pitfalls of not recognizing the presence of the small Lower Tertiary faults. Changing polarity of fault dips or hangingwall roll-over on closely spaced listric faults can be

mistaken for stratigraphic mound morphologies. Bain (1993, Fig. 5a) illustrates one such 'mound' from the central North Sea. When it was drilled by the operator it was found to contain no sand and the subsequent interpretation was a series of closely spaced listric normal faults. The stratal rotation within fault blocks was responsible for the apparent mound.

As previously discussed, the complex 3D fault pattern means that any seismic section contains low-angle intersections with faults parallel and oblique to the orientation of the seismic section. The resultant low-angle and subtle offsets to horizons of interest may be misinterpreted as 'stratigraphic' onlap and downlap features or even facies changes.

Poor interpretation of faults or even ignoring them can lead to substantially different and potentially erroneous reservoir correlations. Figure 9 illustrates a realistic situation where a reservoir correlation between sandstones picked in several neighbouring wells could be made in two totally contrasting ways. In the first case (Fig. 9A), the sandstones are correlated assuming a depositional model of a channelized submarine fan. This leads to a reservoir geometry of several isolated lensoid sand bodies. In the second case (Fig. 9B), the same well picks are correlated with due attention paid to fault patterns recognized on the seismic data. The resultant correlation is radically different from the strati-graphically-driven solution, and would have important consequences for reserve calculations and choice of development drilling locations.
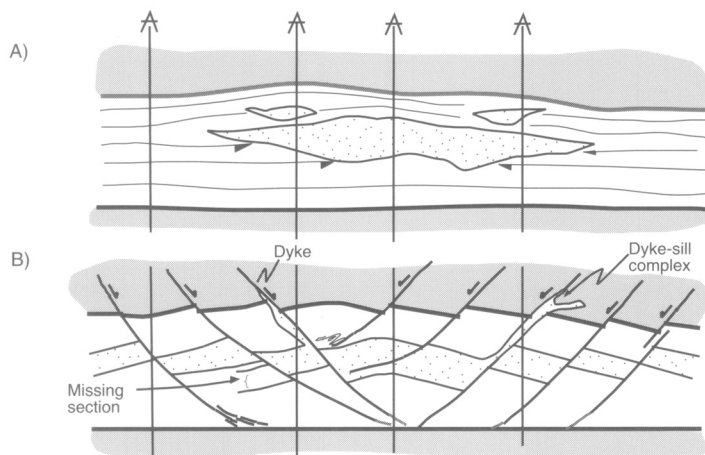
Fig. 9. Comparison of well correlations for reservoir sandstones based on (**A**) stratigraphic model, and (**B**) structural model incorporating polygonal faults. The sandstone picks are identical in both cases but in (A) the correlation depicts isolated sandstone bodies, whereas in (B) the correlation takes account of remobilization of sandstone along fault planes in the form of dykes and sills. Note also in (B) the missing section due to fault cut-out which is shown in (A) as channel incision.

Integration of the complex faulted structure into reservoir correlation schemes may in some cases reduce connectivity and downgrade the potential of an accumulation, but in other cases, syn-sedimentary faulting during reservoir deposition could lead to increased reserve potential in otherwise unexpected trapping configurations. Ignoring the complex fault system simply because it is difficult to map will lead to an incomplete assessment of potential reserves.

Depositional models

The Eocene sandstone reservoirs are distinctive in that they are predominantly massive, high-porosity sandstones with very few preserved sedimentary structures, except for dish and pillar dewatering structures (Armstrong *et al.* 1987; Brewster 1991; Mattingly & Bretthauer 1992; Newton & Flanagan 1993; Alexander *et al.* 1993; Newman *et al.* 1993; Jenssen *et al.* 1993; Shanmugam *et al.* 1995; Dixon *et al.* 1995). Sandstone bodies can be up to 100 m thick but exhibit rapid lateral thickness variation and often pinch out over distances of less than 500 m. Post-depositional modification of the massive sandstone bodies is a common feature of many Eocene reservoirs. Soft-sediment deformation structures and sand and mud injection features have been described in cored intervals through the Alba, Forth, Gryphon and Balder fields (Mattingly & Bretthauer 1992; Jaffri 1993; Newton & Flanagan 1993; Alexander *et al.* 1993; Newman *et al.* 1993; Jenssen, *et al.* 1993; Dixon *et al.* 1995). In the Forth and Alba Fields, extensive sandstone dykes and sills have been intruded into the Eocene muds above the main massive sandstone reservoirs (Alexander *et al.* 1993; Newton & Flanagan 1993). In some cases, these sandstone dykes are found to be oil-bearing. More recently Dixon *et al.* (1995) have recognized discordant sandstone intrusions on seismic data that have a lateral extent of 200–300 m.

Recent sedimentary interpretation of the massive sandstone bodies with mounded topography suggests that they are mass-flow deposits (slumps or debris flows) as opposed to sand-rich turbidites (Newman *et al.* 1993; Shanmugam *et al.* 1995). A puzzling feature is the steep-sided slopes (up to 15°) on the sides of the mounds in both the Gryphon and Balder Fields. Such dips are considered too steep to be depositional in origin, even after accounting for compaction (Jenssen *et al.* 1993). Recent work on both the Gryphon and Balder Fields (Newman *et al.* 1993; Jenssen *et al.* 1993; Rye-Larsen 1994),

which benefits from new 3D seismic surveys acquired over the fields, recognizes the importance of small-scale faulting in controlling the geometry of the sandstone mounds. Essentially, the workers on these fields concluded that the faults are the result of slumping. Jenssen *et al.* (1993) and Rye-Larsen (1994) consider that slump faults alone cannot account for the mounding observed in the Balder Field and suggest that some of the mound-like geometries can be attributed to remobilization and injection of sandstones from underlying low-relief turbidite sheet sands. More recently, Dixon *et al.* (1995) have concluded that post-depositional sandstone diapirism and intrusions of clastic dykes and sills associated with major gravity slide faulting are responsible for the reservoir geometries observed in the Forth and Gryphon Fields.

Our studies of the polygonal fault systems imply that minor extensional faults form as part of the compactional dewatering process during early burial and we suggest that the faults recognized locally in the Eocene fields and attributed to gravity sliding or differential compaction are part of this wider polygonal system. The injection and soft-sediment deformation structures widespread in the Eocene sandstone bodies are all consistent with syn-sedimentary and early burial dewatering deformation. The patterns of sandstone dyke injection described by Alexander *et al.* (1993) for the Forth Field in particular are highly reminiscent of the complex polyhedral geometries of the faults described in this paper. Dyke injection requires elevated pore fluid pressures in order to fluidize the sand in the original reservoir unit, and to provide the pressure differential for upward flow (Jaffri 1993). Upward injection would exploit the weaknesses due to the presence of already formed extensional faults in the overlying mudstones. More direct evidence of the inter-relationship between the polygonal faults and final reservoir configurations is provided by a horizon slice through the Alba Field published by Newton & Flanagan (1993, Fig. 8). This illustrates the close spatial relationships between the sandstone reservoirs and the polygonal fault pattern in the surrounding hemipelagic shales. In a number of places the edges of the Alba 'channel' change strike and follow a polygon side, which implies that either the distribution of sandstones in the deep-water Eocene successions was influenced by contemporaneous, near-surface faulting or that faults controlled the post-depositional modifications to the original sedimentary geometry.

Soft-sediment deformation structures are often interpreted as having formed due to slope

instability, but we consider that dewatering and polygonal fault development could lead to a similar range of structures with identical characteristics in core samples. However, the exact role of the polygonal fault deformation system in controlling sand-body geometries requires further study. Syn-sedimentary faulting generating an irregular sea-floor topography (Fig. 5B) may have exerted a primary control on the location of sand-rich mass-flow deposits. Alternatively the effects of faulting may have been more pronounced during early burial by facilitating remobilization and injection of existing sands, thus contributing to the isolated mound-like geometries typical of some Eocene fields. It is possible that in near-surface conditions of generally elevated pore fluid pressures, considerable volumes of sand could have been fluidized, remobilized and injected as large sandstone sills (Jaffri 1993; Dixon *et al.* 1995). Clearly, this possibility raises some interesting questions about final reservoir configurations. Whilst this is speculative at present, this type of process would help to explain the lack of intra-formational mudstones in the Eocene reservoir units, their lack of internal sedimentary structures, and the abundance of dewatering textures. It may also help to explain some of the more enigmatic aspects of the external form of the reservoirs, such as the steep flank dips, the limited erosion at the base of features described as channels and the isolated nature of many sand bodies with no intervening transitional facies. By recognizing the importance of dewatering phenomena, it may be that a reappraisal of traditional depositional models is now required.

Migration of hydrocarbons and sealing potential of shales

There is general consensus that the hydrocarbons in the Tertiary reservoirs are sourced from the Jurassic Kimmeridge Clay Formation (Barnard & Cooper 1981; Cornford 1990) which began to generate oil in the latest Cretaceous and earliest Tertiary in the centres of the Central and Viking Grabens (Cornford 1990). Oil sourced from the Upper Jurassic in isolated lensoid sandstone bodies, sealed above and below by shales, has long posed a problem for the definition of a plausible migration route. Even more enigmatic is the presence of biodegraded oils in some apparently closed Tertiary reservoirs (e.g. Alba), which also requires groundwater carrying bacteria to have entered the reservoirs (Mason *et al.* 1995).

For some fields, such as Gryphon, located above Mesozoic tilted fault blocks, a vertical migration pathway through Mesozoic faults is generally assumed. The fracture system is then assumed to extend into the Tertiary rocks above the structural high in order to facilitate charging of the Tertiary reservoirs (e.g. Newman *et al.* 1993). For other fields, such as Forties, long-distance migration pathways have been proposed. First the oil migrates vertically via salt features in the Central Graben, and then, once it enters the distal facies of the Paleogene reservoir fan sands,
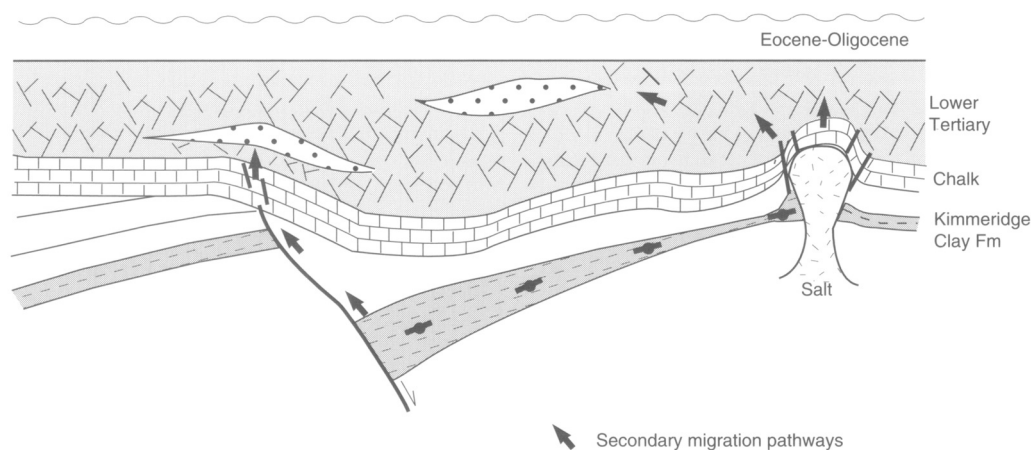
Fig. 10. Hydrocarbons generated from the Kimmeridge Clay Formation in deep kitchens can migrate upwards via basin-bounding faults and salt structures. Once the hydrocarbons encounter the mudrock-dominated lower Tertiary successions, the pervasive system of polygonal faults and fractures facilitates migration into isolated reservoir sandstones.

it migrates laterally up-dip into traps (Cornford *et al.* 1986; Cayley 1987).

The existence of an extensive network of syn-depositional and early-burial faults within the Lower Tertiary shale successions provides an alternative secondary migration pathway for charging the isolated Tertiary reservoirs. Once the oil migrated from the Jurassic kitchens through the Cretaceous by mainly sub-vertical pathways (via basin margin faults and salt structures) it could have encountered the pervasive polygonal fault and fracture system in the mudrocks, allowing migration into isolated sandstones (Fig. 10). Biodegraded oils may be the result of migration into leaky shallow traps where seawater was still present, or, as favoured by Mason *et al.* (1995), aquifers may have been recharged by meteoric waters during the Early Miocene when large areas of the Paleogene shelf were subaerially exposed.

The fact that oil is found in Eocene sandstones means that at some point the fault and fracture network became impermeable and the shale sequences became mainly sealing. The model of fault genesis put forward by Cartwright & Lonergan (1996) proposes that faults were active during early burial when the shales were expelling large volumes of pore water. Once the shales compacted beyond a critical value, the faults ceased to be active and the vertical permeability of the shales was much reduced. Hence the lower Tertiary mudstone units have become better, tighter seals through time.

Conclusions

The chronostratigraphic studies of the Tertiary in the North Sea have clearly aided our understanding of how and when sand was supplied and transported into the slope and basin environments during the lower Tertiary, but until recently subtle structural controls on the Tertiary plays have been considered to be of minor significance. In the Eocene (and possibly in the Paleocene), small-scale extensional faults organized in remarkable polygonal patterns were active during the deposition of the sediments. The role that such faulting played in influencing the locus of sandstone bodies within the depositional environment, and the subsequent modification and remobilization of original reservoir configurations during early burial, has not been adequately considered in reservoir models published to date.

The existence of a dense 3D fault network with extensional throws ranging from 10 to 100 m may explain the compartmentalization of some Tertiary reservoirs discovered during field development. Given the density and pattern of faults observed on the seismic datasets studied so far, there is a high probability that any elongate reservoir sandstone bodies occurring within the mud-dominated slope and deep-water succession of the Eocene in the North Sea Basin will be faulted.

The polygonal faulting is now seen to be an intrinsic product of water loss and compaction in the fine-grained mud-dominated sediments. The faults formed during the earliest phases of burial and acted as active dewatering conduits. They may also have been the migration pathways for the hydrocarbons that charged the isolated Tertiary sandstone reservoirs.

References

ALEXANDER, R. W. S., SCOFIELD, K. & WILLIAMS, M. C. 1993. Understanding the Eocene Reservoirs of the Forth Field, UKCS Block 9/23b. *In*: SPENCER, A. M. (ed.) *Generation, Accumulation and Production of Europe's Hydrocarbons III*. Special Publication, European Association of Petroleum Geoscientists, 3–15.

ARMSTRONG, L. A., TEN HAVE, A. & JOHNSON, H. D. 1987. The geology of the Gannet fields, Central North Sea, UK sector. *In*: BROOKS, J. & GLENNIE, K. (eds) *Petroleum Geology of North west Europe*. Graham & Trotman, London, 533–548.

BAIN, J. S. 1993. Historical overview of exploration of Tertiary plays in the UK North Sea. *In*: PARKER, J. R. (ed.) *Petroleum Geology of Northwest Europe: Proceedings of the 4th Conference*. Geological Society, London, 5–13.

BARNARD, P. C. & COOPER, B. S. 1981. Oils and source rocks of the North Sea area. *In*: ILLING, L. V. & HOBSON, G. D. (eds) *Petroleum Geology of the Continental Shelf of North-West Europe*. Heyden, London, 169–175.

BREWSTER, J. 1991. The Frigg Field, Block 10/1 UK North Sea and 25/1, Norwegian North Sea. *In*: ABBOTTS, I. L. (ed.) *United Kingdom Oil and Gas Fields, 25 years Commemorative Volume*. Geological Society, London, Memoir **14**, 117–126.

CARTWRIGHT, J. A. 1994*a*. Episodic basin-wide fluid expulsion from geopressured shale sequence in the North Sea basin. *Geology* **22**, 447–450.

——1994*b*. Episodic basin-wide hydrofracturing of overpressured Early Cenozoic mudrock sequences in the North Sea Basin. *Marine and Petroleum Geology* **11**, 587–607.

——1996. Polygonal fault systems: A new type of fault structure revealed by 3-D seismic data from the North Sea Basin. *In*: WEIMAR, P. & DAVIS, T. L. (eds) *Application of 3D Seismic Data to Exploration & Production*. AAPG Studies in Geology No **42** and SEG Geophysical Developments Series No **3**, 225–230.

—— & LONERGAN, L. 1996. Volumetric contraction during the compaction of mudrocks: a mechanism for the development of regional-scale polygonal fault systems. *Basin Research* **8**, 183–193.

CAYLEY, G. T. 1987. Hydrocarbon migration in the central North Sea. *In*: BROOKS, J. & GLENNIE, K. (eds) *Petroleum Geology of North West Europe*. Graham & Trotman, London, 549–555.

CLAUSEN, O. R. & KORSTGÅRD, J. A. 1993. Small scale faulting as an indicator of deformation mechanism in the Tertiary sediments of the northern Danish Central Trough. *Journal of Structural Geology*, **15**, 1343–1358.

CORNFORD, C. 1990. Source rocks and hydrocarbons of the North Sea. *In*: GLENNIE, K. W. (ed.) *Introduction to the Petroleum Geology of the North Sea*, 3rd ed., Blackwell, Oxford, 294–361.

——, NEEDHAM, C. E. J. & DE WALQUE, L. 1986. The geochemical habitat of North Sea oils and gases. *In*: SPENCER, A. M. (ed.) *Habitat of Hydrocarbons on the Norwegian Continental Shelf*. Graham & Trotman, London, 39–54.

DIXON, R. J., SCHOFIELD, K., ANDERTON, R., REYNOLDS, A. D., ALEXANDER, R. W. S., WILLIAMS, M. C. & DAVIES, K. G. 1995. Sandstone diapirism and clastic intrusion in the Tertiary sub-marine fans of the Bruce-Beryl Embayment, Quadrant 9, UKCS. *In*: HARTLEY, A. J. & PROSSER, D. J. (eds) *Characterisation of Deep Marine Clastic Systems*. Geological Society, London, Special Publication **94**, 77–94.

DEN HARTOG JAGER, D., GILES, M. R. & GRIFFITHS, G.˜R. 1993. Evolution of Paleogene submarine fans of the North Sea in space and time. *In*: PARKER, J. R. (ed.) *Petroleum Geology of Northwest Europe: Proceedings of the 4th Conference*. Geological Society, London, 59–71.

HARDING, A. W., HUMPHREY, T. J., LATHAM, A., LUNSFORD, M. K. & STRIDER, M. H. 1990. Controls on Eocene submarine fan deposition in the Witch Ground Graben. *In*: HARDMAN, R. F. P. & BROOKS, J. (eds) *Tectonic Events Responsible for Britain's Oil and Gas Reserves*. Geological Society, London, Special Publication **55**, 353–367.

HENRIET, J. P., DE BATIST, M. & VERSCHUREN, M. 1991. Early fracturing of Palaeogene clays, southernmost North Sea: Relevance to mechanisms of primary hydrocarbon migration. *In*: SPENCER, A. M. (ed.) *Generation, Accumulation and Production of Europe's Hydrocarbons*. European Association of Petroleum Geoscientists, Special Publication **1**, 217–227.

HIGGS, W. G. & McCLAY, K. R. 1993. Analogue sandbox modelling of Miocene extensional faulting in the Outer Moray Firth. *In*: WILLIAMS, G. D. & DOBB, A. (eds) *Tectonics and Seismic Sequence Stratigraphy*. Geological Society, London, Special Publication **71**, 141–162.

JAFFRI, F. 1993. *Cross-cutting sand bodies of the Tertiary. Beryl Embayment, North Sea*. PhD Thesis, University of London.

JENSSEN, A. I., BERGSLIEN, D., RYE-LARSEN, M. & LINDHOLM, R. M. 1993. Origin of complex mound geometry of Paleocene submarine-fan sandstone reservoirs, Balder Field, Norway. *In*: PARKER, J. R. (ed.) *Petroleum Geology of Northwest Europe: Proceedings of the 4th Conference*. Geological Society, London, 135–143.

LOVELL, J. P. B. 1990. Cenozoic. *In*: GLENNIE, K. W. (ed.) *Introduction to the Petroleum Geology of the North Sea*, 3rd edition, Blackwell, Oxford, 273–293.

MASON, P. C., BURWOOD, R. & MYCKE, B. 1995. The reservoir geochemistry and petroleum charging histories of Palaeogene-reservoired fields in the Outer Witch Ground Graben. *In*: CUBITT, J. M. & ENGLAND, W. A. (eds) *The Geochemistry of Reservoirs*. Geological Society, London, Special Publication, **86**, 281–301.

MATTINGLY, G. A. & BRETTHAUER, H. H. 1992. The Alba Field. A Middle Eocene deep water channel system in the UK North Sea. *In*: HALBOUTY, M. T. (ed.) *Giant Oil and Gas Fields of the Decade, 1978–1988*. AAPG, Memoir **54**, 78–88.

MILTON, N. J., BERTRAM, G. T. & VANN, I. R. 1990. Early Palaeogene tectonics and sedimentation in the Central North Sea. *In*: HARDMAN, R. F. P. BROOKS, J. (eds) *Tectonic Events Responsible for Britain's Oil and Gas Reserves*. Geological Society, London, Special Publication, **55**, 339–351.

MORTON, A. C. 1979. The provenance and distribution of the Paleocene sands of the Central North Sea. *Journal of Petroleum Geology*, **2**, 11–21.

NEWMAN, M. ST. J., REEDER, M. L., WOODRUFF, A. H. W. & HATTON, I. R. 1993. The geology of the Gryphon oil field. *In*: PARKER, J. R. (ed.) *Petroleum Geology of Northwest Europe: Proceedings of the 4th Conference*. Geological Society, London, 123–133.

NEWTON, S. K. & FLANAGAN, K. P. 1993. The Alba Field: evolution of the depositional model. *In*: PARKER, J. R. (ed.) *Petroleum Geology of Northwest Europe: Proceedings of the 4th Conference*. Geological Society, London, 161–171.

O'CONNOR, S. J. & WALKER, D. 1993. Paleocene reservoirs of the Everest trend. *In*: PARKER, J. R. (ed.) *Petroleum Geology of Northwest Europe: Proceedings of the 4th Conference*. Geological Society, London, 145–160.

PARKER, J. R. 1975. Lower Tertiary sand development in the central North Sea. *In*: WOODLAND, A. W. (ed.) *Petroleum and the Continental Shelf of North-west Europe 1. Geology*. Elsevier, Barking, 447–453.

PARSLEY, A. J. 1990. North Sea hydrocarbon plays. *In*: GLENNIE, K. W. (ed.) *Introduction to the Petroleum Geology of the North Sea*, 3rd edition, Blackwell, Oxford, 362–388.

POSAMENTIER, H. W. & VAIL, P. R. 1988. Eustatic controls on clastic deposition II – sequence and systems tract models. *In*: WILGUS, C. K. *et al.* (eds) *Sea-level Changes: An Integrated Approach*. Society of Economic Palaeontologists & Mineralogists, Special Publication **42**, 125–154.

RUNDBERG, Y. 1989. *Tertiary sedimentary history and basin evolution of the Northern North Sea.* Dr. Ing. Thesis, Trondheim, Norway.

RYE-LARSEN, M. 1994. The Balder Field: refined reservoir interpretation with the aid of high resolution seismic data and seismic attribute mapping. *In*: AASEN, J. O. *et al.* (eds) *North Sea Oil and Gas Reservoirs III.* Kluwer, Dordrecht, 115–124.

SHANMUGAM, G., BLOCH, R. B., MITCHELL, S. M. *et al.* 1995. Basin-floor fans in the North Sea: Sequence stratigraphic models vs. sedimentary facies. *AAPG Bulletin*, **79**, 477–512.

STEWART, I. J. 1987. A revised stratigraphic interpretation of the Early Palaeogene of the central North Sea. *In*: BROOKS, J. & GLENNIE, K. W. (eds) *Petroleum Geology of North-West Europe.* Graham & Trotman, London, 557–576.

VERSCHUREN, M. 1992. *An integrated 3D approach to clay tectonic deformation.* PhD thesis, Ghent University.

Fault and fracture characteristics of a major fault zone in the northern North Sea: analysis of 3D seismic and oriented cores in the Brage Field (Block 31/4)

R. K. AARLAND[1,2*] & J. SKJERVEN[2]

[1] Geological Institute, University of Bergen, Allègt. 41, N-5007 Bergen, Norway
[2] Norsk Hydro a.s, Sandsliveien 90, N-5020 Bergen, Norway

Abstract: Based on three-dimensional (3D) seismic and core data, an analysis of fault geometry and fracture distribution related to a normal fault in the Brage Field, northern North Sea, has been achieved. The fault has a vertical throw of 200–300 m, and exhibits a steep ramp–flat–ramp geometry. Most of the deformation related to this fault is concentrated within a narrow zone in the hangingwall. Both extensional and compressional antithetic structures have been identified. The most intensive fracturing is associated with areas of change in the fault plane orientation. Correspondingly, these areas represent locations where questions regarding sealing capacity arise. The complexity of the fault zone caused difficulties in an exact pick of the fault plane. Oriented cores from one of the production wells in the area include a continuous 120 m long interval across the fault zone itself. Detailed measurements of fracture and bedding orientations were carried out using an automated goniometer as well as manual measuring techniques. Biostratigraphic data show that two faults can be identified within the narrow fault zone, with the main displacement recorded across the upper one. Fracture orientations and fracture distribution pattern versus core depth indicate, however, that the deformation is associated with the lower fault. Based on the core material which exhibits an asymmetrical distribution of deformation in relation to the fault zone, an exact determination of the depth of the fault plane has been possible. It is concluded that the lower interval is the initial main fault. The largest slip has, however, been taken up across the upper interval, representing a hangingwall splay fault.

Analysis of fractures and fracture distributions, their relation to larger structural elements and their textural characteristics, are well-documented from outcrop studies (Harris et al. 1960; Aydin 1978; Aydin & Johnson 1978, 1983; Jamison & Stearns 1982; Underhill & Woodcock 1987; Koestler & Ehrman 1991; Hippler 1993; Antonellini et al. 1994; Fowles & Burley 1994; Knott 1994). These studies show that there are differences in fracture characteristics in the footwall and hangingwall of faults. Such differences are reflected in varying fracture orientation, fracture distribution, deformation products, and displacement distribution across a fault zone. Temporal local stress perturbation is also an important parameter, and may affect the geometry of subsequently developing faults (Gamond 1983; Mandl 1988; Rawnsley et al. 1992).

Similar conclusions have been reported from fault studies in offshore regions, where fault displacement, sand/shale ratio, clay-smear, height of hydrocarbon column, porosity, permeability, capillary pressure, and textural characteristics of fractures obtained from seismic, well data and cores are used to predict sealing efficiency of faults (Smith 1980; Allan 1989; Bouvier et al. 1989; Harding & Tuminas 1989; Knipe 1992; Knott 1993; Anderson et al. 1994; Gibson 1994; Berg & Avery 1995). In addition, numerous fault population studies (e.g. Walsh et al. 1991; Gillespie et al. 1992; Yielding et al. 1992b; Rives et al. 1992) have been carried out in order to obtain a better understanding of the spatial and size distribution of sub-seismic fractures in a reservoir environment. Even so, clustering of different fracture types and the geometry of the deformed zone around a fault have to be known in order to evaluate deformation mechanisms and style, and their effect on sealing capacity. The geometry of the deformed zone (damage zone) associated with a fault, reflects the geometry of the fault and its orientation relative to local tectonic stresses.

Topics addressed in this study are: (1) the deformation style across a cored major fault in the Brage Field, northern North Sea (Fig. 1); and (2) parameters influencing the sealing capacity of the fault. The analysis is based on three-dimensional (3D) seismic, well data and the unique opportunity of characterizing oriented cores through the fault zone.

Fracture frequency, f, is in this study defined as the observed number of natural fractures per

* Presently at Esso Norge AS, Grenseveien 6, N-4033 Forus, Norway
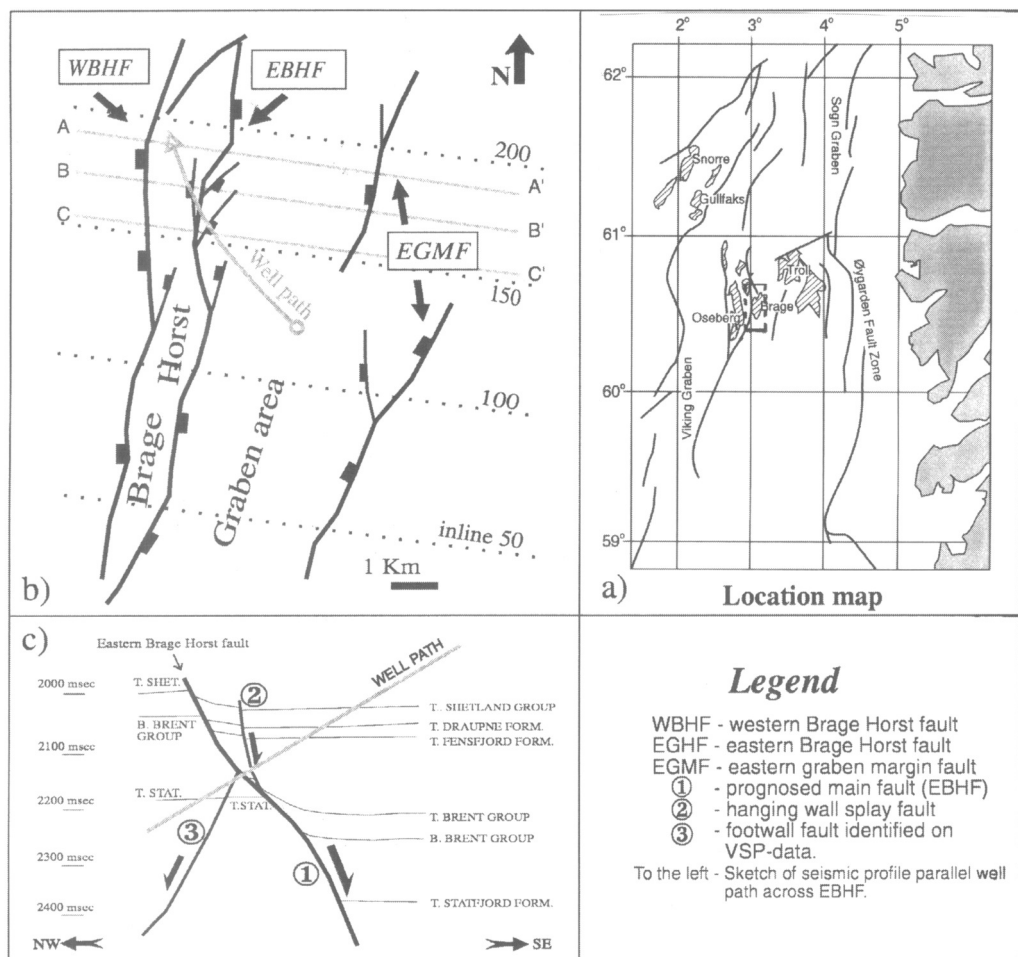
Fig. 1. Location map of the Brage Field and main structural features. Marked are the location of the seismic sections, A–A', B–B' and C–C' presented in Fig. 2, and the well path of well 31/4-A-04.

core metre. Based on examples given in the literature (e.g. Harris *et al.* 1960; Ladeira & Price 1981; Jamison & Stearns 1982; Gabrielsen & Koestler 1987; Huang & Angelier 1989; Gabrielsen & Aarland 1990, 1995; Narr & Suppe 1991), the following relationship seems to control fracture density and distribution in general:

$$f(x) = (d, l, b, x, t, s) \qquad (1)$$

where d represents depth of burial and consolidation stage of the deformed rock body, l refers to the effect of lithology and grain size, b is bed thickness, x is the distance to the nearest major fault, t refers to the effects of local stress patterns and the geometry and orientation of faults in the area investigated, and s is the sampling effect related to well orientation (according to Barton &

Zoback (1990) and Peacock & Sanderson (1993)). The above relationship may account both for mode I, II and III fracture distributions. However, in this study only natural shear (and hybrid) fractures (mode II (and III)) have been identified. These fractures appear in the cores both as open and closed fractures, and may be generated in response to tectonic or non-tectonic processes.

Location of the Brage Field and structural setting

The Brage Field is located in the southwestern corner of Block 31/4, in the transition zone between the Horda Platform and the northern Viking Graben in the Norwegian Sector, northern

North Sea (see Fig. 1). Structurally, the eastern part of the field is characterized by an elongated dome with a NE–SW-trending axis, defining a trap in Bathonian–Oxfordian, bioturbated, off-shore siltstones and fine-grained sandstones of the Fensfjord Formation. To the west a narrow, NNE–SSW-trending horst contains oil-bearing Hettangian to lower Sinemurian fluvio-deltaic sandstones of the Statfjord Formation (Hage et al. 1987). Source rocks for the hydrocarbons in the Brage Field are predominantly the Upper Jurassic shales of the Draupne Formation.

Three major NNE–SSW-trending faults have been identified in the study area (marked WBHF, EBHF and EGMF in Fig. 1). Several faults on the horst block are identified at the top of the Statfjord Formation. A minor westward-dipping fault (marked 3 in Fig. 1), with a normal throw of 10–15 m, is also detected on vertical siesmic profile (VSP) data along the well path. Of the boundary faults of the Brage Horst, the western Brage Horst fault (WBHF) has the largest normal throw (approximately 600 m), whereas the eastern Brage Horst fault (EBHF), with a 200–250 m normal throw, displays the most complex geometry and is the main target for this study.

There is general agreement that the structures in the northern North Sea developed as a consequence of extensional tectonics. Regional studies indicate that some faults in the eastern part of the Viking Graben and on the Horda Platform were initiated during an early Permo-Triassic stretching event (Gabrielsen et al. 1990; Yielding et al. 1992a). Some of these early structures have acted as zones with higher potential for reactivation during the subsequent tectonic phases. However, the majority of the structural elements, including the Brage Horst, were developed during the late Jurassic–early Cretaceous stretching event and the subsequent thermal subsidence (Badley et al. 1984; Hage et al. 1987; Badley et al. 1988). The rifting started after the deposition of the Brent Group, which is eroded on the Brage Horst. The Brage Horst can in general be described as a marginal platform high in a complex of regional structural elements (Gabrielsen 1986), where its orientation may be influenced by the orientation of the stresses during formation as well as pre-existing basement grain.

The eastern Brage Horst fault and location of well 31/4-A-04

The production well 31/4-A-04, drilled in February 1993; is located in the middle part on the Brage Field (Fig. 1). The well plunges 30° towards the NW, across the eastern Brage Horst fault and enters the oil-bearing Statfjord Formation of the Brage Horst. The fault changes orientation along strike from a N–S trend in the south to a NE–SW trend in the north where the well penetrates the eastern Brage Horst fault (Fig. 1). A characteristic ramp–flat–ramp geometry of the fault has initiated various types of accommodation structures. This is seen on NW–SE-trending seismic lines running across the Brage Horst (Fig. 2). Most obvious are the drag effects and the concentration of synthetic and antithetic faults in the hangingwall (Fig. 3).

Oriented cores were taken at two depth intervals. The upper 120 m interval includes the fault zone, which is dominated by heavily fractured rocks. The fault zone is limited by zones of calcite-filled fractures. The well did not penetrate the Brent Group in the hangingwall which was one of the main targets for this well, intending to sample sandstones of the Brent Group juxtaposed against sandstones of the Statfjord Formation in the footwall of the fault. Instead the cores of the upper interval embody the lowermost part of the lower Fensfjord Formation, the silty claystones of the lower Heather Formation, Drake/Cook Formations (located in the fault zone) and the uppermost part of the Amundsen Formation. A detailed biostratigraphic analysis was carried out in this upper cored interval (Fig. 4). Based on the biostratigraphic analysis a vertical section of 100–150 m is shown to be faulted out in an upper 20 cm thick zone which embodies calcite-filled fractures. Additionally, 50 m is faulted out across a lower 80 cm thick zone of calcite-filled fractures in a calcite-cemented matrix. The upper zone corresponds to fault 2 and the lower zone corresponds to fault 1, as shown in Fig. 1c and Fig. 4.

The lower interval of 180 core metres was cored to better describe the Statfjord Formation reservoir within the Brage Horst. Different segments (A–F) in the cored intervals have been defined with reference to deformation intensity and style (see Fig. 4). Core segments E and F are situated in the lower cored interval.

The eastern Brage Horst fault separates water-bearing sandstones within the Brent Group in the hangingwall from oil-bearing sandstones of the underlying Statfjord Formation in the footwall (see Fig. 1c). Across the fault, a pressure difference of approximately 7 bars has been recorded. Questions arise concerning the sealing capacity of the fault, since sandstone is juxtaposed against sandstone across the fault. However, the thick shaly Dunlin Group overlain by the Brent
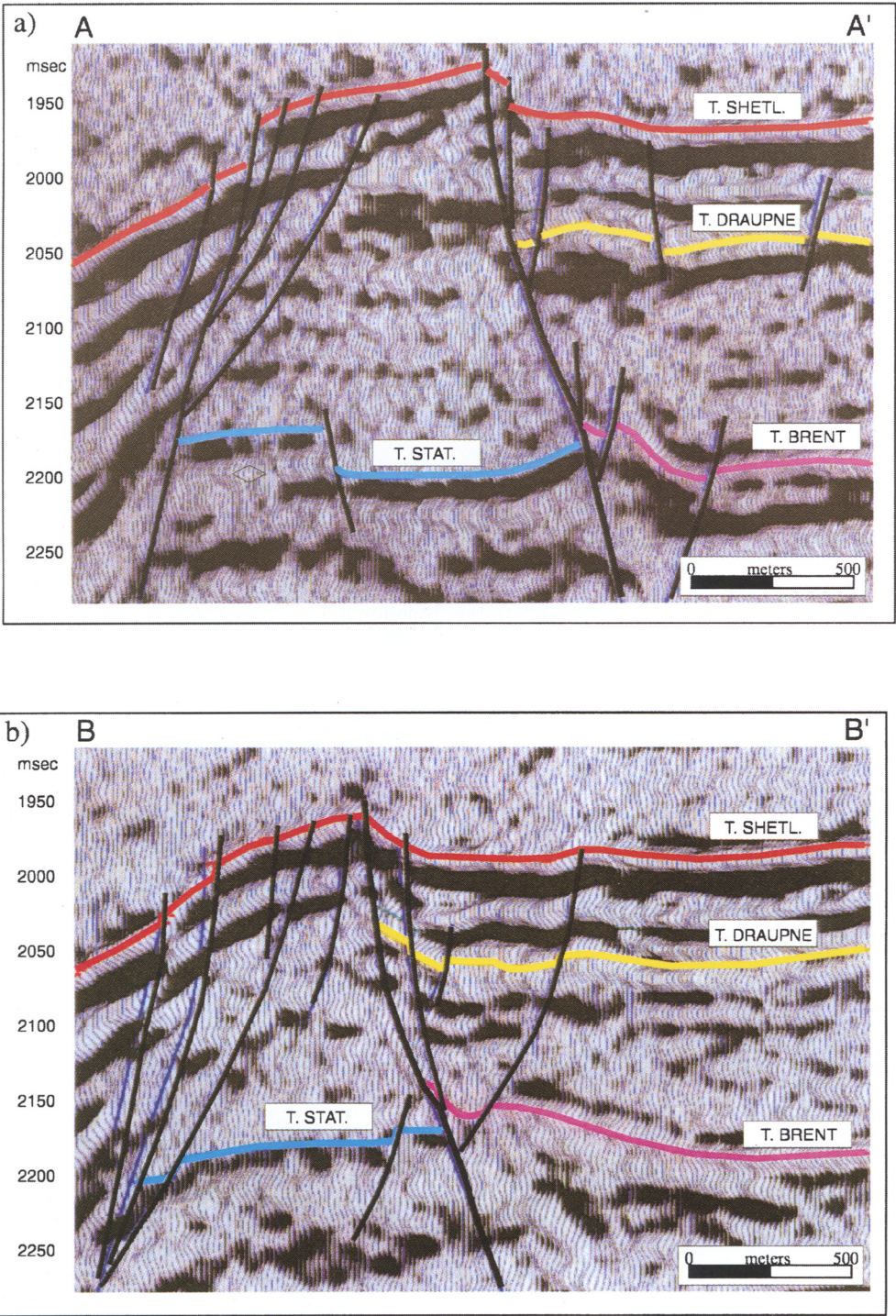
Fig. 2. (a)–(c) Seismic sections (for locations see Fig. 1) across the investigated area illustrating the steep ramp-flat–ramp geometry of the eastern Brage Horst fault.
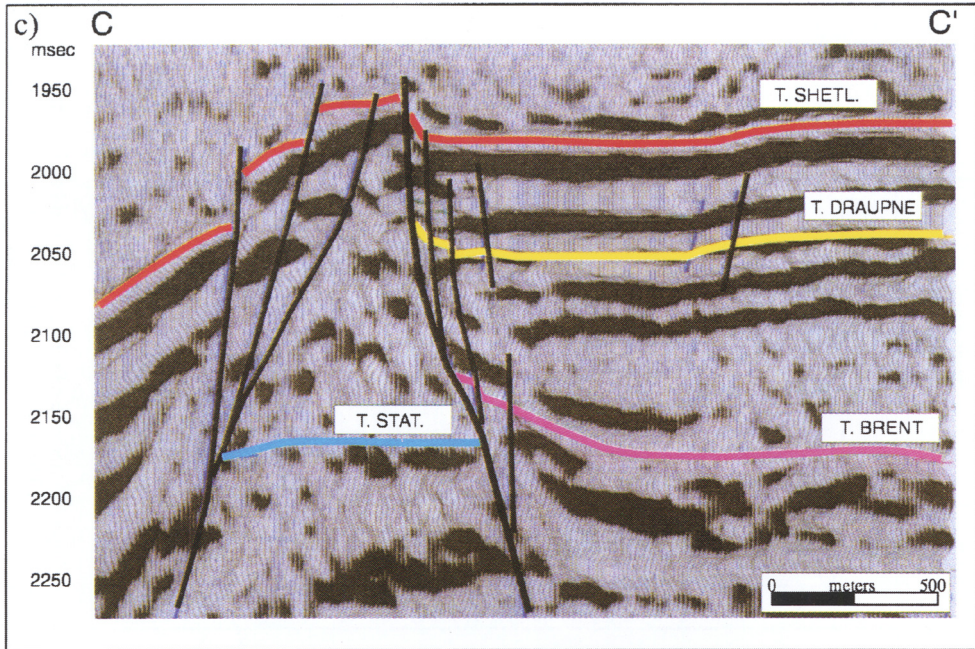
Fig. 2 (c).

Group, and the shaly and silty Heather Formation which locally is onlapping the Brent Group, may provide clay-smearing along the fault plane. An increased sealing capacity across the fault in the level where sand/sand juxtaposition exists would then be expected. As indicated in the strike projection along the eastern Brage Horst fault (Fig. 5), the degree of sand/sand overlap varies along the strike of the fault. Some areas along the fault plane have no
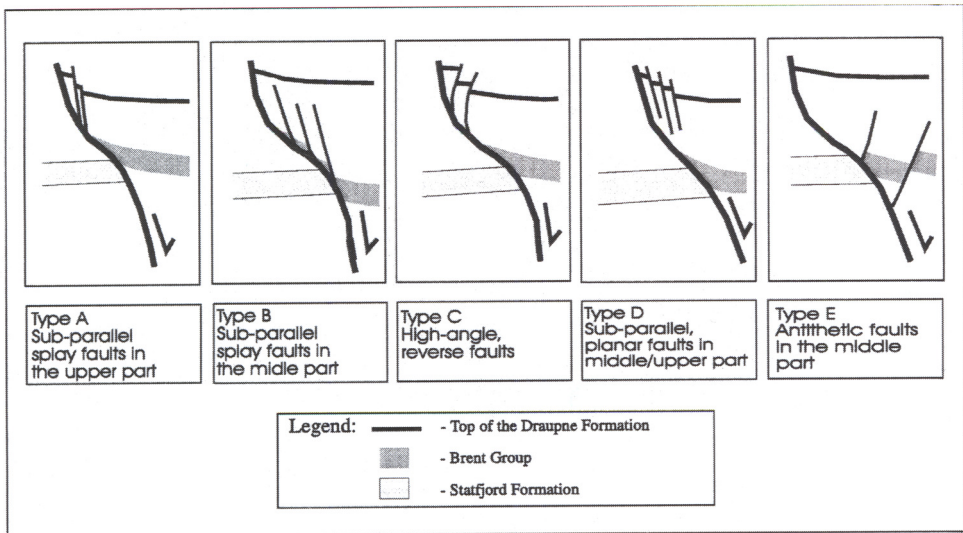
Fig. 3. Classification of hangingwall accommodation faults based on the interpretation of the 3D reflection seismic data.
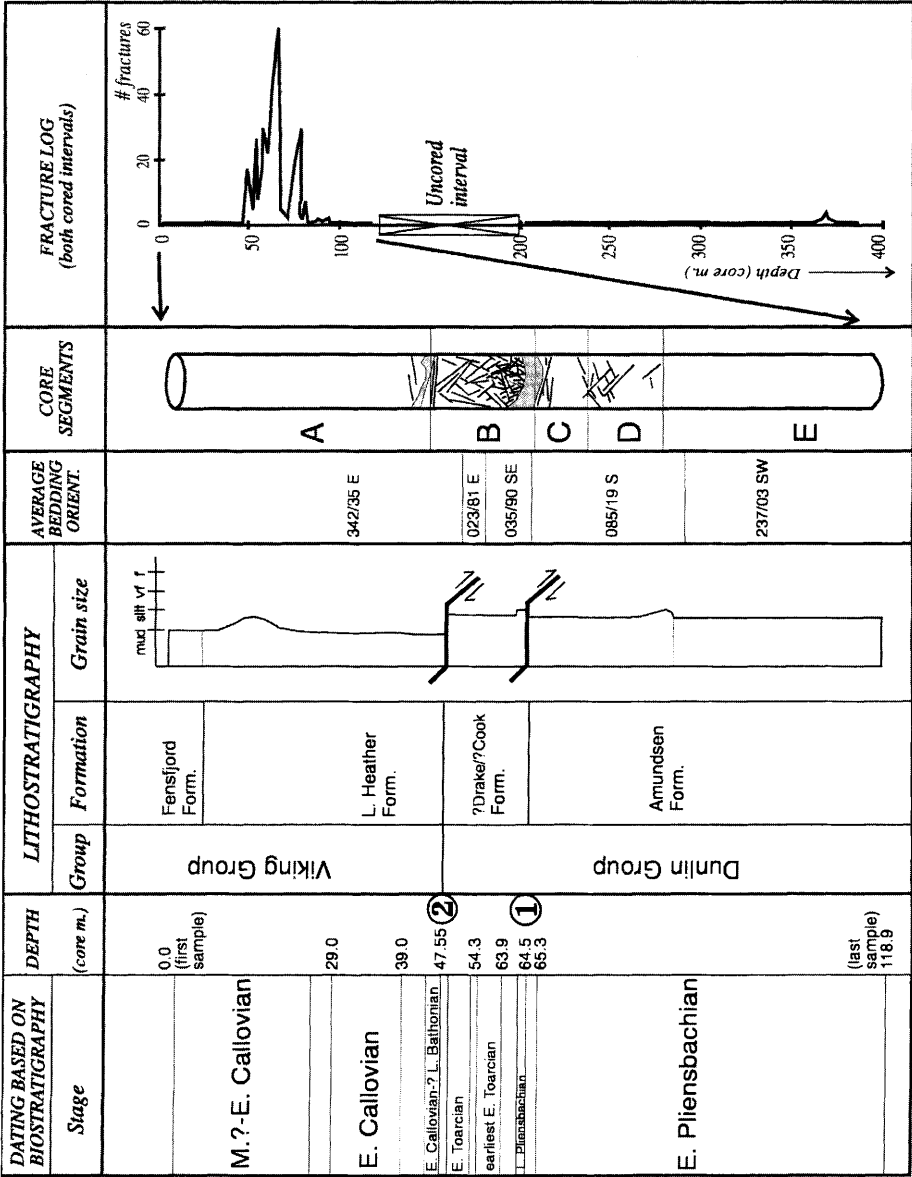
Fig. 4. Lithostratigraphy in the upper cored interval of well 31/4-A-04. (1) and (2) refers to the lower and upper zones where faults are identified based on the biostratigraphical analysis. The columns to the right shows a sedimentary log and fracture distribution in the cores. The cored intervals are divided into different segments, A–F. Not shown here are the remaining part of segment E and segment F in the lower cored level. Note the different zones of bedding throughout the upper cored interval (mean bed orientations in each zone are listed). To the far right is shown a fracture frequency plot versus the core depth for both the two cored intervals.
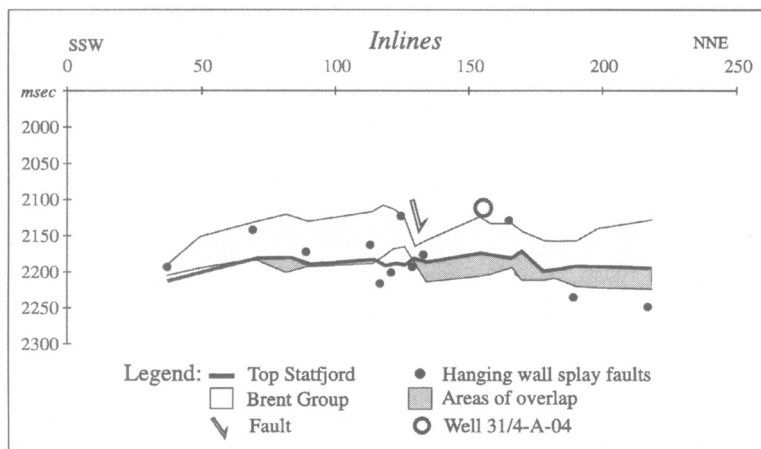
Fig. 5. Fault plane section of the eastern Brage Horst fault showing the water-bearing Brent Group in the hangingwall juxtaposed against the oil-bearing Statfjord Formation in the footwall. The dark zones marks the areas of possible communication across the fault. The arrow indicates the location of a hangingwall fault, affecting the Brent Group.

sand/sand juxtaposition, whereas others have a high degree of overlap. These critical areas may be affected by other parameters which influence sealing capacity, such as fault geometry, splay faults and fracture distribution. The investigated cores from well 31/4-A-04 were taken immediately above one of the areas with a high degree of sand/sand juxtaposition. This means that it was not possible to investigate sand/sand relationships in the cores. However, the effects of fault geometry and fracture distribution pattern could be studied in detail.

Orienting the core

The detailed structural description and interpretation of the core material in this study largely follows the procedures recommended by Nelson (1985). In this study, only natural fractures have been used in the analyses. The criteria used to identify natural and induced fractures are given in Arthur et al. (1980), Nelson (1985), Gabrielsen & Koestler (1987), Kulander et al. (1990) and Özkanli & Standen (1993). Bedding, fracture orientations and lineations have been measured manually throughout the cored intervals. In addition, an automated goniometer has been used to achieve more accurate measurements of bedding and fracture orientations in core segments B–D.

Cores have been oriented by applying an orientation system situated in the inner barrel combined with a magnetic, time-dependent multishot survey instrument. The cores are grooved by three knifes, where the orientation

of the main knife, knife 1, is used as a reference groove with respect to the topside of the hole (Fig. 6). *In situ* measurements can be obtained manually or from a computer-controlled electronic device. To use this equipment the scribe marks during coring and the 'way-up' direction must be clearly defined. The automated goniometer links the acquired bench orientations for the core samples with the survey information (well-path orientation, depth values and reference groove azimuth). Routines to categorize orientations and display their statistics graphically are included in the program.
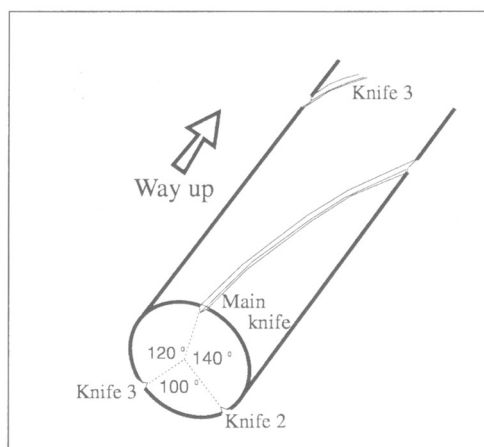
Fig. 6. Reference grooves on cores used for oriented measurement. The angles between each groove may vary from one drilling company to another.
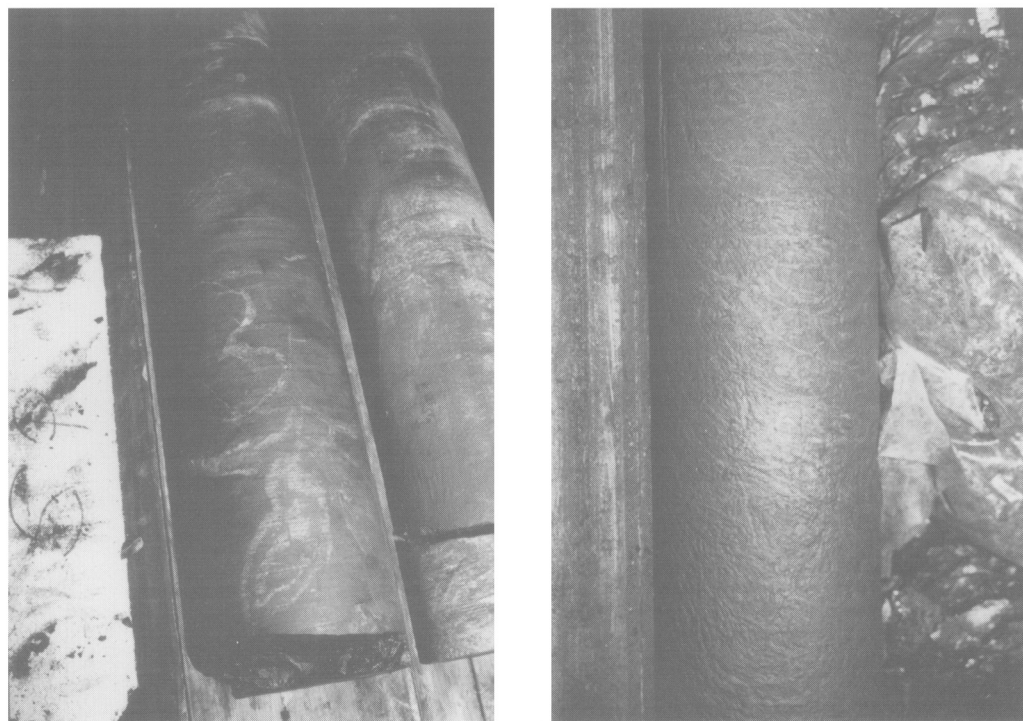
Fig. 7. Calcite-filled fractures. (**a**) Upper zone (marked 2 in previous figures) with calcite-filled fractures. (**b**) Lower zone (marked 1 in previous figures) with calcite-filled fractures is totally intersected by the thin fractures and is associated with calcite cemented matrix of the host rock. Core diameter is 11 cm.

Orientational measurements on cores are connected with many uncertainties. Assuming that initial core-orientation data are of reasonably good quality and that all measurements are executed as precisely as possible, an uncertainty of ±11° may still be associated with the final results derived from manual measurements (Nelson *et al.* 1987). The largest error (±5°) arises from the coring and surveying procedure. An uncertainty estimated to approximately ±3° is connected with the analyst him-/herself, with regard to different individual measuring techniques and levels of accuracy. The uncertainty related to the measuring equipment is thought to be ±1° (Nelson *et al.* 1987). By careful evaluation of the scribe marks in each core metre, and comparing these with the data in the core-orientation report, one should be able to reduce the measuring error by approximately 5°. In addition, the use of an automated goniometer may further reduce the errors in the measurements by 2–3°. The final uncertainty related to automated measurements of the orientation of individual planes or lineations in the core material in this study has thus been minimized to as little as approximately ±4°.

Structural description of the cores

In the cores investigated in the present study the dominating fracture type is the shear (mode II) fracture. Natural mode I fractures are very rare. The shear fractures appear in the cores as both open and closed. It is thought that the open fractures have opened as a result of unloading. Two main classes of shear fractures have been identified, namely fractures related to tectonic processes and fractures related to non-tectonic processes. As shown in Fig. 4, the cores can be divided into different segments according to deformation intensity. Segment A has only a minor number of fractures, which are located in the lowermost part in relation to the upper mineralized zone. Bedding is sub-horizontal in segment A. The most heavily fractured interval is restricted to segment B. Deformation density seems to increase to the lower mineralized zone which is located at the base of segment B. Within this core segment, bedding dip increases and becomes sub-vertical towards the lower mineralized zone. Segment C is characterized by a small number of fractures located in the upper part of the core segment,

and bedding is sub-horizontal. Segment D contains a fracture swarm in its middle part, and bedding is sub-horizontal. No deformation is seen in segment E. Segment F has an interval which is characterized by soft-sedimentary deformation within the Statfjord Formation. Bedding is in general sub-horizontal in both segments E and F. In the following, all descriptions will refer to this sub-division.

Fractures related to tectonic processes

Based on their appearance in the cores, the tectonic fractures can be divided into three sub-groups: calcite-filled fractures, closed and open fractures.

The *calcite-filled fractures* are restricted to segment B, which is bounded on its upper side by a 20 cm thick zone of calcite-filled fractures, and an 80 cm thick zone with calcite-filled fractures in a calcite-cemented matrix on its lower side (Fig. 7). In the upper zone more than ten fractures with calcite infilling are situated in a mudstone sequence interlaminated with siltstones. On its lower side this 20 cm thick zone

is cut by an open fracture with well-developed slickensides, which could represent a fault plane that has taken up the 150 m missing section determined from the biostratigraphic analysis. Mean fracture aperture of the calcite-filled fractures is >5 mm, and these fractures have a curviplanar geometry (Fig. 7a). In the lower zone of calcite-filled fractures, the fractures occur in a massive, calcite-cemented siltstone interval. The cemented interval is totally intersected by the calcite-filled fractures, giving more than 40 fractures in this 80 cm thick interval (Fig. 7b). It has not been possible to measure throw across individual mineralized fractures. Both above and beneath this mineralized and cemented interval, 10 cm thick intervals of totally fragmented material are located. Based on the core description it is not possible to resolve whether they represent faults or not. Mean fracture aperture of the calcite-filled fractures is here <1 mm, and the fractures display very irregular geometries.

The majority of the *closed fractures* are concentrated in segment B, above the lower zone of calcite-filled fractures (Fig. 8). Another interval of closed fractures is identified in

Fig. 8. Overview of segment B, which embodies the lower zone of mineralized fractures (m). The upper interval (2) is located in the cores just to the left, outside this picture. Both fragmented zones (fz), open (o) and closed (c) fractures can be seen. Note the increased fragmentation where intersection of larger fractures occurs (i). Core diameter is 11 cm.
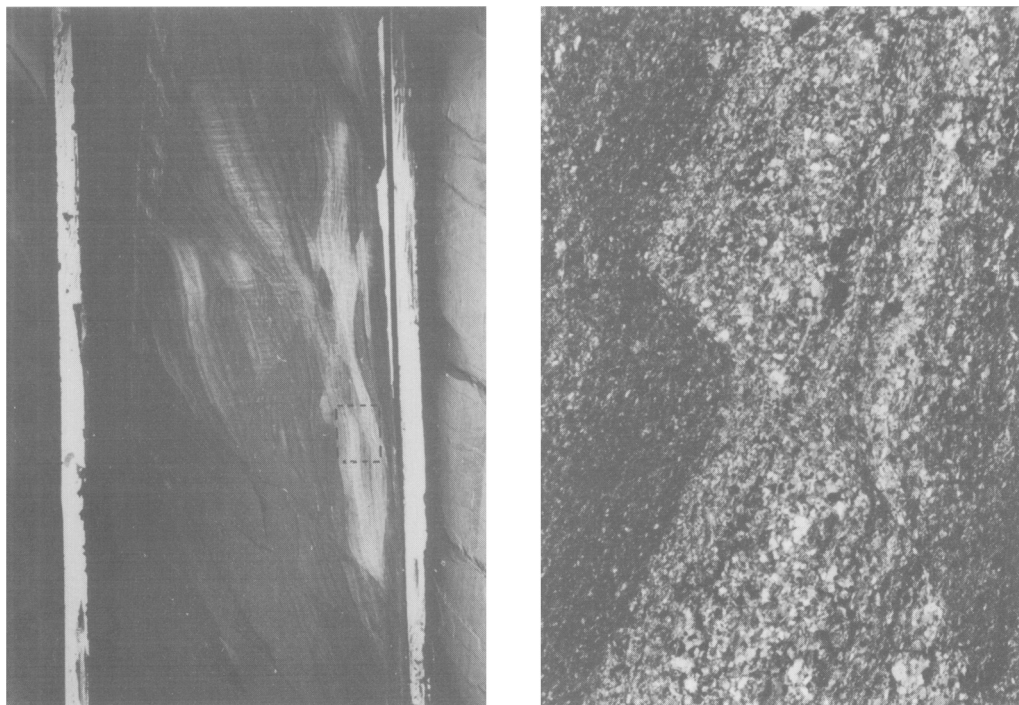
Fig. 9. Close-up of a core interval with predominantly closed fractures. Core diameter is 11 cm. The location of the thin section to the right is marked. As shown in the thin section photo, well-developed drag (reorientation of platy mineral grains) is developed across these fractures. Throw across the microfault is 2 mm.

segment D, where a fracture swarm with 35 individual closed fractures is bounded by open fractures. For all the closed fractures, fracture zone thicknesses are generally <1 mm. The fractures show planar and curved geometries with well-developed normal drag, due to reorientation of platy mineral grains towards the fracture surfaces (Fig. 9). Displacement across individual fractures is of the order of 1–30 mm.

Open fractures are found both as single fractures and as clusters in fragmented zones. A fragmented zone is in the present work associated with a core interval where the fracture density and frequency are extremely high (more than 30 fractures across a 10 cm interval). Based on the macro- and microscopic appearance, open fractures can be regarded as originally closed fractures which have opened during unloading. A pronounced concentration of open fractures is identified in segment B, with increasing frequency towards the lower interval with calcite-filled fractures (see Fig. 8). In segment C, an abrupt decrease in the number of open fractures is seen. Fragmented zones seem to dominate in the most fine-grained lithologies, and where fractures of different orientations

intersect (as shown in Fig. 8). As well as the clustering of open fractures in segment B, another concentration is seen in segment D. The open fractures have well-developed planar to undulating slickensided surfaces (Fig. 10). Morphology, lineation density and orientation seem to vary both on individual fracture surfaces and in response to varying fracture geometry. The measured displacement across individual single open fractures ranges from 0.5 to 10 cm.

Bedding-parallel fractures are evenly distributed throughout the 300 m of core, but a small clustering of these fractures is seen in segment B. In general these fractures show poor development of slickensided surfaces. However, in segment B, some of the open fractures have well-developed slickensides and lineations on the fracture surfaces. These fractures should thus be regarded as tectonic open fractures.

Fractures related to non-tectonic processes

In segment F, in the lower cored interval, both folds and fractures (some with reverse offsets) have been identified. This highly deformed zone

Fig. 10. Open fracture with well-developed slickensides. Note the different lineations orientations on the composite fracture surface. Core diameter is 11 cm.

Fig. 11. Fracture distribution versus core depth (all natural fracture types are included in the diagrams). Shown enlarged is the fracture distribution in segments B–D. (1) and (2) refer to the location of the lower and upper zones with calcite-filled fractures, whereas (3) corresponds to the predicted depth of the minor footwall fault shown in Fig. 1.

is found in association with folded coal fragments and unsystematic laminations. Together with dish structures and other indicators of water-escape, these folds and fractures seem to be initiated by soft-sedimentary deformation during compactional processes. In addition, these soft-sedimentary features are not associated with any identified faults, either in the cores or in the seismic data. These structures are here regarded as non-tectonic. The fractures in segment F are therefore not included in the fracture orientation plots since their orientation has no relevance for the interpretation of the tectonic structures.

Fracture distribution

All natural fractures have been counted and plotted versus core depth (Fig. 11). A total of 361 fractures have been registered in the 300 m of core. Not included are the fractures in the fragmented zones. As indicated in the fracture log (Fig. 4), the majority of fractures and fragmented zones are located in segment B, which is bounded by the two zones of calcite-filled fractures. The upper zone is correlated with fault 2 and the lower one corresponds to fault 1 in Figs 1 and 4.

No fractures are found in core segment A. The first fractures are located immediately above the upper zone of calcite-filled fractures in segment B. Moving downwards to the lower zone of calcite-filled fractures, an increase in the fracture intensity is observed. A corresponding increase

in fragmented zones is also seen towards this zone. No systematic or symmetric decrease in fracture frequency below the lower zone of mineralized fractures is recognized. This implies an asymmetrical fracture distribution across fault 1, which corresponds to the lower mineralized zone.

In segment D, another interval with high fracture intensity is seen. This interval does not seems to be directly associated with the fault zone above, and could represent a minor fault in the footwall of the eastern Brage Horst fault. This interval is comparable with the location of a westward-dipping fault with 5–15 m offset (marked 3 in Fig. 1), detected on the VSP data.

Bedding orientations

Bedding orientations were measured throughout the entire cored interval, except where reference grooves are absent. Based on the variations in strike and dip with depth, various zones with different bedding orientations have been identified (see Fig. 4).

A clear break in dip of bedding is identified between segment B and C, which coincides with the lower zone of mineralized fractures (fault 1) (Fig. 12). The general trend in the hangingwall (segments A and B) is that bedding steepens towards the fault, dips towards the east and
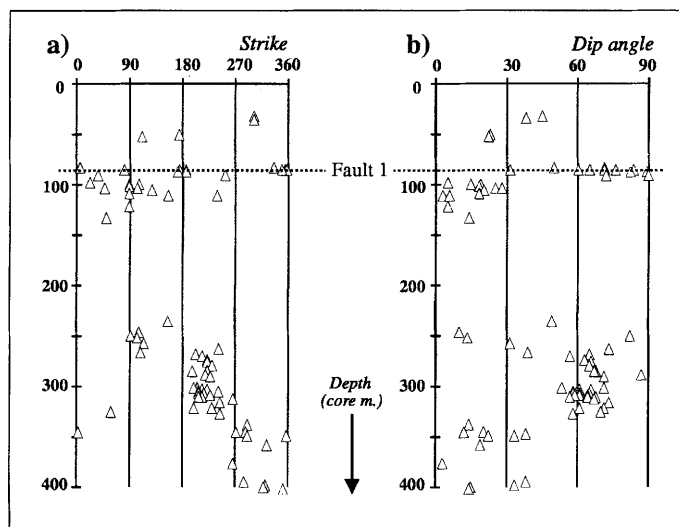
Fig. 12. Distribution of bedding orientations throughout the entire cored intervals. (**a**) Strike distribution diagram, and (**b**) dip distribution diagram versus core depth indicate an increasing drag in the hangingwall towards fault 1. Measurements in the footwall are sub-horizontal.

becomes parallel to the fault. In segments C and D in the footwall of fault 1, bedding is sub-horizontal. This implies an asymmetrical distribution of bedding orientations across fault 1, with well-developed normal drag in the hangingwall and no drag in the footwall. It should be noted that no variations in bedding measurements are observed across faults 2 and 3.

Fracture orientations

Based on the 3D seismic interpretation, the orientation of the eastern Brage Horst fault, where the well intersects the fault, is 020/65 E. The mean orientation of the splay faults in the hangingwall of the eastern Brage Horst fault is 035/75 E. The fault (marked 3 in Fig. 1c) in the footwall of the eastern Brage Horst fault has an orientation of 185/40 W. This orientation is also derived from 3D seismic interpretation.

Automated measurements of fracture orientations have been performed in segment B–E, and cover structures in both the hangingwall and footwall of fault 1. Owing to the absence of fractures in segment A, which corresponds to the hangingwall of fault 2, no variations across this fault have been recognized. A total of 92 fractures were measured with the automated goniometer equipment. Even though the data show some scattering, a clustering around four intervals has been identified: 25–35°, 40–50°, 65–75°, and 80–90° (Fig. 13a). Data on fracture

strike also display clustering of fractures in minor domains (Fig. 13b). However, these diagrams report nothing about the distributional pattern throughout the measured core intervals.

Data on fracture orientation have been plotted versus core depth (Fig. 14), to get a better picture of the spatial distribution of fracture orientation across fault 1. In this fracture scatter diagram, each fracture is represented by a point on both the strike and dip distribution plot. The strike distribution diagram (Fig. 14a) shows that a prominent change in fracture orientation occurs between segments B and C. Fractures in segment B, corresponding to the hangingwall of fault 1, seem to display some clustering in certain intervals. This is confirmed by a statistical uniformity test which demonstrates that three sub-populations exist: 030–050°, 070–100° and 180–230°, regarding fracture strike distribution in the hangingwall of fault 1 exists (Fig. 15). On the other hand, measurements in the footwall (segment C-E), display a clear concentration of fractures trending north-south (320–050°). A corresponding shift in the fracture dip distribution occurs between segments B and C (Fig. 14b). Fractures in the hangingwall of fault 1 (segment B) are predominantly steeply dipping (60–90°), whereas dips of fractures in the footwall are more moderate (30–60°).

The majority of the measured slickenside lineations on the fracture surfaces suggests extensional dip-slip movements. However, some fracture surfaces display strike-slip left-lateral and
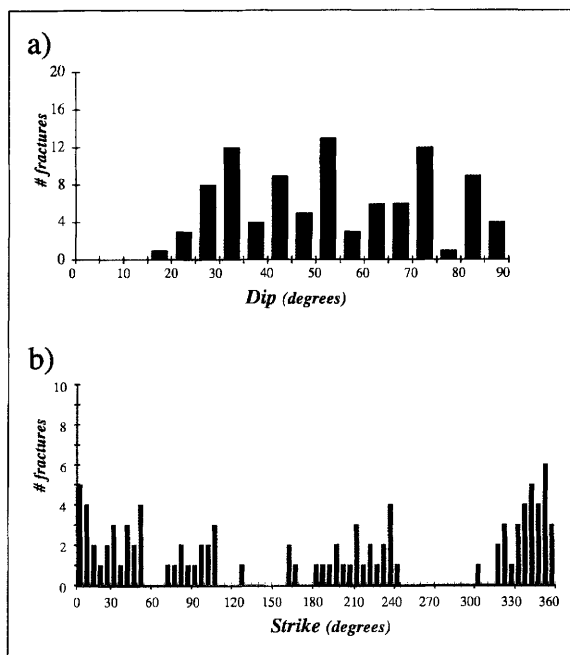
Fig. 13. Fracture orientations in segments B–E ($n = 92$). (**a**) Dip histogram, and (**b**) strike histogram. Measurements are derived from the computerized device.

right-lateral movements. A zonation of lineation directions can be seen versus depth (Table 1). In general, the slip measurements display predominately strike-slip and oblique-slip in segment B, whereas dip-slip is recorded in segments C–E.

Effect of well orientation on recorded fracture distributions and orientations

Both the azimuth and the inclination of the well may lead to an under-representation of fracture strike and dip frequencies in certain intervals.
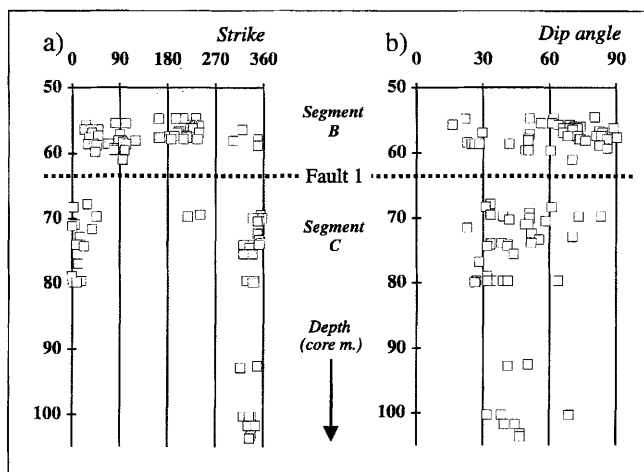
Fig. 14. Distribution of fracture orientations ($n = 97$) versus core depth measured in segments B–E. (**a**) Strike variation, and (**b**) dip variation.

R. K. AARLAND & J. SKJERVEN
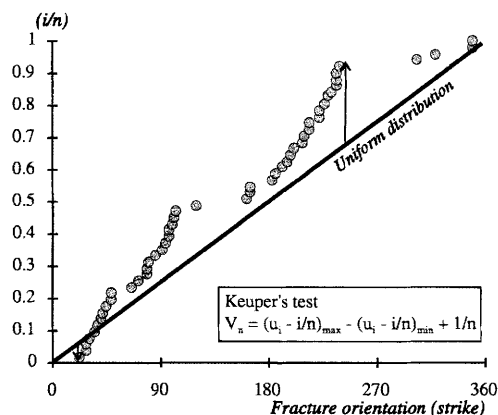
Fig. 15. Uniformity test (Keuper's test) of fracture orientations measured in segment B, situated in the hangingwall of fault 1 (corresponds to the footwall of fault 2). The test showed preferred orientations. Arrows indicate max. and min. deviations from uniform distribution.

This means that any fractures striking sub-parallel (120–130° and 300–310°) to the well, will tend to be under-represented in the current dataset. At the same time, any fractures dipping parallel to the well path (25–35°) will be under-represented. A correlation has been made between these orientation intervals with assumed under-representation, and the fracture distribution diagrams generated. No clear correlation can be seen in the dip distribution plot. Concerning strike distribution, the expected low fracture frequency correlates with intervals of low fracture frequency in the presented strike distribution diagrams. This does not imply that fractures with these orientations are not present in the area, it simply illustrates that these

Table 1. *Zonations versus core depth of lineation measurements on fracture surfaces based on the sense of slip*

Segment	Depth (core m.)	Sense of slip	Zone
A	53.50–56.05	mainly oblique-/strike-slip	I
	56.05–58.20	oblique-slip with strike- and dip-slip	II
B	58.20–60.55	mainly dip-slip	III
	63.80–64.30	dip-slip	IV
	64.80–66.90	dip-slip	V
C	67.10–73.10	mainly dip-slip some oblique-slip	VI
D	73.30–102.60	dip-slip	VII

fractures do not intersect the well path. Nevertheless, the distribution of fracture orientation versus depth still displays a clear difference between the orientation of fractures in the footwall and hangingwall of fault 1.

Discussion

One question that arises in comparing the structural logging with the biostratigraphic analysis, is whether or not the highly fractured and fragmented interval is located in the hangingwall or the footwall of the eastern Brage Horst fault. Alternatively, the whole fractured interval could lie within a fault zone bounded by the main slip surfaces. Another question is whether or not the massive, mineralized/cemented interval (at the base of segment B) represents the mineralized central part of a fault zone, as suggested by Gabrielsen & Aarland (1990), or whether it represents a cemented zone in the footwall of the eastern Brage Horst fault.

Style of deformation

Data on fault zone thickness versus fault throw given in the literature (Smith 1980; Evans 1990; Knott 1993, 1994) have suggested that a linear relationship exists between these parameters, where, for instance a displacement of 100 m should be associated with a 10 m wide fault zone. Other studies (Knipe 1992; Berg & Avery 1995; Gabrielsen & Aarland 1995) have proposed that parameters such as lithology, irregularities along fault planes and local stresses may influence the fault zone thickness, fault geometry and sealing capacity more than the fault throw does. The present study seems to support these observations. Across fault 2, a 20 cm core interval of calcite-filled fractures has accommodated a normal throw of 100–150 m. Across fault 1, 50 m of normal throw is registered and the associated deformation is distributed over 20 core metres, mainly in the hangingwall. This indicates an asymmetric fracture distribution across the lower fault zone, with a higher degree of hangingwall deformation. Additional observations are drawn from bedding orientations (Fig. 12), where an asymmetric hangingwall normal drag is associated with the lower fault. A transition zone, which coincides with fault 1, is located between segment B (easterly, steeply dipping bedding) and segment C (sub-horizontal bedding).

Changes in fracture orientations, fracture distribution, and varying slip indicators from

lineation measurements are seen across the lower zone of mineralized fractures associated with fault 1 (Table 1, Figs 13 and 14). A clear break in dip and strike of fractures is recorded between segments B and C. However, sense of slip, as seen from the slickensides on fracture planes, shows no abrupt change across this zone. Measurements taken in the adjacent areas above and below (zones III and IV, Table 1) indicate pure dip-slip movement on the fracture surfaces. The most prominent anomaly in the orientation of the slickenside lineations is seen in the uppermost part of segment B. Here the kinematic indicators show mainly oblique-slip and strike-slip movement on the fracture surfaces. These measurements are taken in the footwall just below the upper fault (2), which has a slightly oblique orientation relative to fault 1 based on the 3D seimic interpretation. If fault 2 has been formed after the initiation of fault, reactivation of some of the early-formed fractures in the hangingwall of fault 1 is expected. This may have generated secondary movement along some of these fractures, resulting in oblique-slip and strike-slip indicators on these fracture surfaces, as well as enhanced strain in response to movements along fault 2. In their analysis of fractures in the Rhine Graben, Dezayes et al. (1995) demonstrate similar evolution of the lineation pattern and orientation on the fracture surfaces. They suggest that multiple fault slip reactivates earlier fracture systems, and erases the initial slickenside lineations. Both Bürgman & Pollard (1994) and Cashman & Ellis (1994) report analogue conclusions based on fault interaction studies.

Deformation mechanisms

The 3D seismic interpretation of the eastern Brage Horst fault has documented that the fault has associated hangingwall splay faults. It is also seen that the fault changes orientation where the well intersects the fault (Fig. 3). These observations are in accordance with a model in which the measured oblique-slip and strike-slip slickenside lineations on the fracture surfaces (Table 1) are explained as a function of localized lateral movements along fractures with an unfavourable orientation relative to the stretching axis. This is further supported by the measured fracture orientations which exhibit a wide range of values between the two faults (1 and 2), and a more consistent orientation of the fractures in the footwall of fault 1. This is in accordance with an E–W orientation of the least regional principal stress axis during the formation of fractures associated with the initial

movements along the eastern Brage Horst fault in the Late Jurassic.

The present study has documented differences in the fracture dip distribution versus depth (Fig. 14b). The differences in dip values of fractures in the hangingwall and footwall of fault 1 may be explained by the combination of lithological contrasts and the initiation of steep faults in the hangingwall as a response to the ramp–flat–ramp geometry of the eastern Brage Horst fault. Additionally, the dip of the fractures in the footwall of fault 1 could be affected to a higher degree by later compaction, which would help to explain the observed low to moderate dip values of these fractures. However, differential compaction would only be a minor contributor and could by itself never explain the observed dip changes in the fault geometry.

Stress perturbation across the fault plane is likely to occur due to the geometry of the fault. This is caused by later post-depositional rotation of a hangingwall block on a pre-existing fault with a listric geometry, like the upper ramp–flat part of the eastern Brage Horst fault (Fig. 16). Local reverse faulting in the upper part of the hangingwall of fault 1 has been identified in the 3D seismic reflection dataset (Fig. 3). Locally changing stresses which give local variations in fracture orientations have previously been reported both in nature and in experimental studies (Weber et al. 1978; Rawnsley et al. 1992; Yassir & Bell 1995). This stress rotation and redistribution generates fractures with different orientations in the hangingwall and footwall, and will also affect the fracture distribution pattern (Odonne 1990). A similar evolution of fracture initiation and distribution, based on analogue modelling, is described by Withjack et al. (1995), where fault shape is the main parameter responsible for the observed fracture pattern in the hangingwall. Koestler & Ehrman (1991) also show that dilatation jags along the fault plane enhance the clustering of fractures, where increased cementation and stress perturbation could be expected (Knipe 1992). Based on a stress inversion approach, Pollard et al. (1993) demonstrated that slip directions on faults are strongly influenced by local factors, such as fault interactions. Similar observations were made in the studies of Bürgmann & Pollard (1994) and Cashman & Ellis (1994). The data presented on fracture orientation and slip direction from fractures in well 31/4-A-04 illustrate comparable relationships.

Such relations between fault geometry, local stresses, fracture distribution and orientation can be used to predict other highly deformed
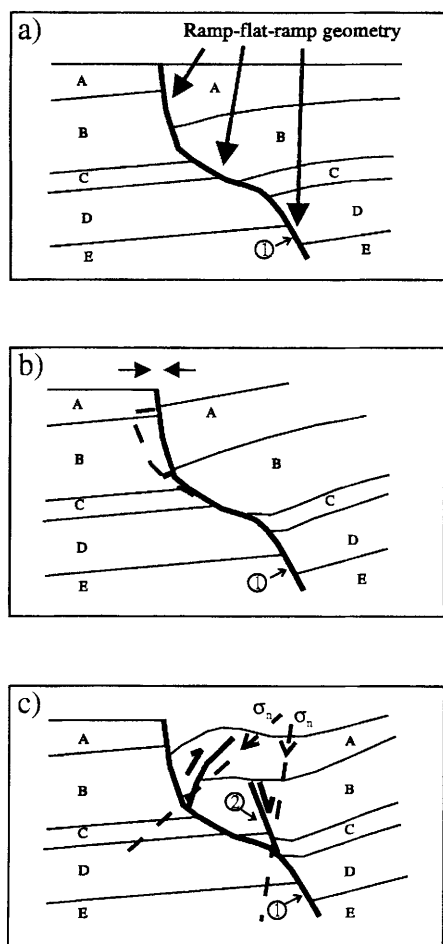
Fig. 16. Schematic model showing effects of stress perturbation across a fault with changing dip geometry, during post-depositional hangingwall block rotation. No scale is added to the model, but it could represent a situation as described for the eastern Brage Horst fault. An overlap in (b) induce volume problems and implies localized compression in the upper concave part of the fault. This will produce additional horizontal stress concentration, and give rise to localized bending of strata and/or reverse faulting in the upper part of the hangingwall, and synthetic normal splay faults in the transition above the flat–ramp segments in the middle–lower part of the hangingwall (c).

areas and their distribution along the fault, in order to evaluate regions that are more critical than others regarding sealing capacity. This depends on the model applied for the geometry of the fractured region (damage zone), and a knowledge of where the investigated sample line is located in such a scheme.

Model for the development of the eastern Brage Horst fault

Based on observations from cores and 3D seismic reflection data, a model for the development of the identified structures from the tectonic core description may be suggested (Fig. 17).

(1) Water-escape processes in some flat-lying sandstone layers during a pre-lithifaction stage of the Statfjord Formation in the Early Jurassic. Resulting deformation is expressed as folds, closed fractures and dish structures. This is comparable to the non-fault-related deformation described by Owen (1987) and Zanchi (1991).

(2) Initiation of eastern Brage Horst fault (fault 1) in Bathonian–Callovian. Deformation associated with fault 1 include hangingwall normal drag, with intense fracturing in the hangingwall. Correspondingly few fractures in the footwall of the fault create an asymmetrical fracture distribution across the fault. The 80 cm thick interval with calcite-filled fractures and cemented matrix located in the central part of the fault zone indicates that the fault acted as a conduit for fluids. This probably occurred during the initial movements along the fault, in a semi-lithified stage of the sediments. The characteristic ramp–flat–ramp geometry of the fault, as identified on the seismic reflection data, may explain the observed differences in fracture intensity and style of deformation in the footwall and hangingwall of fault 1.

(3) Ongoing stretching with a higher degree of vertical movements due to the transition to thermal subsidence in Ryazian favoured dip-slip movements along the eastern Brage Horst fault. This caused localized areas of compression, and areas with a higher potential for splay faults and increased fracturing in the hangingwall. The initiation of the upper fault (2) may have occurred at this time. Fault 3 may have been formed subsequently as an antithetic accommodation structure in the footwall of the eastern Brage Horst fault, or fault 3 could represent an older fault cut by fault 1.

(4) The subsequent evolution of fault 2 may be explained as follows. It is assumed that fault 1 had an unfavourable orientation and geometry in relation to the orientation of the local stress regime. Further movement along this fault became mechanically difficult. The upper part of the eastern
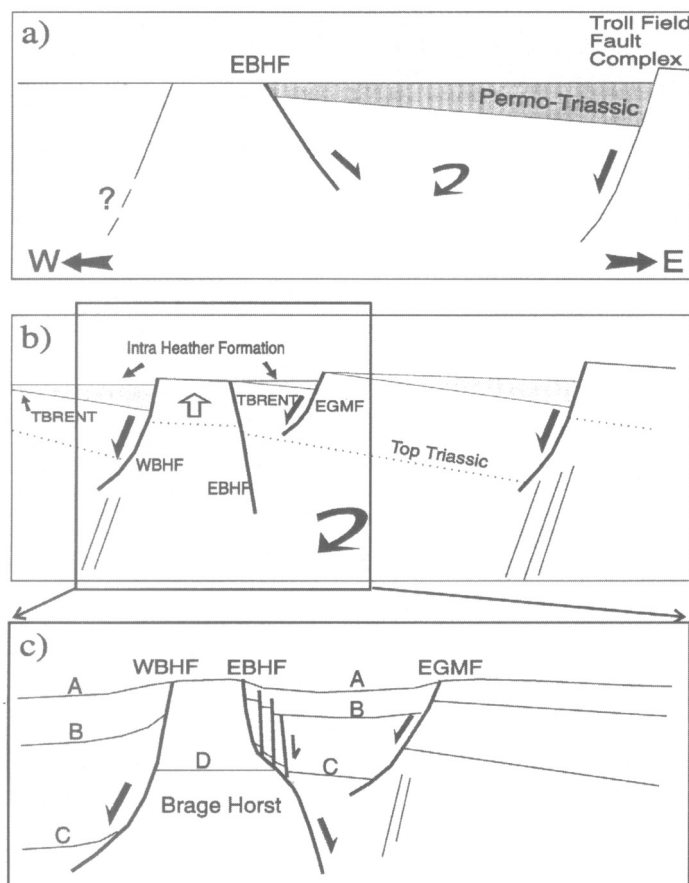
Fig. 17. Schematic model of the structural evolution of the eastern Brage Horst fault in a sub-regional framework. The western and eastern Brage Horst faults are marked WBHF and EBHF respectively. EGMF represent the eastern graben margin fault in the Brage Field. A, B, C and D refer to top of the Shetland Group, top of the Fensfjord Formation, top of the Brent Group and top of the Statfjord Formation respectively.

Brage Horst fault was no longer able to accommodate further movement, and became inactive. The main movement was then taken up by the upper fault (2) at this level. No deformation structures have been observed in the hangingwall of fault 2. Only an approximately 20 cm thick interval with calcite-filled fractures, which is interpreted as the central part of the fault, has been identified. This could imply that a strain-hardening effect occurred in the hangingwall due to the earlier deformation associated with the movements along fault 1. The upper fault (2) was generated in a transition zone with strain-softening, and acted as a hangingwall splay fault which initiated from the transition in the flat–ramp part of the eastern Brage Horst

fault. The fault is easterly dipping, relatively steep and planar. In the upper sedimentary sequence (post-Brent Group) it acted as the main fault during continued stretching.

Sealing properties

The macroscopic appearance, and the orientation and distribution of the fractures identified in the cores indicate that dissimilar fracture types have been identified. The open fractures with well-developed slickensides are dominant, but both closed fractures and calcite-filled fractures are well-represented. In the literature numerous descriptions of the microscopic properties of various fracture types can be found (Dunn *et al.* 1973; Mandl *et al.* 1977; Aydin

1978; Pittman 1981; Gabrielsen & Koestler 1987; Groshong 1988; Gabrielsen & Aarland 1990; Knipe 1992; Sverdrup & Bjørlykke 1992; Gabrielsen *et al.* 1993; Hippler 1993; Antonellini & Aydin 1994; Antonellini *et al.* 1994; Fowles & Burley 1994; Gibson 1994). These studies show that mode II fractures (shear fractures, micro-faults, deformation bands, granulation seams or shear bands) are commonly characterized by internal compaction, grain size reduction and mineralization, and usually give a reduction in the permeability perpendicular to the fractures. The permeability parallel to a fracture will, on the other hand, be increased if the fracture is open and has well-developed slickensides. Lithology will also be an important parameter for the permeability estimation and sealing capacity, since different lithologies engender different textural characteristics of fractures. In this study it was found that fractures in the shaly units are typically open, whereas fractures in silty units are more commonly closed. This difference may depend on the initial clay and mica content in the deforming sediment. A more sediment will tend to develop more closed fractures than a more clay-rich sediment, where 'lubrication' of clays and micas will favour opening of the fracture during later unloading. This means that the fractures are not open at depth. Thin-section studies of the cores of well 31/4-A-04 show that both the open and closed fractures have a high degree of reorientation of clays and micas into the fracture surface, weak cataclasis and no mineralization or cementation.

The sealing capacity of the eastern Brage Horst fault will depend on the degree of juxta-position between the sand bodies across the fault, the fracture pattern expressed as increased deformation towards the lower mineralized fault (2), and the stability of the mineralized intervals observed in well 31/4-A-04. It is reasonable to predict a high sealing capacity across the fault if the remaining part of the fault plane has developed a similar cemented central part as found across fault 1. The stability of cement seals is dependent on the surrounding fault array evolution (Knipe 1992). The movement along fault 1 is thought to be restricted to the post-cementation stage, and stability of the seal is accordingly attained. The difference in thickness of the two intervals of mineralized fractures can be explained as a function of temporal fault movement, dilatation magnitude and strain-hardening. In the lower interval of 80 cm, the calcite-filled fractures are situated in cemented rocks. According to Knipe (1992), this may be described as a composite seal with border zone seals and internal fault zone seals. However,

since the underlying fragmented zone seen in the core could represent the fault plane of fault 1, the lower cemented interval with the minera-lized fractures is interpreted as a central fault zone. Within this fault zone, pre-existing frac-tures were filled by dissolved calcium and the surrounding sediment was affected and cemented by the fluid flow in the hangingwall of the fault.

Anderson *et al.* (1994) have reported several sub-vertical fractures in the hangingwall of a major growth fault in the Gulf of Mexico, and concluded that these fractures could have acted as conduits for hydrocarbons. The observed high frequency of high-angled to sub-vertical frac-tures with well-developed slickensides in the hang-ingwall may then possibly reduce the sealing capacity up along the fault plane of the eastern Brage Horst fault. However, Weber *et al.* (1978) and Berg & Avery (1995) have reported effective seals across sheared zones. Owing to the well-developed drag, a high degree of shearing and clay-smear in the hangingwall of the eastern Brage Horst fault is to be expected. Correspond-ingly, at the critical level (sand/sand juxtaposition seen on the 3D seismic reflection sections), the fault could be regarded as sealing.

The effect of *in situ* stress has not been dis-cussed so far. This parameter is closely linked to the fault mechanisms and hydrocarbon migration. It is well-documented that *in situ* stresses may control the cap-rock seal as well as influencing the shear strength of a fracture zone and its reactivation potential (Sibson 1985, 1990; Grauls & Baleix 1994; Yassir & Bell 1995). In sealing fault studies, the effect of the *in situ* stresses and reactivation potential should be kept in mind.

Conclusions

The structural logging and description of the cored intervals in well 31/4-A-04 have revealed differences in the deformation style across the zone where the well intersects the eastern Brage Horst fault. The following observations and interpretations have been made:

- Two major, easterly dipping faults (1 and 2), both associated with intervals of calcite-filled fractures, have been identified.
- The main deformation is associated with the lower fault (1), which has approximately 50 m of normal throw, whereas the upper fault (2) has a normal throw of 100–150 m.
- An increasing fracture intensity is documen-ted downwards from fault 2 towards fault 1, with an abrupt decrease in fracture frequency

in the footwall of fault 1. No such systematic fracture distribution pattern is seen across the upper fault (2) which has recorded the largest displacement.

• Fracture orientations are different in the hangingwall and footwall of fault 1.

Both the structural description of the cores, the fracture frequency plot, and bedding and fracture orientations have revealed that the most significant break is located between segments B and C. This means that the lower interval of calcite-filled fractures is probably not localized in the footwall of the eastern Brage Host fault, but seems to represent the central part of the fault zone. Another observation is that the fault zone is narrower than expected assuming a linear relationship between fault zone thickness and fault throw. Furthermore, the main displacement seems to be limited to the mineralized intervals and not equally or symmetrically distributed over the whole fractured interval. The style of deformation is asymmetric, and the majority of the structures observed are interpreted to have developed in response to initial movements along fault 1.

Although a high degree of juxtaposition of sand bodies exists across the eastern Brage Horst fault and the majority of the fractures in the cores are open, it is proposed that the deformation structures observed in the cores still contribute to the sealing capacity of the eastern Brage Horst fault. The possibility of a stable seal is further supported by a well-developed normal drag in the hangingwall, which contributes to enhanced clay-smearing along the fault plane.

References

ALLAN, U. S. 1989. Model for hydrocarbon migration and entrapment within faulted structures. *AAPG Bulletin*, **73**, 803–811.

ANDERSON, R. N., FLEMINGS, P., LOSH, S., AUSTIN, J. & WOODHAMS, R. 1994. Gulf of Mexico growth fault drilled, seen as oil, gas migration pathway. *Oil & Gas Journal*, June 6, 97–104.

ANTONELLINI, M. A. & AYDIN, A. 1994. Effect of faulting and fluid flow in porous sandstones: petrophysical properties. *AAPG Bulletin*, **78**, 355–377.

——, —— & POLLARD, D. D. 1994. Microstructure of deformation bands in porous sandstones at Arches National Park, Utah. *Journal of Structural Geology*, **7**, 961–970.

ARTHUR, E., CARSON, B. & VON HUENE, R. 1980. Initial tectonic deformation of hemipelagic sediment at the leading edge of the Japan convergent margin. *Initial Report Deep Sea Drilling Project*, **56**, 569–613.

AYDIN, A. 1978. Small faults formed as deformation bands in sandstones. *Pure and Applied Geophysics*, **116**, 913–930.

—— & JOHNSON, A. M. 1978. Development of faults as zones of deformation bands and as subsurfaces in sandstone. *Pure and Applied Geophysics*, **116**, 931–942.

AYDIN, A. & JOHNSON, A. 1983. Analysis of faulting in porous sandstones. *Journal of Structural Geology*, **5**, 19–31.

BADLEY, M. E., EGEBERG, T. & NIPEN, O. 1984. Development of rift basins illustrated by the structural evolution of the Oseberg structure, Block 30/6, offshore Norway. *Journal of the Geological Society, London*, **141**, 639–649.

——, PRICE, J. D., RAMBECH DAHL, C. & AGDESTEIN, T. 1988. The structural evolution of the northern Viking Graben and its bearing upon extensional modes of graben formation. *Journal of the Geological Society, London*, **145**, 455–472.

BARTON, C. A. & ZOBACK, M. D. 1990. Self-similar distribution of macroscopic fractures at depth in crystalline rock in the Cajon Pass scientific drillhole. *In:* BARTON, N. & STEPHANSSON, O. (eds) *Rock Joints*. Balkema, Rotterdam, 163–170.

BERG, R. R. & AVERY, A. H. 1995. Sealing properties of Tertiary growth faults, Texas Gulf Coast. *AAPG Bulletin*, **79**, 375–393.

BOUVIER, J. D., KAARS-SIJPESTEIJN, C. H., KLUESNER, D. F., ONYEJEKWE, C. C. & VAN DER PAL, R. C. 1989. Three-dimensional seismic interpretation and fault sealing investigations, Nun River Field, Nigeria. *AAPG Bulletin*, **73**, 1397–1414.

BÜRGMANN, R. & POLLARD, D. D. 1994. Slip distributions on faults: effects of stress gradients, inelastic deformation, heterogeneous host-rock stiffness, and fault interaction. *Journal of Structural Geology*, **16**, 1675–1690.

CASHMAN, P. H. & ELLIS, M. A. 1994. Fault interaction may generate multiple slip vectors on a single fault surface. *Geology*, **22**, 1123–1126.

DEZAYES, CH., VILLEMIN, T., GENTER, A., TRAINEAU, H. & ANGELIER, J. 1995. Analysis of fractures in boreholes of the Hot Dry Rock project at Soultz-sous-Forêts (Rhine graben, France). *Scientific Drilling*, **5**, 31–41.

DUNN, D. E., LA FOUNTAIN, L. J. & JACKSON, R. E. 1973. Porosity dependence and mechanism of brittle fracture in sandstones. *Journal of Geophysical Research*, **78**, 2403–2416.

EVANS, J. P. 1990. Thickness–displacement relationships for fault zones. *Journal of Structural Geology*, **12**, 1061–1065.

FOWLES, J. & BURLEY, S. 1994. Textural and permeability characteristics of faulted, high porosity sandstones. *Marine and Petroleum Geology*, **11**, 608–623.

GABRIELSEN, R. H. 1986. Structural elements in graben systems and their influence on hydrocarbon trap types. *In*: SPENCER, A. M. *et al.* (eds) *Habitat of Hydrocarbons on the Norwegian Continental Shelf*. Norwegian Petroleum Society, Graham & Trotman, London, 55–60.

—— & AARLAND, R.-K. 1990. Characteristics of pre- and syn-consolidation structures and tectonic joints and microfaults in fine to medium-grained sandstones. *In*: BARTON, N. & STEPHANSSON, O (eds) *Rock Joints*. Balkema, Rotterdam, 45–50.

—— & ——1995. How can fracture analysis contribute to the understanding of previous and recent stress systems? *In*: MYRVANG, A. & FEJERSKOV, M. (eds) *Proceedings to the Workshop on Rock Stresses in the North Sea*. Trondheim, 38–48.

—— & KOESTLER, A. G. 1987. Description and structural implications of fractures in late Jurassic sandstones of the Troll Field, northern North Sea. *Norsk Geologisk Tidsskrift*, **67**, 371–381.

——, AARLAND, R.-K. & PEDERSEN, T. A. 1993. Distribution and genesis of natural fracture systems in clastic sediments. *In*: BANKS, S. & BANKS, D. (eds) *Hydrogeology of Hard Rocks*. Memoirs of the XXIVth Congress, International Association of Hydrogeologists, Ås, Oslo, 52–73.

——, FÆRSETH, R. B., STEEL, R. J. & KLØVJAN, O. S. 1990. Architectural styles of basin fill in the northern Viking Graben. *In*: BLUNDELL, D. J. & GIBBS, A. D. (eds) *Tectonic Evolution of the North Sea Rifts*. Oxford Science, ILP, **181**, 158–179.

GAMOND, J. F. 1983. Displacement features associated with fault zones: a comparison between observed examples and experimental models. *Journal of Structural Geology*, **5**, 33–45.

GIBSON, R. G. 1994. Fault-zone seals in siliclastic strata of the Columbus Basin, offshore Trinidad. *AAPG Bulletin*, **78**, 1372–1385.

GILLESPIE, P. A., WALSH, J. J. & WATTERSON, J. 1992. Limitations of dimension and displacement data analysis and interpretation. *Journal of Structural Geology*, **14**, 1157–1172.

GRAULS, D. J. & BALEIX, J. M. 1994. Role of overpressures and *in situ* stresses in fault-controlled hydrocarbon migration: a case study. *Marine and Petroleum Geology*, **11**, 734–742.

GROSHONG, R. H. Jr 1988. Low-temperature deformation mechanisms and their interpretation. *Geological Society of America Bulletin*, **100**, 1329–1360.

HAGE, A., BOMSTAD, K. & STRAND, J. E. 1987. Brage. *In*: SPENCER, A. M. *et al.* (eds) *Geology of the Norwegian Oil and Gas Fields*. Norwegian Petroleum Society, Graham & Trotman, London, 371–378.

HARDING, T. P. & TUMINAS, A. C. 1989. Structural interpretation of hydrocarbon traps sealed by basement normal block faults at stable flank of foredeep basins and at rift basins. *AAPG Bulletin*, **73**, 812–840.

HARRIS, J. F., TAYLOR, G. L. & WALPER, J. L. 1960. Relation of deformational fractures in sedimentary rocks to regional and local structure. *AAPG Bulletin*, **44**, 1853–1873.

HIPPLER, S. J. 1993. Deformation microstructures and diagenesis in sandstone adjacent to an extensional fault: implications for the flow and entrapment of hydrocarbons. *AAPG Bulletin*, **77**, 625–637.

HUANG, Q. & ANGELIER, J. 1989. Fracture spacing and its relation to bed thickness. *Geological Magazine*, **126**, 355–362.

JAMISON, W. R. & STEARNS, D. W. 1982. Tectonic deformation of Wingate Sandstone, Colorado National Monument. *AAPG Bulletin*, **66**, 2584–2608.

KNIPE, R. J. 1992. Faulting processes and fault seal. *In*: LARSEN, R. M., BREKKE, H., LARSEN, B. T. & TALLERAAS, E. (eds) *Structural and Tectonic Modelling and its Application to Petroleum Geology*. Norwegian Petroleum Society Special Publication **1**, Elsevier, Amsterdam, 325–342.

KNOTT, S. D. 1993. Fault seal analysis in the North Sea. *AAPG Bulletin*, **77**, 778–792.

——1994. Fault zone thickness versus displacement in the Permo-Triassic sandstones of NW England. *Journal of the Geological Society, London*, **151**, 17–25.

KOESTLER, A. G. & EHRMAN, W. U. 1991. Description of brittle extensional features in chalk on the crest of a salt ridge (NW Germany). *In*: ROBERTS, A. M., YIELDING, G. & FREEMAN, B. (eds) *The Geometry of Normal Faults*. Geological Society, London, Special Publication **56**, 113–123.

KULANDER, B. R., DEAN, S. L. & WARD, B. J. Jr 1990. *Fractured Core Analysis: Interpretation, Logging, and Use of Natural and Induced Fractures in Core*. AAPG, Methods in Exploration Series, **8**.

LADEIRA, F. L. & PRICE, N. J. 1981. Relationships between fracture spacing and bed thickness. *Journal of Structural Geology*, **3**, 179–183.

MANDL, G. 1988. *Mechanics of Tectonic Faulting. Models and Basic Concepts*. Elsevier.

——, JONG, L. N. J. & MALTHA, A. 1977. Shear zones in granular material – An experimental study of their structure and mechanical genesis. *Rock Mechanics*, **9**, 95–144.

NARR, W. & SUPPE, J. 1991. Joint spacing in sedimentary rocks. *Journal of Structural Geology*, **13**, 1037–1048.

NELSON, R. A. 1985. *Geologic Analysis of naturally Fractured Reservoirs*. Contributions in Petroleum Geology and Engineering **1**, 320 pp.

——, LENOX, L. C. & WARD, B. J. Jr 1987. Oriented core: its use, error, and uncertainty. *AAPG Bulletin*, **71**, 357–367.

ODONNE, F. 1990. The control of deformation intensity around a fault: natural and experimental examples. *Journal of Structural Geology*, **12**, 911–921.

OWEN, G. 1987. Deformation processes in unconsolidated sands. *In*: JONES, M. E. & PRESTON, R. M. F. (eds) *Deformation of Sediments and Sedimentary Rocks*. Geological Society, London, Special Publications **29**, 11–24.

ÖZKANLI, M. & STANDEN, E. J. W. 1993. Fracture morphology in Cretaceous carbonate reservoirs from south-east Turkey. *First Break*, **11**, 323–333.

PEACOCK, D. C. P. & SANDERSON, D. J. 1993. Estimating strain from fault slip using a line sample. *Journal of Structural Geology*, **15**, 1513–1516.

PITTMAN, E. D. 1981. Effect of fault-related granulation on porosity and permeability of quartz sandstones, Simpson Group (Ordovician), Oklahoma. *AAPG Bulletin*, **65**, 2381–2387.

POLLARD, D. D., SALTZER, S. D. & RUBIN, A. M. 1993. Stress inversion methods: are they based on faulty assumptions? *Journal of Structural Geology*, **15**, 1045–1054.

RAWNSLEY, K. D., RIVES, T., PETIT, J.-P., HENCHER, S. R. & LUMSDEN, A. C. 1992. Joint development in perturbed stress fields near faults. *Journal of Structural Geology*, **14**, 939–951.

RIVES, T., RAZAK, M., PETIT, J.-P. & RAWNSLEY, K. D. 1992. Joint spacing: analogue and numerical simulations. *Journal of Structural Geology*, **14**, 925–937.

SIBSON, R. H. 1985. A note on fault reactivation. *Journal of Structural Geology*, **7**, 752–754.

—— 1990. Rupture nucleation on unfavorably oriented faults. *Bulletin of the Seismological Society of America*, **80**, 1580–1604.

SMITH, D. A. 1980. Sealing and non-sealing faults in Louisiana Gulf Coast Salt Basin. *AAPG Bulletin*, **64**, 145–172.

SVERDRUP, E. & BJØRLYKKE, K. 1992. Small faults in sandstones from Spitsbergen and Haltenbanken. A study of diagenetic and deformation structures and their relation to fluid flow. *In*: LARSEN, R. M.,

BREKKE, H., LARSEN, B. T. & TALLERAAS, E. (eds) *Structural and Tectonic Modelling and its Application to Petroleum Geology*. Norwegian Petroleum Society, Special Publication **1**, Elsevier, Amsterdam, 507–517.

UNDERHILL, J. R. & WOODCOCK, N. H. 1987. Faulting mechanisms in high-porosity sandstones. *In*: JONES, M. E. & PRESTON, R. M. F. (eds) *Deformation of Sediments and Sedimentary Rocks*. Geological Society, London, Special Publication **29**, 91–105.

WALSH, J., WATTERSON, J. & YIELDING, G. 1991. The importance of small-scale faulting in regional extension. *Nature*, **351**, 391–393

WEBER, K. J., MANDL, G., PILAAR, W. F., LENER, F. & PRECIOUS, R. G. 1978. The role of faults in hydrocarbon migration and trapping in Nigerian growth fault structures. *Tenth Annual Offshore Technology Conference Proceedings*, **4**, 2643–2653.

WITHJACK, M. O., ISLAM, Q. T. & LA POINTE, P. R. 1995. Normal faults and their hanging-wall deformation: An experimental study. *AAPG Bulletin*, **79**, 1–18.

YASSIR, N. A. & BELL, J. S. 1995. Relationships between pore pressures, stresses, and present-day geodynamics in the Scotian Shelf, Offshore Eastern Canada. *AAPG Bulletin*, **78**, 1863–1880.

YIELDING, G., BADLEY, M. E. & ROBERTS, A. M. 1992*a*. The structural evolution of the Brent Province. *In*: HAZELDINE, A. C. *et al.* (eds) *Geology of the Brent Group*. Geological Society, London, Special Publication **61**, 27–43.

——, WALSH, J. & WATTERSON, J. 1992*b*, The prediction of small-scale faulting in reservoirs. *First Break*, **10**, 449–460.

ZANCHI, A. 1991. Tectonic and liquefaction structures in the Loreto basin, Baja California (Mexico): synsedimentary deformation along a fossil fault plane. *Geodinamica Acta* (Paris), **5**, 187–202.

Structural geology of the Gullfaks Field, northern North Sea

HAAKON FOSSEN[1] & JONNY HESTHAMMER[2]

[1] Department of Geology, University of Bergen, Allégt. 41, N-5007 Bergen, Norway
[2] Statoil, N-5020 Bergen, Norway

Abstract: The large amount of structural data available from the Gullfaks Field have been used to unravel the structural characteristics of the area. Two structurally distinct sub-areas have been revealed (a major domino system and an eastern horst complex) that show significant differences with respect to fault geometry, rotation and internal block deformation. The main faults have very low dips in the domino system (25–30°) as compared to the horst complex (65°), whereas most minor faults are steep in all parts of the field. Forward modelling indicates that the horst complex balances with rigid block operations. However, the domino area underwent significant internal deformation, reflected by the low acute angle between bedding and faults, and by non-planar bedding geometries. The internal deformation is modelled as a shear synthetic to, but steeper than, the main domino faults. This deformation explains a large-scale (kilometre sized) drag zone that has a triangular geometry in cross-section. Much of this shear deformation occurred by strain-dependent grain reorganization in the poorly consolidated Jurassic sediments, which led to a decrease in porosity. A strain map is presented for the domino area, indicating where the porosity is likely to have been decreased due to internal shear. Hangingwalls are generally more deformed (sheared) than footwalls. This is seen on both the kilometre scale (large-scale drag) and the metre scale (local drag).

There has been a rapidly growing interest in understanding extensional crustal deformation at various scales during the last few decades. Common approaches include physical modelling (Horsfield 1977; McClay & Ellis 1987; Vendeville *et al.* 1987; Withjack *et al.* 1995), theoretical/numerical modelling (Jarvis & McKenzie 1980; Houseman & England 1986; Kusznir & Ziegler 1992; Childs *et al.* 1990), seismic studies (Blundell *et al.* 1985; Beach 1986; Klemperer 1988) and field studies (Jackson *et al.* 1988; Davison *et al.* 1994). While theoretical and physical modelling are indeed important tools, they must be guided by and tested against data and observations of naturally deformed rocks. Detailed observations and careful collection of field data are therefore crucial.

Although some well-exposed portions of rift systems do exist (e.g. the gulfs of Corinth and Suez), most rift systems are buried by syn-rift or post-rift sedimentary sequences and/or water. Exposed examples may have been brought to the surface by contractional crustal movements, causing reactivation and reworking of the original extensional structures. However, an overwhelming amount of geological and geophysical data have accumulated in parts of rift systems where moderate to large oil-fields are located. We believe that systematic and integrated structural analysis of the various types of geo-data available from oil-fields in the North Sea and elsewhere is a key not only to improving well planning and reservoir management in the region, but also to increasing our general understanding of extensional deformation.

The present work is a contribution from the Gullfaks Oil-field in the North Sea, where more than 170 wells have been drilled and extensive well data of various types are collected. In addition, three-dimensional (3D) seismic data have recently been reprocessed and reinterpreted together with other field data in an integrated process. It represents an attempt to use and combine the many different types of data that are available from a producing oil-field to obtain the best understanding possible of the structural geology of the area.

Regional setting

The Gullfaks Field is located on the western flank of the Viking Graben (Fig. 1), where it occupies the eastern half of a 10–25 km wide, NNE–SSW-trending fault block named the Gullfaks fault block in this article. The Gullfaks fault block is one of a series of large (first-order) fault blocks that are easily identified on regional seismic lines across the North Sea. The general trend of these larger faults in the northern North Sea is N–S to NNE–SSW, reflecting the overall E–W extension across the rift.

The extensional history of the North Sea dates back to the Devonian extensional phase shortly after the Caledonian collision (e.g. McClay *et al.* 1986). Onshore kinematic studies support the
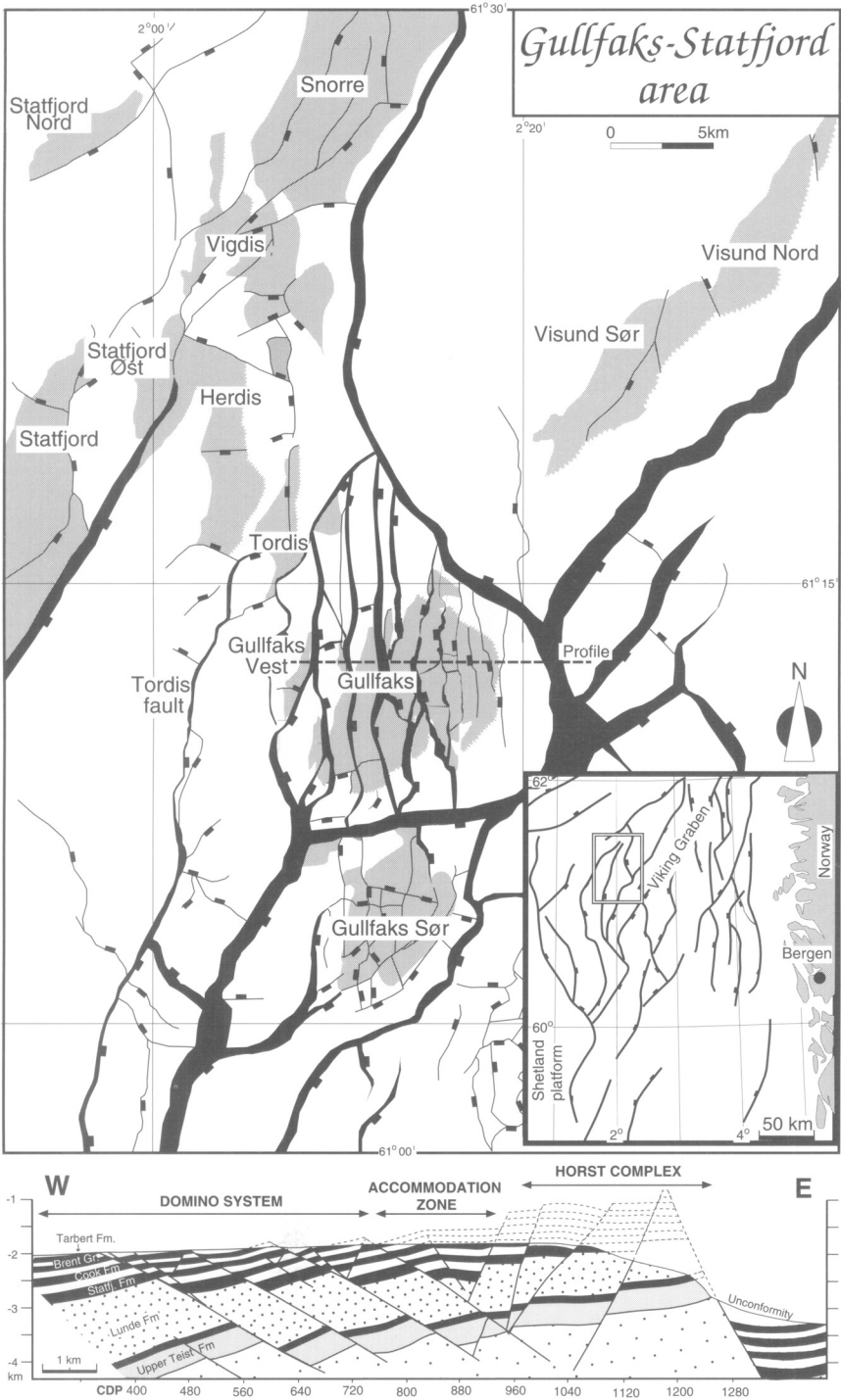
Fig. 1. Regional map of the northern North Sea (inset map) and of the Gullfaks–Statfjord area, and a profile across the Gullfaks Field.

idea of plate-scale divergent movements in the Devonian (Fossen 1992). The main subsequent rifting phases are commonly referred to as the Permo-Triassic and late Jurassic phases (e.g. Badley *et al.* 1988; Gabrielsen *et al.* 1990). Whereas the extension involved in the Permo-Triassic event is significant (Roberts *et al.* 1995), the late Jurassic deformation of the Jurassic sequence is more obvious on commercial seismic lines, and best known from well data. The present study is concerned with deformation of Late Triassic–Jurassic layers in the Gullfaks area, and thus with the late Jurassic extension phase.

The Gullfaks Field

The Gullfaks Field (Petterson *et al.* 1990) is situated east of the Statfjord Field and south of the Snorre Field (Fig. 1), and has been under production since 1986. Covering an area of *c.* 75 km², the field is developed by three concrete platforms under a fully Norwegian license group consisting of Statoil (operator), Norsk Hydro a.s. and Saga Petroleum a.s. Total recoverable reserves amount to about 310×10^6 Sm³ of oil and some 30×10^9 Sm³ of gas, located in the Jurassic Brent Group, Cook Formation and Statfjord Formation.

Stratigraphy

The deepest well in the Gullfaks area (34/10-13) was drilled to about 3350 m depth, and penetrated 1340 m of Triassic sands and shales of the Lunde and Lomvi Formations (Hegre Group). The base of the Triassic has never been reached in this part of the northern North Sea, and little is therefore known about early and pre-Triassic strata. From gravity surveys, palinspastic reconstructions and regional, deep-seismic lines, it is, however, inferred that only thin sequences of sediments are present between the Triassic clastics and Devonian or metamorphic/crystalline basement in this area.

The Triassic Hegre Group consists of inter-bedded intervals of sandstones, claystones and shales, all deposited in a continental environment. The upper part of the Hegre Group (the Lunde Formation) consists of medium-grained, fluvial sandstones and contains reserves in the eastern Gullfaks area. Overlying the Hegre Group is the Rhaetian–Sinemurian Statfjord Formation which consists of 180–200 m of sandstones deposited in an alluvial environment that

changed its character from a well-drained semi-arid setting to a more humid alluvial plain.

The 370–420 m thick Dunlin Group is sub-divided into the Amundsen, Burton, Cook and Drake Formations. The Amundsen and Burton Formations consist 170–180 m of marine clay-stones and siltstones overlain by the regressive, marine, silty claystones of the lower part of the 110–160 m thick Cook Formation, and in turn by muddy sandstones, sands and shales of the upper part of the Cook Formation. The 75–120 m thick Drake Formation comprises marine shales with varying amounts of silt.

The Brent Group of mainly Bajocian–Early Bathonian age forms the upper and main part of the reservoirs. It is sub-divided into the Broom (8–12 m), Rannoch (50–90 m), Etive (15–40 m), Ness (85–110 m) and Tarbert (75–105 m) Formations, all deposited in a deltaic environment. A broad lithological sub-division can be made between the shaly Ness Formation and the sandy intervals below and above.

A major time gap (up to 100 Ma) is represented by the base Cretaceous (late Cimmerian) unconformity on the Gullfaks Field, separating Upper Cretaceous sediments from Jurassic or Triassic sediments, and post-dating the major part of the faulting history of the area. Up to 100 m of Upper Jurassic shales (Heather Formation) are locally preserved in the hangingwalls to the main faults in the Gullfaks Field, particularly in the western part.

Structural outline

The Gullfaks Field is characterized by two structurally contrasting compartments (Fig. 1, profile): a western domino system with typical domino-style fault block geometry, and a deeply eroded eastern horst complex of elevated sub-horizontal layers and steep faults. These two regions are significantly different as far as structural development is concerned, and will be treated separately below. Between the western and eastern regions is a transitional accommodation zone (graben system) which is identified as a modified fold structure.

The distribution of these structurally different areas is shown in Fig. 2, which displays an east-stepping occurrence of the accommodation zone as one goes from the north to the south. The stepping occurs across E–W transfer faults with high displacement gradients (rapidly decreasing displacement to the west). These E–W faults thus separate domains of contrasting dips.
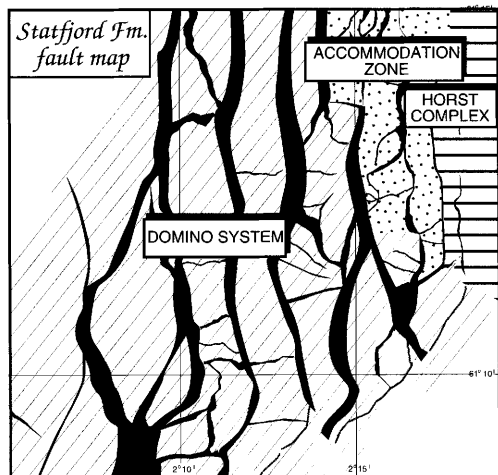
Fig. 2. The areal distribution of the domino system, the horst complex and the accommodation zone on the top Statfjord fault map.

Data and method

The structural analysis and discussion presented in this work are based on the multitude of exploration and production data from the Gullfaks Field. Ten thousand kilometres of reprocessed 3D seismic data (ST8511) were interpreted (1992–93). Reflections closely corresponding to base Cretaceous, top Rannoch Formation, top Amundsen Formation, top Statfjord Formation and an intra-Teist Formation were interpreted in the entire area. Other formation boundaries were partly interpreted and partly constructed from these formation boundaries by use of time-converted isochore maps. Seismic attribute maps, dipmeter data and other information from the approximately 170 wells through the Gullfaks reservoirs were used extensively during interpretation. Both the time-interpreted horizons and faults were depth-converted for structural analysis, using a linear velocity function combined with available well velocity (vertical seismic profile (VSP) and synthetic seismogram) information. The geometrical characteristics of the mapped formations (horizons) and faults are presented as maps, stereoplots and graphs that form a foundation for further analysis and discussion of the structural geology of the Gullfaks Field.

Two maps (top Rannoch and top Statfjord Formations, Figs 3 and 4) were selected for structural analysis, because they coincide or closely coincide with the best reflectors on the seismic lines, and they represent a significant (450 m)

difference in depth. The orientation of the bedding was extracted by sub-dividing depth maps into squares of 312.5 m×312.5 m in which the average strike and dip of the bedding was estimated. Similarly, fault maps were sub-divided along strike into segments of 250 m length, and the average strike and dip were measured/calculated at or close to reservoir level (mostly at the Amundsen–Statfjord level). This length was found to be small enough to pick up all significant undulations in the fault plane geometry, and sufficiently large to even out some of the 'noise' that occurs from inaccurate interpretation (the faults were systematically interpreted every 100 m at the work station).

The domino area

The western domino region constitutes the main part of the Gullfaks Field. The deformation in this part of the field has resulted in a series of generally N–S-trending fault blocks. The faults defining these blocks are named F1, F2 etc. (see Fig. 5). They have displacements in the range 50–500 m, and will be termed main faults in this work. As will be discussed in more detail below, the block-bounding faults in this area have unusually low dips (25–30° to the east) whereas the sedimentary strata dip gently (typically about 15°) to the west. The domino fault blocks are compartmentalized by a series of smaller faults with throws generally below 50 m. These faults, which are referred to as minor faults, have more variable trends, including a marked E–W trend.

Geometry of main faults

Orientation data extracted from depth-converted fault contour maps of main faults were plotted in stereonets as poles to planes. The results (Fig. 6a–e) demonstrate well the non-planar geometry of the main faults, and the poles to the faults are remarkably well-distributed along great circles. The latter phenomenon, which was also noted by Koestler et al. (1992) for two faults in the western part of the domino area, reflects the cylindrical geometry of the non-planar faults at reservoir level. The poles to the best-fit great circles (β-axes of Ramsay (1967)) define the axis of curvature of the fault surfaces. Obviously, the easiest slip direction for the fault blocks is parallel to the β-axes. Movements oblique to this direction would imply serious compatibility problems which could be resolved only to a certain extent by internal deformation
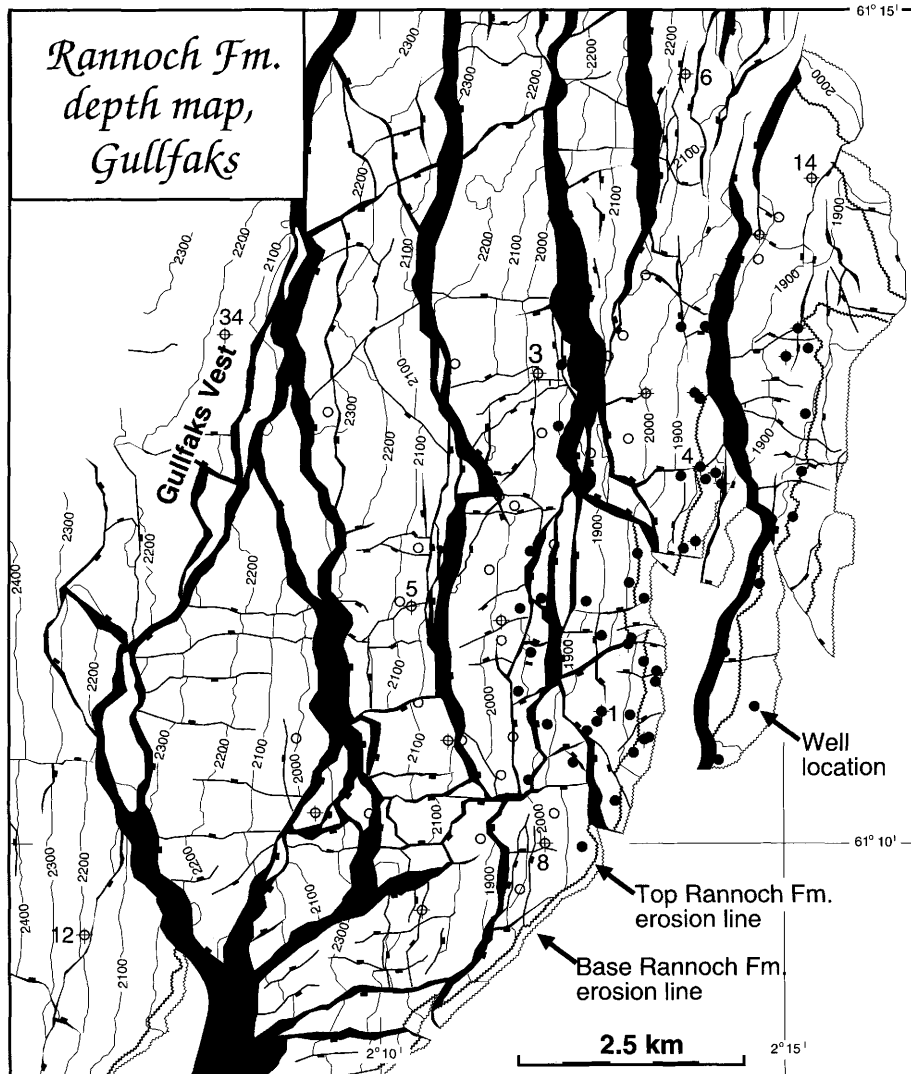
Fig. 3. Depth map of the Rannoch Formation in the Gullfaks Field.

near the fault. The poles to the best-fit great circles must therefore be close to the mean slip direction to the main faults. Figure 6 constrains the mean slip direction to an easterly trend (090 ± 10) with a plunge of about 25–30°. It can also be seen from Fig. 6a–e that the lowest dips (dips of N–S-striking fault segments) vary from 30° in the west to 25° in the east.

Geometry of minor faults

Minor faults show a much wider range in orientation than the main faults (Fig. 6f), and include:

(1) N–S-striking minor faults sub-parallel (synthetic) to the main faults; (2) E–W-striking minor faults; (3) diagonal; and (4) steep N–S-striking minor faults antithetic to the main faults.

The first category have dips that are slightly steeper than the main faults if they occur in the hangingwall (hangingwall collapse, Fig. 7), and somewhat lower dips if they are related to footwall collapse. Hangingwall and footwall collapse have been mapped in several places, but may be difficult to identify from seismic data alone. Exploration of the Gullfaks Vest structure (Figs 3 and 4) is an example of the latter, where, after three pilots and two long horizontal wells,
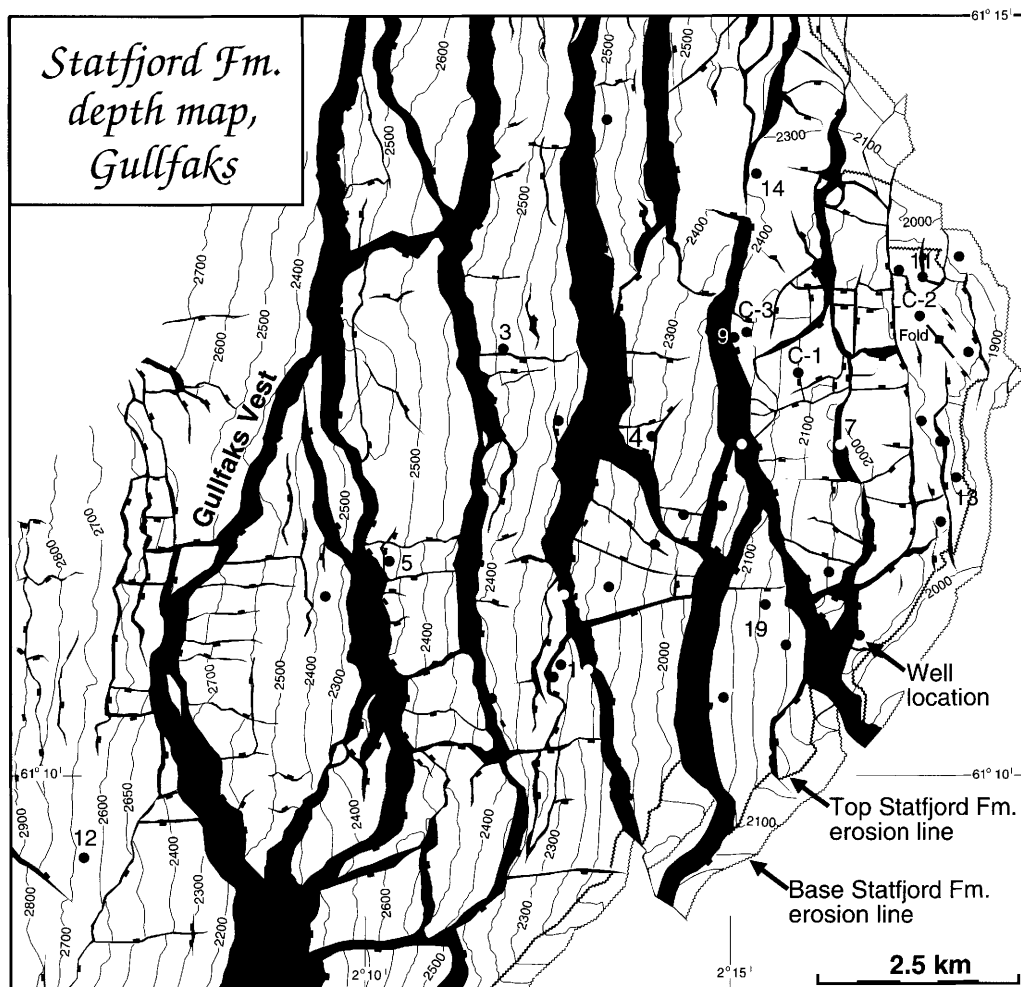
Fig. 4. Depth map of the Statfjord Formation in the Gullfaks Field.

the map pattern changed from a simple footwall geometry to a much more complex collapsed footwall rim. In this particular example, the collapse structures were largely restricted to the Brent Group (compare fault patterns of Figs 3 and 4), and were therefore not reflected in the well-defined but deeper Amundsen and Statfjord reflectors.

E–W-striking minor faults are typically steep (45–90°) and restricted to single domino blocks. They must therefore be related to internal block deformation, and are best interpreted as accommodation structures formed during a history of differential slip along the main faults. They are also characterized by small throws (many <20 m and almost all <50 m). From the stereo-

graphic projections (Fig. 6f) it appears that the N-dipping faults of this type are very steep, whereas a series of S-dipping E–W faults have somewhat lower (although still quite steep) dips.

Diagonal minor faults, i.e. NW–SE- or NE–SW-striking faults, are mapped in most of the Gullfaks area. These faults have variable throws and, like the other minor faults, most are restricted to single fault blocks. They have intermediate dips, and categories (1), (2) and (3) together define a great circle similar to the main faults (Fig. 6f).

Most antithetic faults are steep to sub-vertical and somewhat variable, but mostly N–S-striking. These faults have small (<20 m) throws, and are less common than the other
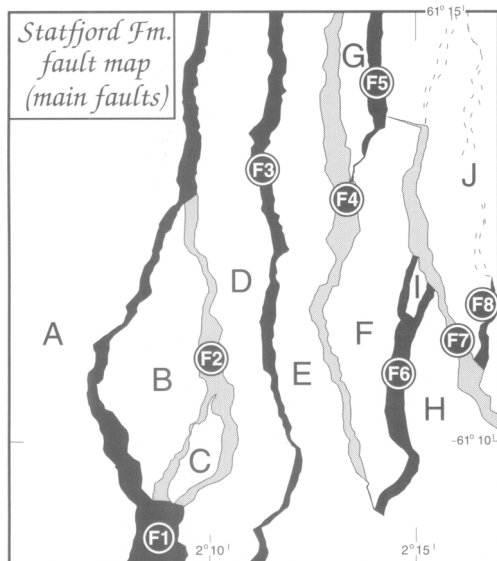
Fig. 5. Labelling of main faults and fault blocks on the Gullfaks Field.

types of minor faults. This expression of internal block deformation is interpreted as adjustment structures related to, for example, irregular block-boundary conditions.

Dipmeter data have proved useful for identification of sub-seismic minor faults. In order to identify small-scale faults by use of dipmeter data, a change in dip and/or dip direction of strata must exist. Such changes can occur as discrete discontinuities, or the changes may be gradual if drag exists (i.e. a deflection of layering adjacent to the fault surface).

Since the degree of bedding deflection around faults is related to fault dip, it is often possible to roughly estimate a minimum dip and dip direction of minor faults. Analysis of dipmeter data from the Gullfaks Field based on statistical curvature analysis techniques (Bengtson 1981) shows two major concentrations of dip directions of faults with drag: one to the east or southeast, and one to the west, i.e. synthetic and antithetic to the main domino faults (Fig. 8). The synthetic set appears to be more common. This corresponds to the higher number of synthetic than antithetic minor faults mapped on the seismic data (Figs 3, 4 and 6f). The E–W-striking minor faults identified from seismic interpretation are, however, not readily observed on dipmeter data, suggesting that they did not develop associated drag.

Fault zone characteristics

Analysis of core material has demonstrated the presence of a relatively narrow 'damage zone' along both major and minor faults, i.e. a zone with an anomalously high density of minor fractures. The width of such zones is typically less than 10 m for the minor faults, and apparently not much wider for the main faults.

On a somewhat larger scale, there is seismic and well evidence for minor faults that splay out from the main fault into the side walls to form hangingwall or footwall collapse structures (Fig. 7). In effect, these structures display an upward dissipation of deformation from the Statfjord Formation towards the base Cretaceous unconformity, i.e. the loose sands of the Brent Group responded differently to deformation than the deeper and more compacted strata. The deformation dissipation may therefore be the result of more active strain-hardening processes up-section during deformation.

Drag, i.e. deflection of bedding adjacent to the fault surface, is an expression of continuous or 'ductile' deformation near the fault, where the non-planar bedding in principle can be traced continuously through the drag zone. In the sense used here, the deformation associated with drag is microscopic, i.e. associated discrete (discontinuous) deformation is not visible in cores. This deformation is identifiable from dipmeter data, and analyses indicate that drag zones up to several tens of metres wide are developed for more than half of the faults that intersect wells with dipmeter data.

The common method of identifying faults from well-log correlation is by recognizing intervals of missing section. Since more than half of all faults on the Gullfaks Field have associated drag, it is clear that the 'total offset' (i.e. offset of a stratigraphic marker across the area affected by drag) will commonly be larger than the amount of missing section. In order to quantify the difference between 'total offset' and missing section, a profile was constructed through a drag zone identified from dipmeter data in the Amundsen Formation in well 34/10-C-3 (Fig. 9a). Dipmeter data suggest that the fault dips 45° or more to the west. Nine metres of missing section was identified from other well logs. Dip isogons were constructed parallel to the fault, thus assuming that the drag zone developed along a fault-parallel shear zone. The resulting profile shows that even though the missing section in the well is only 9 m, 'total offset' amounts to about 100 m in this extreme case. It is thus obvious that construction of geological profiles based on stratigraphic correlations
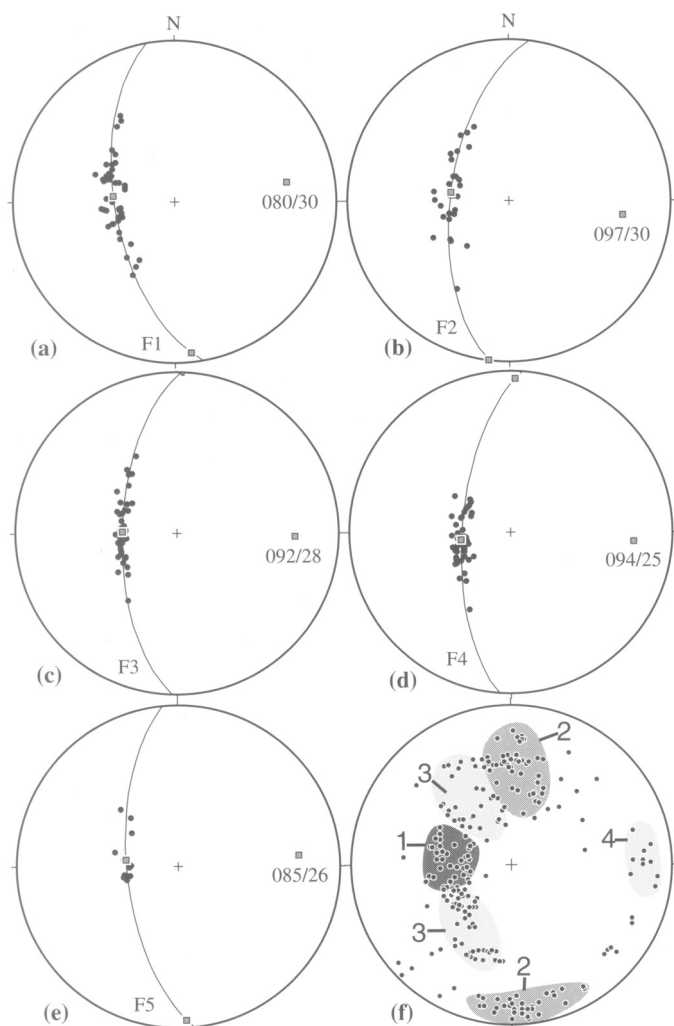
Fig. 6. Equal-area stereographic projections of poles to five main faults (F1–F5, see Fig. 5) (**a**)–(**e**) and minor faults in the domino area (**f**). The best-fit circle and its pole (calculated by Bingham analysis) are shown. The poles are expected to indicate the general slip direction associated with the main faults. The minor faults (f) are distinguished into four different groups: (1) minor faults synthetic to the main faults; (2) steep E–W-trending faults; (3) NE–SW and NW–SE-striking faults; and (4) sub-vertical N–S-trending faults.

alone can lead to serious under-estimates of displacement along faults. In addition, since drag may affect the geometry of the reservoirs, an improved understanding of drag may lead to more correct volume estimates and identification of unknown hydrocarbon prospects.

Drag zones around faults have been determined from dipmeter analysis to be less than 100 m wide. The drag zone is consistently wider in the hangingwall than in the footwall to faults (Fig. 9b), indicating stronger deformation of the hangingwall side of the fault.

Geometry of bedding

The bedding orientation data in the domino area were treated individually for each domino fault block (Fig. 5). Because of the low dips of the bedding, these data are best displayed as dip azimuth/dip plots rather than plots of poles to bedding.

Figures 10 and 11 show that the orientation of the bedding is fairly constant within each fault block as well as between the blocks. The average dips of the top of the Rannoch and Statfjord Formations are 13° and 16.6°, respectively
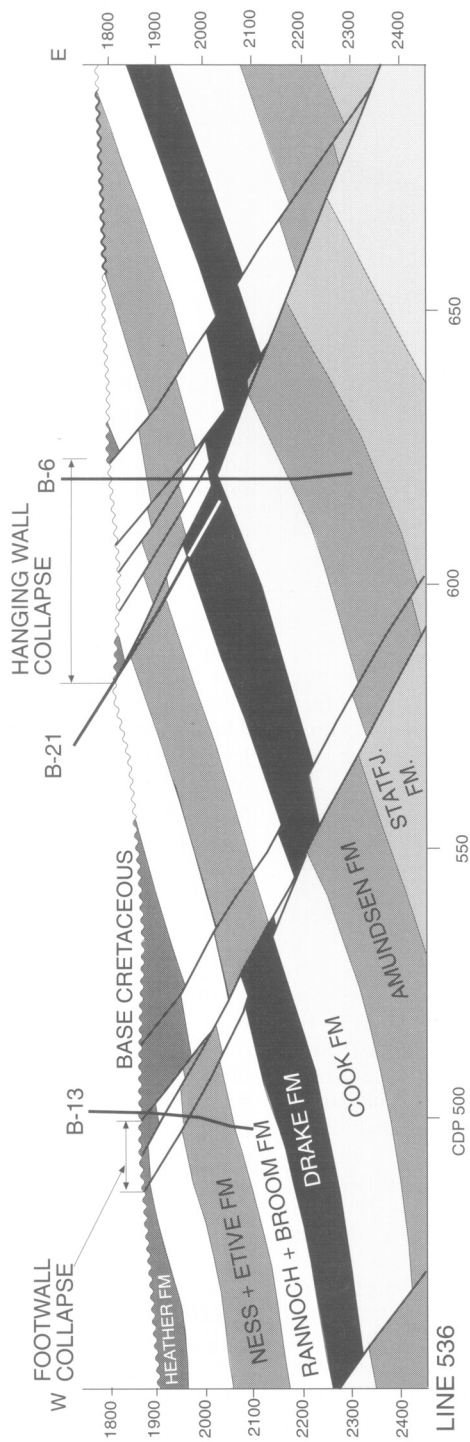
Fig. 7. Profile showing examples of hangingwall and footwall collapse in the domino system.
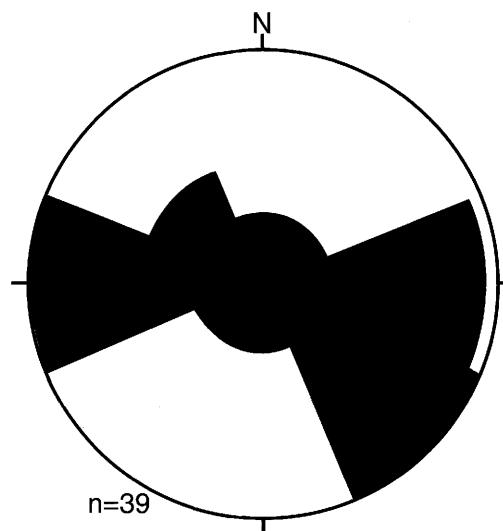
Fig. 8. Rose diagram showing dip directions of faults with associated drag. The diagram shows that N and S-dipping (i.e. E–W-striking) faults have not developed drag structures detectable from dipmeter data.

(Fig. 12). This difference in average dip of about 3.6° indicates a decrease in dip from the Statfjord Formation and upwards through the Brent Group, a difference that locally can be seen directly on the seismic (Fig. 13).

There is a general decrease in dip from the east (footwall position) to the west (hangingwall position) within the domino fault blocks, although variations exist within, as well as between, the blocks. A schematic illustration of the general geometry is given in Fig. 14 (inset). In order to better describe and quantify these changes, the dip of the bedding was plotted with respect to the distance from the nearest main fault to the west. This was done for each fault block defined in Fig. 5 for the top Rannoch and top Statfjord Formations, and the results are given in Table 1.

Figure 14 shows the result of the analysis for fault block B (Fig. 5). A linear regression analysis indicates an average change in dip of 4.6 and 3.6° km^{-1} for the top Rannoch and top Statfjord Formations, respectively. Table 1 shows that the dip gradient generally falls between 1 and 5° km^{-1} in the domino system. This gradient, which is different for the top Statfjord and Rannoch Formations, varies from block to block. The difference in dip gradient between the two horizons is largest in block D (difference of c. 2° km^{-1}) and E (difference of c. 3.5° km^{-1}), and particularly in block G where the gradients have opposite signs.

A map coded with respect to dip categories of most of the domino area displays the general geometry described above (Fig. 15). This general picture is confirmed by analysis of dipmeter data. Well 34/10-8 is a vertical exploration well located within the domino system in the southern part of the Gullfaks Field. A seismic section through the area (Fig. 16) shows that the uppermost part of the well in the reservoir zone is located in the middle of a large fault block. Towards the base, the well penetrates three minor east-dipping faults and approaches, without penetrating, a fourth east-dipping fault with somewhat larger offset (several tens of metres).

Stereonet plots of the different formations penetrated by the well (Fig. 17) show that beds in the Tarbert to Rannoch Formations dip to the west, and dip is clearly decreasing with depth. Beds in the Drake Formation are sub-horizontal or dip very gently to the west, whereas in the Cook Formation, beds dip to the east.

Dipmeter data from well 34/10-8 show that it penetrates the axial surface and the crestal surface (the crestal surface joins the position of lines connecting points of minimum dip of successive layers). Since the well is vertical, such an intersection is only possible if the axial and crestal surfaces are inclined. The simplest interpretation is an east-dipping axial surface. This is consistent with folding of strata due to large-scale drag related to the east-dipping main fault recognized from seismic data. This major drag zone may be described as a triangular zone (Fig. 18). The zone is bounded by the main fault to the west and a less well-defined eastern boundary (there may be a gradual transition from the area affected by drag to the area relatively unaffected by drag). Seismic data indicate that the eastern boundary and the dip isogons in the zone have steeper dips than the main fault, and therefore intersect the main fault at depth (usually at the stratigraphic level of the Statfjord Formation or deeper). The triangular drag zone developed in the hangingwall to main faults is a large-scale expression of more deformation of the hangingwall than of the footwall. A similar relationship was found for minor faults (Fig. 9b).

Relationship between strike of faults and bedding

The strike of the bedding is seen from Fig. 19 to be mostly N–S with a slight NE–SW component. Average strike direction from Bingham analysis (Bingham 1964; Cheeney 1983) for the top
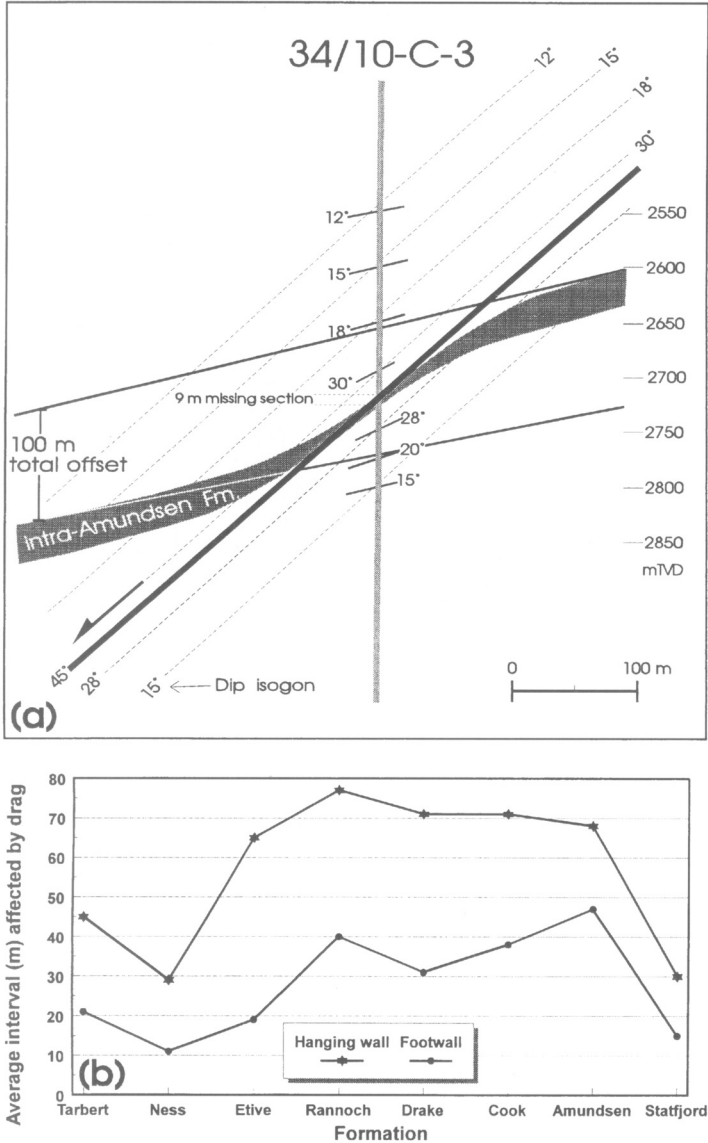
Fig. 9. (a) Construction of bedding geometry around a minor fault encountered in well 34/10-C-3, based on detailed dipmeter analysis. There is 9 m of missing section in the well, whereas the total offset across the deformation zone (including local drag deformation) is about 100 m. (b) Average interval affected by drag for 46 minor faults in the various Jurassic formations in the Gullfaks Field. The drag zone is wider in the hangingwall than in the footwall.

Rannoch and Statfjord Formations are 009 and 006, respectively. Ideally, the strike of the bedding and the faults would be expected to be parallel in a simple domino system. However, the faults show an average strike that is slightly west of north, with a maximum around 350 (Fig. 20). This difference in strike of 15–20° can

also be seen on the contour maps, particularly in blocks D–F where the contour lines can be traced southwards from the eastern side of the fault block to the western side (Fig. 4). An explanation for this discrepancy is that the rotation of the layers in the Gullfaks area was not solely controlled by the domino faults within the Gullfaks

S_O, TOP RANNOCH FM.

277.1/12.9
Block A
N = 169

280.1/13.7
Block E
N = 126

274.5/11.5
Block B
N = 90

284.9/14.1
Block F
N = 74

265.0/12.9
Block C
N = 20

279.0/13.5
Block G
N = 28

281.7/12.2
Block D
N = 173

277.3/14.2
Block I
N = 4
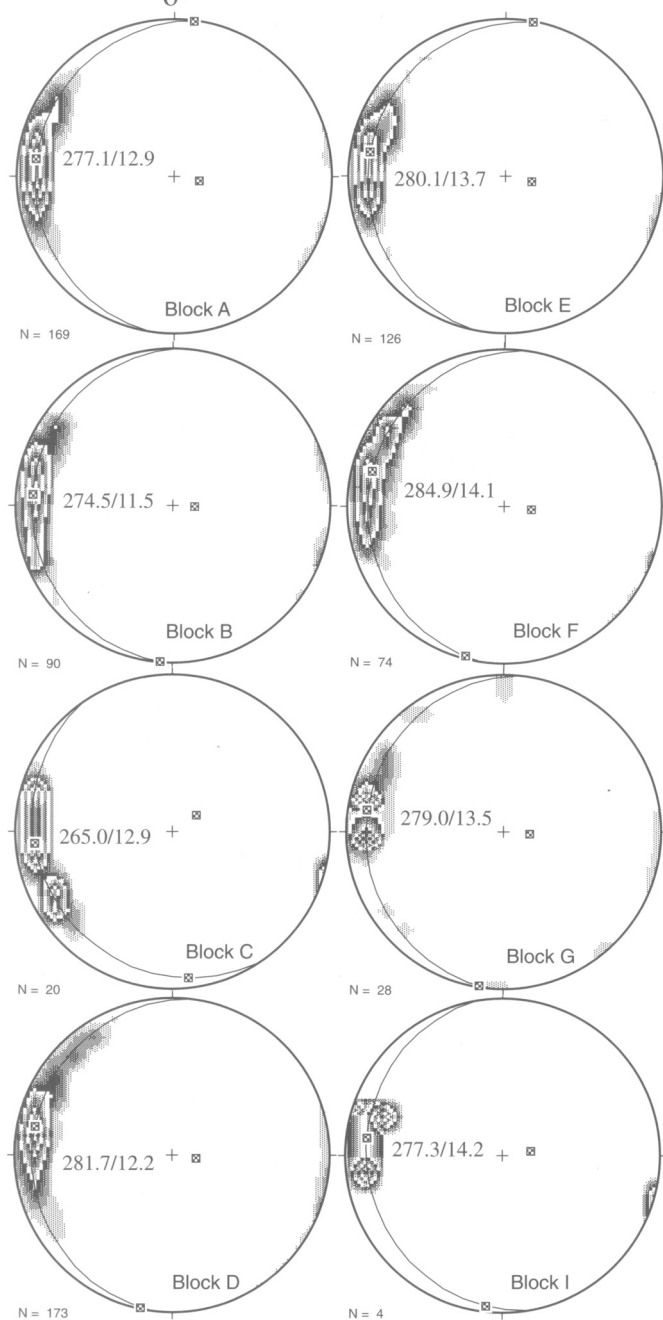
Fig. 10. Dip azimuth/dip of bedding plots for the top Rannoch Formation. Block numbers correspond to domino blocks labelled in Fig. 5.

S_O, TOP STATFJORD FM.

274.8/14.9
Block A
N = 233

276.2/18.5
Block E
N = 152

272.5/14.2
Block B
N = 96

279.0/18.7
Block F
N = 93

266.4/15.1
Block C
N = 16

270.8/20.0
Block G
N = 30

279.3/15.9
Block D
N = 178

270.6/18.7
Block H
N = 38
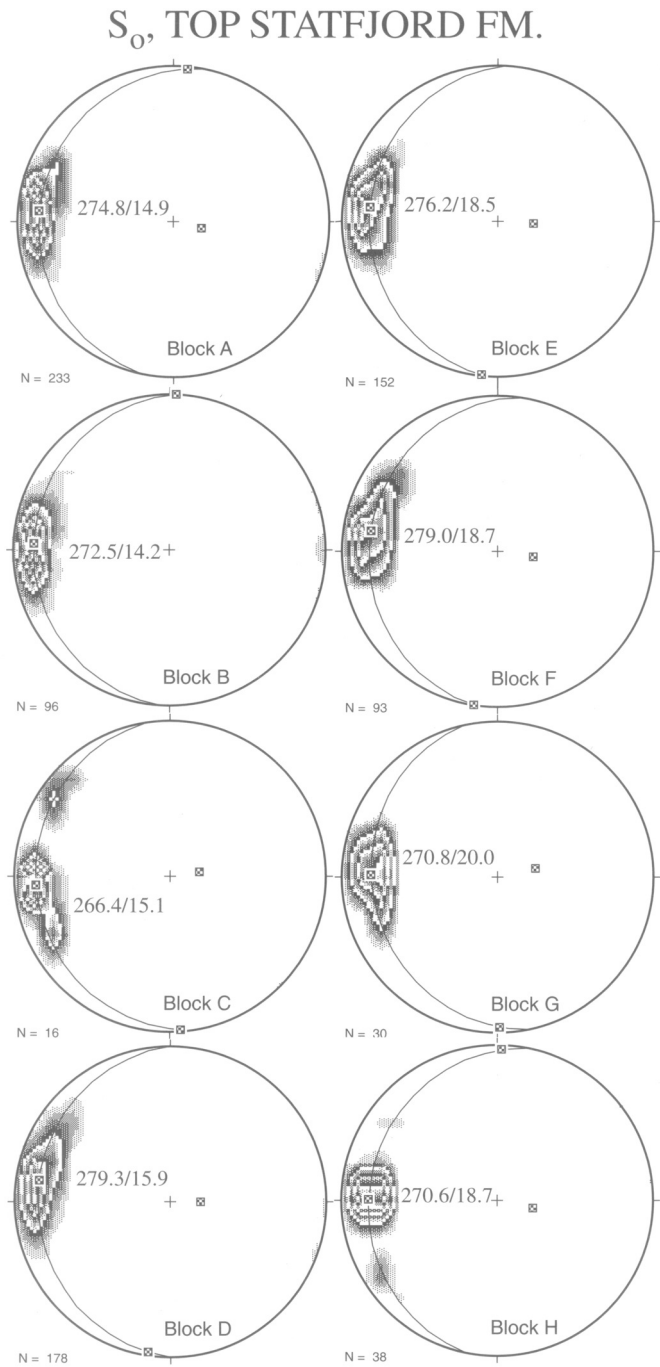
Fig. 11. Same as Fig. 10, but for the top Statfjord Formation.
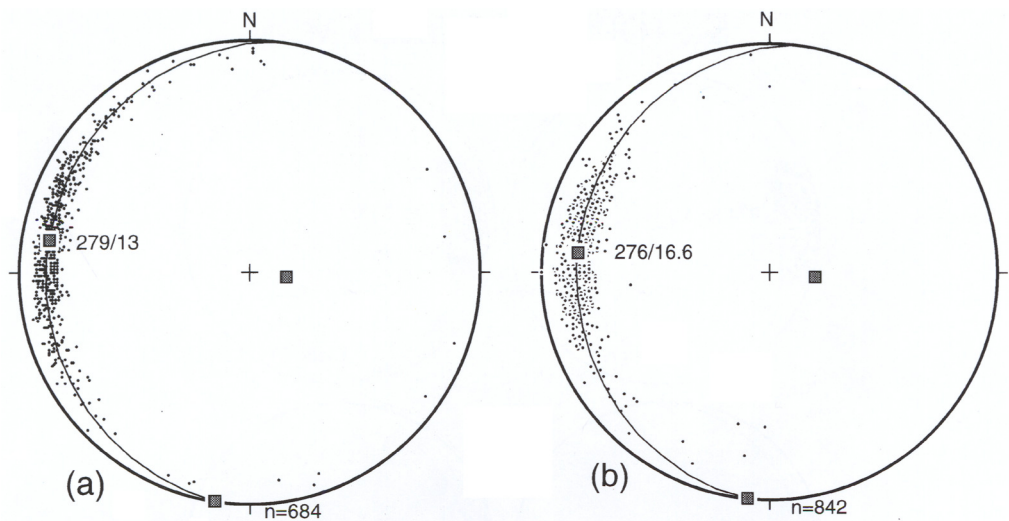
Fig. 12. Dip azimuth/dip plots of bedding from the domino area for (**a**) the top Rannoch Formation, and (**b**) the top Statfjord Formation.
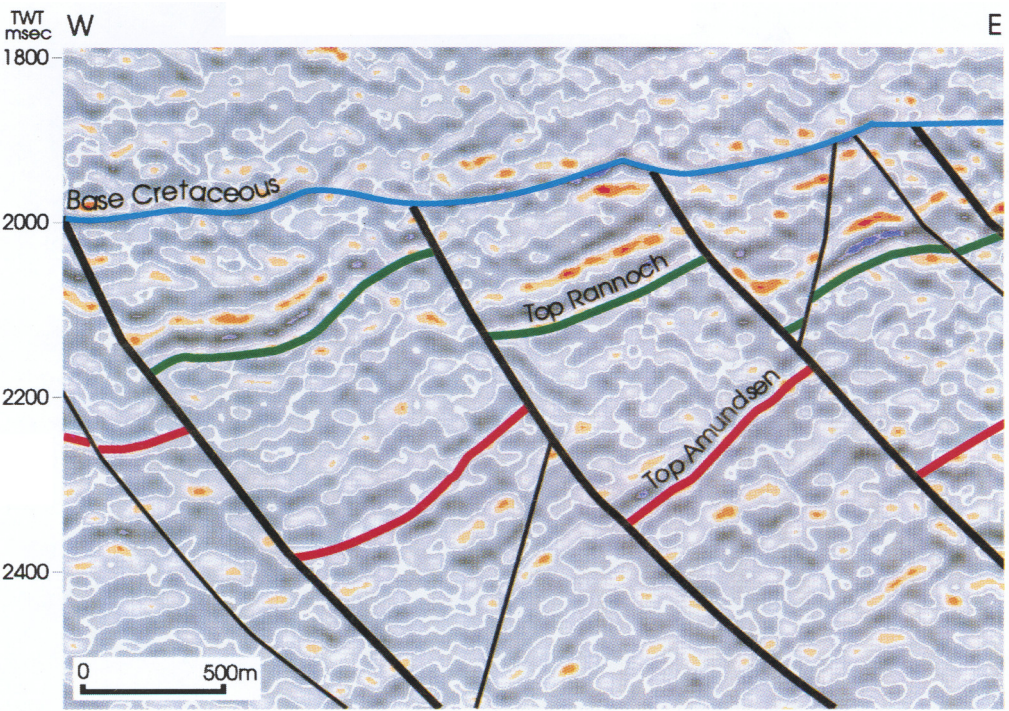
Fig. 13. Seismic line showing difference in dip between the Brent Group and the Statfjord Formation.
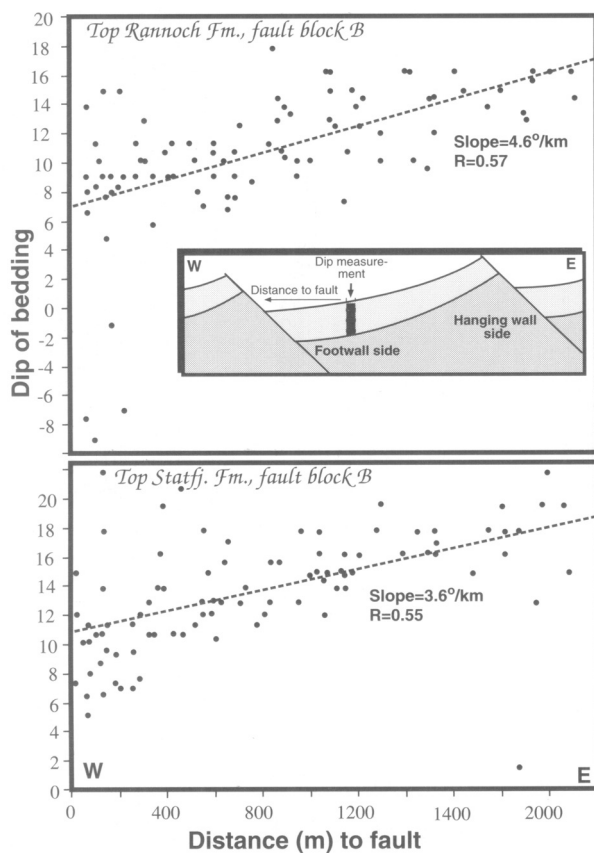
Fig. 14. Dip–distance plot for the top Statfjord and the top Rannoch Formations, fault block B (see Fig. 5 for location). The data indicate a general geometry similar to the one shown in the inset sketch, i.e. steepening bedding to the east across the fault block.

Table 1. *Statistical dip versus distance data for domino blocks defined in Fig. 5*

Block	Rannoch Fm.			Block	Statfjord Fm.		
	Grad (°/km)	R	n		Grad (°/km)	R	n
B	4.58	0.567	90	B	3.58	0.550	90
C	(2.13)	0.182	20	C	(5.5)	0.412	20
D	4.67	0.371	173	D	2.64	0.243	173
E	6.61	0.515	126	E	3.13	0.300	126
F	3.21	0.307	74	F	2.6	0.315	74
G	8.05	0.351	28	G	−7.04	0.522	28

With the exception of block C, all the listed fault blocks contain data that conform to significant linear correlations for a chosen risk of error of 5%. *R*, coefficient of linear correlation; *n*, number of observations.
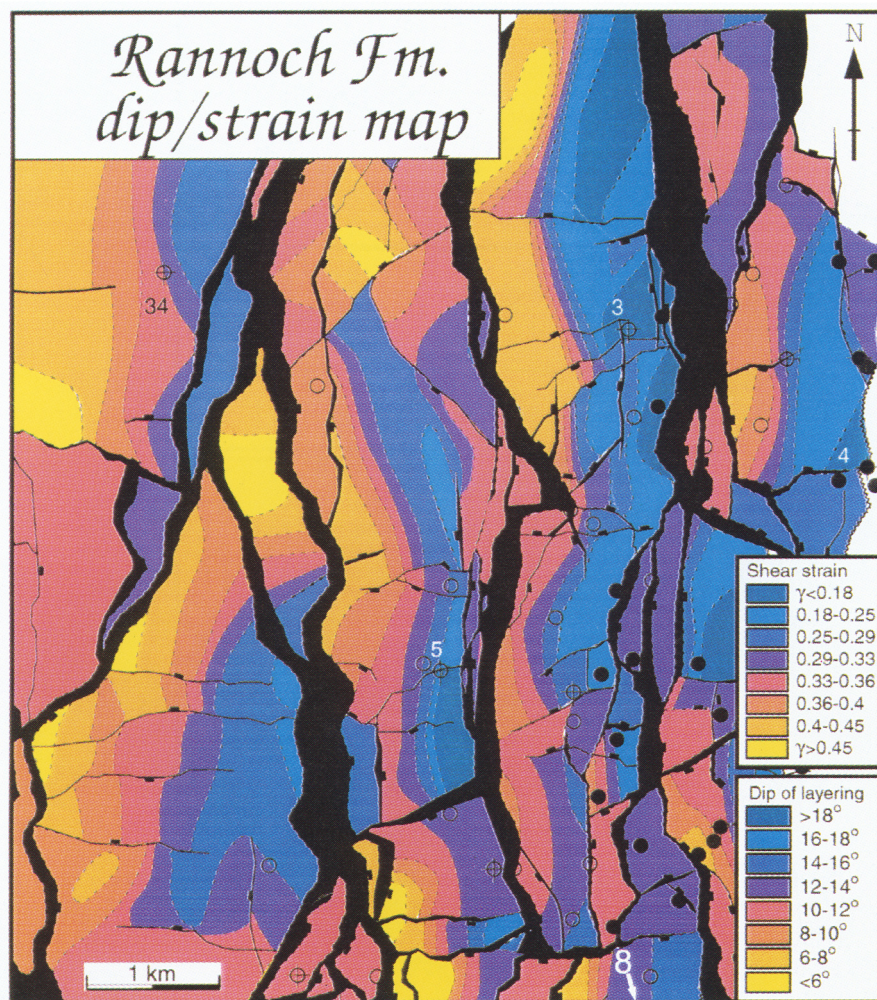
Fig. 15. Colour-coded dip map for the main part of the domino area. The general steepening bedding to the east across domino fault blocks is seen across the area. An additional code indicates shear strain according to the relationship between bedding and shear strain indicated in Eqn 8.

Field, but also by the more NNE–SSW-trending, first-order faults separating the Gullfaks fault block from the Statfjord Field (Fig. 1). The strike of the bedding falls somewhere between the strike of the first- and second-order faults, and may thus have been affected by rotation related to both sets of faults.

The eastern horst complex

Geometry of faults

The main faults in the horst complex are con-siderably steeper than those in the domino area. Dips of about 60–70° are common, and both E- and W-dipping faults occur (Fig. 20a). A very constant N–S strike is characteristic for the main faults, and these faults are more planar than the main faults in the domino system to the west.

The Jurassic sediments that generate good reflectors in the main part of the Gullfaks Field are eroded in the horst complex. This makes mapping of minor faults more uncertain in the horst complex. Most mapped minor faults are relatively steep (45–70°) and run sub-parallel to the main faults.
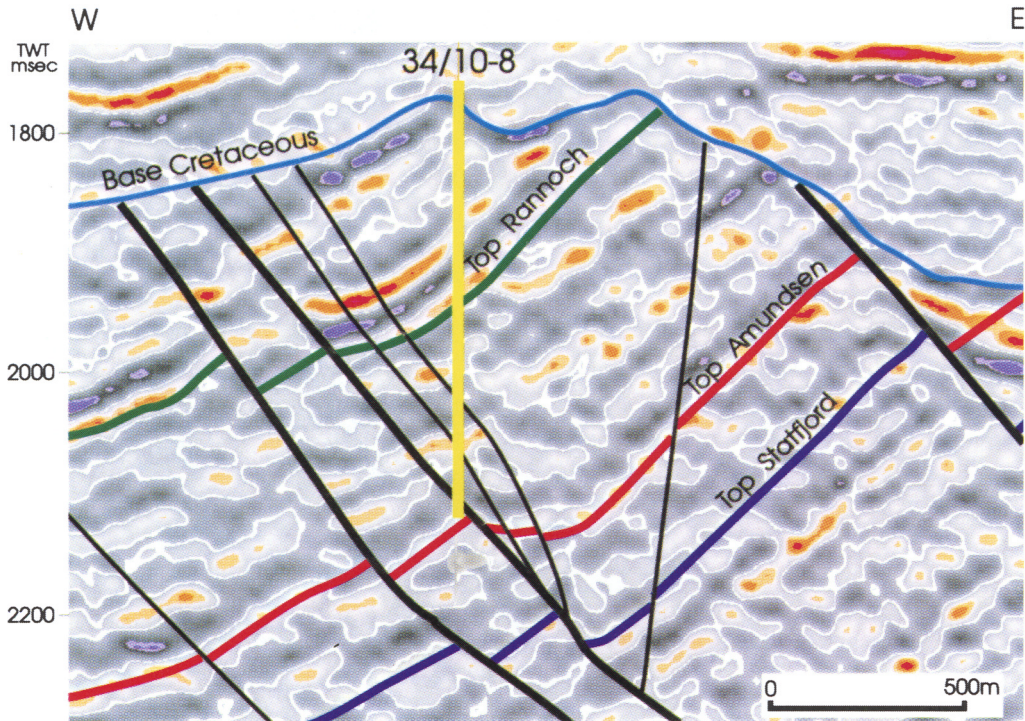
Fig. 16. Seismic line through well 34/10-8. Note pronounced flattening of beds in the western parts of the fault blocks (large-scale drag).

Geometry of bedding

The bedding in the horst complex is sub-horizontal with a weakly preferred westerly dip direction. A perturbation of the bedding is seen in the northern part of this area (around well 34/10-C-2) where a doubly plunging fold with shallowly plunging, NW–SE-trending axial trace and steep axial surface has been mapped.

Dipmeter data from the horst complex support the seismic interpretation, suggesting sub-horizontal dips or shallow dips to the west or to the south.

The transitional accommodation zone

The zone between the domino system and the horst complex accommodates the difference in structural style between the two areas, particularly the difference in dip of bedding and faults on either side of the zone. The accommodation zone is a graben structure, and the bedding defines a fold with a W-dipping western limb and a sub-horizontal to gently E-dipping eastern limb.

Fault geometry

The main faults associated with the accommodation zone are the easternmost domino fault, i.e. a relatively low-angle (25–30°) fault, and the steeper (65°) W-dipping fault bounding the horst complex to the east. Minor faults show a preference of N–S and E–W strikes with variable dip (Fig. 20b). Physical modelling suggests that this is an area of many small faults of which we have been able to identify only a small fraction (Fig. 21).

Geometry of bedding

The bedding in this zone defines a somewhat modified (faulted) fold with a western limb that dips about 15° to the west, and an eastern, gently E- to ENE-dipping limb. The axial trace of the fold trends approximately NNW–SSE, and the fold axis plunges very gently to the NNW. From the measured poles to bedding at Cook level in the fold area, the fold axis was estimated to be oriented at 345/06 (Fig. 22a). The opening angle of the fold is c. 160°, and the axial plane appears to be steep.

Fig. 17. Stereographic projections of dipmeter data (dip azimuth/dip of bedding measurements) from well 34/10-8. A change from westerly dipping beds in the upper part of the well to easterly dips in the lower part confirms the seismic expression seen in Fig. 16.
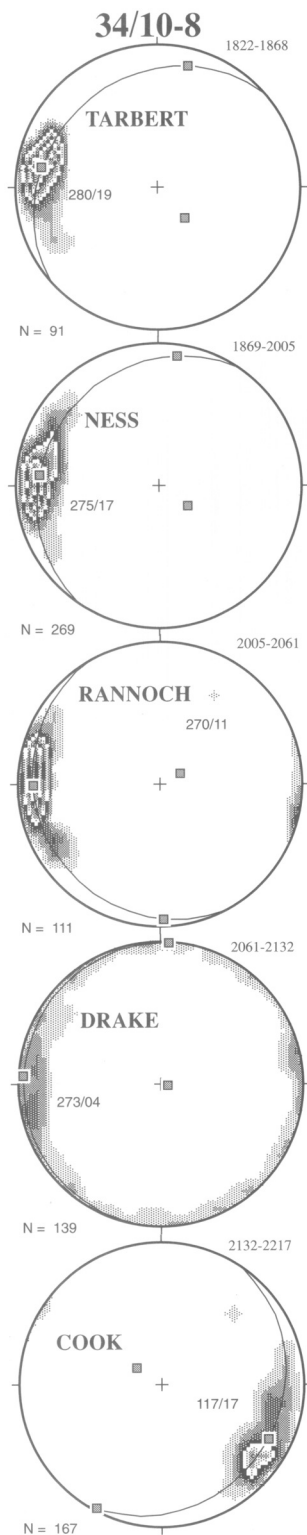
Well 34/10-C-1 is located within the accommodation zone (Fig. 4). The well is drilled in a southwesterly direction and penetrates the eastern limb, the axial surface, and the western limb of a seismically defined gentle fold (Fig. 23). The fold displays a slightly east-dipping eastern limb, and a more steeply dipping western limb. Dipmeter data from this well show relatively shallow easterly dips in the uppermost strata in the reservoir zone (eastern limb) (Fig. 24). Sub-horizontal dips dominate in the hinge zone, changing to gradually steeper (up to 22°) westerly dips as one enters the western limb. The intersection between the axial surface of the fold and the well is interpreted to be within the Statfjord Formation. Plotting the maximum concentration of poles to bedding from the two limbs gives a sub-horizontal fold axis with a southerly trend (176/01, Fig. 22b).

The effect of compaction

Compaction leads to a reduction in both dip and length of non-horizontal and non-vertical faults and beds. The angular changes involved can be expressed by the simple trigonometric relationship:

$$\theta = \tan^{-1}[(1 + \Delta)\tan\theta_0] \qquad (1)$$

where θ and θ_0 are the present and initial dips of the fault in question. The present fault dip is normally known and, assuming a compaction factor Δ, one wants to calculate the initial dip of the fault. Equation 1 can then be rewritten as:

$$\theta_0 = \tan^{-1}[\tan\theta/(1 + \Delta)] \qquad (2)$$

On the Gullfaks Field, the main faulting initiated during, or immediately after, the deposition of the Tarbert Formation, i.e. the top of the Brent Group was at the surface at the time of faulting. The fault surfaces were deformed by the subsequent compaction history of the sediments, which mainly occurred while the structure was buried in Late Cretaceous time and overlain by some 2 km of mostly Tertiary sediments. Near-sea bottom measurements of sand porosity generally fall within 38–43% (Perrier & Quiblier 1974), although the porosity is quickly reduced during burial. Hence, we can assume the original porosity of the sandy intervals of the Brent
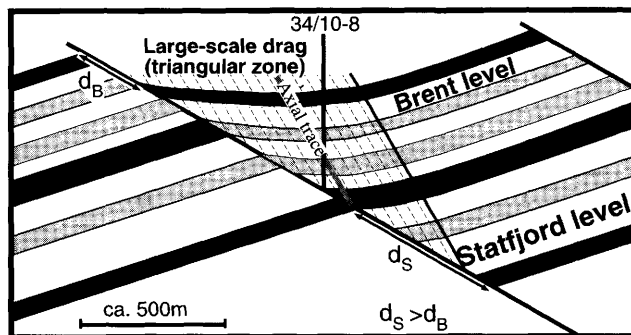
Fig. 18. A generalized section through a domino block, showing the triangle-shaped large-scale drag zone. The displacement at deeper reservoir levels (d_S) is larger than at higher levels (d_B) due to the dissipation of deformation upwards into the hangingwall. The principal location of well 34/10-8 is indicated.

Group to have been around 40% ($\phi_0 = 0.4$). Shale, on the other hand, has a considerably higher initial porosity (85–50% within the upper 10 m of a clay sequence), but decreases rapidly with depth.

The present porosity of the oil-filled sandstones of the Brent Group varies from $\phi = 0.2$–0.34 with a maximum close to 0.3. Their porosity can therefore be assumed to have changed from about 40% near sea-bottom to the present 30%. For $\theta = 0.3$, using the relationship

$$\Delta = [(1 - \phi_0)/(1 - \phi)] - 1 \qquad (3)$$

which yields $\Delta = -0.14$ (i.e. 14% vertical shortening).

Fig. 19. Orientation (strike) of main faults and bedding (Rannoch and Statfjord Formations) in the domino system, Gullfaks. A difference of about 10–20° between the fault orientations and the bedding is evident from the rose diagrams. See text for discussion.
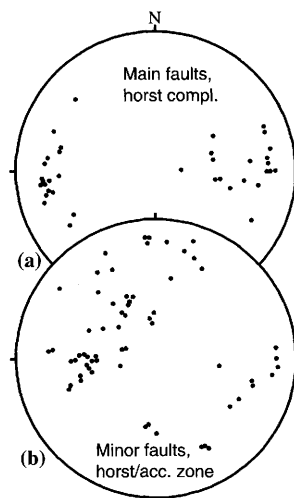
Fig. 20. (a) Poles to major faults in the horst complex, (b) minor faults in the accommodation zone and horst complex.
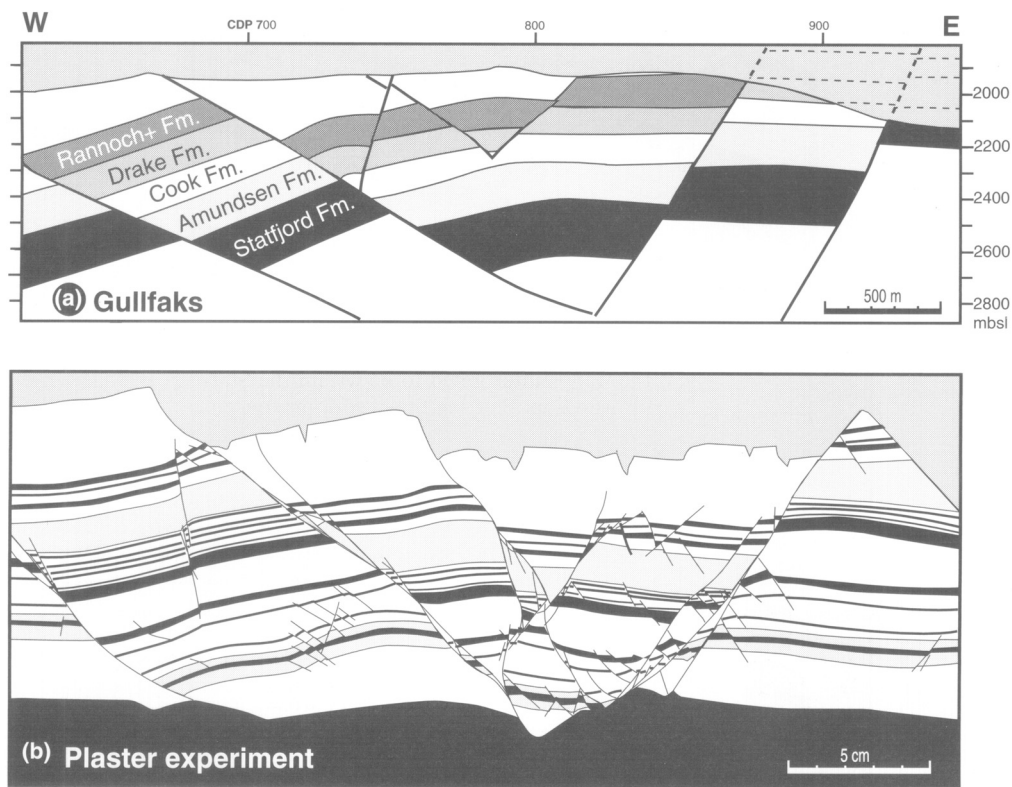
Fig. 21. (a) Seismic line (912) across the accommodation zone, showing a gently collapsed fold structure. (b) Part of plaster model (detailed part of experiment shown in Fossen & Gabrielsen (1996)), showing a remarkably similar geometry to (a), but with a large amount of additional small-scale faults and fractures.

The Brent Group consists of c. 77% sand, of which the upper and lower 100 m contain 90% sand and the middle part (Ness Formation) about 50% sand. For pure sandstones, faults with present dips of 25–30° (Fig. 6) in the uppermost part of the Brent Group would have had pre-compactional dips of 28.5–33.9° according to the numbers above (Eqn 2). Hence, it can be concluded that the lowering of fault dips due to compaction may be in the order of 4° for the uppermost part of the Brent Group, decreasing downwards through the reservoir.

Shales of the Ness Formation were buried to depths of 100–200 m during faulting. Considerable dewatering (compaction) had therefore already taken place prior to faulting. The subsequent reduction in porosity is assumed to be quite similar to the adjacent sandstones. The effect of this type of compaction history on initially planar faults is to form slightly convex-upward or 'anti-listric' fault geometries in the upper part of the reservoir because of the decreasing effect of post-faulting compaction with depth.

Alternatively, if the fault had a gently listric initial geometry, it has been straightened out during the post-faulting compaction history.

In addition to the effect on fault geometry, compaction would also influence the orientation of the bedding. For layers now dipping at 12–14° (Rannoch Formation, Fig. 10), a change in porosity from $\phi_0 = 0.4$ to $\phi_0 = 0.3$ gives a pre-compactional dip of 14–16°. Hence compaction may have lowered the dip of the bedding by an amount of c. 2.4° in the uppermost part of the Brent Group, rapidly decreasing downwards. Hence, the post-tectonic dip is unlikely to have changed significantly during the post-rift burial history of the pre-Tarbert Formation section, and the difference in average dip between the Rannoch and Statfjord Formations indicated in Fig. 12 is largely caused by tectonic deformation.

Vertical changes in post-faulting compaction could in principle give rise to large-scale drag or hangingwall synclines of the type shown in Fig. 18, but modelling shows that this effect is negligible on Gullfaks.
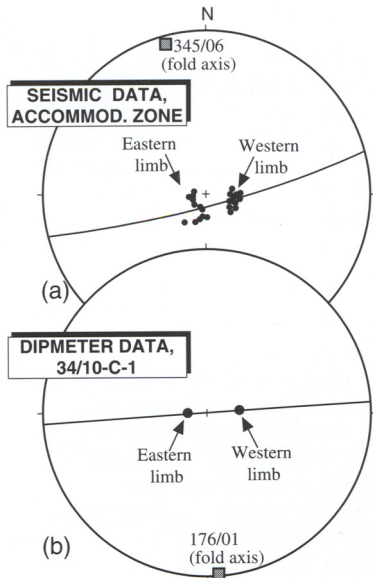
Fig. 22. (a) Poles to bedding in the accommodation zone/fold area from seismic interpretation, and (b) maximum concentrations of bedding from dipmeter data in well 34/10-C1. In both cases, an almost N–S-trending sub-horizontal fold axis is indicated.

Fault geometry, forward modelling and internal block deformation

Initial fault dips

One of the puzzling features of the Gullfaks Field is the anomalously low dips of the fault planes in the domino area, compared to the low dips of the sedimentary layers and to the moderate amount of regional Jurassic extension. In general, the well-known Navier–Coulomb criterion for brittle failure can be expressed as:

$$\tau = C + \sigma_n \mu \tag{4}$$

where τ and σ_n are the shear and normal stresses, respectively, acting on the potential fracture plane, and μ is the coefficient of internal friction ($\mu = \tan \eta$, where η is the angle of sliding friction). C is the cohesion or inherent shear strength of the rock. From this criterion, the angle φ between the shear plane (fault) and the axis of maximum principal stress (σ_1) can be predicted to be:

$$\varphi = \pm(45° - \eta/2) \tag{5}$$

(e.g. Price & Cosgrove 1990). During extensional deformation σ_1 is vertical, and the initial dip
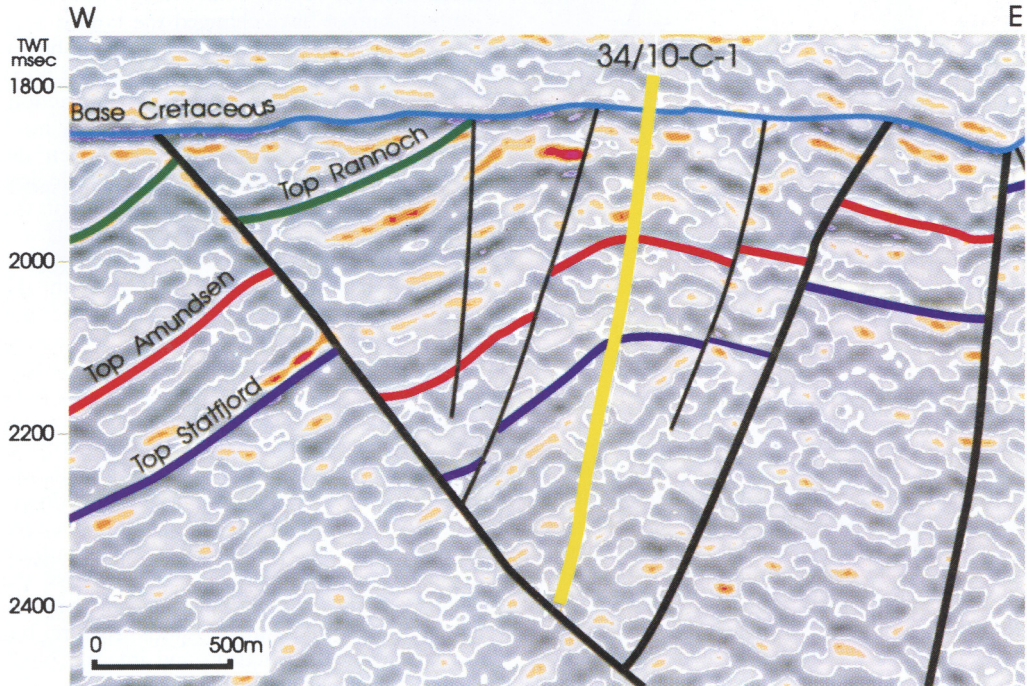
Fig. 23. Seismic line through well 34/10-C-1. According to the seismic interpretation, the well penetrates the fold in the accommodation zone.

34/10-C-1

N = 442   2070-2290

+
E limb

+
Hinge zone

N = 249   2290-2415

+
W limb

N = 391   2415-2610
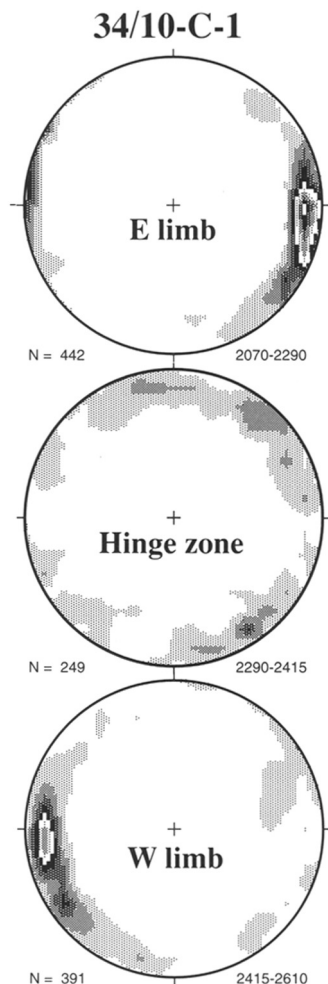
Fig. 24. Dipmeter data (dip azimuth/dip) from well 34/10-C-1 from what is interpreted as the east limb, the hinge zone and the west limb according to the seismic interpretation (see Fig. 23). The dipmeter data support the seismic interpretation.

$(\theta_0 = 90 - \varphi)$ of a normal fault will be higher than 45° by an amount depending on η. Based on studies of fault-plane solution data, Jackson (1987) argued that θ_0 is typically about 60°, as suggested by Anderson (1951). Walsh & Watterson (1988), on the other hand, presented fault dip measurements from British Coalfields, and found that the mean dip of normal faults is about 70° rather than the commonly accepted value of 60°. They also refer to several studies where the mean dip angle is, or is inferred to have initiated at values between 60 and 75°. Their data were collected from consolidated rocks (depth of faulting is 2–3 km), except for four syn-sedimentary faults

which exhibited lower dips. However, faults in poorly consolidated sands and conglomerates also exhibit fault dips in the order of 60–70° in many extensional settings, e.g. in the Lake Havasu/Whipple Mountains area of Arizona/California (unpublished data) and in sandbox experiments, and the existing data therefore do not suggest a significantly shallower angle of faulting in poorly consolidated sediments.

Initial fault dips on Gullfaks

The main faults in the Gullfaks Field formed in mostly consolidated rocks, and only the uppermost part of the fault planes affected what was poorly consolidated sediments at the time of faulting. The dip of the Gullfaks faults was estimated at Statfjord level (at 800–1000 m depth during faulting), and fault dips remain constant at least into the Teist Formation some 1–2 km further down (Fig. 1, profile). According to the discussion above, one would expect initial fault dips in the order of 60–70°.

The present dip of the main faults in the horst complex on the Gullfaks Field is found to be about 60–65°. The effect of post-faulting compaction must have been small in the Triassic–Lower Jurassic layers, and even in the Brent Group it cannot have changed the fault dip by much more than 4° (see discussion above). Also, a very gentle westward tilting of the horst complex counteracts the effect of compaction. The initial dip of the faults in this area must therefore have been about 60–70°. Given the fact that there is no difference in the lithological or mechanical properties of the sediments in the horst and domino area, it is likely that this was also the initial dip of the faults in the domino area, i.e. that the main faults in both the domino area and the horst area started out with approximately the same dip. Otherwise, the maximum principal stress (σ_1) must have deviated considerably from vertical over a very short distance, an unlikely situation on this scale in an extensional rift setting. Furthermore, the change from steep faults in the horst area to low-angle faults in the domino area is closely associated with a change from flat to inclined bedding. This closely associated change in fault and bed geometry occurs rapidly across the accommodation zone, and suggests that the change in fault dip is not an initial feature, but rather is related to rotation and internal block deformation.

The domino faults of the Gullfaks Field appear to be rooted in a low-angle detachment fault (Fossen et al. in press), and thus occur in

the upper plate of a detachment system. Upper plate faults typically initiate as high-angle faults that correspond well with mechanical models of fault initiation. Hence, there is no reason to expect that the main faults in the domino area on Gullfaks should not have originated as high-angle normal faults. Based on the discussion above, we will in the rest of this paper assume that all the main faults initiated with 60–70° dips. It is emphasized that the alternative model, where the faults in the domino area originated at considerably lower angles, would change some of the results presented below.

The rigid domino model

The (rigid) domino or bookshelf model (e.g. Jackson 1987; Mandl 1987; Axen 1988; Davison 1989) is the simplest model that explains the development of sub-rectangular fault blocks separated by straight faults in a cross-section. The main assumption is that the fault blocks, and therefore also the associated faults, rotate rigidly during deformation. No internal deformation takes place within the domino blocks in this model. This implies that the cut-off angle between the faults and the layers remains constant throughout deformation, and both bedding and faults will rotate at the same rate and by the same amount. If α is the dip of the bedding and θ is the dip of the fault plane, then the initial dip of the fault (θ_0) is simply:

$$\theta_0 = \theta + \alpha \qquad (6)$$

For the Gullfaks domino area $\alpha \approx 15°$ (average pre-compactional dip, Rannoch Formation), and $\theta \approx 30°$ for the main faults. The rigid domino model thus gives $\theta_0 = 45°$, which from the discussion above is unrealistically low. Similarly, if the main faults in the domino area initiated with dips of about 65°, their present dips (25–30°) indicate a rotation of the faults in the order of 35° (anti-clockwise when looking north). This contrasts to the rotation of the bedding in the domino area, which is about 15°. From this, and from the fact that bedding is not planar, it can be concluded that the rigid domino model does not work satisfactorily for the main, western part of the Gullfaks Field (see also Koestler et al. 1992).

The soft domino model

The soft domino model is similar to the rigid domino model except that it allows for additional internal deformation of fault blocks.

Simple models describe internal deformation as distributed (homogeneous or heterogeneous) vertical shear (Westaway & Kusznir 1993), inclined shear synthetic or antithetic to the domino faults (e.g. White et al. 1986) or layer-parallel slip (a special case of inclined shear) (e.g. Higgs et al. 1991).

A general E–W section through the Gullfaks Field was constructed for forward modelling purposes (Fig. 25). Starting with the domino area, we assume from the discussion above that the initial angle of faulting was everywhere 60°. Applying 30% extension (more in the domino area and less in the horst complex) (Fig. 25b) and vertical movements leads to Fig. 25c. The geometry in the horst complex is already similar to the Gullfaks horst complex geometry, and neither block rotation nor internal deformation is required here.

The domino area, however, needs rotation after stage (c) in Fig. 25. This results in either steeply (30°) W-dipping bedding (as shown in Fig. 25d), or steeply (55°) E-dipping faults if bedding is balanced. Some additional deformation must therefore be applied to achieve the observed geometry, for example a combination of rigid rotation and inclined shear parallel (synthetic) to the main faults (Fig. 25e). This model is, however, only one of many possible deformations that could lead to the desired geometric relationships. Fault-parallel shear (Fig. 26b), antithetic shear alone (Fig. 26c), or a combination of rigid rotation and layer-parallel (antithetic) shear as in Fig. 26d can lead to exactly the same angular relationship. Vertical shear, on the other hand, cannot produce the desired geometry (Fig. 26e).

To assess this problem, it is necessary to take into account the non-planar geometry of bedding within the domino blocks. Dips of bedding up to 25° are mapped in the footwall to faults, which by rigid body rotation would give initial fault dips of 55°. Little internal deformation is therefore required here if the faults initiated with angles of 60–70°. In the hangingwall parts of the blocks, bedding typically approaches horizontal and the cut-off angle thus approaches 30°. This demonstrates that there is an increasing amount of internal deformation from the east to the west within the domino blocks, i.e. the domino faults separate areas of different strain intensities and thus represent strain discontinuities in the domino system.

The synthetic shear model can be modified to account for the non-planar bedding geometry. To model the observed low-dip triangle zone in the hangingwall to the domino faults, the shear plane must be steeper than the finite dip of the
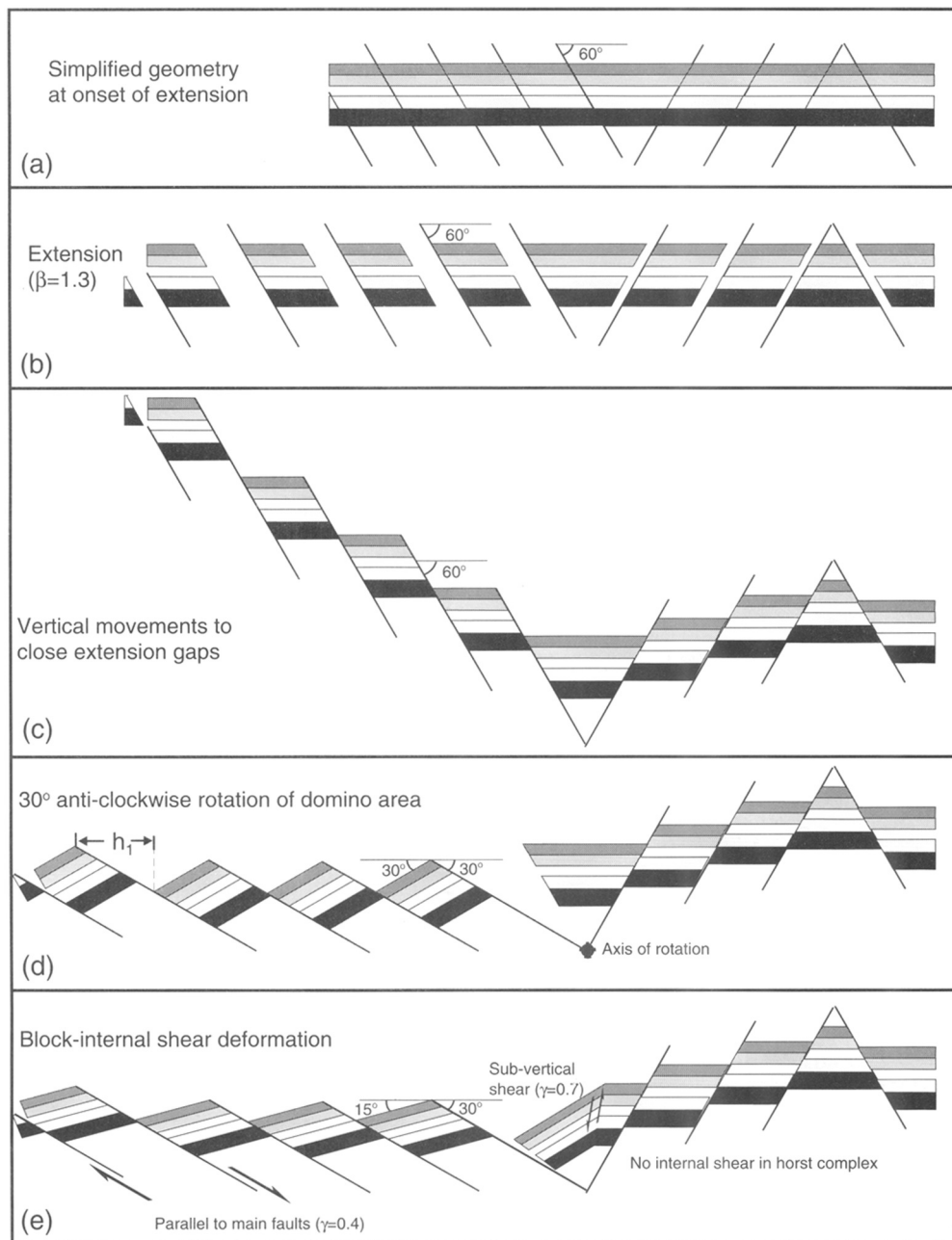
Fig. 25. Forward modelling of the Gullfaks Field by use of a generalized E–W section. (**a**) Initial fault dips are chosen to be 60°. (**b**) Application of 30% extension. (**c**) vertical movements to fill the evolving gaps. Note that the horst complex is adequately modelled at this point. (**d**) Rotation of the domino system so that a 30° dip of the domino faults is achieved. The bedding is now dipping steeply to the left (west), and some internal block deformation must be applied. (**e**) Application of fault-parallel shear gives the wanted dip of the bedding. Similarly, steep W-dipping shear in the accommodation zone helps fill the open gap between the horst complex and the domino system.
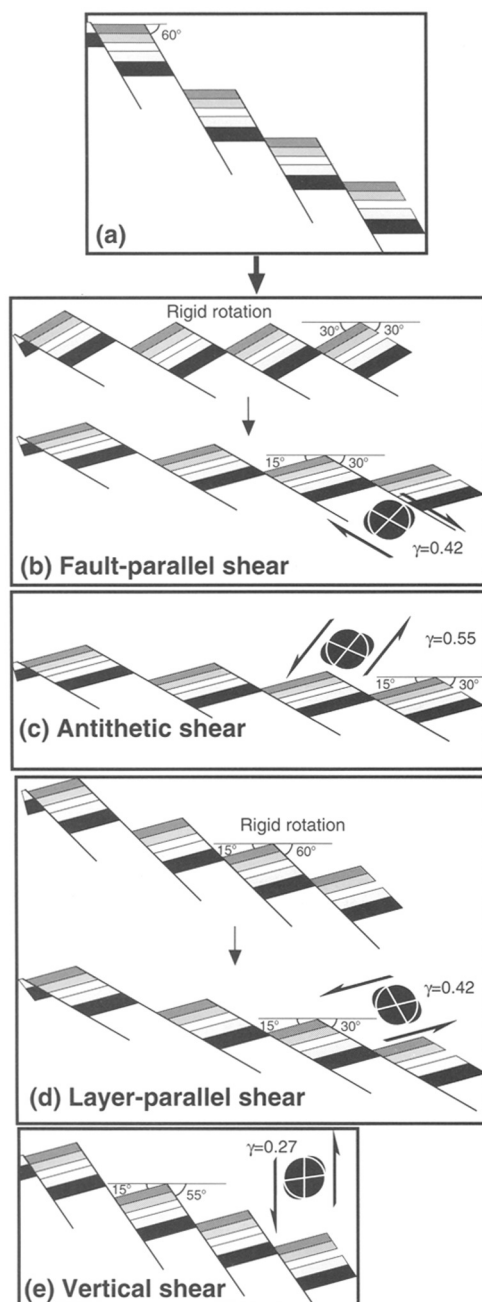
Fig. 26. (a) Going from stage (c) in the domino area in Fig. 25, one can end up with faults dipping 30° and bedding dipping 15° not only by fault-parallel (synthetic) shear (b), but also by antithetic shear (c) or by rigid rotation + bedding-parallel shear (d). Vertical shear (e) can never produce the observed angular relationship between faults and bedding.

faults (Fig. 27b). Because this simple shear model elegantly explains both the geometry of the bedding and the angular relationship between the faults and the bedding in a simple way, it is accepted as a realistic model for the internal block deformation in the domino area. It also bears geometrical similarities with the model presented by Roberts & Yielding (1993, p. 240).

In contrast, the antithetic shear model predicts a positive relationship between dip of bedding and shear strain (Fig. 27c, d). Hence, for the geometry indicated in Fig. 27a, there must be a triangle in the western and upper part of the block that is unsheared or less sheared than the eastern part. However, this implies compatibility problems if one wants to create the observed abrupt change in dip across the domino faults (open void in Fig. 27d). Compatibility can be maintained by a banded shear model, but faults then become highly non-planar, and bedding geometries at deeper parts of the reservoir do not conform with the actual observations (Fig. 27c). A simple antithetic shear model can therefore be rejected.

The horst complex and the accommodation zone

We assume that the horst and the domino area on the Gullfaks Field formed and deformed more or less simultaneously, and that the main faults were established at an early stage of the extensional history. The relatively flat bedding in the horst complex indicates that this area did not experience any finite rotation during the following extension, i.e. no internal deformation is geometrically necessary (Fig. 25c). An open gap evolves as the domino area undergoes anti-clockwise rotation in Fig. 25d, and the area between the horst complex and the domino system must somehow collapse to accommodate this development. This collapse could be modelled by sub-vertical (steeply west-dipping) shear, as indicated in Fig. 25e. However, there is also some evidence (seismic and well data) for a conjugate set of faults that is more pronounced in the upper part of the accommodation zone (Fig. 21a). Plaster experiments (Fig. 21b) indicate that this fault pattern is feasible, but that there is a significant amount of small-scale deformation that is not incorporated in the present interpretation.

Expressions of the internal block deformation

The deformation within the fault blocks on the Gullfaks Field can be sub-divided into minor
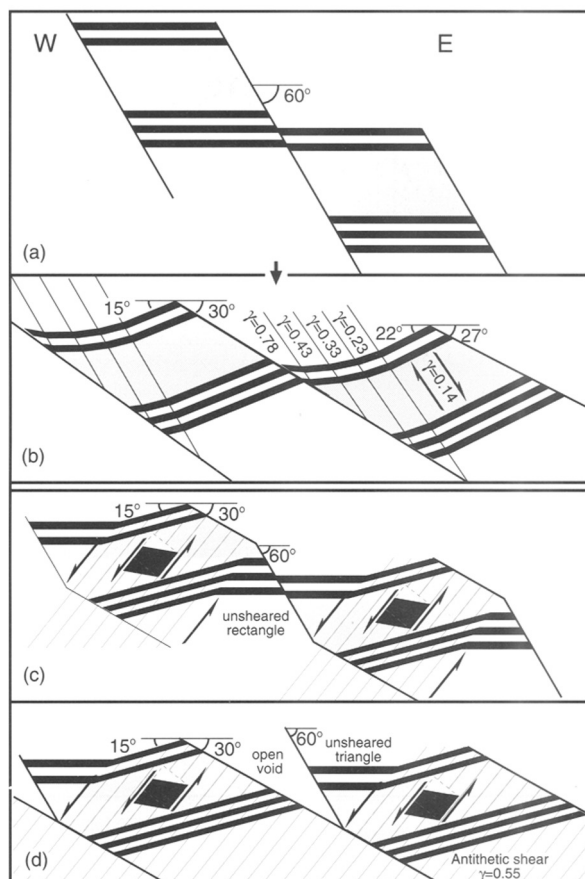
Fig. 27. Forward modelling, taking into account the non-planar geometry of the bedding revealed in this study. (a) Horizontal bedding offset by faults dipping 60°. (b) A synthetic shear model, where the shear plane is steeper (60°) than the domino faults (30°), produces the desired geometric properties. (c) A banded antithetic shear model provides strain compatibility, but the geometry of faults and bedding in the deeper parts of the sequence does not confirm the geometric data from the Gullfaks domino area. (d) Antithetic shear, leaving a triangle in the hangingwall unsheared to obtain the low-dip triangle zone. Note the resulting open void.

faults (seismically resolvable), sub-seismic (discrete) fractures, and continuous ('ductile') deformation (Fig. 28). A statistical fault population study (Fossen & Rørnes 1996) shows that the total seismically resolvable fault population is not fractal, and that a segmented throw population curve exists in log–log space within the range of seismic resolution. However, minor faults define sub-populations that follow exponential scaling laws, although it is uncertain if these laws can be extended into the sub-seismic domain.

The geometries and spatial distribution of sub-seismic faults are hard to predict. Comparing the orientation of the main faults with the seismically resolvable minor faults (Figs 3 and 4) reveals

a significant difference in orientation, and sub-seismic faults may or may not reflect the orientations of either large or small seismically resolvable faults.

As an example of the difficulties involved in predicting sub-seismic fault orientation, we refer to a recent study of fault block B (see Fig. 5). The sub-seismic (1–50 m displacement) fault pattern was modelled numerically (Fig. 29a), based on quantitative data from an onshore field area (Koestler et al. 1994) and assuming that sub-seismic faults are more or less parallel to the seismic faults. The modelling was based on an old (1987) seismic interpretation of the block. The seismic data resolution has since been improved by reprocessing, and seismic attribute
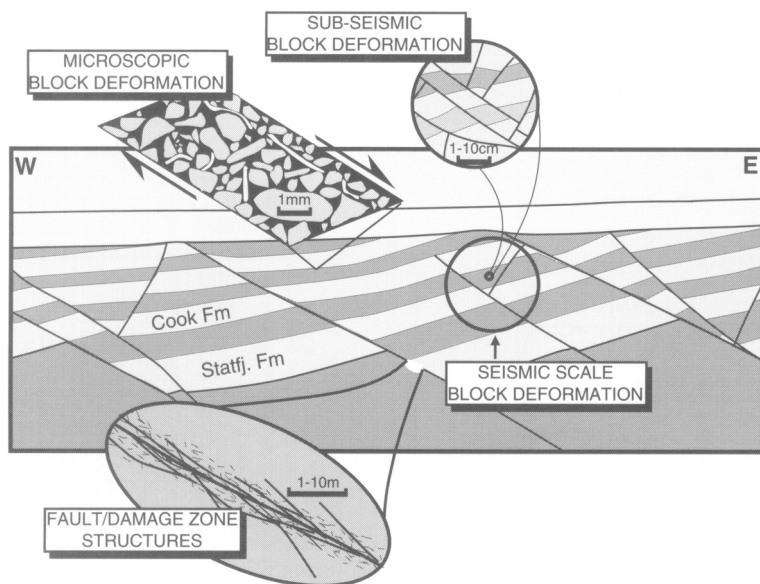
Fig. 28. The various expressions of small-scale deformation in the domino area. See text for discussion.
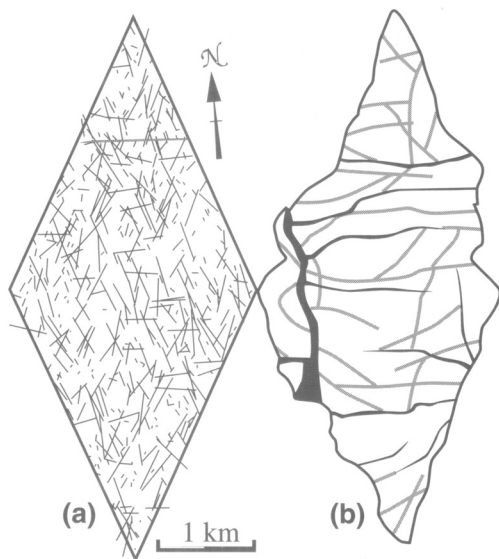
Fig. 29. (a) Result of numerical simulation of fault/ fracture pattern in fault block B (Fig. 5) (redrawn from Koestler *et al.* 1994). (b) Recently remapped fault pattern of the same block after reprocessing of data and application of attribute analysis. Grey lines indicate lineaments on attribute maps that may or may not represent additional minor faults. See text for discussion.

analyses have been applied to identify small faults. This allows us to test the quality of the numerical simulation, at least for a displacement range of 50–15m.

Comparing the numerical model (Fig. 29a) with the improved seismic interpretation (Fig. 29b) reveals significant differences, particularly regarding the length of the internal faults, but also in terms of orientation. Many of the newly mapped faults are much longer than simulated, and an E–W trend is more clearly present in the seismic interpretation than in the model. In conclusion, the distribution of seismically extractable small faults in the domino area cannot explain the strain variation predicted by the model and the non-planar bedding geometries described above.

Sub-seismic faults would be recorded in the more than 6 km of cores collected from the field. Ongoing core studies have revealed suprisingly few sub-seismic faults and fractures more than 10 m away from seismically mappable faults. It is therefore concluded that much of the internal deformation occurs on the microscale.

Microscale deformation within the domino blocks must have involved rotation and translation (sliding) of individual grains. The overall simple shear displacement field predicted by the proposed shear model (Fig. 27b) is accompanied by anisotropic volume loss resulting from deformation-induced grain packing. Grain reorganization, with little grain-size reducing processes,

is a likely process in unconsolidated, shallowly buried and/or overpressured sediments.

The model predicts a direct relationship between dip of bedding and shear strain (Fig. 27b), which can be used to make a strain map of the domino area. Assuming that the rigid rotation preceded the internal shear deformation, the shear strain is found by the relationship:

$$\gamma = \cot(\delta + \alpha) - \cot(\delta + \alpha') \qquad (7)$$

where δ is the dip of the shear plane, α' is the dip of the bedding after the rigid block rotation but prior to the shear deformation, and α is the finite (post-deformation) dip of the bedding. For the special case with the shear plane dipping 60°, a fault cut-off angle of the same magnitude and a rigid block rotation of 30°, the shear strain is simply

$$\gamma = \tan(30° - \alpha) \qquad (8)$$

The general model with decreasing dip of beds towards the west across the domino blocks is masked by local deformation associated with minor, block-internal faults. However, in large areas it is possible to apply this simple relationship between dip and shear strain to construct tentative shear strain maps (Fig. 15). This simple relationship between dip and internal block strain is clearly disturbed by minor faults within the domino blocks, and the shear strain values also depend on the orientation of the shear plane (60° in Fig. 15). Nevertheless, it gives a good overview of the general strain distribution in the domino area. Assuming that there is a negative correlation between shear strain and porosity or permeability due to the shear-related packing of grains, the map may be utilized in future well planning. In this perspective, areas of high γ-values are more affected by internal shear and therefore represent areas of reduced permeability and vice versa. The map thus reflects the variation in porosity and permeability due to intra-block shearing which is imprinted on variations caused by sedimentological and diagenetic factors.

Stretching estimates

There are a number of different techniques that may be used to estimate extension in extended terranes, each of which implies certain fundamental assumptions about the deformation history. For the domino area, we have already discussed two different types of models: the rigid and soft domino models. Although the rigid domino model has been shown to be an unrealistic one in the case of Gullfaks, it is still useful to consider this model further because it provides a minimum estimate of extension in the domino area.

The *rigid domino model* assumes that the fault blocks, and therefore also the faults, rotate rigidly so that the angular relationship between faults and bedding is maintained throughout the deformation. If we assume that the bedding and the faults rotated rigidly by an amount of 15° (i.e. assuming initial fault dips of 45°),we can use the general formula:

$$\beta = \sin(\alpha + \theta)/\sin\theta \qquad (9)$$

to obtain a minimum estimate for the extension in the domino area ($\theta =$ present fault dip, $\alpha =$ dip of bedding). The angular relationships from the domino area on the Gullfaks Field ($\alpha = 15°$, $\theta = 30°$) indicate a β value of 1.41 (i.e. 41% extension). Similar numbers were obtained by summing the fault heaves along interpreted seismic lines (Rannoch Formation) across the domino area, and by plan-view restoration of the top Statfjord map (Rouby et al. 1996). If we use the higher dips in the easternmost part of the domino blocks (20°) and correct for compaction, Eqn 9 shows that β could be as high as 1.6 according to this model.

The *soft domino model* implied a (theoretical) rigid rotation of the bedding from horizontal to about 30° (Fig. 25d). The contribution from this rigid rotation part of the deformation can be found from Eqn 9 to be $\beta = 1.7–1.8$ (inserting $\alpha = 28–30°$, $\theta = 30°$). The additional heterogeneous shear synthetic to the domino faults (Figs 25e, 27b) implies an additional stretch. The contribution of the shear depends on the shear angle and the lateral and vertical variations in shear strain (see Fig. 27b), which makes it more difficult to estimate. It appears, however, that the soft domino model implies a total extension in the domino area in the order of 80%.

The stretching of the horst area is significantly smaller than in the domino area, both because the faults are steeper and thus contribute less to the total extension of the area, and because little internal ('ductile') strain appears to have occurred. Hence, the total extension of the Gullfaks Field (domino area + horst complex) is less than that of the domino area itself.

Conclusions

The present study of the Gullfaks Field shows the result of a three-stage process: (1) an

integrated analysis of seismic data, well data and other available information, resulting in a detailed structural interpretation; (2) geometric analysis of the interpretation, including analysis of faults and bedding, section balancing techniques, and compaction calculations; (3) application of the results to reservoir development. The result is a much more detailed knowledge about the reservoir. The main conclusions from this study are listed below.

- The Gullfaks Field can be structurally subdivided into a major domino system, an eastern horst complex, and an intermediate accommodation zone with a gentle fold structure.
- The main faults dip c. 25–30° to the E in the domino area, and c. 65° to the W or E in the horst complex.
- Dips of the minor faults are generally larger than 45°, i.e. significantly steeper than the main domino faults.
- The main faults show increasing complexity towards higher reservoir levels, with the development of hangingwall and/or footwall collapse structures.
- The average dip of the bedding in the domino area is 13.0° and 16.6° for the Rannoch Formation and the Statfjord Formation, respectively. This downward increase in dip is related to a vertical variation in block-internal deformation (large-scale drag) and to a lesser extent to differential post-deformational compaction.
- Large-scale drag affects a significant part of the hangingwall side of the fault block. Local drag in the vicinity of the main faults is more strongly developed, and affects strata in both the hangingwall and footwall of the faults.
- Local drag is detected for more than 50% of the minor faults. However, E–W-oriented minor faults do not exhibit detectable drag.
- As a result of large-scale drag, there is a general decrease in dip to the W within the domino fault blocks. The average dip gradient, which varies from block to block, can be as high as 6° km^{-1}.
- Large-scale drag structures are better developed in the Brent Group than in the deeper formations, and a triangular drag zone is identifiable in cross-section.
- Continuous or 'ductile' deformation, as expressed by both local and large-scale drag, affects a wider zone in the hangingwall to faults than in the footwall.
- Faults and bedding have slightly different strike directions. The rotation of the bedding

on Gullfaks is thus thought to be related to the large fault(s) to the west rather than to the main faults within the Gullfaks Field.
- Forward modelling indicates that the domino area and the accommodation zone experienced considerably more internal deformation than the horst complex, and a soft domino model with considerable internal block deformation is suggested to explain the geometrical relationships observed within the domino area.
- The soft domino model (assuming initial fault dips of 60–70°) implies an extension of the domino area that is in the order of 80%, i.e. considerably more than the c. 40–50% indicated by the rigid domino model.
- Grain reorganization processes are thought to constitute an important part of the internal block deformation.
- A general relationship is suggested between dip and internal block deformation, and therefore between dip and porosity, in the domino area.

References

ANDERSON, E. M. 1951. *The Dynamics of Faulting.* Oliver & Boyd, Edinburgh.

AXEN, G. J. 1988. The geometry of planar domino-style normal faults above a dipping basal detachment. *Journal of Structural Geology*, **10**, 405–411.

BADLEY, M. E., PRICE, J. D., DAHL, C. R. & AGDESTEIN, T. 1988. The structural evolution of the northern Viking Graben and its bearing upon extensional modes of basin formation. *Journal of Geological Society, London*, **145**, 455–472.

BEACH, A. 1986. A deep seismic reflection profile across the northern North Sea. *Nature*, **323**, 53–55.

BENGTSON, C. A. 1981. Statistical curvature analysis techniques for structural interpretation of dipmeter data. *AAPG Bulletin*, **65**, 312–332.

BINGHAM, C. 1964. *Distributions on the sphere and on the projective plane.* PhD thesis, Yale University.

BLUNDELL, D. J., HURICH, C. A. & SMITHSON, S. B. 1985. A model for the MOIST seismic reflection profile, N Scotland. *Journal of the Geological Society, London*, **142**, 245–258.

CHEENEY, R. F. 1983. *Statistical Methods in Geology.* George Allen and Unwin, Boston.

CHILDS, C., WALSH, J. J. & WATTERSON, J. 1990. A method for estimation of the density of fault displacements below the limits of seismic resolution in reservoir formations. *In: North Sea Oil and Gas Reservoirs – II.* Norwegian Institute of Technology, Graham & Trotman, London, 309–318.

DAVISON, I. 1989. Extensional domino fault tectonics: kinematics and geometrical constraints. *Annales Tectonicae,* **III,** 12–24.

—— et al. 1994. Geological evolution of the southeastern Red Sea Rift margin, Republic of Yemen. *Geological Society of Amercia Bulletin,* **106,** 1474–1493.

FOSSEN, H. 1992. The role of extensional tectonics in the Caledonides of South Norway. *Journal of Structural Geology,* **14,** 1033–1046.

—— & RØRNES, A. 1996. Properties of fault populations in the Gullfaks Field, northern North Sea. *Journal of Structural Geology,* **18,** 179–180.

—— & GABRIELSEN, R. H. 1996. Experimental modelling of extensional fault systems. *Journal of Structural Geology,* **18,** 673–687.

——, ODINSEN, T., FAERSETH, R. B. & GABRIELSEN, R. H. in press. Detachments and low-angle faults in the northern North Sea rift system. *In:* NØTTVEDT, A. (ed.) *Integrated Basin Studies: Dynamics of the Norwegian margins.* Geological Society, London, Special Publication.

GABRIELSEN, R. H., FAERSETH, R. B., STEEL, R. J., IDIL, S. & KLØVJAN, O. S. 1990. Architectural styles of basin fill in the northern Viking Graben. *In:* BLUNDELL, D. J. &. GIBBS., A. D. (eds) *Tectonic Evolution of the North Sea Rifts.* Clarendon, Oxford. 158–183.

HIGGS, W. G., WILLIAMS, G. D. & POWELL, C. M. 1991. Evidence for flexural shear folding associated with extensional faults. *Geological Society of Amercia Bulletin,* **103,** 710–717.

HORSFIELD, W. T. 1977. An experimental approach to basement controlled faulting. *Geologie en Mijnbouw,* **56,** 363–370.

HOUSEMAN, G. & ENGLAND, P. 1986. A dynamical model of lithosphere extension and sedimentary basin formation. *Journal of Geophysical Research,* **91,** 719–729.

JACKSON, J. A. 1987. Active normal faults and crustal extension. *In:* COWARD, M. P., DEWEY, J. F. & HANCOCK, P. L. (eds) *Continental Extensional Tectonics.* Geological Society, London, Special Publication **28,** 3–17.

——, WHITE, N. J., GARFUNKEL, Z. & ANDERSON, H. 1988. Relations between normal-fault geometry, tilting and vertical motions in extensional terrains: an example from the southern Gulf of Suez. *Journal of Structural Geology,* **10,** 155–170.

JARVIS, G. & McKENZIE, D. P. 1980. Sedimentary basin formation with finite extension rates. *Earth and Planetary Science Letters,* **48,** 42–52.

KLEMPERER, S. L. 1988. Crustal thinning and nature of extension in the northern North Sea from deep seismic reflection profiling. *Tectonics,* **7,** 803–821.

KOESTLER, A. G., BULLER, A. T., MILNES, A. G. & OLSEN, T. S. 1994. A structural simulation tool for faulted sandstone reservoirs: exploratory study using field data from Utah and Gullfaks. *In:* AASEN, J. O. et al. (eds) *North Sea Oil and Gas Reservoirs – III.* Kluwer, Dordrecht, 157–165.

——, MILNES, A. G. & STORLI, A. 1992. Complex hanging-wall deformation above an extensional detachment – example: Gullfaks Field, northern North Sea:. *In:* LARSEN, R. M. et al. (eds) *Tectonic Modelling and its Application to Petroleum Geology.* NPF Special Publication 1, Elsevier, Amsterdam, 243–251.

KUSZNIR, N. J. & ZIEGLER, P. A. 1992. The mechanics of continental extension and sedimentary basin formation: a simple-shear/pure shear flexural cantilever model. *Tectonophysics,* **215,** 117–131.

McCLAY, K. R. & ELLIS, P. G. 1987. Geometries of extensional fault systems developed in model experiments. *Geology,* **15,** 341–344.

——, NORTON, M. G., CONEY, P. & DAVIS, G. H. 1986. Collapse of the Caledonian orogen and the Old Red Sandstone. *Nature,* **323,** 147–149.

MANDL, G. 1987. Tectonic deformation by rotating parallel faults: the "bookshelf" mechanism. *Tectonophysics,* **141,** 277–316.

PERRIER, R. & QUIBLIER, J. 1974. Thickness changes in sedimentary layers during compaction history: methods for qualitative evaluation. *AAPG Bulletin,* **58,** 507–520.

PETTERSON, O., STORLI, A., LJOSLAND, E. & MASSIE, I. 1990. The Gullfaks Field: geology and reservoir development. *In: North Sea Oil and Gas Reservoirs – II.* Norwegian Institute of Technology. Graham & Trotman, London, 67–90.

PRICE, N. J. & COSGROVE, J. W. 1990. *Analysis of Geological Structures.* Cambridge University Press, Cambridge.

RAMSAY, J. G. 1967. *Folding and Fracturing of Rocks.* McGraw-Hill, New York.

ROBERTS, A. M. & YIELDING, G. 1993. Continental extensional tectonics. *In:* HANCOCK, P. L. (ed.) *New Concepts in Tectonics.* Pergamon, Oxford.

——, ——, KUSZNIR, N. J., WALKER, I. M. & DORN-LOPEZ, D. 1995. Quantitative analysis of Triassic extension in the northern Viking Graben. *Journal of the Geological Society, London,* **152,** 15–26.

ROUBY, D., FOSSEN, H. & COBBOLD, P. 1996. Extension, displacements and block rotations in the larger Gullfaks area, northern North Sea, as determined from plan view restoration. *AAPG Bulletin,* **80,** 875–890.

VENDEVILLE, B., COBBOLD, P. R., DAVY, P., BRUN, J. P. & CHOUKROUNE, P. 1987. Physical models of extensional tectonics at various scales. *In:* COWARD, M. P., DEWEY, J. F. & HANCOCK, P. L. (eds) *Continental Extensional Tectonics.* Geological Society, London, Special Publication, **28,** 95–107.

WALSH, J. J. & WATTERSON, J. 1988. Dips of normal faults in British coal measures and other sedimentary sequences. *Journal of the Geological Society, London,* **145,** 859–873.

WESTAWAY, R. & KUSZNIR, N. 1993. Fault and bed "rotation" during continental extension: block rotation or vertical shear? *Journal of Structural Geology,* **15**, 753–770.

WHITE, N. J., JACKSON, J. A. & McKENZIE, D. P. 1986. The relationship between the geometry of normal faults and that of the sedimentary layers in the hanging walls. *Journal of Structural Geology,* **8**, 897–909.

WITHJACK, M. O., ISLAM, Q. T. & LA POINTE, P. R. 1995. Normal faults and their hanging-wall deformation: an experimental study. *AAPG Bulletin,* **79**, 1–18.

Index

Structural Geology in Reservoir Characterization

edited by

M. P. Coward, T. S. Daltaban and H. Johnson
(Royal School of Mines, Imperial College, London, UK)

The two main aims of this Special Publication are to capture the wide range of rapidly expanding research in this area, which reflects the increasing importance of comprehensive 'structural characterization' in static reservoir descriptions, and to help promote synergy between the geosciences and petroleum engineering disciplines. The first aim is addressed by the sixteen papers of the volume, the majority of which cover a range of structural geological features, particularly faulted and fractured reservoirs, fault gouge properties, fault seal potential and fluid flow/simulation modelling in faulted and fractured reservoirs. The papers draw heavily on experience obtained in the North Sea.

This volume is for geologists, geophysicists and reservoir simulation/petroleum engineers studying faulted and fractured reservoirs, particularly those interested in studying petroleum traps, predicting fluid flow or modelling structurally heterogeneous reservoirs.

The volume is divided into three main sections: introductory material; theoretical, numerical and experimental studies of faults and fractures; field studies of faulted and fractured petroleum reservoirs. The volume is 266 pages long, includes 199 illustrations and has a detailed index...papers are well written and can be understood without an extensive background in structural or petroleum geology.

W. L. Taylor in *Economic Geology*, **93**, 1110

I would highly recommend the purchase of a copy of this text to structural geologists or to those working in fractured and faulted reservoirs who want to develop a broader perspective into current European structural geology research, and the application of these innovative methodologies to their exploration and development projects.

T. E. Hoak in *AAPG Bulletin*, May 1998

ISBN 1-897799-94-2

9 781897 799949 >

Cover *illustration*: Structural map in two-way travel time of interpreted Lower Miocene horizon (see page 195).